

# HighNESS Conceptual Design Report

V. Santoro<sup>1,2</sup>, O. Abou El Kheir<sup>3</sup>, D. Acharya<sup>3</sup>, M. Akhyani<sup>4</sup>, K.H. Andersen<sup>5</sup>, J. Barrow<sup>6,7</sup>, P. Bentley<sup>1</sup>, M. Bernasconi<sup>3</sup>, M. Bertelsen<sup>1</sup>, Y. Beßler<sup>8</sup>, A. Bianchi<sup>1</sup>, G. Brooijmans<sup>9</sup>, L. Broussard<sup>10</sup>, T. Brys<sup>1</sup>, M. Busi<sup>11</sup>, D. Campi<sup>3</sup>, A. Chambon<sup>12</sup>, J. Chen<sup>8</sup>, V. Czamler<sup>13</sup>, P. Deen<sup>1</sup>, D. D. DiJulio<sup>1</sup>, E. Dian<sup>14,15</sup>, L. Draskovits<sup>15</sup>, K. Dunne<sup>16</sup>, M. El Barbari<sup>8</sup>, M. J. Ferreira,<sup>1</sup> P. Fierlinger<sup>17</sup>, V. T. Fröst<sup>18</sup>, B.T. Folsom<sup>1,3</sup>, U. Friman-Gayer<sup>1</sup>, A. Gaye<sup>1</sup>, G. Gorini<sup>3</sup>, A. Gustafsson<sup>18</sup>, C. Happe<sup>8</sup>, M. Hartl<sup>1</sup>, M. Holl<sup>1</sup>, A. Jackson<sup>1</sup>, E. Kemp<sup>19</sup>, Y. Kamyshevko<sup>20</sup>, T. Kittelmann<sup>1</sup>, E.B. Klinkby<sup>12</sup>, T. Kittelmann<sup>1</sup>, R. Kolevatov<sup>21</sup>, S.I. Laporte<sup>3</sup>, B. Lauritzen<sup>12</sup>, W. Lejon<sup>16</sup>, R. Linander<sup>1</sup>, M. Lindroos<sup>1</sup>, M. Marko<sup>15</sup>, J.I. Marquez Damian<sup>1</sup>, T. C. McClanahan<sup>10</sup>, B. Meirose<sup>16,2</sup>, F. Mezei<sup>14</sup>, K. Michel<sup>1</sup>, D. Milstead<sup>16</sup>, G. Muhrer<sup>1</sup>, A. Nepomuceno<sup>22</sup>, V. Neshvizhevsky<sup>13</sup>, T. Nilsson<sup>23</sup>, U. Odén<sup>1</sup>, T. Plivelic<sup>24</sup>, K. Ramic<sup>1</sup>, B. Rataj<sup>1,2</sup>, I. Remec<sup>10</sup>, N. Rizzi<sup>12</sup>, E. Rosenthal<sup>8</sup>, L. Rosta<sup>15</sup>, U. Rücker<sup>8</sup>, S. Samothrakitis<sup>11</sup>, J. R. Selknaes<sup>1</sup>, H. Shuai<sup>12</sup>, S. Silverstein<sup>16</sup>, W.M. Snow<sup>25</sup>, M. Strobl<sup>11</sup>, M. Strothmann<sup>8</sup>, A. Takabayev<sup>1</sup>, R. Wagner<sup>13</sup>, P. Willendrup<sup>1,12</sup>, S. Xu<sup>1</sup>, S.C. Yiu<sup>16</sup>, L. Yngwe<sup>18</sup>, A.R. Young<sup>26</sup>, M. Wolke<sup>27</sup>, P. Zakalek<sup>8</sup>, L. Zavorka<sup>10</sup>, L. Zanini<sup>1</sup>, and O. Zimmer<sup>13</sup>

<sup>1</sup>European Spallation Source ERIC, Lund, Sweden

<sup>2</sup>Lund University, Lund, Sweden

<sup>3</sup>University of Milano-Bicocca, Milano, Italy

<sup>4</sup>École Polytechnique Fédérale de Lausanne (EPFL), Lausanne, Switzerland

<sup>5</sup>Oak Ridge National Laboratory, Oak Ridge, USA

<sup>6</sup>Massachusetts Institute of Technology (MIT), Cambridge, MA, 02139, USA

<sup>7</sup>Tel Aviv University, Tel Aviv, Israel, 69978

<sup>8</sup>Forschungszentrum Juelich GmbH, Germany

<sup>9</sup>Department of Physics, Columbia University, USA

<sup>10</sup>Oak Ridge National Laboratory, Oak Ridge, USA

<sup>11</sup>Paul Scherrer Institut, PSI Villigen, Switzerland

<sup>12</sup>DTU Physics, Technical University of Denmark

<sup>13</sup>Institut Laue-Langevin ILL, Grenoble, France

<sup>14</sup>Mirrotron Ltd., Budapest, Hungary

<sup>15</sup>Centre for Energy Research, Budapest, Hungary

<sup>16</sup>Stockholm University, Stockholm, Sweden

<sup>17</sup>Technical University Munich, Garching, Germany

<sup>18</sup>Sweco AB, Sweden

<sup>19</sup>University of Campinas, Campinas, Brazil

<sup>20</sup>The University of Tennessee, Knoxville, TN 37996, USA

<sup>21</sup>ESS consultant, Norway

<sup>22</sup>Departamento de Ciências da Natureza, Universidade Federal Fluminense, RJ, Brazil

<sup>23</sup>Institutionen för Fysik, Chalmers Tekniska Högskola, Sweden

<sup>24</sup>MAX IV Synchrotron, Lund University, Sweden

<sup>25</sup>Department of Physics, Indiana University USA

<sup>26</sup>Department of Physics, North Carolina State University, USA

<sup>27</sup>Department of Physics and Astronomy, Uppsala University, Uppsala, Sweden

September 29, 2023

## Abstract

The European Spallation Source, currently under construction in Lund, Sweden, is a multidisciplinary international laboratory. Once completed to full specifications, it will operate the world's most powerful pulsed neutron source. Supported by a 3 million Euro Research and Innovation Action within the EU Horizon 2020 program, a design study (HighNESS) has been completed to develop a second neutron source located below the spallation target. Compared to the first source, designed for high cold and thermal brightness, the new source has been optimized to deliver higher intensity, and a shift to longer wavelengths in the spectral regions of cold (CN, 2–20 Å), very cold (VCN, 10–120 Å), and ultracold (UCN, > 500 Å) neutrons. The second source comprises a large liquid deuterium moderator designed to produce CN and support secondary VCN and UCN sources. Various options have been explored in the proposed designs, aiming for world-leading performance in neutronics. These designs will enable the development of several new instrument concepts and facilitate the implementation of a high-sensitivity neutron-antineutron oscillation experiment (NNBAR). This document serves as the Conceptual Design Report for the HighNESS project, representing its final deliverable.

# Contents

<b>1</b>	<b>Introduction and Scientific Motivations</b>	<b>10</b>
1.1	The European Spallation Source . . . . .	10
1.1.1	The ESS current moderator system . . . . .	11
1.1.2	The ESS upgrade area . . . . .	14
1.1.3	ESS timeline and beam power projections . . . . .	18
1.2	HighNESS scientific motivations . . . . .	18
1.3	HighNESS objectives . . . . .	18
1.4	The HighNESS project in the neutron landscape . . . . .	19
1.5	HighNESS project structure . . . . .	19
<b>2</b>	<b>Design of the cold source</b>	<b>21</b>
2.1	General Description of the ESS Moderator Area . . . . .	21
2.2	Figures of merit . . . . .	22
2.2.1	Figures of Merit for condensed matter . . . . .	24
2.2.2	Figures of Merit for fundamental physics . . . . .	24
2.2.3	NNBAR . . . . .	24
2.2.4	Figure of merit for UCN . . . . .	26
2.2.5	Figure of merit for VCN . . . . .	26
2.2.6	Summary of FOMs . . . . .	26
2.3	Neutronic design . . . . .	26
2.3.1	Iterative design process . . . . .	27
2.3.2	Summary of the results with a single opening cylindrical moderator . . . . .	27
2.3.3	Design optimization . . . . .	28
2.3.4	First iteration . . . . .	28
2.3.5	Second iteration . . . . .	30
2.3.6	Third iteration . . . . .	31
2.3.7	Effect of Be filter and reentrant hole . . . . .	32
2.3.8	Shape of the reentrant hole . . . . .	32
2.3.9	Moderator characterization . . . . .	42
2.3.10	Effects of engineering design on neutronic performance . . . . .	44
2.4	Rounded shape model . . . . .	45
2.5	Summary of the cold moderator design . . . . .	46
<b>3</b>	<b>Engineering design of the liquid deuterium moderator</b>	<b>53</b>
3.1	Moderator Engineering - Introduction . . . . .	53
3.2	Definition of fluid parameters & cooling process concept design . . . . .	54
3.3	Costs estimation of LD <sub>2</sub> infrastructure . . . . .	58
3.4	Selection of materials and overall design . . . . .	58
3.5	Design overview of the lower moderator plug . . . . .	58
3.6	Assembly and welding of the moderator . . . . .	60
3.7	Structural mechanical calculations . . . . .	62
3.8	Analysis of weld seams . . . . .	64
3.9	Thermohydraulic simulations . . . . .	67
3.10	Design solution of the vacuum vessel . . . . .	68
3.11	Integrability into the ESS twister . . . . .	77
3.12	Summary and outlook: engineering implementation of deuterium moderator . . . . .	78

<b>4 Design of a Very Cold Neutron Source</b>	<b>80</b>
4.1 VCN: a long-wished-for source . . . . .	80
4.2 VCN neutrons: a brief introduction . . . . .	80
4.3 Fundamental physics with VCN . . . . .	80
4.3.1 Beam Experiments . . . . .	80
4.3.2 Wave-Optical Experiments . . . . .	81
4.4 VCNs in condensed matter research . . . . .	82
4.5 VCN design options . . . . .	83
4.5.1 Dedicated VCN moderator . . . . .	83
4.5.2 Use of advanced reflectors . . . . .	84
4.5.3 Hybrid design . . . . .	84
4.6 Solid ortho-D <sub>2</sub> . . . . .	84
4.7 Dedicated SD <sub>2</sub> source . . . . .	85
4.7.1 Internal Cooling Structure . . . . .	89
4.7.2 Hydrogen and Para-D <sub>2</sub> impurities . . . . .	90
4.7.3 Crystal Imperfections . . . . .	92
4.7.4 SD <sub>2</sub> Source Summary . . . . .	93
4.8 Combined option . . . . .	94
4.8.1 NNBAR side . . . . .	94
4.8.2 Optimization of the ideal case . . . . .	96
4.8.3 Engineering details . . . . .	96
4.8.4 Improvements to the design . . . . .	98
4.8.5 Converter for neutron scattering instruments . . . . .	100
4.8.6 Gains at small angles . . . . .	103
4.9 Beam Extraction with nanodiamonds . . . . .	105
4.10 Comparison of the different options . . . . .	107
<b>5 Deuterated clathrates hydrates</b>	<b>112</b>
5.1 Experimental characterization of clathrate hydrates . . . . .	112
5.1.1 Manufacturing of THF-hydrates . . . . .	112
5.1.2 Neutron diffraction on fully deuterated THF-hydrates . . . . .	113
5.2 Structural details . . . . .	114
5.2.1 Time of flight spectroscopy . . . . .	115
5.3 Low-Energy Excitations of THF-Hydrates . . . . .	116
5.4 Simulation of a clathrate hydrate moderator . . . . .	117
<b>6 Design of the ESS Ultra Cold Neutron source</b>	<b>123</b>
6.1 UCN scientific case and general overview of the field . . . . .	123
6.1.1 VCN to Feed UCN Production . . . . .	124
6.2 In-pile and in-beam UCN sources . . . . .	124
6.3 UCN production . . . . .	125
6.4 Methods for calculating the UCN production rate density P <sub>UCN</sub> . . . . .	126
6.4.1 Calculating P <sub>UCN</sub> in SD <sub>2</sub> . . . . .	126
6.4.2 Calculating P <sub>UCN</sub> in He-II . . . . .	127
6.4.3 UCN production rates as a function of the distance from the LD <sub>2</sub> moderator . . . . .	128
6.5 SD <sub>2</sub> source in twister . . . . .	128
6.5.1 Thin-slab external converter . . . . .	129
6.5.2 Delayed heat deposition from activation . . . . .	131
6.5.3 Reentrant hole design . . . . .	132
6.5.4 Cylindrical 3-opening design . . . . .	132
6.5.5 SD <sub>2</sub> as primary moderator . . . . .	134
6.6 In-Twister He-II UCN Source . . . . .	135

6.7	SD <sub>2</sub> in MCB . . . . .	136
6.8	He-II in MCB . . . . .	141
6.8.1	Recommended further engineering investigations . . . . .	143
6.9	He-II in LBP . . . . .	144
6.9.1	Bismuth Filter for Gamma Shielding . . . . .	145
6.9.2	LD <sub>2</sub> as a CN reflector . . . . .	147
6.9.3	Adding engineering details . . . . .	148
6.9.4	Outlook . . . . .	148
6.10	In-beam UCN source . . . . .	149
6.10.1	Basic principles of an in-beam UCN source . . . . .	150
6.10.2	In-beam UCN source implementation at the ESS . . . . .	151
6.11	Comparison of the UCN sources . . . . .	153
<b>7</b>	<b>Integration of the CN, VCN and UCN sources</b>	<b>155</b>
7.1	Summary of the main results for CN, VCN and UCN sources . . . . .	155
7.2	Integration options based on an LD <sub>2</sub> primary source . . . . .	156
7.2.1	LD <sub>2</sub> in twister, UCN in the MCB . . . . .	156
7.2.2	LD <sub>2</sub> in twister, followed by UCN in LBP after NNBAR . . . . .	156
7.2.3	LD <sub>2</sub> in twister, UCN in regular beamport . . . . .	157
7.3	Integration option based on an LD <sub>2</sub> primary source, upgraded to deliver also VCN and UCN . . . . .	157
7.4	A full-SD <sub>2</sub> source for CN, VCN and UCN? . . . . .	157
7.5	Comparison of the different scenarios . . . . .	158
<b>8</b>	<b>Neutron scattering instruments for the ESS second source</b>	<b>159</b>
8.1	Moderator alternatives . . . . .	159
8.2	Optimization of small-angle neutron scattering instruments . . . . .	160
8.2.1	Conventional SANS . . . . .	160
8.2.2	SANS with Wolter focusing optics . . . . .	161
8.2.3	FOM Definition . . . . .	163
8.2.4	Performance of conceptual SANS instruments . . . . .	164
8.2.5	Performance comparison to ESS instruments . . . . .	164
8.2.6	SANS Conclusion . . . . .	166
8.3	Optimization of imaging instrument . . . . .	167
8.3.1	FOM Definition . . . . .	168
8.3.2	Imaging instrument performance . . . . .	168
8.3.3	Performance comparison to ESS instrument . . . . .	170
8.4	Achromatic optics for long wavelengths . . . . .	172
8.5	Neutron Scattering instrumentation summary and cost estimation . . . . .	174
<b>9</b>	<b>The NNBAR Experiment</b>	<b>176</b>
9.1	Introduction . . . . .	176
9.2	Scientific Motivation and the modelling of neutron conversions . . . . .	176
9.2.1	Neutron oscillations and baryon number violation . . . . .	177
9.2.2	Neutron oscillations in scenarios of physics beyond the Standard Model . . . . .	177
9.2.3	Free and bound neutron-antineutron conversions . . . . .	178
9.2.4	Antineutron-nucleon annihilation . . . . .	179
9.2.5	Previous searches . . . . .	179
9.3	Software . . . . .	180
9.4	NNBAR moderator design . . . . .	181
9.5	The NNBAR beamline . . . . .	181
9.5.1	NNBAR beamline simulation in the bunker area . . . . .	182

9.5.2	The NNBAR Tunnel . . . . .	184
9.5.3	The interface between the NNBAR beamline and the instruments gallery . . . . .	185
9.5.4	The NNBAR Cave and Beamstop . . . . .	186
9.6	Civil Engineering aspects for the NNBAR Project . . . . .	188
9.6.1	Modifications to the bunker area and the D03 instrument hall . . . . .	188
9.6.2	The area outside the D03 instrument hall . . . . .	188
9.6.3	Interface between the NNBAR and the instrument gallery . . . . .	190
9.6.4	Future investigations connected to the instrument gallery . . . . .	191
9.7	The NNBAR focusing reflector . . . . .	196
9.7.1	The optimization of the focusing reflector . . . . .	196
9.7.2	Nested mirror optics . . . . .	196
9.7.3	Magnification of an elliptical reflector . . . . .	198
9.7.4	Basic Reflector Setup and Simulations . . . . .	199
9.7.5	Construction of the Nested Optics . . . . .	202
9.8	Baseline design and differential reflector . . . . .	203
9.8.1	Optimization of the Nested mirror reflector options . . . . .	205
9.8.2	Summary of the simulation results . . . . .	205
9.8.3	Simulations for a physical model of the experiment . . . . .	206
9.8.4	Utilizing the ESS pulse shape . . . . .	209
9.9	Magnetic Shielding . . . . .	210
9.9.1	Magnetic shielding concept . . . . .	210
9.10	NNBAR vacuum . . . . .	213
9.11	The NNBAR detector . . . . .	215
9.11.1	Detector choices . . . . .	216
9.11.2	Overview of the detector . . . . .	216
9.11.3	Scintillator staves . . . . .	220
9.11.4	Lead-glass calorimeter . . . . .	222
9.11.5	Object definition . . . . .	223
9.11.6	Signal . . . . .	226
9.11.7	Backgrounds . . . . .	228
9.11.8	High energy spallation background . . . . .	229
9.11.9	Skyshine . . . . .	229
9.11.10	Cosmic ray background . . . . .	230
9.11.11	Cosmic ray interactions in the detector . . . . .	235
9.11.12	Machine Learning . . . . .	235
9.11.13	Comparison with the ILL experiment . . . . .	237
9.11.14	Pile-up . . . . .	239
9.11.15	DAQ for NNBAR . . . . .	240
9.11.16	Mechanical construction . . . . .	243
9.11.17	Future steps . . . . .	245
9.12	Cost estimation of the experiment . . . . .	248
9.12.1	Parametric Costing Analysis . . . . .	248
9.13	Sensitivity of the experiment . . . . .	251
9.14	Summary . . . . .	252
<b>10</b>	<b>Thermal Scattering Libraries</b> . . . . .	<b>254</b>
10.1	Introduction . . . . .	254
10.2	Molecular Modelling . . . . .	254
10.2.1	Molecular modelling for MgH <sub>2</sub> / MgD <sub>2</sub> . . . . .	254
10.2.2	Nanodiamonds . . . . .	255
10.2.3	Graphitic compounds . . . . .	256
10.2.4	Clathrate hydrates . . . . .	257

10.3	Advancements in Nuclear Data Libraries . . . . .	260
10.3.1	MgH <sub>2</sub> / MgD <sub>2</sub> . . . . .	262
10.3.2	Other materials . . . . .	262
10.3.3	Libraries for the THF- and TDF-clathrates . . . . .	263
10.3.4	Libraries for graphitic compounds . . . . .	264
10.4	Extensions of NCystal to include new physics . . . . .	266
10.4.1	Small-angle neutron scattering plugin . . . . .	266
10.4.2	Magnetic scattering plugin . . . . .	267
10.4.3	Texture plugin . . . . .	270
10.5	Experimental investigations of graphitic compounds . . . . .	271
10.6	Advances on NCystal . . . . .	273
10.7	Contents of the HighNESS repository . . . . .	276
10.8	Conclusions . . . . .	276
<b>11</b>	<b>Experimental campaign with advanced reflectors</b>	<b>278</b>
11.1	Mock-up experiment at the Budapest Neutron Center . . . . .	278
11.1.1	Introduction to CMTF and the HighNESS experiment . . . . .	278
11.1.2	Neutronic modeling . . . . .	280
11.1.3	Optimization of the source aperture . . . . .	282
11.1.4	Optimization of the source reflector . . . . .	284
11.1.5	Optimization of the extraction system . . . . .	284
11.1.6	Global optimization . . . . .	285
11.1.7	Expected performance . . . . .	287
11.1.8	Dose and background calculations . . . . .	288
11.1.9	Background . . . . .	291
11.1.10	Dose rate . . . . .	292
11.1.11	Activation calculations . . . . .	298
11.2	Engineering of the experimental setup . . . . .	300
11.2.1	Assembly and welding of the components . . . . .	301
11.2.2	Assembly of the moderator & beam extraction system into the test facility . . . . .	304
11.2.3	Results and discussion . . . . .	307
11.3	Experiment at the JULIC Neutron Platform . . . . .	311
11.3.1	Experimental setup . . . . .	311
11.3.2	Materials and Methods . . . . .	314
11.3.3	Data Analysis . . . . .	316
11.3.4	Results . . . . .	318
11.3.5	Discussion . . . . .	321
<b>12</b>	<b>Conclusions</b>	<b>325</b>
<b>13</b>	<b>Outlook</b>	<b>327</b>
<b>14</b>	<b>Acknowledgements</b>	<b>328</b>

## List of Acronyms

Acronym/term	Meaning
BNV	Baryon number violation
BZ	Brillouin zone
BNC	Budapest Neutron Center
CAD	Computer Aided Design
COMSOL	A finite element analysis and simulation software package
CDR	conceptual design report
CEF	Current ENDF Format
CMTF	Cold Moderator Test Facility
CN	cold neutron
CNS	Cold neutron source
COSY	COoler SYnchrotron
DF-DND	Deagglomerated F-DND
DFPT	Density Functional Perturbation Theory
DFT	Density Functional Theory
DFTB	Density Functional Tight Binding
DOS	Density of States
DND	Detonation Nanodiamond
EDM	electric dipole moment
EGO	efficient global optimization
ESS	European Spallation Source
F-DND	Fluorinated DND
FOM	figure of merit
FRM-II	Forschungsreaktor München II
FZH	Forschungszentrum Jülic
GEANT4	A Monte Carlo simulation program for GEometry AND Tracking
HDPE	high-density polyethylene
HiCANS	High Current Accelerator-driven Neutron Source
HighNESS	High intensity Neutron Source at the European Spallation Source
IKP	Institute of Nuclear Physics
ILL	Institut Laue Langevin
JCNS	Jülich Centre for Neutron Science
JULIC	JUelich Light Ion Cyclotron
LANSCE	Los Alamos Neutron Science Center
LANL	Los Alamos National Laboratory
LBP	large beamport
LD <sub>2</sub>	liquid deuterium
LH <sub>2</sub>	liquid hydrogen
MCB	moderator cooling block
MCNP	Monte Carlo N Particle
MCPL	Monte Carlo Particle Lists
ML	Machine Learning
MSD	mean squared displacement
MEF	Mixed Elastic Format
ND	Nanodiamond
NMO	Nested Mirror Optics
NW	North-west
MP	Monoplanar reflector
NNBAR	An experiment to search for neutrons converting to anti-neutrons at the ESS
ND	Nanodiamond

## List of Acronyms (cont.)

Acronym/term	Meaning
PBE	Perdew-Burke-Ernzerhof
PHITS	Particle and Heavy Ion Transport code System
PMT	Photo-Multiplier Tube
PSI	Paul Scherrer Institut
R&D	research and development
SiPM	Silicon photomultiplier
SANS	Small Angle Neutron Scattering
SD <sub>2</sub>	solid deuterium
SNR	Signal-to-Noise ratio
SW	South-west
TEM	Transmission electron microscopy
TMR	Target-Moderator-Reflector
SNS	Spallation Neutron Source
TSL	Thermal Scattering Library
UCN	ultra cold neutron
VCN	very cold neutron
VDOS	Vibrational density of states
WP	work package

# 1 Introduction and Scientific Motivations

## 1.1 The European Spallation Source

The European Spallation Source (ESS) is a cutting-edge scientific research facility currently under construction in Lund, Sweden. When completed to full specifications, it will be the world's most powerful accelerator-based source of neutrons for scientific research [1]. This unparalleled capability will open new scientific avenues across various disciplines, including materials science, life sciences, energy research, environmental technology, and fundamental physics.

Currently, the ESS is actively constructing 15 instruments, which represent a subset of the envisioned 22-instrument suite essential for fulfilling the facility's scientific mission, as outlined in the ESS statutes. Notably, the ESS mandate encompasses a fundamental physics program and the absence of a dedicated beamline for fundamental physics has been identified as a critical gap [2].

The remarkable neutron flux produced by ESS is due to its housing the world's most powerful linear accelerator and the high beam power directed on target. At full design capability, the proton beam operates at a current of 62.5 mA and is accelerated to 2 GeV, employing a 14 Hz pulse structure, with each pulse lasting 2.86 ms. Consequently, this configuration yields an average power of 5 MW and a peak power of 125 MW.

Once the proton beam reaches its final energy, it impacts a rotating tungsten target (see Figure 1), inducing spallation and primarily generating evaporation neutrons with energies around 2 MeV. The high-energy spallation neutrons are decelerated within the neutron moderators situated inside the moderator-reflector plug, as described in Section 1.1.1 and shown in Figure 2.

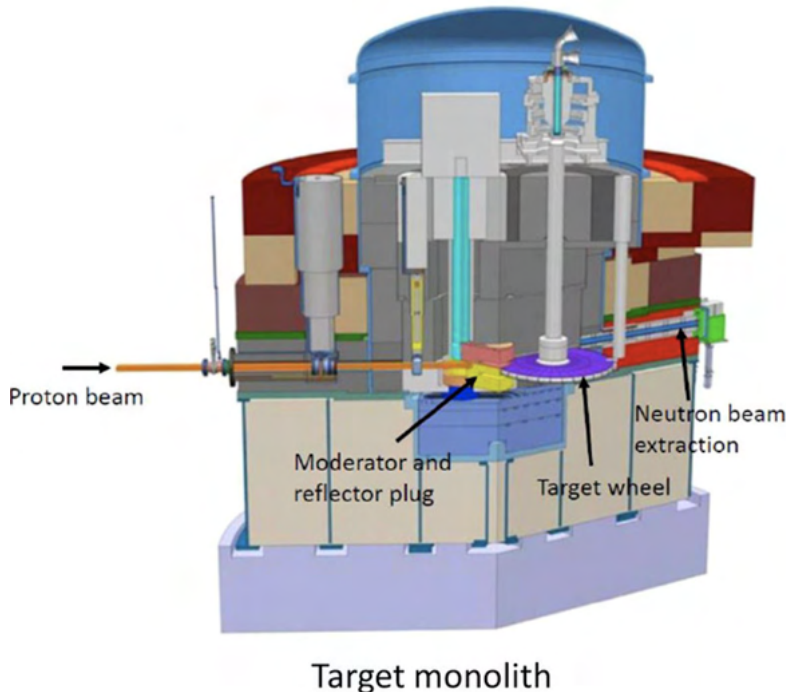


**Figure 1:** The ESS target monolith with key components indicated: moderator and reflector plug, spallation target, and one of the 42 neutron beam ports.

The target area is encircled by a cylindrical steel structure with an 11-meter diameter. This structure, consisting of 6000 tons of steel shielding, is known as the 'monolith'. The monolith is designed to absorb most of the beam power and is capable of withstanding the heat generated during operations. Additionally, the monolith includes a cooling system that utilizes pressurized helium gas. This cooling system effectively reduces the peak temperature by 150°C between successive beam shots. This structure also houses the neutron beam ports, which are essential for extracting thermal and cold neutrons from

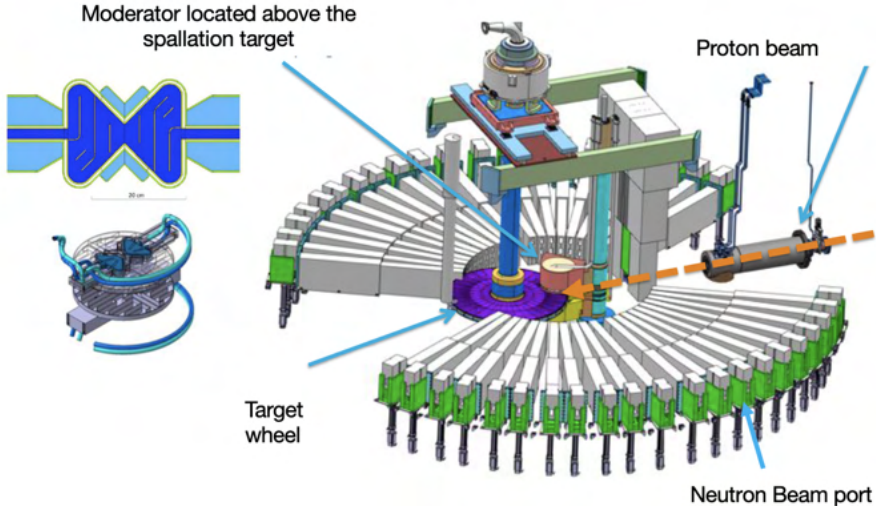


**Figure 2:** The ESS target-moderator system. The picture depicts the proton beam, the spallation target, the structure housing the moderator, and the neutron beam port.

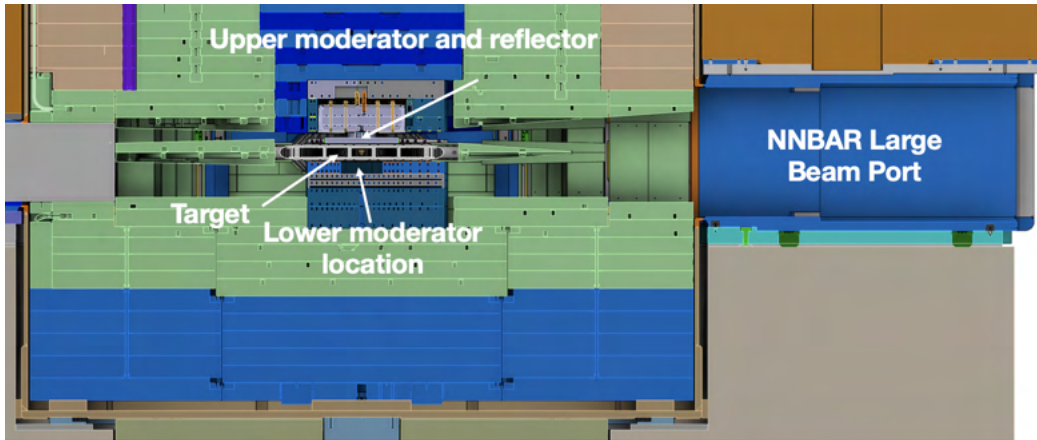


**Figure 3:** Cross-sectional view of the ESS target/moderator area and inner shielding. The figure displays the location of the ESS moderator above the spallation target, referred to as the “upper moderator”, and the moderator below the spallation target, referred to as the “lower moderator”. The NNBAR experiment (see Section 1.1.2) will utilize both moderators.

the moderators. ESS has positioned its beam port system around the moderators, allowing for neutron extraction both above and below the target as shown in Figure 3.

Beyond the ESS monolith, the beamlines reside in the bunker, as referenced in [3]. The bunker serves as a crucial shielding area, enveloping the ESS monolith and shielding the instrument area from the significant ionizing radiation generated during operation. The shielding structure of the bunker consists of 3.5-meter-thick walls (see Figure 4) constructed from heavy magnetite concrete, complemented by a roof of variable thickness, also composed of heavy concrete.

Figure 5 shows the completed bunker in the instrument hall. After the bunker, the neutron instruments reach the instrument halls, as shown in Figure 6. The instrument hall areas are located in the D01, D03, and E01 buildings. Figure 7 shows the complete layout of the facility.

### 1.1.1 The ESS current moderator system

Initially, the spallation source will be equipped with a single compact, low-dimensional moderator specifically designed to produce high-brightness neutron beams for condensed matter experiments. This de-

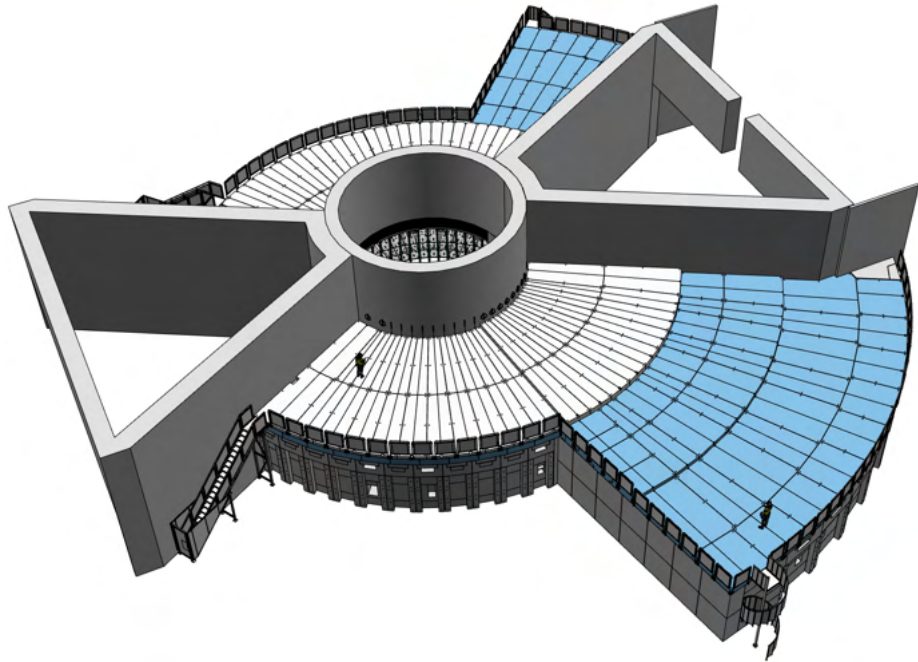


**Figure 4:** The ESS bunker.



**Figure 5:** Overview of the complete bunker area in the ESS D03 instrument hall.

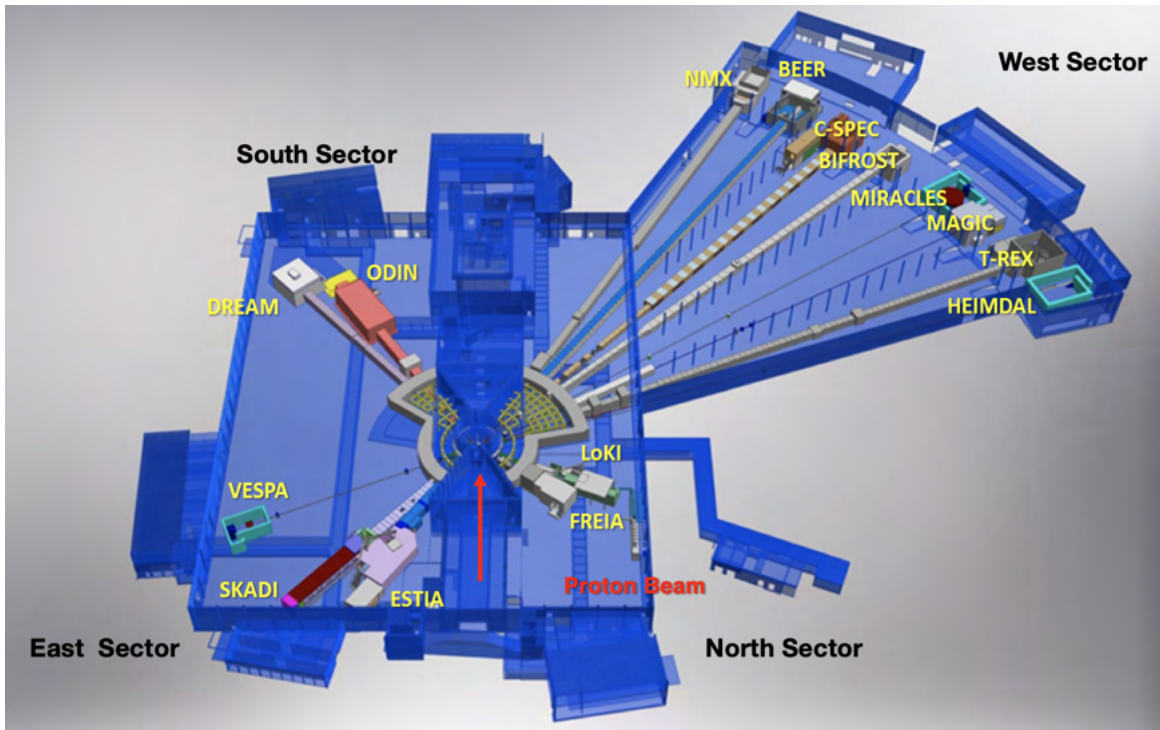


**Figure 6:** Overview of the 15 instruments currently under construction at the ESS and the instrument halls.



**Figure 7:** ESS layout and building description.

sign is optimized for small samples and offers flexibility for parametric studies. In Figure 2, the left side showcases the high-brightness moderator, while the right side illustrates the current configuration of the ESS target-moderator-reflector system.

The core neutron production at ESS happens in the two moderator-reflector systems positioned both above and below the spallation target, as shown at the center of Figure 8. A cylindrical steel structure (shown in dark red) located above the target houses the moderator and reflector, from which neutrons are extracted for the beamlines. A similar container (depicted in yellow) is positioned below the target.

Figure 2 shows the openings in the shielding, which are the beam extraction channels and are present above and below the spallation target. These channels allow for the extraction of neutrons from either or both moderators. The space shown in Figure 3 below the spallation target is presently occupied by a steel plug and currently un-utilized. This space has the potential to accommodate an additional moderator-reflector system. The design of such a system constitutes one of the primary objectives of the HighNESS project.

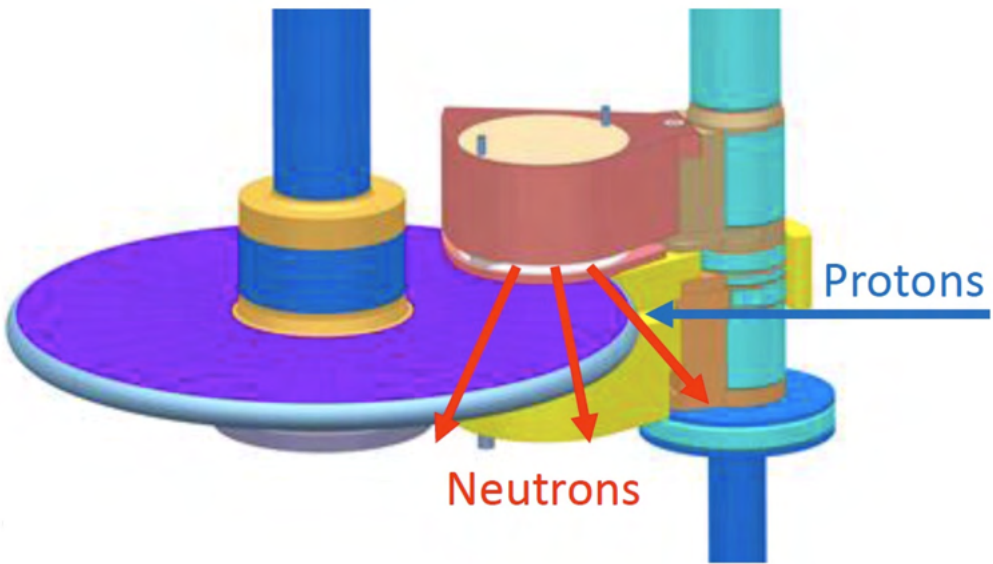


**Figure 8:** Schematic view of the ESS target-moderator-reflector system. The proton beam impinges on a rotating target consisting of tungsten (purple target in the figure). A cylindrical steel structure (dark red) placed above the target contains the moderator and reflector from which neutrons are extracted to the beam lines (red arrows). A similar container (yellow) is placed below the target, and is the intended location for the placement of the high-intensity moderator in the HighNESS project. These two structures and the shaft (light blue) form the so-called twister.

### 1.1.2 The ESS upgrade area

The HighNESS project will also make use of the availability of extra beam ports. Figure 9 shows the available sectors of experimental zones, the distribution of the 15 instruments of the initial suite, and the additional beam ports and areas still available for additional future instruments that can be fed by a second moderator system. These areas, highlighted in green in Figure 9, serve as the primary locations for designing instruments and experiments that will utilize the moderators developed in the HighNESS project.

In addition to the extra beam ports, ESS is also equipped with a large beam port in the shielding of the monolith for neutron extraction. This beam port, often referred to as the Large Beam Port (LBP), due to its size, is equivalent in size to three standard ESS beam ports and is illustrated in Figures 10 and 11. This infrastructure has been installed in anticipation of the Neutron-to-Antineutron Oscillation Experiment, NNBAR [4, 5], in order for the experiment to achieve its design goals (see Section 9). At

the time of this writing, no other existing or planned neutron facility will have a beam port of similar dimensions, making ESS the best possible facility worldwide for the NNBAR experiment. The LBP also serves a broader purpose beyond the NNBAR experiment, since it can be used for various potential designs of Ultra-Cold Neutron (UCN) sources, as detailed in Section 6.

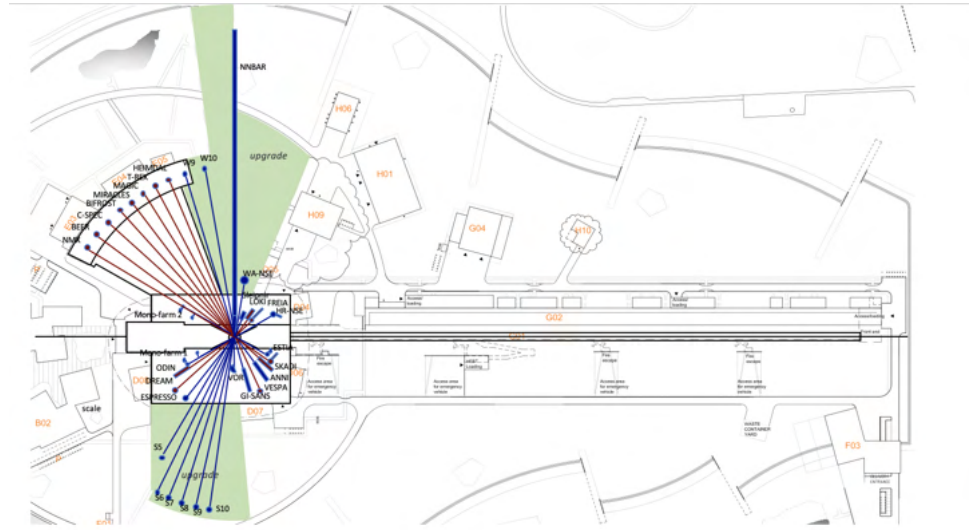


**Figure 9:** The ESS facility. The location of the instruments of the initial suite, plus some additional instruments beyond the initial 15, are shown. In green the upgrade areas, where the HighNESS instruments and experiments could be placed, are highlighted.

Figures 12 and 13 depict how the NNBAR experiment will require an extension of the instrument hall. The current building perimeter extends approximately 21 meters away from the moderator. This area is available for future upgrades and will be used by the NNBAR experiment as shown in Figure 9 (see Section 9.6 for more information) .



**Figure 10:** Photograph of the monolith beam ports around the ESS Large Beam Port. An overlaid drawing shows the visible surface of the upper and lower moderators, with a shielding block in between.

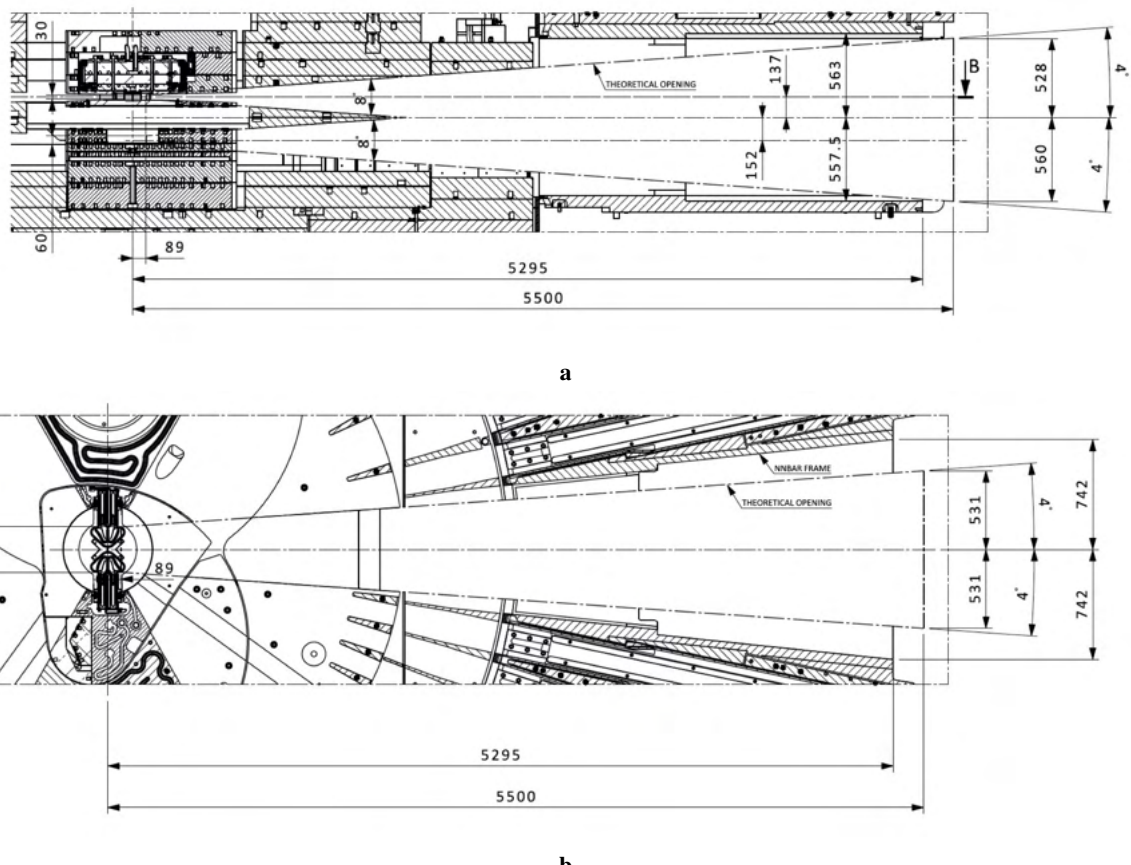


**Figure 11:** (a) Side view of opening in correspondence of NNBAR. (b) Top view of the large beam-port opening for NNBAR

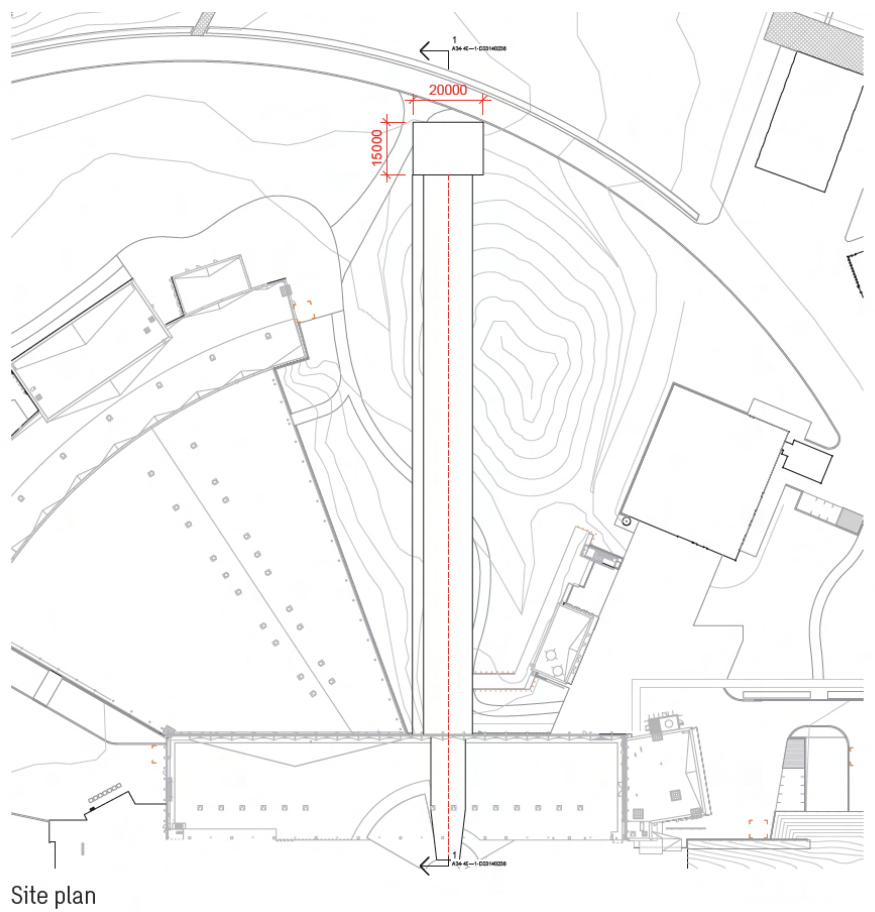


**Figure 12:** Overview of the NNBAR beamline extension from the current ESS building.



**Figure 13:** The NNBAR beamline and the detector hall located 200m from the source

### 1.1.3 ESS timeline and beam power projections

Owing to delays from the covid-19 pandemic and other technical challenges, the ESS in 2021 conducted a rebaseline exercise to revise its construction and commissioning schedule<sup>1</sup>. The revised baseline plan introduces a two-year delay with respect to the previous schedule and will enable the ESS to start full operations and be open for scientific users working with up to fifteen instruments in late 2027. The maximum accelerator power and proton beam energies will be 2 MW and 800 MeV, respectively. The possibility of operating the accelerator at its nominal design power of 5 MW is taken as part of an ESS upgrade project.

The installation of the ESS second moderator would occur after 2030. At the time of the writing, it is challenging to predict whether this moderator will be installed before ESS reaches the 5 MW design power. As a consequence, the majority of the findings presented in this work have been developed with consideration of both the 2 MW and 5 MW options.

## 1.2 HighNESS scientific motivations

As described in the previous section, the flexible design of ESS, with only one moderator located above the target, leaves a great opportunity to implement a second source with complementary characteristics going well beyond the initial goals of the facility development. This new infrastructure has been designed with the purpose of delivering the highest possible total intensity (as opposed to brightness which was the main design criterion for the first source) of cold neutrons with wavelengths above 4 Å (see Section 2), including neutrons in the long-wavelength part of the spectrum, referred to as Very Cold Neutrons (VCN) and Ultra Cold Neutrons (UCN). With these new source capabilities, various condensed matter instrument concepts have been considered, as detailed in Section 8. Furthermore, the presence of a high-intensity neutron source is of paramount importance for the NNBAR experiment and for the development of UCN and VCN sources.

## 1.3 HighNESS objectives

The HighNESS project, [6, 7], is an EU-funded 3-year project, that commenced in October 2020. The primary objective of the project is to develop a second cold neutron source at ESS that complements the first source located above the spallation target. For the initial instrument suite, the emphasis was on creating a source capable of providing a high brightness of thermal and cold neutrons. In contrast, the new sources, designed as part of the HighNESS project, focused on two distinct aspects:

- Increase in Source Intensity: this entails boosting the total number of neutrons emitted from the source. Achieving a more intense source necessitates larger moderators and emission surfaces to enhance the count rate for instruments or experiments that require high flux.
- Shift toward colder neutrons: this shift has manifested in the development of a very-cold neutron source and an ultra-cold neutron source, in addition to the second cold neutron source. To create a highly intense VCN source as part of the project, we have invested significant effort in extensively characterizing promising candidate materials. This comprehensive characterization is essential for fully developing the capabilities required to design a source utilizing these materials. The HighNESS project has placed specific emphasis on some distinct materials: solid deuterium and deuterated clathrate hydrates, that can be used as dedicated VCN moderator materials; nanodiamonds, graphite intercalation compounds, magnesium hydride, and clathrate hydrates as advanced reflectors to increase the VCN flux.

The second source was designed as a liquid-deuterium ( $LD_2$ ) moderator based on proven technology. One of the main results of this work is a complete engineering design of the  $LD_2$  moderator, taking into account the actual layout of the ESS target station. In addition to this, the project has explored several

---

<sup>1</sup><https://europeanspallationsource.se/article/2021/12/10/ess-revises-project-plan-and-budget>

designs for VCN and UCN sources. These designs possibilities are described in Section 4, and Section 6 respectively. Furthermore, the project has successfully developed a set of neutron scattering instruments (see Section 8) and conducted a conceptual design study for the NNBAR experiment in Section 9.

As mentioned previously, the first 15 instruments for the user program of ESS will view the top moderator. The start of operation of ESS will be at low power, which will be increased stepwise to finally reach the time average power of 2 MW. It is planned to reach 2 MW power around 2028. Beyond 2030, a second moderator system, like the one proposed herein, could become available. Around that date the facility would ideally be equipped with two separate neutron sources with the following features:

- A high brightness bi-spectral (thermal–cold) moderator, based on water and liquid para-hydrogen, placed above the spallation target and able to serve all the 42 beam ports of the ESS grid with a thermal and cold brightness spectrum higher than anywhere other facility worldwide.
- A high-intensity LD<sub>2</sub> moderator, placed below the target station, capable of directly serving instruments demanding a cold-neutron flux of unprecedented intensity or acting as a primary source for secondary VCN and UCN sources for experiments requiring sub-cold neutrons. In particular, the ESS would provide the first high-intensity VCN source in the world.

Thus, in this scenario of separate moderators optimized for separate neutron characteristics, ESS would offer a versatile neutron source of outstanding performance, spanning a large neutron wavelength range and without compromising performance (which is inevitable for a single-moderator case). This will enable a plethora of multi-disciplinary activities which fit the original plan for ESS but offer many more possibilities beyond, for which there is strong topical scientific demand.

## 1.4 The HighNESS project in the neutron landscape

HighNESS aims at serving instruments and experiments with high intensity beams of neutrons, and preferably of lower energy than what is typically available at existing neutron sources. Some examples are already given in this introduction, but more are outlined in Section 4, Section 8, and Section 9. It is crucial to emphasize that there is currently no alternative source with comparable parameters to ESS to enable the experiments mentioned. There are two other high-power, MW-class, pulsed spallation sources in the world. These are J-PARC in Japan and SNS in the USA. Both facilities have upgrade plans for the implementation of second target stations, and in both cases, the focus is on using low-dimensional high-brightness moderators, similar to the approach of the ESS first source.

These upgrades aim to achieve peak brightness superior to that of the ESS first source, with a potential increase of up to a factor of 5. However, the time-average brightness is expected to remain approximately 5 times lower than that of the first ESS source when operating at 5 MW. For the majority of applications targeted by the HighNESS project, a high time-average intensity is essential. This requirement implies that even with the upgrades, such facilities would not be able to compete with ESS. Furthermore, it's worth noting that the upgrades at SNS and J-PARC primarily focus on cold neutron ranges.

Neither of these facilities have plans to install a VCN source near the spallation target. As a result, ESS, with its intense source and focus on delivering longer wavelengths, could significantly outperform these planned upgrades in the long-wavelength regime by more than an order of magnitude.

The installation of a long-wavelength facility at the ESS is uniquely favorable due to the high proton power and long-pulse time structure. In other words, no existing facilities can be upgraded in this way. Furthermore, it is worth highlighting that no other facility houses a feature akin to ESS's Large Beam Port, which opens exceptional opportunities not only for the NNBAR experiment but also for the development of world-leading UCN sources.

## 1.5 HighNESS project structure

The HighNESS project is organized into ten distinct Work Packages (WPs), as illustrated in Figure 14. WP1, titled “Project Coordination”, serves as the central hub for coordinating all project activities. WP2,

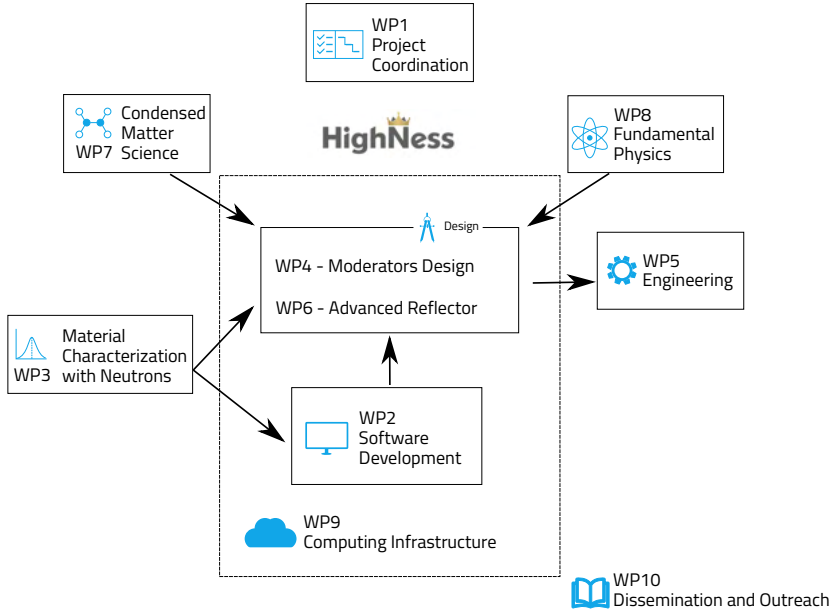


**Figure 14:** HighNESS project Work Package structure

known as “Software Development”, focuses on creating the necessary computational tools required for the analysis and design of high-intensity moderators.

The computational tools developed in WP2 rely on experimental measurements conducted in WP3, titled “Material Characterization with Neutrons”. This work package provides material-property data, essential for generating thermal-neutron scattering kernels and validating the required models.

WP4 and WP6, designated as “Moderator Design” and “Advanced Reflectors”, respectively, serve as the foundation for neutron design efforts, specifically the development of cold sources (CN), very-cold sources, and ultra-cold sources. These two work packages require input and specifications from the scientific-oriented WPs, WP7 (“Condensed Matter Science”) and WP8 (“Fundamental Physics”). These scientific WPs efforts ensure that the source designs deliver the necessary neutron fluxes and spectra, enabling groundbreaking scientific experiments at ESS that are beyond the capabilities of high-brightness moderators. WP5 (“Engineering”) is responsible for handling all engineering aspects related to the different sources.

The objective of WP9 (“Computing Infrastructure”) is to make software and data developments carried out by WP2 and WP6 accessible to the public through the creation of cloud computing resources. Subsequently, WP10 manages the distribution of all scientific content generated as part of this project.

## 2 Design of the cold source

The design of the LD<sub>2</sub> moderator is one of the main objective of the HighNESS project. This moderator has been designed to outperform the low-dimensional moderator located above the spallation target in terms of intensity, thus delivering a world-leading flux of cold neutrons to beamlines serving condensed matter research and fundamental physics.

The design of the LD<sub>2</sub> moderator has been carried out using the MCNP6 [8] code. The work has been performed incrementally, considering initial, simple figures of merit (FOMs), and later in the project using those developed and reported in Deliverable 4.1 of the HighNESS project [9]. Likewise, the work started considering a single opening (channel for neutron extraction), and then moved to a configuration closer to the one needed for ESS, with openings for both fundamental physics and condensed matter experiments. The results from the study with a single opening are detailed in [10] and will not be described in this document where the focus will be on the design with two openings.

### 2.1 General Description of the ESS Moderator Area

The neutron production core at ESS comprises two moderator-reflector systems, one positioned above the spallation target (referred to as the "upper moderator") and the other located below the target (referred to as the "lower moderator"). In Figure 8, one can see a cross-sectional view of the target system, highlighting the locations of these two moderators.

Figure 15 shows the openings available below the target for the neutron extraction. Overall, they cover two areas of 120° each. Neutrons are emitted towards four sectors which are conventionally labelled with their cardinal directions (see Figure 9).

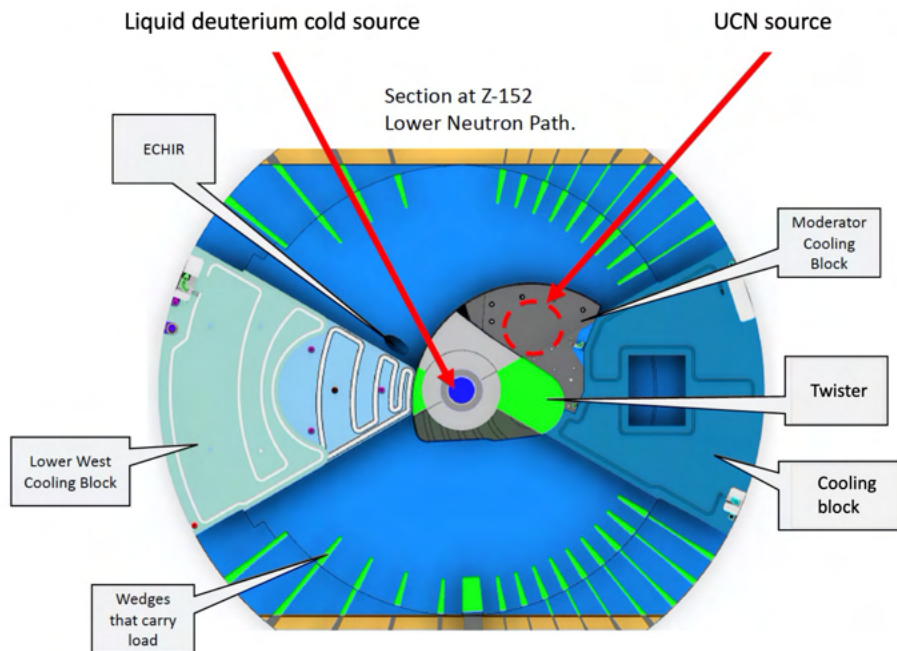


**Figure 15:** Horizontal cut in the geometry of the target monolith in correspondence to the center of the lower moderator, courtesy of R. Holmberg. The grey circle inside the twister represents the maximum available space for a Be reflector (maximum diameter 72 cm). The blue circle inside represents the location of the lower moderator. In the picture is also shown one of several candidate UCN source locations is indicated with the red dotted circle. For more details see Section 6

The lower moderator system will be installed within the twister structure. The coordinate system used to describe the geometry is the so-called TCS (Target Coordinate System) which has the origin inside

the spallation target, with the vertical axis ( $X, Y=0$ ) passing through the center of the upper moderator. We have the following constraints for the liquid deuterium moderator and reflector: 400 mm in height, and 720 cm in diameter. This corresponds to between -78 mm and -478 mm along the Z-TCS. The twister starts at -610 mm with respect to Z-TCS, hence we have 132 mm between the maximum size of the liquid deuterium moderator and the inner shielding. However, some of this space, depending on the engineering design, must be reserved for the structural support of the lower moderator-reflector plug.

In addition to the space inside the twister structure (which contains the moderator and reflector) below the spallation target, another potential location for a moderator system was identified during the early stages of the HighNESS project: the Moderator Cooling Block (MCB). The MCB (as shown in Figure 16) is essentially a block of shielding material that is water-cooled and positioned adjacent to the twister. Its location has been considered for the placement of a secondary source, such as a UCN source see Section 6 for more information. The placement of a source in that location would require a modification of the MCB. This possibility has been discussed with the ESS Target management and is considered feasible. It has therefore been explored, along with a variety of other UCN-source candidate locations, as part of the HighNESS project (see Section 6). Figure 16 and Figure 17 show the twister and the MCB next to each other. Such a source embedded in the MCB could serve more easily beamlines placed in the North sector.

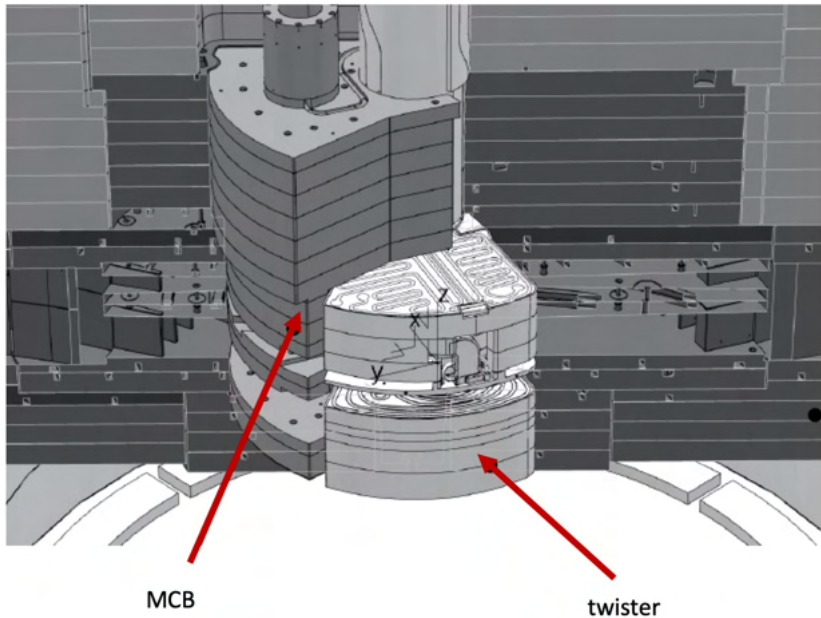


**Figure 16:** Twister and moderator cooling block (MCB). The twister consists of two steel structures containing the upper and lower moderator-reflectors assemblies, and its name is derived from the fact that it rotates around its shaft during the periodic exchange procedures. Drawing courtesy of C. Jones, ESS. See explanation in the text.

## 2.2 Figures of merit

It is important to define the wavelength ranges for the three groups of neutrons of interest in HighNESS (Table 1). Cold neutrons are defined in the range from about 2 Å to about 20 Å, (i.e. the typical range for the instruments using the cold neutrons from the upper moderator [11]). Then, VCNs as defined in [12], are neutrons in the range between about 10 Å and 120 Å. It is worth noting that the lower range, 10–40 Å, is of particular interest for condensed matter research, while the upper range, 40–120 Å, is more applicable to fundamental physics experiments. Finally, UCNs are defined as neutrons with wavelengths above 500 Å. The present section reports on the design and optimization of the lower moderator in terms of CN production, in order to establish a high-intensity baseline in order to complement the high-brightness upper moderator; the design for this moderator was produced with the Monte Carlo code

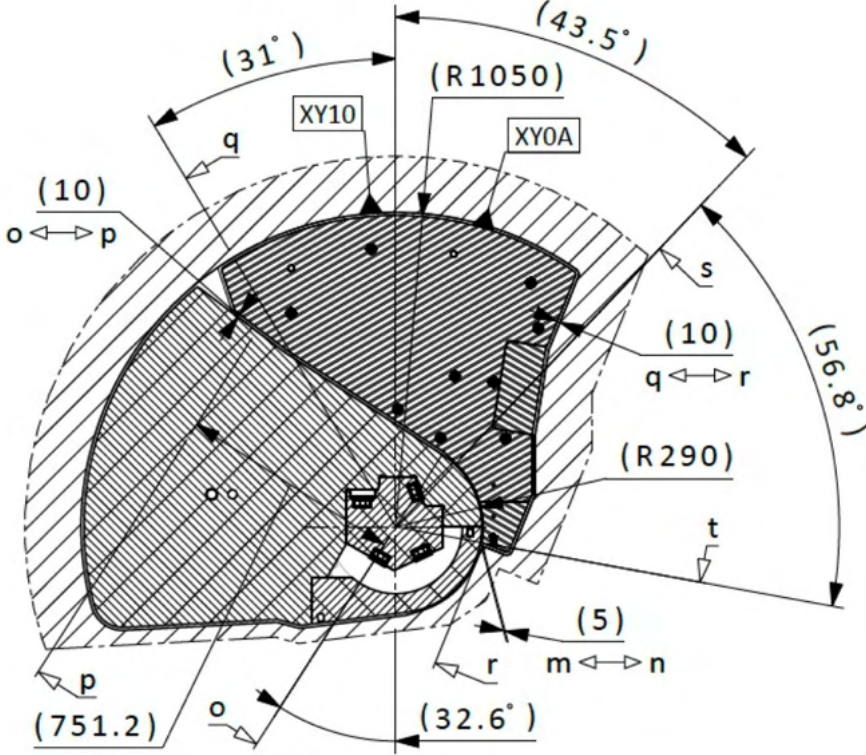


**Figure 17:** Twister (left block) and moderator cooling block (MCB, right block), top view. The twister is the location for both the upper liquid parahydrogen moderator and the lower liquid deuterium moderator (the main HighNESS source). The MCB is a potential location for a UCN in-pile source.

MCNP versions 6.2 [13]. The refinements of this lower moderator and/or addition source placements for producing VCNs and UCNs are discussed in Section 4 and Section 6 .

**Table 1:** The wavelength range that defines cold, very cold, and ultra cold neutrons.

cold	2-20 Å
very cold	$\sim$ 10-120 Å
ultracold	> 500 Å

To design the best possible neutron source, one must consider the whole process from neutron moderation to the transport to the experimental area: the performance of an experiment is determined by the count rate of the desired neutrons (in terms of wavelength and divergence) at the experimental position. The transport to the experimental station is therefore essential to the design of the experiment or instrument, and is linked to the performance of the source (the moderator) and its simulation with MCNP. In other words, the design of the source must be done taking into account both the MCNP for initial CN flux calculation as well as the neutron transport using ray-tracing Monte Carlo simulations using the McStas code [14].

The two processes are done at different stages. In the case of the HighNESS project, MCNP simulations are done by the neutronic team (Work Package 4 of the HighNESS project see Section 1.5 ), while the McStas ones are mainly performed by instrument designers for both condensed matter instruments and fundamental physics experiments. In order to link the two parts, MCNP must provide a source file to be used in McStas. This can be done in several ways, such as by fitting neutron spectra from the moderator, or by writing individual neutron trajectories in a text file (MCPL format [15]), which is then read by McStas. The latter is the preferred option within HighNESS.

There is an additional parameter that complicates the work of the source designers in HighNESS, this is the use of advanced reflectors that are intended to increase the flux from the source to the instruments.

Various options have been investigated, such as the use of nanodiamond layers at the exit of the moderator, which increase the flux towards the neutron guides via quasi-specular reflection. Other materials have also been considered. To investigate these options, thermal scattering libraries were developed and included in the MCNP simulations, as well as in other particle transport tools (see Section 11).

To optimized the moderator design it is necessary to define a metric, or FOM. Several FOMs are needed, to accommodate the needs of the various instruments.

### 2.2.1 Figures of Merit for condensed matter

For the neutron scattering instrument designs developed by HighNESS, what is essential for the instrument optimization is the number of neutrons reaching the sample, within the desired wavelength range and divergence.

As far as the FOM is concerned, this is not always as straightforward as for instance in the case of NNBAR (see below). The reasons are as follows: first, there are three classes of instruments under study: SANS, imaging, and spin-echo. Second, for a given class of instruments, different solutions for the optics can be considered, which might work best for competing features of a moderator.

In general, however, a few guidelines have been established, that can be used to define the way of working and a useful FOM. Since the neutron divergence at the sample can only be studied with McStas, and it is not a parameter controlled with MCNP it has been omitted from the FOM. The FOM to be used in designing the source should rather concentrate on the intensity and spectrum:

- Different emissions surfaces from the moderator are of interest *a priori* for the relevant instruments. The reference emission surfaces are:  $5 \times 5 \text{ cm}^2$ ,  $10 \times 10 \text{ cm}^2$ ,  $15 \times 15 \text{ cm}^2$ ,  $20 \times 20 \text{ cm}^2$ .
- For each of these surfaces, an optimization of the moderator can be done, using as FOM the integrated intensity for wavelengths up to  $2.5 \text{ \AA}$ .
- For some instruments, in particular spin-echo – and potentially future SANS instruments – the instrument design team (WP7) is also interested in a colder spectrum. That is, an increase in the spectrum for wavelengths greater than  $10 \text{ \AA}$ . For this purpose, the combined efforts of WP4 and the advanced reflector team, WP6, were needed (i.e., using advanced reflectors to enhance the coldest part of the spectrum from the cold moderator). It is likely that the greatest increase will be achieved using a smaller viewing surface than the reference ones under study by WP7. This could be obtained with a smaller extraction surface, such as  $3 \times 3 \text{ cm}^2$ , surrounded by a layer of advanced reflectors such as nanodiamonds. This option has also been investigated, and in this case smaller openings will also be considered, in addition to the larger openings mentioned above.

### 2.2.2 Figures of Merit for fundamental physics

#### 2.2.3 NNBAR

The NNBAR experiment will search for baryon number violation (BNV) via neutron ( $n$ ) antineutron ( $\bar{n}$ ) oscillation. The full experiment and its scientific motivation are described in Section 9. In Figure 18 a schematic overview of the planned NNBAR experiment [4] is depicted. Neutrons that are generated in the target are moderated and traverse the LBP. A system of elliptically shaped neutron guides is placed in the region after the LBP's exit to focus the neutrons in the direction of the detector located downstream. After having passed the optics, neutrons fly free from perturbation to the detector region at the end of the instrument. The moderator-to-detector distance is 200 m.

The probability of an oscillation is proportional to the (uninterrupted) flight time squared  $t^2$  of the neutrons. The FOM of the NNBAR experiment is then defined as  $\sum_i N_i t_i^2$  with  $N_i$  being the number of neutrons with a specific flight time  $t_i$ . Thus, slower neutrons are favored and a trade-off between intensity and wavelength will be established.

In the lower plot of Figure 19, the distribution of wavelengths and how they contribute to the FOM is shown for a representative simulation result. The upper plot displays the wavelength distribution in the LD<sub>2</sub> source for comparison.

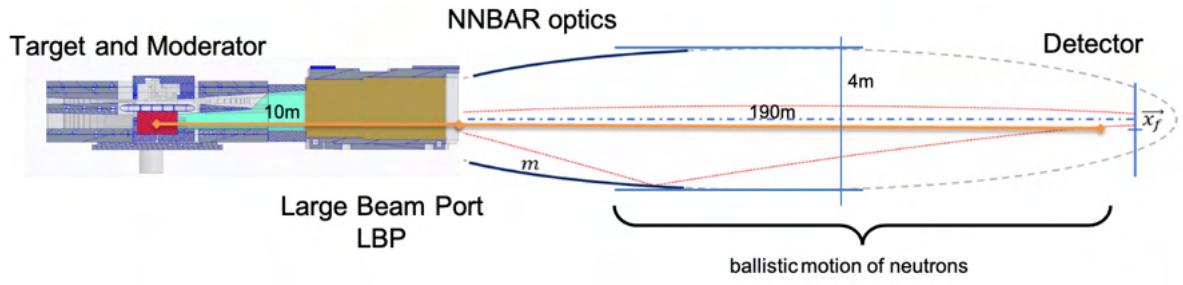


**Figure 18:** Schematics of the NNBAR Experiment (not to scale).

A possible FOM for the moderator optimization can therefore be the wavelength intensity distribution that covers the solid angle defined by the exit of the LBP in the range above 5 Å (or alternatively, 2.5 Å) at the detector and weighted with  $\lambda^2$ . We note that there will be a natural cutoff at  $\lambda$  of about 15 Å, due to the effect of gravity on neutrons with longer wavelengths. For example, for neutrons of wavelength 12.5 Å the vertical drop due to gravity would already be 2 m. Thus, neutrons with wavelengths that are too long will not be able to reach the detector, which has a radius 1 m. Moderator designs that perform better under this criteria should lead to a higher FOM for NNBAR.

The FOM used for the moderator design for NNBAR is therefore the intensity of neutrons, weighted with  $\lambda^2$ , for two ranges of neutrons: above 2.5 Å and above 5 Å, with an upper cut of about 15 Å.

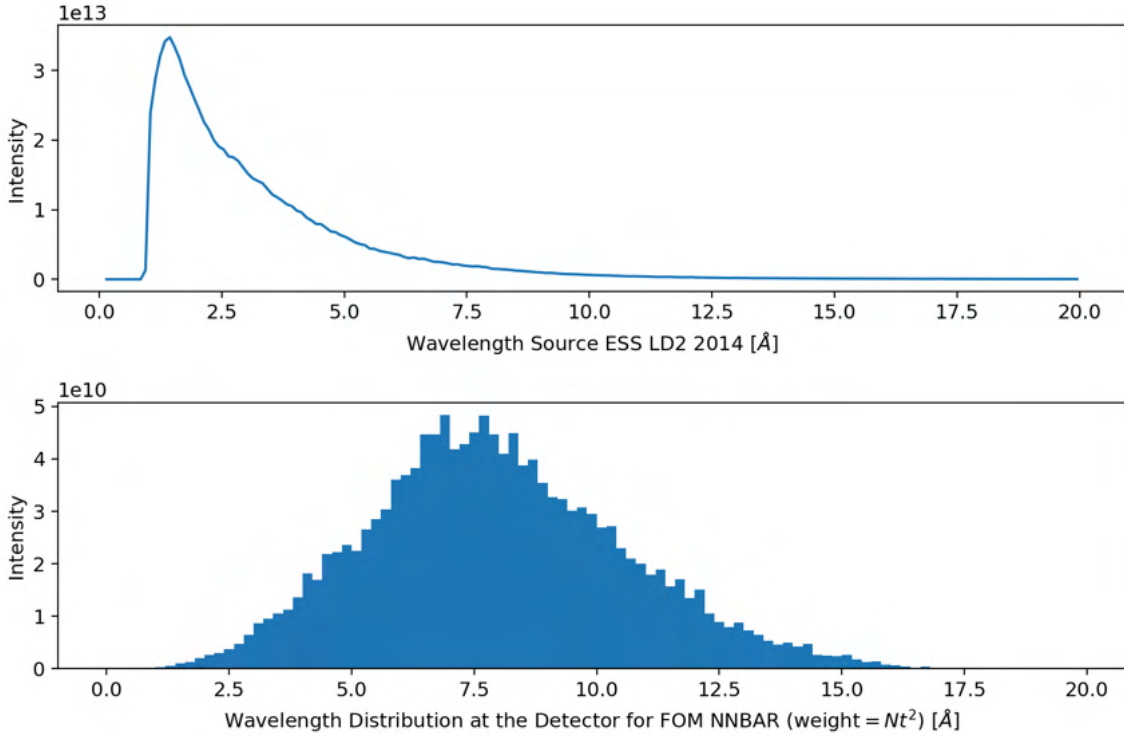


**Figure 19:** Wavelength spectrum of the LD<sub>2</sub> source (upper plot) and the distribution of wavelength contribution to FOM for NNBAR (lower plot).

#### 2.2.4 Figure of merit for UCN

A further goal of the HighNESS project is to design and simulate a source of ultra cold neutrons. This UCN source can be located in-pile or in-beam. For example, the moderator cooling block discussed previously (see Section 2.1) has been investigated as possible location for the in-pile option. These designs are described in detail in Section 6, but we discuss a FOM also here for completeness.

Such a moderator can be a large volume of superfluid helium as converter material, fed by the beam of cold neutrons emanating from the liquid deuterium moderator, as proposed in [16].

The two most relevant parameters for UCN production with liquid He4 sources are:

- 9 Å flux in the UCN source area that contains superfluid helium [17].
- stability of the cooling temperature of the converter material liquid.

For the former, in [16] it is reported that a flux of  $\Phi_{9\text{\AA}} = 10^9 \text{ cm}^{-2} \text{ s}^{-1} \text{\AA}^{-1}$  at 9 Å leads to a UCN density of  $\rho_{UCN} = 1.3 \times 10^3 \text{ cm}^{-3}$  in the source volume. The FOM for UCN production has to take this into account and will consist of the  $\Phi_{9\text{\AA}}$  inside the designated volume of the UCN moderator. This has been used as the initial FOM, with later refinements adding slightly larger wavelength range (roughly 8–10 Å).

For the later engineering design stages, the stability of the cooling temperature was also considered. Designs that minimize the heat impact on the UCN converter module will be preferred.

Other possible converter materials than liquid He have also been investigated, particularly solid deuterium ( $\text{SD}_2$ ) which produces UCNs primarily from 2.5–7 Å neutrons, and has a superior UCN production rate per volume compared to He-II. However, the lifetime of UCNs within the bulk of the  $\text{SD}_2$  is dramatically reduced compared with He-II, thus allowing only thin segments to be used effectively for extraction (see Section 6.5).

#### 2.2.5 Figure of merit for VCN

The emphasis on colder neutron spectra is one of the key aspects of HighNESS, and consequently a great effort has been devoted to the design of a source delivering high intensity of neutrons above 10 Å.

Concerning the FOM, for fundamental physics applications using VCNs, we are mostly interested in neutrons in the range 40–120 Å.

For condensed matter applications, the range of 10–40 Å is in general more useful (see Section 8), as neutron scattering experiments are interested in extending existing techniques such as SANS and spin-echo to the use of neutrons of longer wavelengths than traditionally used.

#### 2.2.6 Summary of FOMs

In Table 2 the FOMs to be used for the designs of the moderators in WP4 are summarized. In the intensity calculations with MCNP, a point detector tally is placed at a distance  $r$  large compared to the moderator, and an artificial collimator limits the view to the emission surface from the moderator. For the option of the VCN source where advanced reflectors are used to increase the transport of VCNs, the viewed surface must also include the reflectors.

### 2.3 Neutronic design

The purpose of the cold moderator is to provide cold neutrons to beamlines for fundamental physics and neutron scattering instruments. The “NNBAR opening” is intended for both fundamental physics experiments and the NNBAR experiment, while the opening for one or more neutron scattering instruments is referred to as the “WP7 opening”.

**Table 2:** List of FOMs.  $I_P$  is the proton beam intensity (for 2.5 mA is  $1.56 \cdot 10^{16}$  protons/s).  $\Delta\Omega$  is the solid angle defined by the emission surface and the distance at which the tally is calculated. The integral in  $dA$  is over the emission surface of the moderator; as per definition of f5 tally, the integral in  $d\Omega$  is over  $4\pi$  sr and the integral in  $dt$  is over all times; the integral in  $d\lambda$  over the two values of wavelength is performed in MCNP by specifying the corresponding values of neutron kinetic energy in the tally energy bin. Collimators are used in the calculations to limit integration to the desired  $\Delta\Omega$ .

COLD SOURCE	
NNBAR	$\frac{I_P}{\Delta\Omega} \int dA \int d\Omega \int dt \int_{\lambda=2.5\text{\AA}}^{15\text{\AA}} d\lambda \phi(\lambda, \Omega, \mathbf{r}, t) \lambda^2$
condensed matter	$\frac{I_P}{\Delta\Omega} \int dA \int d\Omega \int dt \int_{\lambda=5\text{\AA}}^{15\text{\AA}} d\lambda \phi(\lambda, \Omega, \mathbf{r}, t) \lambda^2$
<hr/>	
VERY COLD SOURCE	
fundamental physics	$\frac{I_P}{\Delta\Omega} \int dA \int d\Omega \int dt \int_{\lambda=40\text{\AA}}^{120\text{\AA}} d\lambda \phi(\lambda, \Omega, \mathbf{r}, t)$
condensed matter	$\frac{I_P}{\Delta\Omega} \int dA \int d\Omega \int dt \int_{\lambda=10\text{\AA}}^{40\text{\AA}} d\lambda \phi(\lambda, \Omega, \mathbf{r}, t)$
<hr/>	
ULTRA COLD SOURCE	
He-II	Flux of 9 Å neutrons inside the helium converter
SD <sub>2</sub>	Flux of 2.5–7 Å neutrons inside the SD <sub>2</sub> volume

### 2.3.1 Iterative design process

The design of the cold moderator has followed several iterations, which are summarized in the following Sections. The following design steps were performed:

- Preliminary neutronic studies using a cylindrical moderator shape and one opening for beam extraction (Ref. [10] and Section 2.3.2).
- First neutronic optimization ([10] and Section 2.3.4). In this step, a box shape of the moderator was selected, and the design was performed with two openings. The FOM used for the optimization was the intensity of cold neutrons above 4 Å.
- Second neutronic optimization (Ref.[10] and Section 2.3.5). The optimization from the previous step was repeated using the FOM from Table 2.
- Engineering study based on the model from second neutronic optimization resulting in new engineering requirement for adding aluminum into LD<sub>2</sub>.
- Third neutronic optimization, see Section 2.3.6, motivated by updated constraint on adding aluminum into LD<sub>2</sub> and the effort to minimize heatload by reducing the volume of the moderator.
- Engineering design based on the model from third neutronic optimization, see Section 3.
- Evaluation of the impact of the engineering design on neutronic performance, Section 2.3.10.
- Additional neutronic model with separated LD<sub>2</sub> box and Be filter, U-shaped reentrant hole and rounded walls of the LD<sub>2</sub> box based on new engineering study which is in preliminary stage, see Section 2.4

### 2.3.2 Summary of the results with a single opening cylindrical moderator

The first part of the neutronic design of the LD<sub>2</sub> moderator explored the sensitivity of the performance to a large set of parameters. It used a reference cylindrical geometry of the moderator, and a single opening for neutron extraction [10].

Here we summarize the most important results, which provide important recommendations for the design, before reporting on results for the two-openings model, and with the study of different shapes of the moderator vessel.

- **Ortho-para deuterium fraction.** A 100% orthodeuterium composition gives 7 % higher CN intensity

than the natural composition (67 % ortho - 33% para). It may therefore be beneficial to use a catalyzer to increase the fraction of orthodeuterium.

- **Temperature effect.** A comparison of intensities was performed with scattering kernels at different temperatures, ranging from 19 K to 23 K, for a composition of (67% ortho - 33% para). The results indicate that the lower the temperature, the higher the intensity. A temperature of 20 K gives an intensity 7 % higher than at 23 K. It is therefore recommended to run at a temperature closer to 20 K.
- **Top premoderator thickness.** The top premoderator (i.e. the water layer between moderator and target) was found to have an ideal thickness of approximately 3 cm.
- **Bottom premoderator thickness.** The bottom premoderator (i.e. the water layer below the moderator, between moderator and reflector) has an ideal thickness of approximately 1 cm.
- **Radial premoderator thickness.** The radial premoderator should be 1 cm thick. An interesting effect was observed, that there is a large (28%) difference between having 1 cm water layer, and having no layer at all. The reason for this effect may require further investigation.
- **Size of emission window.** For a given, fixed moderator size, the intensity increases linearly with the height of the emission window opening, as expected.
- **MgH<sub>2</sub> as side and bottom premoderator.** In the cylindrical configuration considered, there is no gain in using a MgH<sub>2</sub> side and bottom layer instead of the water layer.
- **Use of HD.** With the tests performed so far, little (if any) gain in intensity is observed using a small amount of hydrogen in the liquid deuterium.
- **Intensity vs moderator size for a fixed 24×24 cm<sup>2</sup> opening.** The general trend observed is that the intensity is increased with the moderator size.
- **Reentrant hole.** A preliminary study of the effect of a reentrant hole on the intensity of a 10×10 cm<sup>2</sup> emission window indicated strong increases, at the level of 30 % in the intensity. A box-shaped reentrant hole was found a preferable option over the wedge-shaped reentrant hole after assessing the neutronic performance of both options.
- **Be filter/reflector.** A first study of the effect of a Be filter/reflector on the intensity was performed. The study was done also with two openings. The first results, later investigated in more detail, indicate very promising gains, especially for the NNBAR experiment.

### 2.3.3 Design optimization

The design of the cold source is extremely important, as two objectives must be achieved: first, to provide high-intensity cold beams to the experiments; second, to serve as primary source for a secondary VCN or UCN source. Therefore, the following design study of the cold source was performed throughout the whole duration of the HighNESS project.

### 2.3.4 First iteration

For the first baseline model to be sent to the engineering team (WP5), it was selected the box-shaped geometry, which was found to have better neutronic performance than the cylindrical-shaped moderator. An alternative box-shaped geometry was analyzed in [10], and, while the performance was comparable to the selected geometry, the heat load was significantly higher, and therefore it was discarded.

For the selection of the dimensions, among the three optimization criteria chosen for input into the optimization code Dakota [18] (sum of intensities, sum of brightness, and NNBAR intensity), it was selected the sum of brightness. The reason for this choice is that, for a fixed dimension of the emission window (as was the case in all these optimizations), the sum of brightness gives equal weights to NNBAR and WP7, and is the de facto equivalent to optimizing for intensity, when the size of the window is fixed. However, among the many results provided by Dakota, with the criteria of maximization of the sum of brightness, it was selected the one that gives more intensity to NNBAR, while still having a high intensity to WP7. Such geometry has the following parameters:

The Be filter was introduced into this model adjacent to the NNBAR and WP7 emission surfaces as an efficient reflector of neutrons with wavelengths below about 4 Å leading to a considerable gain in cold

neutron intensity (see Section 2.3.7).

The dimensions of the moderator are  $45\text{ cm} \times 47\text{ cm} \times 24\text{ cm}$  for width (parallel to the proton beam), length (perpendicular to the proton beam) and height, and two  $11\text{ cm}$  thick Be filters on both the NNBAR and WP7 sides.

For this configuration, the NNBAR intensity for neutrons above  $> 4\text{ \AA}$  is  $6.89 \times 10^{15}$  and for WP7 intensity for the same energy range is  $2.50 \times 10^{15}$ , with heat load of  $56.4\text{ kW}$ . This model is illustrated in Figure 20.

Below is the description of this “1st iteration” model of the LD<sub>2</sub> moderator.

**A.** The LD<sub>2</sub> moderator is represented by a rectangular vessel made of aluminum. Its inner dimensions are:

- 450 mm long in the proton beam direction (“width”),
- 470 mm long in the direction transverse to proton beam direction (“length”),
- 240 mm long in the vertical direction (“height”).

In neutronics calculations, the thickness of the vessel Al walls was set to 3 mm for the sake of consistency and comparison with work on the upper moderator. The vessel itself is filled with liquid ortho-deuterium at 20 K and the cold Be filters are immersed in deuterium.

**B.** There are two openings, both perpendicular to the incoming proton beam, but in opposite directions:

- NNBAR opening serving the North-west (NW) sector (see Figure 6);
- WP7 opening serving the defined South-east (SW) sector (see Figure 6).

The NNBAR opening has an emission surface of 400 mm width by 240 mm height, while the WP7 opening has an emission surface of 150 mm width by 150 mm height. The geometric centers of both emission surfaces and of the LD<sub>2</sub> moderator are situated at the same level, -237 mm below the center of the spallation target.

The emission surfaces are covered from the inside by rectangular cold Be filters. The filters are 110 mm thick each, while their widths and heights correspond to those of their respective emission surfaces. Cold Be filters are in direct contact with deuterium, however, it is important to note that the bulk temperature of cold Be filters is not required to be 20 K: as long as their temperature is kept below about 80 K, they will provide the expected performance increase.

**C.** The LD<sub>2</sub> moderator is placed inside a “standard” moderator plug, thus, surrounded by the following layers:

- 3 mm thick Al vessel around LD<sub>2</sub> and Be filter;
- 5 mm vacuum gap around the Al vessel (engineering constraint);
- 3 mm thick Al walls surrounding the H<sub>2</sub>O premoderator and Be reflector (engineering constraint);
- 10 mm thick layer of H<sub>2</sub>O below and on the sides to serve as a premoderator, as a result of the neutronic optimization,
- 25 mm H<sub>2</sub>O layer above (between the moderator and the target), as a result of the neutronic optimization
- Be reflector below and on the side to serve as reflector, with as much volume as possible.

The materials in the list above (Al, H<sub>2</sub>O, Be) are at ambient temperature.

**D.** Heat load on cryogenic parts of the MR plug:

The summary of the expected performances, integrated over various wavelength ranges, is shown in Table 3.

**Table 3:** Neutronic performance and characteristics of the model from first iteration of cold moderator. Brightness and intensity integrated over different wavelength ranges (NNBAR and WP7 openings) and compared with the upper moderator. The values for the upper moderator are from Ref [19]. To calculate the intensity we considered the following size of emission windows: NNBAR:  $960 \text{ cm}^2$ ; WP7:  $225 \text{ cm}^2$ ; upper moderator:  $42 \text{ cm}^2$ . The heatload on Be filter accounts for both the contribution at NNBAR and WP7 openings. The moderator volume is the sum of volume of the  $\text{LD}_2$  box and Be filter.

	BRIGHNESS [ $\text{n}/\text{cm}^2/\text{s}/\text{sr}$ ]		
	$> 2 \text{\AA}$	$> 4 \text{\AA}$	$> 10 \text{\AA}$
NNBAR	$9.11 \times 10^{12}$	$7.04 \times 10^{12}$	$5.51 \times 10^{11}$
WP7	$1.45 \times 10^{13}$	$1.08 \times 10^{13}$	$8.13 \times 10^{11}$
upper moderator	$5.3 \times 10^{13}$	$1.7 \times 10^{13}$	$9.9 \times 10^{11}$
	INTENSITY [ $\text{n}/\text{s}/\text{sr}$ ]		
	$> 2 \text{\AA}$	$> 4 \text{\AA}$	$> 10 \text{\AA}$
NNBAR	$8.74 \times 10^{15}$	$6.76 \times 10^{15}$	$5.29 \times 10^{14}$
WP7	$3.26 \times 10^{15}$	$2.42 \times 10^{15}$	$1.83 \times 10^{14}$
upper moderator	$2.2 \times 10^{15}$	$7.0 \times 10^{14}$	$4.2 \times 10^{13}$
NNBAR FOM	$3.00 \times 10^{17} [\text{n}/\text{s}/\text{sr} \times \lambda^2]$		
WP7 FOM	$2.96 \times 10^{15} [\text{n}/\text{s}/\text{sr}]$		
Heatload on $\text{LD}_2$ moderator	$29.3 [\text{kW}]$		
Heatload on Be filter	$20.0 [\text{kW}]$		
Heatload on Al vessel	$7.1 [\text{kW}]$		
Total heatload	$56.4 [\text{kW}]$		
Moderator volume	$50.8 [\text{liters}]$		

### 2.3.5 Second iteration

In the first iteration, all the optimizations and calculations were done where the FOM was the intensity for neutrons above  $4 \text{\AA}$ . This was a FOM meant to generally target cold neutrons in the early optimization steps. The second round of optimization was performed using the more elaborate FOMs, cf. Table 2. Moreover, a reentrant hole (REH) was introduced at the emission surface of the WP7 opening replacing the Be filter, providing a considerable gain in cold neutron intensity and brightness (see Section 2.3.7)).

The optimization is described in detail in [10].

The design of this moderator optimized according to the procedure outlined above gives the intensity of the source at the NNBAR side, integrated above  $4 \text{\AA}$  of  $6.7 \times 10^{15} \text{ n/s/sr}$ . This is the intensity of the emission window of  $24 \times 40 \text{ cm}^2$ , for 5 MW of beam power (i.e. 2 GeV for 2.5 mA average proton current). The intensity at the WP7 side is lower, because of the smaller size of the opening, although it has a greater brightness. For a beam power of 2 MW (800 MeV for 2.5 mA average proton beam current) the intensity is simply a factor of 2.5 lower, because as shown in Figure 32, the difference in emitted spectra from the moderator between 800 MeV and 2 GeV proton beam is negligible. Therefore, at 2 MW the intensity of the moderator is  $2.7 \times 10^{15} \text{ n/s/sr}$ .

To have an idea of what these numbers mean in terms of performance of the experiments intended to use this moderator, we can compare with the original calculations done for the NNBAR experiment in [20]: at 5 MW beam power, the intensity was predicted to be  $2.9 \times 10^{15} \text{ n/s/sr}$ . That calculation was the basis for the original estimate of the performance increase of NNBAR compared to the ILL measurement [21]. It would therefore mean that the NNBAR performance estimate of this second iteration of the moderator at 2 MW is equivalent to the previous estimate for 5 MW. However, a large part of this gain is due to the increase in the size of the emission window (nearly a factor 2 increase).

A summary of the expected performances for this iteration, integrated in different wavelength ranges, is shown in Table 4.

**Table 4:** Neutronic performance and characteristics of the model from second iteration of cold moderator. Brightness and intensity integrated over different wavelength ranges (NNBAR and WP7 openings) and compared with the upper moderator. The values for the upper moderator are from Ref [19]. To calculate the intensity we considered the following size of emission windows: NNBAR: 960 cm<sup>2</sup>; WP7: 225 cm<sup>2</sup>; upper moderator: 42 cm<sup>2</sup>. The moderator volume is the sum of volume of the LD<sub>2</sub> box and Be filter.

BRIGHNESS [n/cm <sup>2</sup> /s/sr]			
	> 2 Å	> 4 Å	> 10 Å
NNBAR	$8.87 \times 10^{12}$	$6.95 \times 10^{12}$	$5.77 \times 10^{11}$
WP7	$1.79 \times 10^{13}$	$1.07 \times 10^{13}$	$9.16 \times 10^{11}$
upper moderator	$5.3 \times 10^{13}$	$1.7 \times 10^{13}$	$9.9 \times 10^{11}$
INTENSITY [n/s/sr]			
	> 2 Å	> 4 Å	> 10 Å
NNBAR	$8.52 \times 10^{15}$	$6.67 \times 10^{15}$	$5.54 \times 10^{14}$
WP7	$4.03 \times 10^{15}$	$2.42 \times 10^{15}$	$2.06 \times 10^{14}$
upper moderator	$2.2 \times 10^{15}$	$7.0 \times 10^{14}$	$4.2 \times 10^{13}$
NNBAR FOM	$3.03 \times 10^{17}$ [n/s/sr × λ <sup>2</sup> ]		
WP7 FOM	$3.68 \times 10^{15}$ [n/s/sr]		
Heatload on LD <sub>2</sub> moderator	29.8 [kW]		
Heatload on Be filter	15.1 [kW]		
Heatload on Al vessel	7.2 [kW]		
Total heatload	52.1 [kW]		
Moderator volume	49.6 [liters]		

### 2.3.6 Third iteration

A third optimization was performed using Dakota with the model from the second iteration updated by the engineering constraint of requiring a 2.5% volume of aluminum in LD<sub>2</sub> to account for flow guides and support structures. Moreover, the third neutronic optimization was also motivated by an attempt to reduce the heat load in the moderator while preserving or even improving its performance. The temperature of LD<sub>2</sub> in the moderator vessel was increased from 20 K to 22 K.

For the purpose of third iteration of optimisation, a parametric model of the moderator was used with the following variable parameters:

- Moderator length;
- Moderator width;
- Be filter thickness;
- Reentrant hole depth.

The height of the moderator was fixed at 24 cm. The listed parameters (see Figure 21) were optimised with respect to NNBAR and WP7 FOMs. A multi-objective genetic algorithm (MOGA) [22] was implemented resulting in the set of solutions over a wide range of NNBAR and WP7 FOMs (see Figure 22). In the subsequent analysis of possible solutions, NNBAR and WP7 FOMs vs moderator length (see Figure 24), moderator width (see Figure 25), Be filter thickness (see Figure 26) and the depth of reentrant hole (see Figure 27) were plotted. A subsequent analysis of these figures resulted in setting the following limits on variable parameters used in the optimisation to maximize NNBAR and WP7 FOMs:

- 45 cm ≤ moderator length ≤ 50 cm;
- 40 cm ≤ moderator width ≤ 45 cm;
- 11 cm ≤ Be filter thickness ≤ 15 cm;
- 9 cm ≤ depth of reentrant hole ≤ 15 cm;

- Gain wrt baseline  $\geq 1$ .

A smaller subset of solutions was then filtered out based on these limits (see Figure 23). The goal was to select a solution that is close to the utopia point (idealized point with highest recorded performance for both NNBAR and WP7 FOMs), and which also minimizes the moderator volume in order to reduce heatload. In the end, this combination of parameters, was selected for the LD<sub>2</sub> moderator:

- Moderator length = 48 cm;
- Moderator width = 41 cm;
- Be filter thickness = 13 cm;
- Reentrant hole depth = 10 cm;
- Volume of LD<sub>2</sub> in moderator = 32.2 l.

For reference, we can also compare the intensity of the lower cold moderator from this neutronic optimization with the model of upper moderator. The upper moderator has a higher brightness, however, because of the smaller size, its intensity is lower. This can be seen in Figure 28(a) and (b) which show the time-averaged brightness and intensity respectively for the thermal and cold neutrons measured at the NNBAR and WP7 openings including the time-averaged brightness and intensity calculated for the upper moderator. For the upper moderator, the size of the emission window depends on the angle of extraction: at the NNBAR location, an emission window with a surface of about 42 cm<sup>2</sup> would be available, and this give an intensity of the upper moderator above 4 Å of  $7 \times 10^{14}$  n/s/sr (i.e. 10 times lower than for the NNBAR opening of the lower moderator).

After completion of the third iteration of optimisation, the model of cold moderator was delivered to the engineering team, WP5 where a thorough engineering study was conducted.

A summary of the expected performances, integrated in different wavelength ranges, is shown in Table 5. There is a decrease in NNBAR and WP7 FOMs in comparison to the model from second iteration of neutronic optimisation (see Table 4) due to increase in temperature of LD<sub>2</sub> from 20 K to 22 K and the presence of 2.5 vol% Al in LD<sub>2</sub>.

### 2.3.7 Effect of Be filter and reentrant hole

A quantification of the effect of the Be filter and reentrant hole on the neutronic performance was done in the third iteration of optimisation. Figure 26a clearly shows that the NNBAR side benefits from the presence of the Be filter. The gain in the NNBAR FOM observed when comparing the case with no Be filter (Be filter thickness = 0 cm) and the cases with Be filters having thicknesses between about 10 and 15 cm was about 30%. Similarly, the WP7 side benefits from the presence of reentrant hole (see Figure 27a). In this case, the WP7 FOM increases by about 20% for reentrant holes with depths between about 10 and 15 cm.

### 2.3.8 Shape of the reentrant hole

The development of the cold moderator continued with a study of the impact of different shapes of reentrant holes. More specifically, the initially rectangular shaped reentrant hole was replaced by, for example, a wedge-shaped reentrant hole with variable depth (see Figure 29). Subsequently, the neutronic performance on the WP7 side was estimated with this shape of reentrant hole for the beamport adjacent to S11 (S" stands for South Sector, and "11" refers to the number of the beamport. In this case, it is the beamport perpendicular to both the incoming proton beam and the emission surface of the moderator at the WP7 side.), namely the S9 beamport with an offset of 6° with respect to S11 (see Figure 30 for a depiction of the beamport positions). The calculated values of the WP7 FOM at various reentrant hole depths are shown in Figure 31. The maximal gain with respect to the baseline rectangular reentrant hole at the S9 beamport was of about 5%, but with a penalty to the WP7 FOM for the S11 beamport of about 3%. Other shapes of reentrant holes were investigated, but with a consistent result that the gain for the off-axis beamport S9 was only marginal with a small loss for the on-axis S11 beamport at the same time. Therefore, the shape of the reentrant hole was kept rectangular also for this round of optimization.

**Table 5:** Neutronic performance and characteristics of the model from third iteration of cold moderator. Brightness and intensity integrated over different wavelength ranges, for the third iteration of lower moderator (NNBAR and WP7 openings) and compared with the upper moderator. The values for the upper moderator are from [19]. To calculate the intensity we considered the following emission window sizes: NNBAR: 960 cm<sup>2</sup>; WP7: 225 cm<sup>2</sup>; upper moderator: 42 cm<sup>2</sup>. The moderator volume is the sum of volume of the LD<sub>2</sub> box and Be filter.

BRIGHNESS [n/cm <sup>2</sup> /s/sr]			
	> 2 Å	> 4 Å	> 10 Å
NNBAR	$7.89 \times 10^{12}$	$6.07 \times 10^{12}$	$4.46 \times 10^{11}$
WP7	$1.60 \times 10^{13}$	$8.76 \times 10^{12}$	$6.89 \times 10^{11}$
upper moderator	$5.3 \times 10^{13}$	$1.7 \times 10^{13}$	$9.9 \times 10^{11}$
INTENSITY [n/s/sr]			
	> 2 Å	> 4 Å	> 10 Å
NNBAR	$7.57 \times 10^{15}$	$5.83 \times 10^{15}$	$4.28 \times 10^{14}$
WP7	$3.60 \times 10^{15}$	$1.97 \times 10^{15}$	$1.55 \times 10^{14}$
upper moderator	$2.2 \times 10^{15}$	$7.0 \times 10^{14}$	$4.2 \times 10^{13}$
NNBAR FOM	$2.51 \times 10^{17}$ [n/s/sr × λ <sup>2</sup> ]		
WP7 FOM	$3.22 \times 10^{15}$ [n/s/sr]		
Heatload on LD <sub>2</sub> moderator	28.5 [kW]		
Heatload on Be filter	19.5 [kW]		
Heatload on Al vessel	7.3 [kW]		
Total heatload	55.3 [kW]		
Moderator volume	45.0 [liters]		

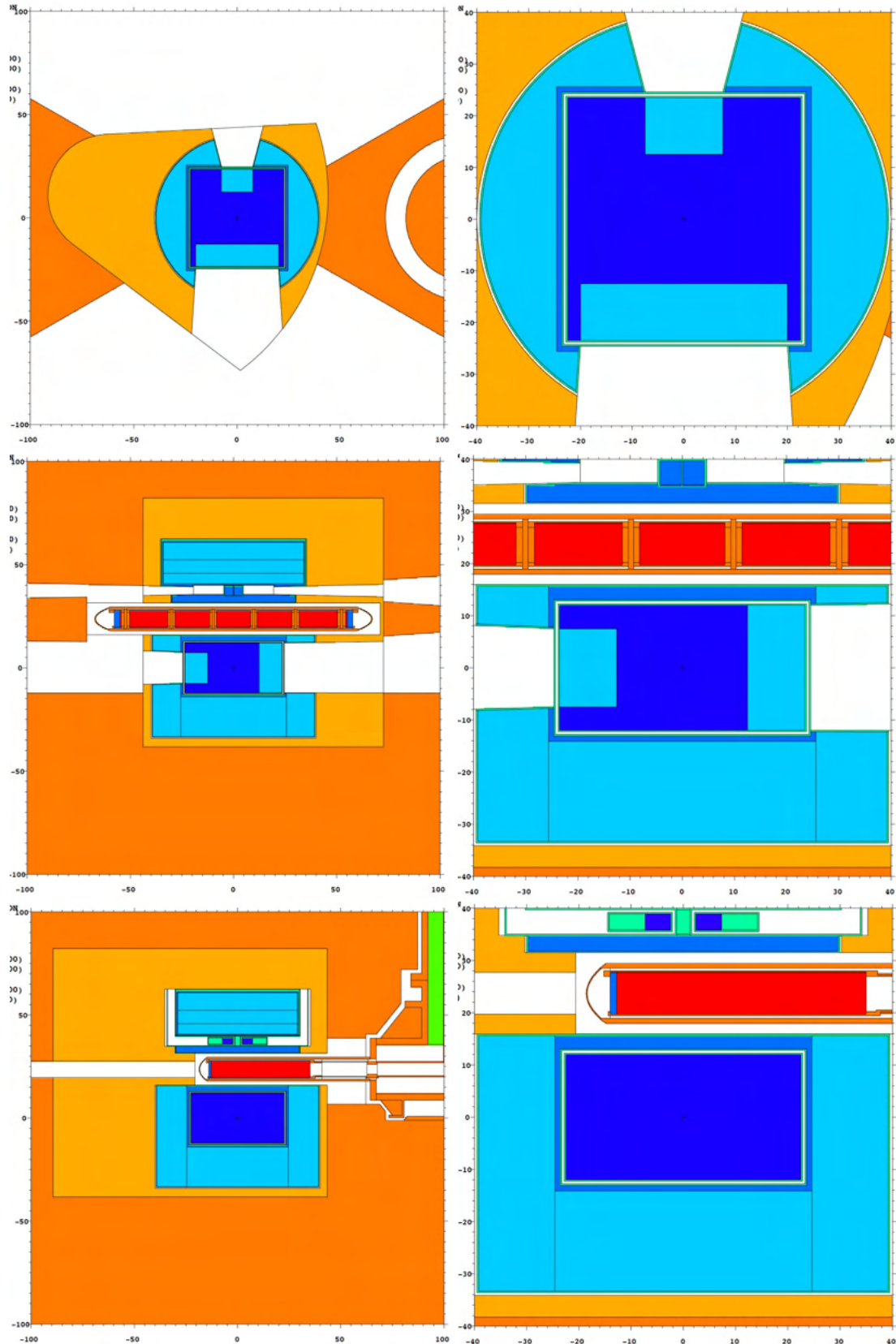


**Figure 20:** Graphical representation of baseline design for the LD<sub>2</sub> moderator submitted to WP5 for engineering studies. The color codes are the following: orange: steel (twister frame, inner shielding, etc); dark blue: liquid ortho-deuterium; blue: light water; light blue: beryllium; green: aluminum. Note that cold Be filters and ambient Be reflector are shown using the same color; the same note applies to Al.

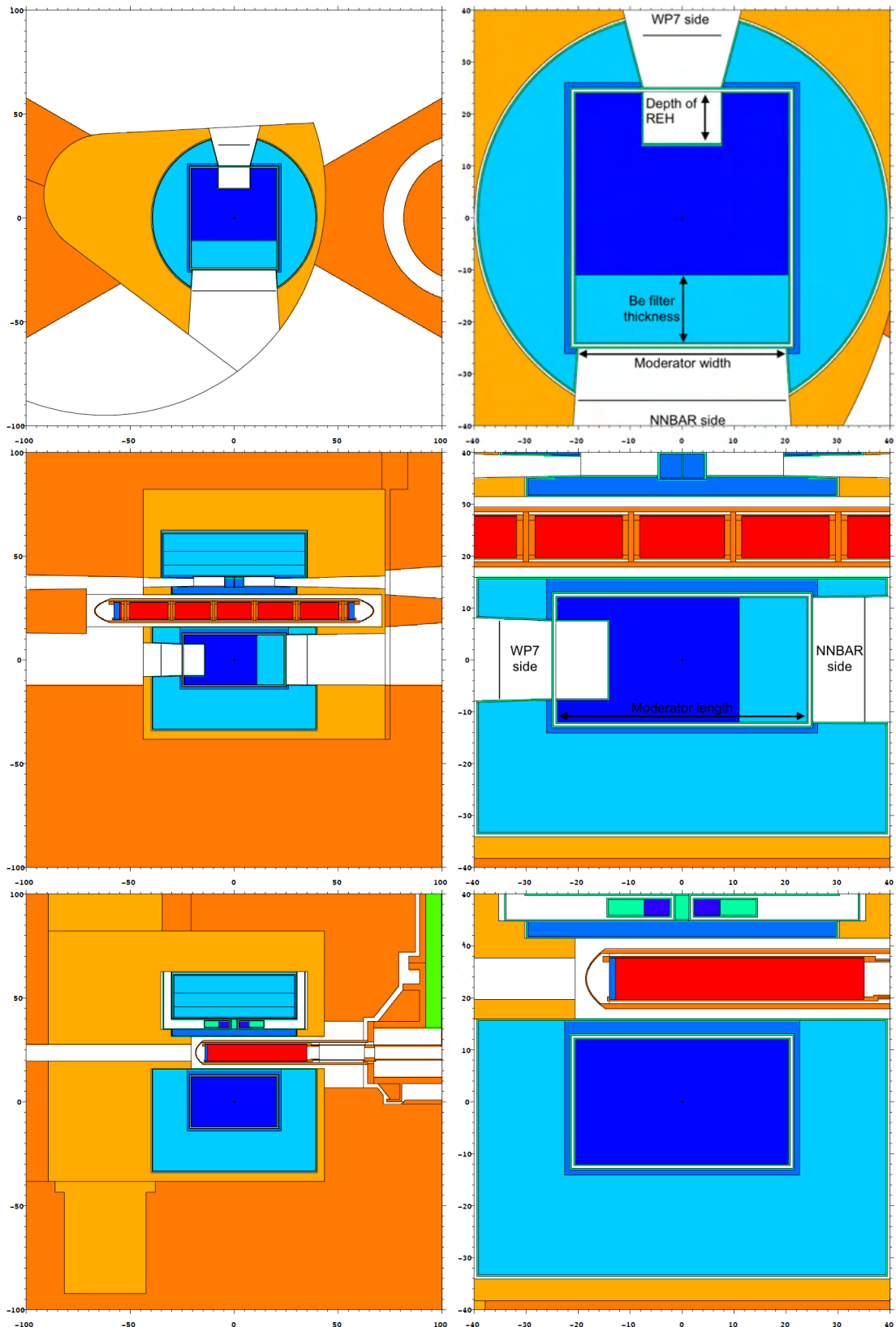


**Figure 21:** Graphical representation of design for LD<sub>2</sub> moderator after the third iteration. The color codes are the following: orange: steel (twister frame, inner shielding, etc); dark blue: liquid ortho-deuterium; blue: light water; light blue: beryllium; green: aluminum. Note that cold Be filters and ambient Be reflector are shown using the same color; the same note applies to Al.

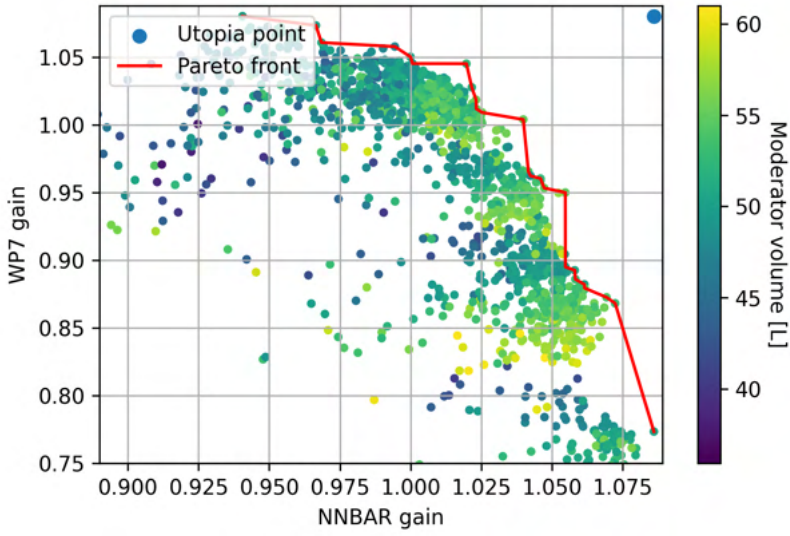


**Figure 22:** Third iteration optimization: each point represents the gain with respect to NNBAR and WP7 figures of merit of the model from second neutronic iteration for a given set of parameters. The Pareto front was fitted through points closest to Utopia point, idealized point with highest possible NNBAR and WP7 gains. The aim is to select a model with parameters that lies as close as possible to Utopia point. The moderator volume is the sum of volume of LD<sub>2</sub> box and Be filter.

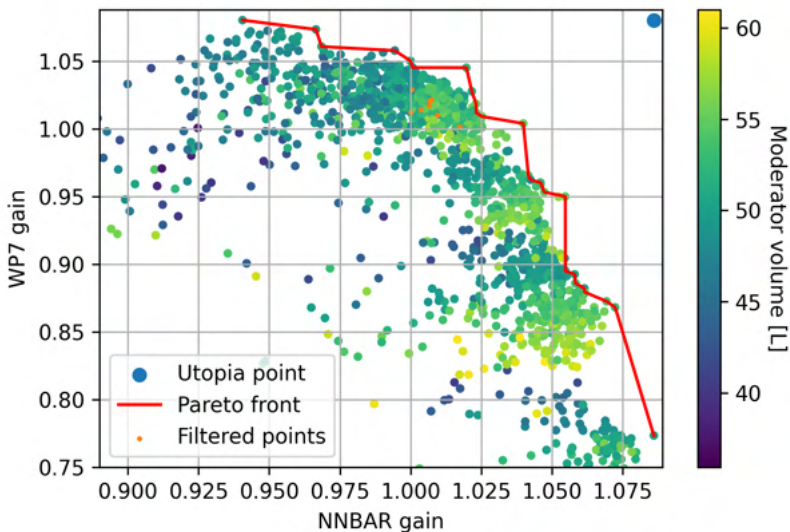


**Figure 23:** Selected models (yellow circles) from the optimisation according after applying the limits on moderator parameters.

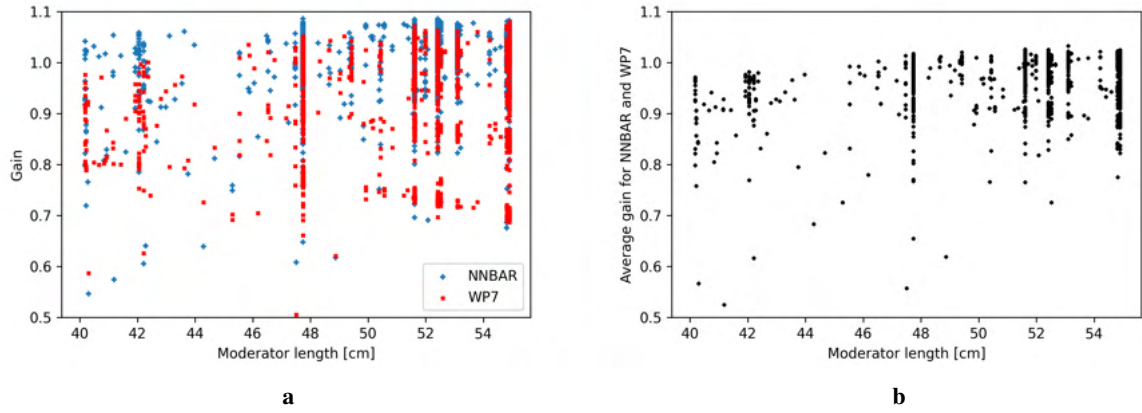


**Figure 24:** Performance of models with respect to moderator length. (a) Gain in NNBAR and WP7 FOM with respect to the baseline model (b) Average gain in NNBAR and WP7 FOM with respect to the baseline model.

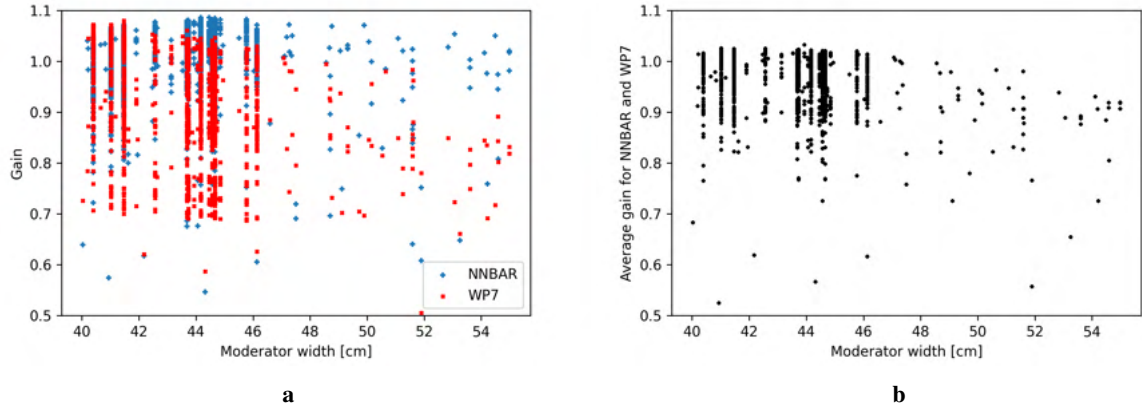


**Figure 25:** Performance of models with respect to moderator width. (a) Gain in NNBAR and WP7 FOM with respect to the baseline model (b) Average gain in NNBAR and WP7 FOM with respect to the baseline model.

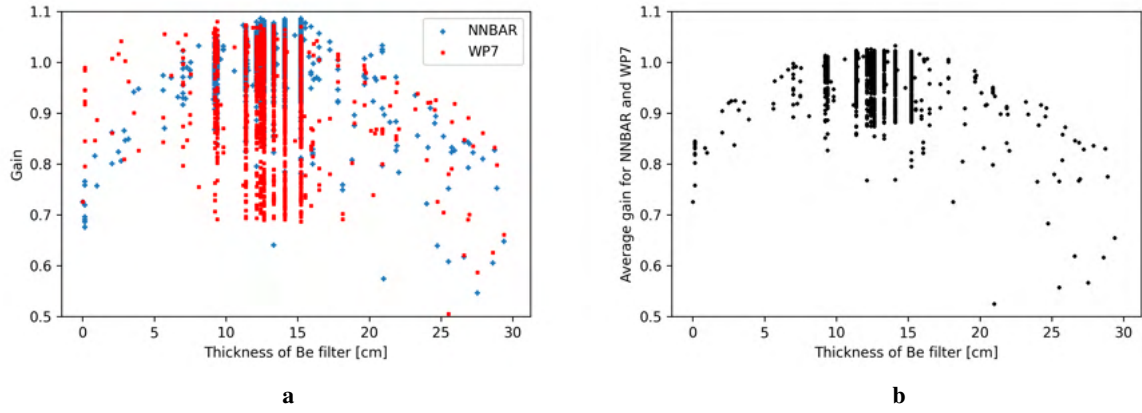


**Figure 26:** Performance of models with respect to Be filter thickness. (a) Gain in NNBAR and WP7 FOM with respect to the baseline model (b) Average gain in NNBAR and WP7 FOM with respect to the baseline model.

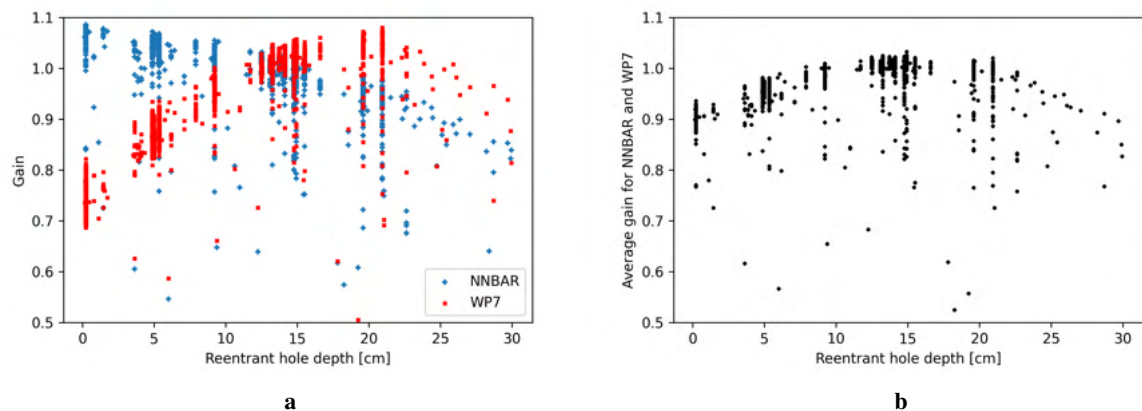
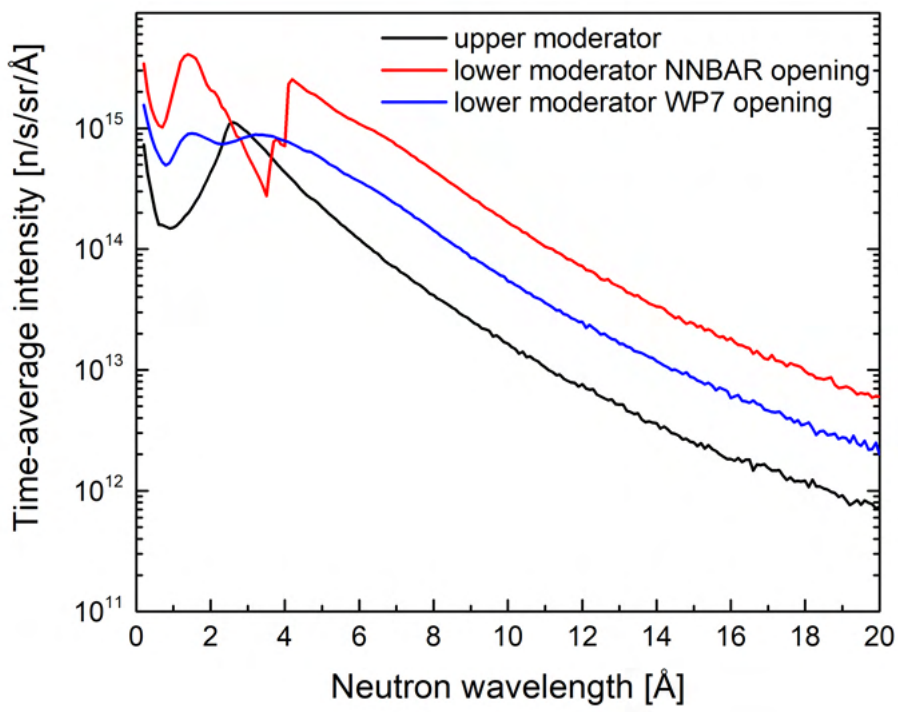
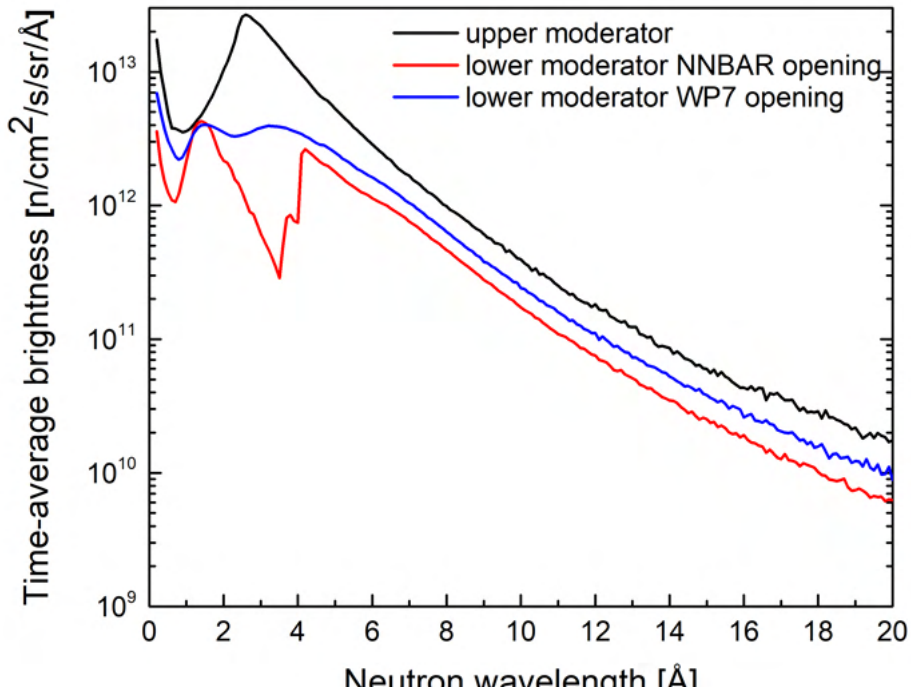


**Figure 27:** Performance of models with respect to the reentrant-hole depth. (a) Gain in NNBAR and WP7 FOM with respect to the baseline model (b) Average gain in NNBAR and WP7 FOM with respect to the baseline model.



(a)



(b)

**Figure 28:** Comparison of neutron spectra for the lower and upper moderators for the third iteration of optimisation. (a) Time-averaged intensity. (b) Time-averaged brightness.

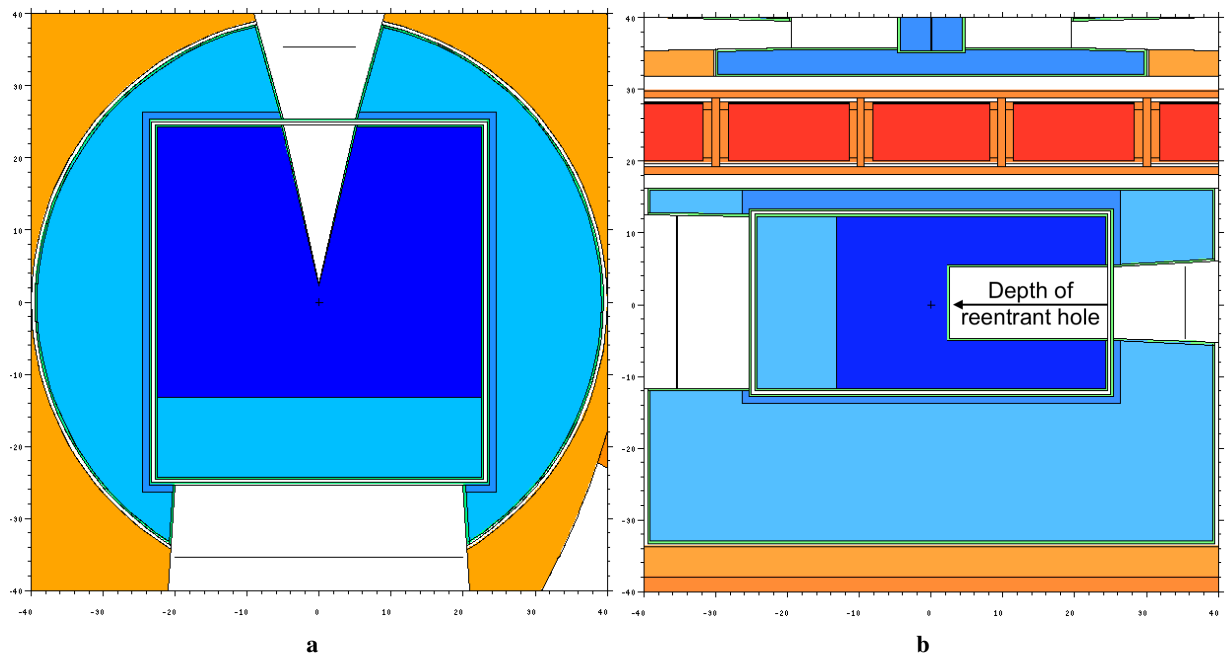


**Figure 29:** Model of the wedge-shaped reentrant hole. (a) Horizontal view of the wedge-shaped reentrant hole. (b) Vertical view of the wedge-shaped reentrant hole.

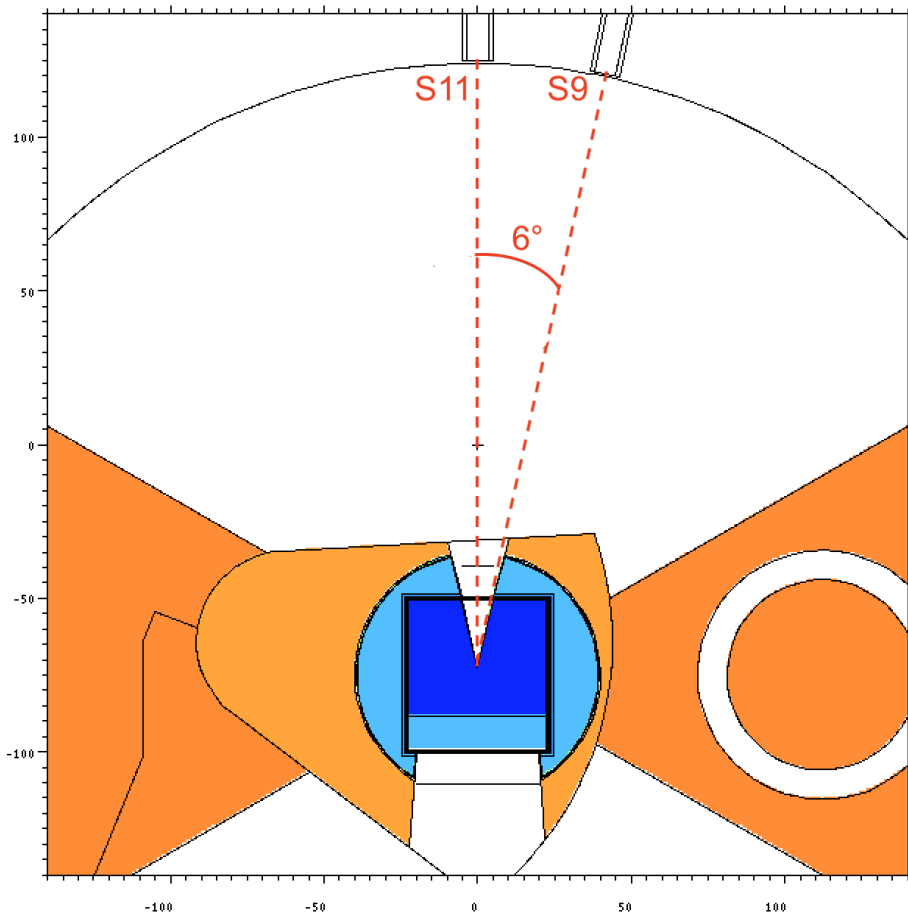


**Figure 30:** Horizontal view of the wedge-shaped reentrant hole and on-axis S11 and off-axis S9 beamports.

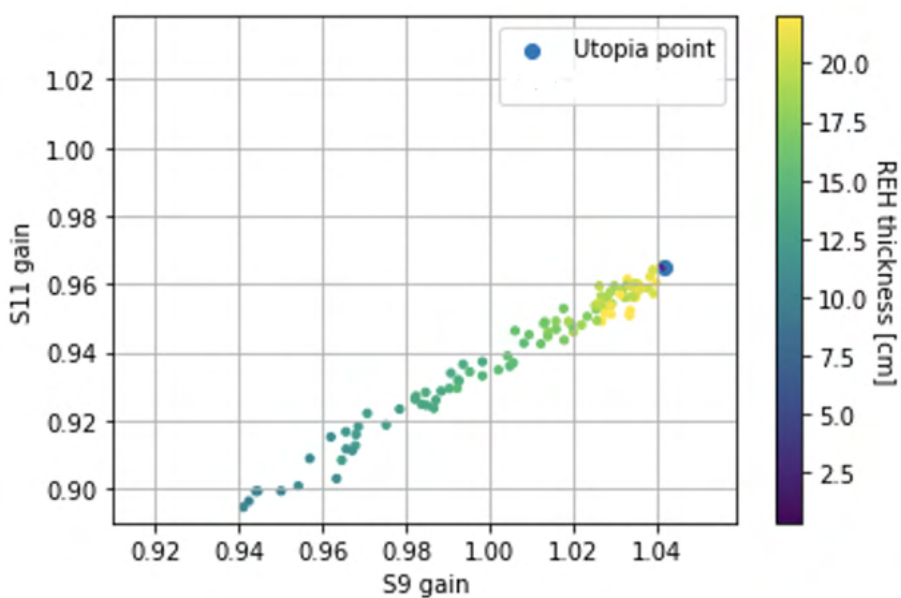


**Figure 31:** Performance of wedge-shaped reentrant hole at different depths.

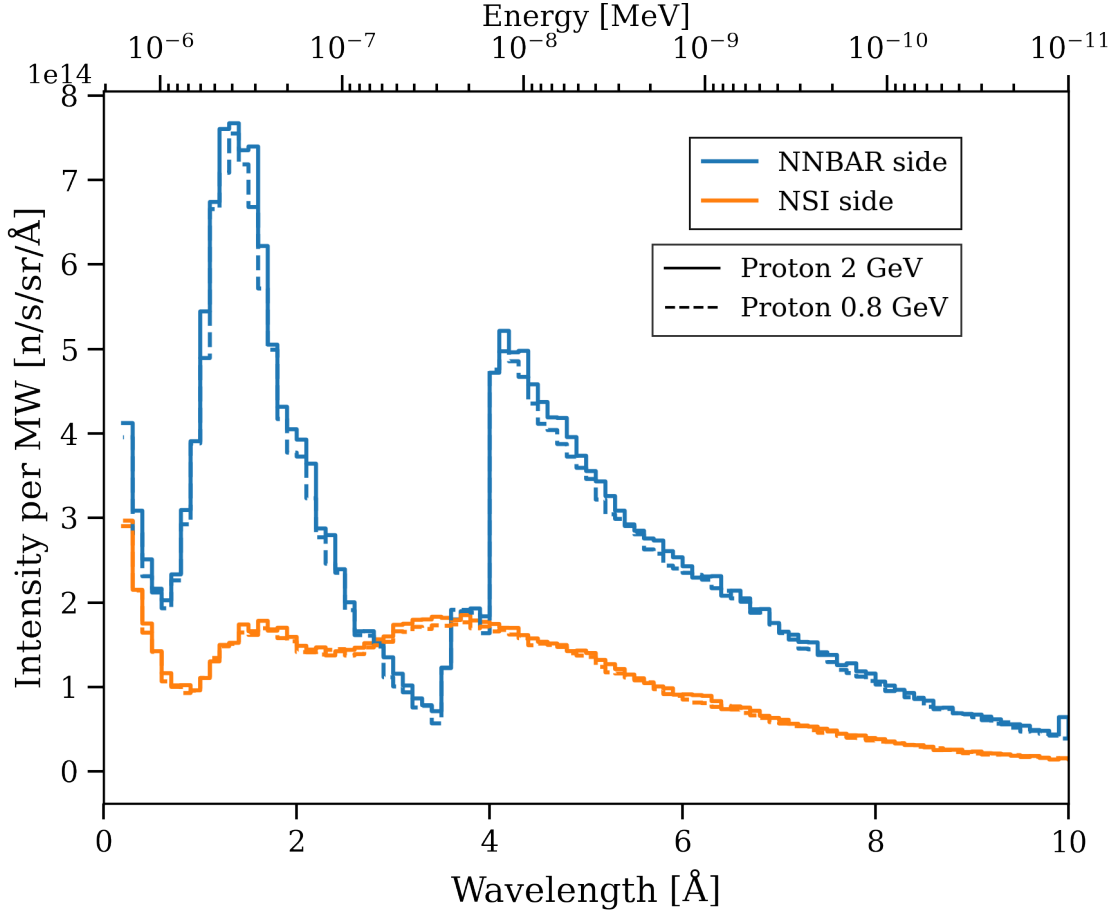


**Figure 32:** Spectra comparison for NNBAR the WP7 neutron-scattering instruments (NSI) sides of the LD<sub>2</sub> using MOGA optimization for protons impinging on the target at 2 GeV (baseline for the design) and 800 MeV, per unit power, respectively.

### 2.3.9 Moderator characterization

The model of the cold moderator from the second neutronic iteration was used to perform a comprehensive moderator characterization. Its characteristics in this context are comparable to the performance of cold moderator from the third iteration.

The energy distribution binned in wavelength for the MOGA optimization is shown in Figure 32 (this was the best-performing optimization approach for a variety of algorithms, for a comparison of these methods see [10].) The baseline case has protons impinging on the target at 2 GeV, and the additional case shows protons at 800 MeV. Both cases are normalized to the accelerator power in MW, respectively 5 and 2 MW. The fact that spectra match for the two openings suggests that lowering the power of the accelerator will not affect the energy distribution besides the obvious drop in absolute intensity.

The main feature of the wavelength distribution on the NNBAR side is the very sharp cut-off at 4 Å due to the Be filter. The peak between 1 Å to 2 Å is not likely due to a thermal peak, but rather a feature introduced by the filter. The thermal and cold peaks are instead clearly visible on the neutron scattering instruments (WP7) opening.

The neutrons spatial distribution coming out of the surface of the moderator was studied with a pinhole-camera tally integrated in MCNP. The pinholes are placed 2 m away from the center of the moderator along the central axis for both openings, while the detectors are 2 m away from the pinholes on the same axis and have dimensions of 50 cm × 50 cm and 30 cm × 30 cm for the NNBAR and WP7 sides, respectively. The results are shown in Figure 33 (NNBAR on the left and WP7 on the right) for three wavelength ranges:  $\lambda < 4 \text{ Å}$ ,  $\lambda > 4 \text{ Å}$ , and  $\lambda > 9 \text{ Å}$ . The distribution of the neutrons is quite different between the two openings. The bigger and shallower NNBAR opening has a nonuniform

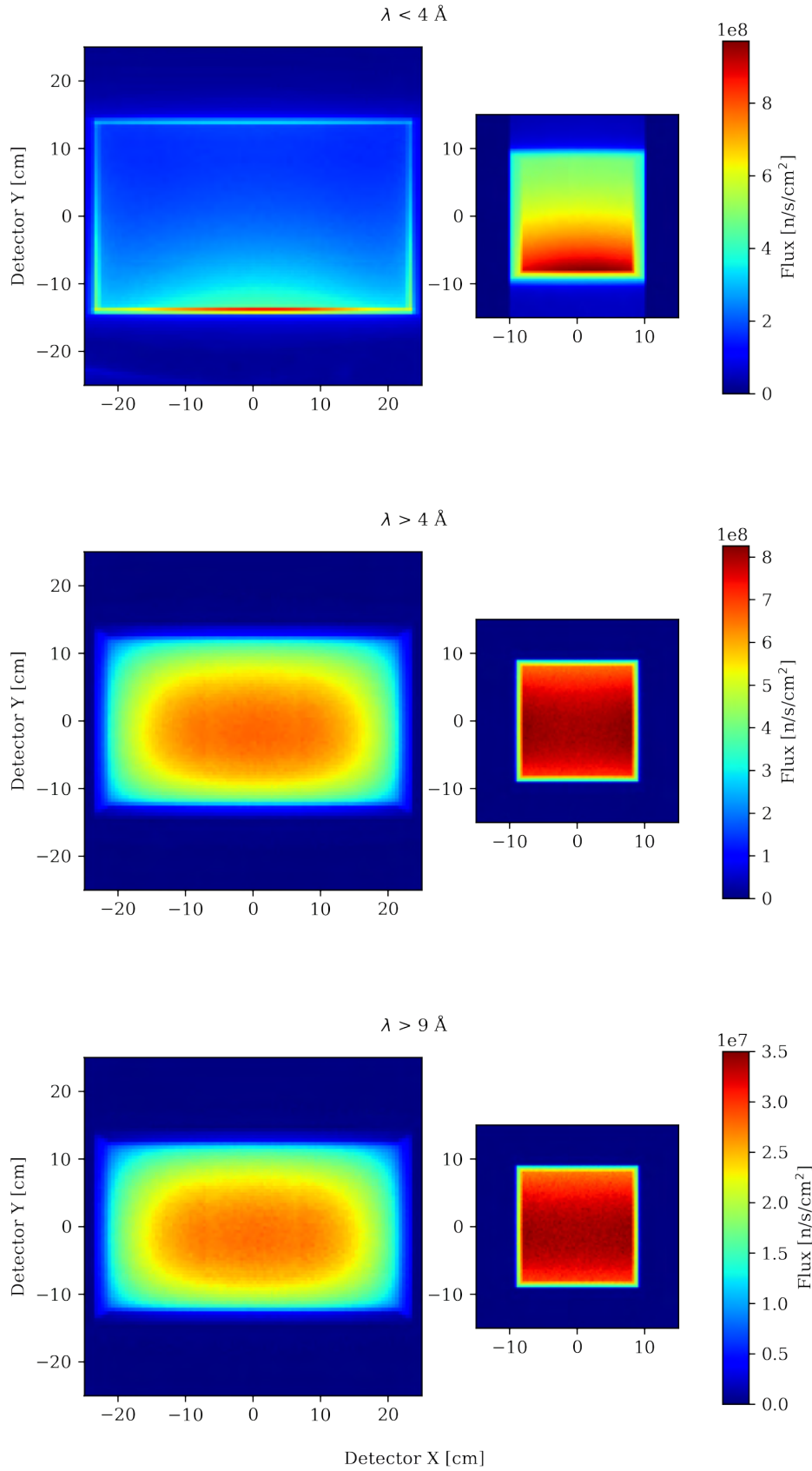


**Figure 33:** Pinhole images of the 24 cm  $\times$  40 cm NNBAR opening (left) and the 15 cm  $\times$  15 cm WP7 opening (right) with filters for neutrons at different energies. The pinholes are placed 2 m away from the center of the moderator along the central axis, while the detectors are 2 m away from the pinholes on the same axis and with the dimensions 50 cm  $\times$  50 cm and 30 cm  $\times$  30 cm for NNBAR and WP7, respectively. The pictures have the same scale and appear inverted along the vertical direction due to the camera obscura effect.

profile along both axes, with a central hot-spot slightly off-centered toward the top of the moderator (the pinhole images appear inverted in the vertical direction). The smaller and deeper opening for the neutron scattering instruments, instead, is a more uniform source. Although the integrated intensity is higher on the NNBAR side, the effective contribution of the neutrons from the corners is quite limited due to current optics design [23]. In any case, the advantage of having such a large opening in the moderator has been established, but further improvement can be made to increase the intensity farther from the center.

Finally, in Figure 34 the pulse shape of the neutrons coming out of the moderator at 2 Å, 4 Å, and 9 Å is presented. The curves were obtained by recording the neutrons crossing outward the moderator surface on the NNBAR side through a SSW card [13]. The neutrons were then filtered in energy using the Monte Carlo Particle Lists (MCPL) interface [15] and binned in elapsed time in ms. The histograms were normalized in order to be comparable and smoothed with Gaussian kernel density estimation. The pulse width is significantly broader than the proton pulse (2.86 ms). This is due to the slow LD<sub>2</sub> thermalization time and will likely impact neutron scattering experiments. In particular, the use of choppers in conventional neutron scattering experiments will certainly lead to a reduction in peak fluxes. On the other hand, for NNBAR there is no foreseen impact since the interesting quantity is the time-averaged flux.

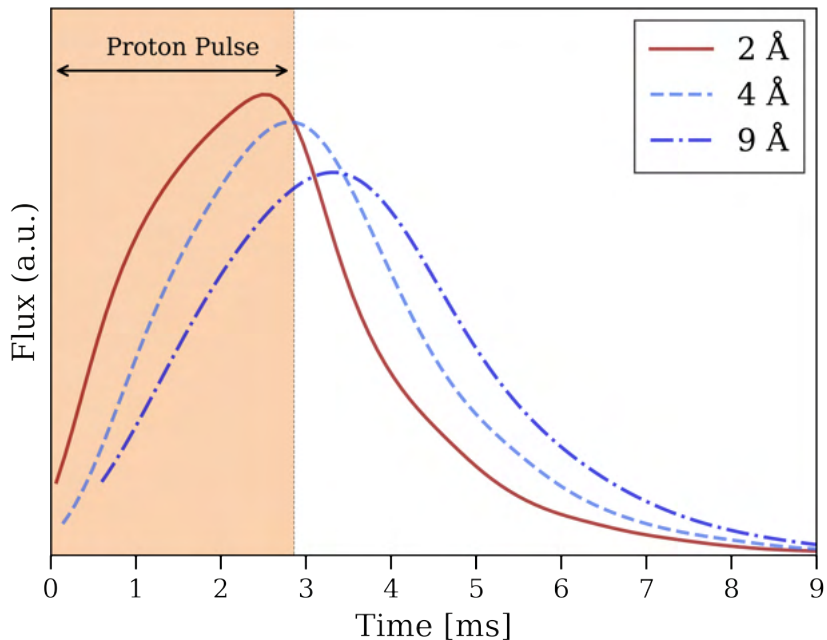


**Figure 34:** Pulse shape of the neutrons coming out of the moderator at 2, 4, and 9 Å. The proton beam impinging on the target lasts 2.86 ms, indicated by the shaded region on the left. The neutrons are binned in elapsed time in milliseconds and the respective histograms are normalized to probability density functions (a.u.) for comparison. The smoothed curves are obtained with Gaussian kernel density estimation.

### 2.3.10 Effects of engineering design on neutronic performance

An engineering design was made based on the optimized neutronic model (see Section 3). In this section, the impact of various engineering solutions on the neutronic performance is analyzed. Two features of the engineering design were found to particularly affect the neutronic performance: first, the large thickness (8 mm) of the Al vessel required for the engineering design of a vessel with flat walls; second, the relatively complex design of the Al flow channels, due to the presence of a reentrant hole on the neutron scattering side.

Additionally, a recommendation came from the engineering designers, that it would be better to place the beryllium outside the LD<sub>2</sub> moderator, for the following reasons: 1) there is a significant reduction

of the heat load which has to be handled by the LD<sub>2</sub> stream inside the moderator when the beryllium is not inside. 2) There was an issue with film boiling in the slit in between the beryllium blocks in the thermomechanical simulations when the blocks are inside the LD<sub>2</sub>. That issue is solved by placing them outside the LD<sub>2</sub> vessel.

Finally, the engineering team suggested a simplification of the flow structure, that would reduce the amount of Al inside the vessel. This implied a change of the shape of the reentrant hole from the square shape, designed by the neutronic team, to a U-shape of the same width (15 cm) but with the height of the moderator vessel (24 cm).

To quantify the effects of these design changes, a set of tests was performed with modifications of the models:

- LD<sub>2</sub> with Al flow guides modeled explicitly, and wall thickness increased from 3 mm to 8 mm (Figure 36).
- Be filter separated from LD<sub>2</sub> moderator (Figure 37).
- Reentrant hole with U-shape and a few parameters slightly changed to streamline the model (Figure 38).
- LD<sub>2</sub> with Al flow guides modeled explicitly, and wall thickness increased from 3 mm to 4 mm (Figure 39).
- rectangular REH is tapered (Figure 40).

The conclusions from this analysis are that a thickness of 8 mm of Al gives too much neutronic penalty and should be reduced. On the other hand, moving the Be filter outside the Al vessel (and envisaging a separate cooling) and using a simplified, U-shape reentrant hole, does not give a large penalty.

**Table 6:** Impact of engineering refinements on neutronic performance, normalized to the optimized LD<sub>2</sub> baseline.

	NNBAR	WP7
Figure 35	100	100
Figure 36	75	77
Figure 37	92	98
Figure 38	91	93
Figure 39	94	93
Figure 40	94	94

The solution to reduce the thickness of Al vessel to 4 mm proposed by WP5 was to round the walls of moderator and to model the U-shaped reentrant hole on the WP7 side to simplify the flow. The WP5 team also provided a detailed CAD model of the LD<sub>2</sub> moderator with Al vessel. It was additionally required to separate LD<sub>2</sub> and Be vessels with a gap of thickness of 5 mm. An MCNP model was designed according to this CAD model (see Figure 44a and Figure 44b). This last step of the design is described in Section 2.4.

## 2.4 Rounded shape model

As a final step of the design of the liquid deuterium moderator, we investigated a model updated following a preliminary engineering study based on the model from third neutronic optimisation of cold moderator (Figures 41 and 42). This study revealed that 8 mm thick Al vessel and additional Al flow guides would be required given the engineering constraints (see model on Figure 36) leading to a significant drop in NNBAR FOM of about 25 % (see Table 6). To reduce this negative impact on the neutronic performance of the cold moderator, it was proposed to round the walls of LD<sub>2</sub> box and Al vessel around it. Moreover, the Be filter and LD<sub>2</sub> box was separated and the shape of reentrant hole was simplified to U-shaped reentrant hole. This allowed reducing the thickness of Al vessel to 4 mm.

We note that there was no time available in the project to perform a full engineering study of this option, and the neutronic design of this model was not optimized. Nevertheless, we report these results

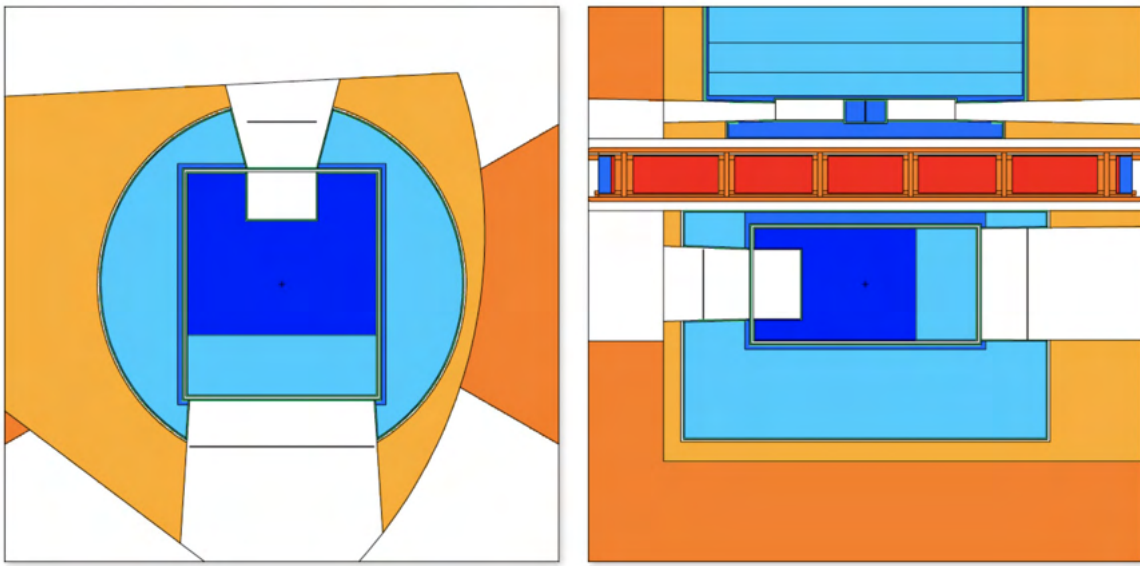


**Figure 35:** Original optimized design for the LD<sub>2</sub> source.

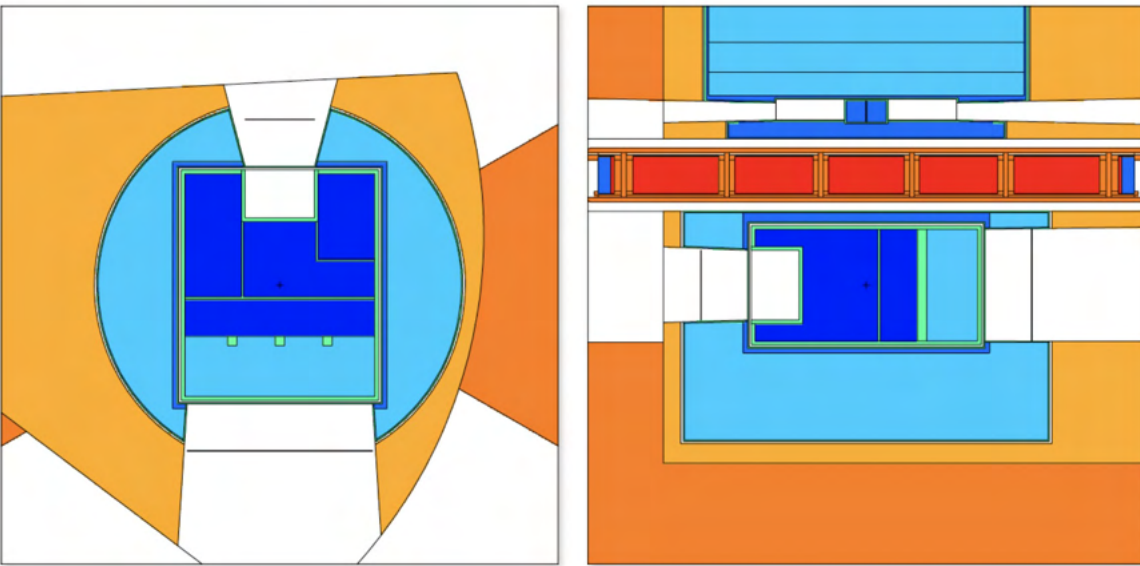


**Figure 36:** As in Figure 35, but Al flow guides modeled explicitly, and wall thickness increased from 3 mm to 8 mm.

in this document since it should be further investigated in future projects.

The MCNP model is shown in Figures 43 and 44. The summary of the expected performances, integrated in different wavelength ranges, is shown in Table 7.

## 2.5 Summary of the cold moderator design

We have successfully designed a cold source with a neutron intensity above 4 Å exceeding the one from the upper moderator by a factor of 10. This accomplishment aligns with one of the primary objectives of HighNESS, which aimed to create a complementary source capable of supporting various experiments where neutron intensity holds greater significance than brightness. This has been achieved using the

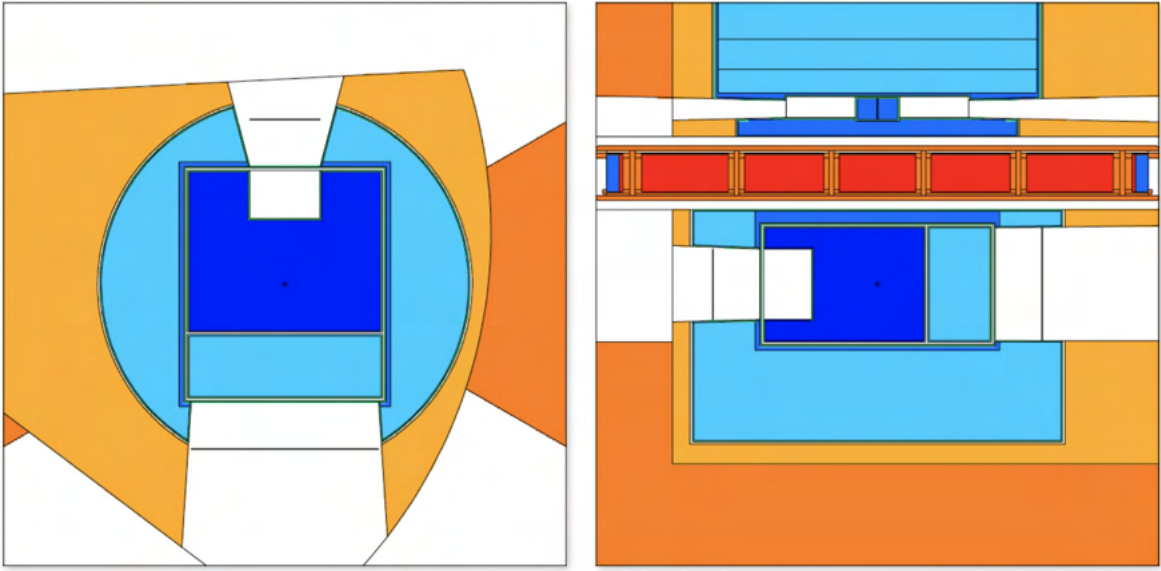


**Figure 37:** As in Figure 35, but Be filter separated from LD<sub>2</sub> moderator.

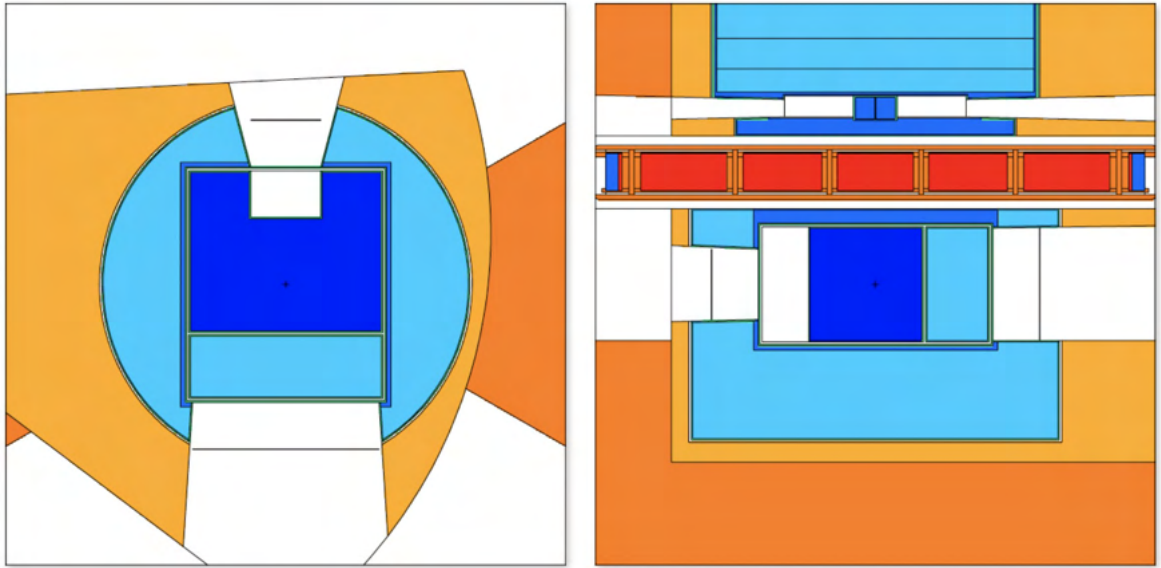


**Figure 38:** As in Figure 37, but with an alternative reentrant hole shape and a few parameters slightly changed to streamline the model.

proven technology of liquid deuterium moderators which are the workhorses at high power research reactors and continuous sources like SINQ<sup>2</sup>. The design of the cold moderator has been refined throughout the whole duration of the project, with several iterations with the engineering teams. Details on the engineering design are provided in the next section. Although an engineering design of the latest model with the rounded shapes has not been performed, due to time constraints, there are strong indications that this approach could be the best one for the cold source and should be further investigated.

---

<sup>2</sup><https://www.psi.ch/en/sinq>

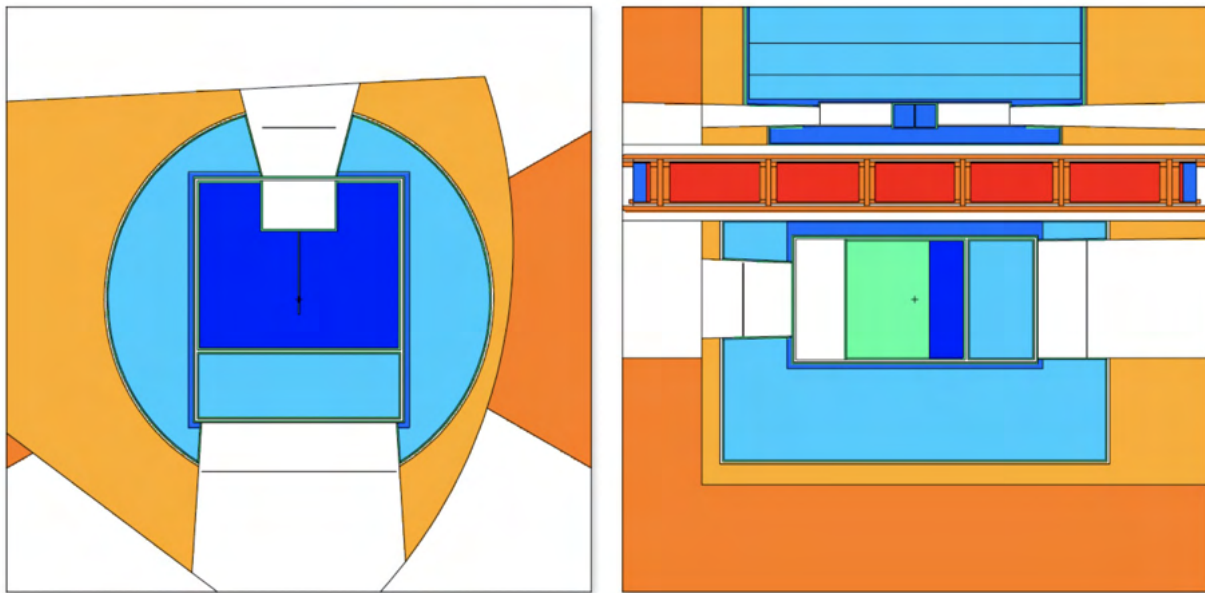


**Figure 39:** As in Figure 38, but Al flow guides modeled explicitly, and wall thickness increased from 3 mm to 4 mm.

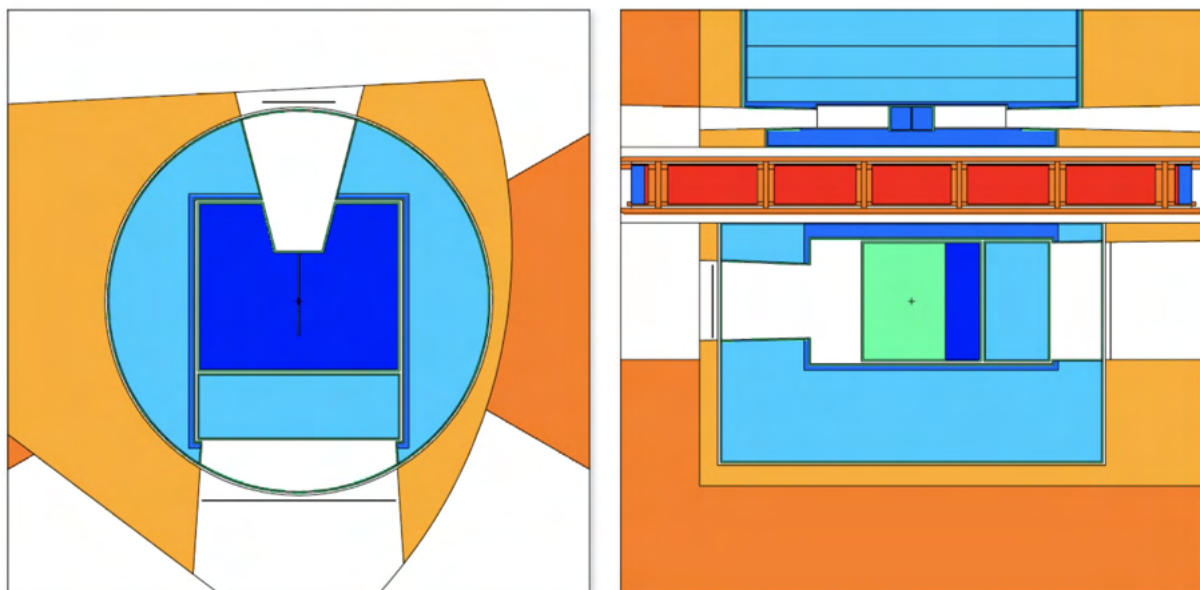


**Figure 40:** As in Figure 39, but rectangular REH is tapered and the geometry is slightly changed to increase the overall performance.

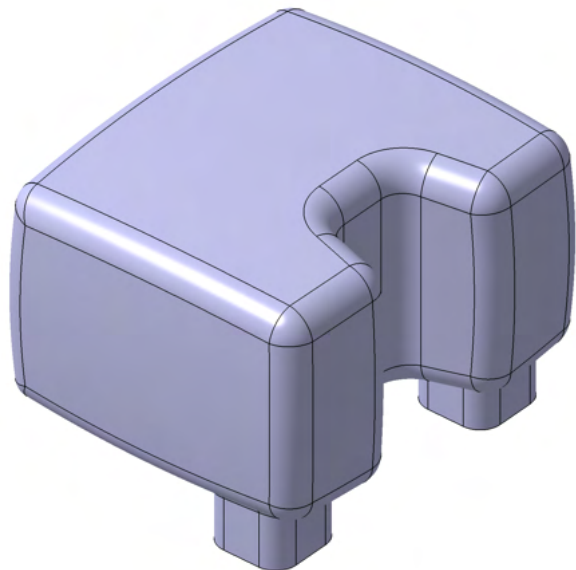


**Figure 41:** Design of LD<sub>2</sub> moderator with rounded shape, developed by the engineering team.

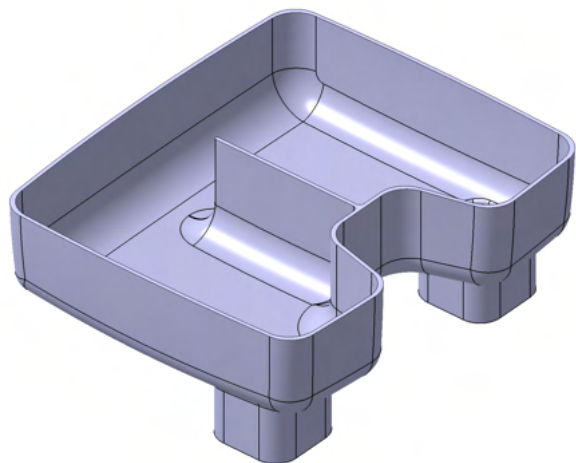


**Figure 42:** LD<sub>2</sub> moderator with rounded shape shown with horizontal cut, developed by the engineering team.

**Table 7:** Neutronic performance and characteristics of the most recent model of cold moderator updated based on the preliminary engineering study. Brightness and intensity integrated over different wavelength ranges, for the last iteration of lower moderator (NNBAR and WP7 openings) and compared with the upper moderator. The values for the upper moderator are from Ref [19]. To calculate the intensity we considered the following size of emission windows: NNBAR: 960 cm<sup>2</sup>; WP7: 225 cm<sup>2</sup>; upper moderator: 42 cm<sup>2</sup>.

BRIGHNESS [n/cm <sup>2</sup> /s/sr]			
	> 2 Å	> 4 Å	> 10 Å
NNBAR	$7.05 \times 10^{12}$	$5.40 \times 10^{12}$	$3.92 \times 10^{11}$
WP7	$1.47 \times 10^{13}$	$7.77 \times 10^{12}$	$6.22 \times 10^{11}$
upper moderator	$5.3 \times 10^{13}$	$1.7 \times 10^{13}$	$9.9 \times 10^{11}$
INTENSITY [n/s/sr]			
	> 2 Å	> 4 Å	> 10 Å
NNBAR	$6.77 \times 10^{15}$	$5.18 \times 10^{15}$	$3.76 \times 10^{14}$
WP7	$3.30 \times 10^{15}$	$1.75 \times 10^{15}$	$1.40 \times 10^{14}$
upper moderator	$2.2 \times 10^{15}$	$7.0 \times 10^{14}$	$4.2 \times 10^{13}$
NNBAR FOM	$2.24 \times 10^{17}$ [n/s/sr × λ <sup>2</sup> ]		
WP7 FOM	$2.91 \times 10^{15}$ [n/s/sr]		
Heatload on LD <sub>2</sub> moderator	25.8 [kW]		
Heatload on Be filter	16.3 [kW]		
Heatload on Al vessel	10.5 [kW]		
Total heatload	52.6 [kW]		

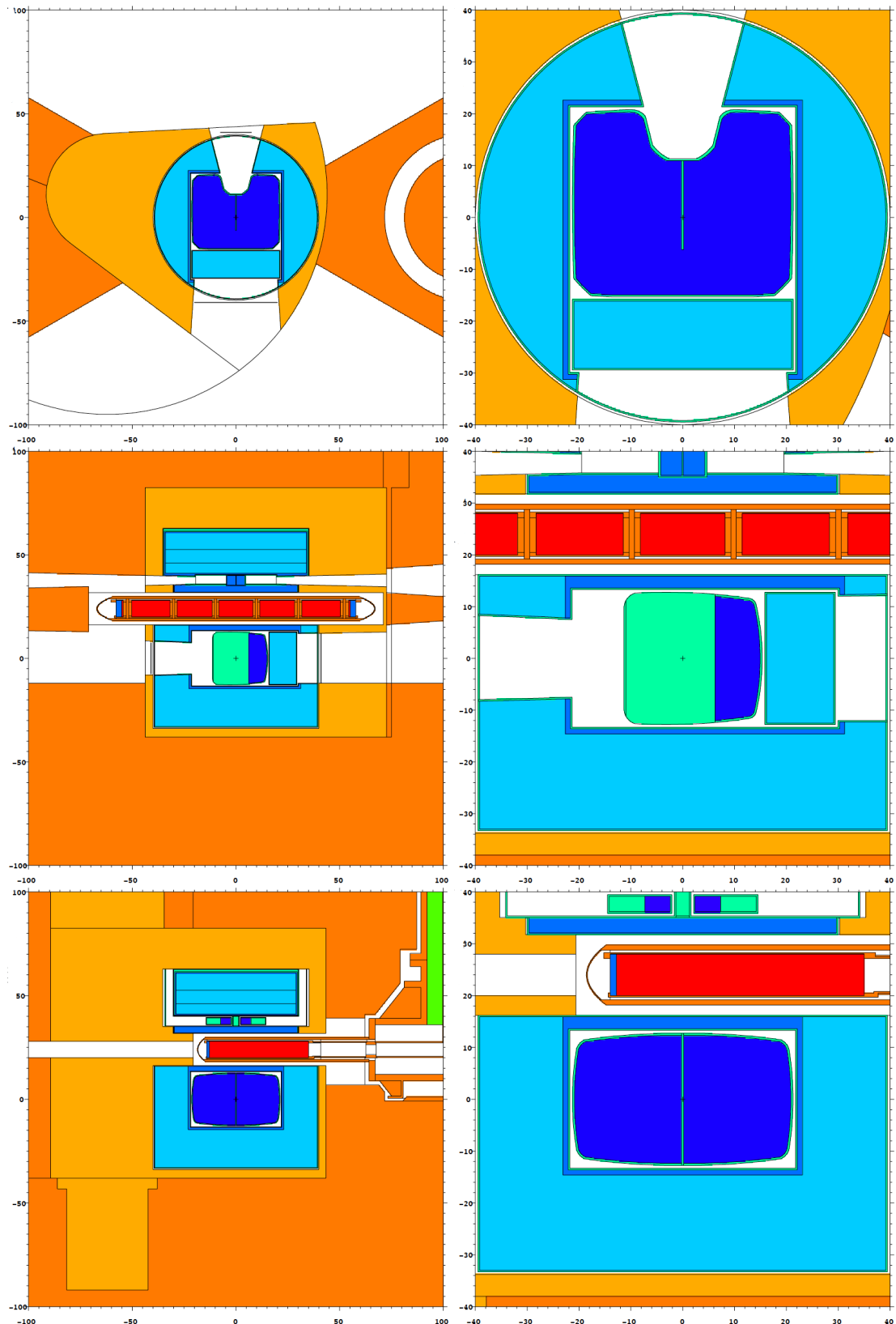


**Figure 43:** Graphical representation of the final design for LD<sub>2</sub> moderator with U-shaped reentrant hole, separated Be filter and LD<sub>2</sub> and rounded walls. The color codes are the following: orange: steel (twister frame, inner shielding, etc); dark blue: liquid ortho-deuterium; blue: light water; light blue: beryllium; green: aluminum. Note that cold Be filters and ambient Be reflector are shown using the same color; the same note applies to Al.

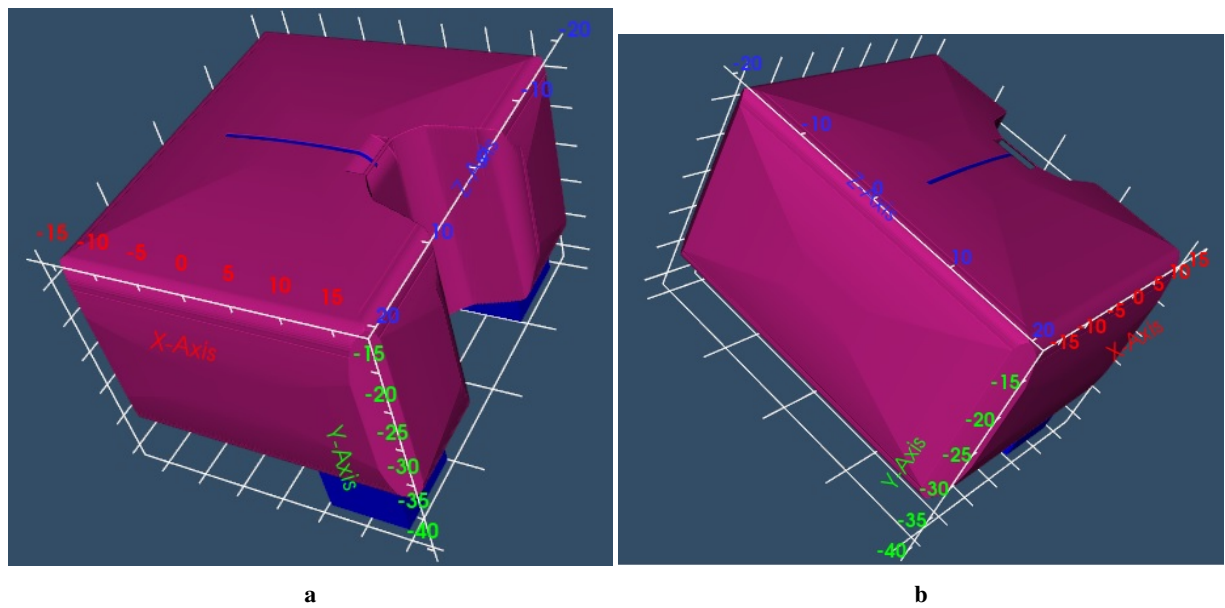


**Figure 44:** MCNP model of the cold moderator vessel with rounded shapes, according to the technical drawing from the engineering team.

### 3 Engineering design of the liquid deuterium moderator

The first moderator and reflector system (so called twister I) will have two liquid parahydrogen moderators above the target wheel only. However, there is available space below the target wheel (lower moderator plug), which has been reserved for future moderator upgrades that could be used for a LD<sub>2</sub> volume moderator. In the HighNESS project, Work Package 5 (WP5) is in charge of the engineering implementation of new cold moderator concepts. This includes the definition of fluid parameters; cooling process concept design; structural materials choice; detailed CAD design of the advanced moderator concepts for the lower moderator plug including manufacturability verification; weldability analysis; structural-mechanics and fluid-dynamics simulations; and integrability into the ESS facility [24].

From an engineering point of view, the cooling and integration into the existing facility of such a large cryogenic pressure vessel in the high-power spallation source ESS is critical and must be analyzed in combination with the mechanical design [25].

#### 3.1 Moderator Engineering - Introduction

The first generation ESS moderator system consists of two liquid parahydrogen low-dimensional moderators, located above the tungsten target wheel. As mentioned previously, the moderator support structure, the twister, also allows for the use of the space below the target wheel for future moderator upgrades. Figure 45 shows the isometric view of the ESS Target Monolith. The colored components are subjects of the planned upgrades of the ESS Target station [6].

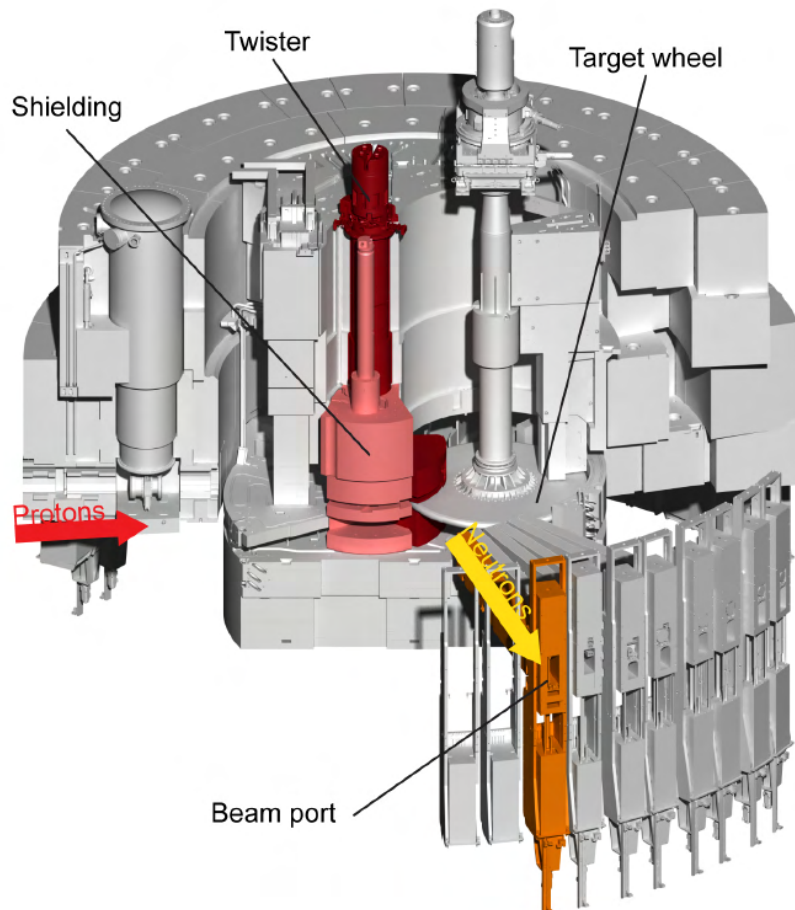


**Figure 45:** ESS Target Monolith, isometric cutaway view.

The major engineering challenge here is to handle the enormous heat load into the LD<sub>2</sub> moderator of around 60 kW resulting from the spallation process of a 5 MW accelerator-driven neutron source. Following the several iterations discussed in the previous section, the following preliminary engineering design of the LD<sub>2</sub> moderator was developed. The moderator vessel consists of high-strength Aluminum alloy EN AW-6061 T6, which allows local stresses up to 87 MPa and will be filled with approximately 30 L of liquid deuterium. The cold moderator is surrounded by a vacuum jacket followed by a light water premoderator and a warm beryllium reflector. In addition, one cold beryllium filter ( $\leq 80$  K) is installed inside the cold moderator vessel on the NNBAR side serving the large beam port (see Figure 46 blue block) [24].

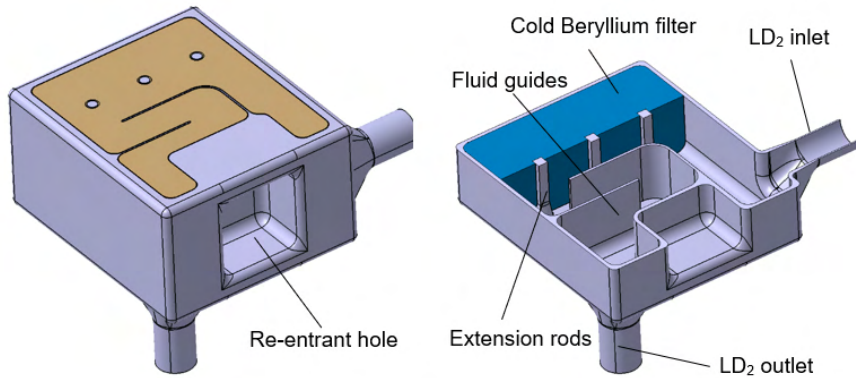


**Figure 46:** Pre-design of the LD<sub>2</sub> moderator

The fluid guides ensure that flow separation, dead areas, and swirls do not occur. The extension rods ensure additional mechanical stability since the vessel walls are flat and need to be as thin as possible to minimize neutron losses. The moderator will be milled and partially Electrical Discharge Machining (EDM) machined from a solid block of aluminum EN AW-6061 T6, and the cover will be finally welded to the main body with “low-distortion” electron beam welding. In addition to the usual structural and fluid mechanics issues, the integrability must also be checked, since the components must be installed into an existing source. Originally, the twister was designed for low-dimensional hydrogen moderators only. The integrability is critical, since the LD<sub>2</sub> volume moderator has a substantially larger volume and thus dissipates significantly more heat. Therefore, larger supply and dissipation cross-sections are required. All supply lines must be routed through the twister shaft. However, the diameter of the shaft cannot be increased because it is surrounded by non-replaceable shielding elements. Figure 47 shows the twister with the upper moderator on the left-hand side and on the right-hand side the integrated volume LD<sub>2</sub> moderator in the lower moderator plug. [24]

### 3.2 Definition of fluid parameters & cooling process concept design

The fluid parameters of liquid deuterium are defined in the following section, since these are required for the following designs and calculations of the new cold moderator system. Figure 46 shows a simplified representation of LD<sub>2</sub> (blue line) at the chosen operation pressure of 5 bar. It can be seen that the deuterium solidifies at a temperature of  $\approx 19$  K and vaporizes at  $\approx 30$  K, which defines the temperature range in the liquid phase for the moderator system. In order to avoid freezing during operation, the minimum temperature at the outlet of the heat exchanger is set to 20 K. In addition, it is assumed that additional heat load from the circulation pumps and insulation losses will increase the deuterium temperature by 1 K before it arrives at the moderator inlet. The average temperature increases in the moderator due to particle heating of 59.8 kW will be up to 3 K, which means that the average outlet temperature will be around 24 K. As a result, there is still a contingency factor for local temperature peaks of approximately 6 K before the deuterium evaporates.

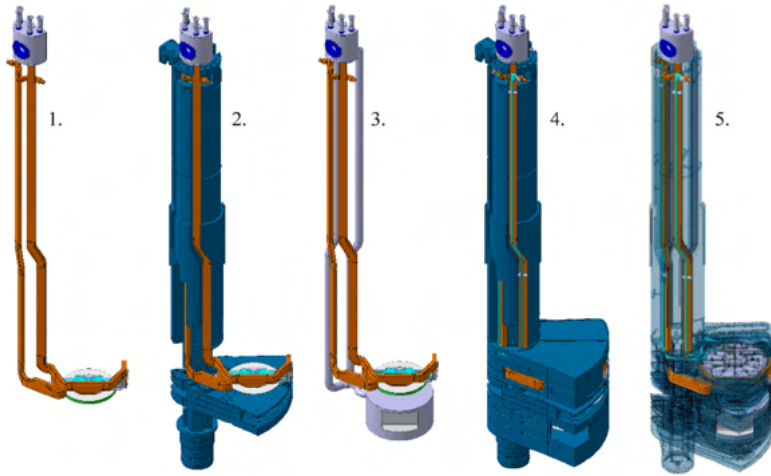


**Figure 47:** Integration of LD<sub>2</sub> moderator: 1. Upper moderator plug; 2. upper moderator plug in the moderator support structure; 3. moderator plug with LD<sub>2</sub> moderator; 4. and 5. moderator plug in the moderator support structure near the outer reflector [24].

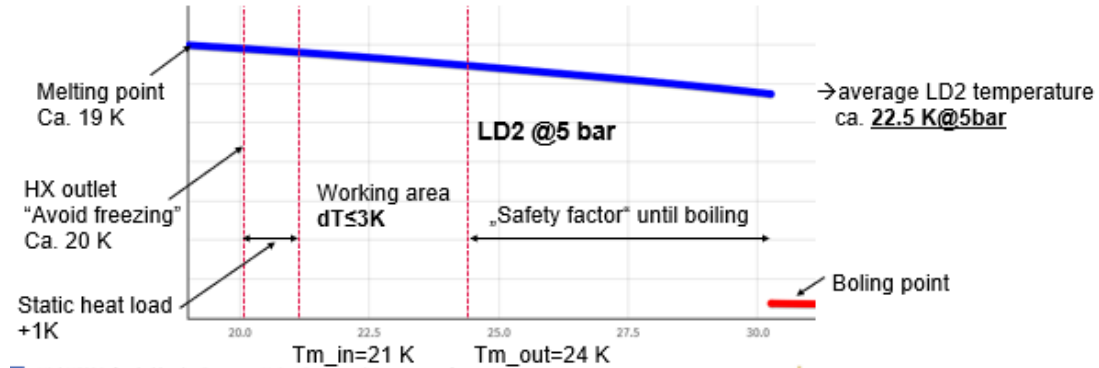


**Figure 48:** Definition of fluid parameters for the moderator LD<sub>2</sub> volume.

The mass flow can now be estimated by using the chosen operating pressure, the inlet- and outlet-temperature, and the heat load. A mass flow of at least 3400 g s<sup>-1</sup> liquid deuterium is needed to remove the enormous particle heat and to keep the average temperature increase below  $\leq 3$  K. Assuming a flow velocity of up to  $\leq 5$  m s<sup>-1</sup>, an inlet\outlet pipe diameter of 70 mm would be required, which has to fit into the existing twister structure.

With the defined fluid parameters, a first piping and instrumentation diagram (P& ID, see Figure 49) was created, and a working CAD design of the lower moderator plug was completed for use in structural mechanical simulations and fluid dynamic simulations. The P& ID in Figure 49 is a simplified system flow diagram of the cryogenic deuterium moderator system (CDMS), consisting of the helium refrigeration system (TMCP II) with 75 kW cryo-power at 20 K, the helium transfer lines (HTL), the deuterium liquefaction cryostat (CDMS Cold Box), the deuterium transfer lines (DTL), and finally the twister with the lower moderator plug.

The helium refrigeration system is responsible for providing the required cryo-power to the deuterium cryostat to liquify the gaseous deuterium and to remove the heat load of the moderator system during operation. For this, gaseous helium is pumped in a closed loop at a minimum temperature of 20 K via the helium transfer lines to the deuterium cryostat heat exchanger and back to the helium refrigeration system. The main components of the deuterium cryostat itself are the heat exchanger, the circulation pumps, the ortho–para converter and the pressure control buffer. The circulation pumps are installed in the deuterium cryostat to supply the moderator with the liquefied deuterium in a closed circuit. In ad-

**Table 8:** Critical design parameters.

Liquid ortho-Deuterium volume	$V_{Mo} \approx 30 \text{ L}$
Heat load into oLD <sub>2</sub> -moderator	$\Sigma Q_{Mo} = 59.8 \text{ kW (@ 5 MW)}$
Total heat load	$\Sigma Q_{To} \approx 70 \text{ kW (60 kW + 10 kW)}$
Average pressure (Moderator)	$p = 5 \text{ bar}$
Average density	$\rho = 173.8 \text{ kg m}^{-3}$
Flow velocity	$w \leq 5 \text{ m s}^{-1}$
Average mass flow	$\dot{m} \geq 3400 \text{ g s}^{-1}$
Average temperature increase (mo.)	$dT \leq 3 \text{ K}$
Average temperature	$T_{Av} = 22.5 \text{ K}$
Average inlet temperature	$T_{AVI} = 21 \text{ K}$
Average outlet temperature	$T_{AVO} = 24 \text{ K}$

dition, the para-deuterium content is converted into almost 100% ortho deuterium by using a catalyst in the cryostat, since this has better moderator properties. An active heated pressure-control buffer is also installed in the cryostat to compensate pressure changes caused by the pulsed proton beam and beam trips.

The cryostat provides the needed liquid deuterium to the moderator via the deuterium transfer lines, where the deuterium is heated up by particle interactions and returned to the heat exchanger of the cryostat to cool the deuterium down again. In addition, a storage tank for the deuterium will be necessary since deuterium produces tritium under irradiation. Therefore, the deuterium cannot be vented like hydrogen, for example, when maintenance work or similar actions have to take place. For this reason, in case of maintenance work, the deuterium will be heated and then fed into the storage tank using a heater and compressor. Then, completing maintenance, the deuterium would be reused.

This is also advantageous, because of the high cost of deuterium. The size of the storage tank is determined by the total inventory of the circuit, cryostat and moderator, which must be kept as small as possible for safety and costs reasons. Therefore, it is very important to place the cryostate as close as possible to the moderator to reduce the total amount of deuterium. Since selecting a final location of the components was not within the framework of the HighNESS project, this will be necessary in the final design phase.

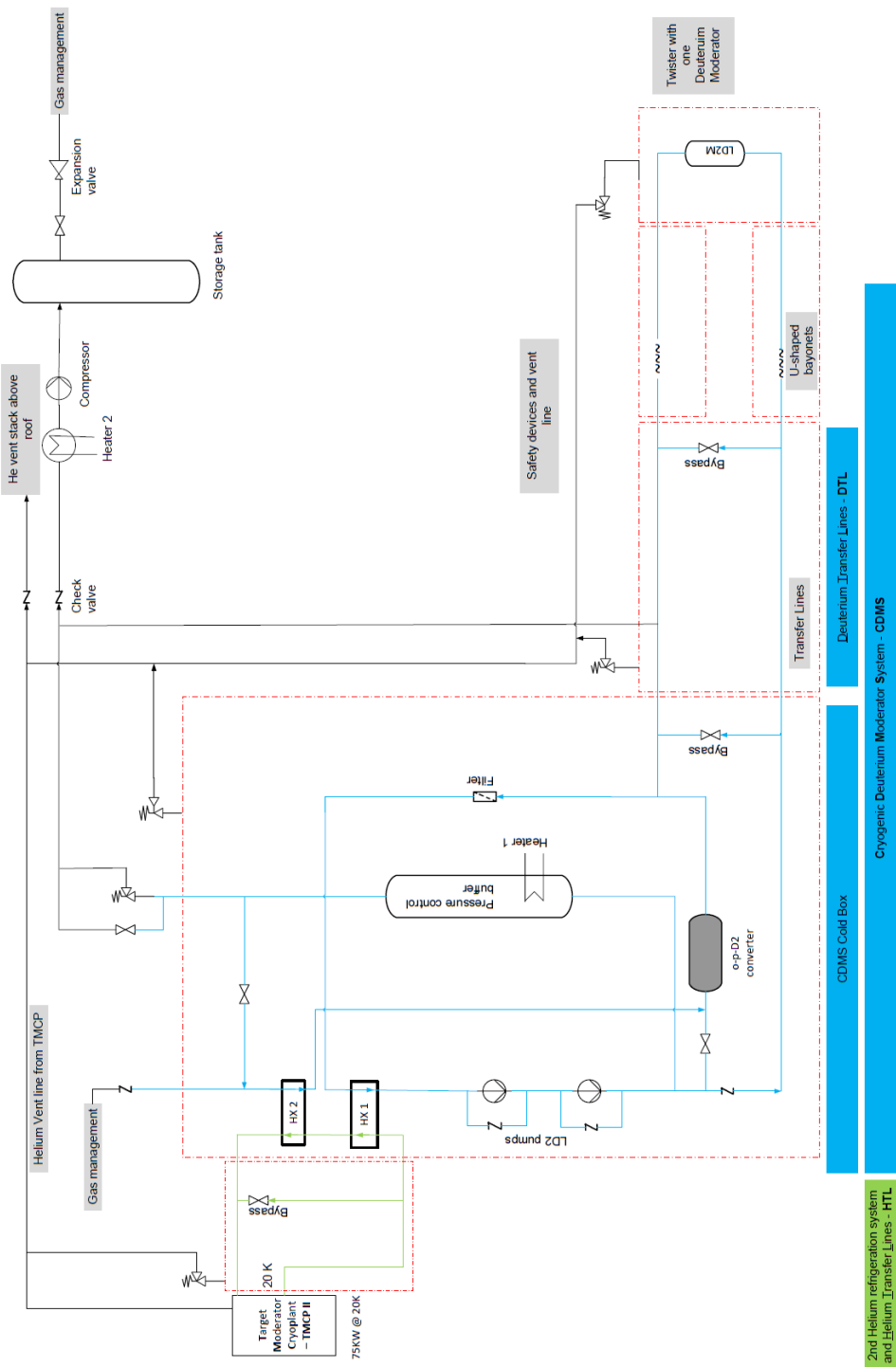


**Figure 49:** Piping and instrumentation diagram for the LD<sub>2</sub> moderator system.

### 3.3 Costs estimation of LD<sub>2</sub> infrastructure

The rough cost estimation shown in Table 9 is based on the cost of the existing ESS hydrogen system and is scaled up according to the heat load of the deuterium moderator system (ca. 75 kW) compared to the hydrogen moderator system (ca. 30 kW). In addition, a storage tank system is considered because of the issue mentioned above that deuterium can not be vented in maintenance cases due to tritium production. In addition, significantly higher costs for deuterium itself are considered as well. Since the location of the needed new building for the helium refrigeration system and the location of the deuterium cryostate inside the Target Station building are unknown, the distance to each other is estimated in order to be able to estimate the costs for the respective transfer lines.

**Table 9:** Cost estimation of the LD<sub>2</sub> moderator system.

Item	Cost [M€]	Comments
Helium refrigeration system	35	Ca. 75 kW @ 20 K
Helium transfer lines	1.93	Assumed: 2x100m
D <sub>2</sub> cryostat	14	
LD <sub>2</sub> transfer lines	2.75	Assumed: 2x40m
LD <sub>2</sub> moderator plug	5.5	Complete new twister
D <sub>2</sub> storage system	2.5	
New building for He-refrigeration system room preparation for LD <sub>2</sub> cryostat, ATEX, ...	5	No room selected so far
Total:	66.68	

The real costs can deviate significantly upwards or downwards from the estimated ones if the locations (distance) of components change and if the heat load is lower or higher, for example.

### 3.4 Selection of materials and overall design

For the newly designed moderator, the moderating medium of LD<sub>2</sub> is kept at 20 K. The structural material for the moderator vessel is required to be tolerant to radiation damage, as transparent for neutrons as possible, and suitable for cryogenic temperatures. The chosen structural material shall also be sufficiently ductile for the fast load changes caused by the pulsed proton beam and sufficient in terms of strength to withstand the internal pressure of the LD<sub>2</sub>.

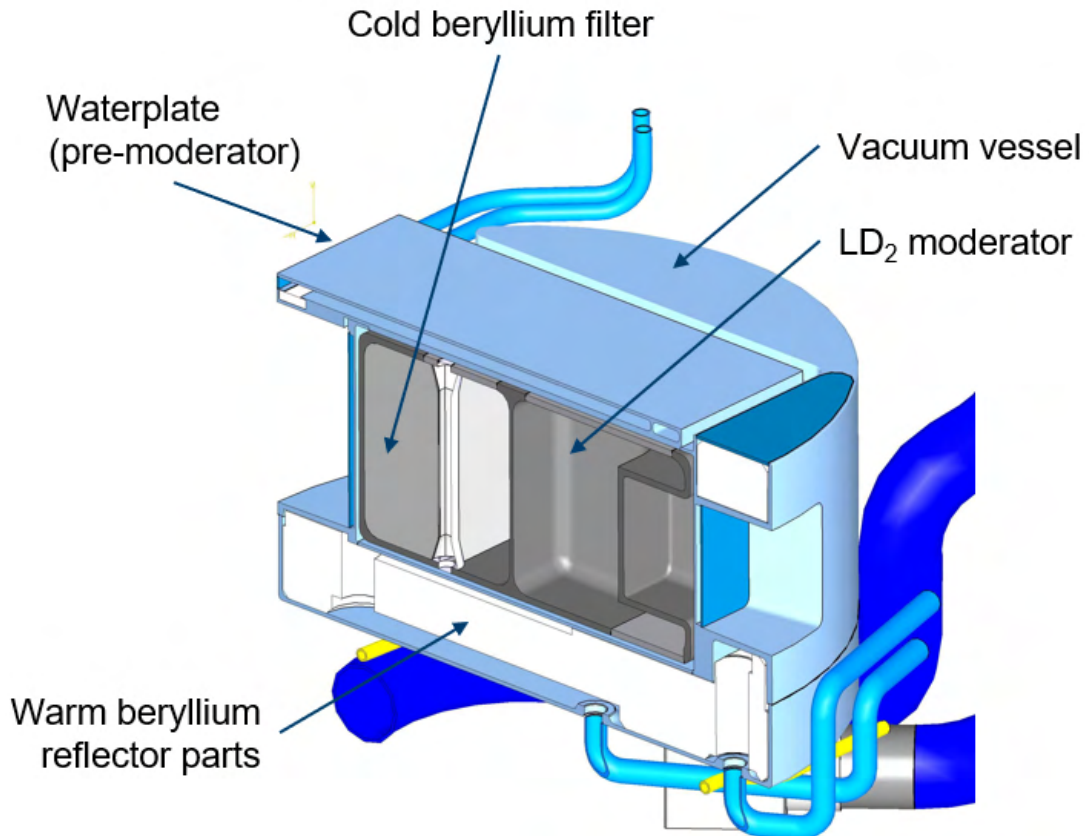
Aluminum is nearly transparent for cold and thermal neutrons and is therefore typically selected as a moderator vessel material. However, the strength of pure aluminum is much too low to keep the stress from inner pressure within the allowable range, especially for large volumes as in the case of the LD<sub>2</sub> moderator. Therefore, heat treatable aluminum alloys (6000 series) or non-heat treatable (5000 series) are the preferred choice [25].

There is no ideal aluminum alloy, with each choice having advantages and drawbacks. Many facilities use EN AW-6061 T6, for example at SNS, J-PARC, and for the liquid hydrogen moderator of ESS. In addition, sufficient data of irradiated samples are available to evaluate the radiation-related lifetime of the moderator vessel [25]. Because of its well-known radiation properties, the high strength values and wide application fields in the frame of spallation sources, it was ultimately decided to use EN AW-6061 T6 for the lower moderator.

### 3.5 Design overview of the lower moderator plug

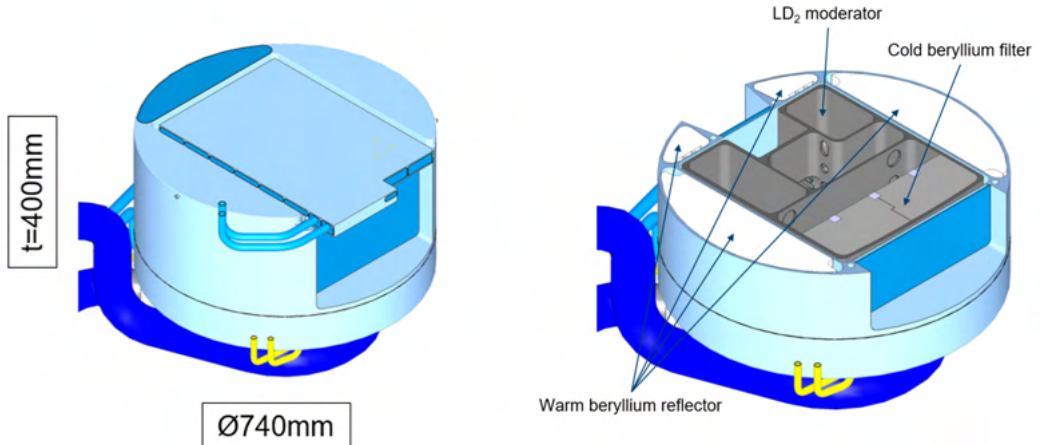
The new moderator is located in the frames of the twister just below the target wheel, as can be seen in Figure 47. All details about the integration of the LD<sub>2</sub> moderator assembly into the already existing ESS twister can be found in Section 3.11. The lower moderator plug consists of the inner LD<sub>2</sub> moderator and a cold beryllium filter, that are surrounded by an insulation vacuum, a warm beryllium reflector, and a

water premoderator on the top side, facing the target wheel. On each side of the outer vacuum vessel there are actively helium-cooled neutron windows (part of the vacuum vessel) where the cold neutrons exit the moderator (see Figure 50).



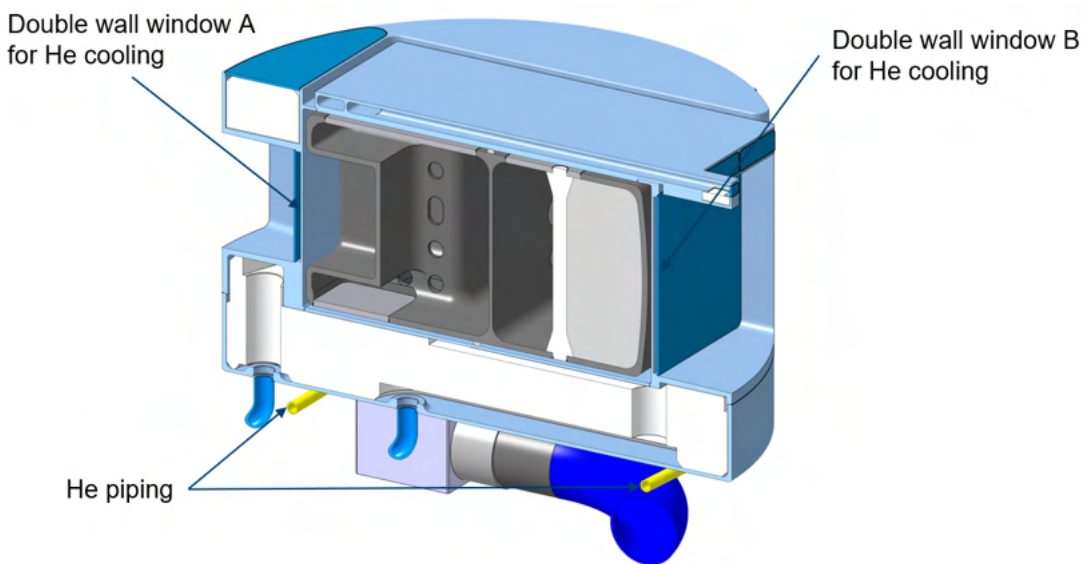
**Figure 50:** 3D cross section illustration of the lower moderator plug.

Figure 51 shows the overall box dimensions of the lower moderator plug without the media supply pipes and a horizontal cross-section of the assembly with the parts inside the plug. In principle, the LD<sub>2</sub> moderator sits within the surrounding vacuum vessel with a 5 mm insulation vacuum gap to the adjacent aluminum walls. A layer of water and the warm beryllium reflector segments surround the moderator, with the reflector segments also placed inside a closed aluminum vessel.



**Figure 51:** Dimensions and layout of the lower moderator plug.

The lower moderator plug has two openings on the front and the back side, one smaller neutron window A (WP7 side) and a larger neutron window B (NNBAR side). Both neutron windows are actively cooled by a transversal helium flow and are therefore designed with a thin double-wall design, as shown in Figure 52.



**Figure 52:** 3D cross-section of the neutron windows.

### 3.6 Assembly and welding of the moderator

A cold beryllium filter is embedded within the LD<sub>2</sub> moderator on the NNBAR side, adjacent window B. This filter element is divided into two pieces for installation purposes. Three stiffening rods are also needed to support the structural integrity of the vessel. The flow guides and restrictors ensure a defined flow of the liquid deuterium from the inlet to the outlet. The whole moderator is milled and eroded from a single piece of EN AW-6061 T6 aluminum. The openings on the top and the bottom side are necessary for inserting the cold beryllium filter parts and for manufacturing reasons. The box dimensions of the moderator vessel with a wall thickness of 8 mm are shown in Figure 53.

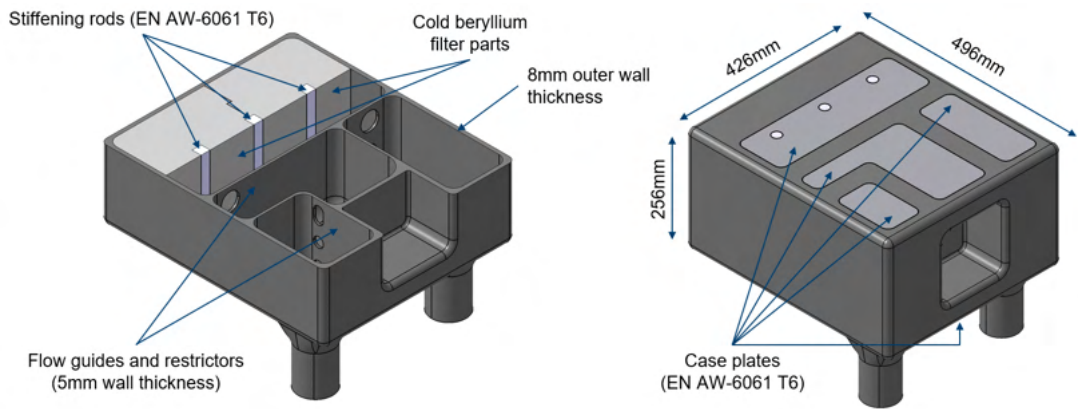


**Figure 53:** Detailed view of the LD<sub>2</sub> moderator structure within the moderator plug.

The assembly sequence of the LD<sub>2</sub> moderator is shown in Figure 54 and Figure 55. First, the parts of the cold beryllium filter are inserted through the top cut-out into the base body of the moderator. Then the 3 stiffening rods are put into the base body and into their grooves in the cold beryllium filter parts, ensuring the correct positioning. Afterwards, the moderator vessel is closed with the case plates.

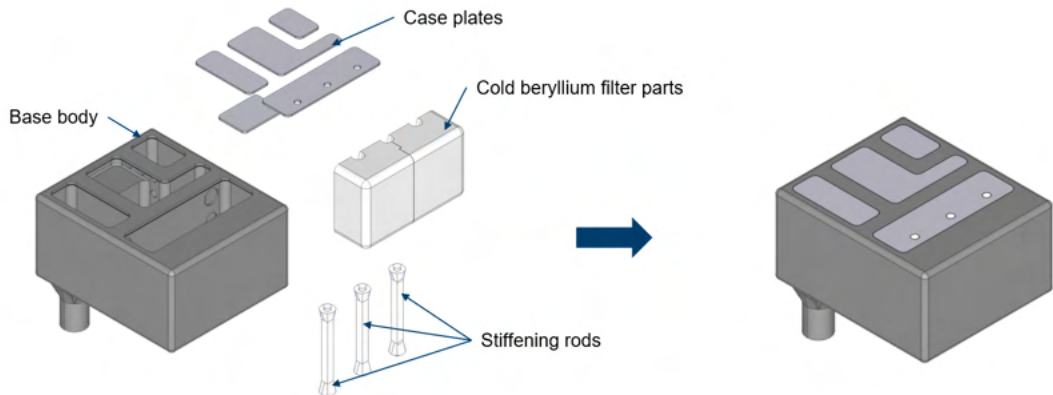


**Figure 54:** Assembly of the LD<sub>2</sub> moderator vessel – parts overview.

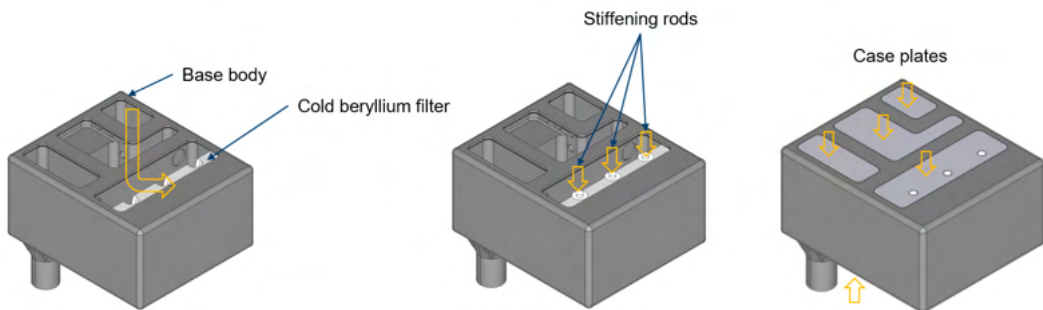


**Figure 55:** Assembly of the LD<sub>2</sub> moderator vessel – assembly sequence.

One challenge when manufacturing the inner LD<sub>2</sub> moderator vessel is the welding process of the case plates, because of the high structural loads that result from the interior operating pressure of the liquid deuterium of 5 bar and the unusual box shape for a pressurized vessel. Figure 56 shows a close-up

of the welding area of one of the case plates. To determine the ideal weld-in depth of the filler material, that is needed to avoid heat cracks during the welding process of the EN AW-6061 T6 aluminum alloy, detailed pre-tests of the welding geometry will be necessary in the future before building of such a vessel can be realized.

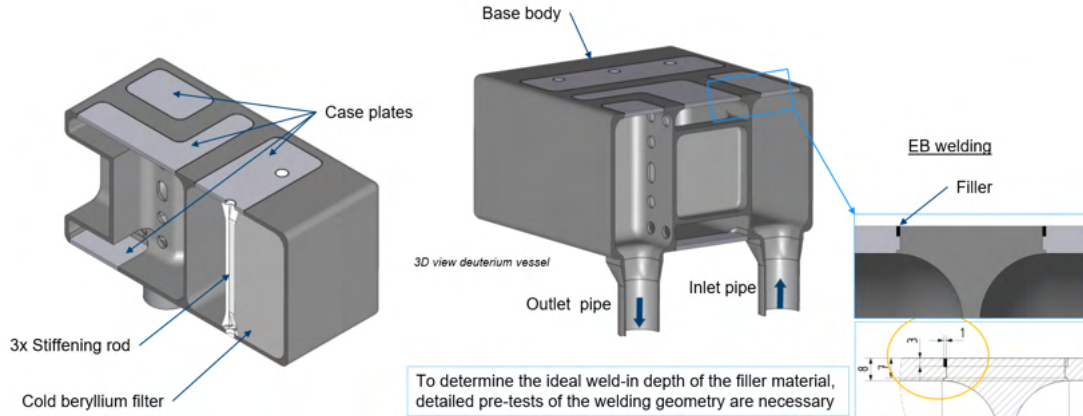


**Figure 56:** EB-welding of the LD<sub>2</sub> moderator vessel.

### 3.7 Structural mechanical calculations

Structural strength simulations with a design pressure of 7 bar (operation pressure 5 bar) following the design rules of RCC-MRx 2012 code were performed to analyze the static behavior of the LD<sub>2</sub> moderator, which basically behaves as a pressure vessel. Figure 57 illustrate that the large flat wall on the front-facing side – where the cold beryllium filter is placed (not included in the simulation) – the stress is particularly high due to the unusual box shape. In this area, the stress exceeds the limit of  $1.5 \cdot S_m$  for EN AW-6061 T6, with  $S_m = 87$  MPa and  $1.5 \cdot S_m = 130.5$  MPa.

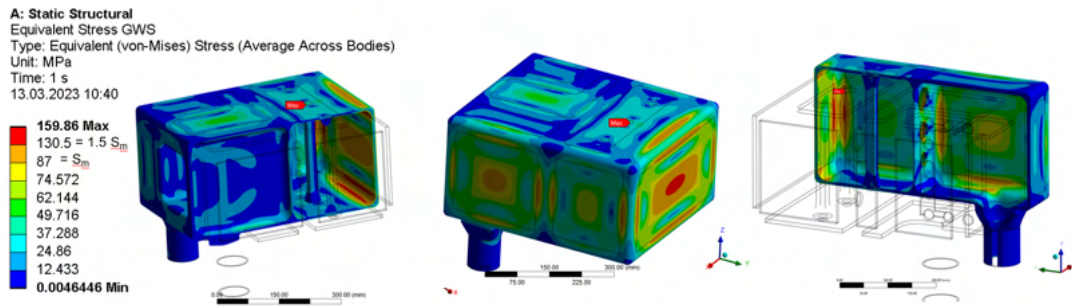


**Figure 57:** Equivalent primary stress at design pressure.

To further optimize the design and meeting the strength criteria regarding the allowable stress, optimizations on this large wall were performed. At first, the wall was shaped cylindrically, which reduced the bending stresses compared to a flat wall. Nevertheless, the sum of the local membrane and bending stress  $P_L + P_b$  on the fillet at the boundary of the rear wall still slightly exceeded the limit of  $1.5 \cdot S_m$ .

Finally, the large and originally flat surface was transformed into a perfectly plastic membrane, which is deformed by pressure to create a shape capable of bearing the load with reduced bending stress. This derived shape is used as a contour for the geometry of the rear wall. This free-formed, or “membrane-shaped” wall under pressure is shown in Figure 58, shown with a 10× magnification of the deformation for visualization. To limit the extent of the free-forming effect, the membrane shape was selected with a maximum deformation of 10 mm.

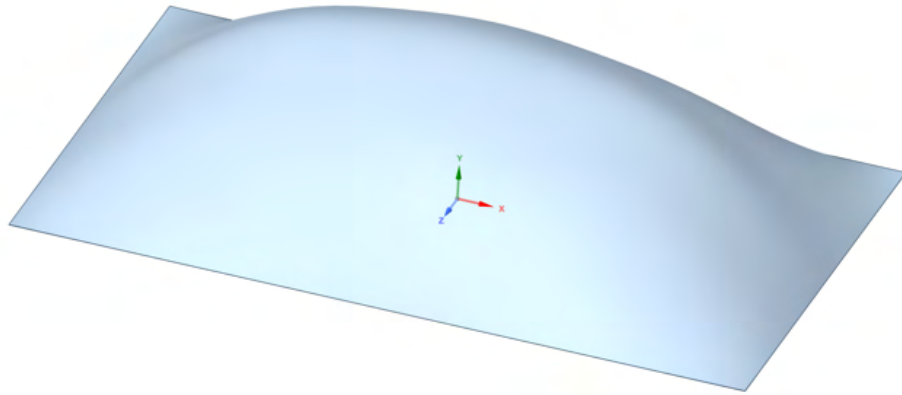


**Figure 58:** Shape of membrane under pressure, magnified 10 $\times$  for visualization purpose

Figure 59 shows the updated equivalent primary stresses at a design pressure of 7 bar. Here, it is indicated that the stress only exceeds the maximum of 130.5 MPa by 0.92 MPa at a single spot in a rounded corner. However, the linearized stresses at surfaces with  $\sigma_{eqv} \geq S_m$  shown in Figure 60 demonstrate that the local primary membrane stress (left) and the primary membrane plus bending stress (right) completely satisfy the allowed strength criteria of  $\overline{P}_m \leq \overline{P}_L \leq S_m(\Theta_m) = 87$  MPa and  $\overline{P}_L + \overline{P}_b \leq 1.5 \cdot S_m(\Theta_m) = 130.5$  MPa.

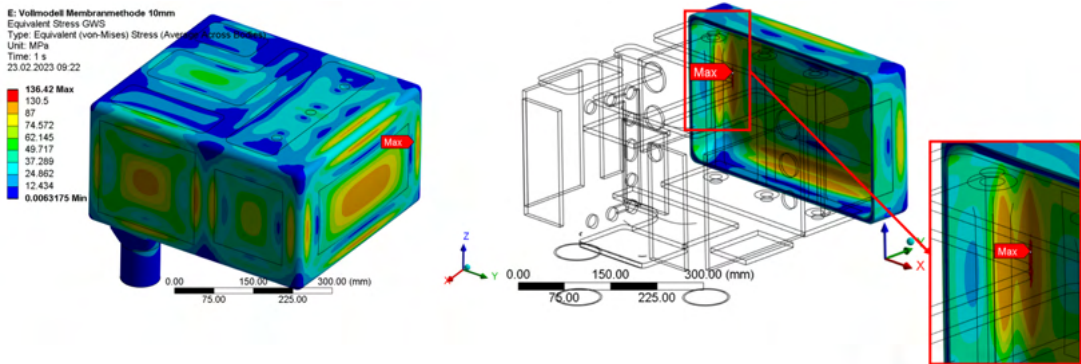


**Figure 59:** Updated equivalent primary stress at design pressure.

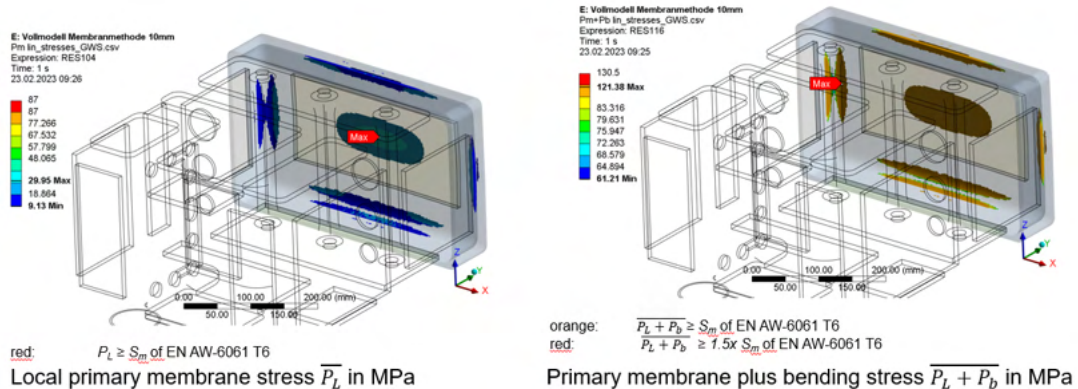


**Figure 60:** Results for membrane stress on the NNBAR-side outer wall.

In summary, a free-shaped rear wall significantly reduces the sum of local membrane and bending stress compared to a flat rear wall or a cylindrical rear wall with identical offset of 10 mm. The sum of local membrane and bending stress  $\overline{P_L} + \overline{P_b}$  on the fillet at the boundary of the rear wall is below the limit of  $1.5 \cdot S_m$ . With this design modification the strength criteria are met.

### 3.8 Analysis of weld seams

In principle, all moderator vessels are welded. Depending on the number of welds, the distance to each other and the welding process itself (TIG, Laser, Electron-Beam, etc.) the entire vessel can lose the additional strength gained by the selected tempered material. The TIG welding process requires a pre-heating of the vessel, which will often damage the previous heat treatments that have been made to achieve the high material strength, such as T6. This can be avoided to a large degree by using electron beam welding (with no pre-heating necessary) and a carefully planned welding design.

Nevertheless, reduced strength must be expected in the area around a weld. Thus, by putting the welds in a low stress area where possible, it is still possible to benefit from the T6 conditions. On the other hand, electron beam (EB) welding requires a very high manufacturing tolerance.

Another issue with using EN AW-6061 T6 is the need of a welding filler to avoid heat crack formation. These heat cracks occur during the rapid solidification of the melt (thanks to the high thermal conductivity of aluminum) and can be mitigated by the alloy composition of the EN AW-6061 T6, particularly owing to the silicon and magnesium content. Therefore, a good choice of filler would have, for example, a relatively high silicon content, which is offered by EN AW-4047A with 12% silicon. Increasing the content of magnesium is not helpful in this case since it evaporates when the aluminum melt is produced.

The filler material needs to be set precisely into the welding area. Also, the weld-in depth is a very sensitive value. For EB welding, it is ideal that there are no gaps between the welded parts and the filler material, because even small gaps  $> 0.1$  mm will result in irregularities in the weld seam and a faulty welding process. This is very challenging for the manufacturing process of the welded parts in terms of accuracy and the manufacturing strategy. The loss of the T6 condition of the aluminum alloy and its influence on the strength of the weld seams and the heat affected zone (HAZ) around them was investigated by simulation. For this purpose, all material within 15 mm of weld seams is assumed to be heat affected and therefore loses the T6 condition, with a significant corresponding loss in strength values which must be considered. This was approximated by conservatively upscaling the observations from previously tested components with lower wall thicknesses. An overview of the heat affected zones of the LD<sub>2</sub> moderator is given in Figure 61.

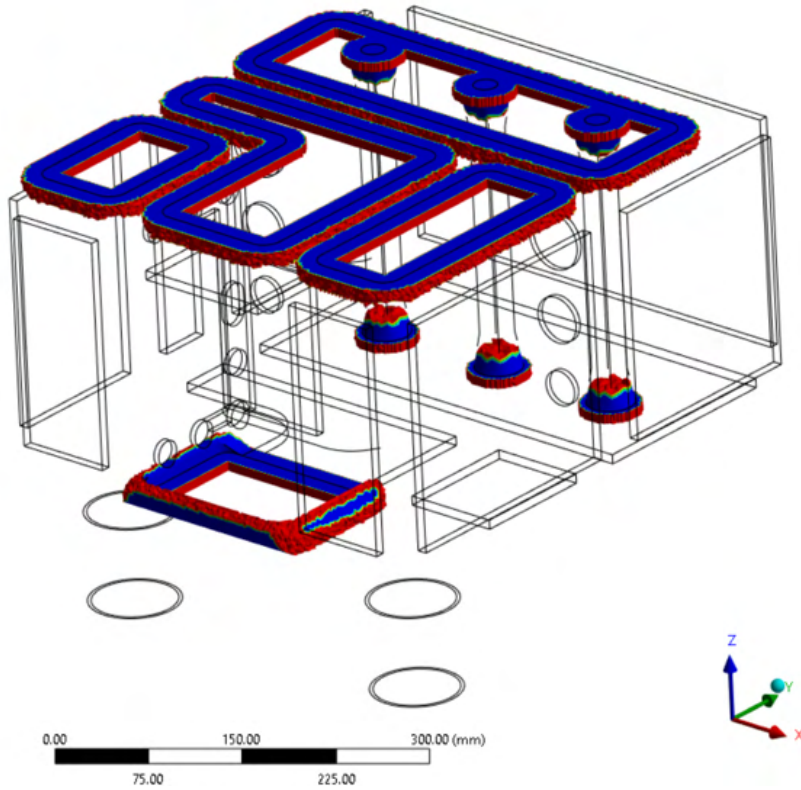


**Figure 61:** Heat affected zones of the LD<sub>2</sub> moderator.

The structural strength simulations with a static design pressure of 7 bar following the design rules of RCC-MRx 2012 code showed that the linearized stresses at the weld seams of the cover plates did satisfy the strength criteria of  $\overline{P_m} \leq \overline{P_L} \leq S_m(\Theta_m) = 47 \text{ MPa}$  at all locations, but the criteria of  $\overline{P_L + P_b} \leq 1.5 \cdot S_m(\Theta_m) = 70.5 \text{ MPa}$  was not satisfied for one weld of one cover plate. These results are visualized in Figure 62.

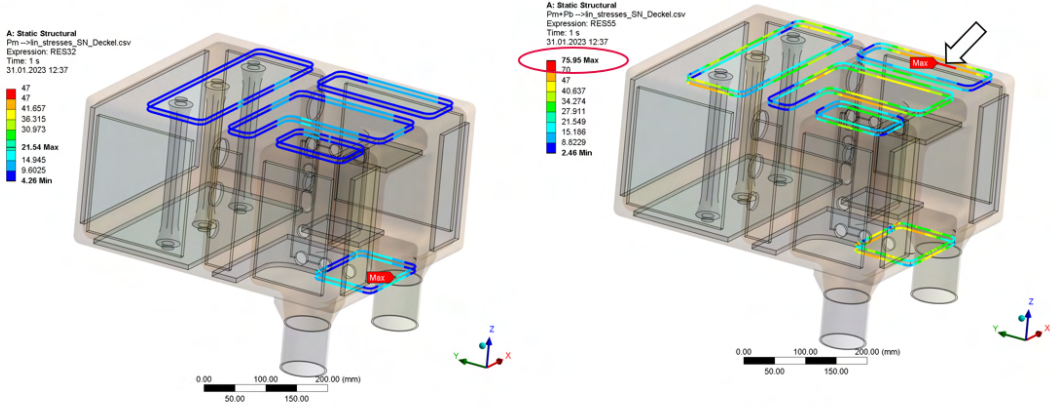


**Figure 62:** Linearized stresses at the weld seams of cover plates.

A further simulation was performed with the same boundary conditions, but an updated design model. In this case the position of the weld seam of the former, unsatisfactory cover plate was moved 6 mm toward a less stressed region of the vessel. Figure 63 shows that the criteria of  $\overline{P_m} \leq \overline{P_L} \leq$

$S_m(\Theta_m) = 47 \text{ MPa}$  as well as the criteria of  $\overline{P_L} + \overline{P_b} \leq 1.5 \cdot S_m(\Theta_m) = 70.5 \text{ MPa}$  are satisfied for the welds of all cover plates.

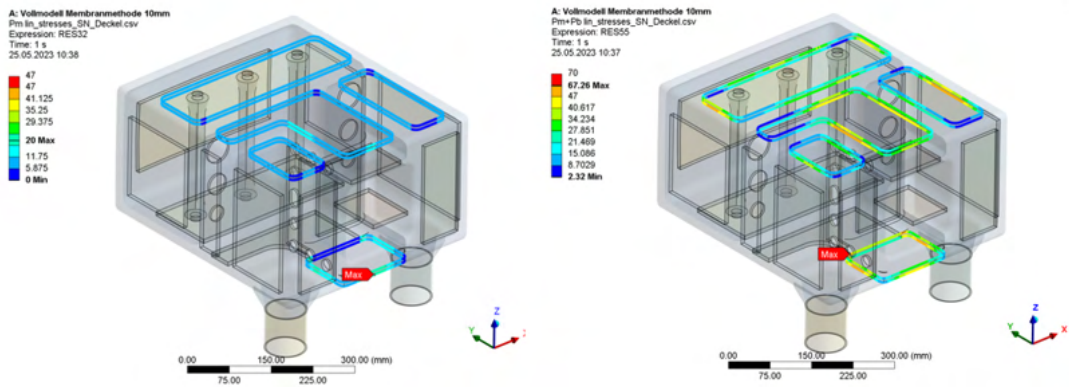
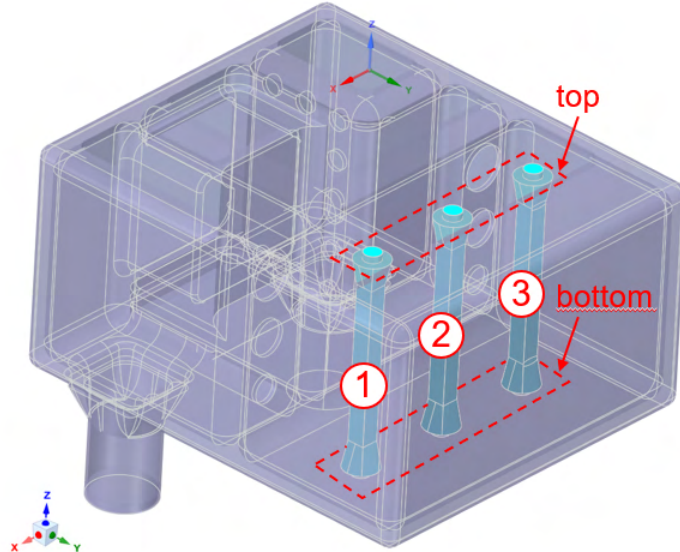


**Figure 63:** Updated linearized stresses at weld seams of cover plates.

The weld seams at the three stiffening rods were also subject of the structural strength simulation. The results overview in Figure 64 shows that the nominal stresses at the weld seams of the stiffening rods all satisfy the strength criteria of  $\overline{P_m} \leq S_m = 27.5 \text{ MPa}$  and  $\overline{P_L} + \overline{P_b} \leq 1.5 \cdot S_m = 41.3 \text{ MPa}$ .



Rod No.	Location	Normal force in kN	Bending moment in Nm	Shear stress caused by normal force in MPa	Shear stress caused by bending moment in MPa	Equivalent stress $\sigma_{eq}$ membrane stress $P_m$	Equivalent stress $\sigma_{eq}$ membrane+bending stress ( $P_m+P_b$ )
1	top	4.3	12.0	8.6	4.8	14.8	23.1
2	top	5.5	10.8	10.9	4.3	19.0	26.4
3	top	4.3	13.5	8.6	5.4	14.8	24.1
1	bottom	4.3	11.1	8.6	4.4	14.8	22.5
2	bottom	5.5	10.4	10.9	4.1	19.0	26.1
3	bottom	4.3	12.8	8.6	5.1	14.8	23.6

**Figure 64:** Nominal stresses on the weld seams of the stiffening rods.

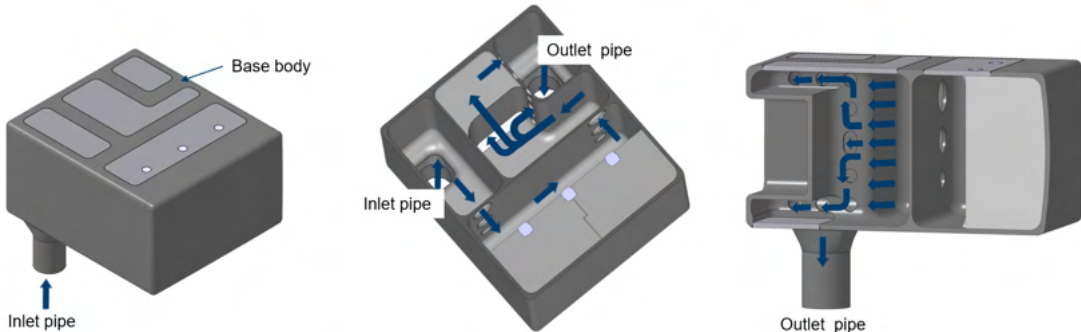
In conclusion, it can be stated that all requirements from a structural mechanical point of view are met, considering the RCC-MRx code.

### 3.9 Thermohydraulic simulations

The fluid parameters and cooling concepts have been verified by full-scale fluid dynamic simulations. Here, the fluid modeled is the subcooled moderating media LD<sub>2</sub> with an average inlet temperature of approximately 21 K. The heat input by neutrons is pulsed, with a 14 Hz pulse frequency and 2.86 ms pulse length based on the ESS proton beam parameters. The allowed temperature increase of deuterium by neutron heat is limited in order to avoid boiling and particularly film boiling. Therefore, the goal for the fluid dynamical simulation is that the fluid temperature does not exceed the boiling temperature at any time.

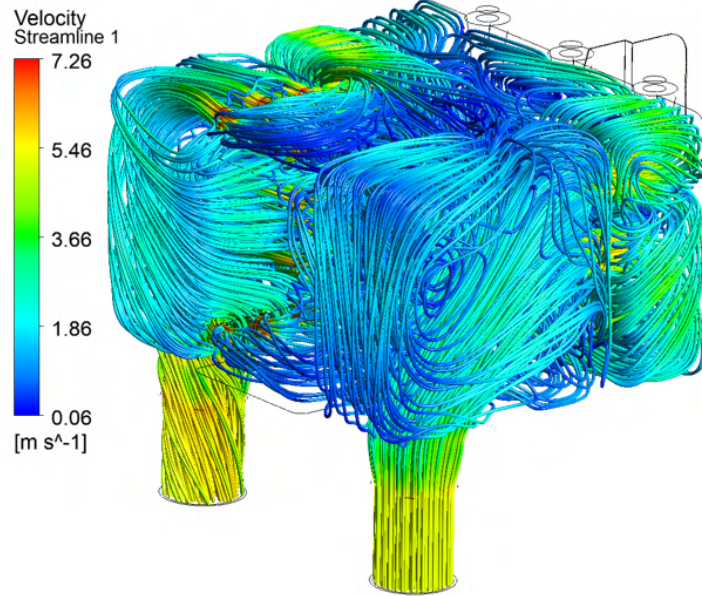
This goal could not be achieved for the 5 MW load case with the given design and requirements. Further details on this issue and remedial measures are discussed in Section 3.12. The simulations were thus carried out using the design shown at reduced beam power 2 MW, since ESS will run at this power in the initial operations phase. A corresponding total heat deposition of 28.4 kW was therefore considered in the simulations, using distribution functions derived for the design of the liquid hydrogen moderator of ESS.

The reentrant hole on the WP7 side (window A) of the moderator, opposite to the cold beryllium filter requires special consideration, since it is fully surrounded by LD<sub>2</sub> on the interior faces of the moderator. To achieve this, a complex flow pattern of the liquid deuterium through the moderator vessel is needed. The deuterium is guided from the inlet to the outlet via flow distributors and restrictors to ensure a homogeneous flow inside the vessel. In the area of the reentrant hole the flow is split, so that the deuterium can flow above and below it (see Figure 65).



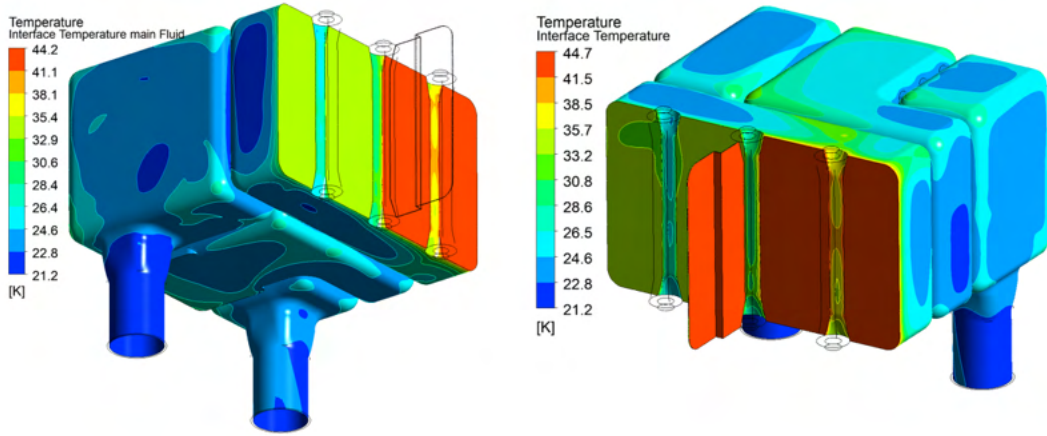
**Figure 65:** Flow pattern of LD<sub>2</sub> through the moderator vessel, below and above the reentrant hole on window A.

Figure 66 shows the velocity streamlines of the liquid deuterium inside the moderator vessel that result from the CFX analysis [26]. Time-averaged results confirm a pressure drop of 0.15 bar in the moderator and a maximum fluid velocity of 7.26 m s<sup>-1</sup> at an inlet velocity of 5.16 m s<sup>-1</sup>.



**Figure 66:** Velocity streamlines of LD<sub>2</sub> inside the moderator vessel

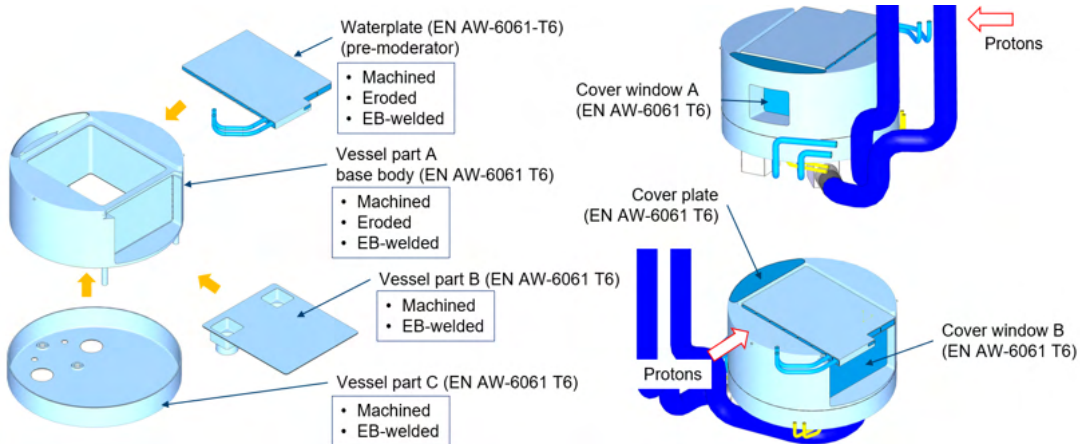
The temperature difference from the inlet to the outlet is 1.4 K with an outlet temperature of 22.4 K (time averaged). The boiling temperature of deuterium at a pressure of 5 bar is 30.6 K. This temperature is reached locally at the inner interface layer between the deuterium and the cold beryllium filter and in the small gap between the cold beryllium filter parts, as shown in Figure 67, but the main flow is still sufficiently subcooled. Therefore, there is no risk of film boiling.



**Figure 67:** Time-averaged fluid temperatures for the LD<sub>2</sub> moderator.

In summary, it can be said that the fluid mechanical requirements for the 2 MW load case are met, if local boiling at the beryllium filter – fluid inner interface is allowed. So, there are no concerns from an operational safety point of view.

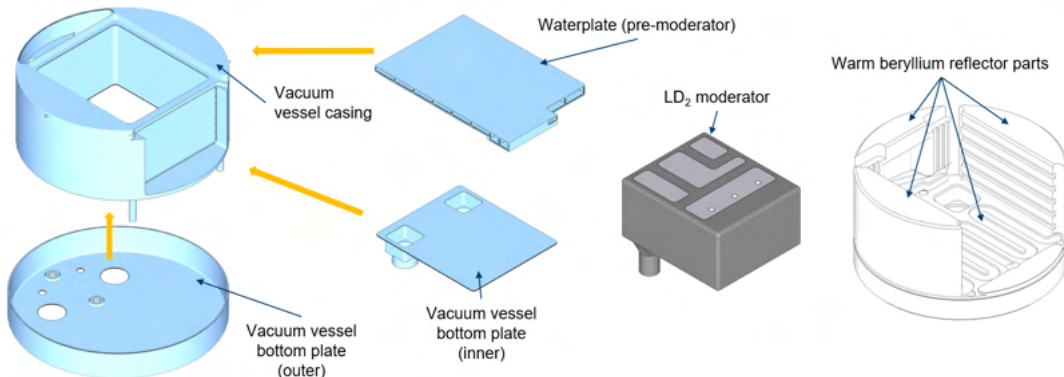
### 3.10 Design solution of the vacuum vessel



**Figure 68:** Assembly of outer vessel for the lower moderator.

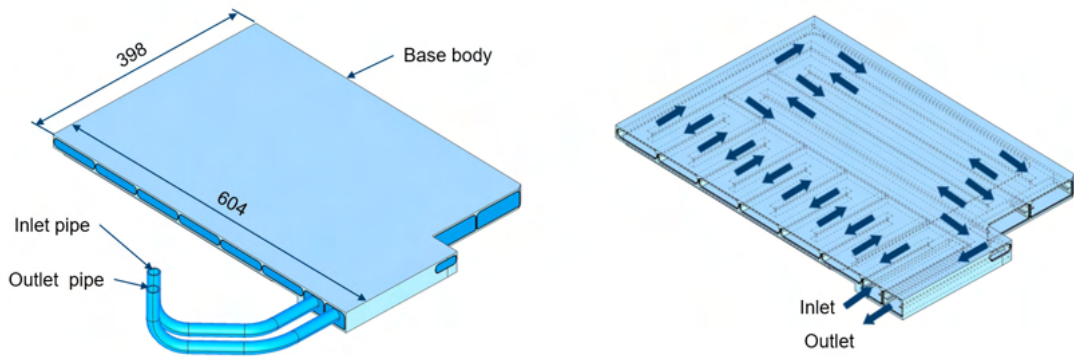
The outer vessel shown in Figure 68 consists of multiple parts that are combined inside a vessel made of EN AW-6061 T6 aluminum alloy. This vessel and the involved reflector parts also enable the water cooling of the beryllium (Be) reflector. Between the Be-reflector and the inner LD<sub>2</sub> moderator there is an insulation vacuum gap of 5 mm to minimize the heat transfer between the cold and warm parts.

Figure 69 shows the different parts of the assembly, that consists of the center LD<sub>2</sub> moderator, the warm beryllium reflector parts, and the outer aluminum vessel.



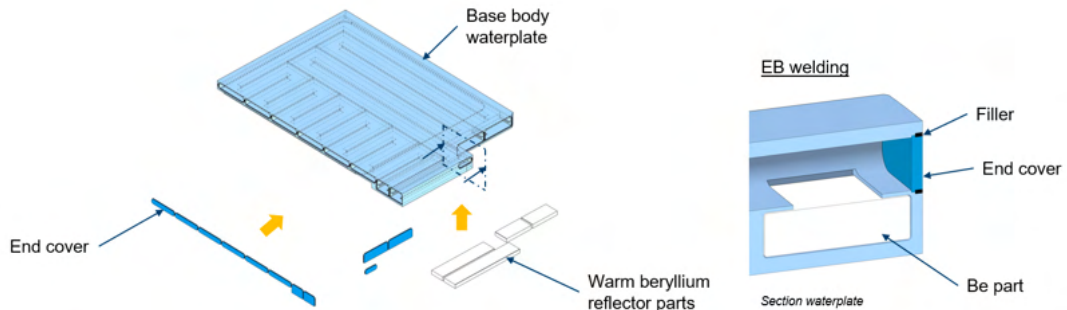
**Figure 69:** Assembly of the lower moderator plug – parts overview.

The water disc on top of the moderator plug assembly works as a premoderator for the fast neutrons released by the tungsten target. Figure 70 shows the flow pattern of water through the premoderator, that is located on top of the lower moderator plug.



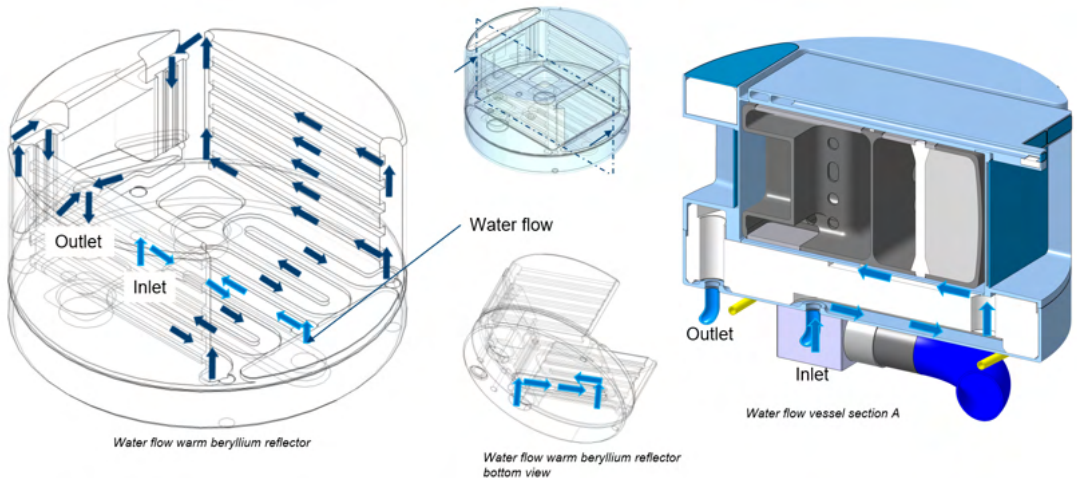
**Figure 70:** Flow pattern of water through the premoderator.

It is assembled as shown in Figure 71. Above the bigger neutron window B, also warm beryllium reflector parts are inserted and the milled and eroded water channels inside the water disc are closed via electron-beam welding.



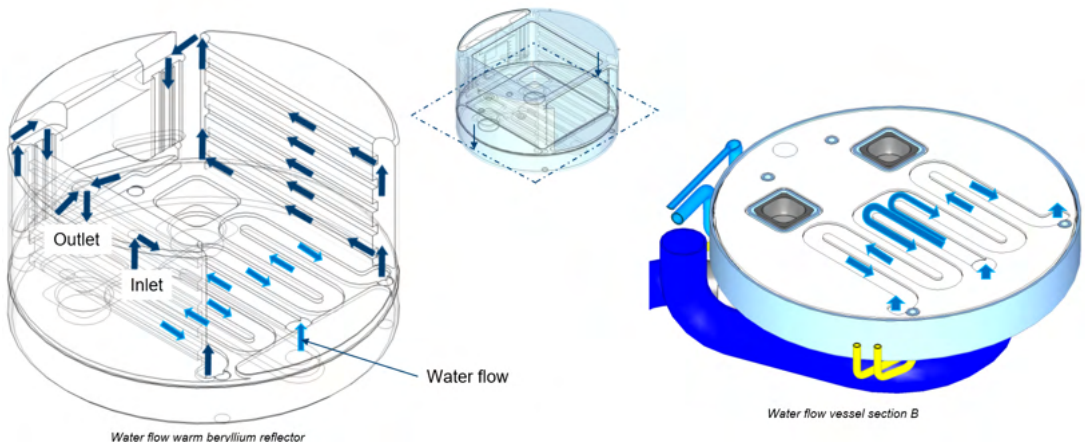
**Figure 71:** Assembly and EB-welding detail of the premoderator.

Figure 72 to Figure 78 show the flow pattern of water through the warm beryllium reflector parts inside the outer vessel, shown in progressive vertical cross-sections. At first the water enters through the inlet on the bottom side of the outer vessel and is afterwards distributed to the bottom part of the warm beryllium reflector.



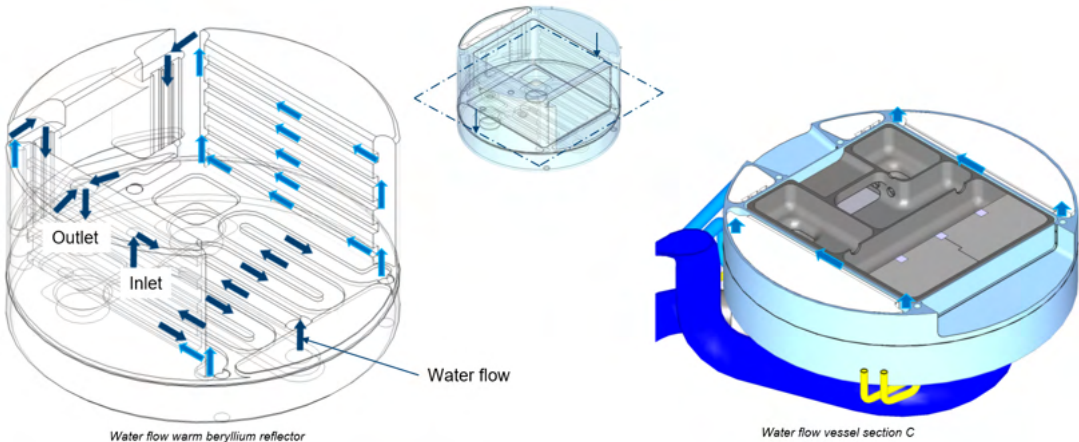
**Figure 72:** Flow pattern of water through the warm beryllium reflector parts, section A.

In this bottom part, the flow is separated into two parallel flows that go upwards along each side of the NNBAR opening (Figure 73).



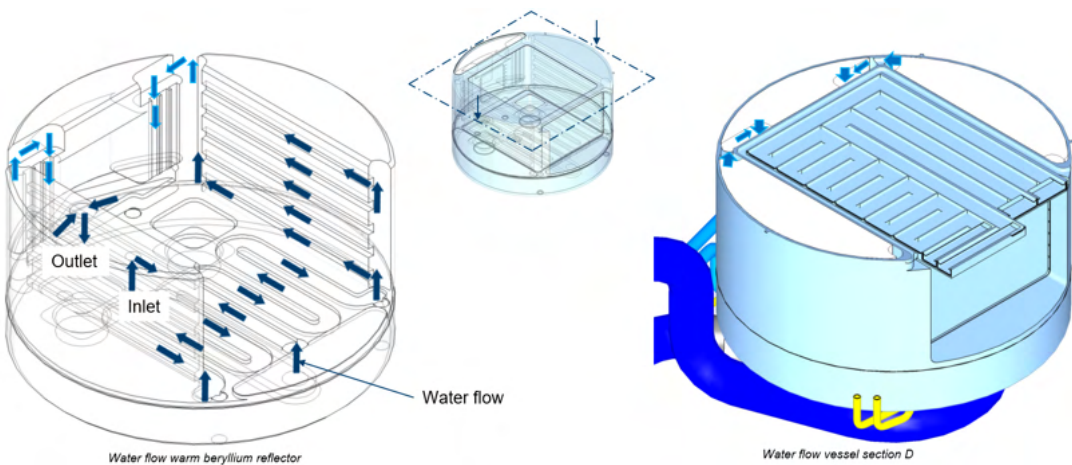
**Figure 73:** Flow pattern of water through the warm beryllium reflector parts, section B.

While flowing toward the top, the water is also distributed alongside the side pieces of the warm beryllium reflector, as shown in Figure 74.

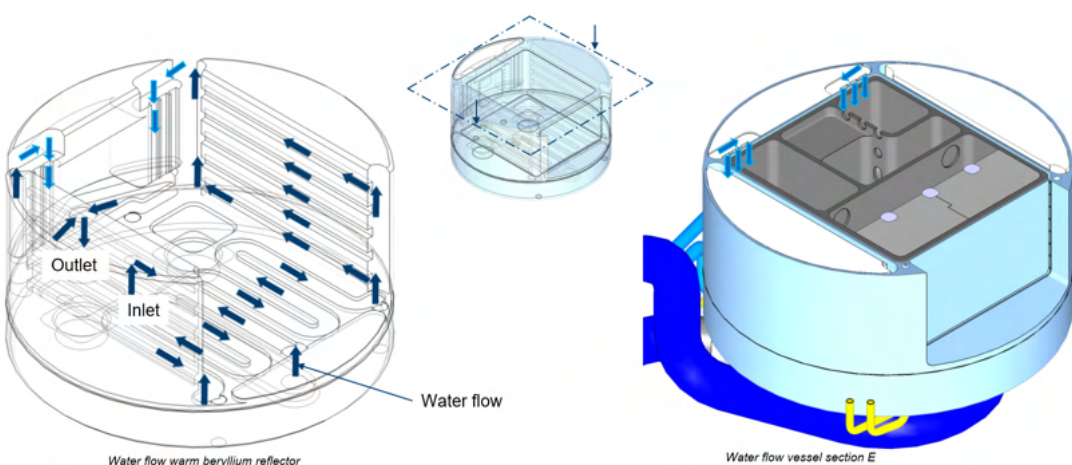


**Figure 74:** Flow pattern of water through the warm beryllium reflector parts, section C.

When the smaller neutron window A opening is reached in Figure 75 and Figure 76, the water flows downwards again.

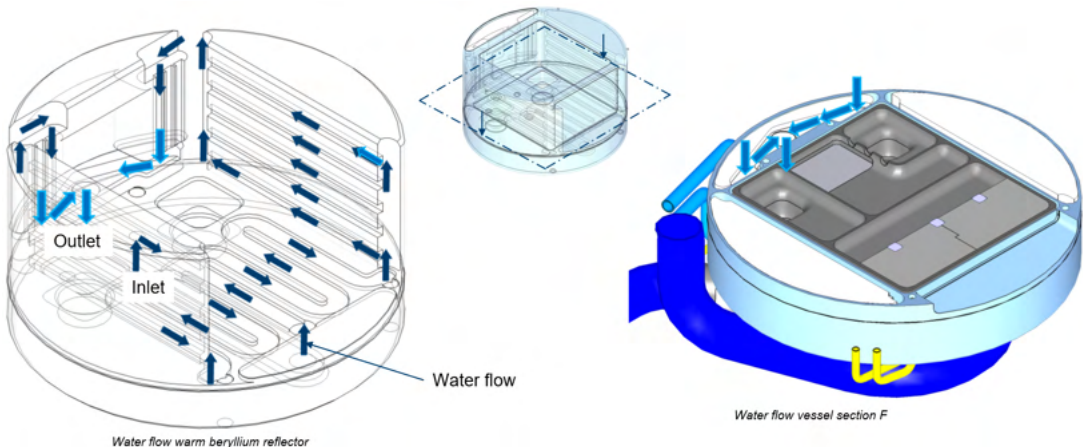


**Figure 75:** Flow pattern of water through the warm beryllium reflector parts, section D.



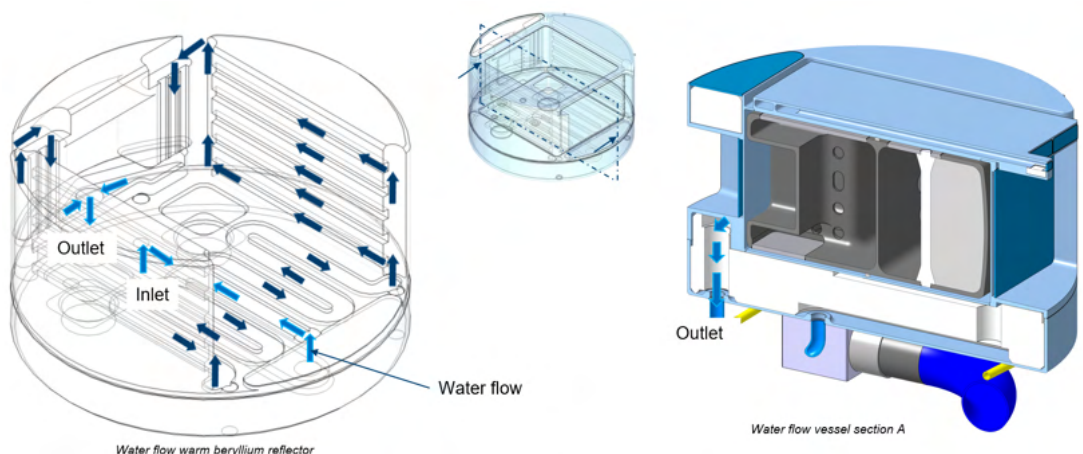
**Figure 76:** Flow pattern of water through the warm beryllium reflector parts, section E.

Next, the water flow is guided below the smaller neutron window A opening, through the warm beryllium filter parts underneath it (Figure 77).



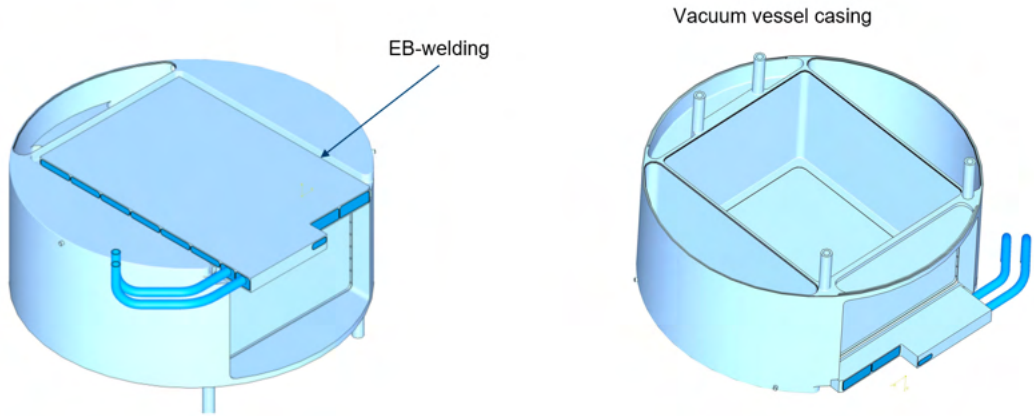
**Figure 77:** Flow pattern of water through the warm beryllium reflector parts

Finally, the flow is guided to the outlet pipe at the bottom side of the lower moderator plug, as shown in Figure 78.



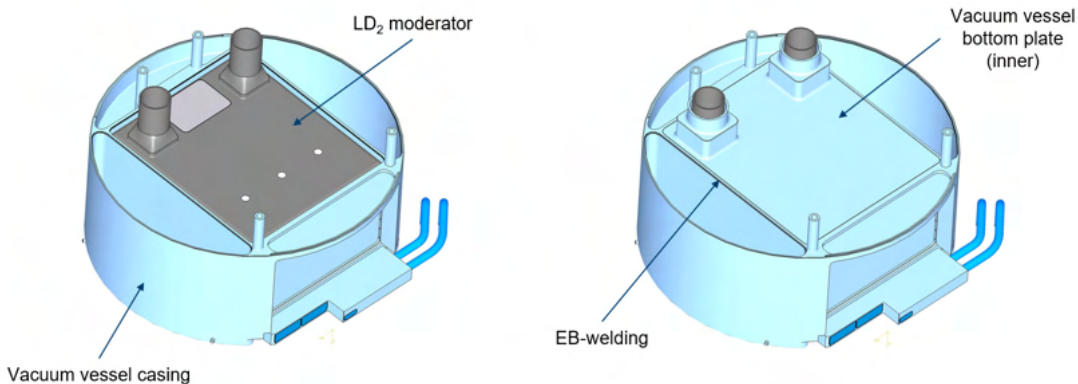
**Figure 78:** Flow pattern of water through the warm beryllium reflector parts

The assembly sequence of the outer vessel is then shown in Figure 79 to Figure 85. At first, the water disc premoderator is welded to the top of the outer vessel via electron-beam welding (Figure 79).



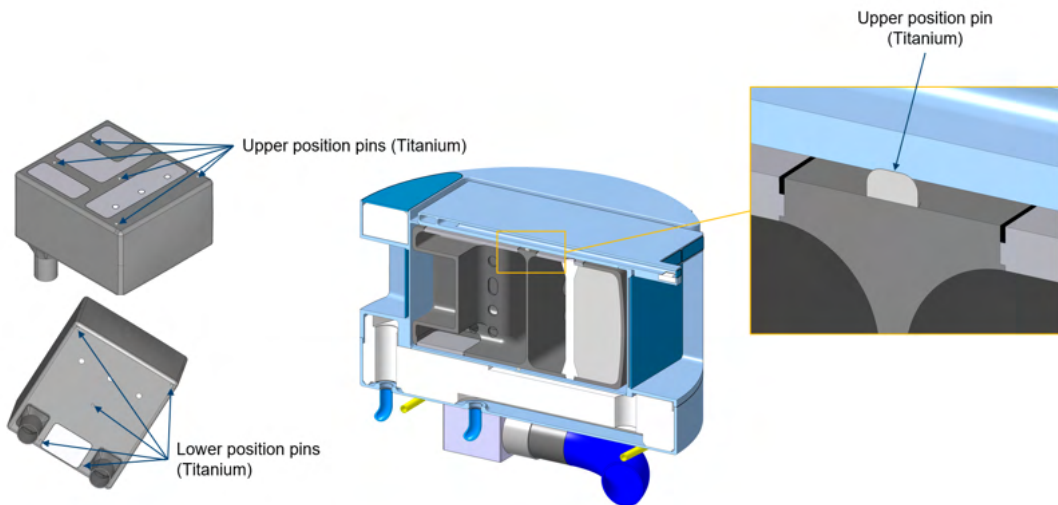
**Figure 79:** Assembly and EB-welding of the vacuum vessel (premoderator).

The vessel is then flipped upside down and the LD<sub>2</sub> moderator is inserted. After this is complete, the inner bottom plate of the vacuum vessel is welded on via electron-beam welding (Figure 80).



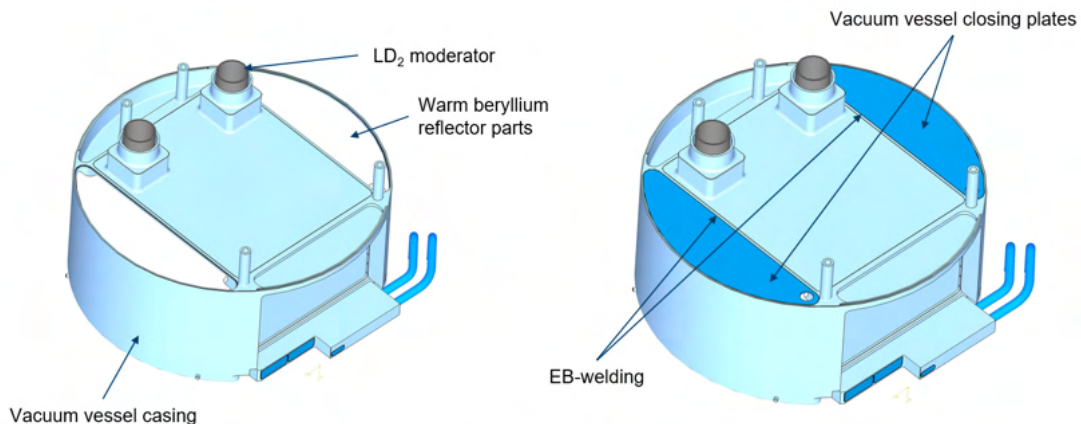
**Figure 80:** Assembly and EB-welding of the vacuum vessel (inner bottom plate).

Figure 81 shows how the moderator is positioned inside the insulation vacuum. It will rest on titanium pins on the top and the bottom of the moderator vessel. Titanium as a material is chosen for the positioning pins, because of its relatively low thermal conductivity – to minimize the heat transfer between the moderator and the vacuum vessel – and for its radiation resistance.



**Figure 81:** Positioning of the LD<sub>2</sub> moderator inside the vacuum vessel.

When the insulation vacuum around the moderator is successfully closed, the side segments of the warm beryllium reflector are inserted and the outer vessel is closed with the vacuum vessel closing discs via electron-beam welding (Figure 82).



**Figure 82:** Assembly and EB-welding of the vacuum vessel (Be reflector side segments).

Then the warm beryllium reflector parts above the WP7 window A (Figure 83) and the large bottom reflector part below the moderator (Figure 84) can be mounted and afterwards covered and sealed via electron-beam welding.

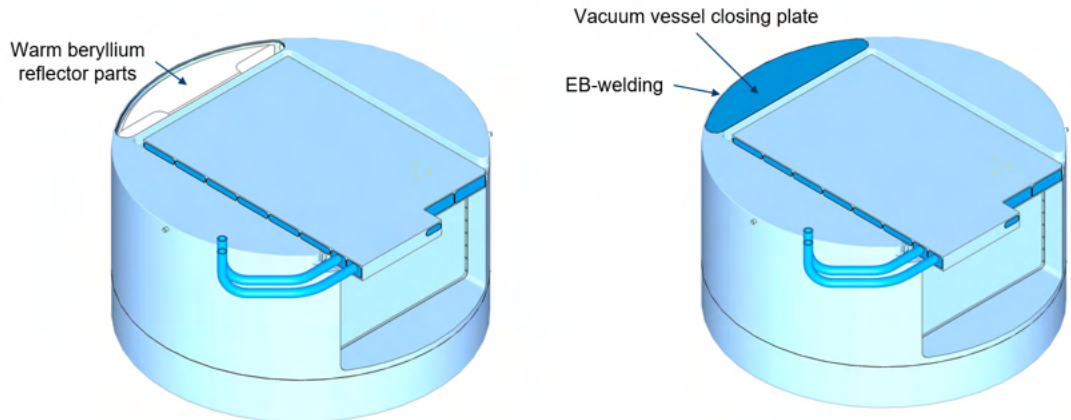


**Figure 83:** Assembly and EB-welding of the vacuum vessel (Be reflector segment above WP7 window A).

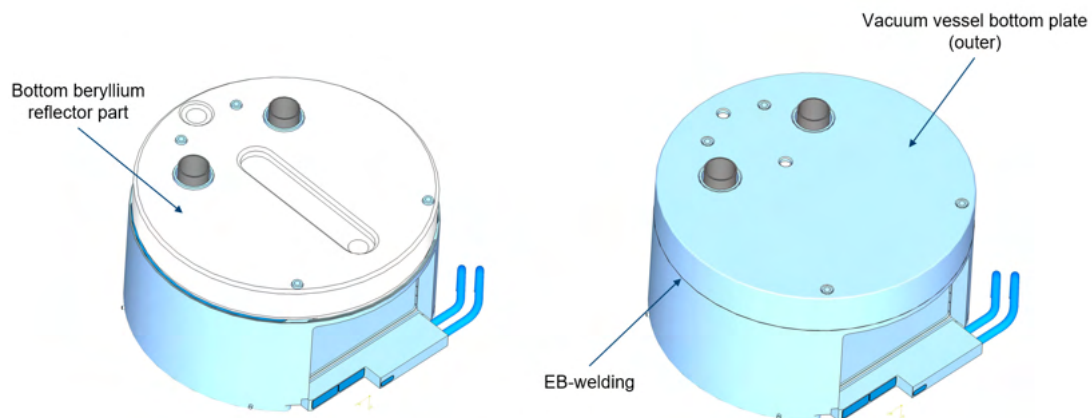


**Figure 84:** Assembly and EB-welding of the vacuum vessel (large Be reflector below the moderator).

In a final step, the cover plates for the actively cooled neutron windows A & B can be welded on via electron-beam welding, as shown in Figure 85.

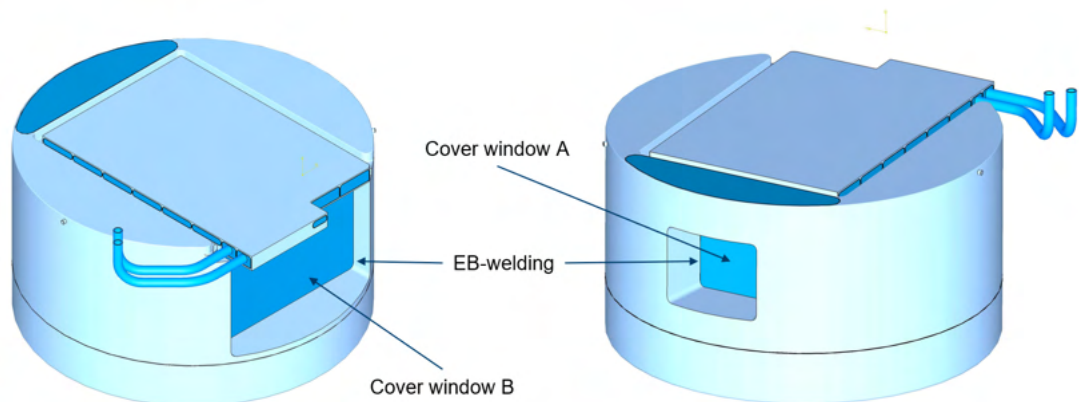


**Figure 85:** Assembly and EB-welding of the vacuum vessel (cover plates for beam windows).

At this point, the pre-assembly is ready for integration into the twister, which will be described in the following section.

### 3.11 Integrability into the ESS twister

The newly designed moderator and reflector plug must fit into the existing twister frame below the target wheel. Also, all media supply for the moderators and the reflectors needs to be guided through the existing design of the twister shaft, since the surrounding shielding elements are not exchangeable and therefore a larger twister shaft diameter is not possible. In addition to the supply media for the first generation LH<sub>2</sub> moderator and its beryllium reflector above the target wheel, the lower moderator plug needs an additional supply lines for liquid deuterium, water for the premoderator, helium for the cooling of the neutron windows, water for the warm beryllium reflector, and vacuum for insulation. The designated location of the different media and the supply-pipe routing through the existing twister shaft are shown in Figures 86 and 87.

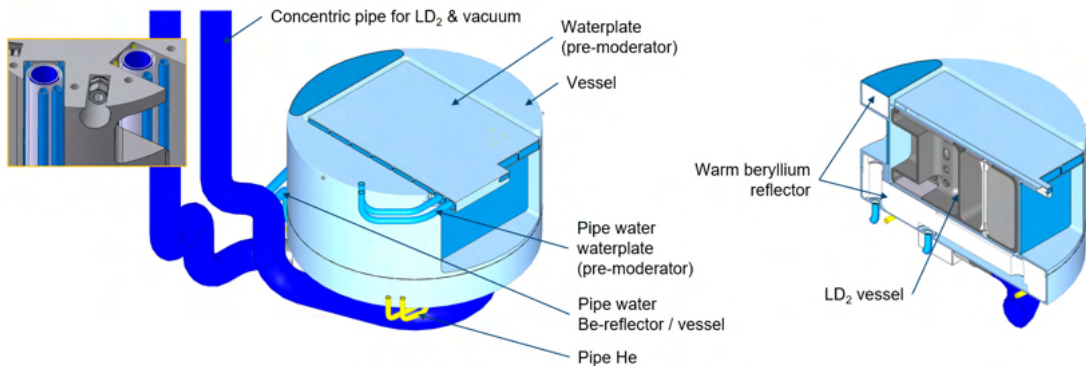


**Figure 86:** Media interfaces on the lower moderator plug.

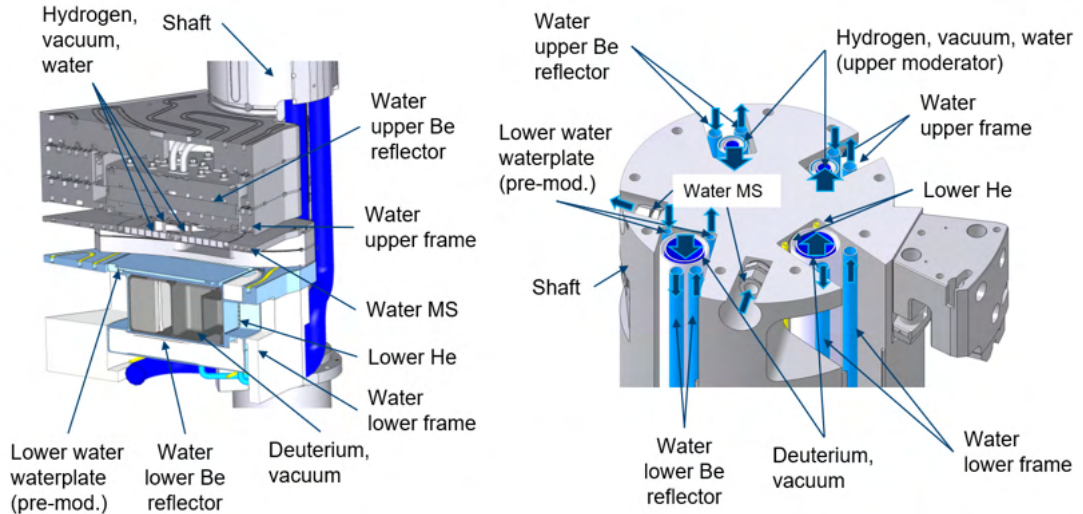


**Figure 87:** Twister integration and interface description.

The attachment and integration of the lower moderator plug into the twister, underneath the target wheel, is illustrated in Figures 88 and 89. The outer vessel has three assembly pins radially installed on the outer cylindrical surface. The corresponding part in the twister is the lower mounting socket, where three slots with a bayonet-catch shape are implemented.

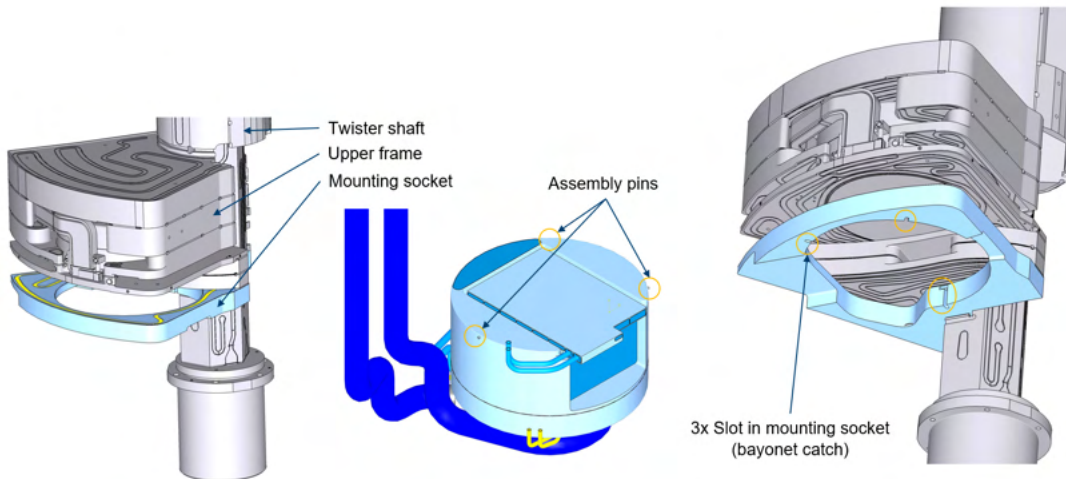


**Figure 88:** Assembly of the lower moderator plug to the twister (mounting details).

With this mechanism, the moderator plug can be inserted into the mounting socket from below and then is aligned to its final position by turning. After the plug is fixed in the mounting socket, the lower frame can be assembled to the twister shaft and welded to the mounting socket, to complete the stainless-steel shielding in this area.

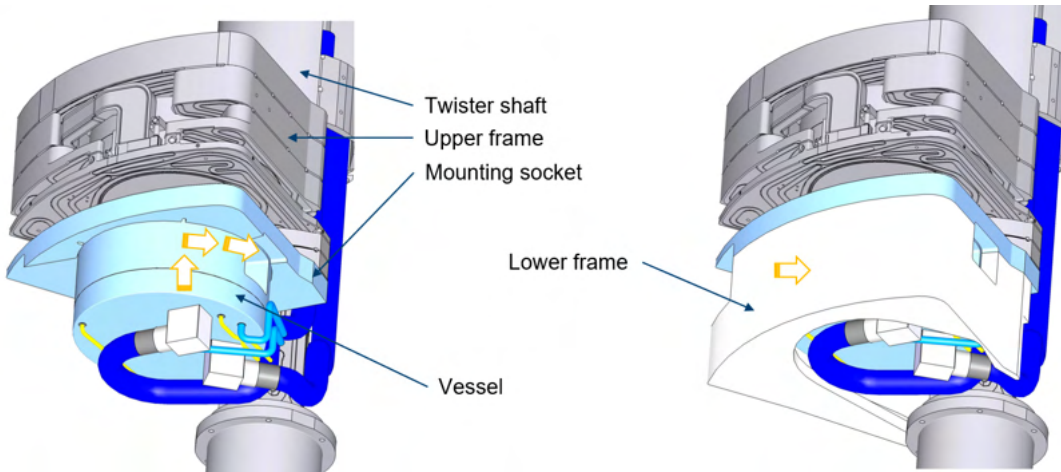


**Figure 89:** Assembly of the lower moderator plug to the twister (insertion and turning).

In summary, it can be stated that the integration of the new LD<sub>2</sub> moderator system into the existing twister is a very complex process, but feasible.

### 3.12 Summary and outlook: engineering implementation of deuterium moderator

In general, it can be concluded that a LD<sub>2</sub> moderator system for ESS appears to be feasible from an engineering point of view. It was demonstrated that a volume moderator, including all necessary process lines, can be integrated into the existing twister structure under the given restrictions. Furthermore, the detailed design shows that the moderator system can withstand all mechanical loads and that the manufacturing and welding, although very complex, is feasible.

The conceptual design for the cooling process describes all the additional infrastructure needed to realize such a moderator upgrade. A key point is to reduce the deuterium inventory as much as possible. On one hand, this can be accomplished by choosing a location for the cryostat as close as possible to the moderator and, on the other hand, by reducing the heat load.

The reduction of the heat load is also decisive from a thermo-mechanical point of view in order to be able to use the moderator at full beam power of 5 MW. Without further optimization, the proton beam power is currently limited to 2 MW. However, the first optimizations have already shown that the separation of the cold beryllium filter already leads to significant improvements. In contrast to the demonstrated box-shaped moderator (worst case), slightly shaped vessel walls would allow for a reduction in the wall thickness, which means in turn that less heat is generated and the neutronic performance of the moderator is improved as well. However, the following recommendations should be examined more closely in a follow-up project, before a final decision for the moderator upgrade will be made:

### **Recommended further engineering investigations**

- Building a full-scale prototype is recommended, because of the stringent requirements on the manufacturing process and specifically because of the welding process. Electron-beam welding of the aluminum alloy EN AW-6061 T6 can be critical, because of the weld-in depth of the needed filler material. Therefore, thorough welding tests should be performed to determine the final design.
- Thermo-hydraulic analysis needs further investigations, especially for 5 MW beam power.
- Separation of the beryllium filter from the LD<sub>2</sub> moderator, to reduce the heat load.
- Reducing aluminum content by changing the shape of the moderator to reduce the heat load and to improve the neutronic performance.
- Better understanding of local nuclear boiling on the wall with subcooled main flow.
- Thermo-hydraulic analysis, considering boiling on the wall (by experiment).
- Possibly relaxing ESS requirements regarding local boiling and measurement of critical heat flux.
- Analysis of the risk of cavitation due to wall boiling in-pulse (by experiment).

## 4 Design of a Very Cold Neutron Source

### 4.1 VCN: a long-wished-for source

An intense VCN source has been a desire of the neutron community for at least 20 years. A dedicated workshop [27] was held in 2005 to discuss ideas for sources and applications. While several ideas on possible materials for VCN were raised (cf. Section 4.6), it was clear at that time that the lack of knowledge of the properties of the candidate materials, and, in particular, the thermal scattering libraries, constituted a major problem for realistic design studies. It is worth recalling that at this workshop a program to study VCN sources was outlined. This included topics such as: 1) experiments on selected moderator types; 2) development of scattering kernels for candidate materials; 3) benchmark measurements of VCN production; 4) investigations of thermal and superthermal production of VCN. The HighNESS project has taken on most of these tasks, thus offering for the first time the concrete possibility of designing realistic VCN sources.

### 4.2 VCN neutrons: a brief introduction

Very cold neutrons cover a wide spectral range within the long-wavelength tail of cold neutron sources<sup>3</sup>, with energies ranging from below 1 meV (9 Å) to few hundreds of neV (> several 100 Å), the domain of UCN. A VCN source offers new possibilities in neutron scattering applications [28] and fundamental physics research. Extended neutron wavelengths ( $\lambda$ ) inherently enhance the capabilities of diverse instrument categories. This impact can be observed in the  $\lambda$  dependencies of the gains in instrumental resolution at fixed geometry and in intensity at fixed resolution. For example, gains in resolutions proportional to  $\lambda^{-1}$ ,  $\lambda^{-3}$  and  $\lambda^{-3}$  are expected for reflectometers, time-of-flight instruments and neutron spin echo (NSE), respectively, while gains in intensity at fixed resolution are expected to be proportional to  $\lambda^2$ ,  $\lambda^2$  and  $\lambda^3$  for these three classes of instruments [27].

Particle physics experiments can benefit from enhanced VCN fluxes, including the search for neutron-antineutron oscillations (described in Section 9), beam experiments looking for a non-zero neutron electric dipole moment and search for novel fundamental forces (discussed in Section 4.3).

In this section, we first provide an overview of the scientific case for VCNs and later describe the different design concepts that have been developed in the course of the HighNESS project.

### 4.3 Fundamental physics with VCN

The primary advantage of VCNs in fundamental physics experiments is their extremely low energy, which results in long interaction times with the experimental apparatus. Unlike UCNs, VCNs can still be considered as beams, allowing for the application of beam optics and related methods. Consequently, VCNs enhance the sensitivity of most fundamental physics experiments that utilize beams of slow neutrons or exploit the wave-optical properties of these beams.

#### 4.3.1 Beam Experiments

Recently suggested particle physics experiments using beams of slow neutrons include:<sup>4</sup>

- In-beam searches for a permanent neutron electric dipole moment (nEDM) [29, 30, 31], and searches for new fundamental forces [32]. These kind of experiments profit linearly from the interaction time  $t$  of the neutron in the apparatus. Therefore, their figure of merit can be considered proportional to  $\lambda$ .
- Measuring the neutron lifetime  $\tau_n$  by means of the *beam method*. Typically these experiments contain a trapping region of some length  $L$  that intercepts a neutron beam. The neutron decay is

<sup>3</sup>The standard cold moderator materials for both spallation and fission sources are liquid or solid deuterium ( $S_2$ ), liquid hydrogen ( $H_2$ ) and liquid or solid hydrocarbons (e.g. methane( $CH_4$ )).

<sup>4</sup>Note that this list is not exhaustive.

observed by detecting decay protons within the volume of these region. In an experiment similar to [33], the mean number of neutrons in the decay region at any time is given by,

$$N_n = L \int_A \int da I(v) \frac{1}{v} dv , \quad (1)$$

where  $A$  is the cross-sectional area of the trap and  $I(v)$  is the velocity-dependent fluence rate [33]. By increasing the VCN flux through such an experiment, the neutron density and hence the observed neutron decay rate increases, which in turn improves the statistical accuracy of the result. Similarly to the nEDM experiments, there is an expected FOM  $\propto \lambda$ . It should be noted that these experiments still suffer from a systematic uncertainty, associated with the determination of the absolute neutron flux. Further progress towards the reduction of this uncertainty, as pointed out in [34], could increase the precision of VCN beam lifetime experiments significantly and shed light on the neutron lifetime puzzle [35].

- Experiments searching for neutron anti-neutron oscillations [36, 5]. Here it is not the interaction time, but quasi-free flight time of VCN that allow to significantly increase the sensitivity of the experiment. Under these conditions the probability for a transition can be expressed by:

$$P_{n \rightarrow \bar{n}} = \left( \frac{t}{\tau_{n \rightarrow \bar{n}}} \right)^2 , \quad (2)$$

with the free oscillation time  $\tau_{n \rightarrow \bar{n}}$  [36]. This results in a FOM =  $N_n t^2$ , with  $N_n$  being the total number of neutrons observed. Due to the proportionality of the (FOM) to  $\lambda^2$ , VCN exhibit specific potential for neutron oscillation experiments.

One should note, that, under the assumption of equivalent phase-space density, in most experiments the long interaction time or the longer free flight time of VCN is in competition with their lower flux. It is therefore crucial, in order to truly increase the sensitivity of the experiments described above, to increase the phase space density of VCN in the source. This has been discussed in [31] and [37].

### 4.3.2 Wave-Optical Experiments

Another class of experiments that could potentially benefit from VCN's exploit the wave-optical properties of the neutron, in terms of diffraction and interferometry. The potential of low wavelength neutrons for wave optics experiment was already pointed out in the 80s and early 90s in the works of A.G. Klein, A. Zeilinger et. al. [38]. An extensive list of fundamental physics experiments utilizing neutron interferometry techniques is provided in [39]. Some of these experiments can benefit from lower energy neutrons. While certain proposed experiments may have become less relevant due to advancements in other fields, wave-optical experiments involving VCN remain an exciting avenue for fundamental physics research.

A dedicated VCN source could for example be used for:

- Further investigation of gravitationally induced quantum interference as measured in the famous COW<sup>5</sup> experiment [40]. While this effect was already measured with VCN [41], the experiment could be significantly improved with higher fluxes, brightness and modern VCN optics.<sup>6</sup> With regard to the latter, especially the field of holographic gratings, as described in [42], made significant progress.
- Improve the current limit on the neutron charge [43] with a Talbot-Lau interferometer [44].
- Measurement of the gravitational constant G by means of an active gravitational mass other then the Earth itself, in a *Cavendish experiment*, as described in [45].

---

<sup>5</sup>Acronym for R. Colella, A. W. Overhauser, and S. A. Werner.

<sup>6</sup>It should be noted that VCN might not be competitive with the accuracy of atom interferometers, as pointed out in [39, p. 263f.].

#### 4.4 VCNs in condensed matter research

In condensed matter research with neutrons, the momentum and energy transfer of scattering events is measured to probe the structure and dynamics of a sample material. Very cold neutrons hold significant potential for advancing this field of study. While low-energy neutrons provide the highest sensitivity to low momentum and energy transfers (and therefore are well suited for maximizing resolution) their usage is hindered by the low available flux in the VCN regime. The flux of VCNs in the tail of a Maxwellian spectrum typically available from conventional cold neutron moderators exhibits a wavelength dependence of  $\lambda^{-5}$ .

High-resolution techniques such as small-angle neutron scattering SANS, time-of-flight spectroscopy, and neutron spin-echo (NSE) are mostly seen as standing to gain from longer-wavelength neutrons [46]. Moreover, other methods such as neutron imaging, which is a real-space technique, might benefit in some cases from improved flux conditions down to the VCN regime.

Small angle scattering is an elastic neutron scattering technique, where the resolution of small angles enables studying large-scale structures on the nanometer scale (i.e. from a few to a few thousand nanometers). Flux limitations typically prohibit probing larger structures up to the micrometer scale with conventional pinhole SANS instrumentation. Other instrumentation exploring even smaller momentum transfers, and thus giving access to the low-micrometer scale, are typically limited to one dimension and require separate measurements. Thus, it is desirable to increase the resolution of conventional SANS instruments.

An elementary analysis shows that a  $\lambda^{-5}$  slope of the long wavelength tail of a moderator spectrum marks the break-even for gaining either efficiency or resolution at longer wavelengths with SANS [27]. This is due to the momentum transfer being  $q = 2\pi/\lambda \sin \theta$ , and thus larger wavelengths enable lower collimation and larger sample sizes in both dimensions across the beam for achieving the same angular resolution. Together with the increased  $d\lambda$  for constant  $d\lambda/\lambda$ , the gain equals  $\lambda^5$ . Hence, a long-wavelength tail that decays at a rate less than  $\lambda^{-5}$  will have corresponding performance gains (either in data rate or resolution, or a balanced gain in both).

However, these simplified considerations do not yet take into account some additional aspects, in particular the downsides, of utilizing very long wavelength neutrons – namely their increased absorption probability and the significant impact of gravity on their trajectories. Increased absorption heightens the requirements on all materials used in the neutron beam, in particular neutron beam windows of sources, guides, and sample cells and environments. The increased absorption along with an increased scattering probability will favor thin samples to avoid absorption losses due to the former effect and multiple scattering from the latter. Effects from gravity can in principle be countered by means of instrumentation but might contribute to complexity and additional absorption issues.

When turning to experimental methods probing energy transfers and thus dynamics, the same break-even principle is found for time-of-flight spectroscopy probing inelastic scattering. Here, basic estimates can take into account that the energy change  $dE \propto dt/\lambda^3$ , where  $dt$  is the time resolution. The estimated gains, taking into account a lower repetition rate, and thus scaling with  $\lambda^5$  again, imply wavelength-independent performance at constant resolution for a long wavelength tail of an Maxwellian spectrum decaying with  $\lambda^{-5}$  [27, 46] (keeping in mind the corresponding relaxation of instrument requirements for monochromatization – initial pulse length – and neutron pulse length at the sample). However, in time-of-flight spectroscopy, the momentum transfer resolution would increase, and relaxing collimation and increased sample size could result, corresponding to the previous considerations for SANS, with gains proportional to  $\lambda^4$ . Only the required momentum-transfer range limits such gains, where for example, for quasi-elastic measurements the wavelength must be limited to  $\lambda < 4\pi/k_{max}$ , where  $k_{max}$  denotes the maximum momentum transfer.

In NSE, longer wavelengths are utilized to improve the energy resolution based on the relation  $dE \propto dt/\lambda^3$ , but without being able to profit from relaxing the requirements on incoming wavelength resolution, divergence, or increased beamsize, like in the cases outlined above. However, results from high-resolution NSE instruments such as IN15 at ILL imply that the current technology of magnetic field configurations does not allow for further gains beyond about 25 Å [46].

For neutron imaging, different considerations have to be taken into account. Currently, neutron imaging reaches resolutions of a few micrometers, enabled by progress in detector technology. However, in the range of single micrometers, the technique meets two limitations. The first one is related to contrast, since only a few materials would provide sufficient image contrast on a thickness scale of micrometers. Here, a colder spectrum is beneficial, since absorption tends to increase with longer wavelengths, thereby enabling the resolution of smaller structures. The second limitation is neutron flux. Current resolutions and the utilization of the entire white beam spectrum already indicate a limitation in flux, suggesting that a decay in flux close to  $\lambda^{-5}$  prevents the effective use of very cold neutrons for high-resolution imaging.

On the other hand, novel lens systems for neutrons promise gains of the order of  $10^4$  [47] and long wavelengths are advantageous for lenses due to the refractive index increasing with  $\lambda^2$ , the focal length with  $\lambda^{-2}$ , and the critical angle with  $\lambda$ . The concern regarding increased absorption makes reflective focusing optics, like Wolter optics [48], an attractive choice. By using shorter focal lengths, the impact of gravity can be minimized. However, it is important to take into account and address any potential aberrations that may arise and require correction [49]. The potential of true neutron microscopy to unlock unexplored applications and fields of study is particularly promising in soft matter and biology, where deuteration can provide unique opportunities for neutron imaging. Moreover, efficient neutron lenses designed for long wavelengths can also have a significant impact, especially in techniques such as SANS.

Finally, in [50] the possible advantages of using VCNs in reflectometry techniques are discussed in several configurations. Gains are expected if there is a shift of the neutron spectrum towards colder energies, provided that the brightness is preserved. The use of VCNs for reflectometry is considered particularly promising for compact sources, due to their intrinsically limited performance and to the fact that new compact sources could be designed for optimal use of VCNs.

## 4.5 VCN design options

In the original proposal of the HighNESS project, two approaches were considered for the design of such a source. One is based on a dedicated VCN source using a suitable material that would provide a high flux of VCNs, while another one, similarly to the PF2 beamline<sup>7</sup> at the ILL, extracts VCNs directly from the cold source. At the dedicated workshop in 2022 [51], an additional concept was suggested, that can be considered a merger of the two approaches [52].

### 4.5.1 Dedicated VCN moderator

Previous studies, using a set of candidate materials for which thermal scattering libraries were available, indicated that solid orthodeuterium and solid methane promise a higher VCN production performance than LD<sub>2</sub> [53]. However, solid methane has the problem of radiolysis-induced radical formation followed by polymerization [54] and is therefore likely not suitable in a high-power spallation facility. SD<sub>2</sub>, on the other hand, is already well-established as an in-pile converter medium for UCN sources (see Section 6.4 and Section 6.5). Another class of candidate materials, whose suitability for moderation to the VCN energy range still needs to be demonstrated experimentally, are fully deuterated clathrate hydrates. In these inclusion compounds, guest molecules occupy cages formed by a rigid network of water molecules. Various local modes can be excited in incoherent inelastic scattering events, which provide a path for cascaded neutron cooling that is not kinematically restricted by a dispersion relation [55]. A strong candidate material investigated within HighNESS is the fully deuterated tetrahydrofuran (THF-d) clathrate hydrate, which has a broad band of low-energy modes, as experimentally demonstrated for its undeuterated version [56].

For both materials, SD<sub>2</sub> and THF-d clathrate hydrate, the highest VCN fluxes are to be expected at source locations near the spallation target. Although both materials are expected to deliver a higher VCN flux than the LD<sub>2</sub> moderator, their use is justified only if they outperform the main source in the

---

<sup>7</sup><https://www.ill.eu/users/instruments/instruments-list/pf2/description/instrument-layout>

wavelength range of VCNs. This is very difficult to achieve, as shown in Ref. [53], and requires the highest possible incident flux, so that the best location for a VCN source would be below the spallation target, thus replacing the cold source. This solution would have to cope with the challenge of cooling the material to the needed temperature. While for  $\text{SD}_2$  a temperature of 5 K seems optimal [57], the THF-d clathrate hydrate would best be operated below 2 K. At such low temperatures, the local modes are predominantly populated in the ground state, which suppresses up-scattering. From a practical point of view, He-II can be used for effective cooling of the weakly thermal-conducting clathrate hydrate.

Designs with dedicated VCN moderators are reported in Section 4.7 for  $\text{SD}_2$  and in Section 5 for deuterated clathrate hydrates.

### 4.5.2 Use of advanced reflectors

The use of advanced reflectors for a VCN source was at the beginning of the HighNESS project intended in combination with the liquid deuterium moderator, as discussed in Section 4.9. However in the course of the project we have developed designs where nanodiamonds have also been applied in the full  $\text{SD}_2$  design, as detailed in Section 4.7, as well as in the Hybrid design, as described in Section 4.8

### 4.5.3 Hybrid design

The hybrid design proposed by Nesvizhevsky supplements the baseline  $\text{LD}_2$  moderator with an adjacent or embedded block of  $\text{SD}_2$ . The original rationale for such an option was to improve the performance for NNBAR. However, potential gains for general VCN performance may also be feasible. As such, this option has been investigated in several configurations, for both the NNBAR and WP7 beam openings, and is discussed in-depth in Section 4.8.

## 4.6 Solid ortho- $\text{D}_2$

In the first workshop dedicated on Applications of a Very Cold Neutron Source [27], the designs proposed for a VCN moderator already made use of solid materials like Be, graphite,  $\text{D}_2$  and  $\text{D}_2\text{O}$  in the configuration of a bed of small pellets between 5 and 10 K with liquid helium at 2 K flowing through the gaps as a coolant. It is well known that deuterium is one of the best neutron moderator materials thanks to its small nuclear mass and absorption cross section. During the workshop, it was acknowledged that deuterium-based materials are expected to be generally better than graphite and beryllium, whose total cross sections has no incoherent contribution and a steep fall for energies below the lowest Bragg edge (5 meV in Be and 2 meV in graphite). However, the higher heat capacities of beryllium and graphite left open the possibility that they might be favored when optimizing the source for the neutron flux weighted on the heating during the accelerator pulse. At the end of the workshop, there was a consensus that the lack of neutron scattering kernels and measurements was hindering the design of a VCN source based on calculations.

A more recent study by Gallmeier et al. [53] looked for a VCN source option for the second target station at SNS. The set of materials investigated was chosen based on the thermal scattering libraries available. In particular, para- $\text{H}_2$ , water ice, beryllium [58, 59], ortho- $\text{D}_2$ [60],  $\text{CH}_4$ [61], and Neon, all solid at cryogenic temperatures of 4-6 K, were compared. The figure of merit in that study was the time-integrated pulse brightness over a liquid para- $\text{H}_2$  moderator at 20 K. The authors indicated that solid ortho-deuterium ( $\text{SD}_2$ ) and solid methane are the most promising material for delivering a higher VCN production than liquid hydrogen, with the former able to outperform a conventional cold source by a factor 2, at the expense of a pulse five time longer. While solid  $\text{CH}_4$  is generally considered a good candidate material for a VCN source due its high hydrogen content, it is likely not suitable in a high-power spallation facility like ESS. Irradiation of methane leads to the formation of radiolysis-induced radicals  $-(\text{CH}_2)_n-$ , followed by polymerization into carbon-based deposits and release of  $\text{H}_2$ , both of which have been observed to accumulate in the moderator vessel [62, 54]. On the other hand, solid ortho-deuterium, well-established as an in-pile converter medium for UCN sources [63, 64, 65, 66, 67, 68],

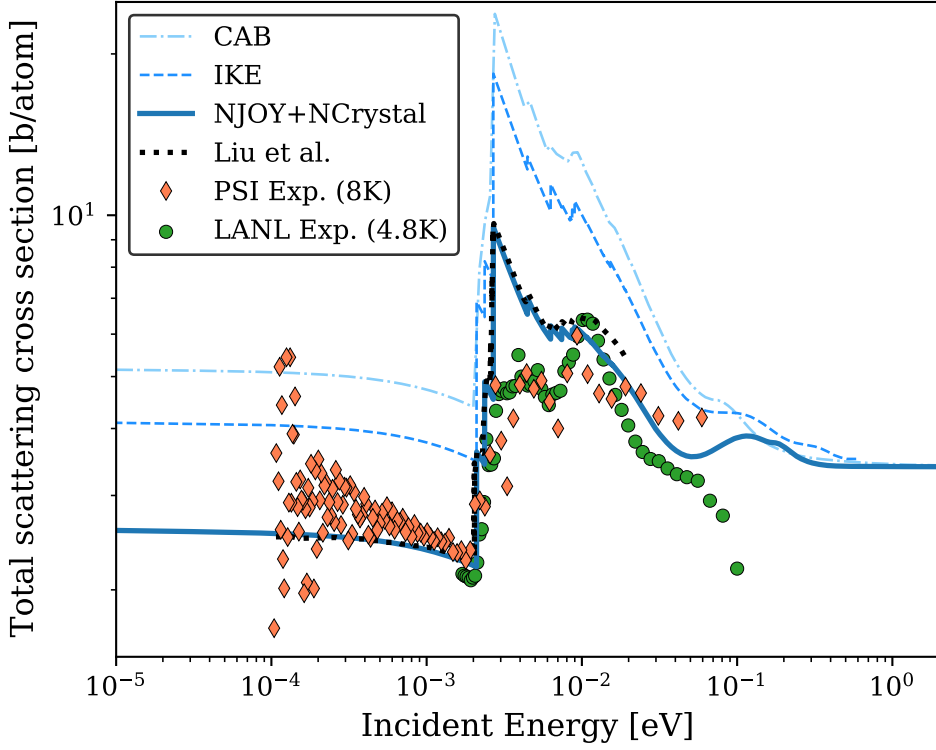


**Figure 90:** Total scattering cross section per atom for  $\text{SD}_2$  as a function of incident energy. Here, NJOY+NCrystal is the new library, CAB is the evaluation generated by *Centro Atomico Bariloche* [60, 69], and IKE is the evaluation from *Institut für Kernenergetik und Energiesysteme* [59]. Also the more recent model developed in [72] is shown for comparison. Models are also validated with measurements from SINQ/PSI [65] and LANL/LANSCE [64]. Only every fourth data point is shown for clarity.

has no physical impediment to the VCN production in high radiation fields, despite the many challenges related to keeping such a source at low temperature.

In this work, a new scattering kernel was used to model the interactions of slow neutrons with  $\text{SD}_2$ . The library, developed by the Spallation Physics Group at ESS, follows the physics of the thermal scattering model from Granada [60, 69], and uses the new mixed-elastic scattering format to correctly include both the coherent and incoherent components of elastic scattering [70]. The cross section and the benchmark against experimental data [65, 64] can be seen in Figure 90. The related files are available in the ESS Gitlab repository [71].

#### 4.7 Dedicated $\text{SD}_2$ source

Neutronics simulations for this analysis used MCNP 6.2 [73]. Our first tests involved a moderator which had a similar total volume to the baseline  $\text{LD}_2$  source, where the total  $\text{LD}_2$  moderator volume was partially displaced by  $\text{SD}_2$ . Different configurations were tested, varying the relative amounts of  $\text{SD}_2$  and  $\text{LD}_2$ . The highest intensity in the VCN region was obtained for  $\text{SD}_2$  completely replacing the  $\text{LD}_2$ . Therefore, the focus in this section is on the properties and performance of a full  $\text{SD}_2$  moderator. Additionally, we have investigated the effect of surrounding the  $\text{SD}_2$  with a layer of nanodiamonds (NDs), see Section 10.2.2. The ND layer is 5 mm thick with a density of  $0.6 \text{ g/cm}^3$  and is separated from the  $\text{SD}_2$  by a 0.5 mm Al sheet. The geometry for the MCNP models of the  $\text{SD}_2$  moderator is shown in Figure 91.

Compared to the  $\text{LD}_2$  baseline, the  $\text{SD}_2$  moderator vessel has thinner Al walls (0.2 cm), which is possible because it exerts less pressure as a solid block, and because it lacks a reentrant hole. A further improvement to the model has been obtained by adding a 20 K beryllium filter on the left-hand side, facing the NNBAR experiment (which demands mainly a high flux for  $\lambda < 15 \text{ Å}$ ). Unlike the baseline,

**Table 10:** Gain factors of the SD<sub>2</sub> moderator over the LD<sub>2</sub> baseline for the left-hand NNBAR opening and the right-hand general-purpose neutron scattering instruments opening (WP7). No internal cooling structures are considered (pure ortho-D<sub>2</sub> is used for both cases).

$\lambda$	2.5 Å to 4 Å	4 Å to 10 Å	10 Å to 40 Å	> 40 Å
<b>WP7</b>	0.7	1.1	2.3	27
<b>NNBAR</b>	0.6	1.3	2.1	14

the Be filter would be added outside the vessel, thus avoiding the need to remove moderator material. This filter would improve the performance on the NNBAR side in the 4 Å to 10 Å range by roughly 40% with respect to the case without filter, while sacrificing 70% in the 2.5 Å to 4 Å and 20% in the >40 Å range. The scattering instruments' opening would also benefit from having the filter on the opposite side, leading to an increase of 5% in flux for the cold and very-cold range.

In Table 10, we report the gain factors for the best performing SD<sub>2</sub> model (Figure 91) over the baseline for different energy ranges.

In Figure 92, the spectral brightness is calculated for the cases with and without ND and compared with the baseline. To obtain the absolute brightness we used the raw counts per proton on the spallation target recorded at the exit of the twister ( $\approx 50$  cm from the emission surface). In particular, we divided the counts within a cone with 2° half opening angle to the surface normal, by the emission surface, by the solid angle defined by this cone and by the bin width in wavelength, and then we multiplied the result by the expected proton current on the ESS target at 5 MW:

$$B \left[ \text{n/s/cm}^2/\text{sr}/\text{\AA} \right] = \frac{C \left[ \text{n/nps} \right] P \left[ \text{nps/s} \right]}{S \left[ \text{cm}^2 \right] \Omega \left[ \text{sr} \right] \Delta\lambda \left[ \text{\AA} \right]} \quad (3)$$

As a benchmark, we compared the LD<sub>2</sub> moderator brightness calculated in this way with the method described in [19, 5]. The reason why this comparison is possible only for the LD<sub>2</sub> case is a technical limitation in the use of a point detector tally (F5), on which the second method relies, when neutrons are transmitted through a ND layer. The comparison showed a difference of 10–20% across the whole energy spectrum, which is deemed reasonable as a systematic approximation of brightness.

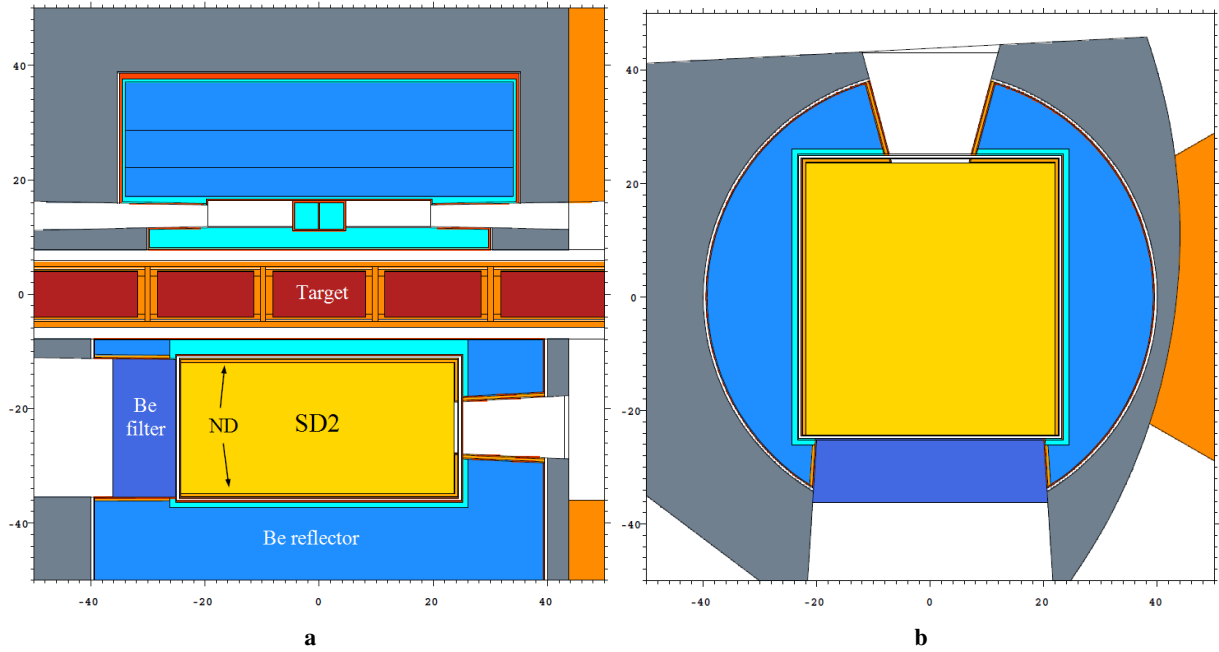


**Figure 91:** MCNP model of the full SD<sub>2</sub> moderator (a) vertical cut, perpendicular to the proton beam direction. (b) cut parallel to the target plane with the neutron beam impinging from the left.

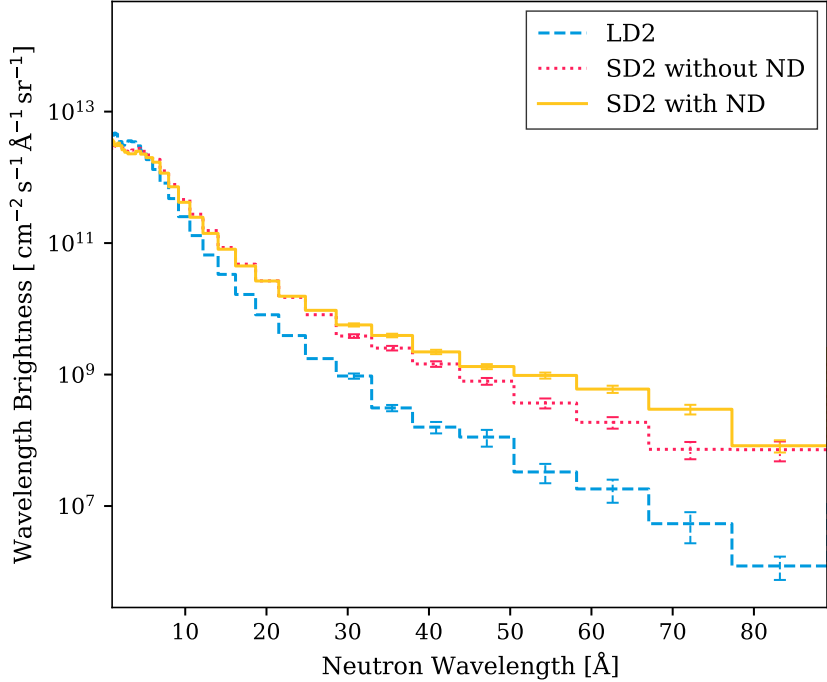


**Figure 92:** Brightness spectra comparison for VCNs emitted by lower-moderator designs using  $\text{LD}_2$ ,  $\text{SD}_2$ , and  $\text{SD}_2 + \text{ND}$  reflection layer. Tallies are taken for neutrons traveling  $\pm 2^\circ$  from the normal of the emission surface; the recording surface is placed at the twister exit in the direction of the beam port for neutron scattering instruments.

Two factors contribute to the improved performance of the  $\text{SD}_2$  moderator with respect to  $\text{LD}_2$ . The first is the high VCN yield of the ortho- $\text{D}_2$  crystal made possible by the very small upscattering cross-section for energies less than 20 meV ( $\lambda > 2 \text{ \AA}$ ) when compared with  $\text{LD}_2$ , see Figure 93. This results in a longer mean free path for upscattering, which produces a significant deviation from a Maxwellian thermalization spectrum at long wavelengths (an estimated  $\propto \lambda^{-3.5}$ , compared with the Maxwellian  $\lambda^{-5}$ ). This effect can be exploited in the design of novel neutron scattering instruments. The second factor yielding even higher gains in the VCN range is the addition of NDs which, due to their high albedo for VCNs, limit losses and trap neutrons in the moderating volume. The fact that NDs are effective in increasing the travel path is evident also from Figure 94, which shows the different moderators' time response at the twister exit for CNs and VCNs. The neutron counts in the figure are normalized to the peak value in the cold energy range. After 7.5 ms, the VCN counts, already much higher in  $\text{SD}_2$  than in  $\text{LD}_2$ , start to drop due to losses when there is no ND reflecting layer around the vessel. Adding the reflective layer reduces these losses and increases the chances for the neutrons to be further moderated. In the cold range, NDs are transparent and there is no significant difference in the time response.

Interestingly, adding an identical thin ND layer to the  $\text{LD}_2$  baseline did not produce the same relative gains described for  $\text{SD}_2$ . A significant 40% increase was calculated only on the NNBAR side for  $\lambda > 40 \text{ \AA}$ , but at the expenses of higher energy neutrons, which are the most relevant for the current NNBAR design. On the WP7 side, no gains at all were observed, but same losses at high energy. This suggests that in  $\text{LD}_2$  the good VCN reflective properties of ND are most likely not enough to counterbalance the upscattering from the medium.

It should be noted that, for neutrons in the  $\lambda > 40 \text{ \AA}$  range, simulations with good statistics are very costly to procure in comparison with shorter wavelengths, especially when incorporating the full geometry of the ESS target monolith and shielding. For mitigation we used the energy-splitting variance reduction technique in MCNP. Nonetheless, the relative error for this range remains at roughly 10% – convergence beyond this precision becomes particularly time consuming, even when simulating with 400+ cores on the ESS computing cluster.

Features that are not included in these basic simulations and that could negatively affect the gains are:

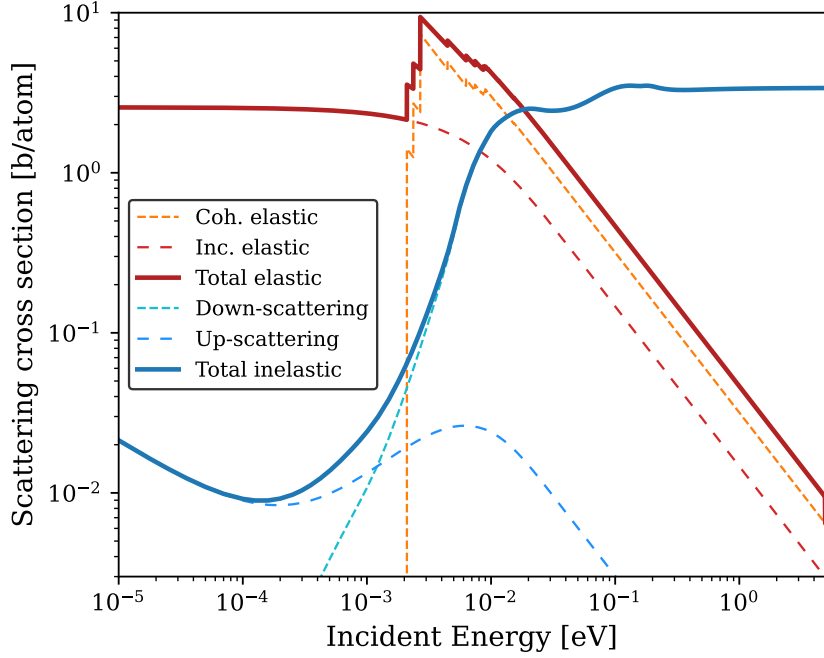


**Figure 93:** Thermal scattering cross section per atom for ortho-SD<sub>2</sub> used in this study. The elastic, both coherent and incoherent, and inelastic contributions are shown. The fall of the upscattering cross section at low energy makes SD<sub>2</sub> an excellent moderator for the VCN range.

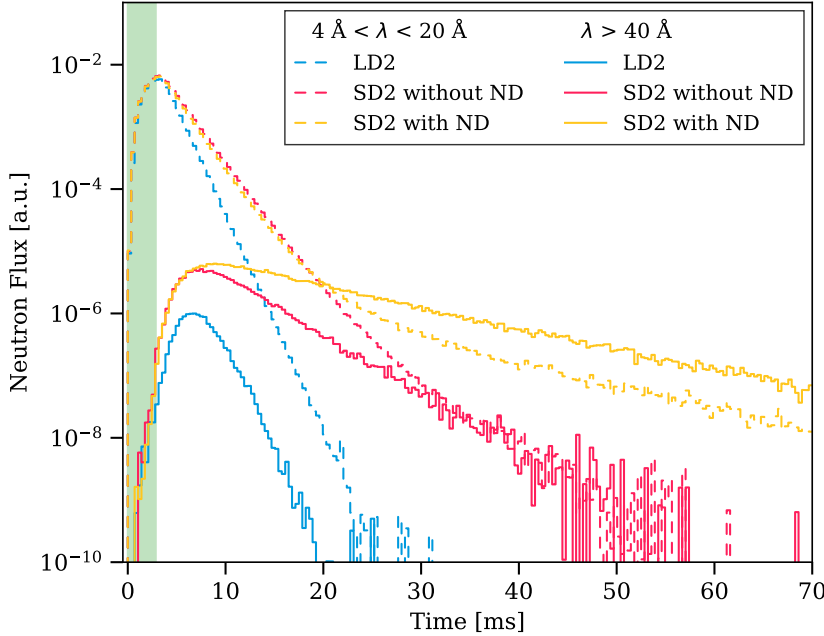


**Figure 94:** Temporal response of the moderator, calculated at the exit of the twister for CN in the range  $4 < \lambda < 20 \text{ \AA}$  (dashed lines) and VCN  $\lambda > 20 \text{ \AA}$  (solid lines) for the LD<sub>2</sub> baseline and the SD<sub>2</sub> moderator with and without ND. Counts are normalized to the maximum values for the  $4 < \lambda < 20 \text{ \AA}$  spectra. The recording surface is placed at the twister exit in the direction of the beam port for neutron scattering instruments.

- Internal structure for cooling;
- Para-D<sub>2</sub> and H impurities in ortho-D<sub>2</sub>
- Cracks and imperfections in the D<sub>2</sub> crystal

While these effects will be covered in the next sections, a full optimization of the moderator's dimensional parameters (size, shape, position, etc.) has not yet been performed. This is expected to positively

**Table 11:** Heat conductivity  $\lambda_{eff} [\text{W m}^{-1} \text{K}^{-1}]$  in different porosities  $\Phi$  for pure aluminum (99.994%).

$\Phi$	0.85	0.93	0.95
$\lambda_{eff}$ (4 K)	85.97	41.02	29.78
$\lambda_{eff}$ (10 K)	200.24	101.90	77.35
$\lambda_{eff}$ (20 K)	213.12	99.59	71.2

impact the final VCN yield. In particular, substantial gains are seen when using ND as reflector in the extraction and reducing the thickness of the 0.5 mm Al sheet located between the D<sub>2</sub> crystal and the ND layer and/or using a different low-absorbing material like beryllium or magnesium [74]. A full optimization which accounts for such engineering considerations is a complicated task – and outside the scope of this early study – but we have assessed the detrimental factors and, when possible, also estimated their impact.

#### 4.7.1 Internal Cooling Structure

A critical aspect in designing a volume SD<sub>2</sub> moderator is the heat load deposited in the interior of the solid block and its aluminum vessel, which is on the scale of tens of kilowatts. As the SD<sub>2</sub> temperature exceeds 5 K, the VCN flux is reduced with respect to its optimum; however, at 15 K near its melting point, SD<sub>2</sub> still outperforms LD<sub>2</sub> by roughly a factor of 5 at wavelengths greater than 10 Å. Nevertheless, there is a greater likelihood for defect formation with greater thermal stress, and the thermal conductivity of the SD<sub>2</sub> itself drops between 5 and 12 K [75] from approximately 30 down to 1 W m<sup>-1</sup> K<sup>-1</sup>; this indicates that it is imperative to keep as much of the SD<sub>2</sub> bulk as possible below roughly 10 K.

Preliminary assumptions for ortho-SD<sub>2</sub> – which has a significantly higher thermal conductivity compared to the natural ortho-para ratio – indicate that it is feasible to realize such a moderator at the foreseen operating temperature even within the ESS environment (2 MW beam power) by implementing an embedded cooling structure. For this structure, two conceptual measures are considered. First, a metallic (aluminum or beryllium) or graphite foam inlay to increase the thermal conductivity of the solid block; and second, an additional inner cooling pipe (or pipes) with liquid helium flows to reduce the distance to the uncooled core of the solid.

Possible material options for the inlay are – considering both neutronic and thermal conductivity – aluminum, beryllium, or graphite [76, 77, 78, 79, 80]. Such foams have been shown to have very high effective thermal conductivities [81, 82, 83, 84], performing comparably with their bulk counterparts at cryogenic temperatures [85, 86, 87, 88, 89]. More complex materials with exceptional thermal conductivity may also be worth studying, such as diamond/copper composites [90] or aluminum/beryllium alloys; but these are not considered further in this work.

The steady state thermal simulation tool of Ansys® Workbench 19.2 was used for the draft analyses. The material data for deuterium with variable ortho-para concentrations, helium, aluminum (99.994% and 6061-T6) and beryllium were considered in the simulation as a function of the temperature. The material data were taken from the MPDB Material Property Database v7.91 [91] except for the deuterium data [92]. The combined thermal conductivity  $\lambda_{eff}$  of solid deuterium with the foam made of pure aluminum (99.994%), aluminum alloy 6061-T6 or beryllium were calculated using the following equation:

$$\lambda_{eff} = f_A(\Phi\lambda_1 + (1 - \Phi)\lambda_2) + \frac{1 - f_A}{\frac{\Phi}{\lambda_1} + \frac{1 - \Phi}{\lambda_2}}, \quad (4)$$

where  $f_A = 0.33$ , the porosity of the foam  $\Phi = 0.85 - 0.95$ , the thermal conductivity of solid deuterium is  $\lambda_1(T)$  and the thermal conductivity of foam is  $\lambda_2(T)$ .

The volumetric heat induced by the spallation reaction was considered as uniformly distributed over the moderator volume and only steady state simulations have been performed (no pulsed heat). Two cases where considered, the full-load operation with 5 MW proton beam power  $Q = 60 \text{ kW}$  and partial-load operation with 2 MW proton beam power  $Q = 24 \text{ kW}$ . The heat is removed by a surface cooling

only. The cooling medium is helium at an average temperature of 3.75 K. The heat transfer coefficient of the He-wall is considered as infinite. The thermal contact of the foam to the aluminum vessel wall is also assumed as optimal. All of the simplifications mentioned must be verified in detailed simulations.

The results of neutronic simulations are summarized in Table 12, where the foam was first approximated in MCNP by a uniform mixture of 85% volume fraction of SD<sub>2</sub> and 15% foam inlay. Gains are reported as count ratios at 2 m (Beam Port Tally) over the baseline LD<sub>2</sub> moderator with 4% aluminum added, which approximates the LD<sub>2</sub> flow channels for fair comparison. We also explored the possibility of reducing the amount of foam material by having an inlay with different densities between the core region and the outer corners, where it is less important. The boundary between these two regions is a sphere of 10 cm radius, and the outer foam volume-percentage is reduced to 7%. This last configuration has a notable advantage over the uniform case in terms of neutron yield, while keeping the required cooling power almost unchanged. We also investigated the increase in heat deposition in the moderator cell as a function of the foam volume percentage (Figure 95).

In general, simulation results show graphite and beryllium outperforming aluminum in terms of neutronics, self-heating, and thermal conductivity. The enhanced performance for beryllium comes at the expense of manufacturing, which becomes more challenging due to the higher melting point and non-standard safety measures in handling beryllium. This leaves graphite as an appealing candidate material in general terms.

However, the thermal conductivity of high-quality bulk beryllium at the relevant temperature range of 5–20 K is particularly high at roughly  $3200 \text{ Wm}^{-1}\text{K}^{-1}$  [93] near the melting point of SD<sub>2</sub> (with an effective thermal conductivity of roughly  $200 \text{ Wm}^{-1}\text{K}^{-1}$  for a porosity of approximately 85%); the thermal conductivity of graphite foam is likely to be lower by at least a factor of two [94, 84]. It should also be noted that the thermal conductivity can vary by orders of magnitude for aluminum and beryllium, depending on purity [85, 95], with ultra-high purity aluminum being shown to exhibit  $35.000 \text{ Wm}^{-1}\text{K}^{-1}$  at 10 K [96].

Regarding the manufacturability of the inlay: a foam with open pores (I) or a 3D printed grid structure (II) would be attractive options worth investigating [97, 98]. For option (I) a melting of the optimized alloy can be frothed by adding a foaming agent. In this process, the density and porosity can be tuned homogeneously for the inlay. Option (II) would be a grid structure manufactured by the 3D printing technique known as selective-laser-sintering (SLS). In this process, a thin layer of metal powder is locally sintered by a laser beam. By repeating this step layer-by-layer, a defined three-dimensional geometry can be created. The advantage of this method over (I) is the capability for tailoring the geometry to the demands of an optimal thermal conduction while minimizing the reduction of SD<sub>2</sub> volume. This overcomes the limitations due to the homogeneous properties of option (I). It should be noted that this heatsink inlay does not need to act as a structural support, its function is entirely to improve thermal conductivity. A critical aspect in incorporating an inlay to the moderator design is its thermal coupling with the surrounding moderator vessel walls and the liquid helium channel, which could be realized by a defined press fit or a soldering process with a matched plumb alloy. Inlay-type (II) would allow for the printing of a thin-wall structure in the geometry to enlarge the connecting interface surface, which would increase the thermal coupling compared with the press fit and soldering option. In this issue, further experimental investigations will be necessary.

#### 4.7.2 Hydrogen and Para-D<sub>2</sub> impurities

Deuterium is one of the best neutron moderator materials thanks to its small nuclear mass and absorption cross section. Research related to the use of SD<sub>2</sub> for UCN production has demonstrated the importance of having high-purity ortho-D<sub>2</sub> crystals [99, 68]. The elements commonly addressed as impurities are hydrogen and para-deuterium, for their respectively higher absorption and upscattering cross sections [99]. With the achievable ortho-D<sub>2</sub> purity, we expect the impact of these impurities on the VCN yield to be small, as discussed in the following.

We simulated the effect of hydrogen impurities by adding increasing percentages of solid para-H<sub>2</sub> at 5 K in the SD<sub>2</sub>. It should be noted that hydrogen impurities have typically been found in the form of HD

**Table 12:** Intensity gain factors in the SD<sub>2</sub> lower moderator at different volume percentages of aluminum (Al), beryllium (Be), and graphite (C) approximating embedded foam densities. Counts are measured at the Beam Port Tally and gains are reported as ratios over the baseline with 4% aluminum added. In the non-uniform cases (second rows), the boundary is a higher-density 10-cm-radius sphere encompassing the SD<sub>2</sub> core; only such non-uniform trials are reported for graphite.

$\lambda$ range	Al %	2.5 Å to 4 Å	4 Å to 10 Å	10 Å to 40 Å	> 40 Å
<b>NS</b>	15%	0.57	0.68	0.95	2.5
	15/7 %	0.68	0.94	1.52	5.73
<b>NNBAR</b>	15%	0.48	0.71	0.95	1.9
	15/7 %	0.56	0.96	1.50	4.15
$\lambda$ range	Be %	2.5 Å to 4 Å	4 Å to 10 Å	10 Å to 40 Å	> 40 Å
<b>NS</b>	15%	0.64	1.10	2.12	10.0
	15/7 %	0.77	1.27	2.47	18.3
<b>NNBAR</b>	15%	0.56	1.10	1.93	10.1
	15/7 %	0.63	1.26	2.33	13.8
$\lambda$ range	C %	2.5 Å to 4 Å	4 Å to 10 Å	10 Å to 40 Å	> 40 Å
<b>NS</b>	15/7 %	0.79	1.28	2.57	22.0
	15/7 %	0.64	1.25	2.42	16.1

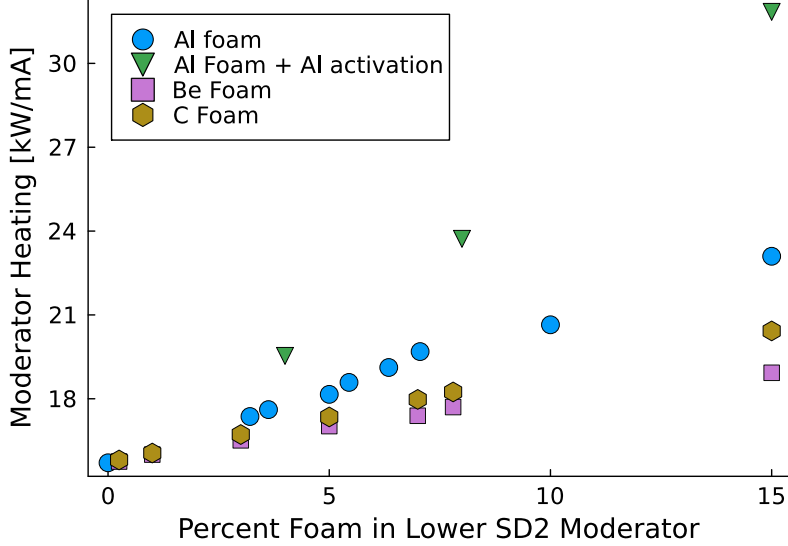


**Figure 95:** Lower-moderator cell heat deposition for metallic (Al and Be) and graphite (C) foam configurations, divided by the proton current in mA impinging on the target (for a 5 MW beam). The green triangles show results accounting for additional heating due to <sup>27</sup>Al activation.

and not para-H<sub>2</sub>. However, since this was the only library available and impurity concentrations in D<sub>2</sub> are usually around 0.2% [68], it was taken as an acceptable approximation for the absorption problem. The impact of the impurities was assessed at the exit of the twister due to the lower statistical uncertainty. The results are shown in Figure 96. For concentrations ranging up to 1%, an average drop was observed of roughly 0.35% in neutron counts for  $\lambda > 40 \text{ \AA}$  for every 0.01% increase in hydrogen concentration. This linear approximation is less accurate for the scattering instruments opening, which exhibit a relatively larger loss, especially for concentrations higher than 0.5%. In any case, considering that an impurity level

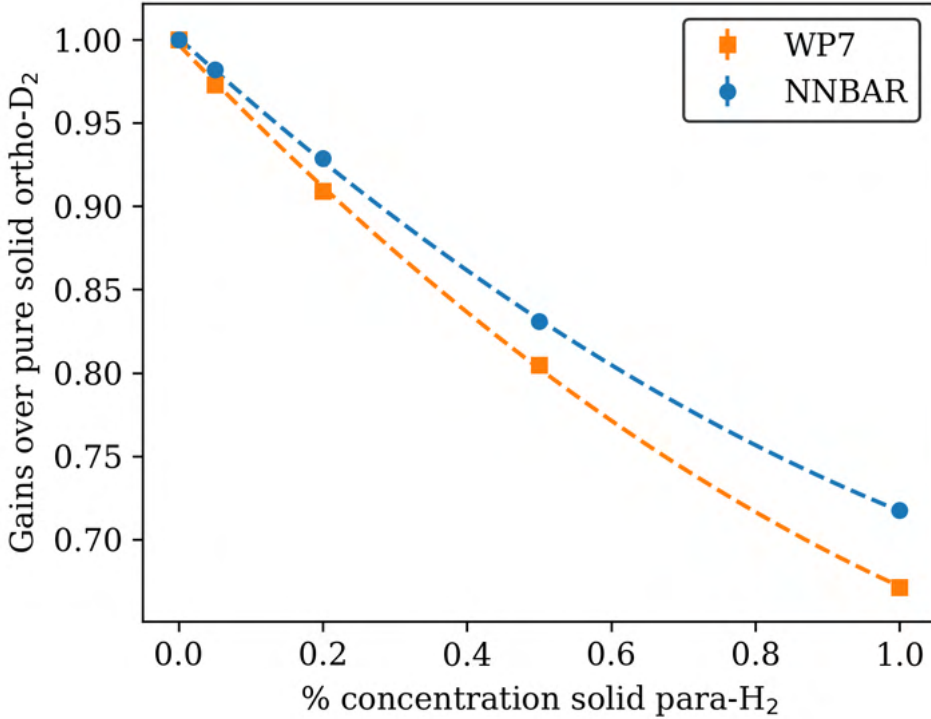


**Figure 96:** Effects of introducing small vol% of solid para-H<sub>2</sub> in the ortho-D<sub>2</sub> crystal for neutrons with  $\lambda > 40 \text{ \AA}$

of 0.2% is achievable in D<sub>2</sub>, with more pure D<sub>2</sub> reaching 0.05%, these effects would hardly downgrade the gains observed with the ideal crystal.

Along the same lines, no significant effects exceeding the statistical uncertainty have been observed at the exit of the twister when adding 1% para-D<sub>2</sub> to the material mix. However, one could expect the para-D<sub>2</sub> concentration to increase as a function of the operation time due to recombination following the radiolysis induced by fast neutrons and gammas. After the radiolysis of an ortho-D<sub>2</sub> molecule, the recombination will produce a para-D<sub>2</sub> molecule 33% of the time, according to the natural proportion of the two spin isomeric forms [100]. Preliminary calculations with a solid para-D<sub>2</sub> thermal scattering library at 5 K showed small losses (less than 5%) for neutrons with  $\lambda > 40 \text{ \AA}$  when adding 30% para-D<sub>2</sub>. This last result is expected, considering how similar the two spin isomers' cross sections are in the VCN energy range. Although the neutronic performance at 5 K is reassuring, high concentrations of para-D<sub>2</sub> would drastically decrease the thermal conductivity of the crystal, making it harder to keep it at 5 K. Because of this, the neutronic effects of para-D<sub>2</sub> at higher temperatures should be investigated in a dedicated study.

#### 4.7.3 Crystal Imperfections

Growing a perfectly transparent SD<sub>2</sub> crystal is notoriously challenging [75, 68, 101, 66, 102, 67]. The goal of perfect optical transparency is hindered by the crystal defects induced by thermal stress. Meanwhile, high-purity ortho-D<sub>2</sub> is achievable. However, cracks and frost buildup on the surface seem inevitable. The former are produced in the cooling phase and during temperature cycling, while the latter is a snow-like layer on the SD<sub>2</sub> surface that is created by a small amount of D<sub>2</sub> undergoing sublimation during a proton pulse.

These defects have been extensively studied because they strongly affect the UCN yield, but there is limited evidence of the interaction with higher energy neutrons in the VCN range. In this section, we address the issue with the available knowledge, keeping in mind that an in-depth study would be needed for further applications.

The influence of cracks on the SD<sub>2</sub> transparency has been studied in [68, 66]. Cracks lead to a sharp

change in potential  $\Delta V_F = 104$  neV at the boundaries between D<sub>2</sub> and vacuum, which results in elastic scattering at the interface. This effect has been observed and quantified in a SANS experiment with cold neutrons in [66]. Due to their low energies, UCN can be totally reflected, thus reducing the transmitted intensity. In the same work, it is also shown how the transmission of a directional VCN beam is heavily affected by a deteriorated crystal. While the small-angle elastic scattering at the boundaries explains the increase in the cross section, it is less clear how a smaller mean-free path could affect the moderation and isotropic emission of VCN.

One possibility is that the assumption of a smaller mean-free path could ultimately lead to the calculation of sub-optimal dimensions for the moderator. Following the method used for ND in [103], SANS could be added to the SD<sub>2</sub> thermal scattering library to model the cracks. The experimental Porod exponents given in [66, 102] could serve as starting point and would allow for the modeling of a real crystal in different cooling conditions. In any case, less damage to the crystal was reported when slowly cooling from the liquid phase and temperature cycling was kept between 5 K and 10 K.

Surface degradation has been extensively treated from both theoretical and experimental perspectives in [75]. The creation of a frost layer at the SD<sub>2</sub>-vacuum interface is due to D<sub>2</sub> sublimation, which is then poorly cooled and poorly attached to the SD<sub>2</sub> surface. The number of layers increases with the number of proton pulses, hence increasing the optical opacity of the surface. Through a procedure called conditioning, it is possible to sublimate and resublimate the frost as better-quality SD<sub>2</sub>, while recovering the UCN yield. The physics behind the neutron loss is a combination of an alteration of the optical potential shape (from a stepped to a smooth profile), specular and non-specular scattering (due to roughness [104]), and diffusion from randomly oriented crystal facets. Each of these mechanisms prevents the extraction of UCN, but as highlighted in [75] these are energy-dependent processes described by the optical laws of reflection. In particular, the probabilities for reflection  $P_R$  and transmission  $P_T$  an interface are:

$$P_R = \left| \frac{\sqrt{E_\perp} - \sqrt{E_\perp - \Delta V_F}}{\sqrt{E_\perp} + \sqrt{E_\perp - \Delta V_F}} \right|^2 \quad (5)$$

$$P_T = 1 - P_R \quad (6)$$

where  $\Delta V_F$  is the change in neutron optical potential at the interface D<sub>2</sub>-vacuum and  $E_\perp$  is the component of kinetic energy perpendicular to the boundary surface before the interaction. It is clear that, for VCN energies of the order of 10<sup>-5</sup> eV,  $P_T$  is approximately 1 for almost all emitted neutrons. In [75] it is experimentally observed that already the fastest UCN (320 neV) are less affected by the frost layers, causing a hardening of the spectrum after continuous pulse operations.

#### 4.7.4 SD<sub>2</sub> Source Summary

Simulations for a full-SD<sub>2</sub> source predict order-of-magnitude gains for  $\lambda > 40$  Å neutrons, along with gains exceeding a factor of two in the  $10 < \lambda < 40$  Å range, in comparison with a conventional LD<sub>2</sub> moderator design of similar volume and following the same engineering constraints required by the existing ESS layout. A significant fraction of these gains are owing to an ND reflecting layer encasing the source, which have a high albedo for VCNs.

Although it is clear that both cracks and surface degradation will need a dedicated study which takes into account the specific conditions and constraints at ESS, it is likely that imperfections in SD<sub>2</sub> – which are generally considered detrimental for UCN production – should not significantly affect higher energies in the VCN range.

Novel heat-extraction solutions are required to make the proposed design feasible, with preliminary studies indicating that embedding a foam structure of beryllium or graphite into the moderator volume would be viable with the ESS initial operating proton beam power of 2 MW. Engineering such a cooling system for the design power of 5 MW may present greater difficulties, and further study would be required.

Implementation of a such VCN moderator can be expected to open new avenues of research in neutron scattering and fundamental physics studies with neutrons.

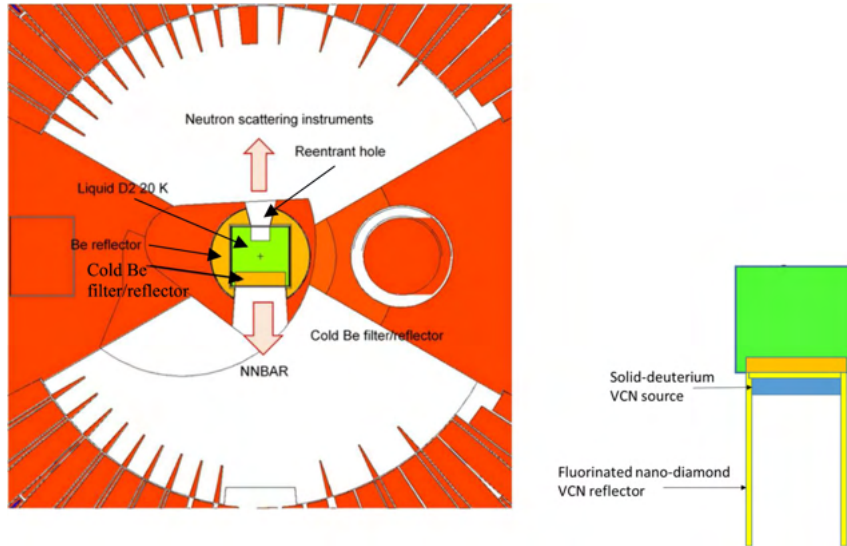


**Figure 97:** Original concept of the  $\text{SD}_2$  converter as presented in [37]

## 4.8 Combined option

The idea of a VCN source combining an  $\text{SD}_2$ -based VCN converter with an existing CN source was proposed at the first HighNESS workshop on UCN and VCN Sources at ESS [37]. The rationale behind the concept is to maximize the VCN flux to the NNBAR experiment. A dedicated VCN source could overcome the well-known low phase-space density (the neutron flux decreases as the square of longitudinal neutron velocity in a cold source), while retaining the sensitivity increase as the square of the free flight time ( $\approx \lambda^2$ ). The net gain factor would then be simply proportional to the increase in the phase-space density over the cold source. The original concept is shown in Figure 97 and it can be described as follows:

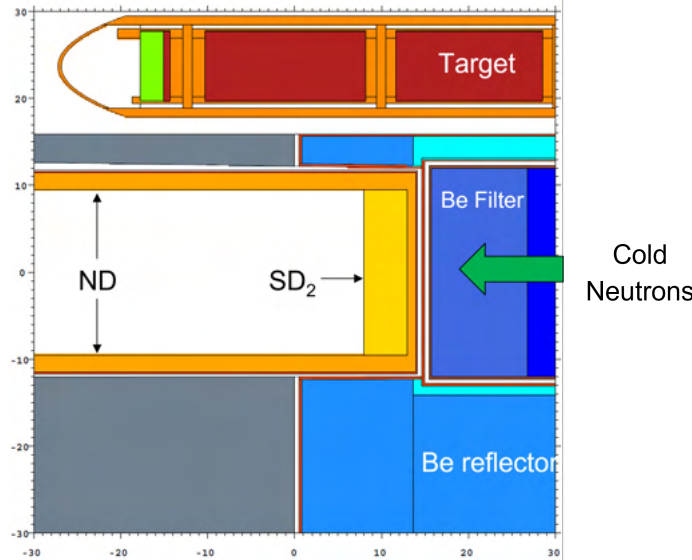
- An  $\text{SD}_2$  VCN converter at a temperature of  $\approx 4\text{ K}$  is placed in front of the  $24\text{ cm} \times 40\text{ cm}$  NNBAR opening.
- A long channel filled with fluorinated detonated nanodiamonds (F-DNDs) is placed at the exit as extraction system, increasing the total flux of VCN at  $2\text{ m}$  due to multiple reflections from the walls and enhanced directional extraction to the experiment.
- A thin F-DND layer is placed between the  $\text{LD}_2$  source and the  $\text{SD}_2$  converter to increase the chance of moderation inside the converter volume. At the same time, such a thin layer is nearly transparent for CNs, hence the incident CNs are virtually unaffected.

Contrary to UCN extraction with  $\text{SD}_2$ , VCNs penetrate through the inhomogeneities in the  $\text{SD}_2$  bulk, and are thus more easily extracted with minimal losses.

The source flexibility and the ease of implementation within the current  $\text{LD}_2$  cold source make this an interesting design for a general-purpose VCN beamline. Therefore, the performance of a possible converter on the WP7 has also been studied.

### 4.8.1 NNBAR side

As a starting point, the simplest study one can imagine is to measure the effect of a thin converter on the VCN flux at the beam port, which is located  $2\text{ m}$  from the center of the moderator. For this test, we put  $5\text{ cm}$  of  $\text{SD}_2$  in a  $170\text{-cm-long}$  ND-filled channel with  $2\text{-cm}$  reflector thickness on the sides and  $1\text{ cm}$  in the direction of the cold neutron beam. The reason for having a thick ND layer is to increase the diffusive transport of VCNs. The very cold energy range is far from the quasi-specular regime; thus, the intense albedo from the powder is exploited instead. The first tests did not have any structure around the converter and for the inner walls. This is clearly an oversimplification, since both the  $\text{D}_2$



Specifications	
Converter thickness	5 cm
Converter vessel	0 mm
ND reflector (sides)	2 cm
ND reflector (back)	1 cm
External Al case	2 mm
Internal Al walls	0 mm

**Figure 98 & Table 13:** (Left) MCNP model of the preliminary test run to check the separate and combined effect of ND and the SD<sub>2</sub> block. (Right) Parameter table for this model.

**Table 14:** Preliminary results at all angles of the SD<sub>2</sub> converter design on the NNBAR side. The tally is measuring the counts at all angles through a fixed surface placed at the beam port. Gains are measured over the third optimized baseline (see Section 2.3.6).

Gains	Al casing	SD <sub>2</sub> only	NDs only	SD <sub>2</sub> + NDs
4 Å < λ < 10 Å	0.98	0.54	1.71	0.87
20 Å < λ < 40 Å	0.95	0.71	0.84	1.76
λ > 40 Å	0.86	0.93	0.44	16.9

(gas) and the NDs (powder) must be stored in a container in reality, but it allows for a verification of the predicted enhancing effect, neglecting the engineering complications. The model used is shown in detail in Figure 98.

The performance of the converter is measured with a current tally (F1) through a fixed surface placed at the beam port with several energy-grouped resolutions and coarse angle bins. The effect on the neutron counts was studied separately for each component of the system. The Table 14 summarizes these preliminary results at all angles.

First, the Al case was added in the opening, which produced overall small losses in the energy ranges studied. Then, only the SD<sub>2</sub> crystal was inserted, without the surrounding NDs. As a result, cold neutron (4 Å to 10 Å) and VCNs from 20 Å to 40 Å are halved, while an increase in the coldest neutron counts ( $\lambda > 40 \text{ Å}$ ) is the first sign of enhanced VCN production over the LD<sub>2</sub> baseline.

Similarly, results for ND reflector but no SD<sub>2</sub> are shown. In this third case, it is possible to observe an increase in the cold counts for the ND guide only, which is due to the quasi-specular reflection. On the other hand, huge losses are observed in the VCN energy region. The difference with the previous model, and cause of the losses, is in the additional layer at the emission surface, which is back-scattering and diffusing the VCNs coming from the LD<sub>2</sub> moderator.

Finally, the two pieces are coupled, SD<sub>2</sub> and NDs in the Al case, and the VCN counts at the beam port increase by more than a factor 2 from 20 Å to 40 Å and a factor 17 above 40 Å. In the next section, this tentative simple case is improved by an optimization of the parameters.

#### 4.8.2 Optimization of the ideal case

For a robust and methodical approach to the optimization task, Dakota [18] and the EGO algorithm were used. The optimization parameters were the thickness of the SD<sub>2</sub> block and the thickness of the ND layer both on the sides of the guide-like system and behind the SD<sub>2</sub> (in front of the emission source) designated as side and back thicknesses, respectively. The FOM chosen to drive the algorithm is the VCN counts at the beam port between 20 and 40 Å and at all angles. In fact, it is more convenient to use this tally since it converges faster while following approximately the same behavior as the VCNs above 40 Å. The results of this multi-dimensional optimization are shown in Figure 99.

Before discussing the results, the content of the plots in Figure 99 should be clarified:

- Each run of the optimization is represented by three vertically aligned points, one for each energy-group of interest and each one with its own scale for the gains over the LD<sub>2</sub> baseline.
- Since we are showing one parameter at a time, the presence of different counts values for the same parameter value is to be interpreted as a run where one (or both) of the other parameters was changed.
- The lines shown are mere trend lines with the sole purpose of guiding the reader's eye and not fitted models.
- The EGO algorithm does not sample uniformly the parameter space, hence the larger clusters of points visible in the plots are formed to better sample the region around the maximum of the FOM. This is also why this approach can be much faster than a simpler evaluation of a parameter grid.

The first important result of the optimization is that large blocks of SD<sub>2</sub> produce the highest VCN yields. Here 20 cm was the upper boundary given to Dakota for the thickness, but it is reasonable to assume that there would be higher gains for larger crystals. However, with approximately 14 L of SD<sub>2</sub>, this moderator has already unprecedented dimensions for a crystal at 5 K, with non-negligible issues pertaining to cooling and engineering (the estimated heat deposition from prompt neutron and gammas is 2.5 kW). The cost for the high gains in the VCN energy range are considerable losses in the cold range around 4 Å. A possible explanation for these losses is in the large SD<sub>2</sub> elastic cross section (see Figure 93) that decreases the mean free path, effectively making the cold source appear further away from the beam port and increasing the chances of absorption or leakage.

Additionally, the thickness of the crystal seems to be the most important parameter by looking at the range of the results, while the thickness of the back ND layer is the least crucial for an optimal design. The latter is due to the relatively high transmission fraction of cold neutron through thick ND layers. Meanwhile, once the neutrons are moderated to VCN energy, that layer, even when few millimeters thin, suddenly becomes opaque, reducing the chances of leakage.

Conversely, the thickness of the ND layer on the sides seems to have a more important role. In particular, both too-thick and too-thin values are penalizing for VCNs. In the first case because there is not enough reflecting material, while in the second case, too much moderating material is lost to accommodate NDs. Also, the emission surface is considerably shaded by the reflector layer, inevitably reducing the neutron counts at the beam port. The optimized model is shown in Figure 100. Compared to the LD<sub>2</sub> baseline, this model is able to deliver 47 times more neutrons above 40 Å and 3 times more neutrons in the range from 20 Å to 40 Å, while retaining only 40% of the cold neutrons between 4 and 10 Å.

#### 4.8.3 Engineering details

In order to make the model more realistic, we added an aluminum vessel 2 mm thick at 5 K around the SD<sub>2</sub> crystal. An additional 5 mm vacuum gap separates the converter vessel from the ND reflector surrounding it. Finally, we add 1 mm of aluminum as internal cladding for the reflector. We have already mentioned that the model without inner Al structure was a simplified test to study the validity of the idea. For a ND guide, this is quite a critical feature, especially in the VCN range. This model is shown in Figure 101.

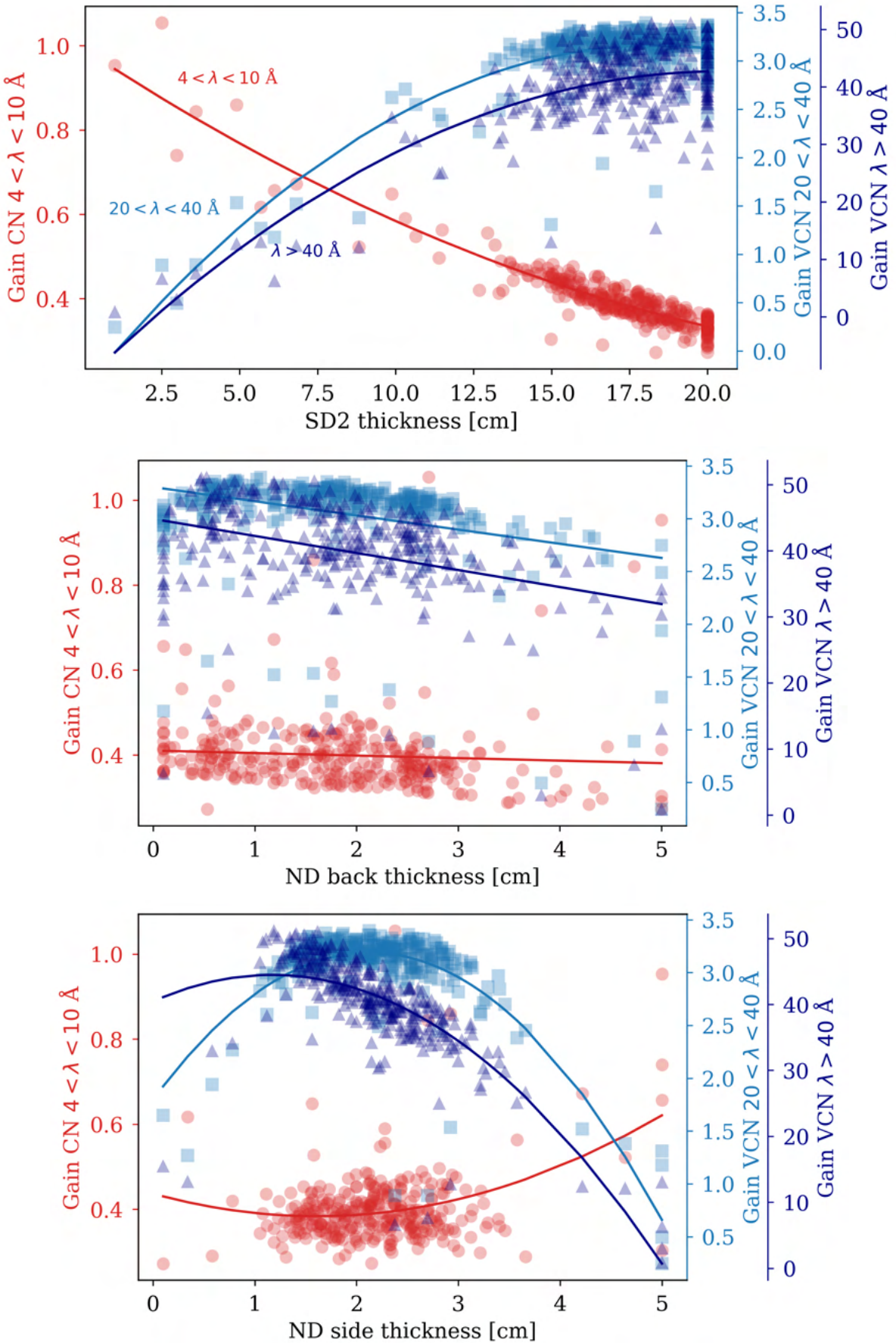
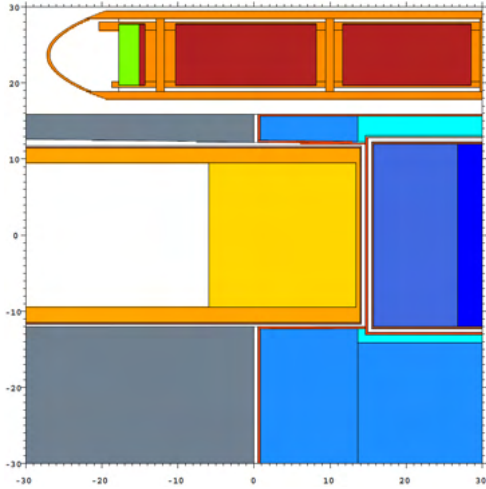
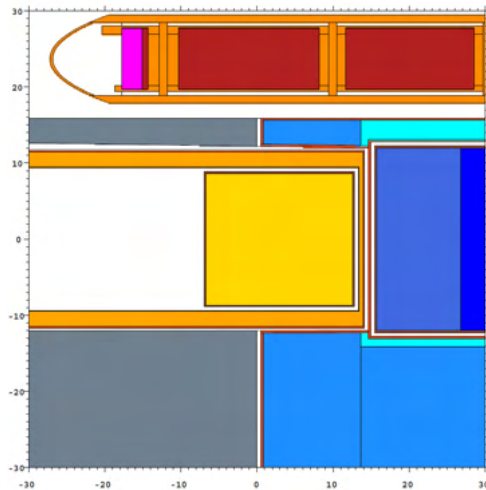


**Figure 99:** Results of the multi-dimensional optimization. Each run of the optimization is represented by three vertically aligned points, one for each energy-group of interest and each one with its own scale for the gains over the LD<sub>2</sub> baseline. Trend lines are shown with the sole purpose of guiding the reader's eye.



Specifications	
<b>Converter thickness</b>	20 cm
Converter vessel	0 mm
<b>ND reflector (sides)</b>	2 cm
<b>ND reflector (back)</b>	0.55 cm
External Al case	2 mm
Internal Al walls	0 mm
Prompt heat-load	2.5 kW

**Figure 100 & Table 15:** (Left) MCNP model of the optimized converter. (Right) Parameter table for this model. The optimized parameter are in bold.



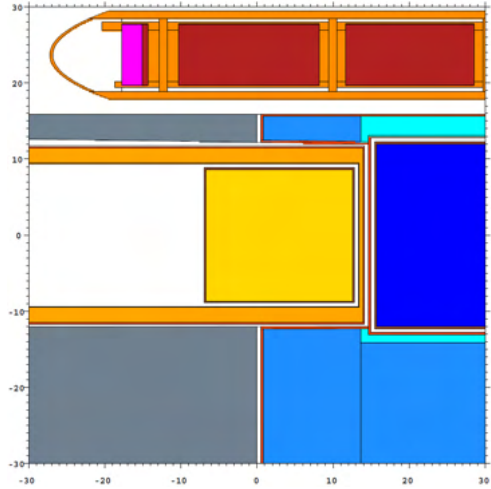
Specifications	
Converter thickness	20 cm
Converter vessel	2 mm
ND reflector (sides)	2 cm
ND reflector (back)	0.55 cm
External Al case	2 mm
Internal Al walls	1 mm
Prompt heat-load	2.5 kW

**Figure 101 & Table 16:** (Left) MCNP model of the optimized converter with engineering details. (Right) Parameter table for this model.

Compared to the ideal case, this model performs much worse. We estimated that, in terms of gain over the baseline, it yields only 2.6 times more neutrons above 40 Å and 10% more neutrons in the range from 20 Å to 40 Å. While 1 mm is already a reasonable thickness, one way to improve the model is to use thinner Al cladding for the extraction. Another way to improve performance would be using other metal foils, like magnesium [74]. Preliminary calculations with 1 mm of pure Mg showed gains over the baseline as high as a factor of 12 for neutrons above 40 Å and a factor of 2 in the range from 20 Å to 40 Å. Here, it is probably most noteworthy that the flexibility of the design could be used to improve the performances, keeping in mind that reducing the thickness of the inner walls or changing the material tends to be beneficial.

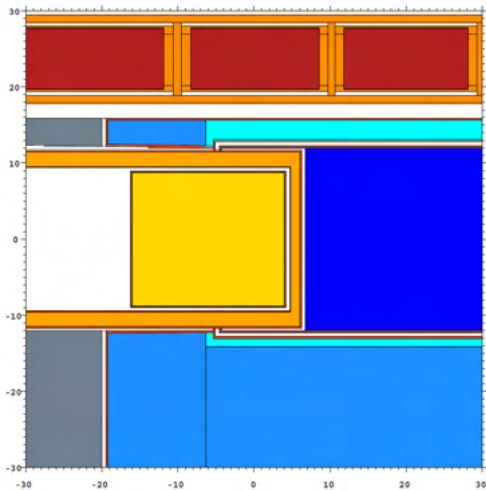
#### 4.8.4 Improvements to the design

The first change we can make to the model that will predictably improve the performance is removing the cold beryllium filter from the LD<sub>2</sub> vessel. The reason for this is that the beryllium at 20 K reflects any neutrons with wavelengths below 4 Å back to the moderator; whereas for longer wavelength neutrons, the crystal is almost transparent. Although this is beneficial for NNBAR, whose FOM is proportional to  $\lambda^2$ , it is detrimental for a VCN converter, given that neutrons in the range from 2 Å to 4 Å contribute significantly to the VCN production in SD<sub>2</sub>. The model without the Be filter is shown in Figure 102.



Specifications	
Converter thickness	20 cm
Converter vessel	2 mm
ND reflector (sides)	2 cm
ND reflector (back)	0.55 cm
External Al case	2 mm
Internal Al walls	1 mm
Prompt heat-load	3 kW

**Figure 102 & Table 17:** (Left) MCNP model of the optimized converter with engineering details and without Be filter in the cold source. (Right) Parameter table for this model.



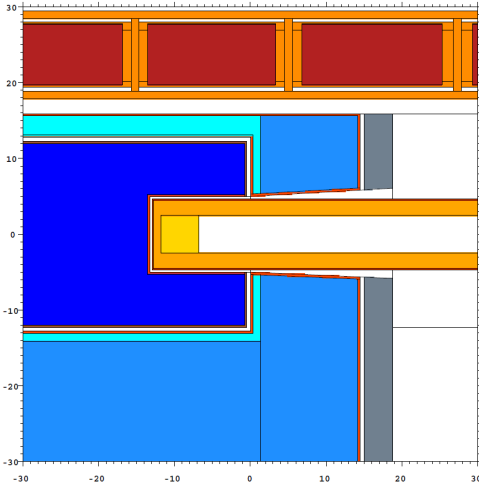
Specifications	
<b>Converter thickness</b>	20 cm
Converter vessel	2 mm
<b>ND reflector (sides)</b>	2 cm
<b>ND reflector (back)</b>	1.25 cm
External Al case	2 mm
Internal Al walls	1 mm
Prompt heat-load	5.8 kW

**Figure 103 & Table 18:** (Left) MCNP model of the optimized converter embedded in the LD<sub>2</sub> cold source. (Right) Parameter table for this model. The optimized parameters are in bold.

Removing the filter to add more moderating LD<sub>2</sub> has the effect of increasing the gains by  $\approx 20\%$  over the case with the filter (Figure 101). Another important result is in the increase to 3 kW of the heat deposition in the moderator volume due to the higher neutron and gamma flux.

Since the thermal and cold neutron flux have an important role in VCN production when with SD<sub>2</sub>, a further improvement to the design should be obtained by moving the converter closer to the source. In other words, it is worth studying the effect of embedding the converter inside the LD<sub>2</sub> vessel, regardless of its feasibility. To this end, we inserted the converter 11 cm deep inside the cold source. Due to the major shift in the design, we chose to optimize this model separately. The parameters are, within the statistical uncertainty, identical to the previous optimization, except for the thickness of the back ND layer which is 1.2 cm (still a low-sensitivity parameter).

The model implementing this idea is shown in Figure 103. In terms of performances, this solution provides an average factor of two improvement for all energies over the case with the Be filter (Figure 101). If we compare the neutron counts over the baseline without a UCN converter, this model is able to deliver 5.7 times more neutrons above 40 Å and 2.5 times more neutrons in the range from 20 Å to 40 Å, while retaining 60% of the cold neutrons between 4 and 10 Å. However, once again, the price to pay for the increased flux is a significant increase in heat-load. We estimate that just moving the converter 11 cm inside the moderator nearly doubles the heat deposition to a value of 5.8 kW.



Specifications	
Opening size	10 × 10 cm <sup>2</sup>
Converter thickness	5 cm
Converter vessel	0 mm
ND reflector (sides)	2 cm
ND reflector (back)	1 cm
External Al case	2 mm
Internal Al walls	0 mm

**Figure 104 & Table 19:** (Left) MCNP model of the converter embedded on the WP7 side for the preliminary test run to check the separate and combined effect of NDs and the SD<sub>2</sub> block. (Right) Parameter table for this model.

#### 4.8.5 Converter for neutron scattering instruments

Similarly to the tests on the NNBAR side, the effects on VCN flux were studied for a thin converter on the WP7 side. The F1 tally measures the current at a fixed surface placed at the beam port, 2 m from the center of the moderator, with the same energy-angle resolution. For this test, the opening is 10 cm × 10 cm and the SD<sub>2</sub> crystal is 5 cm thick. The ND guide is 190 cm long with 2-cm-thick walls on the sides and 1 cm in the direction of the cold neutron beam. No structure is present around the converter and for the inner walls. The model used is shown in detail in Figure 104.

The preliminary test with this tentative setup did not show, compared to the baseline, any gain in using the converter independently from the energy-group considered. To be sure that the bad performances observed is not strictly bound to a particular configuration, the most important parameters of the geometry is optimized with Dakota. Namely, the EGO algorithm found the best values for the SD<sub>2</sub> thickness, the ND layer thickness on both the sides and the back. Similarly to the NNBAR case, the figure of merit of the optimization was the VCN counts between 20 Å and 40 Å and the minimum value set as boundary for the ND layers is 0.1 cm. Despite the precision being lower than the NNBAR case, especially at very long wavelength, the results suggest with a good degree of convergence that the most favorable configuration has only 1 mm of NDs on the sides (Figure 105).

The fact that gains are observed over the baseline in the VCN range suggests that inserting a block of SD<sub>2</sub> has the intended effect of further moderating the cold spectrum coming from the LD<sub>2</sub>. Also, as expected, the system is not very sensitive, within few centimeters, to the thickness of the NDs in the back due to the high neutron transmission in the cold range.

However, the configuration that maximizes the gains between 20 Å and 40 Å is found at the minimum of the ND thickness on the sides. The different behavior observed between WP7 and NNBAR in the optimization of the ND side layer thickness is explained by a poor parameterization of the model. As already mentioned, the increase of the reflector thickness on the side has the effect of reducing the amount of SD<sub>2</sub> and occluding the emission surface. Despite being present also on the NNBAR side, this effect seems to be crippling only on the WP7 side.

One way to fix this is to move the SD<sub>2</sub> block out of the reentrant hole and by changing the thickness of the ND layer outward at the cost of the reflector, not the emission surface. In this setup, the SD<sub>2</sub> block has the same lateral dimensions as the opening and it is decoupled from the NDs. This allows for an unrestricted increase to the ND layers on the sides to reduce the leakage, without occluding the opening. Finally, the thickness of the reflector layer outside the twister (i.e. the guide-like part) is also decoupled and optimized separately. The cost in terms of performance for this setup is a lower cold flux due to the longer distance from the center of the cold source. The optimized model for a 15 cm × 15 cm opening is shown in Figure 106, while in Figure 107 an overview of the results of the optimization is presented.

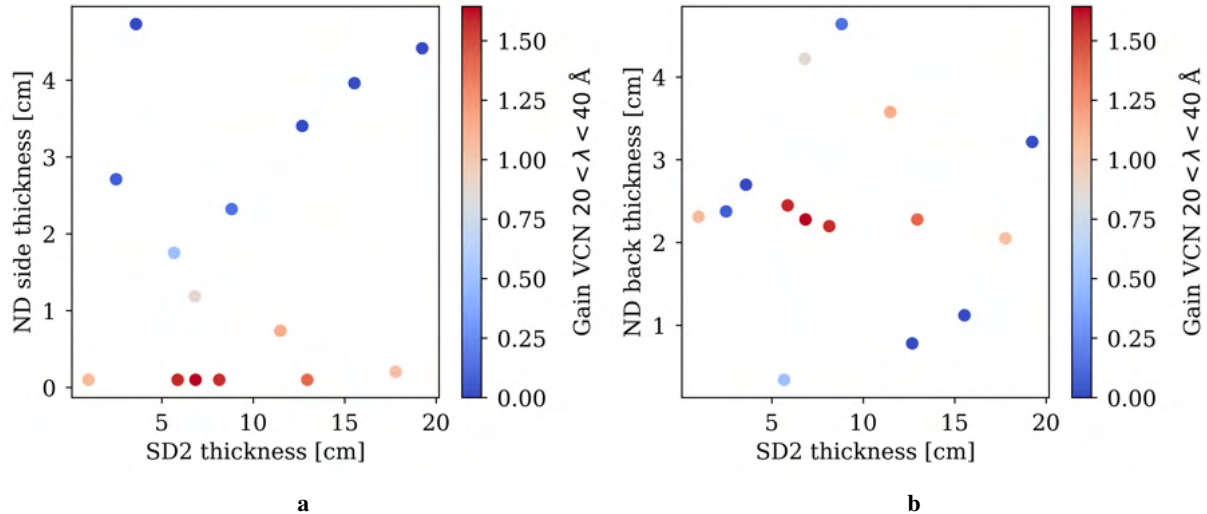
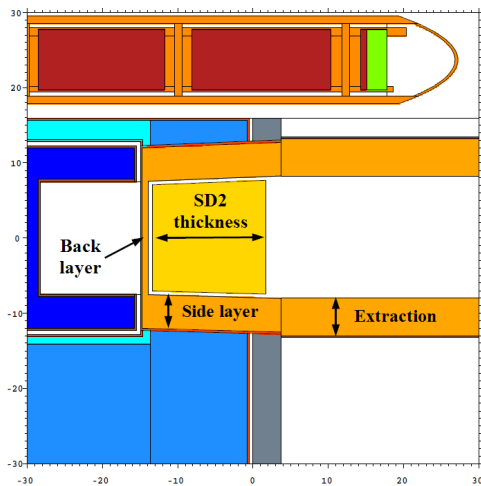


**Figure 105:** Results of the multi-dimensional Dakota optimization of the 10 cm × 10 cm opening for WP7. Each run of the optimization is represented by a point. Only gains for the VCN energy-group from 20 Å to 40 Å are shown. The gains are calculated over the baseline with the same opening. (a) SD<sub>2</sub> thickness vs ND layer side thickness (b) SD<sub>2</sub> thickness vs ND layer back thickness.



Specifications	
Opening size	15 × 15 cm <sup>2</sup>
<b>Converter thickness</b>	15.6 cm
Converter vessel	0 mm
<b>ND reflector (sides)</b>	4.5 cm
<b>ND reflector (back)</b>	0.8 cm
<b>ND reflector (extraction)</b>	5 cm
External Al case	2 mm
Internal Al walls	0 mm
Prompt heat-load	860 W

**Figure 106 & Table 20:** (Left) MCNP model of the converter for the WP7 side with improved parameterization (Right) Parameter table for this model. The optimized parameters are in bold.

From the analysis of the parameter space, the behavior of the improved model is more similar to what was expected by such system. In Figure 107a, the different trends of the gains for different energy groups as a function of the SD<sub>2</sub> thickness are highlighted. It is clear that, for small amounts of SD<sub>2</sub> in the opening, the overall effect of the setup is to increase the CN transport by exploiting the quasi-specular reflection on the ND layers on the sides. Notably, the factor 2 increase in the flux is compatible with the results in Section 4.9 at all angles. As the thickness of the converter increases, the shift at longer wavelengths becomes more and more pronounced. Around 15-20 cm, the converter yields an average gain factor of more than 3 for VCNs between 20 Å and 40 Å and 30 for VCNs at longer wavelengths and at all angles. In Figure 107b and Figure 107c the gains from 20 Å to 40 Å are plotted as function of the SD<sub>2</sub> thickness and ND layer on the sides and in the extraction, respectively. In both cases, a thicker reflector is correlated with higher gains. In the case of the NDs on the sides, the removal of standard reflector does not seem to produce a significant loss.

It should be noted at this point that each step of the optimization is computationally more expensive and tally precision is lower than for the NNBAR opening. This limits the exploration of the parameter space and the extraction of key insights about the system. Despite the lower cold flux on the converter

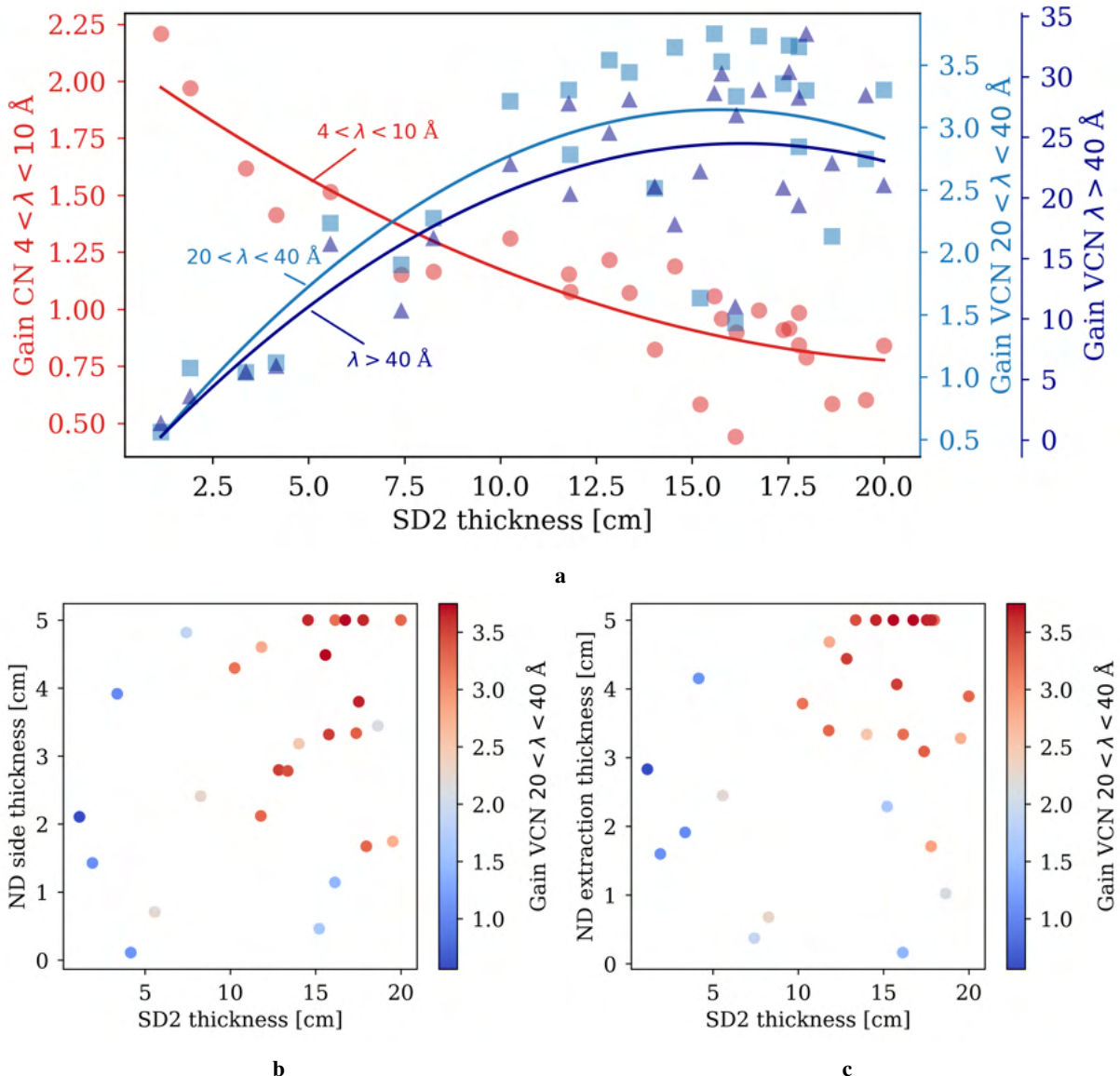


**Figure 107:** Results of the multi-dimensional Dakota optimization of the  $15 \text{ cm} \times 15 \text{ cm}$  opening for WP7. The gains are calculated at all angles over the baseline with the same opening. (a) each run of the optimization is represented by three vertically aligned points, one for each energy-group of interest and each one with its own scale for the gains. Trend lines are shown with the sole purpose of guiding the readers' eye. (b) each run of the optimization is represented by a point. Only gains for the VCN energy-group from  $20 \text{ \AA}$  to  $40 \text{ \AA}$  are shown. The two parameters plotted are: SD<sub>2</sub> thickness vs ND layer side thickness (c) SD<sub>2</sub> thickness vs. ND layer thickness in the extraction.

caused by the longer distance from the center of the moderator, the system is able to deliver order-of-magnitudes gains in the lower VCN range, with potentially smaller impact on the cold flux at the beam port and a smaller heat load to remove (cfr. Figure 106). Finally, in Section 4.8.3 the losses caused by adding the engineering details were discussed for the setup in the NNBAR opening. Similar observations are reasonably valid for the WP7 opening.

#### 4.8.6 Gains at small angles

The results discussed so far are for neutrons reaching the beam port at any angle. The presence of a ND channel allows neutrons with a large divergence to reach the recording surface. However, for most conventional neutron scattering instruments, neutrons with large divergence are collimated along the way and do not contribute to the flux at the sample. The gains for the neutrons with vertical divergence between  $0^\circ$  and  $2^\circ$  are shown in Figure 108a for the NNBAR opening, and Figure 108b for the WP7 opening.

The gains are reported solely as a function of the  $SD_2$  thickness, as the strongest predictor. While the trends are similar to the all-angles cases, the scale of the VCN gains is smaller. Up to 20 Å, there is no advantage in using the converter. The initial VCNs produced inside the  $LD_2$  cannot reach the beam port due to the thin ND layer between the main source and the converter. Since ND channels have proven to be effective in improving the neutron flux at small divergence, the reason for the lower gains can be attributed only to a lesser production in the  $SD_2$ . The neutron flux out of the  $SD_2$  at small divergence does not compensate for the initial VCN flux, yielding an overall loss between 20–30%. Below 40 Å, the neutron production by the  $SD_2$  crystal over the  $LD_2$  baseline is enough to achieve a net gain. Due to the wide applications of low-divergence neutrons, this effect should be studied in detail, in order to tailor the source to the specific needs of the instruments placed at the end of the extraction system.

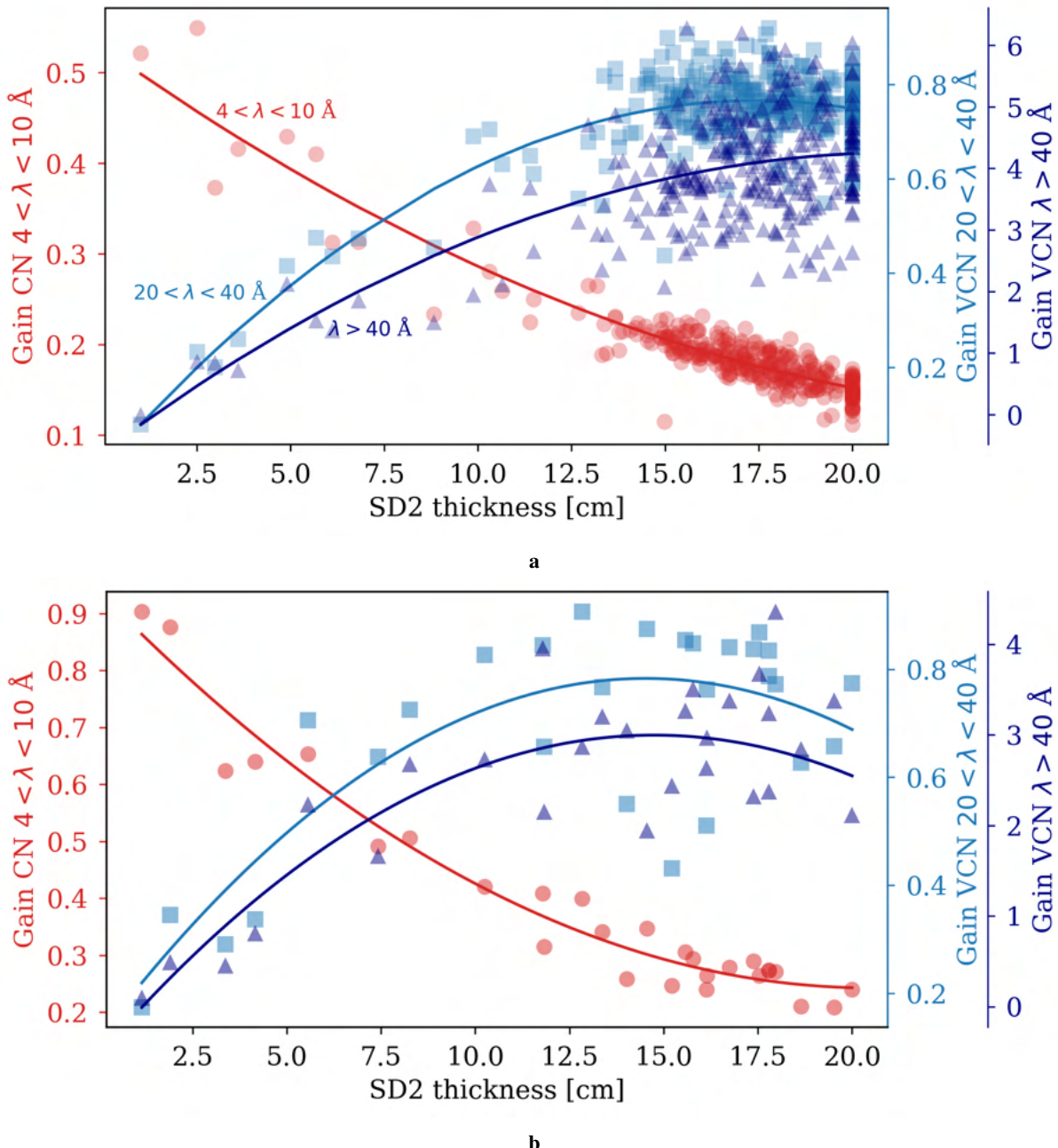


**Figure 108:** Results of the multi-dimensional Dakota optimization of the (a) NNBAR opening and (b) the 15 cm × 15 cm opening for WP7. The gains are calculated at small angle over the baseline with the same opening. Each run of the optimization is represented by three vertically aligned points, one for each energy-group of interest and each one with its own scale for the gains. Only the SD<sub>2</sub> thickness is reported. Trend lines are shown with the sole purpose of guiding the readers' eye.

## 4.9 Beam Extraction with nanodiamonds

An additional options for improving VCN yield regardless of the source configuration is to use a dedicated guide-like system to more efficiently extract the VCN tail from the LD<sub>2</sub> spectrum. In a dedicated study, since the quasi-specular reflection on thin ND powder samples has been experimentally observed [105, 106, 107, 108], a straight ND guide with walls thickness of 5 mm was considered adequate to observe the improvement of extracting CNs and VCNs. Preliminary simulations were conducted on the both sides of the LD<sub>2</sub>. The ND powder had an effective density of 0.6 g/cm<sup>3</sup>, so it was compressed inside the hollow space created by two Al walls. The inner wall was a 0.1 mm thick Al foil, and the outer Al wall had a thickness of 2 mm. The geometry is shown in Figure 109.

The result of the study are summarized in Figures 110 and 111. As expected, the ND guide can transport cold neutrons and can provide on average a factor of 2 gain at 2 m over the baseline. However, most of these gains are obtained for neutrons reaching the beam port with vertical divergence greater than 2°, that is, the more pronounced effect is observed in the region of the phase space where fewer neutrons (or none at all) would be allowed to reach the beam port without the guide. The gain provided by the ND guide reached the maximum at around 10 Å on the WP7 side, and then decrease in the VCN energy range. Here, due to the multiple large-angle interactions, the reflections on the ND layer very quickly produce an isotropic distribution. The large NNBAR beam port is more likely to accept those large divergence neutrons, while in the smaller guide on the neutron scattering side, they are easily lost (absorbed, back-scattered, and so on) after multiple interactions with the ND and the Al walls. The idea of a ND guide between the emission surface and the beam port as a VCN-enhancing system is further investigated in the following section.

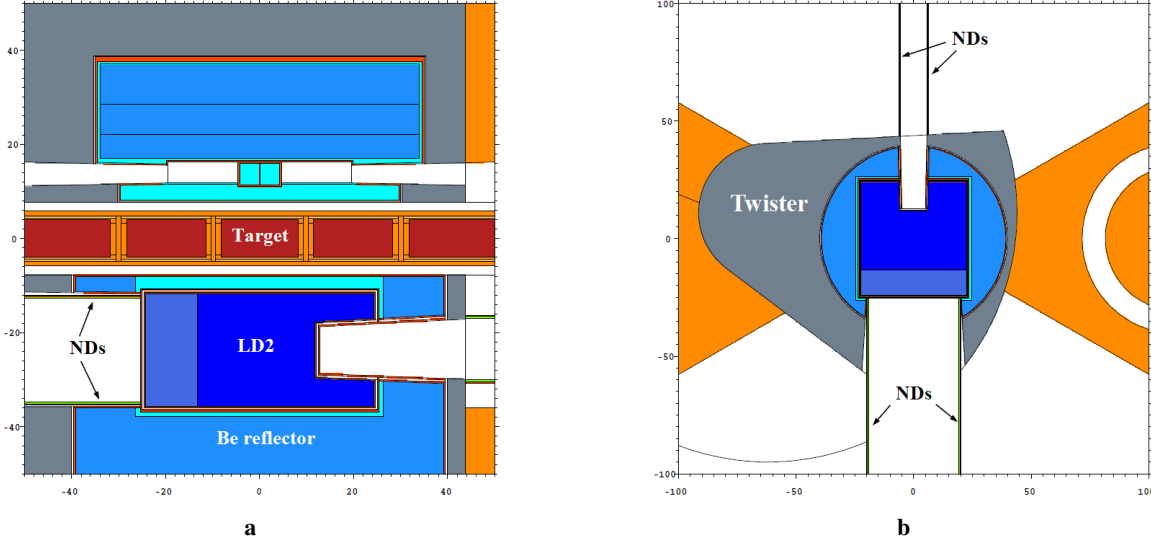


**Figure 109:** MCNP model of the LD<sub>2</sub> baseline with ND extraction system (a) vertical cross section, perpendicular to the proton beam direction. (b) Cross section parallel to the target plane with the neutron beam impinging from the left.

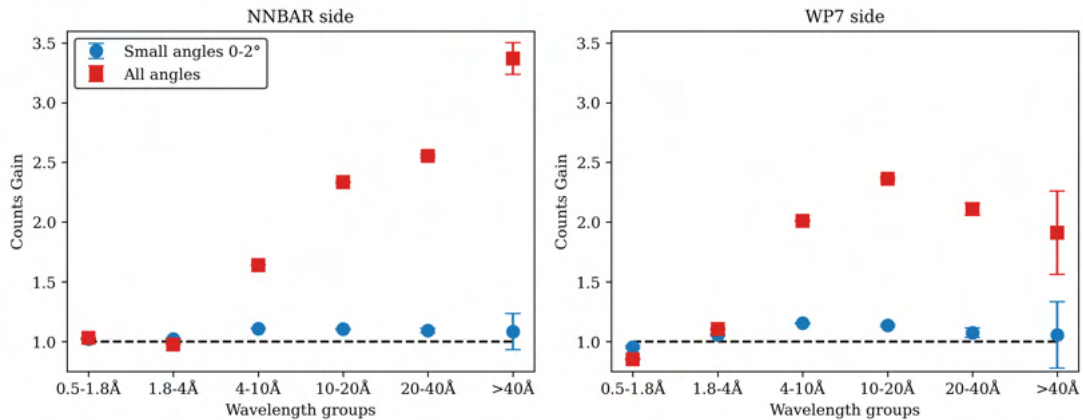


**Figure 110:** Gains with ND guide 2 m away from the center of the moderator (beam port position) as a function of neutron wavelength groups for NNBAR (left) and WP7 (right) openings.

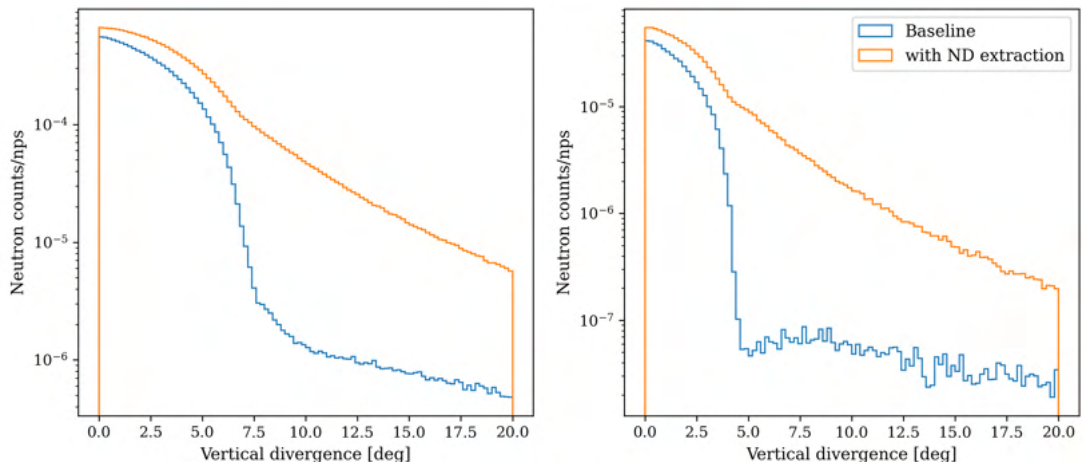


**Figure 111:** Divergence of cold neutrons at the beam port ( $\lambda > 4 \text{ \AA}$ ) for the baseline without (blue) and with (orange) ND guide. Left for the NNBAR opening, right for the WP7 opening. The vertical axis is neutron counts/nps.

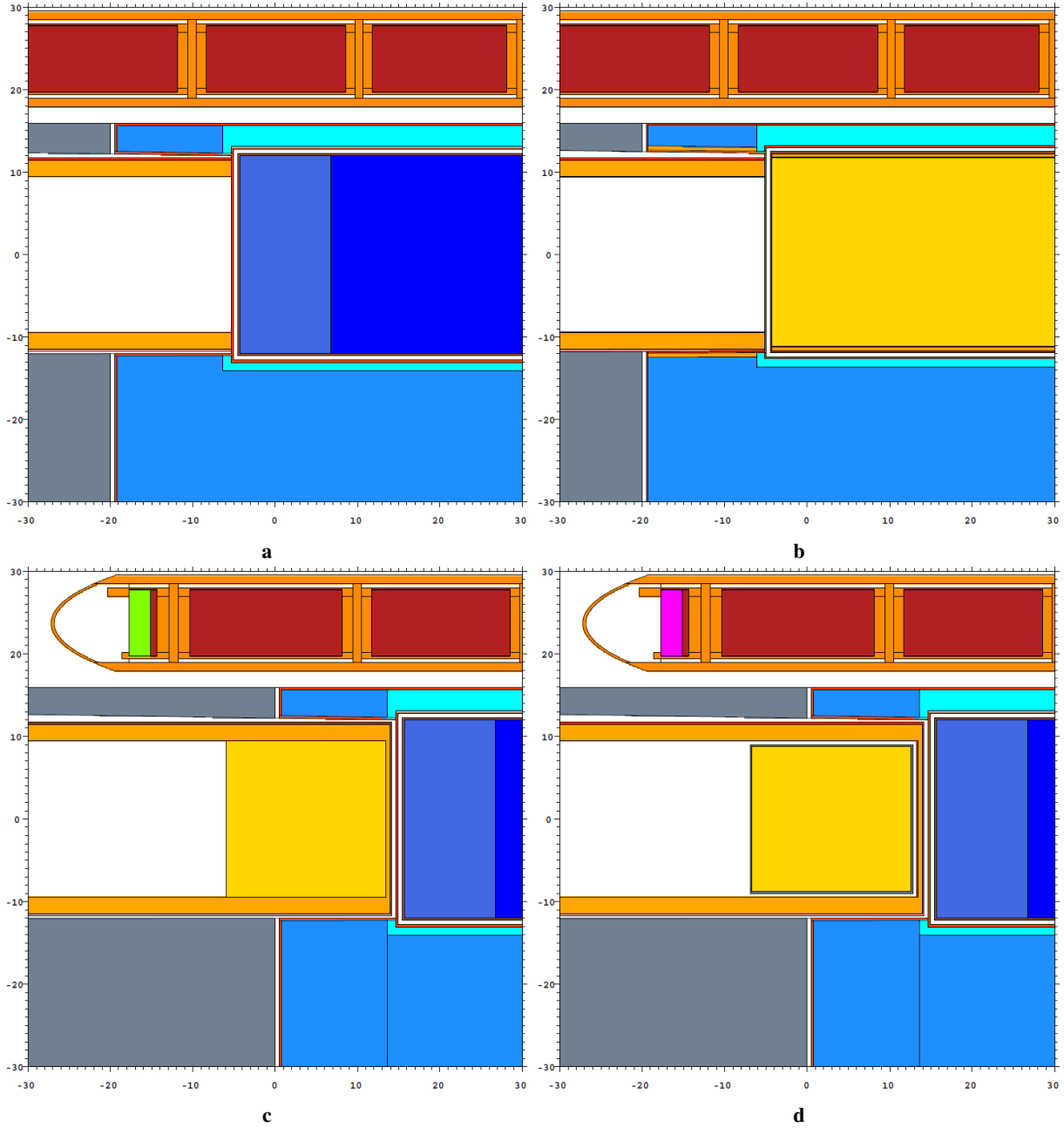


**Figure 112:** MCNP models of the VCN sources compared in this report: (a) standard LD<sub>2</sub> with advanced ND extraction system (b) dedicated SD<sub>2</sub> with advanced ND extraction system (c) combined LD<sub>2</sub> and SD<sub>2</sub> source with ND extraction (ideal case) (d) combined LD<sub>2</sub> and SD<sub>2</sub> source with ND extraction (Al vessel and void gap).

#### 4.10 Comparison of the different options

In this section, we compare the performance of the VCN options presented thus far, except for the clathrates option because it is still at a conceptual level. The models compared here are shown in Figure 112. In order for the comparison to be meaningful, it is important to account for the differences that are not at the core of the design (e.g. the size of the recording surface, or the thickness of the Al walls). Here, we focus only on the NNBAR opening since it is the most similar between the cases and also the most reliable in terms of statistical convergence. Below is a description of each model that is part of the comparison:

- The baseline used is an LD<sub>2</sub> 24 cm × 45 cm × 48.5 cm box at 22 K with a reentrant hole on the neutron scattering side of approximately 10 cm × 10 cm and 12.5 cm and straight walls in the direction

perpendicular to the target. The NNBAR side is 24 cm × 40 cm and an 11-cm cold Be filter at the exit. This baseline was initially conceived to accommodate several equally-illuminated instruments on a plane parallel to the target. The only adjustment to be made to the model in view of the comparison is the dimension of the recording surface at 2 m from the center of the moderator. This is set for all the cases at 19 cm × 35 cm.

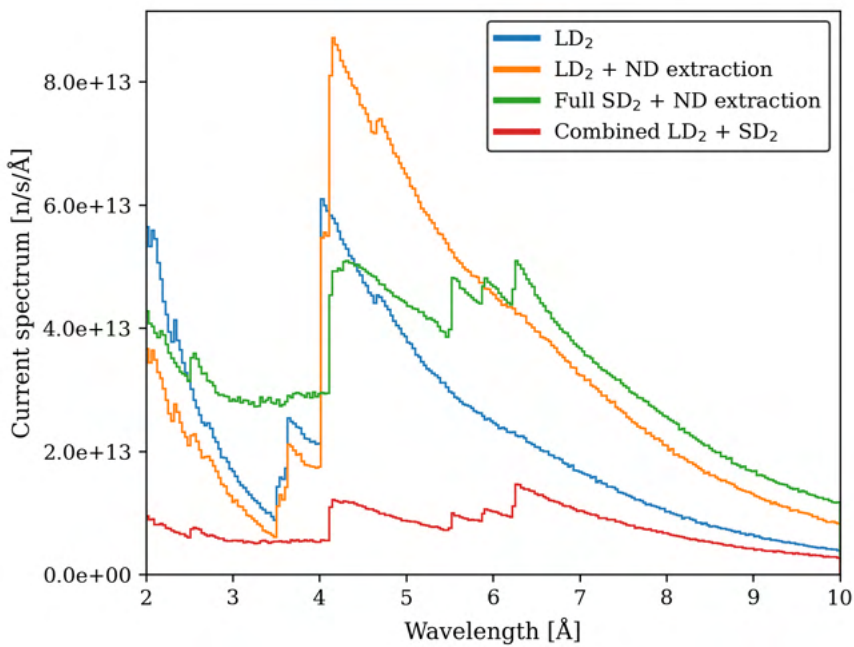
- The ND extraction discussed in Section 4.9 has a thin ND layer on the sides. Here it is increased to 2 cm, which should increase the effect of the enhanced VCN transport at the expense of the cold neutrons. The inner Al wall that contains the ND is 1 mm thick. The model is shown in Figure 112a.
- For the dedicated full SD<sub>2</sub> source, a ND extraction system identical to the previous case was added (Figure 112b). The model for this comparison assumes ideal SD<sub>2</sub> at 5 K with no cooling structure inside the moderating volume. As seen in Section 4.7, this is far from being a realistic description of the moderator, but it is based on the same sets of assumptions that define the baseline (i.e. ideal LD<sub>2</sub> at 22 K with no flow channels inside).
- In the combined option for the NNBAR side, the SD<sub>2</sub> block is 20 cm thick and the ND layer between the source and the SD<sub>2</sub> block is 0.55 cm. The ND extraction system is the same as the previous cases, as well as the recording surface. The difference between the ideal case in Figure 112c and the one in Figure 112d is only the 2 mm Al vessel and the 5 mm vacuum gap surrounding the SD<sub>2</sub>. The only change made for the comparison is adjusting the position and the dimensions of the ND guide to match the previous cases.

For each of these cases, we calculated the current in n/s and the brightness in n/s/cm<sup>2</sup>/sr/Å. The calculation of the absolute brightness for this comparison is similar to what has been done in Section 4.7. First, we recorded the raw counts per spallation proton through the surface at 2 m from the center of the moderator. Then, we divided the counts at ± 2° from the surface normal, by the emission surface, by the solid angle in the 2° cone, and by the wavelength range of the group, then we multiplied the result by the expected proton current on the ESS target at 5 MW, as in Equation (3). All the results in the appropriate units are presented in Table 21. To facilitate the comparison, in Table 22 we calculated the gains over the baseline for each option, while in Figure 113 the current spectra at all angles highlights the effect of ND, SD<sub>2</sub>, and the combination of the two in two wavelength regions.

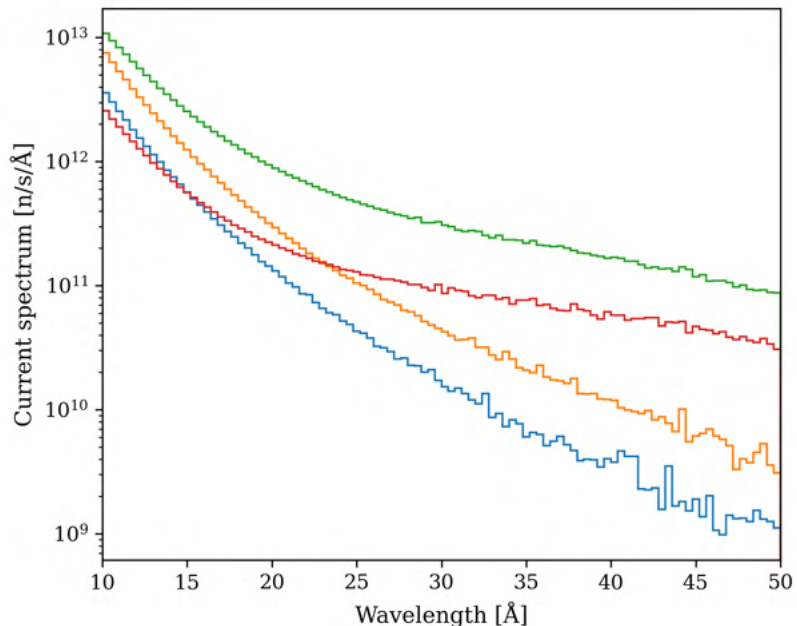
The best option for both the figure of merits studied is undoubtedly the dedicated full SD<sub>2</sub> moderator at 5 K. From the neutronic point of view, order-of-magnitude VCN gains are complemented by a high CN yield. This makes such a moderator an ideal candidate to replace the LD<sub>2</sub> cold source. However, as already highlighted in Section 4.7, this solution comes with great challenges from the engineering point of view.

On the other hand, the easiest solution is using the LD<sub>2</sub> moderator as it is would be to place a guide-like system made of a thick layer of ND and enhance the VCN tail of the cold spectrum. The simulations show that the longer the wavelength, the higher the gain factor for the current; but when it comes to brightness (low angles) the gains are more limited. The interactions with dedicated VCN instruments need to be investigated for a complete overview of the impact of such device. There is, nevertheless, room for further improvement in the design both in terms of materials (e.g. metal walls, packing of the powder etc.) and configuration (e.g. position of the guide) that should be further investigated in a new project.

The option of combining SD<sub>2</sub> and LD<sub>2</sub> is a midpoint between the previous two cases. Even though the possibility of cooling a 5-K D<sub>2</sub> block so close to the spallation target is yet to be determined, this case promises to be much easier to handle if compared to the full SD<sub>2</sub>. At the same time, other challenges would arise in terms of the engineering development (e.g. finding room for the cooling infrastructure in the limited space of the opening, replacing components etc.) that do not need to be faced in the case of a simpler ND guide. In terms of neutronic performance, this option can potentially provide order-of-magnitude gains in the VCN current, without structural changes to the CN baseline. As with the other cases, the optimization of the materials used for the extraction and the containment of the D<sub>2</sub> is crucial to preserve the ideal gains. Lastly, this option takes a significant toll on the CNs, which are drastically reduced at 2 m with the insertion of the SD<sub>2</sub> block. A possible explanation for this effect is the decrease



a



b

**Figure 113:** Current at all angles [ $n/s/\text{\AA}$ ] at 2 m from the moderator center for all the VCN options studied in this section. (a) Bragg peaks from Be Filter, ND and  $D_2$  crystal are visible in the range between 2 and 10  $\text{\AA}$ . (b) VCN tails are highlighted in the range between 10 and 50  $\text{\AA}$ .

of the neutron mean free path due to the elastic scattering inside the  $D_2$  crystal, which increases the effective distance between the moderator surface and the recording surface.

**Table 21:** Neutron current and brightness in wavelength groups for the five VCN sources used in the comparison (Figure 112), calculated for the NNBAR opening. The statistical relative error is also reported.

Current at all angles [n/s]															
	1.8 Å < λ < 4 Å			4 Å < λ < 10 Å			10 Å < λ < 20 Å			20 Å < λ < 40 Å			40 Å < λ < 90 Å		
	Value	% Rel. Err.	Value	% Rel. Err.	Value	% Rel. Err.	Value	% Rel. Err.	Value	% Rel. Err.	Value	% Rel. Err.	Value	% Rel. Err.	
Baseline	$6.20 \times 10^{13}$	0.1	$1.26 \times 10^{14}$	0.1	$9.73 \times 10^{12}$	0.1	$6.17 \times 10^{11}$	0.5	$3.19 \times 10^{10}$	3.7					
Baseline (ND extraction)	$4.42 \times 10^{13}$	0.2	$2.19 \times 10^{14}$	0.1	$2.08 \times 10^{13}$	0.1	$1.50 \times 10^{12}$	0.3	$1.10 \times 10^{11}$	2.0					
Full SD <sub>2</sub> (ND extraction)	$7.15 \times 10^{13}$	0.2	$1.99 \times 10^{14}$	0.1	$3.63 \times 10^{13}$	0.1	$7.44 \times 10^{12}$	0.2	$2.65 \times 10^{12}$	0.6					
Combined option (ideal)	$1.45 \times 10^{13}$	0.3	$4.76 \times 10^{13}$	0.1	$8.30 \times 10^{12}$	0.1	$2.10 \times 10^{12}$	0.4	$1.14 \times 10^{12}$	0.7					
Combined option (Al vessel)	$1.52 \times 10^{13}$	0.3	$5.09 \times 10^{13}$	0.1	$7.22 \times 10^{12}$	0.1	$1.28 \times 10^{12}$	0.4	$3.30 \times 10^{11}$	1.3					
Brightness [n/s/cm <sup>2</sup> /sr/Å]															
Baseline	$7.12 \times 10^{11}$	0.4	$7.67 \times 10^{11}$	0.3	$3.73 \times 10^{10}$	0.3	$1.18 \times 10^9$	1.3	$2.25 \times 10^7$	10					
Baseline (ND extraction)	$9.14 \times 10^{11}$	0.4	$1.10 \times 10^{12}$	0.3	$5.29 \times 10^{10}$	0.3	$1.67 \times 10^9$	1.3	$2.86 \times 10^7$	9.1					
Full SD <sub>2</sub> (ND extraction)	$1.46 \times 10^{12}$	0.5	$9.27 \times 10^{11}$	0.2	$8.66 \times 10^{10}$	0.2	$6.71 \times 10^9$	1.0	$5.64 \times 10^8$	3.5					
Combined option (ideal)	$2.72 \times 10^{11}$	0.8	$1.86 \times 10^{11}$	0.3	$1.71 \times 10^{10}$	0.3	$1.40 \times 10^9$	1.7	$1.80 \times 10^8$	5.1					
Combined option (Al vessel)	$3.35 \times 10^{11}$	0.8	$2.35 \times 10^{11}$	0.3	$1.72 \times 10^{10}$	0.3	$1.00 \times 10^9$	1.8	$5.79 \times 10^7$	9.6					

**Table 22:** Neutron current and brightness gains over Baseline in wavelength groups calculated from Table 21. Propagated statistical error is also reported.

Gain on current at all angles										
	1.8 Å < $\lambda$ < 4 Å		4 Å < $\lambda$ < 10 Å		10 Å < $\lambda$ < 20 Å		20 Å < $\lambda$ < 40 Å		40 Å < $\lambda$ < 90 Å	
	Value	% Rel. Err.	Value	% Rel. Err.	Value	% Rel. Err.	Value	% Rel. Err.	Value	% Rel. Err.
Baseline (ND extraction)	0.7	0.4	1.7	0.1	2.1	0.2	2.4	1.0	3.4	7.4
Full SD <sub>2</sub> (ND extraction)	1.2	0.3	1.6	0.1	3.7	0.2	12	0.8	83	6.0
Combined option (ideal)	0.2	0.3	0.4	0.1	0.9	0.2	3.4	0.9	36	6.1
Combined option (Al vessel)	0.2	0.3	0.4	0.1	0.7	0.2	2.1	0.9	10	6.2

Gain on Brightness										
	1.8 Å < $\lambda$ < 4 Å		4 Å < $\lambda$ < 10 Å		10 Å < $\lambda$ < 20 Å		20 Å < $\lambda$ < 40 Å		40 Å < $\lambda$ < 90 Å	
	Value	% Rel. Err.	Value	% Rel. Err.	Value	% Rel. Err.	Value	% Rel. Err.	Value	% Rel. Err.
Baseline (ND extraction)	1.3	0.6	1.4	0.2	1.4	0.4	1.4	1.9	1.3	14
Full SD <sub>2</sub> (ND extraction)	2.1	0.6	1.2	0.2	2.3	0.4	5.7	1.6	25	11
Combined option (ideal)	0.4	0.9	0.2	0.3	0.5	0.4	1.2	2.1	9.5	11
Combined option (Al vessel)	0.5	0.9	0.3	0.3	0.5	0.4	0.9	2.3	3.1	14

## 5 Deuterated clathrates hydrates

Another set of materials investigated within the HighNESS project are deuterated clathrate hydrates [109] (DCH), which are water-based solids with large crystallographic unit cells. The moderation potential of clathrate hydrates lies in their low energy modes, which are a consequence of the ability of these so-called inclusion compounds to host guest molecules in cages that are formed by networks of hydrogen-bonded water molecules.

While moderation from collective excitations, such as phonons, in a moderator material are kinematically restricted; localized, dispersion-free excitations, such as displacement of confined molecules – often referred to as Einstein modes, molecular rotations, librations or paramagnetic excitations [110] – do not suffer from this limitation and allow for an efficient neutron slowdown even at lowest neutron temperatures [111]. However, their actual moderation capability for the VCN range still needs to be demonstrated experimentally.

Three hydrate systems were investigated within the HighNESS project. The first one hosting deuterated tetrahydrofuran (THF-d) as a guest molecule (molecular formula:  $17\text{D}_2\text{O} \cdot \text{C}_4\text{D}_8\text{O}$ )<sup>8</sup>, the second one hosting molecular oxygen ( $\text{O}_2$ ) as a guest molecule (molecular formula:  $17\text{D}_2\text{O} \cdot \sim 3\text{O}_2$ )<sup>9</sup> and the third one hosting both THF-d and  $\text{O}_2$  (molecular formula:  $17\text{D}_2\text{O} \cdot \text{C}_4\text{D}_8\text{O} \sim 3\text{O}_2$ ). Therein,  $\text{O}_2$  occupies the small cages, which are twice as abundant as the bigger cages occupied by the THF-d.

The biggest advantage of the first system is that it can be manufactured with high yields by freezing a stoichiometric mixture of THF-d and heavy-water ( $\text{D}_2\text{O}$ ). As demonstrated in Section 5.1.1, the  $\text{O}_2$  allows for an additional channel of neutron slow-down. The magnetic triplet ground state of molecular oxygen with its zero-field splitting of 0.4 meV allows for moderation via a cooling cascade mechanism in fully deuterated  $\text{O}_2$ -clathrate hydrates, as described in [110]. It is this low excitation energy (as opposed to modes of several meV of the lattice and the THF) that will significantly enhance the moderation efficiency towards VCN, with the inelastic magnetic scattering providing a final cooling decrement. In this section we present results of the experimental characterization of THF-hydrates (Section 5.1), as well as first results from neutronic simulations using moderators of  $\text{O}_2$ -clathrate (Section 5.4).

### 5.1 Experimental characterization of clathrate hydrates

A necessary characteristic to assess the suitability of a material for moderation purposes is the dynamic structure factor  $S(\mathbf{q}, \omega)$ , which accounts for its structure and excitation spectrum and enters the cross section for VCN production. To determine this quantity in absolute units for the THF-d clathrate hydrate, inelastic scattering experiments using thermal- and cold-neutron time-of-flight instruments at ILL have recently been performed in addition to diffraction experiments for sample characterization. Results of these measurements have been published in [111]<sup>10</sup>. Additional experiments on VCN transmission can provide important complementary information, which determines the maximum depth from which VCNs can be extracted from a moderator to a beam.

#### 5.1.1 Manufacturing of THF-hydrates

A starting point of the experiments described here is establishing a reliable and scalable technique, that allows production of relatively large quantities of hydrates with minimal amounts of residual ice. In this section, this technique is described for THF-hydrates having different protonated and deuterated components. The obtained structures were studied by neutron diffraction at the high-intensity two-axis diffractometer D20. An exemplary powder pattern and details of the associated Rietveld-refinement are given in Section 5.1.2. The structure analysis is followed by a study of the low-energy dynamics of different THF-hydrate samples, as described in Section 5.2.1.

<sup>8</sup>This system was studied before and has shown a broad band of low-energy modes, as experimentally demonstrated by [112] and [113].

<sup>9</sup>The oxygen abundance is, unlike the THF-d, non-stoichiometric and strongly depends on the sample preparation. This is represented by “~”.

<sup>10</sup>For further details consult this article and references therein.

THF (molecular formula C<sub>4</sub>H<sub>8</sub>O) is an organic compound which has a ring structure. A great advantage of THF-hydrates, compared to most other clathrate hydrate compounds, is that they form at ambient pressure from a stoichiometric mixture of its two liquid components, water (H<sub>2</sub>O) and THF (C<sub>4</sub>H<sub>8</sub>O), in a ratio of 17 to 1 [114] at 280 K and below. After carefully weighing and mixing the two liquids with a teflon-coated magnetic stirrer, a cool-down of the solution results in solidification in the CS-II structure (see Table 23). The CS-II structure is the most common among clathrate hydrates and its ideal unit cell contains 136 (H<sub>2</sub>O) molecules forming 16 small and 8 large cages. This structure has been extensively studied previously (see, for example, [115]). The study presented here focuses on the yields of the CS-II structure and quantifying the residual ice, for two different methods to cool down the sample. A great

**Table 23:** Characteristics of the CS-II hydrate crystal cell structure. In the case of THF-hydrates the unit cell formula reduces to 8 THF:136 H<sub>2</sub>O, with the small cages remaining empty. Table adapted from [109, p. 60].

Crystal system	Cubic
Space group	Fd3m (N°227)
Lattice description	Face centered
F Lattice parameters	a = 17.1 Å-17.33 Å α = β = γ = 90°
Number of cages	8 large (5 <sup>12</sup> 6 <sup>4</sup> ), 16 small (5 <sup>12</sup> )
Ideal unit cell formula	8(5 <sup>12</sup> 6 <sup>4</sup> ) · 16(5 <sup>12</sup> ) · 136H <sub>2</sub> O

advantage of the manufacturing technique is, that it allows for a contrast variation between the host and the guest contribution in spectroscopy experiments. By simply substituting one of the liquid components with its deuterated counterpart (water (H<sub>2</sub>O) with heavy water (D<sub>2</sub>O) and THF (C<sub>4</sub>H<sub>8</sub>O) with THF-d (C<sub>4</sub>D<sub>8</sub>O)) one obtains four different samples which are summarized in Table 24.

**Table 24:** Differently deuterated and protonated samples prepared for spectroscopy experiments. The deuteration of either the guest molecule or the host lattice allows to highlight the different parts of the sample in the scattering signal. Note that the fully or partial deuteration is able to slightly change the dynamics of the sample, while the structure remains the one described in Table 23.

	Abbrev.	Host	Guest
Fully protonated	THF · H <sub>2</sub> O	136 H <sub>2</sub> O	8 C <sub>4</sub> H <sub>8</sub> O
Deuterated guest	THF – d · H <sub>2</sub> O	136 H <sub>2</sub> O	8 C <sub>4</sub> D <sub>8</sub> O
Deuterated cage	THF · D <sub>2</sub> O	136 D <sub>2</sub> O	8 C <sub>4</sub> H <sub>8</sub> O
Fully deuterated	THF – d · D <sub>2</sub> O	136 D <sub>2</sub> O	8 C <sub>4</sub> D <sub>8</sub> O

### 5.1.2 Neutron diffraction on fully deuterated THF-hydrates

To characterize the fully deuterated THF-hydrates, the diffractometer was utilized with the (115) reflection from a germanium (113) monochromator, employing a wavelength of  $\lambda = 1.546 \text{ \AA}$ . It operated at a take-off angle of 90°, resulting in a resolution of  $\Delta d/d = 3 \cdot 10^{-3}$ . The sample container, a cylindrical vessel constructed from vanadium with dimensions of 6 mm in diameter and a 0.1 mm wall thickness, was filled with the stoichiometric liquid mixture. This container was then quenched using liquid nitrogen before being placed into the cryogenic sample environment.

After reaching thermal equilibrium at the desired temperature, it took approximately 30 minutes to acquire a diffraction pattern over a scattering angle range of 4° to 150°, achieving satisfactory statistics. This enabled measurements within a temperature range spanning from 2 K to 230 K. Subsequently, the sample was gradually heated above its melting point (around  $\sim 277.5 \text{ K}$ ) and then slowly cooled down at a rate of approximately 7 K per minute, reaching temperatures below 200 K. Interestingly, we observed that the CS-II structure formation occurred under both rapid quenching and gradual cooling of the liquid sample.

Effects of texture of the polycrystalline samples were observed as a dependence of diffraction patterns on sample orientation (which for an ideal powder would be absent). These variations stem from uncontrolled in-situ crystallization, which can result in a limited number of crystallites and eventually deviate from the typical continuous powder patterns, approaching individual points on the Debye-Scherer cones. To alleviate this effect, an approach was made to mitigate it by incrementally rotating the sample in 20° intervals and subsequently combining the resulting nine diffraction patterns. This method aimed to provide a more accurate representation of a powder average. As depicted in Figure 114, an illustrative diffraction pattern acquired using this procedure showcases the process at a temperature of 230 K.

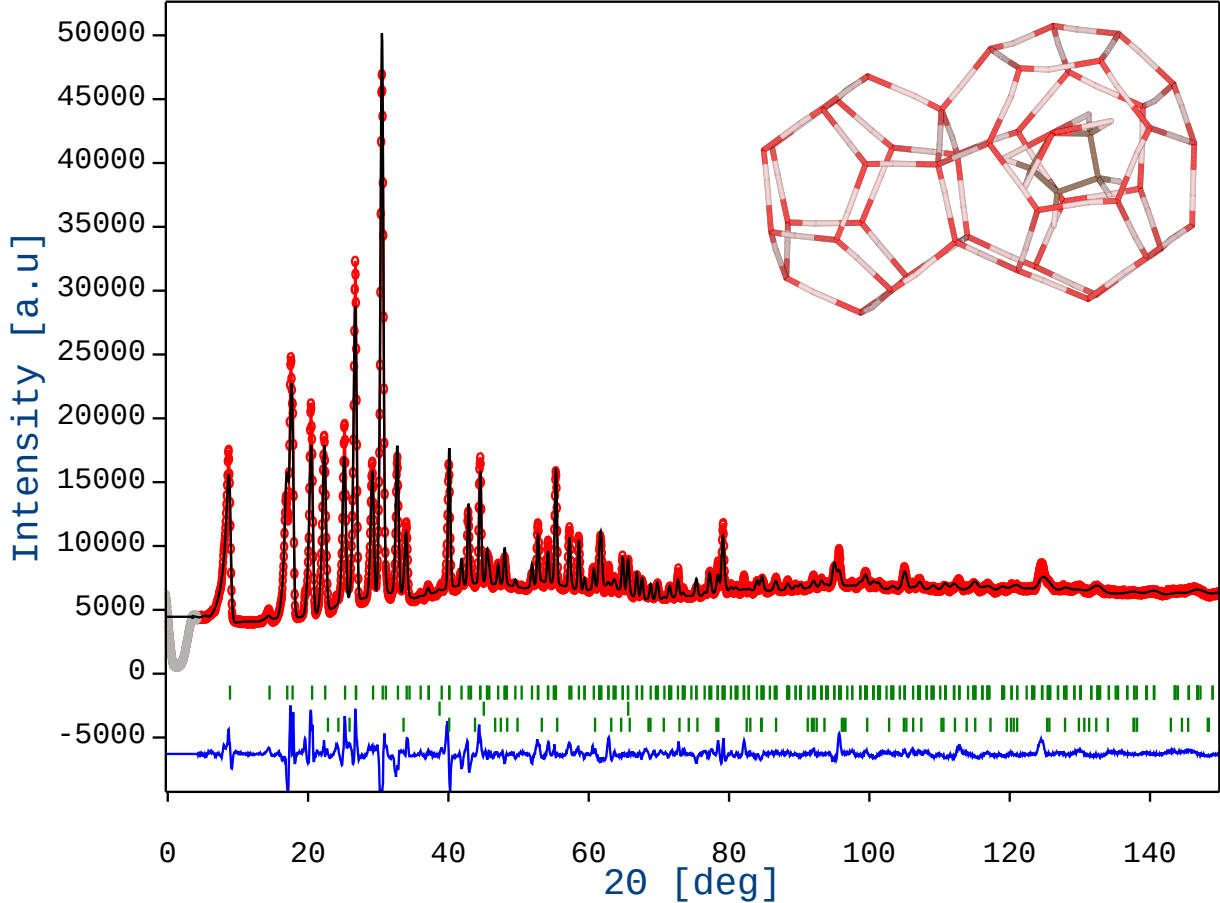


**Figure 114:** Diffraction pattern of fully deuterated THF-hydrates ( $\text{THF} - \text{d} \cdot \text{D}_2\text{O}$ ) formed in situ taken on D20 with  $\lambda = 1.546 \text{ \AA}$  at a temperature of 230 K (red) and the corresponding multi-phase Rietveld-refinement (black). See text for experimental conditions. The experimental data is available in Ref. [116]. The blue line depicts the difference between the data and the fit. The calculated peak positions (green ticks) correspond to phases considered for the refinement, which are, besides the THF-d-hydrate, the aluminum sample environment and residual hexagonal ice (see Section 5.2) for details on the refinement). The upper right corner shows 1 of the 8 large cages ( $5^{12} 6^4$ ) within the unit cell hosting a THF-d molecule, as well as 1 of the 16 empty small cages ( $5^{12}$ ).

## 5.2 Structural details

Data analysis and structure refinement were performed in the program Fullprof [117] [118]. A multi-phase Rietveld-refinement (see e.g. [119]) yields the lattice constants, the positional and thermal parameters, as well as the weight percentage for each crystalline phase present in the sample. In a full refinement procedure the instrumental and background parameters are determined concurrently to the structure, the respective scale factors and the phase fractions. The THF-d molecule was treated as a rigid body, with its position and the orientation within the large cage as free parameters. Aside from the phase under investigation (THF-d-hydrates), the refinement includes the aluminum of the sample environment

**Table 25:** Refinement details of the diffraction pattern depicted in Figure 114. The Bragg R-factor ( $R_B$ ) and the weighted profile R-factor ( $R_{wp}$ ) indicate an acceptable fit.

Phase	THF – d · D <sub>2</sub> O	Ice I <sub>h</sub>
Crystal System	cubic	hexagonal
Space Group	F d -3 m	P 63/m m c
Cell parameters	a = 17.22(7)	a = b = 4.50(7) c = 7.35(4)
$R_B$	10.49	27.92
$R_{wp}$	4.89	4.89

and residual hexagonal ice. The weight percentage  $W_j$  for the phase  $j$  can be calculated as in [120]:

$$W_j = \frac{S_j Z_j M_j V_{cj}}{\sum_i^N S_i Z_i M_i V_{ci}}, \quad (7)$$

with  $S$ ,  $Z$ ,  $M$  and  $V$  being the scale factor, the number of formula units per unit cell, the mass of one formula unit and the unit-cell volume, for each phase  $j$  and  $i$ , respectively. Fullprof also accounts for the multiplicities of each site, for occupation numbers unequal to 1, via the factor  $f_j$ , and the micro absorption of neutrons (Brindley factor  $t_j$ ) of each phase (see Ref. [121] for details):

$$W_j = \frac{S_j Z_j f_j^2 M_j V_j / t_j}{\sum_i^N S_i Z_i f_i^2 M_i V_i / t_i} = \frac{S_j \cdot ATZ \cdot V_j}{\sum_i^N S_i \cdot ATZ_i \cdot V_i}, \quad (8)$$

with  $ATZ = Z_j f_j^2 M_j / t_j$ .

Since our hydrate is stoichiometric ( $f_j = 1$ ) and the two phases in question have very similar absorption ( $t_j \sim 1$ ) Equation (8) reduces to Equation (7).

Depending on the sample, a clathrate weight percentage of  $95.1 \pm 1.5$  % to  $98.4 \pm 1.6$  % was reached for the samples investigated, with the uncertainty being dominated by the quality of the fit. In that context, it is important to note that deviations derived in these kinds of least-squares methods only partly reflect systematic errors which might be introduced by the instrument or sample. The details of the refinement are given in Table 25. The fit suffers substantially from the size of the crystallites, which is due to the texture resulting from formation in situ. Nevertheless, it provides evidence that the clathrate structure is formed with reliable purity from the liquid stoichiometric mixture.

### 5.2.1 Time of flight spectroscopy

After confirming the presence of the CS-II structure in the samples that had undergone solidification through quenching or slower cooldown, we proceeded to study their low-energy excitations. To this end, experiments were conducted on the ILL time of flight (TOF) spectrometers IN5 [122] and Panther [123]. These experiments aimed to measure the dynamic structure function  $S(q, \omega)$  across a substantial portion of the  $(q, \omega)$ -space. This comprehensive study is made possible thanks to the broad and complementary kinematic range offered by these two instruments.

The data obtained from these measurements play a crucial role in benchmarking density functional theory (DFT) and molecular dynamics (MD) simulations, as elaborated in [124]. The four samples described in Table 24 were measured under the configurations summarized in Table 26. Additional measurements of each empty sample holder were conducted in order to subtract their contribution from the respective scattering signals. Vanadium standards were used to normalize our data to absolute units. Particular emphasis was put on selecting the geometries of the sample and the standard to be as identical as possible. By choosing thin hollow cylinders as sample geometry (with a wall thickness of  $d = 0.05$  mm for the partly or fully protonated samples and  $d = 0.1$  mm for the fully deuterated one) the multiple scattering was reduced to a minimum [125]. Note that unlike at D20, the sample containers are made from aluminum. The respective vanadium standard was cut from a sheet of the same thickness and placed inside the sample container without overlap.

The vertical intensity profile of the beam was mapped out prior to taking measurements. This allowed us to place the samples and the vanadium standards in an intensity distribution which would minimize potential systematic effects due to possible small differences in their vertical extensions.

**Table 26:** Configurations for measurements conducted on ILL's TOF spectrometers. The overlap between incident wavelength allows crosschecking of the absolute units calibration.

Instrument	Panther	IN5
Incident wavelength $\lambda_i$ [Å]	1, 2	2, 3
Incident energies $E_i$ [meV]	76, 19	19, 9
Temperature [K]	1.5	1.5

Data reduction, analysis and visualization was done with the software package Mantid [126] [127]. Self-attenuation effects in the sample and the vanadium standard were calculated using a Monte Carlo simulation as described in [128]. The scattering of the sample environment was accounted for by subtracting measurements of the empty sample container in the cryostat. In order to normalize  $S(q, \omega)$  to absolute units, the data is multiplied by a factor  $f$ , derived from the vanadium standard:

$$f = \frac{N_V \sigma_V}{N_S}. \quad (9)$$

Here,  $N_V$  is the number density and  $\sigma_V$  the total scattering cross section of vanadium and  $N_S$  the number density of the sample. The factors  $N_V$  and  $\sigma_V$  are well-known tabulated values, while  $N_S$  can be calculated from the structure given above. It should be noted that it is essential when using this method to know exactly the purity and geometry of both the sample and the vanadium standard.

### 5.3 Low-Energy Excitations of THF-Hydrates

Figures 115a and 115b show two spectra for different THF hydrate samples measured at Panther and IN5, respectively. These spectra are obtained by integration over a given  $q$ -range, providing an average of the coherent signal in this range.

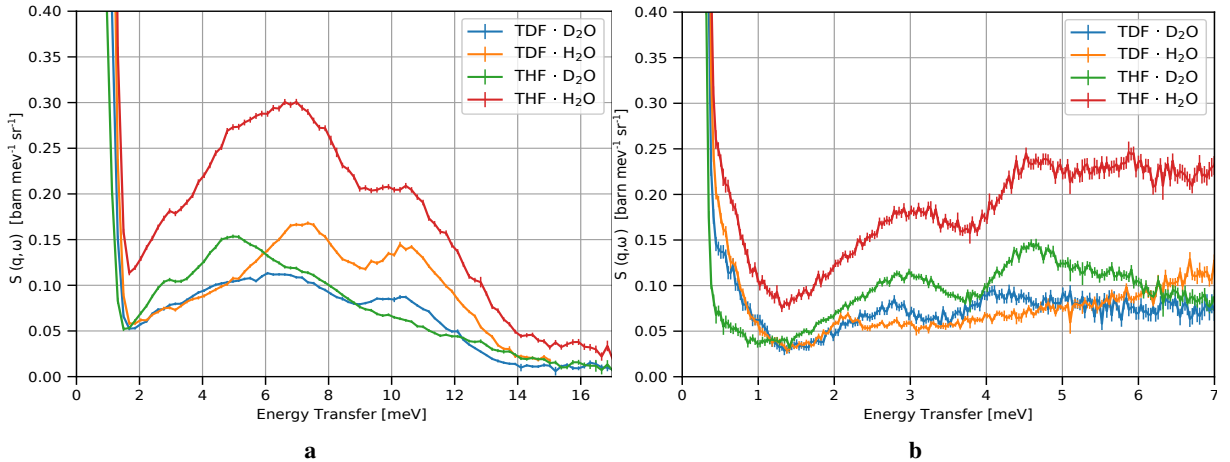


**Figure 115:** (a) Constant  $q$ -slice at  $q = (4 \pm 1) \text{ \AA}^{-1}$  through  $S(q, \omega)$  for different deuteration and protonations of the THF-hydrate measured at **Panther** with an incident energy  $E_i = 19 \text{ meV}$  at a temperature of  $T = 1.5 \text{ K}$ . The characteristic peaks at 7 meV and 10.5 meV of CS-II can be well discerned. Preliminary results, data is available under [129]. (b) Constant  $q$ -slice at  $q = (3.5 \pm 0.75) \text{ \AA}^{-1}$  through  $S(q, \omega)$  at **IN5** with an incident energy  $E_i = 9 \text{ meV}$  at a temperature of  $T = 1.5 \text{ K}$ . The observed peaks are due to localized excitations of the THF molecules (see text). The shoulder of the elastic peak is not a feature of the sample but back scattering of the sample environment. Preliminary result, data is available under [116].

In the investigated energy region, the dynamics of the host structure are dominated by the translational modes of the H<sub>2</sub>O or D<sub>2</sub>O molecule. This leads to two characteristic peaks at about 7 meV

and 10.5 meV of every CS-II hydrate structure (see, for example, Refs. [130],[131],[113],[112],[132]), which can also be observed in Figure 115a for both the protonated and the deuterated host structures. The most pronounced peaks are visible in the THF – d · H<sub>2</sub>O sample (orange), as the contribution of the deuterated guest molecule is suppressed. The excitations of the guest molecule are located at lower energy and show very distinct peaks at about 2.9 meV and 4.7 meV, best visible in the THF · D<sub>2</sub>O sample (green) in Figure 115b. These localized excitations are particularly promising for moderation to the VCN range. As expected, they are shifted to slightly lower energies when substituting hydrogen with deuterium due to the increased mass and thus moment of inertia. This is the case for both translational modes of the host lattice and the excitations of the THF molecule, and consistent with phonon density of states (PDOS) computed by our collaborators [124].

#### 5.4 Simulation of a clathrate hydrate moderator

To study the use of clathrate hydrate as a VCN moderator, a neutron flux in a simple spherical model was initially calculated in OpenMC [133]. In this model, a sphere with radius of 22 cm was filled with the clathrate hydrate at 2 K (see Figure 116a) with a thermal (1 eV) isotropic point source of neutrons located in the center of sphere. The radius of the sphere was chosen so that it has a similar volume as the baseline LD<sub>2</sub> cold moderator. The sphere was subsequently filled with LD<sub>2</sub> and SD<sub>2</sub> for comparison with clathrate.

The neutron energy spectrum for each case can be seen in Figure 118a, and the neutron wavelength spectrum for each case can be seen in Figure 119a and Figure 119b. Here, the SD<sub>2</sub> outperforms the clathrate for both the CN ( $2 \text{ \AA} < \lambda < 10 \text{ \AA}$ ) and VCN range ( $\lambda > 10 \text{ \AA}$ ), while the clathrate was only competitive with LD<sub>2</sub> in the VCN range above 14 Å. The reason for the sudden increase in the neutron flux at 14 Å for the clathrate-filled moderator is that the cross section for the magnetic down-scattering is maximal at that wavelength (see Figure 117). The wavelength spectrum in Figure 119a shows a peak for SD<sub>2</sub> at about 5 Å, which appears due to a sharp peak in the elastic cross section for SD<sub>2</sub> at this wavelength. These results from OpenMC simulation are consistent with those from an identical simulation in MCNP (see Figure 121a).

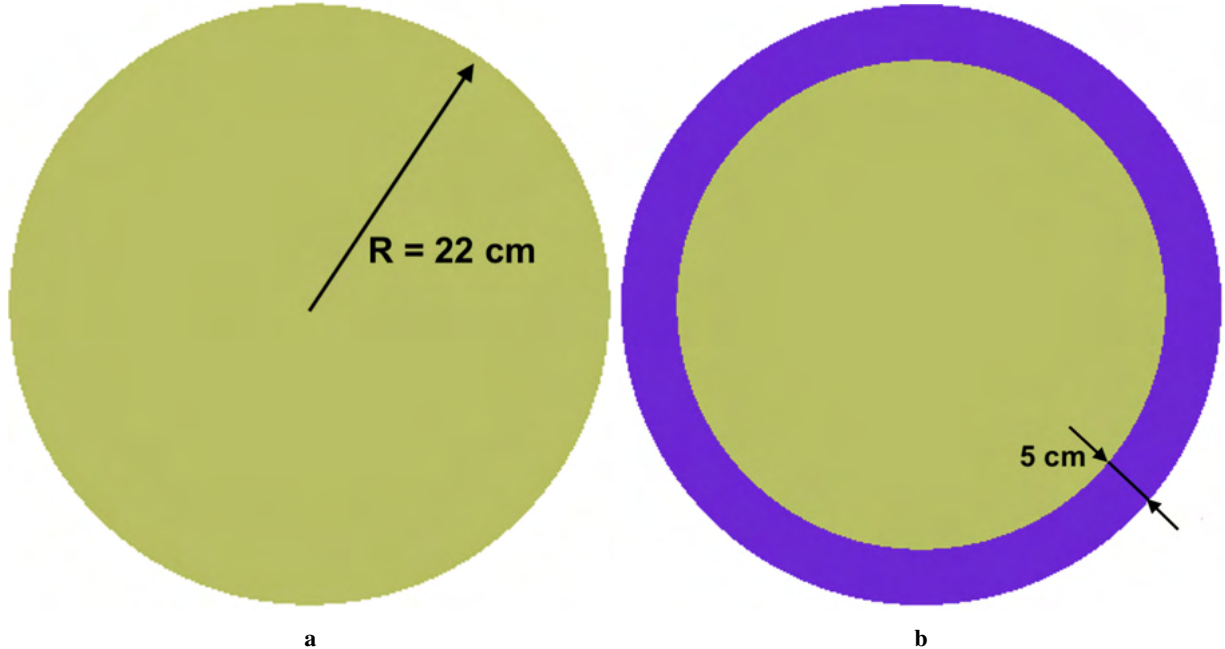


**Figure 116:** An initial model of the clathrate VCN source. (a) Initial model with sphere of radius 22 cm filled with clathrate hydrate. (b) Second model with additional 5 cm thick layer of MgH<sub>2</sub> cold neutron reflector.

A limiting factor of the selected clathrate at 2 K is the large mean free path of cold neutrons, about 30 cm, for magnetic down scattering that can be deduced from Figure 117. The cross sections are

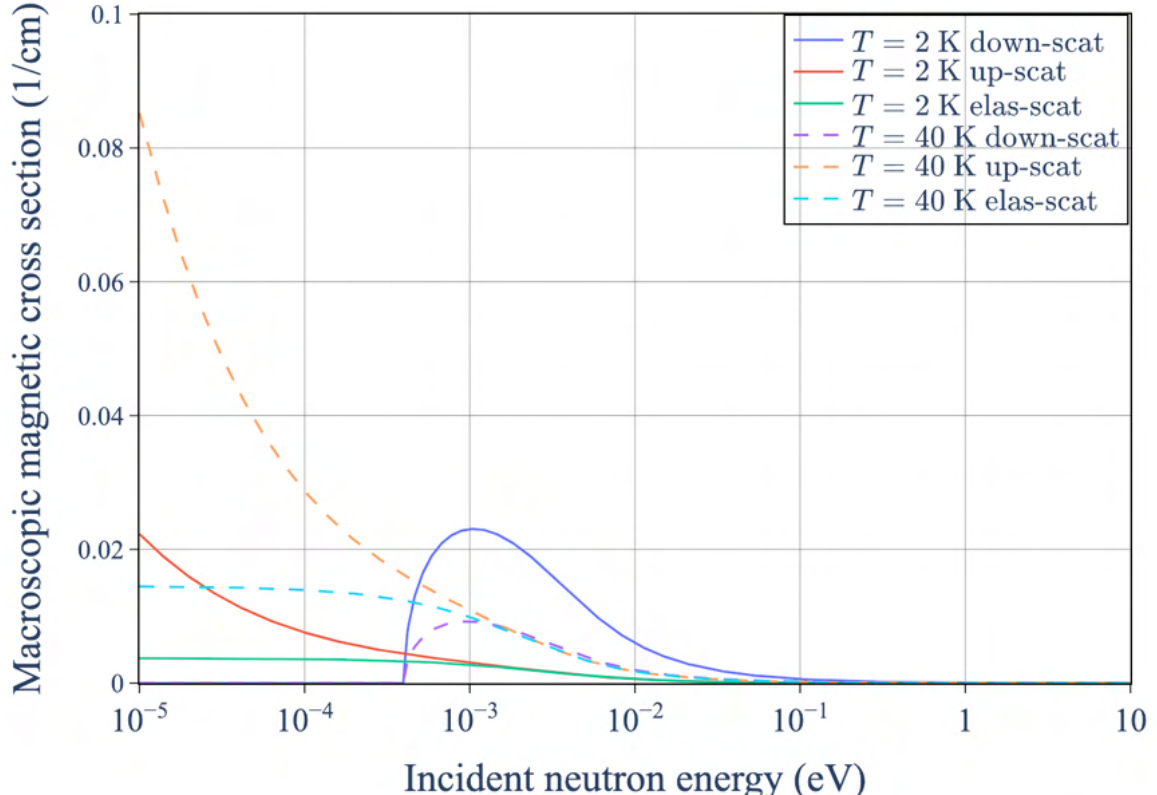


**Figure 117:** Cross-section for the magnetic scattering in O<sub>2</sub>-clathrate hydrate with 136 D<sub>2</sub>O and 24 O<sub>2</sub> in each unit cell. Generated using the tool ncplugin-MagScat presented in Ref. [134].

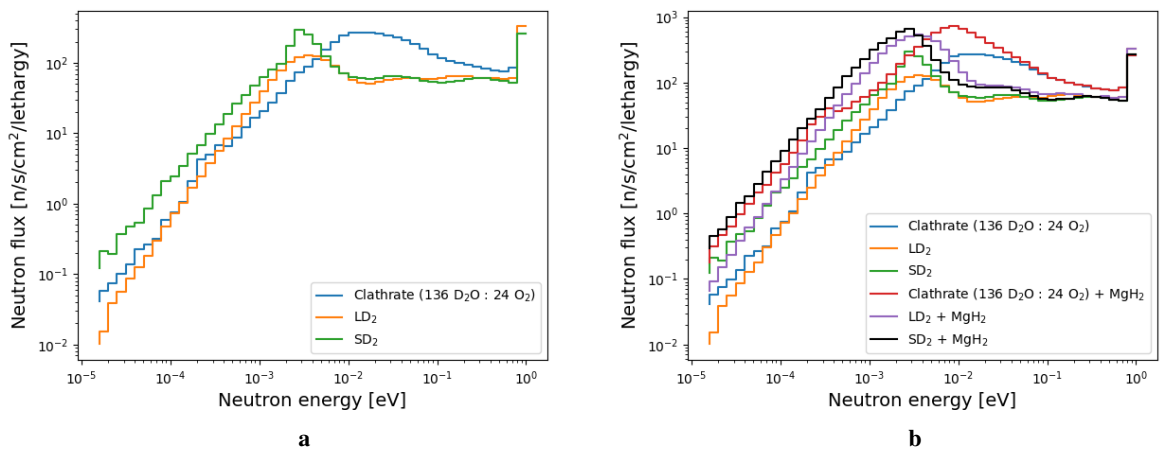


**Figure 118:** Calculated neutron flux inside a sphere filled by O<sub>2</sub>-clathrate, LD<sub>2</sub> or SD<sub>2</sub>. (a) Model without the cold neutron reflector. (b) Comparison of the model with and without the cold neutron reflector, which was is MgH<sub>2</sub> at 20 K.

computed using the tool ncplugin-MagScat in which the physics of inelastic neutron magnetic scattering [110] is implemented [134]. To mitigate this deficiency, a 5 cm thick shell of material to reflect cold neutrons was designed around the sphere to allow for more interactions between cold neutrons and the clathrate (see Figure 116b). This shell was filled with MgH<sub>2</sub> because of its promising properties as a cold neutron reflector, as reported by Granada et al. [135] and based on a study of several neutron reflector materials. This study was conducted using the model in Figure 116b where the 5 cm thick outer shell was filled with several possible cold neutron reflectors (results shown in Figures 122a and 122b). In

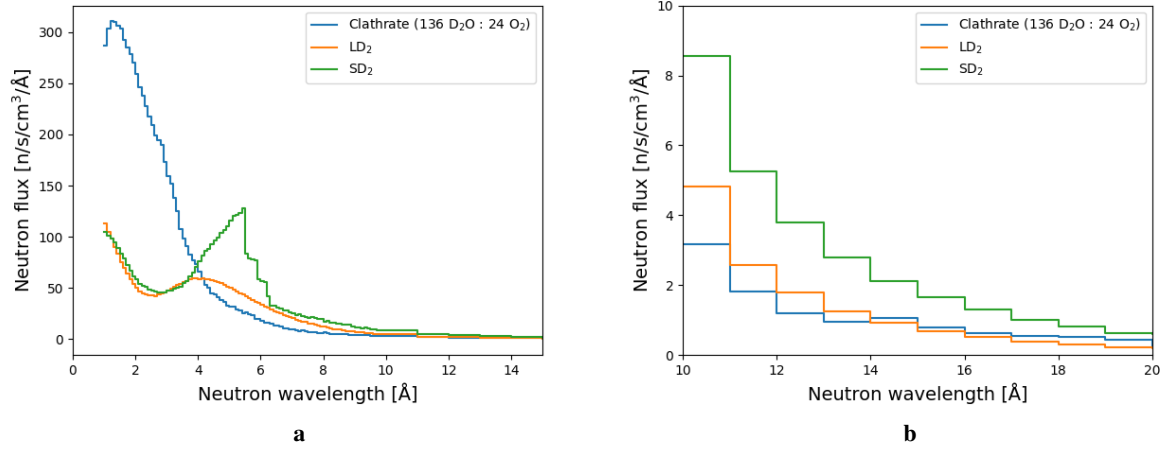


**Figure 119:** Neutron spectrum measured in the sphere filled by O<sub>2</sub>-clathrate, LD<sub>2</sub> or SD<sub>2</sub>. (a) Spectrum between 1 and 15 Å. (b) Spectrum between 10 and 20 Å.

this case, the presence of MgH<sub>2</sub> at 20 K maximized the neutron flux for the cold and very cold regions.

The resulting neutron energy and wavelength spectra for the spherical moderator surrounded by the cold neutron reflector is shown in Figures 118b, 120a and 120b. It is obvious that the presence of the MgH<sub>2</sub> reflector improved the efficiency of the clathrate as a VCN moderator much more than for the case of SD<sub>2</sub> and LD<sub>2</sub>. The performance of clathrate with an MgH<sub>2</sub> reflector nearly reached that of SD<sub>2</sub> with an MgH<sub>2</sub> reflector in this scenario. The peak for the SD<sub>2</sub> spectrum at about 5 Å appears in the case with the MgH<sub>2</sub> reflector as well. This result from OpenMC is again consistent with the result from MCNP (see Figure 121b).

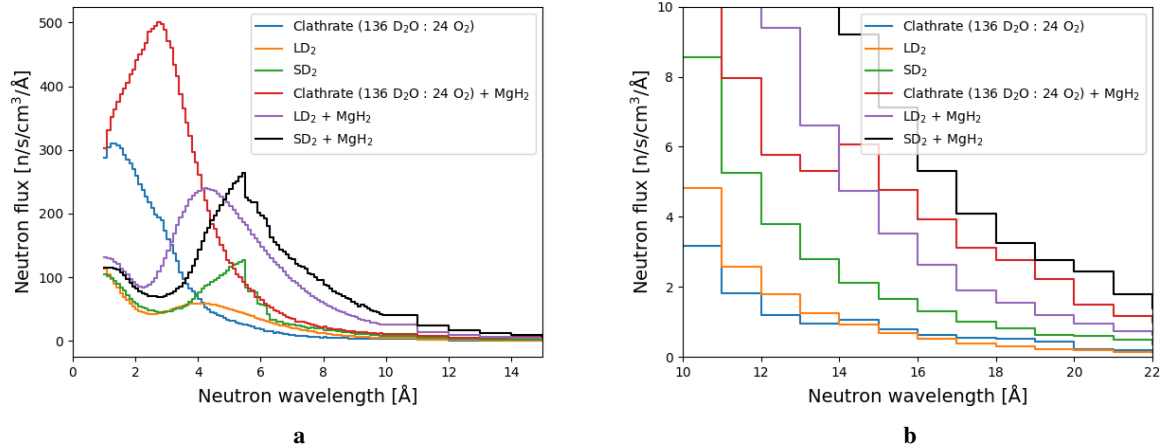


**Figure 120:** Neutron spectrum measured in a sphere filled by O<sub>2</sub>-clathrate, LD<sub>2</sub>, or SD<sub>2</sub>; with or without the MgH<sub>2</sub> reflector at 20 K. (a) Spectrum between 1 and 15 Å. (b) Spectrum between 10 and 22 Å.

A toy model was designed after finishing the initial study to simulate more realistic conditions for a source made of clathrate hydrate inserted below the spallation target at the ESS. This model contained a cell with the thermal reflector filled with Be; a 2-cm thick thermal premoderator filled with H<sub>2</sub>O; a 5-cm thick cold reflector filled with MgH<sub>2</sub>; and a cubic-shaped moderator filled either with the clathrate hydrate, LD<sub>2</sub>, or SD<sub>2</sub>. The emission surface had an area of 20 × 20 cm<sup>2</sup>, designed together with a 50-cm vacuum pipe for neutron extraction. A surface source with area of 40 × 40 cm<sup>2</sup> was located at the top of H<sub>2</sub>O premoderator. The volume of the moderator cell was fixed at 40 × 40 × 40 cm<sup>3</sup> (see Figure 123).

The neutron energy spectrum was calculated (see Figure 124) 50 cm away from the emission surface in the extraction pipe. The neutron wavelength spectra in Figures 125a and 125b show that the clathrate

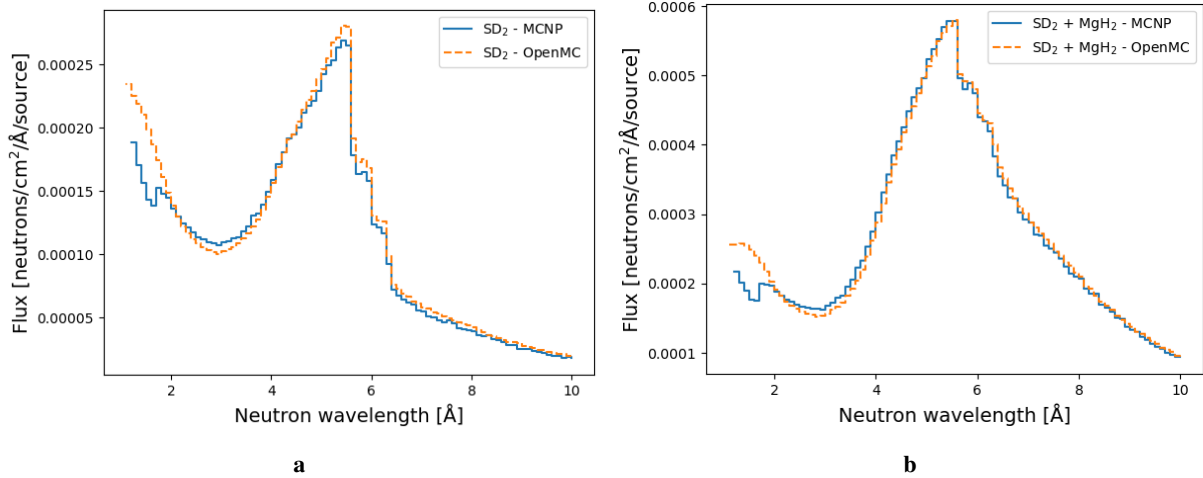


**Figure 121:** Comparison of the neutron wavelength spectra for the spherical moderator filled with  $\text{SD}_2$  calculated in MCNP and OpenMC. (a) Spectra without the  $\text{MgH}_2$  reflector at 20 K. (b) Spectra with the  $\text{MgH}_2$  reflector at 20 K.

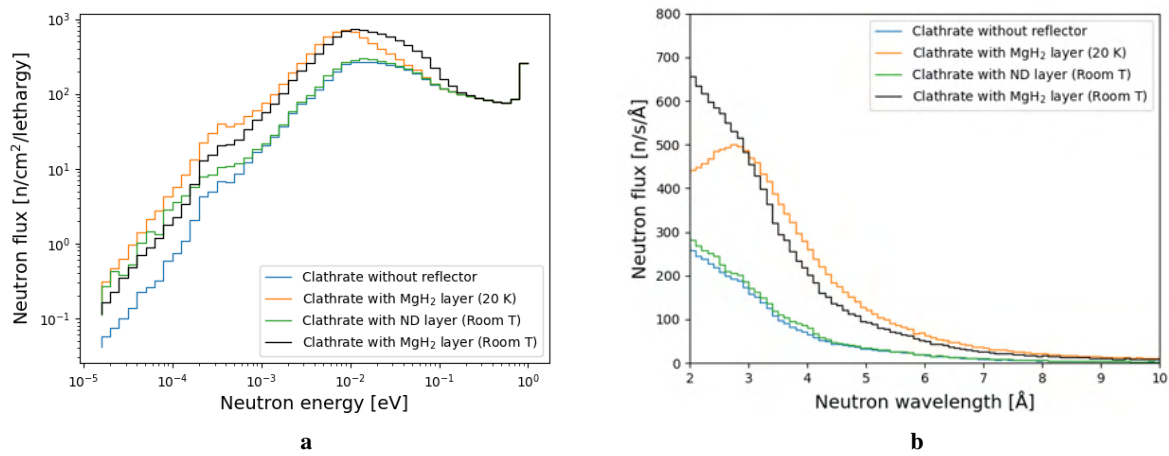


**Figure 122:** Neutron spectra measured in the sphere filled by  $\text{O}_2$ -clathrate and different neutron reflector materials around the moderator. (a) Spectrum in energy. (b) Spectrum in wavelength.

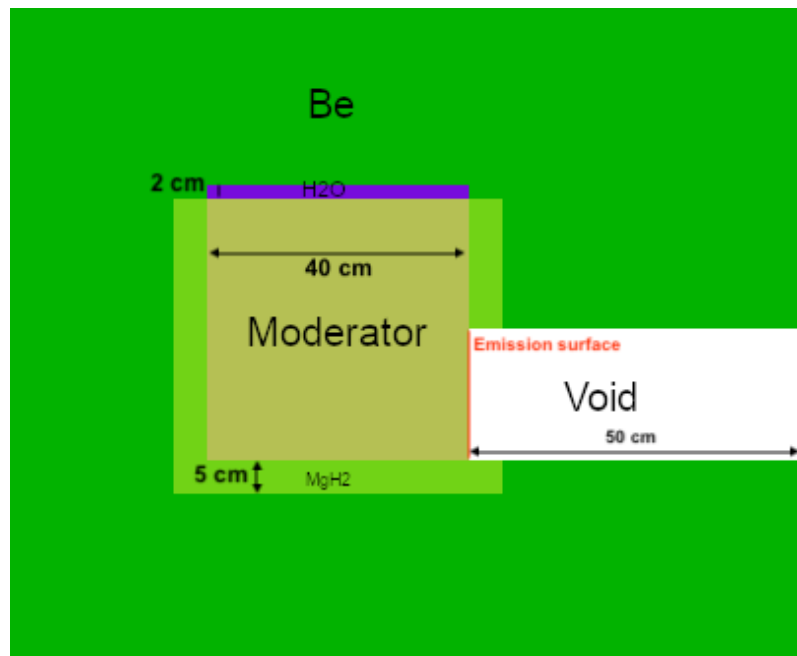


**Figure 123:** A drawing of OpenMC toy model of clathrate moderator with size of moderator box of  $40 \times 40 \times 40$  cm $^3$ .

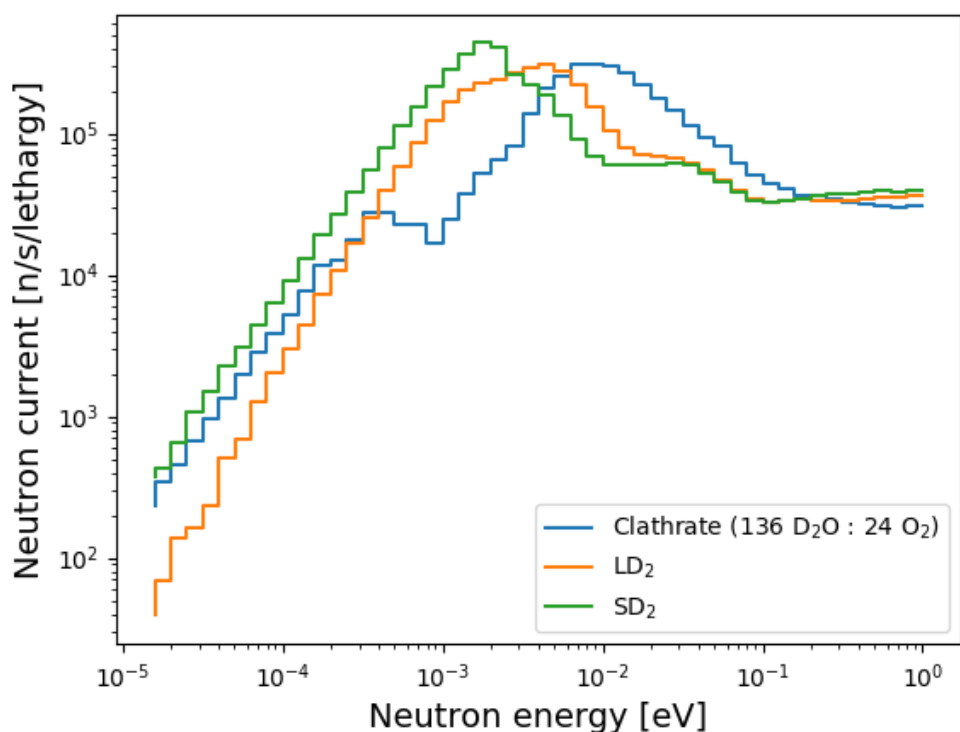


**Figure 124:** Neutron energy spectrum measured 50 cm away from the emission surface with size of moderator box of  $40 \times 40 \times 40$  cm $^3$ .

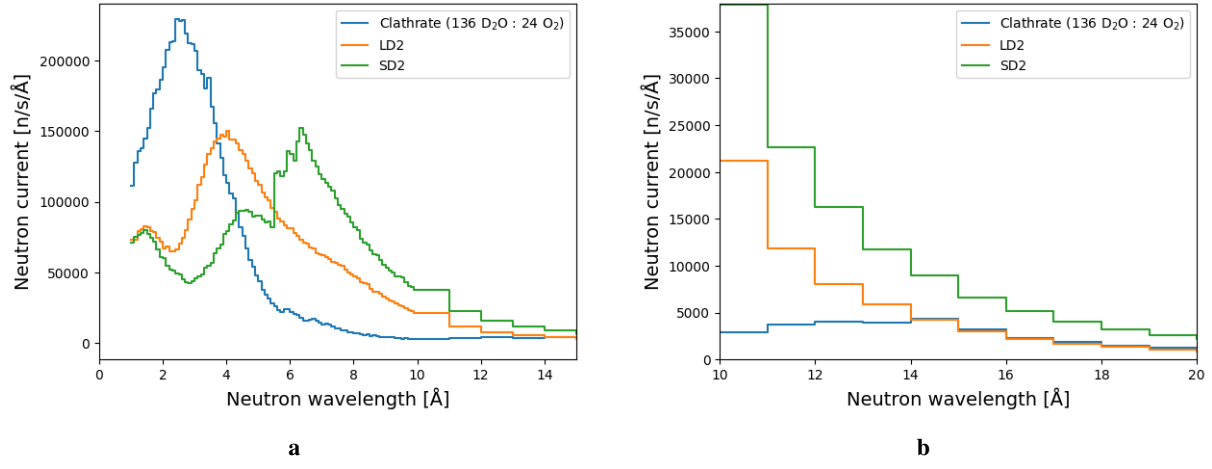


**Figure 125:** Neutron wavelength spectra measured 50 cm away from the emission surface for the model with moderator volume of  $40 \times 40 \times 40 \text{ cm}^3$ . (a) Spectra from 1 to 15 Å. (b) Spectra from 10 to 20 Å.

hydrate became a competitive moderator material with LD<sub>2</sub> above about 14 Å. This result is consistent with the results from the spherical moderator and MgH<sub>2</sub> reflector model. The volume of the box moderator was increased to  $80 \times 80 \times 80 \text{ cm}^3$  while keeping the dimensions of cold reflector, premoderator and extraction pipe aligned to the bottom of moderator. The results are shown in Ref. [134].

## 6 Design of the ESS Ultra Cold Neutron source

### 6.1 UCN scientific case and general overview of the field

The extremely low energy levels of ultracold neutrons, often on the order of several neV, enable them to exhibit unique properties. They can be reflected from various materials at all angles of incidence, depending on the energy range associated with the material. Consequently, UCNs can be stored in material traps[136], magnetic traps[137], or even be subjected to gravitational confinement. UCNs have the potential to remain within experimental setups for extended periods, sometimes spanning several hundred seconds. This characteristic makes them highly responsive to subtle phenomena. In many cases, despite their significantly lower fluxes, UCNs prove to be more sensitive probes compared to thermal and cold neutrons.

It was F.L. Shapiro, who pointed out the possibility of procession measurements with UCN [138], followed by the first reported observations of UCNs [139] [140]. This led to a rapid developments in the field during the 1970s, resulting into substantial enhancements in precision in measuring the neutron lifetime [141]. They also played a crucial role in setting constraints on the neutron's electric dipole moment (EDM) [142], and later to the discovery of gravitational eigenstates of UCN above a flat mirror [143].

Increasing the quantity of ultracold neutrons introduced into experiments remains a valuable approach for improving experimental precision. In cases where the free neutron lifetime isn't the main limiting factor for losses, as observed in neutron EDM measurements, significant enhancements can also be achieved by extending the storage duration<sup>11</sup>. However, it's important to highlight that regardless of the scenario, existing experiments with ultracold neutrons are primarily restricted by counting statistics. For a comprehensive overview of the scientific capabilities of UCNs and the specific needs of respective experiments, please refer to [144].

Currently, there are only a handful of operational UCN sources worldwide, including those at ILL, PSI, TRIGA-Mainz, and LANL. PNPI in Russia has operated several UCN sources in the past, and a new one is currently under construction. Additionally, various UCN sources are either in the construction phase or have been proposed at prominent facilities like FRM-II in Germany, TRIUMF in Canada, LANL and SNS in the USA. For a comprehensive overview of the global UCN landscape, please refer to [145].

The first UCN source developed for user applications is PF2 at the ILL. It is based on the vertical extraction of VCNs from the tail of the Maxwellian distribution of a cold source, followed by final slowdown to UCNs using the *Steyerl-turbine* [146]. All the other sources, operating or under design or construction, are based on neutron conversion, using either SD<sub>2</sub> at about 5 K, or superfluid <sup>4</sup>He (He-II) at about 1 K or less. While other materials have been considered and are still studied (see [147] and references therein), these two materials have been identified as particularly suitable for UCN production. The transition from a cold neutron to an ultracold neutron occurs in both of these materials through a single scattering event. Consequently, the UCN do not reach thermal equilibrium with the medium, leading to the classification of such sources as "superthermal". It is imperative to maintain the medium at extremely low temperatures to minimize the loss of UCN due to up-scattering.

One of HighNESS' primary objectives is to design a UCN source at ESS. Extensive studies has been conducted, drawing from the two materials mentioned earlier. This exploration includes various concepts for UCN sources, ranging from those positioned in close proximity to the neutron-production target (referred to as "in-pile" options) to sources located further away and supplied with a cold neutron beam (referred to as "in-beam" options). You can find a comprehensive list of concepts and potential locations for possible UCN sources at ESS in [148]. The findings presented herein are based on the assumption of ESS operating with a proton beam power of 5 MW, equivalent to a beam energy of 2 GeV and an average current of 2.5 mA. As discussed in Section 1.1.3 ESS will start its operation with the reduced power of 2 MW corresponding to an 800 MeV beam energy and maintaining an average current of 2.5 mA. Given

---

<sup>11</sup>It's important to note that certain experiments depend on a substantial transmitted flux of UCNs rather than a dense storage.

that the neutron spallation yield generally increases linearly with proton energy, the findings regarding UCN performance and heat loads can be easily extrapolated to the 2 MW operational scenario.

### 6.1.1 VCN to Feed UCN Production

The development of a VCN source has a parasitic benefit of improving flux in the wavelength ranges relevant to UCN production (which are discussed in detail in Section 6.4). Thus, the VCN design options proposed in Section 4 may be highly beneficial in terms of UCN production.

For example, as highlighted in [149], superfluid He-II can be utilized as a converter in the production of UCN through a superthermal cooling process of CN or VCN (see Section 6.4.2). This is made possible by the crossing dispersion relations between superfluid He-II and the free neutron, allowing neutrons with wavelengths of approximately 8.9 Å (equivalent to a kinetic energy of 1.0 meV) to be scattered down to the ultracold regime emitting a single phonon. An enhancement of the flux of neutrons with wavelengths around 8.9 Å would be a valuable asset for in-beam UCN-sources exploiting this mechanism. This includes variants with in-situ UCN production and detection approaches, as proposed in [150].

## 6.2 In-pile and in-beam UCN sources

We have divided the possible implementations of UCN sources at ESS into two groups: *in-beam* and *in-pile* UCN sources.

An in-pile source is placed near the primary source of neutrons, i.e., a reactor core, or the target in a spallation source. Thus, an in-pile source has the advantage of receiving a high neutron flux, with the possibility of delivering high UCN yields. This comes however with the challenges related to positioning such a source near the target, and in particular to keep the source at the desired low temperature (about 5 K for an SD<sub>2</sub> source, and below 2 K for a He-II source). Conversely, an in-beam source is placed at some distance (typically several tens of meters) from the primary cold source. Such an in-beam source, fed by a cold neutron beam, will have lower UCN production rate than for an in-pile source, but there are several advantages, such as: easier engineering (for example, more freedom about the placement of the source, more available space); much easier cooling of the source to sub-K temperature; easier access for maintenance.

The list of the identified in-pile and in-beam options is given in [148] and shown in Figure 126. We have adopted the convention to label *in-pile* a source located inside the ESS monolith, i.e., within 5.5 m from the center of the monolith (corresponding to the center of the main moderator). A source located at larger distance is considered *in-beam* (cf. Figure 4 in [148]). In HighNESS, we have investigated only one in-beam concept, which has been published in [147]. This in-beam concept exploits the larger field of view offered by the large beamport, and adopts the novel nested mirror optics [151]. Alternatively, a regular beamline, i.e. from one of the available beamports of ESS, could be used for an in-beam source similar to the ILL SuperSUN [152]. Performance estimates are given in [153].

An alternative approach for UCN studies is to perform the intended experiment in-situ[153]. Such experiments have been previously realized and are proposed for ESS and other facilities. In this approach, the measurements are performed inside the source, which is based on He-II. The proposed experiments are EDM searches, thus requiring polarized neutrons. The detector is also placed inside the source and it can be based on <sup>3</sup>He. The major advantage of in-situ measurements is the fact that transport losses are avoided altogether. There are some challenges, in particular related to the guiding of cold neutrons in the source, in-situ detection of UCN, and balancing UCN accumulation time with measurement time. In-situ measurement might be possible for the in-beam option [147] that we propose which uses a He-II source placed at a distance from the ESS cold source, and nested mirror optics to transport the neutrons from the LBP to the UCN source. Additionally, an in-situ configuration could also be possible for a He-II source placed directly in the LBP at about 2 m from the cold source.

Concerning the possible converter materials for in-beam and in-pile UCN sources, we have adopted the following: in the case of in-pile sources, both SD<sub>2</sub> and He-II are possible candidates; therefore both materials have been studied. For an in-beam source, we considered only the option of He-II. The

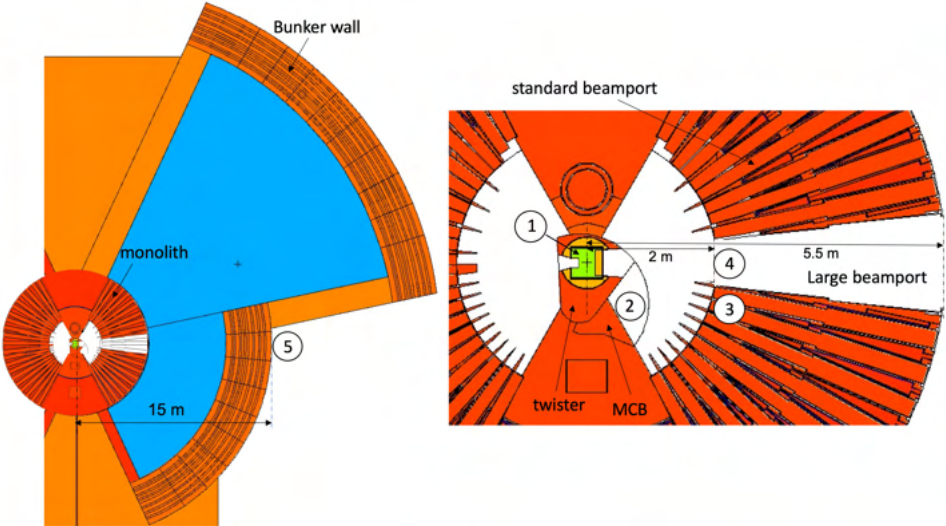


**Figure 126:** A horizontal cut through the target region, at the height of the LD<sub>2</sub> moderator (shown in green) situated below the spallation target (not visible). The cylindrical region of radius 5.5 m around the center represents the shielding monolith (shown in red). The right figure is a zoom of the central part of the left figure. About half of its 42 standard beamports are visible in the cut plane. The possible locations of UCN sources, as studied within the HighNESS project are: (1) inside the “twister”; (2) inside the moderator cooling block; (3) in a standard beamport; (4) in the large beamport (shown as a white segment in the monolith); (5) outside the “bunker”, a heavy concrete shielding structure (shown in orange) placed around the monolith; the minimum distance of this location from the moderator is 15 m. See [148] for details and explanation of options for the various source positions. Reprinted from [148].

reason for this choice is that we expect higher total UCN production in a large He-II converter placed in a cold neutron beam than in a SD<sub>2</sub> converter. The latter, even when placed in beam, would have to be of relatively small volume, to overcome the issue of poor UCN extraction from the bulk of the SD<sub>2</sub> converter. Because of that, SD<sub>2</sub> is considered a valid candidate for a UCN source only in the in-pile option. In fact, all the UCN sources in operation (LANL, PSI) or under construction (FRM-II), based on SD<sub>2</sub>, are in-pile designs.

In summary, the list of possible UCN sources which have been analyzed within the HighNESS project is the following:

- He-II in twister;
- SD<sub>2</sub> in twister;
- He-II in MCB;
- SD<sub>2</sub> in MCB;
- He-II in LBP;
- He-II in beam.

Regarding the last case, He-II in-beam, we have only studied the source’s performance using the LBP where thanks to the large available solid angle, special optics can be employed. Performance of a generic in-beam He-II source at the ESS using a regular beampore, can be estimated rescaling the results obtained from this case.

### 6.3 UCN production

There are several quantities that can be used to characterize the performance of a UCN source:

- UCN production rate density  $P_{UCN}$  [ $\text{cm}^{-3} \text{s}^{-1}$ ]. This is the rate of production of UCN inside the source, per unit volume of the source.
- UCN production rate  $\dot{N}_{UCN}$  [ $\text{s}^{-1}$ ]. Following from integration of  $P_{UCN}$  over the volume of the UCN source, it characterizes the total production rate.

- UCN density in the source  $\rho_{\text{UCN}}$  [cm<sup>-3</sup>]. This quantity is in general time-dependent but here to be understood as the number of UCN per unit volume in the source in steady-state operation. It is sometimes also called saturated UCN density and given by the product of  $P_{\text{UCN}}$  and the lifetime  $\tau$  of UCNs in the source.  $\tau$  is strongly dependent on the material and on its temperature. For SD<sub>2</sub> at 5 K, it is about 40 ms [154, 155]. For He-II, assuming UCN accumulation in a converter vessel with material walls, it is given by the expression [156]

$$\tau^{-1} = \tau_{\beta}^{-1} + \tau_{\text{up}}^{-1} + \tau_{\text{He3}}^{-1} + \tau_{\text{wall}}^{-1} \quad (10)$$

In this expression,  $\tau_{\beta}$  is the mean lifetime of the neutron (880 s);  $\tau_{\text{up}}$  is the up-scattering rate, which for a temperature below 1 K is given by [157, 158]  $\tau_{\text{up}} \approx (T[K])^7/100[s]$ ;  $\tau_{\text{He3}}$  is the rate of UCN absorption by <sup>3</sup>He; and  $\tau_{\text{wall}}$  is the rate of UCN loss due to interaction with the walls of the vessel.

- Total UCN number (or saturated UCN number) in the source  $N_{\text{UCN}}$ . It is given by the production rate  $\dot{N}_{\text{UCN}}$  times the UCN lifetime  $\tau$  in the source.
- UCN density in the storage vessel  $\rho_{\text{UCN, EXP}}$ [cm<sup>-3</sup>]. For an experiment with UCN, the quantity to be optimized is the sensitivity to the effect to be measured, rather than the UCN density in the source. A large UCN density  $\rho_{\text{UCN, EXP}}$  and a large total number of UCNs trapped in an experimental storage vessel,  $N_{\text{UCN, EXP}}$ , are often numbers to be considered and optimized in designing an experiment. To estimate these quantities for a specific UCN source, it is necessary to first have at least a preliminary design of a UCN experiment and then calculate the fraction of UCN losses attributed to various factors, such as extraction losses, transport losses, and losses inside the storage vessel. In general, experiments involving a large vessel, such as some neutron lifetime experiments, often aim at maximizing  $N_{\text{UCN, EXP}}$ . Certain other experiments relying on extreme suppression of systematic effects, such as nEDM experiments, are preferably done with smaller vessels, in which a high value of  $\rho_{\text{UCN, EXP}}$  is then crucial [156].
- Total (saturated) number of UCNs in the storage vessel  $N_{\text{UCN, EXP}}$ . For this quantity, the same considerations as discussed in the previous bullet point apply.

Given the multitude of quantities involved, it becomes evident that there is no single, unambiguous figure of merit for optimizing a UCN source. In our studies, our primary focus was on achieving high  $N$  and  $P$ , with our analysis primarily centered on the source itself. Assessments of UCN experiment performance connected to a source should be conducted in a subsequent stage, during the design of the UCN experiments.

For the same reason, the performance of SD<sub>2</sub>-based and He-II based sources are not directly comparable: the UCN lifetimes in the two materials are very different, of the order of 40 ms for SD<sub>2</sub>, and of the order of hundreds of seconds for He-II below 1 K. The scopes of these two source types are thus different as well. SD<sub>2</sub> close to a primary cold source can produce a large UCN flux which is suitable for experiments in flow-through mode or if large vessels need to be filled, whereas He-II enables UCN accumulation to high saturated UCN densities, which can be advantageous for small storage vessel with a long storage time constant. Finally a prerequisite for in-pile source variants, where the UCN converter medium is installed close to a primary cold source, is the capability to transport UCNs with low losses over large distances of several tens of meters.

## 6.4 Methods for calculating the UCN production rate density $P_{\text{UCN}}$

### 6.4.1 Calculating $P_{\text{UCN}}$ in SD<sub>2</sub>

$P_{\text{UCN}}$  cannot be estimated directly in an MCNP simulation by the conventional method of measuring a neutron flux tally, since MCNP does not transport neutrons in the energy range of UCNs. Therefore,  $P_{\text{UCN}}$  for converters made of SD<sub>2</sub> was estimated by calculating the cold neutron flux and multiplying it by UCN production cross-section. The accuracy of such calculation depends on the accuracy of the thermal scattering libraries used in the MCNP calculation, as well as on the accuracy of the UCN production cross-section in SD<sub>2</sub>. Several SD<sub>2</sub> UCN cross-sections have been published. We adopted the cross section calculated by Frei et al. [159] at the Technical University of Munich. This cross-section was

calculated from a dynamical scattering function extracted from the IN4 experiment conducted at ILL with the SD<sub>2</sub> sample kept at 4 K and incident neutron energy of 67 meV (see Figure 127). This cross-section differs slightly from the one measured in an experiment at the FUNSPIN beamline at PSI with a sample kept at 8 K (see Figure 127). The observed discrepancies between these two cross sections can be, for example, explained by a different crystal orientation, sample temperature, sample purity and crystal quality.

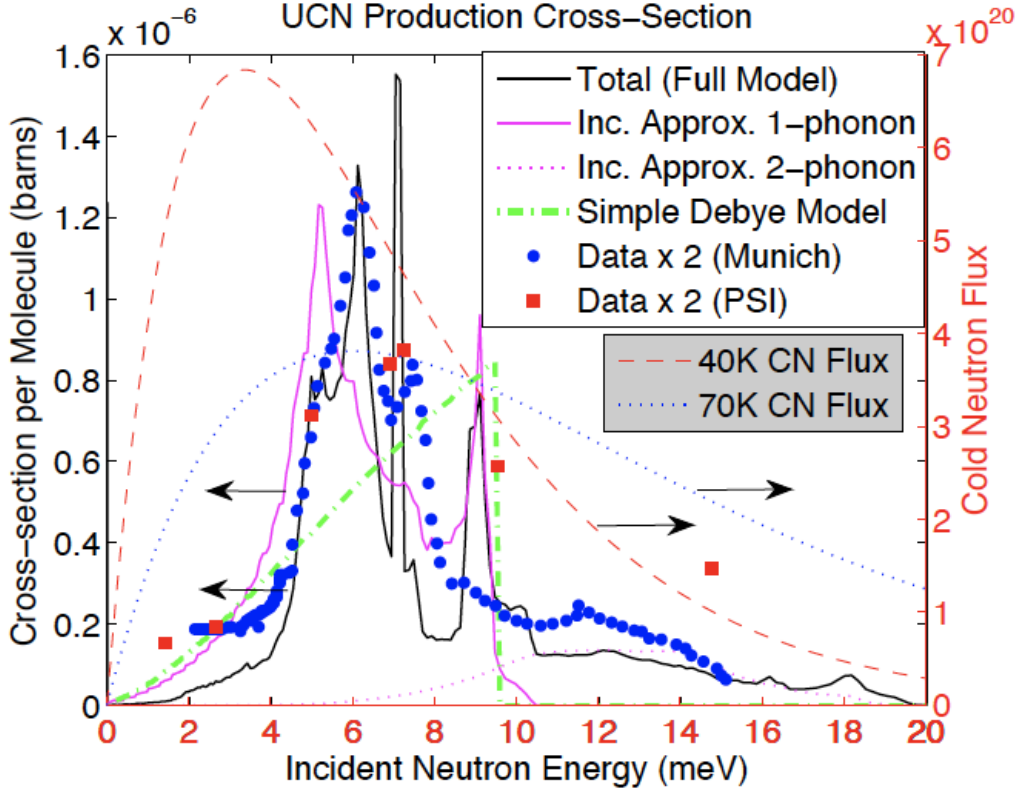


**Figure 127:** The comparison of UCN production cross sections in SD<sub>2</sub>. Adapted from Liu et al. [72]. The red squares depict the cross section measured at PSI [160], whereas the blue circles depict the cross section calculated at TUM in Munich [159]. The calculation of cross section at TUM was based on experimental data from neutron time-of-flight experiment at IN4 (ILL).

#### 6.4.2 Calculating P<sub>UCN</sub> in He-II

The scattering function for He-II,  $s(\lambda)$ , which the UCN production calculations are based on, is shown in Figure 128. The model used for the library generation is based on the separation of the single-phonon excitations, described by the phonon-roton dispersion relation, and the multi-phonon excitations, which have been included using a weighted frequency spectrum with the phonon-expansion approach in the Gaussian approximation [161].

The scattering function can then be derived from this model and has also been determined experimentally [162]. Both functions are shown in Figure 128. ESS Model 1 refers to the version used for this work, while ESS Model 2 is based on a revised methodology [163], which can be used in future work. It can be seen in the figure that the main contribution to the UCN production is given by a narrow wavelength band around 8.9 Å, but also higher energetic neutrons between 2 Å and 6 Å contribute to UCN production (via multi-phonon processes).

Following [162],  $P_{UCN}$  is given by

$$P_{UCN} = N\sigma V_c \frac{k_c}{3\pi} \int_0^\infty \frac{d\phi}{d\lambda} s(\lambda) \lambda d\lambda, \quad (11)$$

where  $N$  is the He number density,  $\sigma=1.34$  b is the bound neutron scattering cross section for  ${}^4\text{He}$ ;  $\hbar k_c = \sqrt{2m_n V_c}$ ;  $V_c$  is the wall potential of the converter vessel with respect to the Fermi potential of He-II (18.5 neV at SVP); we consider as wall material beryllium, with an optical potential of 252 neV; therefore  $V_c=233$  neV;  $s(\lambda)$  is the UCN scattering function as a function of the neutron wavelength  $\lambda$ ;  $\frac{d\phi}{d\lambda}$  is the differential incident flux.

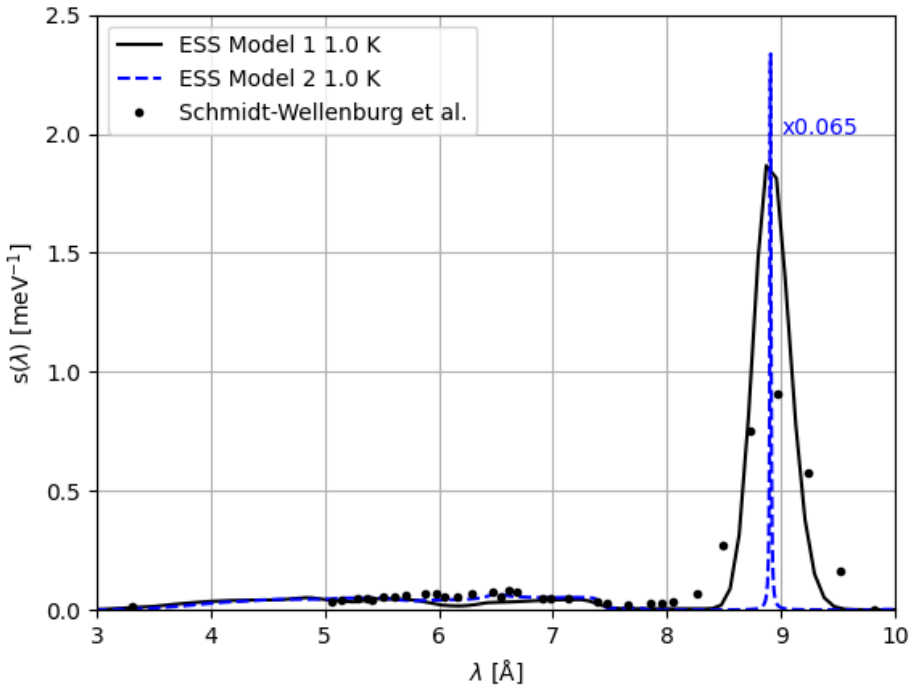


**Figure 128:** The scattering function,  $s(\lambda)$ , for UCN production in He-II. The curve from Schmidt-Wellenburg et al. [162] has been determined experimentally. The ESS model 1 curve was used for this work and is based on an early version of the scattering library [164], while ESS model 2 is an improved version, which can be used for future work [163]. The single-phonon peak for ESS Model 2 has been multiplied by a factor of 0.065 for visualization purposes.

#### 6.4.3 UCN production rates as a function of the distance from the LD<sub>2</sub> moderator

The calculated production rate density in He-II and SD<sub>2</sub>, as a function of the distance from the cold moderator, ranging from the moderator surface to 150 cm away, is shown in Figure 129. These estimates are obtained following the procedure explained in the sections above. Neutron fluxes are calculated at a given distance from the moderator surface; the SD<sub>2</sub> or He-II converters are not modelled. These curves are therefore representative of the production in He-II or thin films of SD<sub>2</sub>, i.e., for configurations where the perturbation of the incoming cold flux, from the converter itself, is negligible.

### 6.5 SD<sub>2</sub> source in twister

The first option that we consider is to place the UCN source as close as possible to the cold source inside the lower moderator plug in the ESS twister. This option corresponds to *option 1* in Figure 126. For an explanation of the geometry and the purpose of the twister, see Section 3.1 in [148]. The rationale behind this concept is to maximize the cold flux delivered to the UCN converter and therefore the UCN production, in agreement with the results shown in Figure 129. This solution requires either to design a dedicated second-generation cold moderator or to find a design that complements the first-generation cold source, without impacting the needs of the NNBAR experiment and of the neutron scattering instruments.

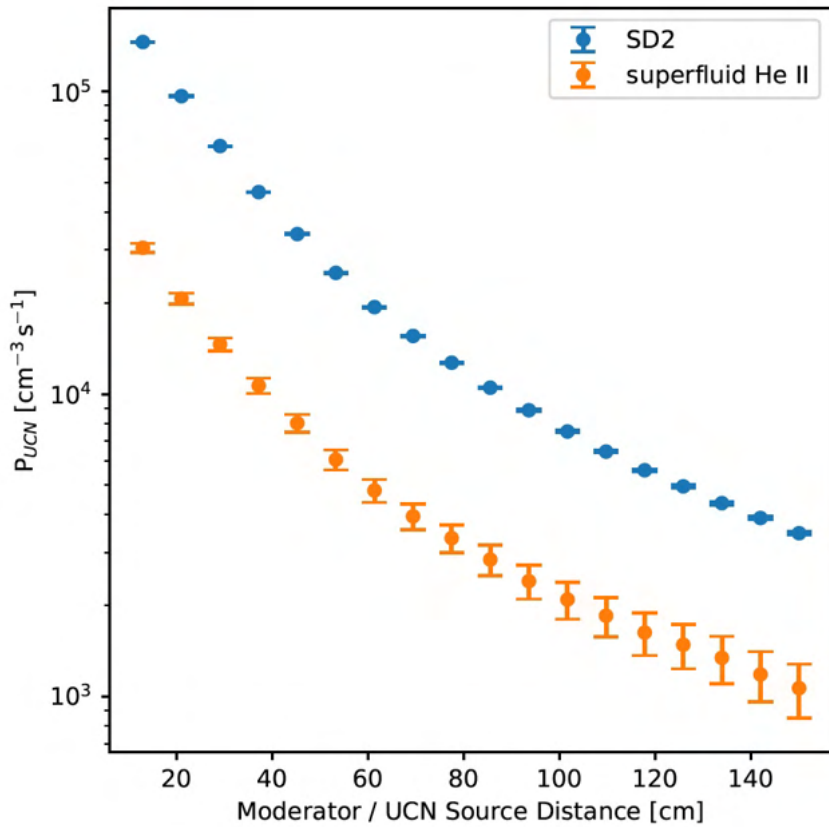


**Figure 129:** Calculated production rate densities for He-II [162] and SD<sub>2</sub> [72] as a function of the distance from the LD<sub>2</sub> moderator. The distances are from the center of the UCN source to the edge of the beryllium filter on the NNBAR side of the lower moderator. The UCN converters are not modelled.

As indicated in [148], a possible design which, thanks to the reduced amount of SD<sub>2</sub> inside the twister, might be possible to cool and operate, consists of a thin slab of SD<sub>2</sub> placed close to the main cold source. We explore several ideas using a thin SD<sub>2</sub> converter in the twister in Sections 6.5.1, 6.5.3 and 6.5.4. A larger volume of SD<sub>2</sub>, if coolable at the high power levels of ESS, could be a very promising source of VCNs, as well as UCNs. This is discussed in Section 6.5.5.

### 6.5.1 Thin-slab external converter

The most straightforward implementation of a UCN source in the twister consists of adding a UCN converter to the current optimized design of the cold source. We added a 2-cm-thick slab of SD<sub>2</sub> at 5 K covering completely the NNBAR opening. The SD<sub>2</sub> volume is embedded in an Al case 2 mm thick, but there is no Al on the extraction side. In a real case, there would be a very thin window. A view of the MCNP model is shown in Figure 130.

The choice of the SD<sub>2</sub> thickness comes from evidence reported in literature [154, 155] on the effective production depth of extracted UCN. In particular, it was estimated that roughly 50% of the UCN produced in the last 2 cm of a 16-cm thick converter are extracted. This percentage drops to 30% between 2 and 4 cm in depth, while making increasingly more inefficient to keep the SD<sub>2</sub> at 5 K. In our concept, the volume of the converter is 1.8 liters. The UCN production rate density from the thin slab, calculated with the method highlighted in Section 6.4.1, was estimated to be  $3.07 \times 10^5$  n/s/cm<sup>3</sup>. The corresponding  $\dot{N}_{UCN}$  is then  $5.56 \times 10^8$  n/s. The estimated prompt heat-load on the converter (both SD<sub>2</sub> and Al vessel) is 760 W. The  $\beta$  and  $\gamma$  contribution from <sup>28</sup>Al and the surrounded activated material has been treated separately in Section 6.5.2.

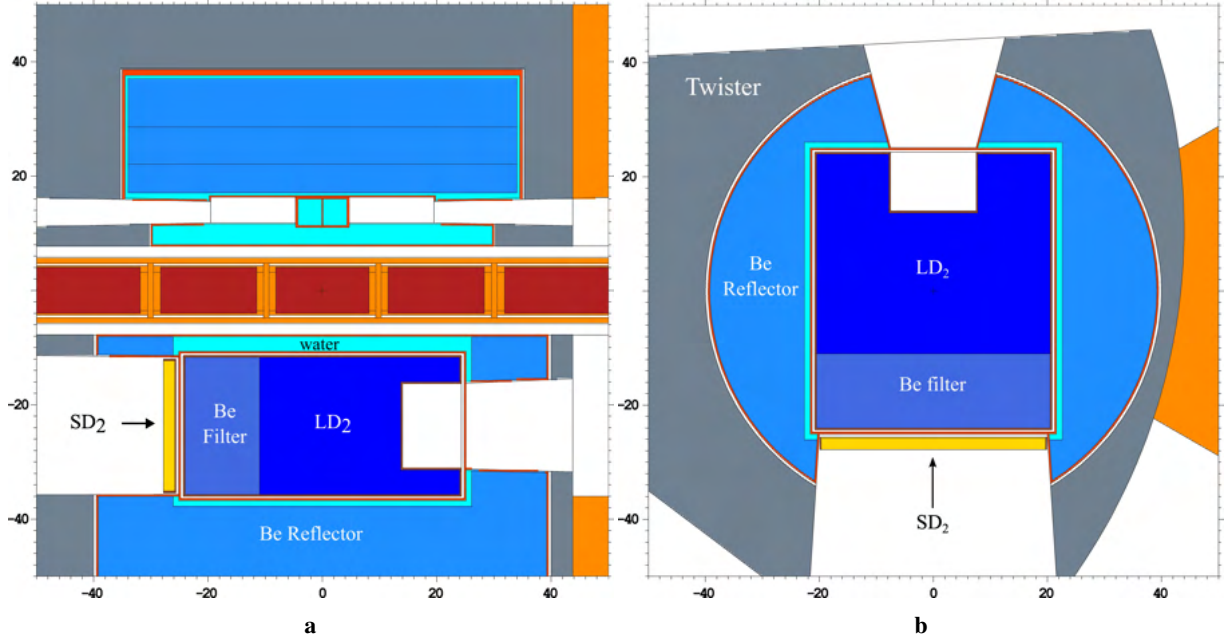


**Figure 130:** MCNP model of a 2-cm-thick SD<sub>2</sub> UCN source complementing the LD<sub>2</sub> baseline for UCN production. (a) vertical cut, perpendicular to the proton beam direction. (b) cut parallel to the target plane with the proton beam impinging from the left.

A first improvement to the design may come from the removal of the cold Be filter. As a matter of fact, the gains for  $\lambda > 4 \text{ \AA}$  produced by the filter come at the expense of neutrons in the range  $2 \text{ \AA}$  to  $4 \text{ \AA}$ , i.e., between 5 meV and 20 meV. While the increase at longer wavelengths is advantageous for NNBAR, whose FOM is proportional to  $\lambda^2$ , it is detrimental for a UCN converter, since neutrons in the range from  $2 \text{ \AA}$  to  $4 \text{ \AA}$  contribute significantly to the UCN production in SD<sub>2</sub> (cfr. Figure 127). Removing the filter to add more moderating LD<sub>2</sub> has the effect of increasing the UCN production rate density up to  $4.70 \times 10^5 \text{ n/s/cm}^3$  (a 53% gain) and the prompt heat-load to 1 kW, while decreasing the neutron yield on the neutron scattering instruments side by 5%. Adopting this solution at ESS would entail achieving a high-intensity UCN source by complementing the pre-existing design without having to design a new moderator. Such solution could be implemented after the NNBAR experiment. The drawbacks are a higher heat-load on the converter, the possible lack of space for cooling infrastructure and the lower performances on the dedicated WP7 opening in case of removal of the Be filter.

It is also of interest to study the performance of the thin-slab converter in the ideal case where the lower moderator would be optimized for UCN production, as opposed to the previous case, where a thin SD<sub>2</sub> layer was added to an existing design. Such a source would still emit CNs and VCNs, but would be optimized for UCNs. This case represents the *non plus ultra* for an in-pile UCN source based on SD<sub>2</sub> (at least when a thin-slab is used), and therefore is a term of comparison for the other cases. We assume the cold moderator to be completely filled with ortho-LD<sub>2</sub> at 22 K (with 2.5 wt% Al) and with only one fixed-dimensions opening  $24 \text{ cm} \times 40 \text{ cm}$ . The vertical dimension is also kept fixed to 24 cm, while we varied the other two (parallel and transverse to the proton beam axis). The center of the moderator-converter system along the transverse-to-proton-beam axis was also a variable for the Dakota optimization (more information on Dakota and the optimization algorithm in [18]). The optimization algorithm found the best  $P_{\text{UCN}}$  for a  $40 \text{ cm} \times 16 \text{ cm} \times 24 \text{ cm}$  cold moderator with the center shifted 4 cm away from the opening, placing the converter closer to the region of highest cold intensity. The MCNP model of the optimum is shown in Figure 131. The estimated  $P_{\text{UCN}}$  and  $\dot{N}_{\text{UCN}}$  are  $7.72 \times 10^5 \text{ n/s/cm}^3$  and  $1.35 \times 10^9 \text{ n/s}$ , respectively, for a total prompt heat-load of 2.91 kW. It should be noted that since the converter's volume does not vary much (it shrinks slightly to fit the divergent opening as it goes deeper), we can consider this case to be also optimal for the production rate  $\dot{N}_{\text{UCN}}$  since it differs from  $P_{\text{UCN}}$  only for a (constant) volume. After the optimization results we can conclude that an ideal thin-slab

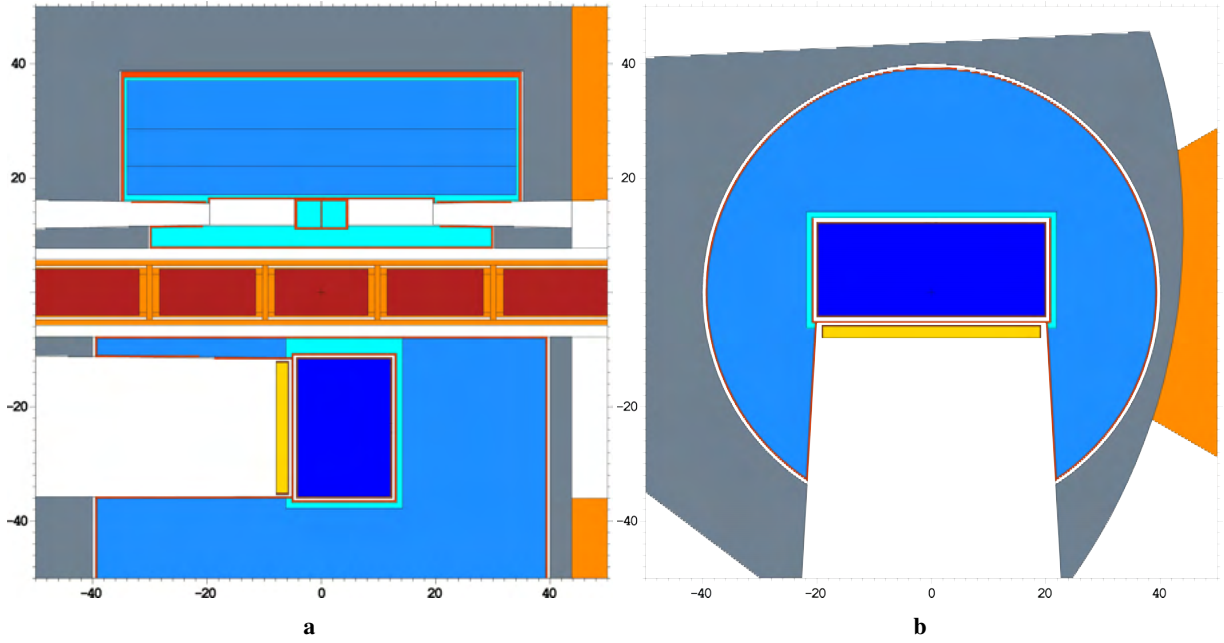
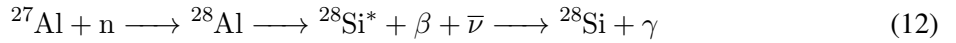


**Figure 131:** Fixed 2-cm SD<sub>2</sub> UCN source with optimized cold LD<sub>2</sub> moderator. (a) vertical cut, perpendicular to the proton beam direction. (b) cut parallel to the target plane with the neutron beam impinging from the left. The figure of merit for the optimization was the mean UCN production rate density inside the SD<sub>2</sub> converter.

SD<sub>2</sub>-based UCN source placed inside the twister does not need large volumes of cold moderator material as long as it is kept close to the hot spot of cold neutron production. Clearly, this higher production rate comes at the expense of a higher heat-load to remove from the converter.

### 6.5.2 Delayed heat deposition from activation

A correct estimation of the heat deposition on the UCN converter is essential for the *in-pile* solution, where the high radiation flux could make it challenging to keep the converter at 5 K. Additional heat-load, which is not taken into account by the F6 tally in MCNP (which only calculated prompt energy deposition), comes from the decay of activation products. Considering the use of Al in the moderator vessels, we expect the most important contributor to be <sup>28</sup>Al:



The half-life of <sup>28</sup>Al is 2.245 min, it decays to a metastable state of <sup>28</sup>Si with the emission of an electron (average energy 1.24 MeV), which in turn decays to stable <sup>28</sup>Si emitting a photon (one line at 1.79 MeV). In MCNP it is possible to estimate the saturation activity of <sup>28</sup>Al from the incident neutron flux using a tally multiplier (FM card). The FM card is used to apply a multiplicative response function from the MCNP6 cross-section libraries. In this case, we used the radiative capture library (n, γ), identified with the ENDF/B (MT) reaction number 102. One tally with the respective FM card was defined for each cell containing aluminum. The volume of the cell is normalized to 1 so that the value obtained is in Bq, instead of the default Bq/cm<sup>3</sup>. The next step is to calculate the energy deposition from the decay electron and γ. The particles are generated uniformly in the cell with intensity equal to the saturation activity. This step is repeated for each particle and for each aluminum cell. The electrons are generated with a continuum β-decay spectrum taken from [165]. The results for the model in Figure 130 obtained with this method are reported in Table 27. The short range of electrons in aluminum, compared to the thickness of the containers, means that the largest contribution to the decay heat-load in the SD<sub>2</sub> Al vessel comes from the β decay in the vessel itself, while the second largest contribution comes from the β decay in the Al vacuum jacket few millimeters away. In the SD<sub>2</sub> cell, the single most important source of decay heat is the β from the Al vessel, while, in total, γ and electrons have a similar impact on the heat-load. The heat deposition from the decay products can be compared with the deposition

**Table 27:** Delayed heat deposition from  $^{28}\text{Al}$  decay. The columns correspond to the source cells. For each cell, the scored heat-load in both the SD<sub>2</sub> and the Al vessel is reported. Two different tables are presented for  $\beta$  and  $\gamma$  particles.

Delayed electron heat-load [W]						
To\From	Flow channels	LD <sub>2</sub> vessel	REH vessel	Vacuum jacket	SD <sub>2</sub> vessel	Total
SD <sub>2</sub>	$6.51 \times 10^{-4}$	$1.95 \times 10^{-2}$	1.63	1.14	10.9	12.1
SD <sub>2</sub> vessel	$2.93 \times 10^{-3}$	$2.24 \times 10^{-1}$	7.33	22.7	47.6	70.5
Total	$3.59 \times 10^{-3}$	$2.44 \times 10^{-1}$	8.96	23.8	58.5	82.6
Delayed $\gamma$ heat-load [W]						
To\From	Flow channels	LD <sub>2</sub> vessel	REH vessel	Vacuum jacket	SD <sub>2</sub> vessel	Total
SD <sub>2</sub>	$5.38 \times 10^{-1}$	3.38	$6.12 \times 10^{-2}$	3.89	1.14	9.01
SD <sub>2</sub> vessel	1.00	6.62	$1.17 \times 10^{-1}$	8.17	3.36	19.3
Total	1.54	9.99	$1.78 \times 10^{-1}$	12.0	4.50	28.3

from the prompt radiation. The prompt heat-load estimated with the F6 tally is 483 W for the SD<sub>2</sub> cell and 275 W for the Al vessel. These estimations point out that the heat deposition from delayed decay products accounts for almost 30% of the heat in the Al vessel, hence it should not be overlooked. For SD<sub>2</sub>, this contribution, while not negligible, is relatively less significant (about 4% increase).

### 6.5.3 Reentrant hole design

In light of the results of the ideal case, we explored also a design that would possibly reconcile the needs of both a neutron scattering instruments opening delivering CN on one side and a UCN source on the other; such design could be adopted after the NNBAR experiment is completed. The two openings compete for the high CN intensity produced at the center of the large LD<sub>2</sub> moderator. For the first tentative design, we added a 2-cm-thick SD<sub>2</sub> converter at the bottom of a 15 cm  $\times$  15 cm  $\times$  15 cm reentrant hole on the NNBAR side. Hence, this converter has a smaller volume of 384 cm<sup>3</sup>. It is important for the UCN extraction that no Al layer is interposed between the converter and the channel. Hence the Al window (3 mm) separating in the previous models the vacuum jacket and extraction channel (also vacuum) is removed. The geometry is shown in Figure 132. The estimated  $P_{\text{UCN}}$  thus obtained is  $1.31 \times 10^6$  n/s/cm<sup>3</sup> with a total prompt heat-load of 0.56 kW. The smaller dimension of this converter is compensated by the high production rate density achieved thanks to the proximity to the LD<sub>2</sub> core. However, this corresponds to  $\dot{N}_{\text{UCN}} = 5.03 \times 10^8$  n/s which is lower than simply putting the converter outside the LD<sub>2</sub> vessel.

### 6.5.4 Cylindrical 3-opening design

We studied the possibility to have a UCN in-pile source together with an opening for NNBAR and one for standard scattering experiment. We deemed not possible to accommodate a third opening in the box geometry presented so far, so we switched the shape of the cold moderator to a cylinder with a 45 cm diameter and 24 cm height. The model is shown in Figure 133. The NNBAR opening is of the same size and in the same position as before, since it is constrained by the position of the large beamport at 2 m. As in the developing of the lower moderator it was found that the cylindrical emission surface in the NNBAR opening was detrimental to the performance, we cut the cylinder to obtain a

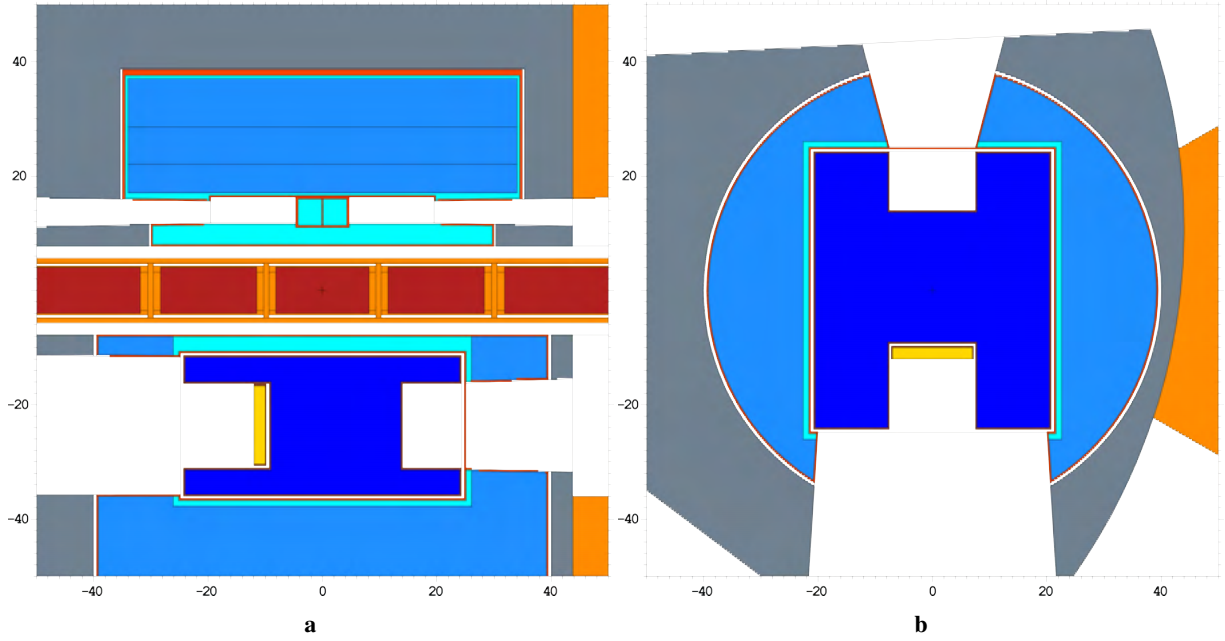


**Figure 132:** Fixed 2-cm SD<sub>2</sub> UCN source in a reentrant hole inside the LD<sub>2</sub> moderator, hence closer to the hot-spot of cold neutrons production. (a) vertical cut, perpendicular to the proton beam direction. (b) cut parallel to the target plane with the neutron beam impinging from the left. The figure of merit for the optimization was the UCN production rate density inside the SD<sub>2</sub> converter.

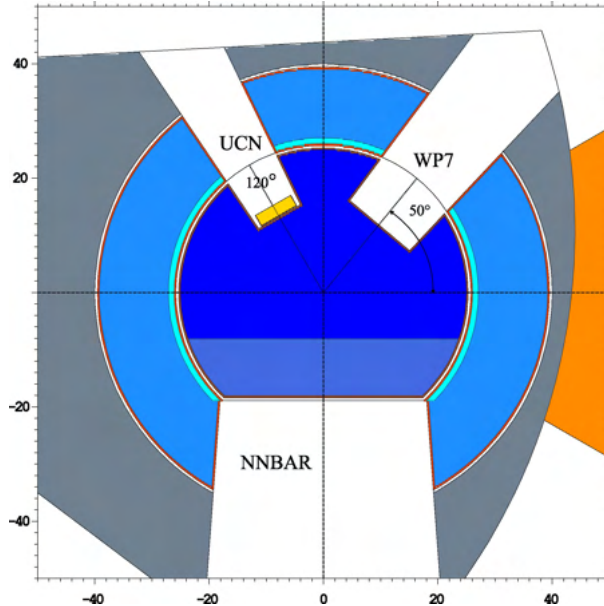


**Figure 133:** Cylindrical cold moderator (45 cm diameter) with three openings for NNBAR, UCN and neutron scattering experiments. The SD<sub>2</sub> converter has a fixed thickness of 2 cm. The cut is parallel to the target plane with the neutron beam impinging from the left.

flat rectangular emission surface. The cold Be filter is also present and it is 10 cm thick. The WP7 opening is a 15 cm × 15 cm square surface 10 cm deep in the moderator, placed at 50° with respect to the proton beam direction (as a comparison, the NNBAR opening is placed at 270° in this coordinate system). Finally, the UCN converter is placed in a 10 cm × 10 cm opening at 120°, also 10 cm deep in the moderator. It has again a fixed thickness of 2 cm for a total SD<sub>2</sub> volume of 128 cm<sup>3</sup>. At this exploratory stage, these dimensions are tentative, but it should be noted that we can apply the same principle of competition for the hot-spot described for the opposing openings. Hence, we opted for a symmetric configuration. The estimated  $P_{UCN}$  is  $1.74 \times 10^6$  n/s/cm<sup>3</sup> while the production rate is  $2.22 \times 10^8$  n/s.

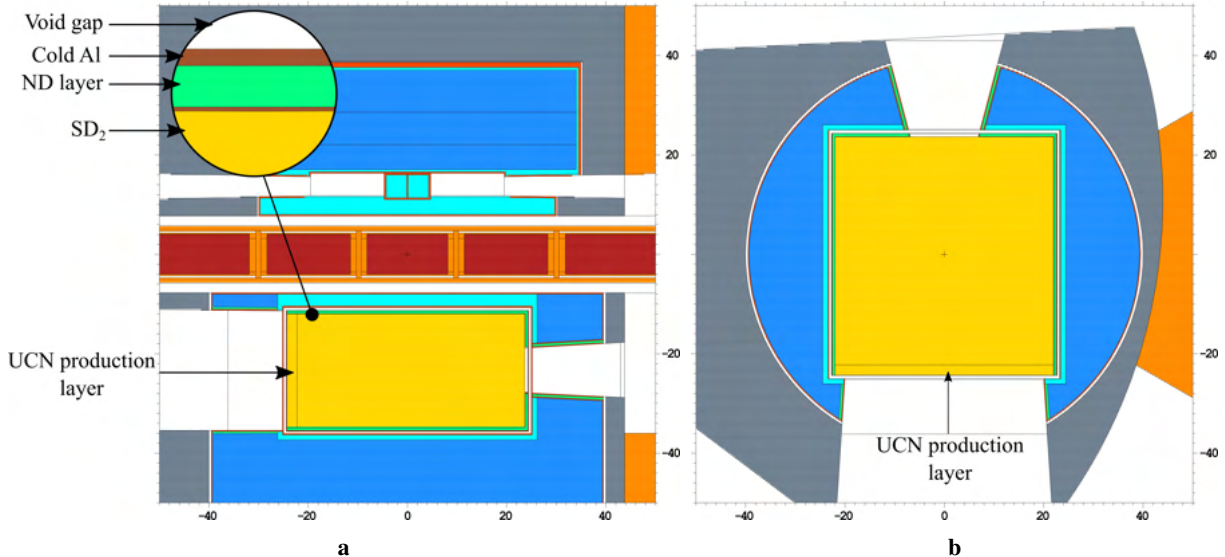


**Figure 134:** MCNP model of a 41 cm × 48 cm × 24 cm SD<sub>2</sub> moderator for VCN and UCN production. (a) vertical cut, perpendicular to the proton beam direction. The inset zooms on the 5-mm ND reflector layer and its aluminum case (b) cut parallel to the target plane with the neutron beam impinging from the left.

The prompt heat-load on this converter is 520 kW. The estimated FOMs for the NNBAR and WP7 openings are  $2.33 \times 10^{17} \text{ nÅ}^2/\text{s}/\text{sr}$  and  $2.84 \times 10^{15} \text{ n/s}/\text{sr}$ . These values should be compared with the ones reported in Table 3 for the original LD<sub>2</sub> baseline. We can see that the two original openings would lose 7% and 12% in this configuration. For a more fair comparison, one should consider the baseline model without the 3 mm Al window at the interface between the vacuum jacket and the opening, since this is not considered in this model. However, regardless of the absolute value of the loss, at this stage we are more interested in showing the concept and its feasibility.

It is clear that this is a limited study and a wider optimization effort, which takes into account all the parameters including the NNBAR and WP7 FOMs, could find one or more better compromises to accommodate the three applications.

### 6.5.5 SD<sub>2</sub> as primary moderator

The last in-twister design is based on the observation that the high-intensity SD<sub>2</sub>-based VCN source not only gave the highest VCN yield, but would also produce UCN, even though only the ones produced in the last few cm of the crystal can be extracted. The geometry is shown in Figure 134.

An extensive description of the model, the method and the results of the VCN performance of this multi-purpose source, which would be the first of its kind, is provided in Section 4.7. Here, we only report the relevant values concerning the UCN production. The total volume of SD<sub>2</sub> is 48.2 L, but only the last 2 L (corresponding to the last 2 cm on the NNBAR side) are considered for the UCN production. The  $P_{UCN}$  in this smaller volume is  $6.56 \times 10^5 \text{ n/s}/\text{cm}^3$ , which means a UCN production rate of  $1.32 \times 10^9 \text{ n/s}$ . Concerning the heatload, the main challenge of this design is to keep a large volume of ortho-D<sub>2</sub> in the solid state at 5 K. We estimated that the heat-load on the moderator would be approximately 40 kW at 5 MW operation, but this number is expected to increase once the decay heat-load from the surrounding aluminum is taken into account. Preliminary simulations of embedded foam-like aluminum and aluminum-beryllium alloy cooling structures have shown promising results in improving the moderator thermal conductivity. In conjunction with a standard liquid-helium cooling pipe, these foams should allow for a rate of heat extraction capable of keeping the solid deuterium well below its melting point, at least for the 2 MW scenario at ESS. In particular, the use of beryllium alloys or graphite in such cooling structures appears to be more favorable in both terms of cooling (due to reduced self-heating) and neutronics. Despite the obvious challenges, this idea opens the door to a completely new future for ESS, where VCN and UCN are produced with an intensity never seen before, allowing scientists to

**Table 28:** Summary table of the calculations for the in-twister options. The optimization was driven by maximising  $P_{UCN}$ , but since the volume is approximately constant, the same result would be obtained by choosing  $\dot{N}_{UCN}$  instead. The reported heat-load is only the prompt radiation heat-load.

	SD <sub>2</sub> Volume [L]	$P_{UCN}$ [n/s/cm <sup>3</sup> ]	$\dot{N}_{UCN}$ [n/s]	Heat-load [W]	WP7 FOM [n/s/sr]	NNBAR FOM [nÅ <sup>2</sup> /s/sr]
<b>Baseline + UCN</b>	1.81	$3.07 \times 10^5$	$5.56 \times 10^8$	760	$3.23 \times 10^{15}$	-
<b>No Be filter + UCN</b>	1.81	$4.70 \times 10^5$	$8.51 \times 10^8$	1000	$3.06 \times 10^{15}$	-
<b>Optimized UCN-only</b>	1.75	$7.72 \times 10^5$	$1.35 \times 10^9$	2910	-	-
<b>Reentrant Hole</b>	0.38	$1.31 \times 10^6$	$5.03 \times 10^8$	560	$2.81 \times 10^{15}$	-
<b>3-openings cylinder</b>	0.13	$1.74 \times 10^6$	$2.22 \times 10^8$	520	$2.84 \times 10^{15}$	$2.33 \times 10^{17}$
<b>Full SD<sub>2</sub> moderator</b>	48.2	$6.56 \times 10^5$	$1.32 \times 10^9$	39886	-	-

explore new instruments concept and, ultimately, generating new science. For further discussion on this design see Section 4.7.

Estimated values for each design in this section are listed in Table 28 for comparison.

## 6.6 In-Twister He-II UCN Source

Similar to the models discussed in Section 6.5, placing a UCN source within the twister has been investigated for cases having He-II as the UCN production material. This solution imposes the most difficulty in terms of heating, while also presenting considerable engineering constraints.

A preliminary model is shown in Figure 135, where the majority of the LD<sub>2</sub> volume is displaced by He-II at a temperature of 1.2 K. Although engineering such an insert to the baseline LD<sub>2</sub> model could be relatively straightforward, the heatload reported in this model in Table 29 is nearly 1 kW. Keeping in mind that for SD<sub>2</sub> a kW-scale heatload may be feasible when considering its optimal temperature range of roughly 4–10 K, whereas He-II is ideally kept below 1 K [157, 158] and heatloads exceeding 100 W are likely unfeasible. Despite this model being impractical, it should be observed that the total neutron production rate exceeds that of  $\dot{N}_{UCN}$  for the Full SD<sub>2</sub> model by roughly a factor of four (and with the Full SD<sub>2</sub> having roughly twice the volume). The two results for this model in Table 29 are for trials with and without a MgH<sub>2</sub> reflective layer enclosing the full moderator volume, with an improvement exceeding a factor of two for the trial with added MgH<sub>2</sub>.

A more realistic model is shown in Figure 136, where the moderator is extended downward with a small 64 cm<sup>3</sup> primary UCN production volume of He-II and an extraction line extending to a beamport adjacent the NNBAR opening. In this case, the single-crystalline bismuth shielding reduces photon heating while being relatively transparent to neutrons in the critical UCN production range for He-II near 9 Å (see Figure 128) [166]. Polycrystalline bismuth was also tested and is an effective gamma-shield, but shows a penalty in UCN production of roughly 4%. The best available thermal scattering kernel for single-crystalline bismuth was at a temperature of 77 K. For further studies a library at a temperature of 22 K would be necessary to match that of the LD<sub>2</sub> moderator; it is expected that this would increase the He-II UCN production by further reducing the bismuth cross-section near 9 Å. (See also: Section 6.9.1.)

From Table 29, one can see that the heatload drops by roughly two orders of magnitude, while the UCN production rate per cm<sup>3</sup> is only reduced by approximately 75%. This reduction can be attributed to the increased distance from the He-II volume to the target, with a small penalty due to the bismuth gamma shield.

A hybrid model is then shown in Figure 137, where a thin slab of SD<sub>2</sub> is added in the critical UCN production volume centered directly below the impact point of protons on target (the proton beam direc-

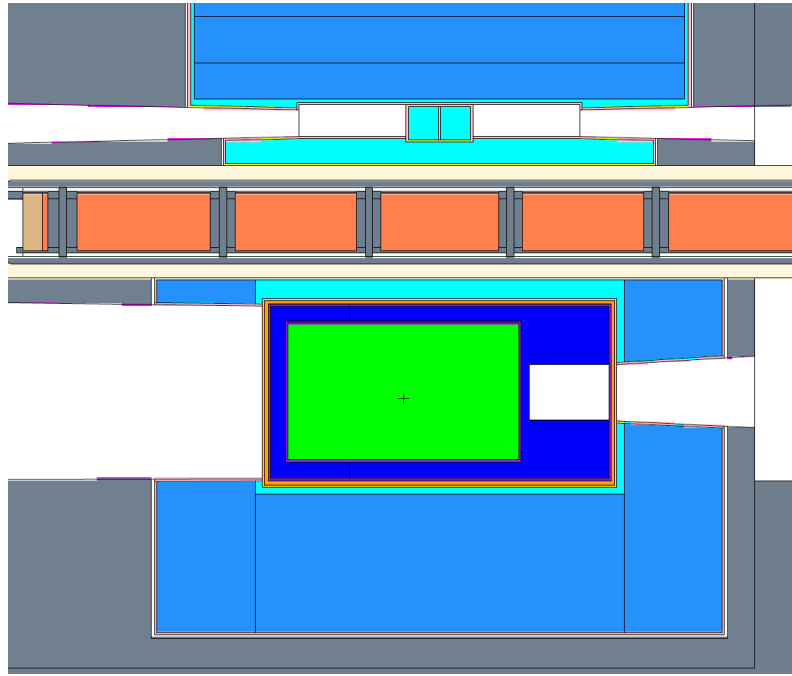


**Figure 135:** In-pile UCN source with He-II (light green) nearly fully displacing the LD<sub>2</sub> (dark blue) moderator volume.

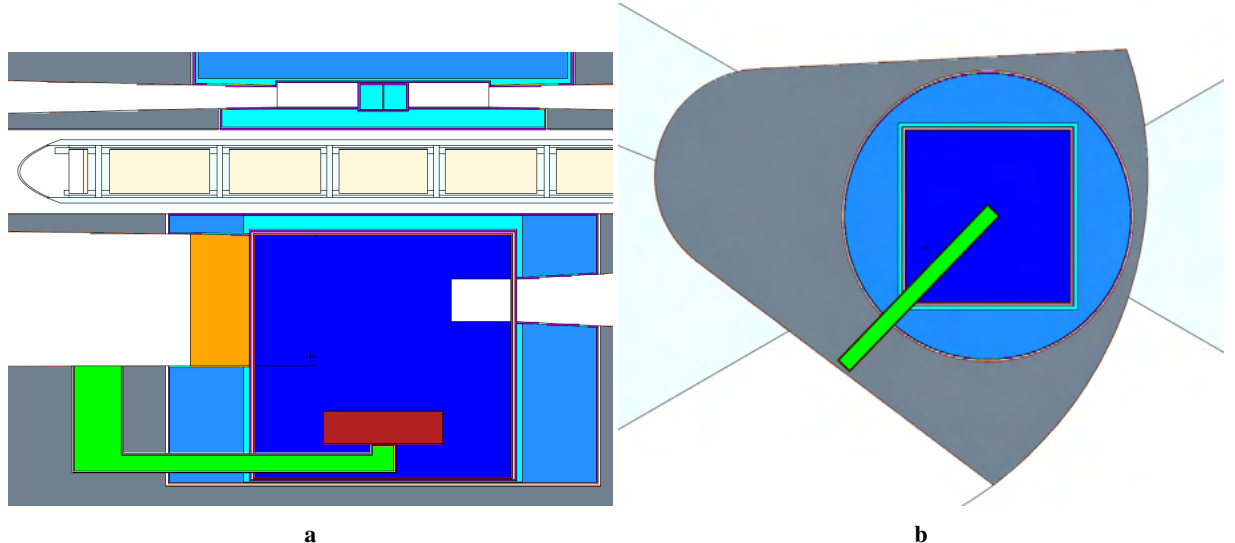


**Figure 136:** In-pile liquid helium UCN source (light green) with extraction channel; vertically extended LD<sub>2</sub> moderator (dark blue); and single-crystalline bismuth gamma shield (red). (a) Cross-section of the extraction channel. (b) Top-down view of the moderator and extraction channel within the twister.

tion goes out the page). For this case, the He-II and SD<sub>2</sub> volumes contribute roughly equal amounts to the total UCN yield in neutrons per second, with the SD<sub>2</sub> being better suited for absorbing the higher heatload and producing orders of magnitude more neutrons per cm<sup>3</sup>, and the longer lifetime of UCNs in He-II allowing for a larger volume.

## 6.7 SD<sub>2</sub> in MCB

The possibility of placing the UCN SD<sub>2</sub> converter into a moderator cooling block was studied. The MCB is a piece made of steel located in the target vessel with the sole purpose of shielding (see Section 3.2 in [148]). A part of the MCB that surrounds the twister and the LD<sub>2</sub> moderator (see Figure 138a) can be potentially modified to fit the UCN converter inside [148]. In this section, we describe the analysis of a

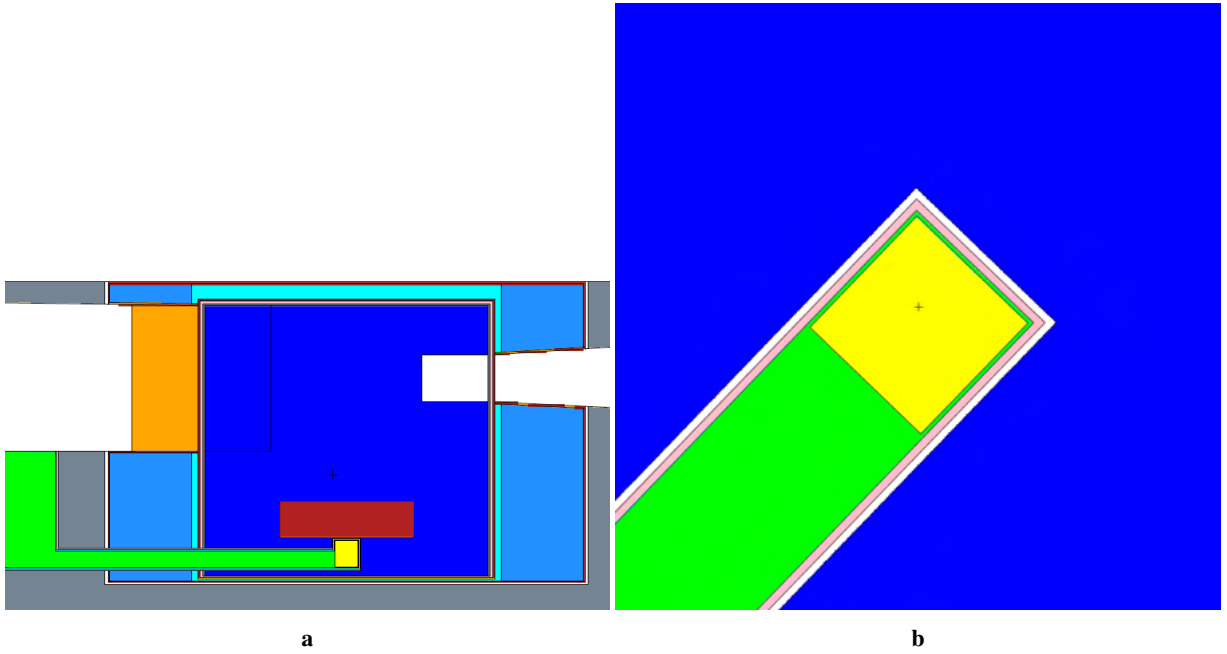


**Figure 137:** In-pile liquid helium UCN source and extraction channel (light green) with added thin-slab SD<sub>2</sub> UCN source (yellow); a vertically extended LD<sub>2</sub> moderator (dark blue); and single-crystalline bismuth gamma shield (red). (a) Cross-section of the hybrid source and extraction channel. (b) Top-down view of the primary UCN production volume.

**Table 29:** Calculations for liquid helium UCN sources placed in-pile. The reported heat-load is only the prompt radiation heat-load.

	He-II/SD <sub>2</sub> Volume [L]	$P_{UCN}$ [n/s/cm <sup>3</sup> ]	$\dot{N}_{UCN}$ [n/s]	Heat-load [W]
<b>Full He-II Moderator + MgH<sub>2</sub> (Figure 135)</b>	21.9	$2.58 \times 10^5$	$5.56 \times 10^9$	9933
<b>Full He-II Moderator + No MgH<sub>2</sub></b>	21.9	$1.23 \times 10^5$	$2.69 \times 10^9$	9915
<b>Small He-II w/extraction (Figure 136)</b>	1.25	$6.3 \times 10^4$	$7.8 \times 10^7$	113
<b>Small He-II + SD<sub>2</sub> slab w/extraction (Figure 137)</b>				
SD <sub>2</sub> slab only	0.06	$1.22 \times 10^6$	$7.7 \times 10^7$	10
He-II extraction line only	1.19	$5.14 \times 10^4$	$6.1 \times 10^7$	99
<b>Total</b>	1.25	–	$1.34 \times 10^8$	109

SD<sub>2</sub> converter, while a He-II converter in the MCB is described in Section 6.8. The basic concept is to place the SD<sub>2</sub> UCN converter into MCB near the cold source (see position 2 of Figure 4 in [148]), which would make use of cold neutrons streaming from the LD<sub>2</sub> moderator to produce UCNs. However, as it is clear from Figure 138b, in the current baseline model few cold neutrons can reach the MCB location, leading to small  $P_{UCN}$ . The solution consists in upgrading the baseline model and, in particular, the Be reflector and steel surrounding the LD<sub>2</sub> moderator, by designing a channel connecting the LD<sub>2</sub> moderator and the MCB.

The initial model that was studied comprised of a cylindrical channel to transport cold neutrons from the surface of the LD<sub>2</sub> moderator to MCB and spherical UCN converter in which  $P_{UCN}$  was calculated (see Figure 139). In this case, the UCN converter was defined as a void cell in the geometry definition in MCNP, so the calculated  $P_{UCN}$  was underestimated since the effect of scattering of cold neutrons

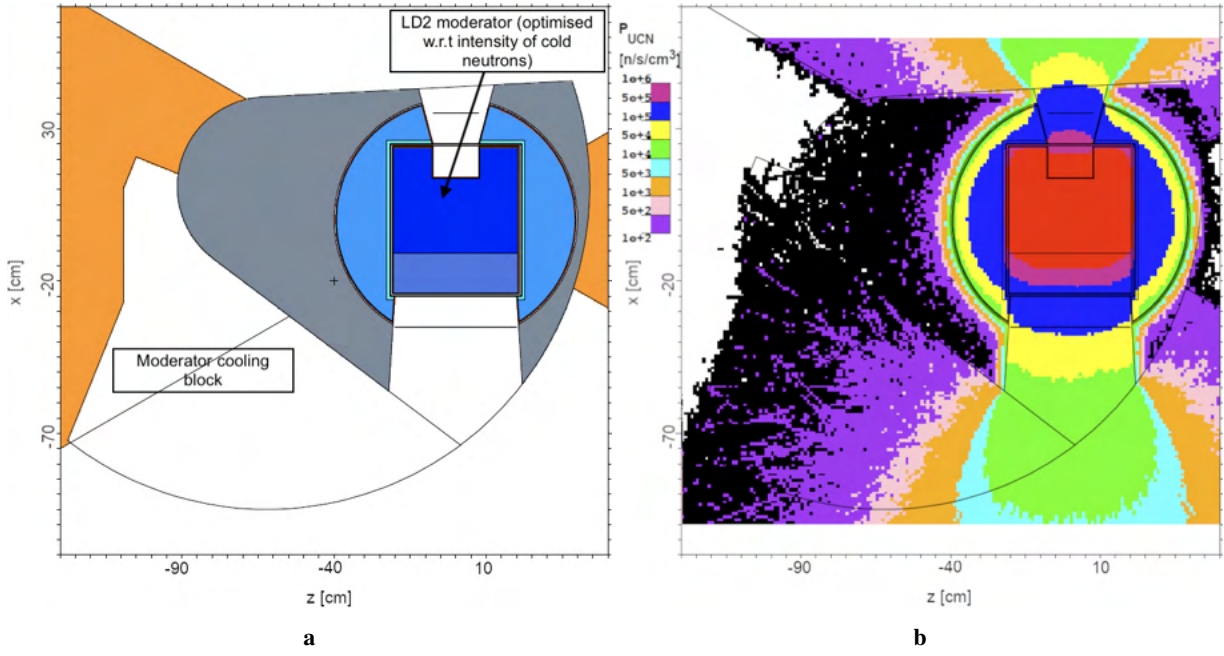


**Figure 138:** (a) The baseline geometry for LD<sub>2</sub> cold neutron moderator and MCB. (b) Map of  $P_{UCN}$ .

within the SD<sub>2</sub> material was not taken into account. However, comparing relative values of  $P_{UCN}$  that were calculated for each set of parameters in the model were sufficient for this initial study. Both the cylindrical channel and the UCN converter were aligned with the center of LD<sub>2</sub> moderator on the plane perpendicular to the y axis.

Subsequently, the model was parametrized such that the horizontal position of the channel's opening at the LD<sub>2</sub> moderator surface X', the channel radius R and the SD<sub>2</sub> spherical converter position in x and z could be varied. First, a general parametric study was performed. Namely, the position of SD<sub>2</sub> converter was varied at a fixed radius of the channel ( $R = 6, 8, \text{ and } 10 \text{ cm}$ ) and a fixed alignment of the opening of the channel with the surface of box-shaped LD<sub>2</sub> moderator. The alignment was either with the LD<sub>2</sub> moderator centre or Be filter. The parametric study revealed that a larger radius of channel gave rise to higher  $P_{UCN}$ , but at the cost of a drop in the NNBAR FOM.

Moreover,  $P_{UCN}$  was at a maximum at a given channel radius when the length of the channel was minimized. Therefore, the channel opening aligned with the Be filter, together with the UCN converter placed in MCB with a slight offset in x and z w.r.t X' to minimize the length of the channel, resulted in the highest observed  $P_{UCN}$ .

This finding was also independently confirmed by the Efficient Global Optimization algorithm that searched for maximal  $P_{UCN}$  by varying all the parameters: x, z, X' and R. Although the Be filter suppressed the spectrum of neutrons below 4 Å, the models with channel opening aligned with the Be filter still performed the best w.r.t  $P_{UCN}$ .

Simultaneously, the drop in NNBAR FOM was minimal. This was an unexpected result since cold neutrons with a wavelength between 2 and 4 Å contributes to  $P_{UCN}$  partially, but the gain from designing a shorter channel overcame this effect. These results together with high  $P_{UCN}$  observed around the NNBAR emission surface (see Figure 138b) motivated a further study of SD<sub>2</sub> converter located in MCB, but with a direct view on the NNBAR emission surface.

We set a maximal tolerance on the drop in NNBAR FOM to be 5% for any model of UCN converter in the MCB. Since the NNBAR FOM of the baseline model without UCN converter and the channel was  $2.53 \times 10^{17}$ , the model with the radius of the channel of 6 cm aligned to the Be filter was selected as a reference model for the scenario of designing a cylindrical channel between the LD<sub>2</sub> moderator and UCN converter. The NNBAR FOM measured for this model was  $2.41 \times 10^{17}$ , so it did not exceed the tolerance level, and it provided the highest observed  $P_{UCN}$  among the models with the drop in NNBAR FOM below 5%. The shape of the UCN converter was redesigned to reflect that UCNs from very thin

layer SD<sub>2</sub> can be extracted only. This resulted in a disc-shaped UCN converter with 2 cm thickness. Filling this UCN converter by SD<sub>2</sub> increased the measured  $P_{UCN}$  to  $1.1 \times 10^4$ .

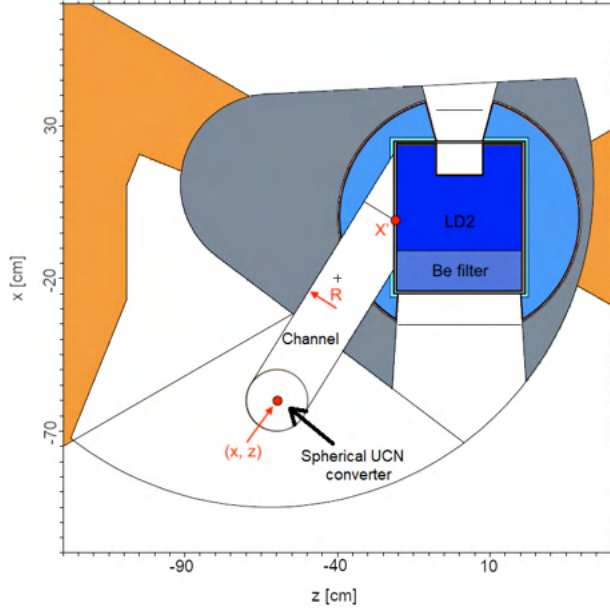


**Figure 139:** Parameterised model of the channel and UCN converter.

Subsequently, the idea of a direct view from the SD<sub>2</sub> converter in the MCB on the NNBAR emission surface was studied. Such design could be modelled by placing the converter further down in MCB with respect to the  $x$  axis, and defining a plane in the twister below which was all material removed. Consequently, cold neutrons emitted from the NNBAR emission surface could reach the SD<sub>2</sub> converter in the MCB without obstacles. Ultimately, a model with horizontal plane in the twister to allow a direct view of the SD<sub>2</sub> converter on the NNBAR surface was studied (see Figure 140a). It was expected based on Figure 140b that the SD<sub>2</sub> converter in MCB could reach the performance of  $P_{UCN}$  of the order of  $10^4 \text{ cm}^{-3}\text{s}^{-1}$ . Subsequently, the model of the SD<sub>2</sub> converter was designed and placed into region with the highest expected  $P_{UCN}$  in MCB (see Figure 141a). The goal was to place the SD<sub>2</sub> UCN converter into the region with  $P_{UCN}$  of the order of  $10^4 \text{ cm}^{-3}\text{s}^{-1}$ , i. e. within the green shaded region. The resulting geometry of a thick box-shaped SD<sub>2</sub> UCN converter with a thickness of 13.4 cm can be seen on Figure 141b. This scenario implies a horizontal extraction of UCNs. The Al container was designed around the SD<sub>2</sub> UCN converter with a wall thickness of 3 mm that was reduced to 0.5 mm on the emission surface of the converter.  $P_{UCN}$  calculated for this converter was  $4.5 \times 10^4 \text{ cm}^{-3}\text{s}^{-1}$ . The initial thick box-shaped SD<sub>2</sub> UCN converter was redesigned since previous experiments [154] showed that it is much easier to extract UCNs from a thin slab of SD<sub>2</sub> converter. This constraint together with the fact that  $P_{UCN}$  of the order of  $10^4 \text{ cm}^{-3}\text{s}^{-1}$  could be reached close to the border between MCB and twister, i. e. at the shortest possible distance to the NNBAR emission surface, favoured a following design of the SD<sub>2</sub> converter (see Figure 142a).  $P_{UCN}$  measured for this thin box-shaped SD<sub>2</sub> UCN converter was  $3.8 \times 10^4 \text{ cm}^{-3}\text{s}^{-1}$ .

Estimating the heat-load on the SD<sub>2</sub> converter and surrounding Al vessel was also an integral part of our study. The prompt heat-load for the thick box-shaped SD<sub>2</sub> UCN converter was 440 W, where the heat deposited by neutrons was 220 W, and the heat deposited by photons was 200 W. However, this estimation did not take into account a contribution due to the neutron activation of isotope <sup>27</sup>Al with subsequent beta decay of <sup>28</sup>Al where both a beta and gamma particle was emitted. The decay heat for the thick UCN SD<sub>2</sub> converter was 18 W. Similarly, the prompt heat-load for a thin box-shaped SD<sub>2</sub> UCN converter was 150 W, where the heat deposited by neutrons was 60 W, and the heat deposited by photons was 80 W. The decay heat of <sup>28</sup>Al was 9 W.

All the calculated variations of  $P_{UCN}$  over a grid in the  $xz$  plane were done within the center of LD<sub>2</sub> moderator lying at  $y = -23.7$  cm in our model. Therefore, it was also important to explore the  $P_{UCN}$  variation in the  $yz$  plane over the NNBAR emission surface (see Figure 142b). It is apparent that

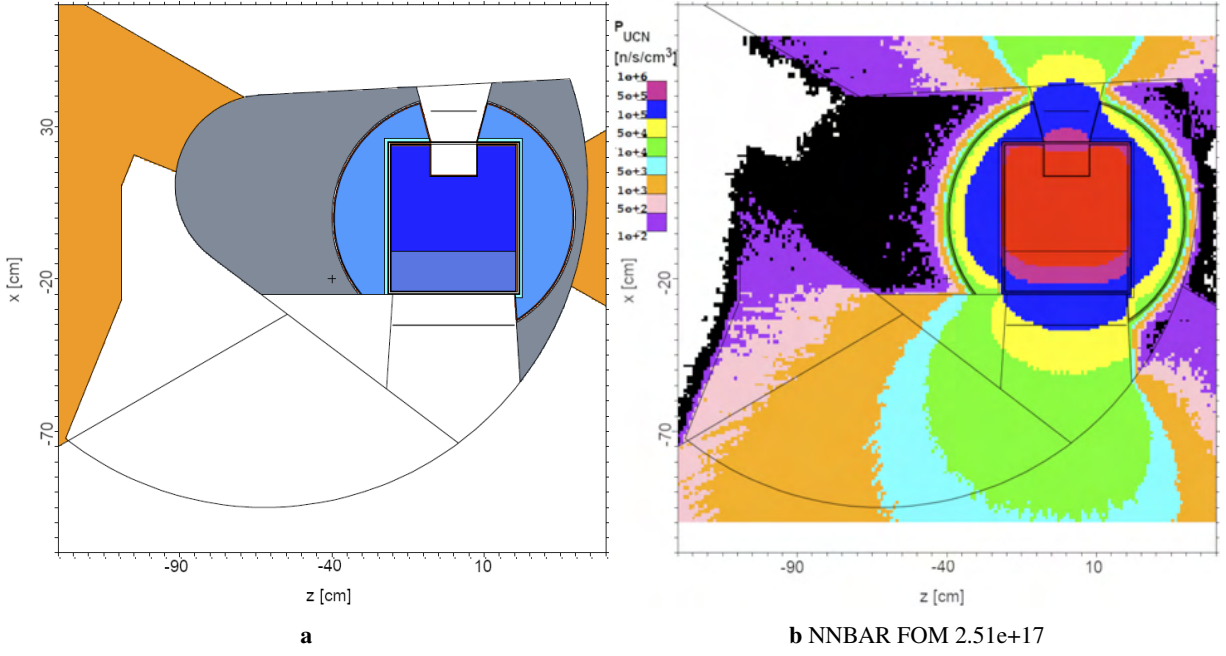


**Figure 140:** A model with material removed in twister below a horizontal plane to allow for a direct view between the SD<sub>2</sub> converter in MCB and NNBAR emission surface (a) Drawing of the model. (b) Map of  $P_{UCN}$ .

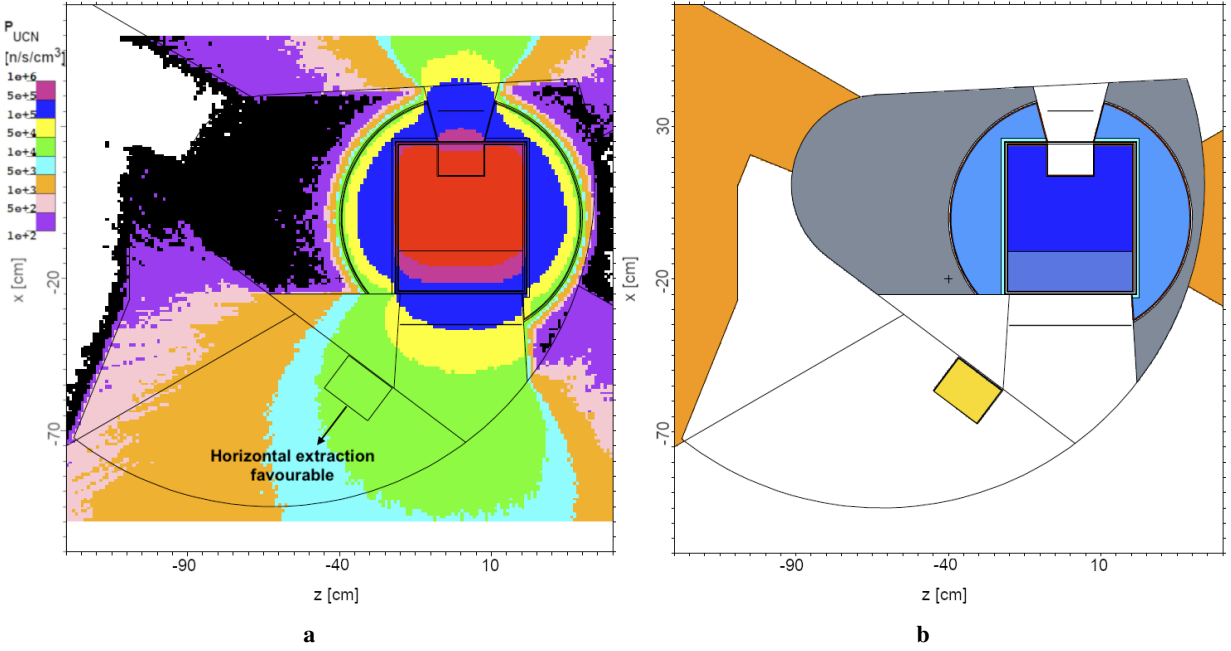


**Figure 141:** (a) The thick SD<sub>2</sub> converter placed within the region with  $P_{UCN}$  of the order of  $10^4 s$  in MCB. (b) The thick SD<sub>2</sub> UCN converter in MCB for which  $P_{UCN}$  and heat-load was estimated.

a slightly higher  $P_{UCN}$  could be reached by placing the SD<sub>2</sub> UCN converter slightly up in  $y$  closer to the water premoderator, where the converter would benefit from neutrons with wavelengths closer to the thermal region. Finally, a preliminary study of the effect of bismuth on reducing the heat-load of photons on the SD<sub>2</sub> UCN converter was performed. For this purpose, a shielding block made of bismuth was inserted into the twister (see Figure 143a). The flux of photons was significantly reduced in the MCB by the effect of the bismuth shielding (see Figure 143b). However, this was at a cost of significant reduction of  $P_{UCN}$  within the SD<sub>2</sub> converter. The reason is that the cold spectrum was strongly suppressed by the bismuth shielding (see Figures 144a and 144b). In fact, bismuth has a Bragg cutoff wavelength larger at 6.6 Å. Therefore, it is probably not interesting for a SD<sub>2</sub> source, which needs these suppressed neutrons.

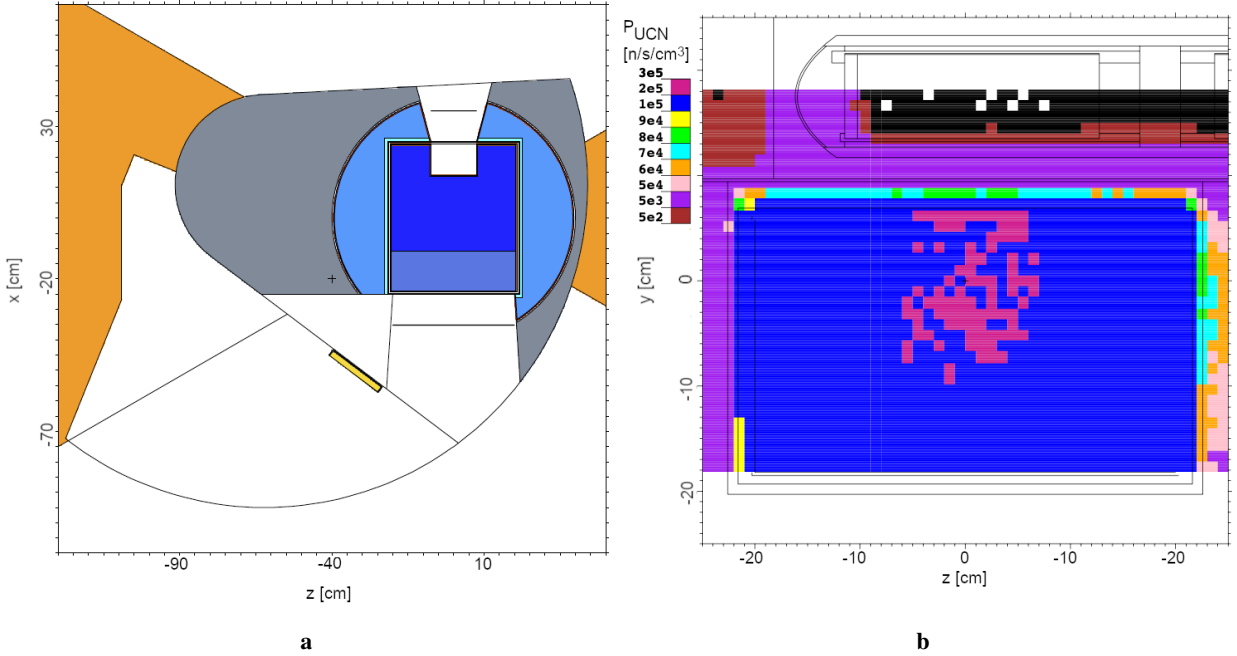


**Figure 142:** (a) Thin box-shaped  $\text{SD}_2$  UCN converter placed in MCB. (b)  $P_{\text{UCN}}$  map in the  $yz$  plane measured at the NNBAR emission surface.

For He-II on the other hand, for which  $8.9 \text{ \AA}$  are most effective for UCN production, the Bi filter is very interesting, as discussed in [145].

## 6.8 He-II in MCB

The option of a UCN moderator placed in the moderator cooling block based on helium in phase-state II (He-II) is investigated in this section. This option is very promising if CN, VCN and UCN sources are intended to be installed and operated in parallel. Therefore, preliminary engineering studies have been performed for this option. The following engineering study is unconstrained by the final decision for an implementation concept in this location.

A three stage coaxial shell moderator concept and a channel option to lead cold neutrons from the  $\text{LD}_2$  moderator to the UCN source has been studied in an attempt to increase the UCN production rate [161]. In the channel case (Figure 139) the result was a loss in the UCN production rate for every channel diameter, reflector material and wall size. Removing parts of the twister as depicted in Figure 145 leads to a gain in the UCN production rate and is therefore the preferred option.

A coaxial-moderator shell design has been evaluated in a parametric study. The baseline model is shown in Figure 145 and consists of an aluminum T6061-T6 vessel with a constant wall size of 3 mm filled with He-II at 1 K. The volume of the He-II content is about 24 L. The shell model consists of two different premoderators encapsulating the He-II vessel. The first premoderator, with thickness  $a$ , is a  $\text{H}_2\text{O}$  layer at room temperature and is supposed to thermalize fast neutrons. Inside there is an additional layer with thickness  $b$  of parahydrogen at 20 K, to moderate thermal neutrons into a cold neutron regime ( $9.8 \text{ \AA}$ ) in which the probability of direct conversion in He-II to the desired UCNs is highly increased (see also diagram Figure 128).

The moderator media are encased by 3 mm Al T6061-T6 spaced with a 5 mm vacuum gap between the vessels as depicted in Figure 145. The variation in the media thicknesses varies between  $a$ : 15 mm to 35 mm for the thermal and  $b$ : 5 mm to 25 mm for the cold moderator.

It can be observed that the maximum gain of  $\approx 2\%$  is reached for a case of thick thermal and thin cold moderator layers. The result is that the shell concept is not highly performing compared to the baseline model, but can be followed up in further simulations with different geometries and moderator media even

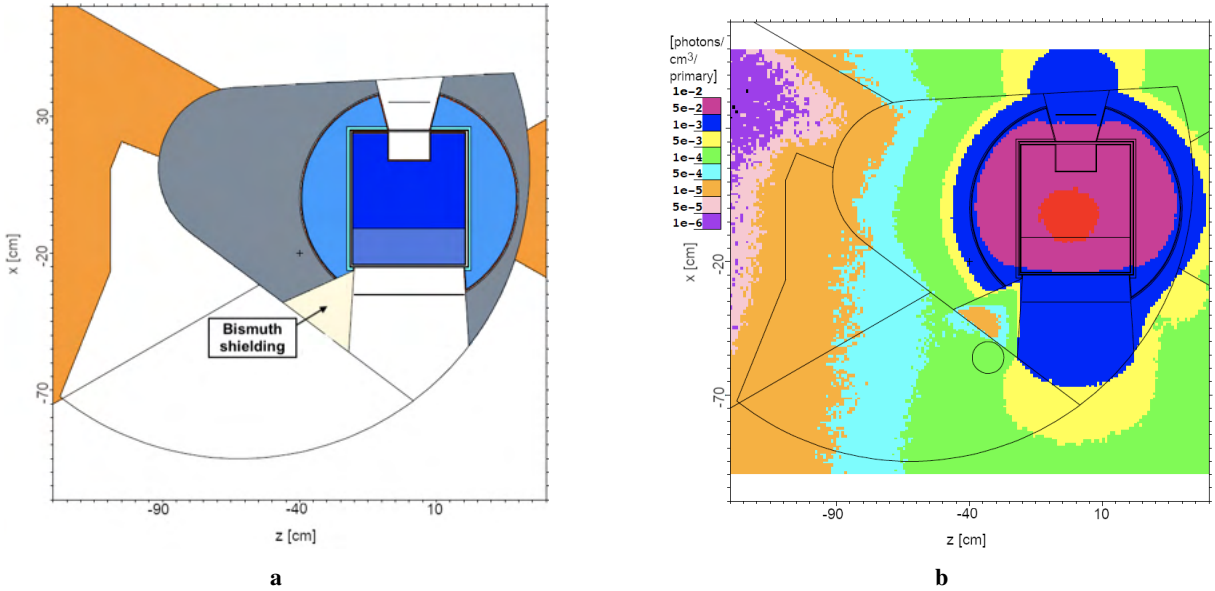


**Figure 143:** (a) Inserting the bismuth shielding into the twister in order to suppress photons before they reach MCB. (b) bismuth shielding in the twister reduced the flux of photons in MCB significantly.

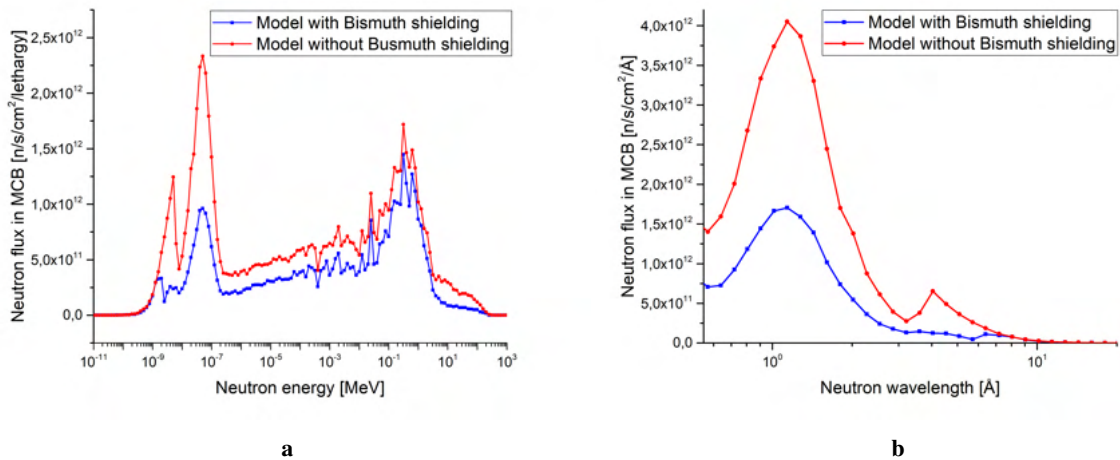


**Figure 144:** (a) The neutron spectrum in MCB. The red line depicts the spectrum without bismuth shielding in the twister, and the blue line depicts the spectrum with bismuth shielding in the twister. (b) The flux of cold and thermal neutrons with wavelengths  $> 1 \text{ \AA}$  was clearly suppressed in MCB by the bismuth shielding.

if an outstanding gain in performance is unlikely. Therefore, the baseline model is the option that will be considered in the further engineering process.

Table 30 shows the expected heat loads on the aluminum structure and on the He-II filling, separated for neutron and gamma radiation. It can be observed that the highest heat load is caused by gamma radiation absorbed in the aluminum structure.

The neutron absorption cross section in most materials increases in general towards lower neutron energies. Therefore, the gain in UCN conversion by He-II is overcome by the loss due to absorption of the premoderated neutrons in aluminum structures needed to add moderation stages; simultaneously the heat load in the system is increased. In Figure 128 it is visible, that for lower neutron wavelength then the narrow 8.9 Å band of high interaction probability with He-II, the interaction probability is significantly lower but still present. In this regime the energy transfer from the neutron to the He-II is mediated in several steps by phonon interactions. Due to He-II's extremely low absorption cross section, higher-energy neutrons are either converted to UCNs as desired or pass through He-II without interaction. The conclusion for the further engineering process is that the He-II vessel of the UCN source should be

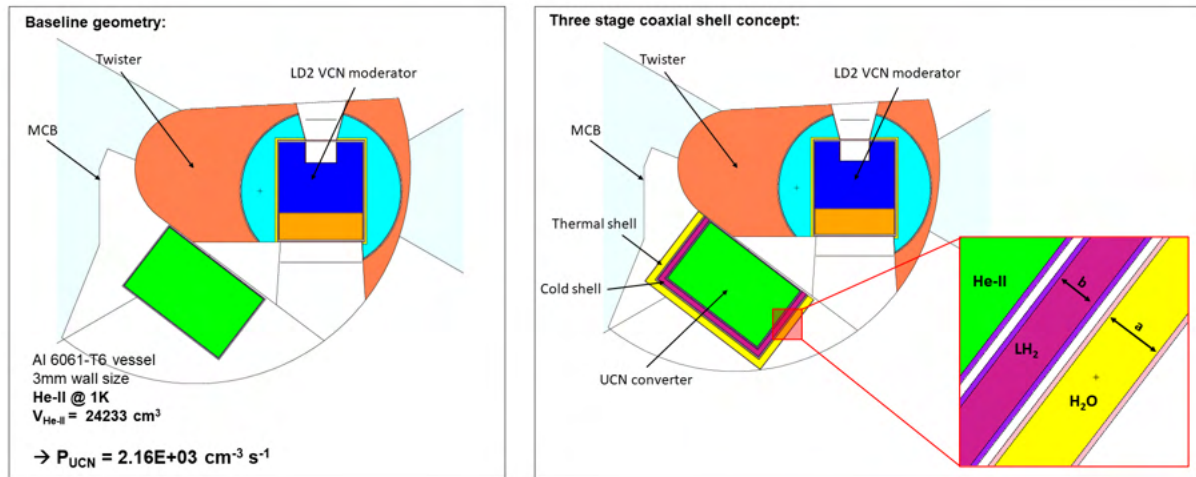


**Figure 145:** MCNP simulation of coaxial-moderator shell design. Horizontal cut through the MCNP simulated geometry. Left: baseline geometry with He-II filled vessel. Right: Coaxial-moderator shell geometry. The moderator shell thickness  $a$  &  $b$  has been varied in a parameter study.

	Al	He-II	$\Sigma$
$\gamma$	173 W	84 W	256 W
n	11 W	61 W	71 W
328 W			

**Table 30:** Heat load on the He-II vessel separated by material and type of radiation.

designed under the premise to minimize the aluminum content to the needed for fulfilling the demands on structural integrity of the nuclear code for pressure vessels while maximizing the encased He-II volume, without additional moderation devices. If in the following engineering process the heat load is above a critical level that can not be handled by available He cryostates, additional gamma filter shells can be considered, which will most likely imply some loss of the UCN performance of the source.

It can also be considered to manufacture the vessel from beryllium or from a beryllium/aluminum alloy which would considerably reduce the heat load on the vessel. These materials are currently not qualified by the RCC-MRx nuclear code for pressure vessels although the material parameters are promising. Therefore an accreditation for the use of these materials can be taken into account.

The mounting position in the moderator cooling block offers the possibility to integrate the UCN source in the existing ESS infrastructure by replacing and rebuilding a minimum of existing components. The moderator cooling block consists of staked and actively cooled stainless steel shielding blocks which can be partially replaced or overworked. Another benefit of the location is the already existing supply infrastructure with cooling water and cold gaseous as well as liquefied He.

In conclusion, the MCB location has, besides a high UCN production rate, different advantages. The UCN source can be implemented by changing and overworking a small number of existing components while most of the existing ESS structure can be left untouched. Furthermore, the location offers existing supply infrastructure with cooling water and helium on different temperature levels.

### 6.8.1 Recommended further engineering investigations

- Engineering on UCN source concept:
  - Guiding of UCN and interfacing to experiments
  - Inner wall coating ( $^{58}\text{Ni}$ )
  - Purification of He-II

**Table 31:** Performance of baseline geometry of He-II UCN source in the LBP.

	He-II Volume [L]	$P_{UCN}$ [n/s/cm <sup>3</sup> ]	$\dot{N}_{UCN}$ [n/s]	Heat-load [W]
<b>He-II in LBP (Baseline)</b>	57.6	368.5	$2.1 \times 10^7$	8.2

- Experimental investigations on He-II regarding:
  - Phase stability
  - Heat conductivity
  - Experimental simulation of ESS conditions based on MCNP simulation results (expected heat load, pulse structure)
- Limits for cross section area for heat transport through He-II

## 6.9 He-II in LBP

Another option for creating a UCNs source at ESS is based on He-II placed at the LBP, which is described extensively in Section 3.4 of [148]. A He-II based UCN source can benefit from the extended lifetime of the UCNs within the neutron absorption-free medium, allowing for storage and therefore, high density of UCNs. Additionally, this location can result in lower heat loads compared to the other options discussed so far. While the LBP is initially intended for use by the NNBAR experiment, it could potentially be repurposed for UCN production at a later stage.

Two different concepts of UCN source that could use the LBP location were identified. In the first option, which is studied in this section, the LBP can host a He-II converter for UCN production (represented as number 4 in Figure 126), placed inside the monolith, with the tip of the source at a distance above approximately 2 m from the center of the lower moderator. As it is described in Section 6.2, we still consider this option as “in-pile”, even though it is a larger distance from the primary source compared to the options in the twister or in the MCB, discussed in the previous sections. This classification is justified by the fact that at that location, a He-II converter will receive a neutron spectrum with a large component of fast neutrons, unlike a pure in-beam converter which will receive mainly cold neutrons and a smaller fraction of background neutrons. In the second option (location 5 in Figure 126, considered as “in-beam”, we still use the LBP, but the source is placed further away, outside the neutron bunker. This option is described in Section 6.10.

For the in-pile option under study in this section, we followed the proposal by Serebrov and Lyamkin [145], consisting of a 58-liter vessel (60 cm × 30 cm × 32 cm) filled with He-II, surrounded by a reflector made of LD<sub>2</sub> and bismuth shielding. The geometry is depicted in Figure 146, and it will be referred to as the baseline geometry henceforth.

Table 31 presents a summary of the UCN production for the baseline geometry [148]. For this study, the He-II thermal scattering library mentioned at Section 6.4.2 is used in MCNP. By implementing the scattering function from ESS model 1, Figure 128 into Equation (11), the UCN production rate density is calculated as 368.5 n/s/cm<sup>3</sup>. The total prompt heat-load only on the He-II converter at the specified source location is 8.2 W. To further enhance this design, it is essential to understand how each component of the UCN source impacts UCN production and heat load.

The main objectives are twofold: first, to maximize the neutron flux within the energy range of 1-10 meV within the He-II converter. Second, to effectively manage the total heat load on the He-II converter. This heat load encompasses contributions from both neutrons and photons on the He-II converter as well as the aluminum shell surrounding the He-II. Additionally, there is a decay heat load resulting from aluminum beta activation, which accounts for about 24 % of the total heat load originating from neutrons and photons [168]. Throughout the optimization process, we maintained the He-II volume constant at the preliminary design value of 57.6 L for comparability. Subsequently, we investigated the impact of each component on the performance of the UCN source.

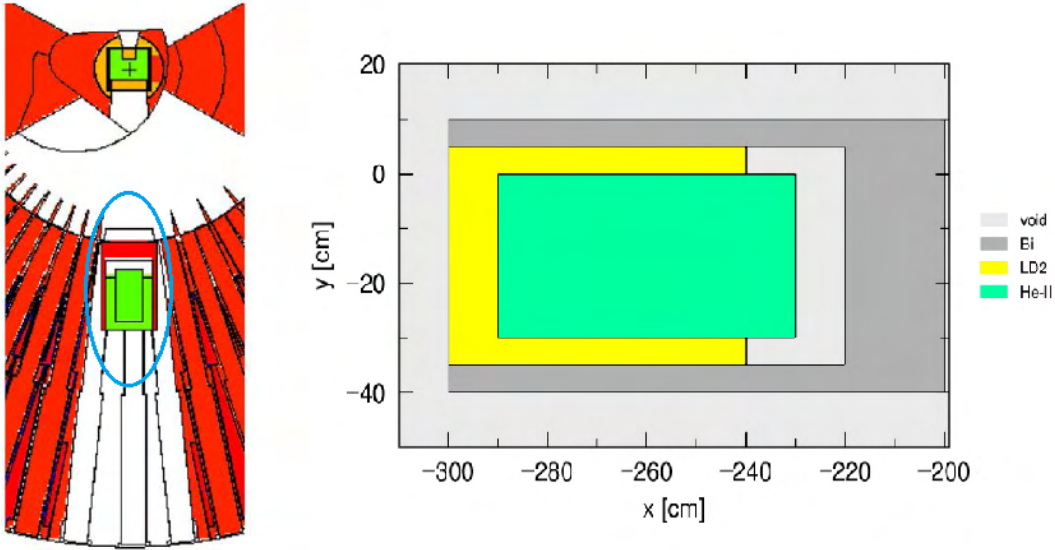


**Figure 146:** *Left:* MCNP geometry showing the He-II source backed by a LD<sub>2</sub> reflector in the large beamport, concept of Serebrov and Lyamkin [145]. *Right:* The geometry and the materials used in the UCN source located at LBP plotted by PHITS 3.27 [167].

### 6.9.1 Bismuth Filter for Gamma Shielding

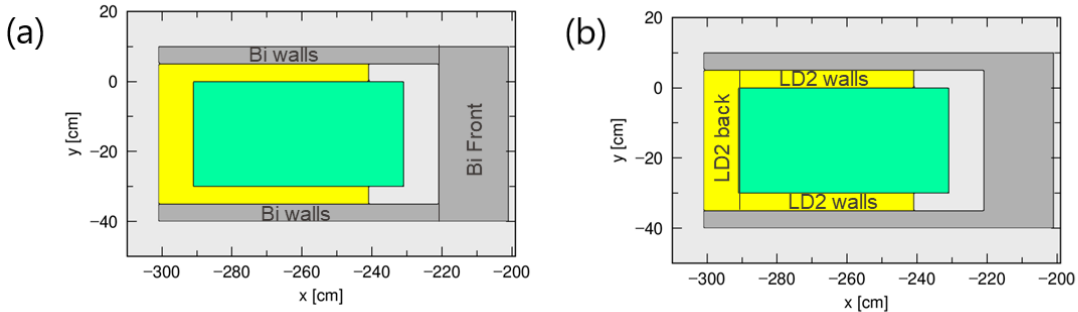


**Figure 147:** Studying the baseline geometry to assess the impact of individual components: (a) Investigation of bismuth shielding by the front section and walls; (b) Examination of the effect of LD<sub>2</sub> by the back section and walls.

To investigate the impact of bismuth on the resulting UCN density and heat load, we segregated this part of the geometry into the front section and the section encompassing the walls, as depicted in Figure 147 (a). The outcomes, outlined in Table 32, indicate that the presence of Bi in the walls does not markedly influence the heat load or the UCN production rate density when compared to the front part. Removing Bi from the front portion results in a doubling of UCN gain, albeit at the cost of increasing the heat load by approximately a factor 6.

The significant impact of removing Bi on UCN gain can be understood by examining the transmission spectrum with and without Bi in the front section, as illustrated in Figure 148. This comparison reveals a substantial drop within the 1-10 meV range, which is crucial for UCN production.

This effect arises from the presence of Bragg peaks in the cross-section of polycrystalline bismuth, as shown in Figure 149 (left). To compensate for this drop, we need to identify a material that scatters neutrons less effectively within the 1-10 meV range. Looking again at Figure 149, oriented single crystal bismuth at 77 K exhibits a minimal scattering cross section within this range. Additionally, beryllium, shown on the right side of the figure, also has a lower scattering cross section.

The results of replacing polycrystalline bismuth in the front section with single crystalline bismuth

**Table 32:** Effect of Bi in the front and in the walls on the relative gain in UCN production rate density and relative heat load compared to the baseline geometry.

	Relative gain $P_{UCN}$	Relative heat load He-II, $n + \gamma$
Baseline	1	1
Baseline-Absence of Bi-walls	0.85	1.3
Baseline-Absence of Bi-Front	2.37	15.7
Baseline-Absence of total Bismuth	1.95	6.7

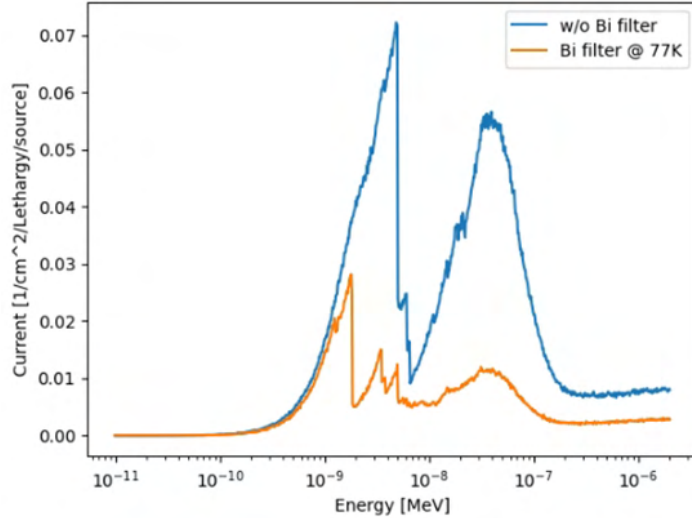


**Figure 148:** The cold source spectrum when there is no bismuth filter and at the presence of bismuth filter at 77 K as a function of energy

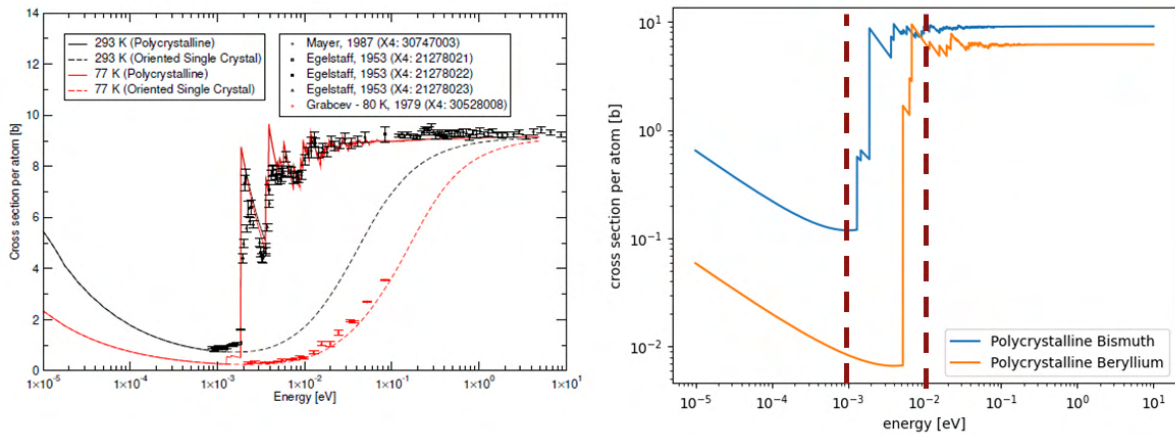


**Figure 149:** Left: Total cross section of neutron for polycrystalline and oriented single crystalline bismuth; Right: Total cross section of neutrons for polycrystalline bismuth and beryllium.

and beryllium are detailed in Table 33. Single crystalline bismuth leads to a 1.75-fold increase in gain compared to the baseline, with only a 30 % increase in heat load. On the other hand, beryllium shows lower performance in both UCN gain (1.6-fold increase) and heat load reduction (1.9-fold increase).

Figure 150(a) displays the transmittance spectrum of various filters, demonstrating the superior transmission of neutrons within the 1-10 meV range for single crystalline bismuth and beryllium. Addition-

**Table 33:** Effect of different front filter materials on the UCN production rate density and the heat load on He-II converter. PC: polycrystalline ; SC: single crystalline

Front Filter	Relative $P_{\text{UCN}}$	He-II heat load ( $n+\gamma$ )
void	2.3	5.2
Bi PC @ 77K	1	1
Bi SC @ 77K	1.75	1.3
Be PC @ 77K	1.6	1.9

**Table 34:** Effect of different parts of LD<sub>2</sub> reflector on the UCN production rate density  $P_{\text{UCN}}$  and total heat load on He-II converter

	Relative gain $P_{\text{UCN}}$	He-II heat load ( $n+\gamma$ )
baseline	1	1
Absence of LD <sub>2</sub> -walls	0.65	1.2
Absence of LD <sub>2</sub> -back	0.87	1.01
Absence of LD <sub>2</sub> -total	0.58	1.21

ally, Figure 150(b) illustrates the neutron spectrum inside the He-II, revealing a greater flux for single crystalline bismuth and beryllium when compared to polycrystalline bismuth. This observation aligns with the findings presented in the table.

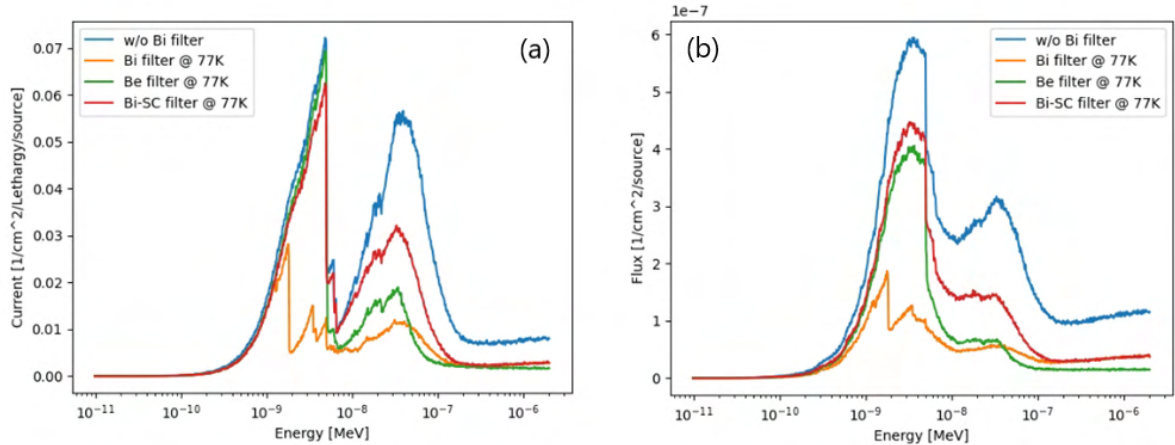


**Figure 150:** (a) Transmittance spectrum of incoming cold neutrons for different materials; (b) Flux of neutrons inside the He-II converter.

### 6.9.2 LD<sub>2</sub> as a CN reflector

Following the same methodology employed for the bismuth studies, we divided the LD<sub>2</sub> into two parts: the back section and the walls, as depicted in Figure 147(b). The impact of each part of the LD<sub>2</sub> reflector is outlined in Table 34. In total, the presence of LD<sub>2</sub> leads to a 42 % gain in UCN production rate density and has a favorable effect on reducing heat load. This is primarily attributed to the implementation of the inverted pre-moderator scheme, allowing cold neutrons a second opportunity for conversion to UCNs upon reflection back into the He-II. The reduction in heat load arises from the fact that a portion of the heat is absorbed by LD<sub>2</sub>, thereby reducing the amount absorbed by the He-II converter.

Apart from using LD<sub>2</sub> as a cold reflector, there are other materials that hold potential as effective reflectors for the cold regime, such as nanodiamonds and MgH<sub>2</sub>. Figure 151 displays the reflectivity of these materials, distinctly highlighting that MgH<sub>2</sub> exhibits better reflection compared to the other two,

**Table 35:** Effect of MgH<sub>2</sub> layer on the UCN production rate density  $P_{\text{UCN}}$  in He-II converter

Geometry	Relative gain $P_{\text{UCN}}$
baseline	1
Absence of Bi walls	0.85
Bi walls replaced by LD <sub>2</sub> @20K	1.24
1 cm MgH <sub>2</sub> @20K + 9 cm LD <sub>2</sub> @20K	1.65
1 cm MgH <sub>2</sub> @293K + 9 cm LD <sub>2</sub> @20K	1.04

specifically for neutrons within the 1-10 meV range. Additionally, maintaining MgH<sub>2</sub> at 20K results in reduced scattering, as illustrated on the right-hand side of the same figure.

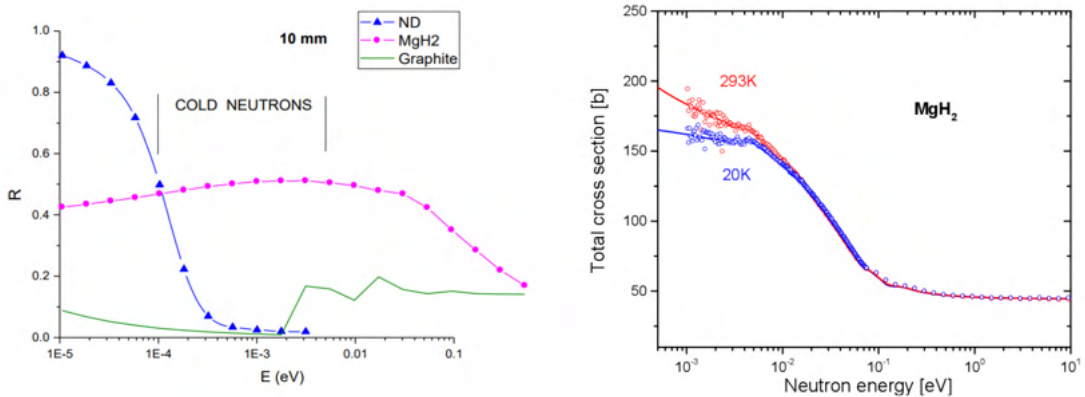


**Figure 151:** Left: Reflectivity of nanodiamonds, graphite and MgH<sub>2</sub> as a function of neutron energy [135]; Right: Total cross section of MgH<sub>2</sub> at 20K and 293K [169].

Table 35 provides a comparison of the relative UCN production rate density in scenarios without bismuth walls and with the substitution of LD<sub>2</sub>, resulting in a 39 % increase in gain. This gain factor could see another 41 percent improvement with the addition of a 1-cm layer of MgH<sub>2</sub> surrounding the He-II converter. However, increasing the temperature of MgH<sub>2</sub> leads to a loss in performance, almost equivalent to the baseline geometry. This is likely attributed to up-scattering events, which diminish the flux of cold neutrons within the He-II medium, and underscores the significance of keeping the source at low temperatures.

### 6.9.3 Adding engineering details

Until now, our discussion has been based on an idealized design concept. In reality, maintaining He-II at 1K, MgH<sub>2</sub> at 20K, and Bi at 77 K requires proper isolation of each component through the use of vacuum insulation. Furthermore, both He-II and LD<sub>2</sub> are fluids and necessitate the presence of a vessel, along with considerations for the vessel's material, and the inclusion of vacuum gaps within the design. As per the technical designs, a 3 mm aluminum vessel encompassing all components and a 10 mm vacuum gap can adequately fulfill these requirements, as illustrated in Figure 152.

### 6.9.4 Outlook

According to the calculations, employing single crystalline bismuth at 77 K and MgH<sub>2</sub> at 20 K presents an opportunity to enhance UCN gain while still maintaining the heat load below 100 W. While this design did not account for the UCN extraction scheme, it is worth noting that being situated within a large beam port provides enough space for implementing extraction channels. Additionally, considering the specific instrument and UCN experiment, there may be room for optimization in the volume of He-II. Table 37

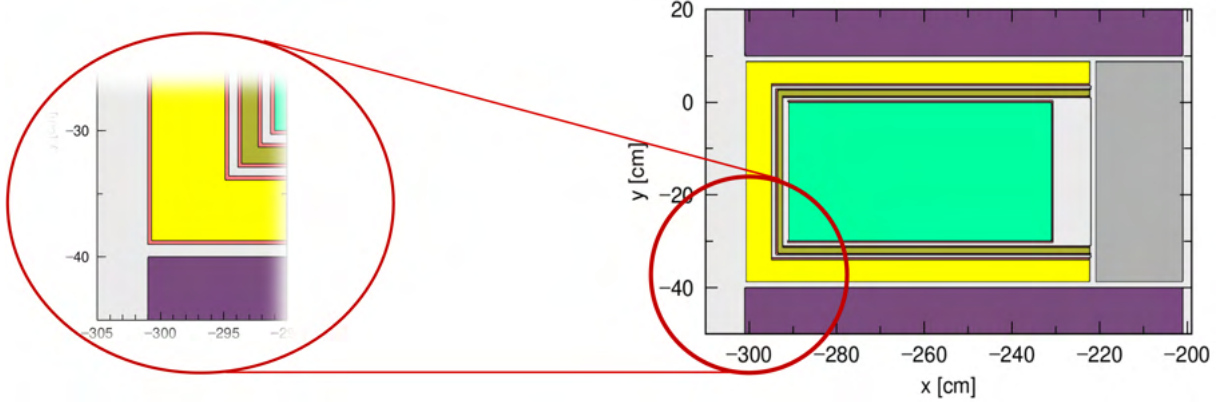


**Figure 152:** Adding engineering details, including aluminum vessel and vacuum gaps to the source design. A close-up view is provided for better clarity.

**Table 36:** Effect of adding engineering details on the UCN production rate density  $P_{UCN}$  in He-II converter

Geometry	Relative gain $P_{UCN}$	Heat load [W] He-II ( $n+\gamma$ )	Heat load [W] Al ( $n+\gamma$ )	Heat load [W] Al ( $\beta$ )	Total Heat load [W]
Baseline (Ideal)	1	8.0	-	-	8.0
Baseline	0.76	9.3	3.05	2.26	14.6
Optimized (MgH <sub>2</sub> +LD <sub>2</sub> + Bi PC)	1.02	10.6	7.0	5.2	22.8
Optimized (MgH <sub>2</sub> +LD <sub>2</sub> + Bi SC)	1.6	13.5	10.7	8.0	32.2
Optimized (MgH <sub>2</sub> +LD <sub>2</sub> + Be)	1.52	19.5	17.8	13.2	50.5

**Table 37:** Performance of optimized geometry of He-II UCN source in the LBP.

	He-II Volume [Liters]	$P_{UCN}$ [n/s/cm <sup>3</sup> ]	$\dot{N}_{UCN}$ [n/s]	Heat-load [W]
<b>He-II in LBP (Final design)</b>	57.6	590	$3.4 \times 10^7$	32.2

shows the final values for the optimized geometry of the UCN source at LBP considering the engineering details.

## 6.10 In-beam UCN source

In this section the design and possible performance of an in-beam UCN source for the ESS are described. More details can be found in a recent publication [147]).

The central component of in-beam UCN source is a neutron delivery system consisting of nested-mirror optics (NMO). The bright neutron emission surface of the large liquid-deuterium moderator has to be imaged onto the UCN source, a remotely located superfluid-helium converter. This approach allows the converter to be placed far away from the high-radiation area in the ESS shielding bunker. The focused beam illuminates the converter under a solid angle that may significantly exceed the solid angle transportable by a straight guide equipped with the most advanced supermirror coating. In this way a large gain in flux density and hence UCN production rate density is achieved.

### 6.10.1 Basic principles of an in-beam UCN source

The three main components to an in-beam UCN source are: a cold neutron moderator, a neutron optical delivery system (NODS), and a converter vessel, filled with superfluid Helium (He-II). The problem of optimizing the UCN production according to a particular set of desired characteristics requires a careful consideration of not only the many parameters describing these three components, but also the interplay between them.

A possible architecture for the transport system for neutrons diverging from a source to a target region is an elliptical guide, with its focal points coinciding with the center of the source and the detector, respectively [151, 170]. The layers of several guides can then be nested to build up a spatial tight component (see Figure 153) to form a NMO system. These devices accept neutrons within a wide, geometrically defined angular range. Two main implementations of NMO can be considered, either with a toroidal or with a planar symmetry (see inlays in Figure 153). In the former case, the device is rotationally symmetric about the optical axis; each mirror surface is a section of an ellipsoid of revolution, and a single reflection transports a neutron from source to target. In the planar case, the mirrors have a local translational symmetry in a direction transverse to the optical axis. Refocusing the beam in both transverse dimensions then requires a combination of two planar NMO rotated by 90° about the optical axis. Such a system images the beam by two reflections, one for each transverse dimension.

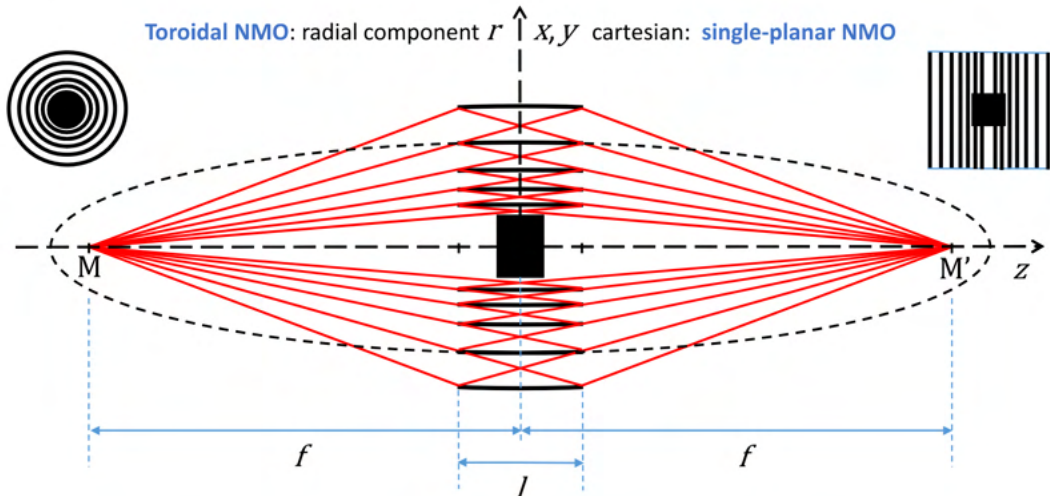


**Figure 153:** Schematic of an elliptic nested mirror optical (NMO) system.  $M$  and  $M'$ , separated by  $2f$ , are the common foci of a set of ellipses, one of which is indicated by a dashed line. The mirror surfaces are formed by truncating the ellipses to the common length  $l$ . See [151] for details of the mathematical construction. The two types of symmetry about the optical axis of the NMO are indicated in the upper corners; the views show the NMO surfaces projected onto a surface normal to the optical axis  $z$ .

The in-beam UCN source for this report is proposed to be of the “superthermal” type. The mechanism was proposed 1975 by Golub and Pendlebury [149] and in contrast to UCN production by neutron moderation, cold neutrons are “converted” to UCN by imparting nearly their entire kinetic energy to elementary excitations – most commonly phonons – of the source medium in single scattering events. In Figure 154 the process for superfluid  $^4\text{He}$  (He-II) is depicted. The dispersion relations of the free neutron and the phonon-roton of the superfluid helium cross at an energy  $E^* \approx 1.04\text{meV}$ , corresponding to a wavelength  $\lambda^* \approx 8.9\text{\AA}$ . A cold neutron with an energy resp. wavelength centered around this value can lose almost all its energy to the converter medium and become ultra-cold by exiting a phonon. Besides this dominant “single-phonon” process a second contribution to UCN production accounts for inelastic scattering of cold neutrons that involves several phonons. Such “multi-phonon” processes occur over a wider range of the neutron spectrum, but, for typical cold beams delivered by neutron guides, contribute less than 30% to the total UCN production [171, 172]. The simulations and estimates for the studies

in this section did only take the single-phonon contribution into consideration. The production rate for UCNs up to a maximum energy  $V_c = 233(2)$ , defined by the wall potential of the converter vessel is [162]:

$$P_I(V_c) = 4.97(38) \cdot 10^{-8} \frac{\text{Å}}{\text{cm d}\lambda} \left. \frac{d\phi}{d\lambda} \right|_{\lambda^*} \quad (13)$$

where  $\left. \frac{d\phi}{d\lambda} \right|_{\lambda^*}$  is the flux at the converter evaluated at the conversion wavelength  $\lambda^*$  of 8.9 Å.

This makes clear that for such an in-beam UCN device the goal becomes to maximize the average of  $\left. \frac{d\phi}{d\lambda} \right|_{\lambda^*}$  at the converter.

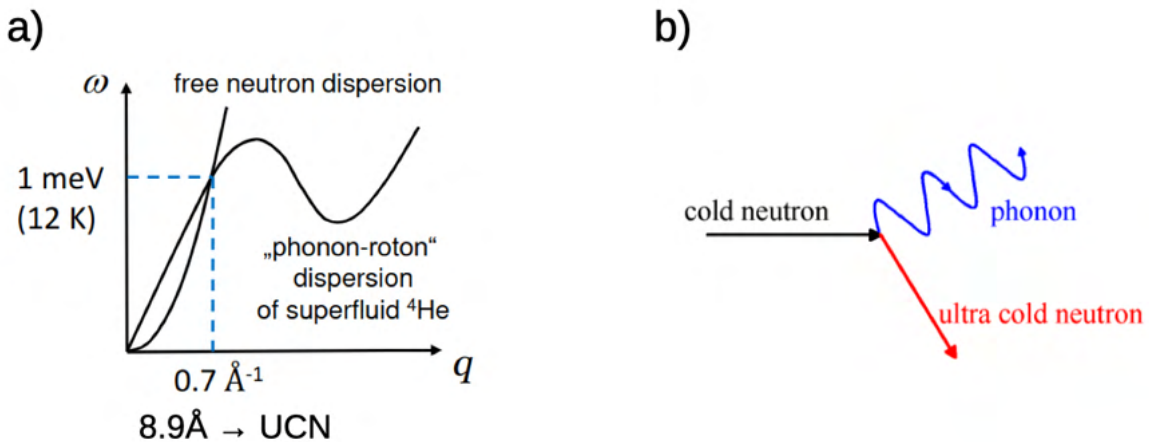


**Figure 154:** a) Dispersion curves of free neutrons and phonons in superfluid helium  $^4\text{He}$ . b) Elastic scattering process. A cold neutron emits a phonon and becomes ultra cold

### 6.10.2 In-beam UCN source implementation at the ESS

The concepts pointed out in the previous section shall now be applied to an implementation at the ESS in order to estimate the UCN densities that may be possible using NMO to transport cold neutrons to a He-II converter vessel. The ideal location for such a UCN source would make use of the LBP, through which moderators in the vicinity of the spallation target wheel can be viewed with large solid angle. The emission parameters of the LD<sub>2</sub> moderator are

$$A_{LD2} = 40_x \times 24_y \text{ cm}^2 \quad \text{and} \quad b_{LD2}^* = 3.4 \times 10^{11} \text{ s}^{-1} \text{ cm}^{-2} \text{ sr}^{-1} \quad \text{at } 5 \text{ MW}, \quad (14)$$

with  $b_{LD2}^*$  being the mean brilliance at 8.9 Å over the moderator surface  $A_{LD2}$ . In Figure 155 a simulated intensity map of neutrons with wavelengths near 8.9 Å emitted by the surface of LD<sub>2</sub> moderator is shown. An efficient extraction of the divergent beam at 8.9 Å from the LD<sub>2</sub> moderator by an elliptic NMO requires covering of a large solid angle. A double-planar elliptic NMO would be best adapted to image the beam, whose horizontal and vertical extents are defined at the moderator surface and guide end, respectively, onto the He-II converter. In the vertical direction, access is limited from the bottom by a 2 m long horizontal shielding plate, which is flat rather than tapered and cuts into the field of view; see Figure 5 in [148]. In order to minimize losses of neutrons emitted downward, the bottom plate should be covered by a mirror starting close to the moderator. If one then places a second mirror, parallel to this, one obtains a vertical, “one-dimensional” guide of the height of the moderator and its length extending to the LBP (see Figure 156 for a schematic). The planar elliptic NMO with horizontal mirrors can then extract neutrons from the “virtual source” defined by the end of this guide. It would have a different focal length than its vertical counterpart. The He-II converter would be installed at a distance of 35 m.

To determine the performance of the proposed system has been simulated in McStas. The NMO have been realized using the library developed for the NNBAR reflector (see Section 9). The recorded flux

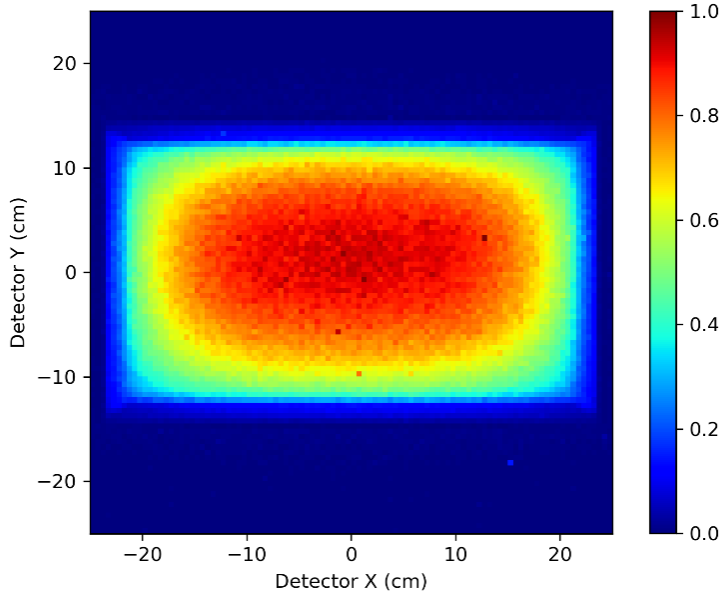


**Figure 155:** Simulated intensity map of the te ESS LD<sub>2</sub> moderator surface of neutrons with wavelengths near 8.9 Å. The data shown, which are normalized to the maximum, correspond to neutrons detected at 4 m from the emission surface after having passed through a “pinhole” halfway between the detector and moderator. Note that an image produced by such a “camera obscura” is inverted, and that the map shown has been mirrored up-down and left-right to represent the moderator surface as it would be seen looking through the LBP. The maximum intensity occurs closer to the upper end, above which the target wheel is situated.

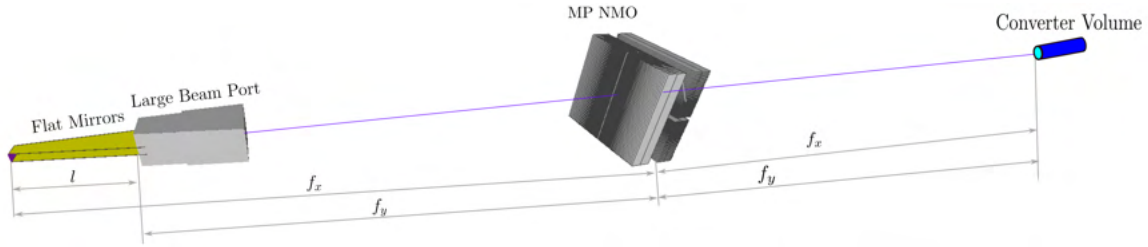


**Figure 156:** Schematic of the proposed Neutron Optical Delivery System for the Large Beam Port at the ESS. The parameters quoted below have been used for the McStas simulations. The distance between the moderator, at left, and the converter entrance, at right, is 35 m. Neutrons are emitted at the LD<sub>2</sub> moderator surface from an area  $w_{mod} \times h_{mod}$ , where the physical height  $h_{mod} = 24$  cm. and width  $w_{mod} = 40$  cm, respectively. Neutrons are initially guided in the vertical direction by two parallel, flat mirrors that end at the LBP at 2.67 m. The beam is imaged onto the entry of the converter by two planar elliptic NMO that consist of mirrors of lengths  $l = 0.5$  m. The semi-minor axis of the outermost mirror of both devices is  $b_{0,x} = b_{0,y} = 1.85$  m. The vertically focusing NMO has a focal length of  $f_y = 16.165$  m and is placed halfway between converter and the end of the flat mirrors, whereas the horizontally focusing NMO ( $f_x = 17.5$  m) is centred between the converter and the moderator. All mirrors of the NODS are coated with the same broadband  $m = 6$  supermirror.

at the converter area is converted to a production rate using Equation (13). In Figure 157 the plots of the relative and total productions rates at the converter and the total UCN production rate for converter volumes of different radii are shown. For a converter with diameter 22 cm and taking into account loses

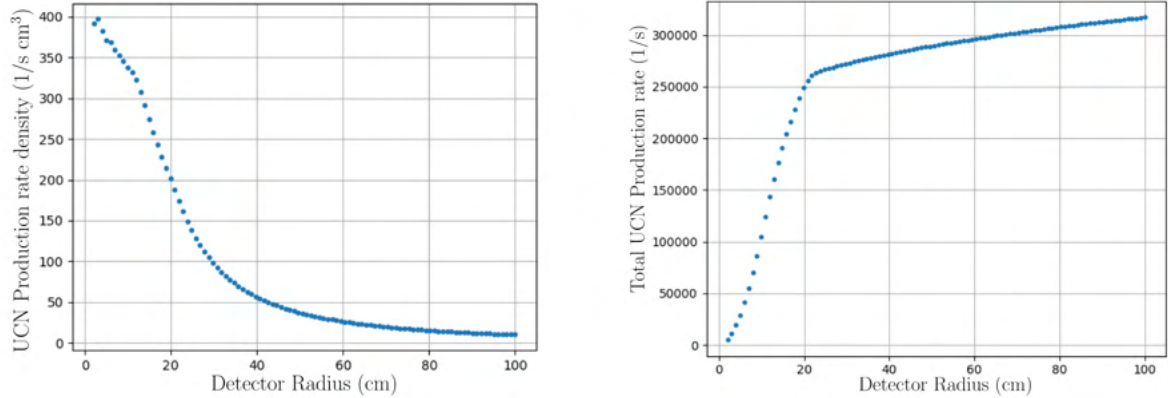


**Figure 157:** Relative (left) and total (right) production rates at the UCN converter volume as a function of the radius.

due to the thickness of the NMO layers of 22 % we obtain a production rate of:

$$p_I = 269 \text{ s}^{-1} \text{ cm}^{-3} \quad (15)$$

Assuming the UCN storage time constant of the converter to be  $\tau = 300\text{s}$ , the corresponding saturated UCN density will be (using  $\rho = \tau \times p_I$ ):

$$\rho_{sat} = 8.06 \times 10^4 \text{ cm}^{-3} \quad (16)$$

in a short converter.

It can be concluded that the parameters of the UCN in-beam type source described in this section propose a very attractive option since it offers a saturated UCN density at the top of the range of other current projects, which rely on UCN production in vicinity of a strong primary cold neutron source. This kind of UCN source is complementary to in-pile type proposals, which generally possess a much higher UCN production rate, but have to overcome cooling and extraction difficulties. It's also important to consider the practical advantages of having the converter located remotely from the primary source. By being far removed from strong radiation fields, the required cooling power is significantly reduced, and the UCN source is easily accessible for troubleshooting. Moreover, UCN transportation is limited to short distances, and nuclear licensing procedures are less likely to pose direct obstacles to the project.

## 6.11 Comparison of the UCN sources

In Table 38 the performances of the different concepts are compared. Overall, we have analyzed several solutions with  $SD_2$  in the twister and in the MCB, and different solutions using He-II in twister, MCB, LBP and in-beam with a NMO system. Some general conclusions are:

- $P_{UCN}$  is higher in  $SD_2$  than in He-II, in agreement with previous studies. The most direct comparison can be done for location 2, where we tested both  $SD_2$  and He-II sources.
- High  $\dot{N}_{UCN}$  values can be reached by all the concepts. For the case of He-II, higher values are reached thanks to the larger volumes of the converters.
- Heat-loads are much lower for the He-II placed further away from the spallation target, compared to the other options. This is a clear advantage for a solution based on a He-II source placed at least 2 m away from the spallation target, or in-beam outside the ESS neutron bunker.

**Table 38:** Summary table with the performance of different UCN source concepts. For details, see discussions in the corresponding sections. The source locations are the ones from Figure 126. The beam values from [173] have been corrected with a 10 % reduction to account for differences in the MCNP models used.

Option	Volume [L]	$P_{UCN}$ [cm $^{-3}$ s $^{-1}$ ]	$\dot{N}_{UCN}$ [s $^{-1}$ ]	Heat [Watt]
SD <sub>2</sub> thin slab in twister - location 1				
Figure 130	1.81	$3.1 \times 10^5$	$5.6 \times 10^8$	760
Figure 131	1.75	$7.7 \times 10^5$	$1.4 \times 10^9$	2910
Figure 132	0.38	$1.3 \times 10^6$	$5.0 \times 10^8$	560
Figure 133	0.13	$1.7 \times 10^6$	$2.2 \times 10^8$	520
Full He-II in twister - location 1				
Figure 135	21.9	$2.58 \times 10^5$	$5.65 \times 10^9$	9933
Thin He-II in twister w/extraction - location 1				
Figure 136	1.25	$6.3 \times 10^4$	$7.8 \times 10^7$	113
Thin SD <sub>2</sub> + He-II in twister w/extraction - location 1				
Figure 137	1.25	—	$1.34 \times 10^8$	109
(SD <sub>2</sub> Only)	0.06	$1.22 \times 10^6$	$7.7 \times 10^7$	10
(He-II Only)	1.19	$5.14 \times 10^4$	$6.1 \times 10^7$	99
Full SD <sub>2</sub> in twister - location 1				
Figure 134	48.2	$6.56 \times 10^5$	$1.32 \times 10^9$	39886
SD <sub>2</sub> thin slab in MCB - location 2				
Figure 142a	0.91	$3.8 \times 10^4$	$3.4 \times 10^7$	159
He-II in MCB - location 2				
Figure 145	24.3	2160	$5.23 \times 10^7$	328
He-II in MCB + 77 K Bi Shield - location 2				
Figure 145	24.3	1435	$3.49 \times 10^7$	153
He-II in MCB + 293.6 K Bi Shield - location 2				
Figure 145	24.3	1150	$2.79 \times 10^7$	145
He-II in LBP - location 4				
Figure 146	58	369	$2.1 \times 10^7$	8
He-II in beam - location 5				
Figure 156	114	234	$1.53 \times 10^7$	

- In-source  $\rho_{UCN}$  values can be obtained by multiplying  $P_{UCN}$  by the UCN lifetime in the medium. As previously discussed, this is about 40 ms in SD<sub>2</sub>, while it is of hundreds of seconds for He-II. However, even the shorter lifetime of UCNs in SD<sub>2</sub> allows for a large release fraction (of roughly 50%) for a thin SD<sub>2</sub> converter of 2 cm or less thickness [154]. A comparison of in-source  $\rho_{UCN}$  between He-II and SD<sub>2</sub> is not necessarily conclusive because the two sources are typically used in different ways, as discussed in Section 6.3.
- It worth noting that  $P_{UCN}$  and  $\dot{N}_{UCN}$  are similar between He-II in LBP and He-II in-beam, despite the He-II in the LBP being at a much closer distance. This is an indication that the nested-mirror optics in the in-beam design (see [173]) allows the transport of the cold beam within a divergence range which is similar to the beam divergence defined by the solid angle of the source placed in the LBP at about 2 m from the moderator center. Results can change once the designs will be further optimized; for instance the He-II design can be optimized by improving the geometry and the reflectors surrounding the He-II vessel. These optimization are beyond the scope of the HighNESS project but should be investigated in future projects.

## 7 Integration of the CN, VCN and UCN sources

### 7.1 Summary of the main results for CN, VCN and UCN sources

As presented in the previous sections, the HighNESS project explored various potential solutions for CN, VCN, and UCN sources. It's important to recall that HighNESS had two primary objectives: designing intense neutron sources and shifting the neutron spectrum towards colder energies. These goals can be achieved through several approaches.

In the following discussion, we will first summarize and discuss the results for each type of source individually. Then, we will explore how these different sources can be integrated most efficiently.

The second ESS source is centered around the CN moderator designed in HighNESS. The reference design, utilizing LD<sub>2</sub> and a Be filter/reflector, achieves an order-of-magnitude increase in intensity compared to the upper moderator. This source is expected to serve both NNBAR experiments and various neutron scattering studies. It's worth noting that this CN source is the only one that has been fully designed. This is not surprising, as it utilizes LD<sub>2</sub>, a well-established high-intensity cold source with decades of proven experience.

There is, however, an alternative to this design, namely a SD<sub>2</sub> moderator, that was discussed in the context of VCN and UCN sources. While preliminary engineering design considerations seem promising for operating such a moderator at least up to 2 MW, further in-depth R&D would be necessary to realize and operate this source in a high-temperature, strong-radiation environment. As a result, implementing this source would only be possible after years of research, therefore the most likely scenario is that this source will be installed at a later stage, likely after the completion of the NNBAR experiment. It can then be concluded that the ESS second source should be based on the LD<sub>2</sub> moderator for the first several years of operation .

Unlike the CN source, the VCN moderator presented several promising options for investigation. Our study followed two distinct but interconnected paths: one involved the use of dedicated VCN materials, while the other explored the use of advanced reflectors to enhance VCN source performance. In the dedicated materials category, we considered SD<sub>2</sub> and deuterated clathrate hydrates. Additionally, we explored advanced reflectors such as nanodiamonds and MgH<sub>2</sub>, which could be employed not only with dedicated VCN materials but also with LD<sub>2</sub>.

Furthermore, a variety of hybrid configurations using both LD<sub>2</sub> and SD<sub>2</sub> were analyzed, thanks also to the availability of accurate thermal scattering libraries (several of which were calculated in the framework of the HighNESS project). Among the various options, it seems that the most promising ones in the foreseeable future are based on the use of SD<sub>2</sub> in conjunction with nanodiamond reflectors, where LD<sub>2</sub> is fully displaced as the moderating medium. Deuterated clathrate hydrates have been explored for the first time for the development of a practical VCN source. The first results in HighNESS indicate that larger volumes of moderating materials such moderating materials would be necessary, compared to SD<sub>2</sub>. This would probably make them impractical for ESS as primary VCN-source options; nevertheless the potential for the use of this material is established, and investigations should be extended to their use as reflectors, or in conjunction with a primary source.

A full SD<sub>2</sub> source is expected to deliver an order-of-magnitude increase in VCN brightness above 40 Å. This result was not anticipated at the outset of the HighNESS project: there were no prior works with VCN sources placed so near a spallation target, and reliable thermal scattering libraries needed development or improvement. This result is therefore very important and could be groundbreaking in the field of neutron scattering, if such a source was realized.

Regarding UCN sources, HighNESS explored a wider range of concepts compared to VCN sources. The project identified various in-pile options both in the initial proposal and during its course. Furthermore, the availability of two proven materials, SD<sub>2</sub> and He-II, expanded the array of potential options. To provide a comprehensive overview, the in-pile performances are summarized in Table 38. Additionally, the project conducted an in-depth study of an in-beam option.

## 7.2 Integration options based on an LD<sub>2</sub> primary source

This option was considered the most promising in the HighNESS proposal. The rationale behind this concept involves having a primary high-intensity cold source that can also serve as a source to feed secondary VCN and UCN sources. Consequently, the project dedicated significant effort to explore this possibility, which culminated in a detailed design of the LD<sub>2</sub> moderator. This design underwent several phases of neutronic and engineering optimization.

For this option we explored two possibilities for the placement of the secondary source: the MCB as can be seen on Figure 158, and the LBP.

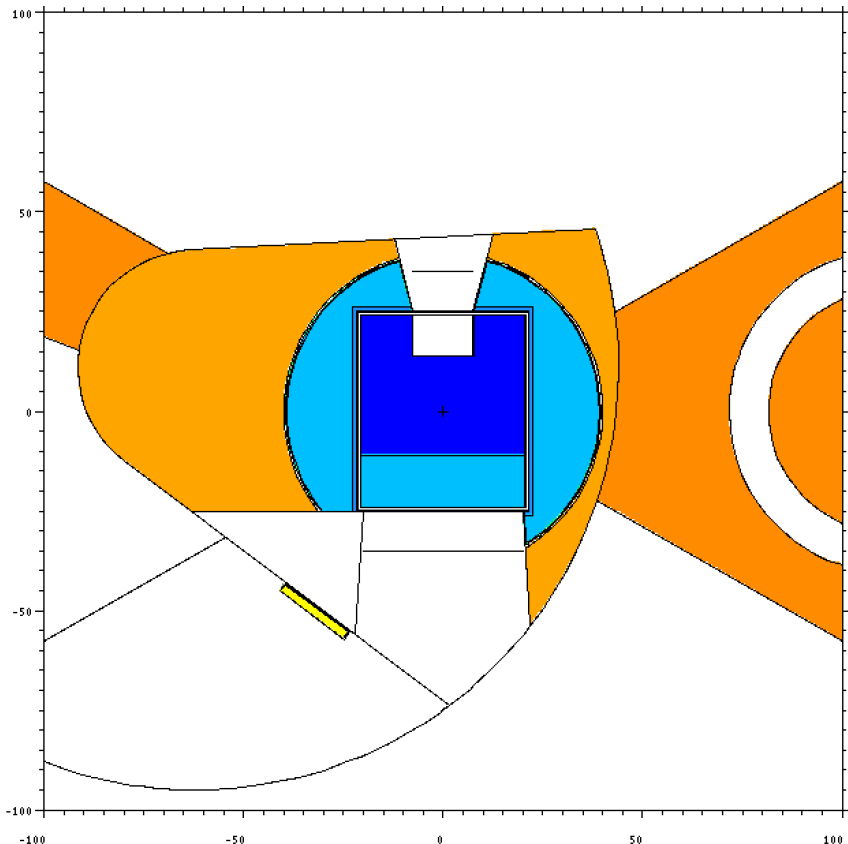


**Figure 158:** An example of integration of primary cold neutron source made of LD<sub>2</sub> and secondary UCN source made of SD<sub>2</sub>. LD<sub>2</sub> is depicted by dark blue color and SD<sub>2</sub> is depicted by yellow color. The Be filter on NNBAR opening is depicted by the light blue color.

### 7.2.1 LD<sub>2</sub> in twister, UCN in the MCB

For this option, from day one ESS has an intense CN source and a UCN source in the MCB, which has no interference with the operation of NNBAR. Neutronic design of this option has been investigated for UCN sources both based on SD<sub>2</sub> and He-II, showing great potential for a high-performance source.

### 7.2.2 LD<sub>2</sub> in twister, followed by UCN in LBP after NNBAR

In this scenario, ESS initially uses the LD<sub>2</sub> moderator alone, and the NNBAR experiment is conducted for several years. Once the NNBAR experiment is completed, the LBP can be repurposed for other applications. We have conducted detailed studies of two options for this case: the in-pile option (see Figure 159) and the in-beam option using nested mirror optics.

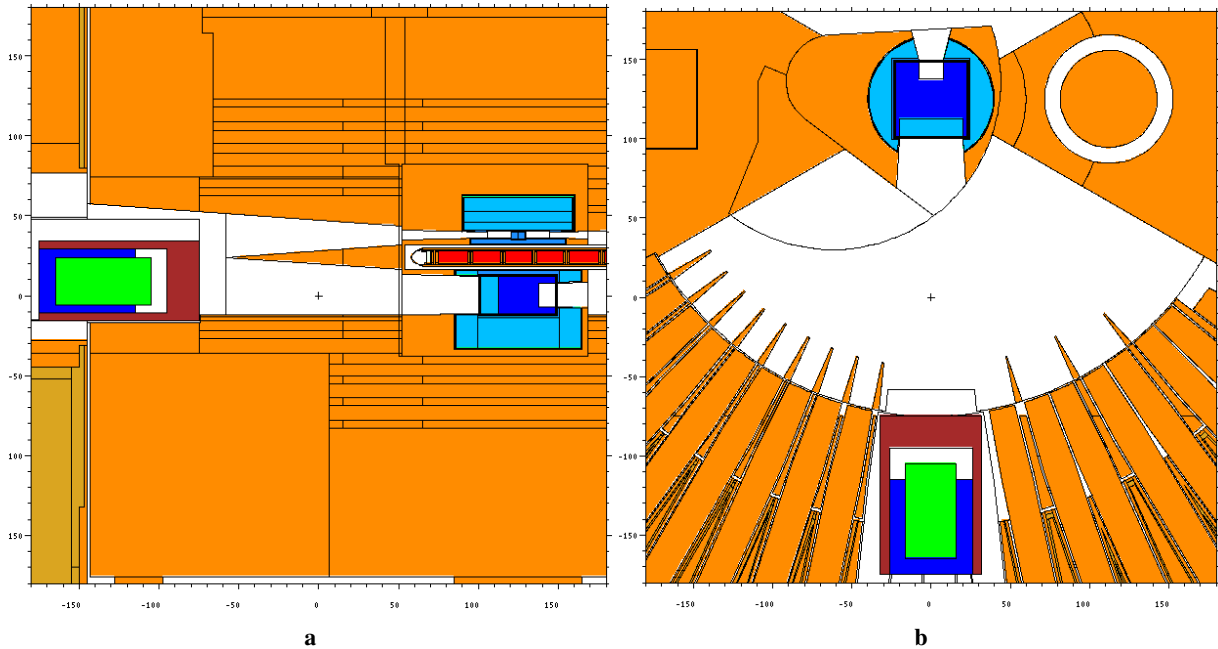


**Figure 159:** Integration of the primary cold source made of LD<sub>2</sub> depicted by the dark blue color located below the target and secondary UCN source made of He-II depicted by the green color located in the NNBAR beamport. The model is based on the proposal from Serebrov. The red color depicts the ESS target made of tungsten. The dark red color around He-II converter depicts the shileding made of bismuth.

### 7.2.3 LD<sub>2</sub> in twister, UCN in regular beamport

This configuration represents a third option for a secondary UCN source fed by the LD<sub>2</sub> moderator, wherein a regular beamport is utilized in order to avoid interfering with the NNBAR experiment. Additionally, in this case the UCN source can be in-pile, inside the monolith, or in-beam. We did not perform a neutronic study of this in-beam option, however its performance can be estimated by either scaling the results for the LBP in-pile solution see Section 7.2.2, or from estimated performed at the HighNESS workshop [174].

## 7.3 Integration option based on an LD<sub>2</sub> primary source, upgraded to deliver also VCN and UCN

The options based on using the LD<sub>2</sub> moderator as primary source described above do not have a dedicated VCN source. This is due to the fact that, for a VCN source to outperform the performance of an LD<sub>2</sub> moderator, in the wavelength range of the VCNs, such a source must necessarily be placed inside the twister, close to the hot spot of neutron production. The only other possibility for a VCN source without using a dedicated material that has been explored in HighNESS is the use of advanced reflectors (NDs) to more efficiently transport the coldest part of the spectrum to an instrument or guide entrance. However, it has been found to have a significant effect only at large divergence angles, which is not immediately relevant for the intended applications of the second source. An upgraded LD<sub>2</sub> cold source, with the addition of a SD<sub>2</sub> slab on one of its extraction sides – or in one of the more complex hybrid options detailed in Section 6.5 – could be a valid alternative for a combined CN/VCN source.

## 7.4 A full-SD<sub>2</sub> source for CN, VCN and UCN?

In HighNESS we also designed a VCN source that is based on full SD<sub>2</sub> at 5 K. With respect to the LD<sub>2</sub> source, an SD<sub>2</sub> moderator delivers more neutrons for wavelengths above about 6 Å, while the performance below this range is lower. However, it would provide a slight increase in the FOM of NNBAR, which would make it very interesting as it would be a source of CN, VCN and UCN.

In this scenario, ESS would start with a  $\text{LD}_2$  moderator located below the target; later the  $\text{LD}_2$  moderator would be replaced with a  $\text{SD}_2$  moderator with the same dimensions. This scenario would be possible only if the big cooling challenges to operate a solid deuterium source at high power would be solved; by the time ESS will reach the 5 MW average power, a compromise design solution should probably be adopted, where the moderator is part  $\text{LD}_2$  and part  $\text{SD}_2$ .

## 7.5 Comparison of the different scenarios

Based on the above considerations, it is evident that there are several competitive possibilities for providing a second source that complements the upper high-brightness bi-spectral moderator. To select the most promising option among these, several factors need to be taken into account, particularly focusing on performance, operability, and technical feasibility.

**Table 39:** The different integration scenarios.

option	CN source	VCN source	UCN source
1	$\text{LD}_2$	none	none
2	$\text{LD}_2$	none	$\text{SD}_2$ or He-II in MCB
3 <sup>a</sup>	$\text{LD}_2$	none	He-II in beam in regular beamport
4 <sup>b</sup>	$\text{LD}_2$	none	He-II in LBP
5 <sup>b</sup>	$\text{LD}_2$	none	He-II in beam in LBP (NMO)
6 <sup>c</sup>	Hybrid $\text{LD}_2/\text{SD}_2$	$\text{SD}_2+\text{ND}$	$\text{SD}_2$
7 <sup>d</sup>	Hybrid $\text{LD}_2/\text{SD}_2$	$\text{SD}_2+\text{ND}$	He-II in beam
8 <sup>e</sup>	$\text{SD}_2$	$\text{SD}_2$	$\text{SD}_2$

*a:* not studied in HighNESS, performance can be estimated from SuperSUN at ILL.

*b:* UCN in beam, use of NMO; installed after NNBAR is completed

*c:* UCN extracted from  $\text{SD}_2$

*d:* full  $\text{SD}_2$  option, needs R&D

The list of possible options for an integrated source is in Table 39.

The eight rows in Table 39 could be loosely considered as a possible sequence of possible configurations for the lower moderator plug. Starting from having only the  $\text{LD}_2$  moderator in the twister, it would be possible to add in parallel a UCN source in the MCB, or a UCN source in beam using a regular beamport other than the LBP.

Different options for UCN sources could be implemented after NNBAR is completed and the LBP is available (options 3 and 4).

To establish a high-intensity VCN source, we have determined that the use of a dedicated material in the twister is essential. However, the development of technology to operate a 5 K moderator in close proximity to the spallation target is required. Additionally, the need to commence operation of the lower moderator with a high-intensity cold moderator suggests that the implementation of a strong VCN source would likely occur at a later stage, potentially after the NNBAR experiment is completed. In terms of performance, a full  $\text{SD}_2$  moderator is comparable to an  $\text{LD}_2$  moderator, but it delivers an order of magnitude or more VCNs and is also a proven material for UCN. Therefore, option 8 could potentially represent the final stage of the HighNESS source, where a single  $\text{SD}_2$  moderator can offer competitive CN fluxes, unprecedented VCN fluxes, and a world-leading UCN source.

## 8 Neutron scattering instruments for the ESS second source

During the late stages of the design of the European Spallation Source it was realized that reducing the height of the cold hydrogen moderator could significantly increase its brightness, presenting a new opportunity for both moderator and instrument design [175]. The increase in brilliance did not fully compensate for the decrease in height, meaning the height would directly control the trade-off between intensity and brilliance. The optics for all instruments, which will be served by the newly designed butterfly moderator [176], were reoptimized for a range of moderator heights [175], and a choice was made to reduce the height from 10 cm to 3 cm, as this benefitted almost all instruments, and in some cases increased the simulated flux on sample with over 150 %.

There were however a few science cases that proved to be more difficult on the smaller moderator, for example imaging, which benefits from a larger moderator due to better homogeneity and field of view. Some types of instruments can tolerate a large divergence, for example backscattering instruments or time-of-flight spectrometers, and their performance is more closely related to the intensity of the moderator than its brilliance. For these reasons it was natural for the HighNESS project to investigate larger moderators to complement the butterfly moderator with its small height. The butterfly moderator has a bispectral design with both a thermal water part and cold hydrogen part [176]. On the other hand, the HighNESS, larger moderator focus on the cold side, and provide a colder spectrum which can potentially benefit SANS, imaging and spin-echo instruments.

In order to optimize the moderator proposed by HighNESS, a number of instrument concepts that would utilize this new moderator were considered along with suitable figures of merits. This allowed an iterative approach for moderator design. Each new design could be evaluated using these instrument concepts to assess the moderator's performance, considering not only the flux at its surface but also its impact on the performance of the instruments reliant on the moderator.

In this section we share the final design of the instruments along with their performance for each of the 4 proposed moderator sizes (see Section 2.2.1), providing the necessary data to choose the best of the 4 options. The considered instruments were two SANS instruments, one using conventional optics and the other using focusing optics, as well as an imaging instrument. The work on a spin-echo instrument using focusing optics was not finished within the time constraints of the project but shows promising results and should further developed in future studies. Each conceptual instrument is compared with the relevant ESS instruments under construction to ensure they add new capabilities and avoid replicating existing capabilities in the instrument suite.

As described previously the HighNESS project has also investigated a solid deuterium moderator which would have significantly better performance in the VCN wavelength range. When considering instrumentation for such a source, it is important to have optical tools for counteracting the effects of gravity. The last part of this section investigates the use of prisms in combination with focusing optics to create achromatic optics, which will be an essential tool for future VCN-neutron scattering instruments.

### 8.1 Moderator alternatives

The moderator optimization process arrived at a large liquid deuterium vessel with different sizes of exits towards the condensed matter instruments investigated here. The final four candidates were the following sizes,

$$3 \times 3 \text{ cm}^2, 5 \times 5 \text{ cm}^2, 10 \times 10 \text{ cm}^2, \text{ and } 15 \times 15 \text{ cm}^2.$$

In Figure 160 the brilliance and intensity of these four moderators are plotted along with the corresponding values for the cold part of the butterfly moderator. While the smaller openings do have a higher brightness, this effect is much smaller for the deuterium moderator than the hydrogen-based butterfly, meaning that differences in brilliance are less pronounced. At wavelengths larger than 5 Å the brilliance of the larger moderators is very similar to the butterfly, while the two smaller moderators have brilliance

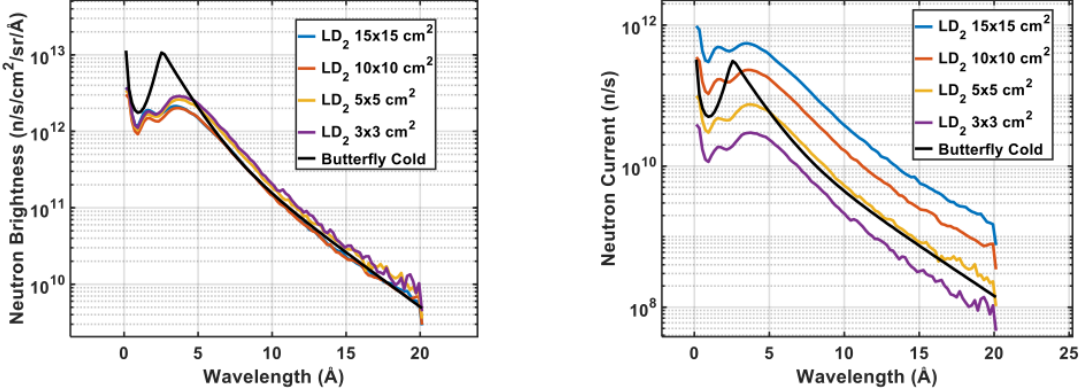


**Figure 160:** 1 Spectrum for the proposed liquid deuterium moderators at 2 m distance measured over the beamport.

slightly higher than the butterfly. With the similar brilliance, the larger moderators ( $> 5 \times 5 \text{ cm}^2$ ) have a significantly larger neutron intensity when compared to the butterfly moderator.

## 8.2 Optimization of small-angle neutron scattering instruments

The SANS science case for a larger moderator would naturally focus on larger samples, though the large source can also be utilized by focusing optics. As such, two different designs were investigated, a conventional SANS named ConvSANS and a Wolter optics-based SANS instrument named WOFSANS. There are two SANS instruments under construction at the ESS, the short LOKI and the medium length SKADI. For ConvSANS to be complementary to these instruments, it is chosen to increase its length to achieve better resolution and smaller minimum  $Q$ . The WOFSANS instrument uses focusing optics to benefit from the large moderator area and due to the focusing properties can avoid a long collimation section, resulting in a shorter instrument with greater bandwidth.

### 8.2.1 Conventional SANS

The Conventional SANS (ConvSANS) conceptual design presented here is based on a typical pinhole collimation geometry. A schematic of the instrument is given in Figure 161. The current design consists of a single block 30 m long collimation, thus having, for initial assessment, a constant collimation distance ( $L_1$ ). In a practical realization the collimation will consist of sections to enable to relax resolution and adapt to different sample sizes. Currently, two fixed-position detectors are placed at 3 m (wide angles) and 30 m (small angles) from the sample, respectively. The combination of the long collimation with the two detector positions, will allow for a large  $Q$ -range coverage, allowing at the same time to maintain high  $Q$  resolution for large sample sizes. The relatively long total instrument length, set at 80 m, leads to good wavelength resolution, while the long collimation provides high angular resolution, which can be traded for large samples and thus high intensity. The total length of the instrument limits the wavelength bandwidth to about 3.5 Å when operating in the standard 14 Hz mode, however, this can be extended to about 7.0 Å in the pulse skipping 7 Hz mode of operation.

The present instrument design assumes a constant guide size of  $6 \times 6 \text{ cm}^2$  throughout the instrument. The start of the neutron guide is at 2 m from the moderator surface, at the beginning of the monolith wall. The instrument makes use of a pair of benders located in the monolith and the bunker wall, respectively, that are used to avoid direct line-of-sight to the moderator and act as a short wavelength cut-off filter. The benders are designed with a radius of curvature of 61.25 m and a length of 3.5 m. The use of the bender pair provides for twice out of line-of-sight curvature to minimize the intrinsic background, and offsets the beamline down vertically by 0.55 m. In the in-between space of the monolith wall and the bunker wall, two tilted straight neutron guides, 1 m and 5 m in length, respectively, connect the two benders, with a small gap between them for chopper installation. After the second bender, a straight guide of 5 m in length brings the beam back into horizontal position and connects the bender with the collimation

system. After initial Monte Carlo investigations, all neutron guides and benders are coated with  $m=4$  supermirrors, however, this should be subjected to further optimization. The 30 m collimator starts at 20 m from the moderator, where a first aperture, hereafter referred to as source aperture ( $D1$ ), is located, and ends at 50 m from the moderator, where the sample aperture ( $D2$ ) is located.

Wavelength selection and frame overlap prevention is performed using two double-disc choppers. A bandwidth double-disk chopper is placed in the in-bunker section of the instrument, between the two tilted neutron guides, at 6.5 m from the moderator. An additional pair of choppers is placed right after the bunker wall, at 15 m, downstream of the second bender, to suppress frame overlap. A third pair of choppers can also be added further downstream, at 40 m within the collimation section, to further suppress frame overlap.

The detector configuration employed for the current set-up is based on a "window-frame" design (see Figure 161). The front detector is at a fixed position, 53 m from the moderator and 3 m from the sample position. It has a  $3 \times 3 \text{ m}^2$  surface area with a  $0.327 \times 0.327 \text{ m}^2$  window opening at the center. The rear detector, also at fixed position, is located at 80 m from the moderator and 30 m from the sample position, with a  $3 \times 3 \text{ m}^2$  surface area. In the current design, there is no specific detector technology considered (e.g.,  ${}^3\text{He}$  gas detector or  ${}^{10}\text{B}$ -based detector), however a standard pixel size of 1 cm is conservatively assumed for  $Q$ , and  $Q$ -resolution calculations.

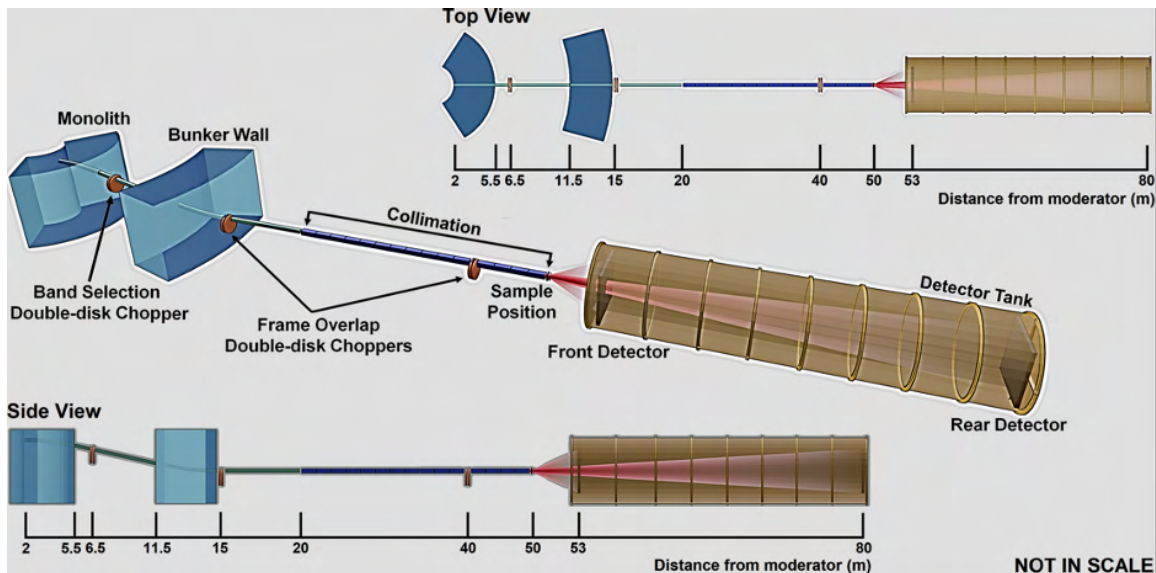


**Figure 161:** Overview of ConvSANS instrument geometry.

While the instrument has flexible collimation for different samples, it was chosen to investigate the flux on sample for the configuration believed to be most often used, here a source aperture of 3 cm and a sample aperture of 1.5 cm. The spectrum on the sample with the choppers open can be seen in Figure 162. In this configuration the performance is similar for all moderators, only the smallest delivers a significantly lower intensity. For configurations intended for larger samples and lower resolution, the benefit from the larger moderators increases, though it is important to note that even for the chosen high resolution configuration, the largest moderator achieves the highest intensity.

### 8.2.2 SANS with Wolter focusing optics

The WOF-SANS design makes use of a pair of reflective Type I Wolter optics [177] to take advantage of the large moderator surface and thus increase the neutron intensity at the sample position. The concept of such a focusing SANS instrument is described in [178]. A schematic of the current instrument design can be seen in Figure 163. The total length of the instrument is 29.5 m defining a wavelength bandwidth of 9.5 Å when operating with the 14 Hz source frequency and can be extended to about 19 Å at pulse skipping mode.

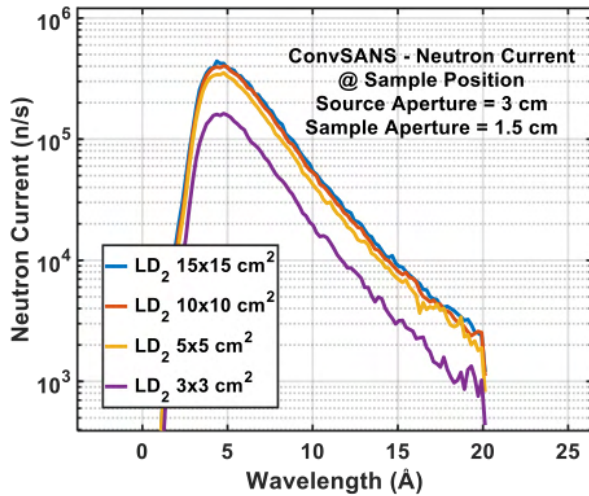


**Figure 162:** Intensity on sample for ConvSANS instrument for each proposed moderator size.

The first Wolter optics system is used as a condenser lens, and it is located in the in-bunker section of the instrument, 10 m from the moderator (considering its middle point). It is designed accordingly to have the highest possible throughput. For an initial assessment, it consists of 28 nested paired parabolic and hyperbolic (P-H) sections, currently 1.3 m and 1.0 m in length, respectively (2.3 m total length), with a total radius of 7.5 cm. The innermost radius of 1.0 cm is not covered and might be filled with an absorber. The focal length of the condenser is 5.5 m thus its focal point is 15.5 m from the moderator. The use of parabolic mirrors as the first point of contact for the incoming beam, implies that predominantly the lowest divergence component of the phase space will be focused. The mirrors are coated, for initial assessment, with supermirror coating of  $m = 3.0$ . Lower coating quality is anticipated to suffice, as highly divergent portions of the beam, similar to the conventional SANS approach, will not be taken into account. Instead, a larger area of the moderator will be considered. An aperture of 4 mm in diameter is placed downstream of the bunker wall, at the focal point of the condenser, to suppress any out-of-focus rays and any neutrons that pass through the condenser without reflecting. This position will be heavily shielded and the aperture will be designed to deal with such a situation and to shield the large diameter beam of background radiation.

The second Wolter optics system is used as an objective lens and it is located 23.5 m from the moderator (considering its middle point). Its focal lengths, aperture-to-objective (LC) and objective-to-detector (LD), are 8 m and 6 m, respectively, resulting in a (de)magnification  $M = 0.75$ . As such, the beam spot size on the detector center is expected to be 3 mm in diameter. The objective lens consists of 25 nested paired elliptical and hyperbolic (E-H) sections, 0.9 m and 0.82 m in length, respectively (1.72 m total length). Its maximum radius is 10 cm, allowing it to collect the full divergence coming from the aperture (i.e., from the condenser). The E-H mirrors are also coated supermirror of  $m = 3.0$ , however, this is subject to optimization. The sample is placed between the objective lens and the detector. Different positions are possible with corresponding impact on illuminated sample size (beam size), Q-range, and resolution. A bandwidth double-disk chopper is placed right after the bunker wall and the slit of the focusing position, at 16 m. An additional pair of choppers can be placed before the objective lens to suppress frame overlap. The position sensitive detector is considered to have a surface area of  $3 \times 3 \text{ m}^2$  and is placed at a fixed position matching the focal point of the E-H optics, at 29.5 m from the moderator. As in the case of ConvSANS there is no assumption of specific detector technology, however a pixel size of 0.3 cm is used for subsequent Q and Q-resolution calculations.

The spectrum on the detector position with all choppers open can be seen in Figure 164. Due to the focusing of the instrument, this is equivalent to the intensity at the sample regardless of position (when neglecting losses from air scattering). The WOF-SANS instrument shows higher sensitivity to the size of the moderator, partly due to the use of a parabolic section that performs better with larger sources.

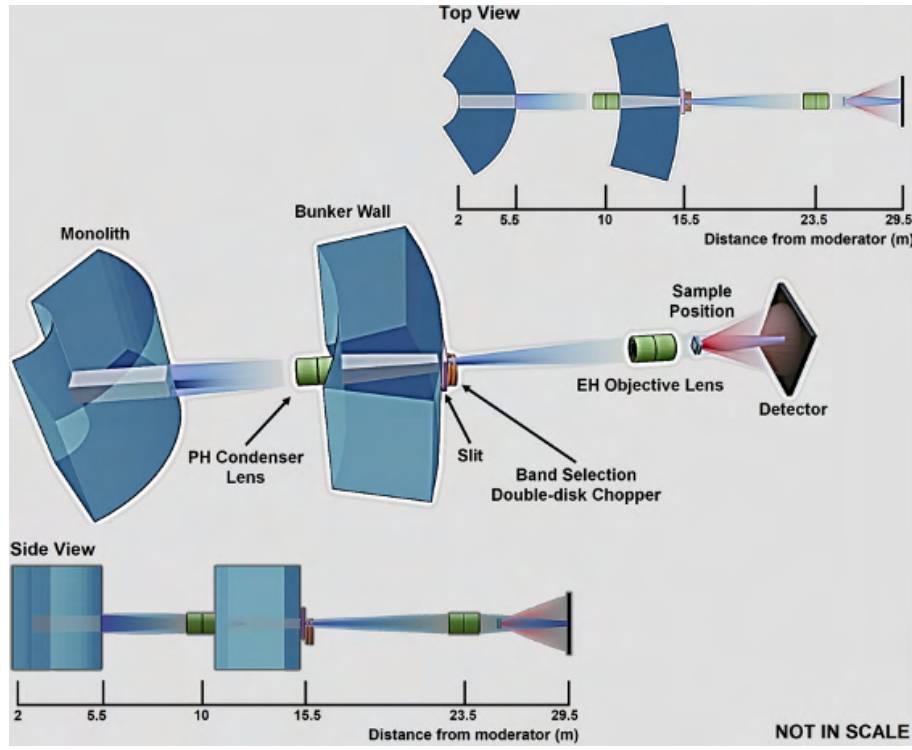


**Figure 163:** Overview of WOF-SANS instrument geometry.

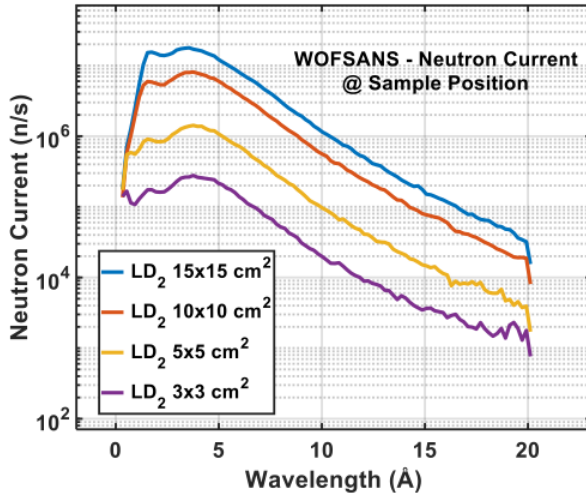


**Figure 164:** Intensity on sample for WOF-SANS instrument for each proposed moderator size.

### 8.2.3 FOM Definition

In general, determining the FOM of a SANS instrument can be complex since there are many parameters coming into play and of course different sets of samples and/or configurations need to be taken into account. For our SANS instruments, at this early stage of conceptual design, the useful parameters that can be considered are the intensities at the sample position ( $I_{sample}$ ), as calculated from the simulations, the  $Q_{min}$  and  $Q_{max}$  values, as well as  $\Delta Q/Q$  for every  $Q$  value within a range of interest. Similar to the FOM defined by information theory, we can define the following simple FOM formula:

$$FOM(\Delta Q/Q) = \frac{I_{sample}}{\Delta Q/Q} \cdot \ln \left( \frac{Q_{max}}{Q_{min}} \right) \quad (17)$$

With the above FOM definition we see that the FOM is proportional to the intensity, as well as the

ratio of Qmax and Qmin. The Q-resolution is inversely proportional to the FOM since of course lower Q-resolution value (improved resolution) will thus increase the FOM.

#### 8.2.4 Performance of conceptual SANS instruments

With the clear definition of the figure of merit, both the SANS instruments and moderator candidates can now be directly compared. In Figure 165 the figure of merit is shown for both instruments and all moderators as a function of Q, showing the WOF-SANS generally has higher performance than the conventional instrument.

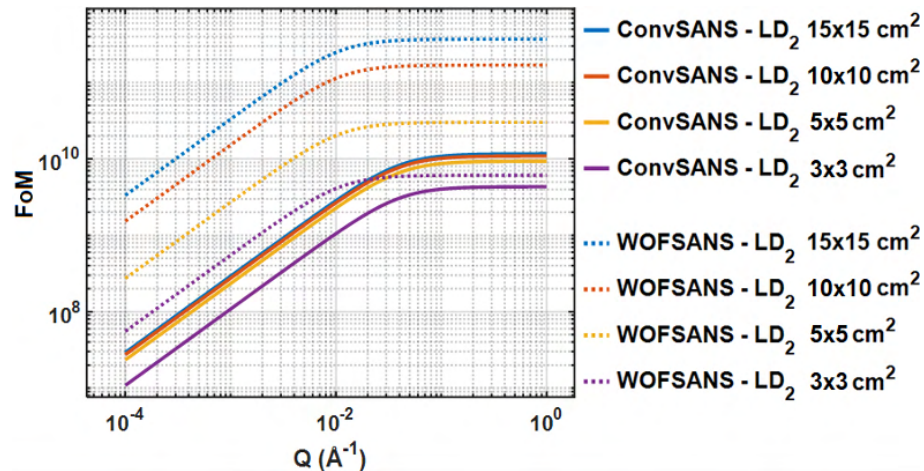


**Figure 165:** Figure of merit as function of scattering vector magnitude for both SANS instrument concepts and all proposed moderators.

To clearly show the performance of the instruments as a function of moderator size, the figure of merit at  $Q = 1.0E-4 \text{ Å}^{-1}$  is plotted for each moderator in Figure 166, from which is clear that both SANS instrument concepts perform best at the largest source.

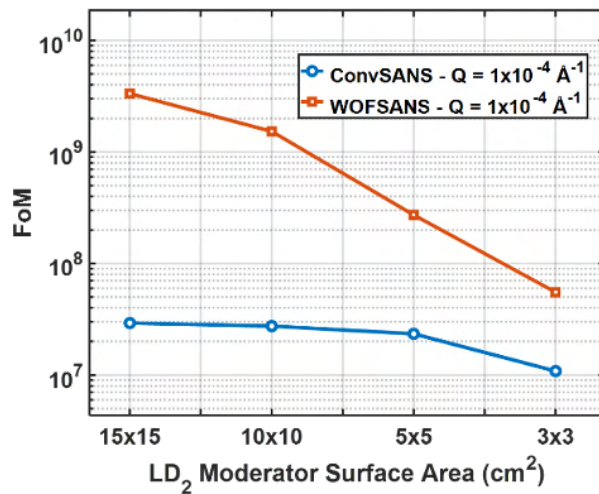


**Figure 166:** Figure of merit at fixed scattering vector magnitude as function of moderator size.

#### 8.2.5 Performance comparison to ESS instruments

In addition to comparing the two conceptual SANS instruments with each other for each proposed moderator, it is important to view their performance in the context of the SANS instruments already under

construction at the ESS. In this section it is assumed the  $15 \times 15 \text{ cm}^2$  moderator is selected and the performance of the SANS instruments LOKI and SKADI is sourced from [11]. The  $Q$ -range and resolution is shown for all 4 instruments in Figure 167, where the longest configurations are used. The conventional instruments ConvSANS, LOKI and SKADI used source aperture of 2 cm diameter and sample aperture of 1 cm diameter, while the WOF-SANS instrument had the sample immediately after the focusing optic. The conventional instruments used 1 cm pixel resolution while the WOF-SANS used 4 mm due to the different modes of operation. Additional details on instrument configurations can be seen in Table 40. The conventional SANS achieves a smaller minimum  $Q$  along with better resolution due to both the total instrument length and length of the collimation section, though this length also limits its bandwidth. The WOF-SANS instrument has significantly different characteristics, showing both a better minimum  $Q$ , resolution and bandwidth. The resolutions of the four instruments are compared directly at three  $Q$ -values in Table 41.

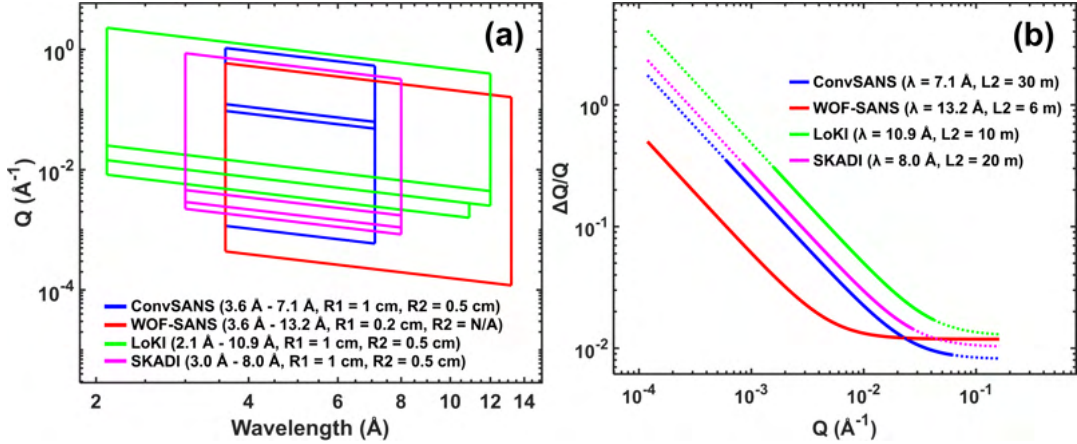


**Figure 167:** (a)  $Q$ -ranges as a function of wavelength for ConvSANS and WOF-SANS in comparison to the  $Q$ -ranges reported for LoKI and SKADI [11]. (b) FWHM of the  $Q$  resolution as a function of scattering vector  $Q$  for ConvSANS and WOF-SANS in comparison to the  $Q$  resolutions of LoKI and SKADI. All resolutions were calculated for  $\lambda_{max}$ , as given in (a), and for the longest configuration of each instrument. The dashed lines are extensions of the curves to match the  $Q$ -range of WOF-SANS for visual comparison.

**Table 40:** Parameters and results of  $Q$  and  $\Delta Q/Q$  calculations of Figure 167.

Instrument	L1 (m)	L2 (m)	$\lambda$ ( $\text{\AA}$ )	R1 (cm)	R2 (cm)	$Q_{min}$ ( $\text{\AA}^{-1}$ )	$Q_{max}$ ( $\text{\AA}^{-1}$ )	$\Delta Q/Q$
ConvSANS	30	30	7.1	1	0.5	5.9E-4	-	0.3536
	30	3	3.6	1	0.5	-	1.06	0.0243
WOF-SANS	8	6	13.2	0.2	N/A	1.2E-4	-	0.4960
	8	6	3.6	0.2	N/A	-	0.6	0.0435
LoKI	8	10	10.9	1	0.5	1.6E-3	-	0.3032
	3	1.5	2.1	1	0.5	-	2.3	0.0881
SKADI	20	20	8.0	1	0.5	8.4E-4	-	0.3307
	4	1.6	3.0	1	0.5	-	8.7E-1	0.0409

The instruments are also compared on wavelength spectrum and flux on sample, the results can be seen on Figure 168. Compared to the ESS instruments LOKI and SKADI, the ConvSANS instrument sacrifices some flux especially at the smallest sample sizes to achieve the better resolution characteristics already discussed. The WOF-SANS instrument is capable of outperforming all other instruments in terms of flux. However, it should be noted that achieving the best resolution requires a large sample, which can be placed further away from the detector. According to a 2016 paper, LoKI is predicted to have the highest flux worldwide among SANS instruments [179]. Therefore, the WOF-SANS instrument, which is able to outperform LoKI, is expected to become the world-leading instrument in this field.

**Table 41:**  $Q$  resolution at same  $Q$  values of  $0.001 \text{ \AA}^{-1}$ ,  $0.01 \text{ \AA}^{-1}$ , and  $0.1 \text{ \AA}^{-1}$  for all four instruments.

Instrument	$Q (\text{\AA}^{-1})$	$\Delta Q/Q$
ConvSANS	0.001	0.2087
WOF-SANS		0.0607
LoKI		0.4849
SKADI		0.2779
ConvSANS	0.01	0.0224
WOF-SANS		0.0133
LoKI		0.0501
SKADI		0.0296
ConvSANS	0.1	0.0084
WOF-SANS		0.0119
LoKI		0.0135
SKADI		0.0106

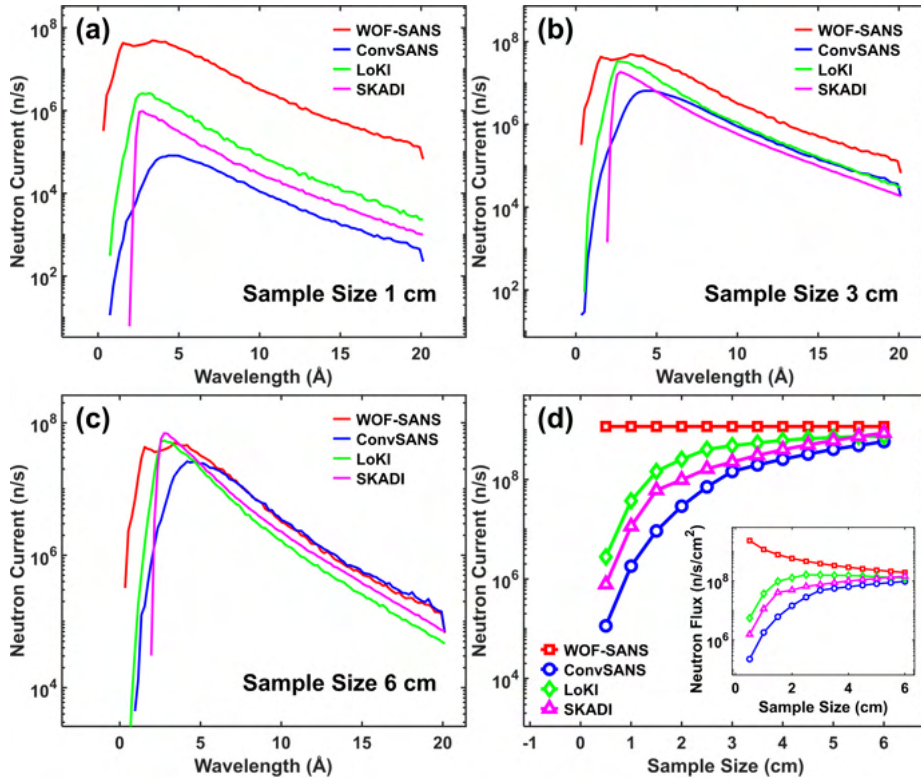


**Figure 168:** (a,b,c) Simulated spectra at the sample position of WOF-SANS, ConvSANS, LoKI, and SKADI for 1, 3 and 6 cm sample sizes. (d) Total neutron current and total neutron flux at the sample position of WOF-SANS, ConvSANS, LoKI, and SKADI as a function of sample size.

The defined Figure of Merit is used to calculate a figure of merit curve as a function of  $Q$  for all instruments and for 3 and 6 cm sample sizes. This comparison can be seen on Figure 169. From the results it is clear the WOF-SANS is significantly different from the three conventional instruments and in general has superior performance.

### 8.2.6 SANS Conclusion

It was shown that both conceptual SANS instruments, ConvSANS and WOF-SANS, perform best on the largest  $15 \times 15 \text{ cm}^2$  moderator. Using this moderator, the ConvSANS instrument was able to fit into the suite of ESS SANS instruments by extending the minimum  $Q$  and providing a slightly better resolution

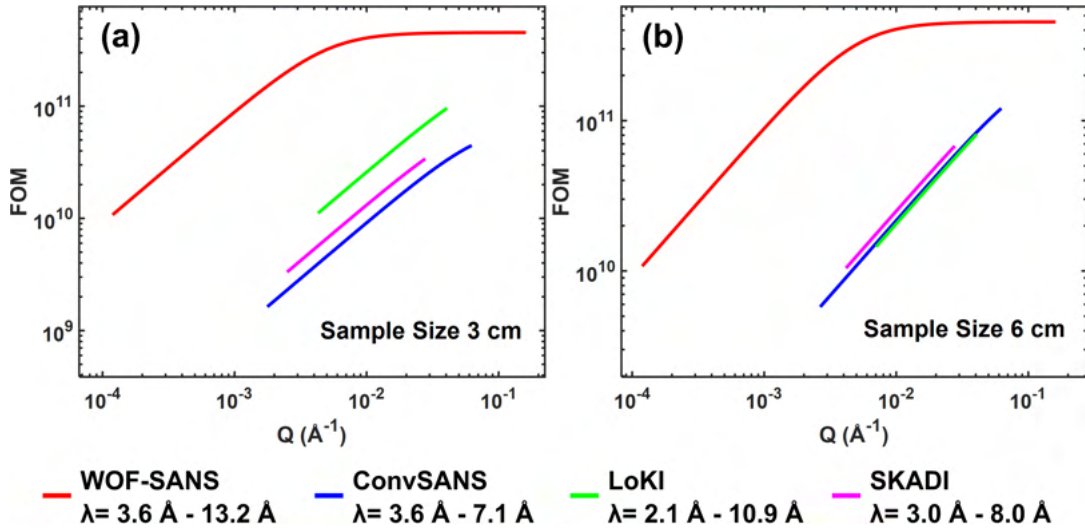


**Figure 169:** FOM as a function of the scattering vector  $Q$  for WOF-SANS, ConvSANS, LoKI, and SKADI. The calculations were performed for two different sample sizes, 3 cm and 6 cm.

at the cost of some flux. The WOF-SANS with its different mode of operation was shown to perform significantly better than ESS instruments under construction, though with the caveat of requiring large samples for the best resolution and potential high cost for Wolter optics.

### 8.3 Optimization of imaging instrument

The ESS instrument suite already has an imaging instrument under construction, namely ODIN [11], which uses a complex chopper system and a neutron guide to achieve enhanced wavelength resolutions necessary for Bragg edge analyses and other wavelength resolved imaging methods. Not all experiments will require these capabilities, and thus one simple way to compliment ODIN is a simple pinhole based imaging instrument that would exploit the larger field of view from a larger moderator, a more homogeneous field of view and e.g., very moderate wavelength resolution. Given the known positions of the monolith and bunker, as well as the requirement for a wide field of view, it was determined that the pinhole should be located 8 meters from the moderator, with the detector situated up to 24 meters away. The geometry can be seen in Figure 170. With the maximum distance between the detector and the pinhole being twice that between the pinhole and the moderator, the anticipated maximum field of view will be twice the width and height of the moderator.

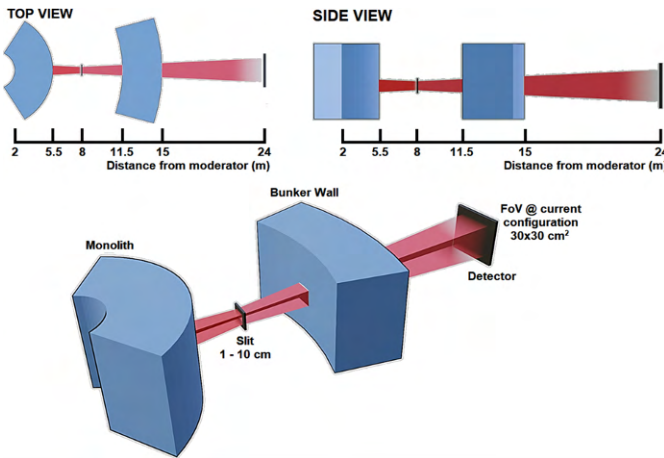


**Figure 170:** Overview of the imaging instrument geometry.

The spectrum reaching the detector with a pinhole of  $2 \times 2 \text{ cm}^2$  can be seen in Figure 171, this scales

with the moderator intensity as expected. In this work square pinholes are used over the usual circular counterpart in order to allow comparisons when using the moderator itself as a pinhole.

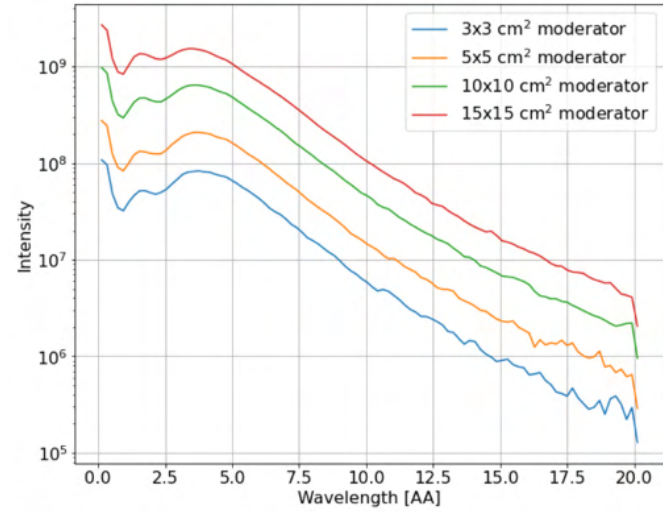


**Figure 171:** Intensity on detector for the imaging instrument when using a  $2 \times 2 \text{ cm}^2$  pinhole with each of the different proposed moderators

### 8.3.1 FOM Definition

For an imaging instrument there are several factors that should contribute to the figure of merit. In the following intensity refers to intensity on the detector,  $L$  the distance from pinhole to detector and  $D$  the size of the pinhole.

- Intensity: The figure of merit should increase when the required exposure time is decreased, which is here determined by the intensity in the pixel on the detector with the lowest intensity within the defined field of view.
- Field of View: the figure of merit would be higher for an instrument that can provide a larger field of view, so the figure of merit is multiplied by the field of view area. Unless otherwise specified, the field of view is found as the largest square area centered on the detector where no pixel is less than 75% of the maximum intensity.
- Collimation: the figure of merit should be normalized to the collimation provided by the instrument, changing the  $L/D$  ratio results in a  $(D/L)^2$  change in the intensity. To normalize for a linear increase in intensity, the figure of merit is thus multiplied by the square root of  $L/D$ .
- Evenness: The figure of merit should decrease as the image becomes less flat. Here, we assess flatness using the standard deviation of intensity in the detector pixels within the defined field of view. This assessment is represented as the square root of the inverse of the standard deviation

The full expression for the figure of merit of an imaging instrument used in this work can thus be written as,

$$FOM = I_{\min} \cdot FOV \cdot \sqrt{L/D} \cdot \sqrt{\frac{1}{std(I)}} \quad (18)$$

### 8.3.2 Imaging instrument performance

The imaging instrument can adjust its collimation using the pinhole and the sample-detector position along the beam outside the bunker (on an optical bench), for the purpose of this report we have investigated four different configurations, for simplicity only using the outmost measurement position at 24 m, as shown in Table 42.

**Table 42:** Investigated distance and pinhole configurations for imaging instrument.

L (cm)	Pinhole detector distance	D (cm)	pinhole size	L/D
	1600 cm		1 cm	1600
	1600 cm		2 cm	800
	1600 cm		3 cm	533
	1600 cm		5 cm	320

If we assume the optimal field of view for each configuration is twice the dimensions of the viewed moderator, we can then evaluate the figure of merit for each moderator at each configuration, the result is shown in Figure 172. Generally, the larger moderators perform better, and this trend is stronger at high collimation ratios than at low ratios.

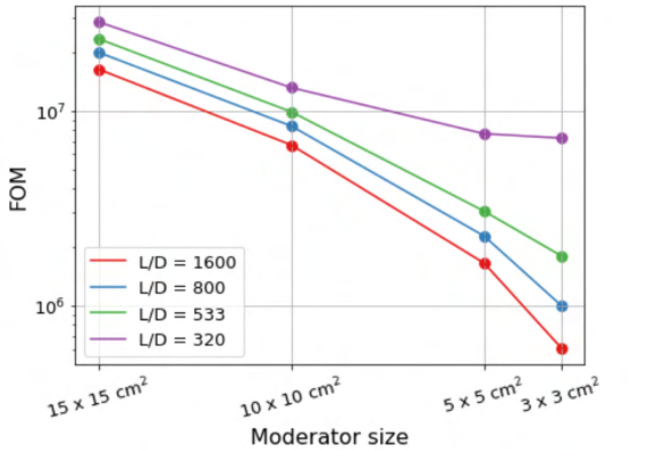


**Figure 172:** Figure of merit for the imaging instrument with different pinhole sizes resulting in different  $L/D$  values for all proposed moderators.

Since the two smallest moderators correspond directly to the pinholes used for the two lowest  $L/D$  values, it is possible to reconfigure the instrument to not use a pinhole for these configurations as seen in Table 43.

**Table 43:** Configurations of imaging instrument that use the moderator itself as pinhole definition when possible.

Moderator Size ( $\text{cm}^2$ )	$L/D = 20$ $D = 5 \times 5 \text{ cm}^2$	$L/D = 533$ $D = 3 \times 3 \text{ cm}^2$	$L/D = 800$ $D = 2 \times 2 \text{ cm}^2$	$L/D = 1600$ $D = 1 \times 1 \text{ cm}^2$
$15 \times 15$				Pinhole 8 m from moderator
$10 \times 10$				Detector 24 m from moderator
$5 \times 5$	No pinhole Detector 16 m from moderator $L = 16 \text{ m}$			$L = 16 \text{ m}$
$3 \times 3$	No pinhole, $D = 3 \times 3 \text{ cm}^2$ Detector 9.6 m from moderator $L = 9.6 \text{ m}$	No pinhole Detector 16 m from moderator $L = 16 \text{ m}$		

The configurations using a 16 m distance from the moderator would be limited by restrictions in allowed size of gaps in the bunker wall, which ends 15 m from the moderator. Here we assume that these gaps can be increased by additional shielding around the instrument cave. The lowest  $L/D$  of 320 for the  $3 \times 3 \text{ cm}^2$  moderator can only be achieved by moving the detector position into the bunker. Even though this is most likely not feasible, we included it for completeness. Assuming the field of views would be twice the one of the moderator, these configurations result in the figure of merit shown in Figure 173. Note that the low collimation options for the smallest moderators now achieve the highest figure of merit.

Viewed as a whole, the imaging instrument with the small moderators excels at lower collimation, but struggles with high collimation.

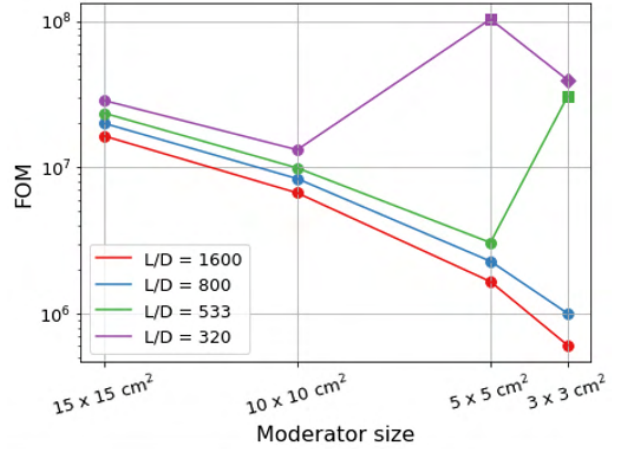


**Figure 173:** Figure of merit for the imaging instrument with different pinhole sizes resulting in different L/D for all proposed moderators, and here using the moderator as pinhole when feasible, these are shown as square points. The single diamond configuration represents the case where the distance had to be reduced to 9.6 m to achieve desired L/D.

The feasibility of using the moderator as pinhole is doubtful as neutrons could scatter close to it and still reach the image, blurring the image. The required opening in the shielding would be much larger than the other configurations, resulting in severely increased background. The configurations using the moderator as pinhole were studied for completeness, but it was decided not to continue investigation despite their impressive low collimation performance.

So far the field of view has been assumed to be twice that of the moderator. The beam for each configuration is now examined to find the field of view corresponding to the intensity at the edge falling to no less than 75% of the maximum intensity. An example of such an investigation is seen in Figure 174. The smallest moderator is almost the same size as the pinhole, and thus suffers in terms of evenness, yet the larger moderators each have a successively larger homogenous area. They also have increased brightness in the area nearest the target at top of the moderator, which after inversion from the pinhole camera correspond to a larger intensity near the bottom of the detector, detracting from the flatness of the distribution. The same procedure is followed for all configurations.

If we plot the achieved field of view and corresponding FOM for each configuration of pinhole and moderator size (Figure 175), it can be seen, that the actual field of view is less than twice the moderator size, except for a single configuration of the smallest moderator. The overall trend in the figure of merit is similar to the fixed fields of view with pinholes in all configurations, and thus we conclude that the fixed field version is sufficient for further analysis.

### 8.3.3 Performance comparison to ESS instrument

In order to investigate whether the conceptual imaging instrument is relevant for ESS it is compared to the ODIN imaging instrument already under construction. Here it is assumed, that the  $15 \times 15 \text{ cm}^2$  moderator is chosen for the conceptual instrument, while the performance of ODIN is calculated using the butterfly moderator with same proton power on target. For this comparison it is important to note that ODIN uses a guide to extend the instrument length and thus significantly improves energy resolution, along with a comprehensive chopper setup that allows it to customize this resolution on demand. Such options are much more limited for the conceptual instrument without a guide. A comparison of flux as a function of  $L/D$  can be seen in Figure 176 where the conceptual instrument achieves a higher flux at all resolutions.

The figure of merit used in this section for the two instruments are also compared as a function

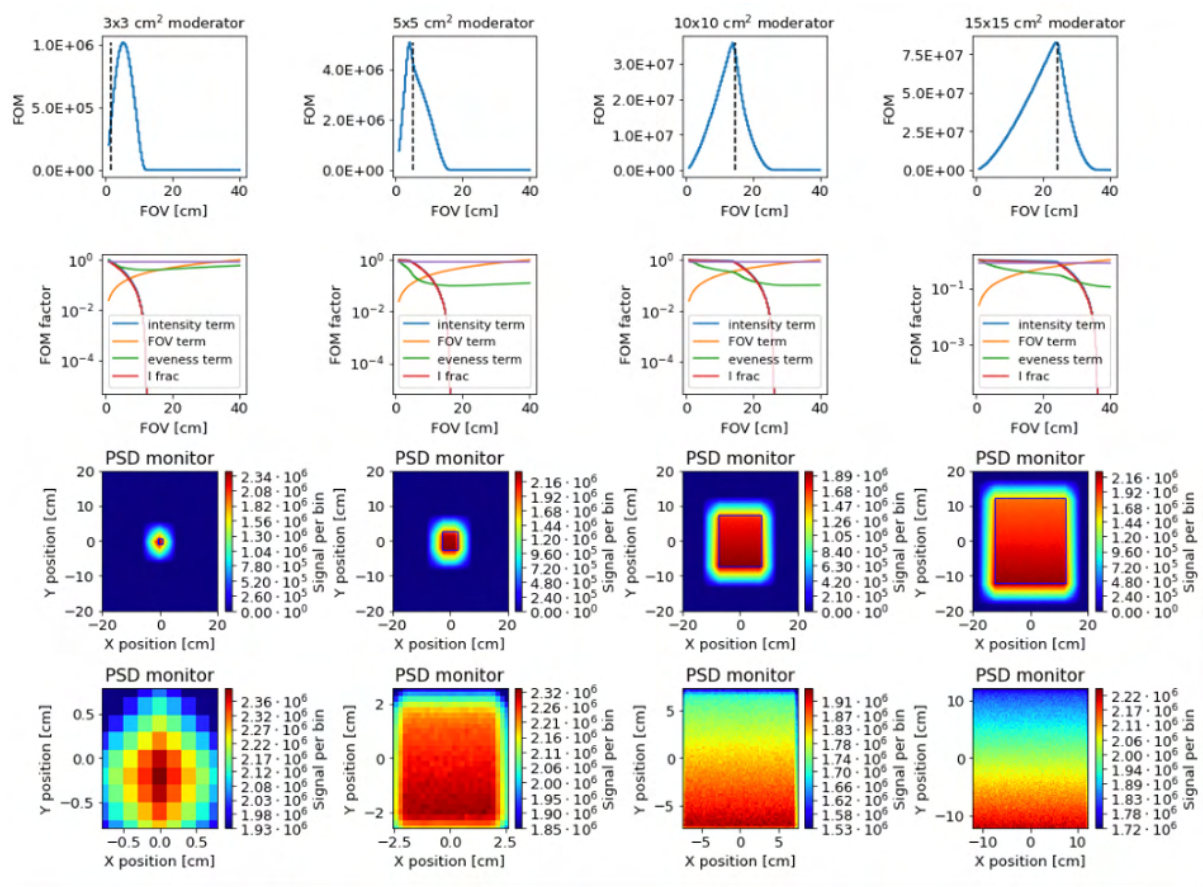


**Figure 174:** Example of FOM calculation for all moderators with  $2 \times 2 \text{ cm}^2$  pinhole corresponding to a  $L/D$  of 800. Each column corresponds to a moderator size. The top graph is the FOM as function of used FOV with the dashed line showing the used FOV where falloff of 75 % of maximum intensity is used. The second row is a decomposition of the factors included in the FOM along with the ratio between lowest and highest intensity. The third row is the full detector with a black box showing the FOV. The last row is the FOV cut from the detector showing the homogeneity, notice the limited color scale.

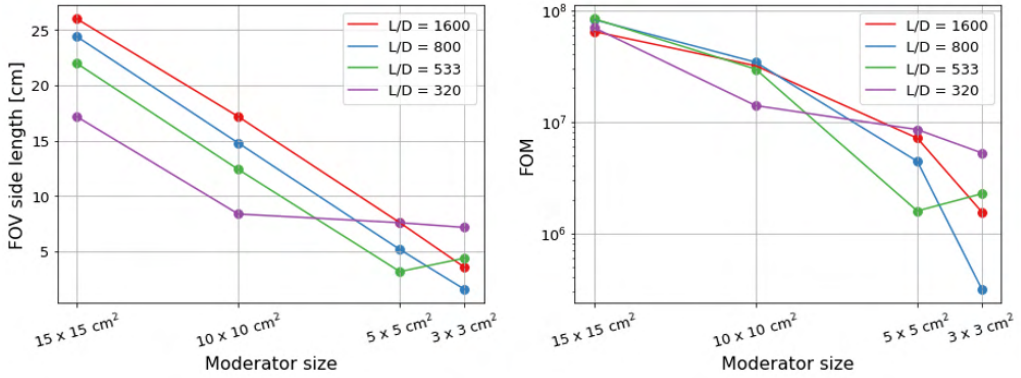


**Figure 175:** Left: Field of view where the minimum intensity is 75 % of maximum for all configurations of moderators and pinholes. Right: The corresponding figure of merit for all configurations of moderators and pinholes.

of  $L/D$ , the result is shown in Figure 177. Here the conceptual imaging instrument achieves a higher FOM over the  $L/D$  range, which is primarily caused by the lack of energy resolution in the figure of merit. This is however justified by the requirement of optimizing an instrument that should compliment ODIN. While the conceptual "simple" imaging instrument can handle the presumably large subset of experiments that do not require energy resolution with significantly shorter measurement times, ODIN could focus on experiments, where customizable energy resolution is necessary.

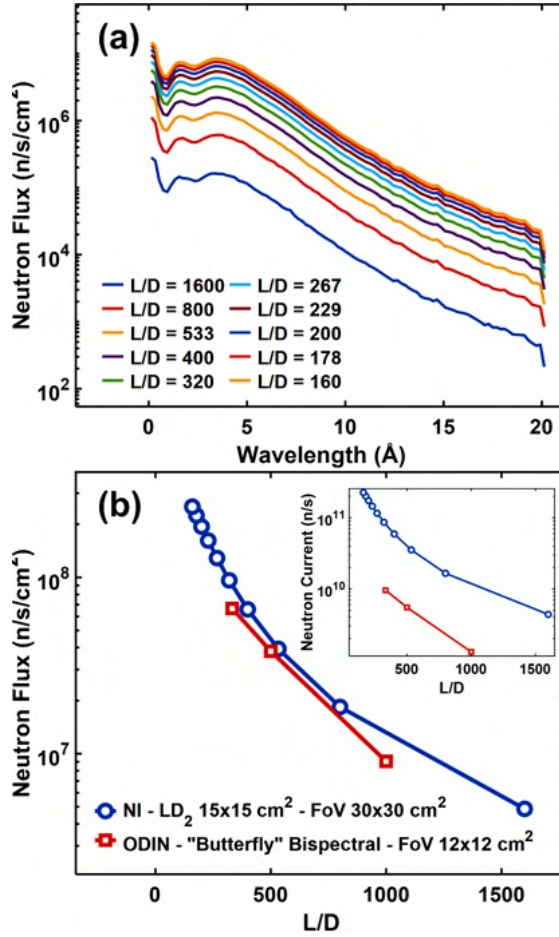


**Figure 176:** (a) Simulated spectra of the NI instrument at the sample position for different  $L/D$  values. (b) Total neutron flux and neutron intensity at the sample position of NI and ODIN as a function of  $L/D$ .

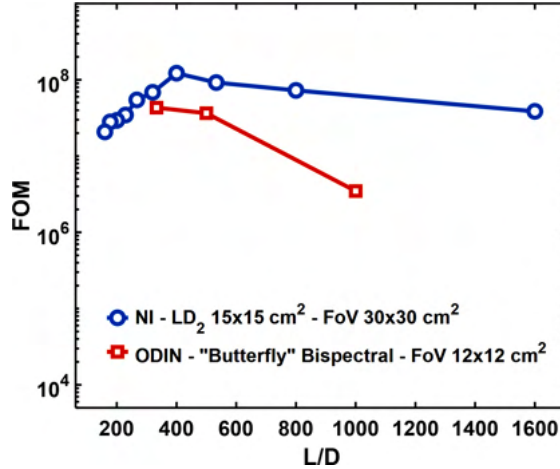


**Figure 177:** FOM as a function of  $L/D$  for NI and ODIN. The ODIN FOM is restricted to the simulated data for  $L/D = 1000, 500$ , and  $333$ .

#### 8.4 Achromatic optics for long wavelengths

Typically condensed matter instrumentation for neutron scattering can ignore the effect of gravity, though when going to the VCN region, this becomes a serious issue. While they can be transported with traditional guides, any long collimation section or focusing can be problematic. As part of HighNESS project it was studied how prisms could be used to counteract gravity when used in conjunction with focusing optics.

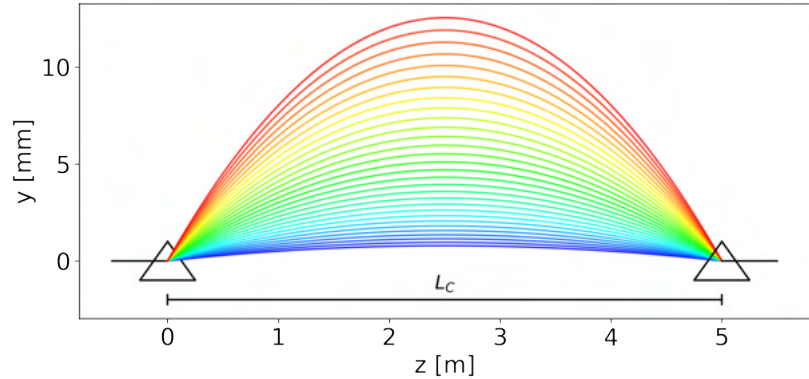


**Figure 178:** Illustration of prisms canceling gravity over a characteristic length depending on the material and geometry of the prisms. (Not to scale and not illustrating the actual path within the prisms.)

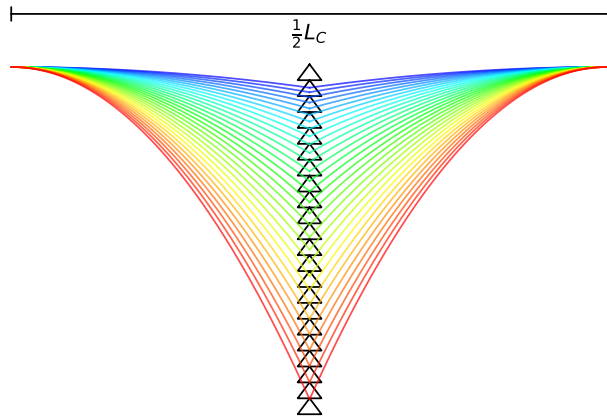


**Figure 179:** Illustration of prisms canceling gravity over half a characteristic length as they are placed halfway between the source and destination. (Not to scale and not illustrating the actual path within the prism.)

A well-collimated white beam incident on a prism will be split according to wavelength such that all the trajectories meet at a later point. The distance to this point correspond on the properties of the prism, both its geometry and material, this is here called the critical distance for a prism. At this point the beam will be divergent, but can be recombined with a second prism, as seen in Figure 178. For some applications it is unwanted to have a prism close to the destination of a beam, here an alternative geometry can be used with a stack of prism halfway between the origin and target, though the distance covered in this configuration is only half the characteristic length, see Figure 179.

These configurations have been tested with the Monte Carlo ray-tracing simulation tool McStas and work as expected, even for beams with some divergence, which act as if there was no gravity in the corrected region.

To demonstrate further we combine these techniques with focusing Wolter optics. As they have limited depth, the majority of the flight path would be in free space where the prism systems can counteract the vertical displacement due to gravity. This system is shown in Figure 180. The instrument starts with a point source and is followed by a stack of Be prisms after 4.88 m which correspond to their characteristic length. The focusing optics are placed right after the prisms. Gravity correction of the focused beam is performed with a stack at the halfway point, again using Be prisms. The focal points of the focusing optics are thus on the source and 2.44 m after the end of the focusing optic.

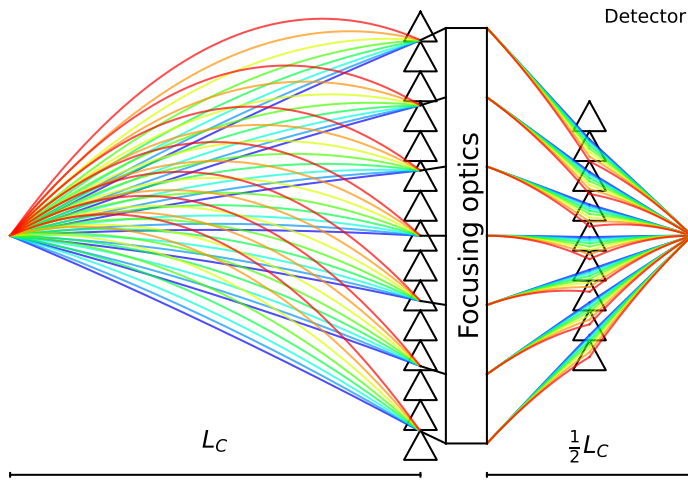


**Figure 180:** Overview of gravity-corrected Wolter optics for VCN.

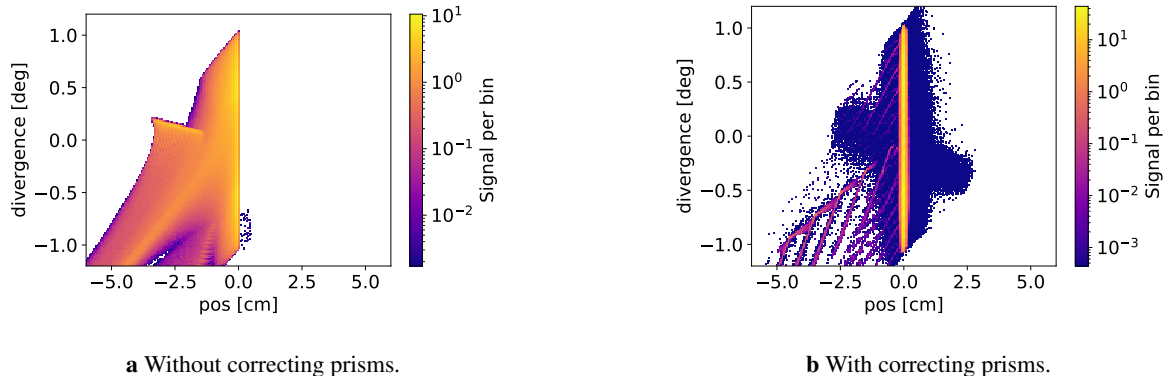


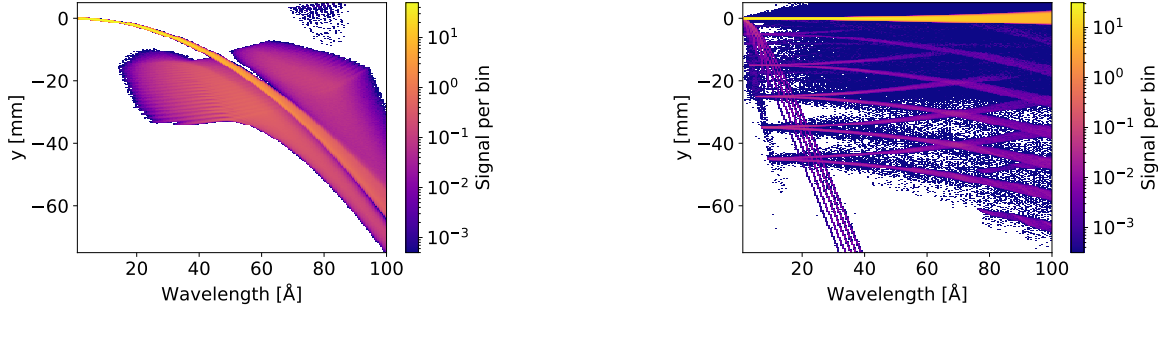
**Figure 181:** Acceptance diagram of vertical divergence and position at the detector with a white beam 10–70 Å

On Figure 181a and Figure 181b the beam quality of this system is compared to a version without the correcting prisms. The difference in beam quality is stark, with the uncorrected version having a drop and complex correlations between position and divergence. The corrected instrument does have artifacts, these are however at intensities 3 orders of magnitude lower than the intended beam. The beam drop as a function of wavelength is investigated in the same manner on Figure 182a and Figure 182b, here it is again evident that even over such small distances, correcting measures are necessary for the VCN wavelength range.

Such an optical system can be a part of the solution for creating efficient and accurate instrumentation that functions over a very broad wavelength range. The system could for example be used to create a SANS instrument, where additional length could be achieved with multiple columns of prisms. These preliminary studies are promising and warrant further investigation in future research.

## 8.5 Neutron Scattering instrumentation summary and cost estimation

This section investigated the performance of three conceptual instruments, a conventional SANS instrument, a Wolter optics-based SANS instrument and an imaging instrument for four moderator candidates of varying size. The smaller moderators had a higher brilliance, but in contrast to the similar survey for the butterfly moderator, all investigated instruments preferred the largest moderator as seen Figure 183. The trade-off between brilliance and size for the investigated liquid deuterium moderator was simply smaller than for the hydrogen-based butterfly moderator, resulting in the opposite outcome. The large



a Without correcting prisms.

b With correcting prisms.

**Figure 182:** Height distribution of the focused beam as a function of wavelength.

liquid deuterium moderator thus complements the butterfly moderator well as it provides a large surface with a similar brilliance at wavelengths over 5 Å, and is especially suited to instruments with performance scaling driven by moderator size or neutron intensity.

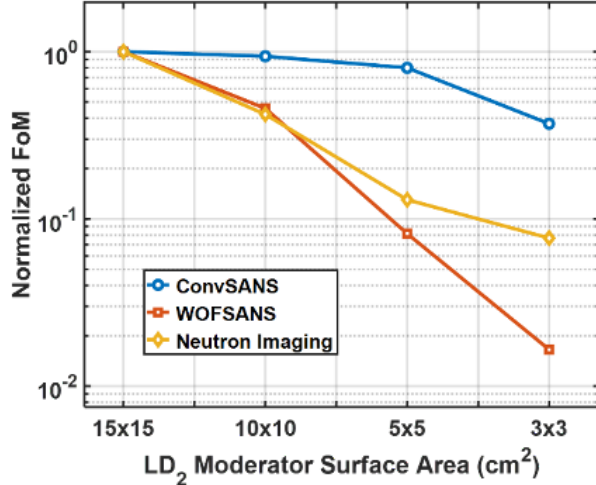


**Figure 183:** Normalized figure of merit as function of moderator size for the three instruments, all normalized to the 15x15 cm<sup>2</sup> moderator. The SANS instruments are for  $Q=1.0E-4 \text{ \AA}^{-1}$  while the imaging instrument is fixed FOV, L/D=533 and with pinholes for all moderator sizes.

It was shown that when using the proposed 15x15 cm<sup>2</sup> moderator, the conceptual instruments are all highly competitive with the ESS instruments under construction and are complementary as they avoid covering exactly the same usecases while offering new capabilities. A rough estimate of the cost for each instrument can be found in Table 44

**Table 44:** Cost estimates of conceptual instruments.

Instrument	Cost estimate [M€]
ConvSANS	20-30
WOFSANS	20-30
Imaging instrument	15-20

Furthermore, it was investigated how to counteract gravity when transporting neutron beams with a large wavelength range; here, prisms were shown to work well in conjunction with Wolter focusing optics.

## 9 The NNBAR Experiment

### 9.1 Introduction

As described previously, the ESS will be the world’s brightest neutron source. To exploit the unique potential of the ESS for fundamental physics [144], the HIBEAM/NNBAR collaboration is planning a two-stage program of high precision searches for neutron conversions corresponding to a range of baryon number violation (BNV) channels [4, 5]. These culminate in an ultimate sensitivity increase for a search for free  $n \rightarrow \bar{n}$  conversions which is three orders of magnitude beyond that previously achieved at the Institut Laue-Langevin (ILL) [21]. Such leaps in sensitivity in tests of a global symmetry are rare. In this section we describe the conceptual design report for the NNBAR experiment.

An observation of BNV via neutron oscillations would be a discovery of fundamental significance which would falsify the Standard Model (SM) of particle physics and address a number of key, open questions in modern physics [180]. These include the origin of the matter-antimatter asymmetry (baryogenesis), the possible unification of fundamental forces, and the origin of neutrino mass [181, 182, 183, 184, 185, 180].

The first stage of the program, HIBEAM (High Intensity Baryon Extraction and Measurement), would use a dedicated fundamental physics beamline for searches for feeble interactions of neutrons with sterile neutrons  $n'$  from a “dark” sector of particles [186, 187, 188]. HIBEAM also allows the test and prototype experiments for the second stage, NNBAR. The program exploits the unique capability of the ESS for high precision neutron conversions and fits well in the future experimental physics landscape. It should also be noted that tests of fundamental symmetries and searches for dark sector particles and feebly interacting particles are regarded as “essential activities” in the 2020 European Particle Physics Strategy [189].

The Figure of Merit (FOM) for a free  $n \rightarrow \bar{n}$  search is given by  $\text{FOM} = N \cdot \langle t^2 \rangle$ , where  $N$  is the number of free neutrons arriving at the carbon target after a propagating over a time  $t$ . A high sensitivity search therefore requires a large intensity and neutron propagation time. This has driven the design of the experiment, which is described in this paper. A bespoke liquid deuterium moderator provides a shift of the wavelength range towards colder neutrons compared with the upper moderator. The availability of the LBP, which corresponds to three normal-sized beam ports, contributes to a high neutron rate. Highly efficient neutron transmission and focusing is then provided by a system of neutron guides placed in the region behind the LBP. Neutrons are focused through a magnetic field region of less than around 5 nT to focus the neutrons in the direction of the detector located upstream. The target is surrounded by a detector to measure the multi-pion signature arising from the annihilation of baryon number via the interaction of an antineutron and a nucleon in a carbon nucleus.

This section is organised as follows. In Section 9.2 the scientific motivation of the project is described. Software and the moderator are covered in Sections 9.3 and 9.4, respectively. The beamline, stretching from the target monolith, through the ESS instrument and to a beamedump 200 m away is described in Section 9.5 together with estimates of the radiation shielding which is needed. The optics system, together with expected performance, is outlined in Section 9.7 and is followed by descriptions of the magnetic shielding and (Section 9.9) vacuum design (Section 9.10). The design of the annihilation detector and its expected performance for signal reconstruction and background rejection is given in Section 9.11. Following Section 9.6 which covers civil engineering aspects to this work, the experiment costing is described in Section 9.12. The experiment’s sensitivity is then discussed (Section 9.13) before a conclusion and outlook are given.

### 9.2 Scientific Motivation and the modelling of neutron conversions

This Section describes the motivation for searching for  $n \rightarrow \bar{n}$  and the phenomenology of the conversion process which informs the strategy for the search.

### 9.2.1 Neutron oscillations and baryon number violation

Of all of the empirically observed conservation laws, that associated with baryon number is arguably the most fragile. As Sakharov showed, baryon number violation is an essential condition for a theory to explain the origin of the observed matter-antimatter asymmetry[190]. Furthermore, like lepton number ( $\mathcal{L}$ ), baryon number corresponds to a so-called accidental symmetry of the SM, which is typically broken when the SM is extended [183, 191, 192, 192, 182].

BNV is even expected to be violated in the SM itself, albeit at tiny rates via non-perturbative sphaleron processes [193, 194, 195, 196]. It should in fact be pointed out that sphalerons provide an intriguing symbiosis between  $n \rightarrow \bar{n}$  and two other candles of new physics, proton decay and neutrinoless double beta decay. The sphaleron interaction can be represented as a nine-quark-three lepton interaction:  $QQQQQQQ\ QQQL\ LL$ . This is a combination of  $n \rightarrow \bar{n}$ , proton decay and a  $\Delta\mathcal{L} = 2$  process. Since sphalerons are fundamental predictions of the SM, this implies that if any two of these processes exist, the third is expected.

A strictly empirical view of BNV searches highlights the need for  $n \rightarrow \bar{n}$  searches, as a BNV-only process in which baryon number is the only hitherto conserved quantity which is violated. Single nucleon two-body decay searches (e.g.  $p \rightarrow \pi^0 e^+$  or  $p \rightarrow \pi^+ \nu$ ) require simultaneous lepton and baryon number violation to ensure angular momentum conservation. The  $\Delta\mathcal{B} = 2$  processes of  $n \rightarrow \bar{n}$  transitions and dinucleon decays would lead to matter decay. This has have been sought at various experiments, most recently at Super-Kamiokande [197, 198, 199, 200, 201]. However, only searches for free neutron conversions provide a theoretically clean and high-precision way to search for BNV-only processes.

A high precision search for free neutrons converting to an antineutrons violates baryon number by two units ( $\Delta\mathcal{B} = 2$ ) which would occupy a unique and complementary experimental role in the landscape of searches for new physics.

### 9.2.2 Neutron oscillations in scenarios of physics beyond the Standard Model

In an effective field theory approach, the  $n \rightarrow \bar{n}$  transition can be described with dimension-nine operators  $\mathcal{O}_{n-\bar{n}} \propto (udd)^2/\Lambda^5$  where  $\Lambda$  is the scale for the new physics [202, 203]. Dimensional reasoning thus implies a sensitivity to  $\Lambda \sim \mathcal{O}(10) - \mathcal{O}(1000)$  TeV for an NNBAR search which would exceed the previous ILL search by three orders of magnitude in sensitivity. Such a scale is beyond the sensitivity reach of current or planned colliders [204].

Calculations for  $n \rightarrow \bar{n}$  within ultraviolet extensions of the Standard Model depend on the low-energy dynamics of quantum chromodynamics (QCD). Since the scales for new physics and for quark confinement are different, predictions are made for the coefficients of the six-quark operators while the matrix elements between neutron and antineutron states are determined by nonperturbative QCD. These latter calculations have been performed with the MIT bag model [205, 206] and, more recently, with lattice QCD (LQCD) [207, 208, 209, 210].

Models which predict observable  $n \rightarrow \bar{n}$  arising from BNV at TeV and PeV scales include scenarios of  $R$ -parity violating supersymmetry and extra dimensions [181, 183]. The extra dimensional models have their origin in superstring theory [211]. One such type of model [191, 212] gives an example of how proton decay can be strongly suppressed but  $n \rightarrow \bar{n}$  transformations take place at observable rates. This is also seen in an extra-dimensional model with a left-right gauge symmetry broken at a scale  $\mathcal{O}(10^3)$  TeV [213]. Neutron-antineutron oscillations are predicted in various scenarios of baryogenesis [184, 203, 214, 215, 185, 216]. One example of a class of models predicting observable  $n \rightarrow \bar{n}$  transitions are UV-complete models of post-sphaleron baryogenesis (PSB) [203, 184, 217, 185]. Figure 184 shows the likelihood probability for a PSB model parameter as a function of the transition time. The Figure also shows the sensitivity of the  $n \rightarrow \bar{n}$  oscillation time to a mass scale in a  $R$ -parity violating supersymmetry scenario. Limits from earlier searches [21, 197] are shown (see Section 9.2.5 for more details) as is the sensitivity of NNBAR assuming a factor of 1000 improvement in the FOM compared with the ILL experiment.

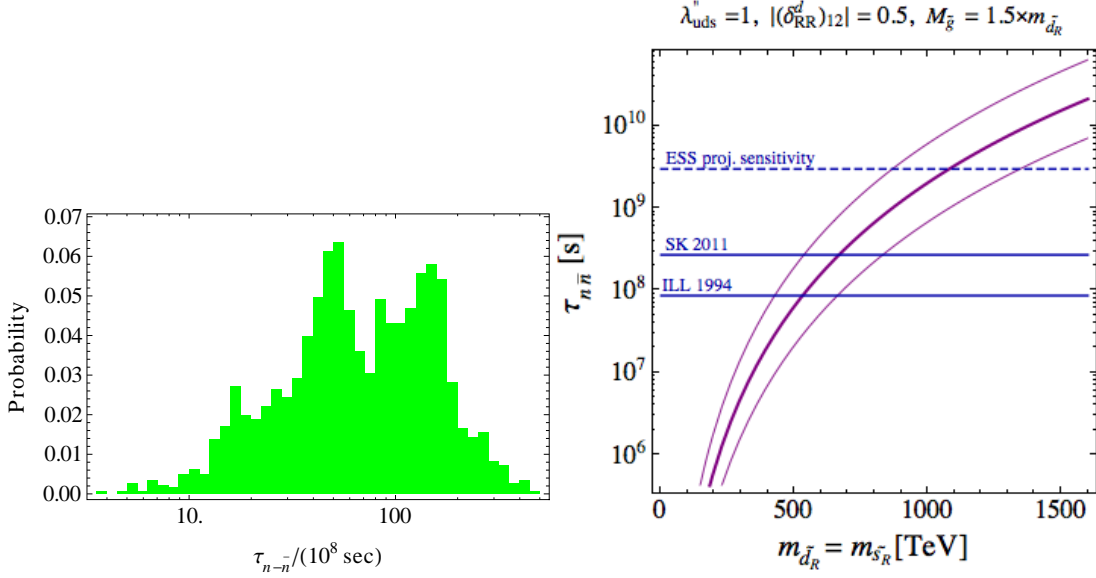


**Figure 184:** Left: likelihood probability for a PSB model parameter as a function of the  $n \rightarrow \bar{n}$  oscillation time. From Reference [185]. Right: relationship between the oscillation time and a mass scale in a R-parity violating supersymmetry scenario. From Reference [218]. Limits from the ILL [21] and Super-Kamiokande [197] searches are shown together with the approximate sensitivity of the NNBAR experiment.

Another open question which  $n \rightarrow \bar{n}$  processes may address is the origin of neutrino mass. A symbiosis exists between  $n \rightarrow \bar{n}$  transitions and neutrinoless double  $\beta$  decays. They are the baryonic or leptonic equivalent of each other. Each process violates  $\mathcal{B} - \mathcal{L}$  (the quantity associated with the anomaly-free SM symmetry) by two units and imply Majorana masses. Both processes are connected in unification models, such as in left-right-symmetric scenarios [219, 220, 221].

### 9.2.3 Free and bound neutron-antineutron conversions

The Hamiltonian for the evolution of an initial beam of slow moving neutrons which can convert to antineutrons after a time  $t$  is shown in Equation (19).

$$i \frac{\partial}{\partial t} \begin{pmatrix} n \\ \bar{n} \end{pmatrix} = \begin{pmatrix} E_n & \epsilon_{n\bar{n}} \\ \epsilon_{n\bar{n}} & E_{\bar{n}} \end{pmatrix} \begin{pmatrix} n \\ \bar{n} \end{pmatrix} \quad (19)$$

The term  $\epsilon_{n\bar{n}}$ , to be calculated from a theory of new physics, drives the  $n - \bar{n}$  mixing.

The probability that a neutron has transformed to an antineutron at time  $t$  is given by Section 9.2.3

$$P_{\bar{n}}(t) = \frac{4\epsilon_{n\bar{n}}^2}{(\Delta E)^2 + 4\epsilon_{n\bar{n}}^2} \sin^2\left(\frac{t}{2}\sqrt{(\Delta E)^2 + 4\epsilon_{n\bar{n}}^2}\right) \quad (20)$$

Here  $\Delta E = E_n - E_{\bar{n}}$  is the difference in energy of the neutron and antineutron. It is assumed that  $t$  is much shorter than the neutron lifetime.

It can be seen that the conversion probability becomes strongly suppressed when the energy degeneracy between neutron and antineutron is broken, whereas the degeneracy can be protected with magnetically shielding [222, 223, 224]. Free ( $\Delta E \cdot t \ll 1$ ) and bound neutron ( $\Delta E \cdot t \gg 1$ ) oscillations correspond to the limits in  $P_{n \rightarrow \bar{n}}$  given in Equations (21) and (22), respectively.

$$P_{n \rightarrow \bar{n}} \sim (\epsilon_{n\bar{n}}^2 \cdot t)^2 \equiv \left(\frac{t}{\tau_{n-\bar{n}}}\right)^2 \quad (21)$$

$$P_{n \rightarrow \bar{n}} \sim \frac{2 \cdot \epsilon_{n\bar{n}}^2}{(\Delta E)^2} \quad (22)$$

### 9.2.4 Antineutron-nucleon annihilation

The composition and properties of the visible final state produced following an extranuclear  $\bar{n}$  annihilation upon a target nucleus fundamentally impacts the design of any annihilation detector system for NNBAR/HIBEAM.

A model of  $\bar{n}C$  annihilation [225, 226, 227] is used in this work which considers  $\sim 100$  independent annihilation branching channels and includes heavy resonances. The simulations have been bench-marked against available  $\bar{p}\text{-}p$  and  $\bar{p}^{12}\text{C}$  data-sets. Annihilation channels for  $\bar{n}n$  are assumed to be identical to those for  $\bar{p}p$ . Annihilation channels for  $\bar{n}p$  are charge-conjugated to those for  $\bar{p}n$ . The intranuclear cascade and particle transport through the nuclear medium (so-called final state interactions, FSIs) is also modelled.

Table 45 shows the simulated and measured particle multiplicities and the total energy of final state particles, produced after  $\bar{p}^{12}\text{C}$  interactions. The data and simulation agree well. Pionic final states are produced following the decay of heavy resonances.

**Table 45:** Average particle multiplicities compared between data and simulation. From Reference [4].

	$M(\pi)$	$M(\pi^+)$	$M(\pi^-)$	$M(\pi^0)$	$E_{tot}$ (MeV)	$M(p)$	$M(n)$
$\bar{p}\text{C}$ Experiment	$4.57 \pm 0.15$	$1.25 \pm 0.06$	$1.59 \pm 0.09$	$1.73 \pm 0.10$	$1758 \pm 59$	—	—
$\bar{p}\text{C}$ Simulation	4.60	1.22	1.65	1.73	1762	0.96	1.03

### 9.2.5 Previous searches

Free neutron searches have been made at the Pavia Triga Mark II reactor [228, 229] and at the ILL [230, 21]. These are based on the principle underlying NNBAR i.e. a pionic final state induced by the annihilation of baryon number when an antineutron and nuclear interact. The last ILL search [21] gave a limit on the free neutron oscillation time of  $\sim 8.6 \times 10^7$ . This remains the most competitive limit with free neutrons.

Searches have also been made with bound neutrons at large volume detectors. Such searches look for a signature of pions and photons arising from a  $\bar{n}N$  annihilation process occurring inside a nucleus. Searches have been performed at Homestake [231], KGF [232], NUSEX [233], IMB [234], Kamiokande [235], Frejus [236], Soudan-2 [237], the Sudbury Neutrino Observatory [238], and Super-Kamiokande [197, 198].

Limits on conversion times for neutrons bound in nuclei ( $\tau_{nucl}$ ) can be converted to an equivalent limit on free neutron conversion time using the relationship in Equation (23) developed from nuclear physics models [239, 240, 241, 242, 243, 244, 245, 227]. Each nucleus has its own value of  $R$ .

$$\tau_{nucl} = R \cdot \tau_{n \rightarrow \bar{n}}^2 \sim \left( \frac{10^8 \text{ s}}{\tau_{n\bar{n}}} \right)^2 \times 10^{31} \text{ yr.} \quad (23)$$

Super-Kamiokande has currently provided the most competitive inferred limit on the free neutron conversion time. A limit of  $\tau_{n\bar{n}} > 4.7 \times 10^8$  s for neutrons converting in oxygen has been obtained [201]. Super-Kamiokande has also searched for dinucleon decays producing various final states [246, 247, 199].

Figure 185 shows limits on conversion time which have so far been achieved with bound and free neutron searches. Projected sensitivities for the future DUNE experiment [248] are shown. The sensitivity of the future Hyper-Kamiokande experiment has not yet been published.

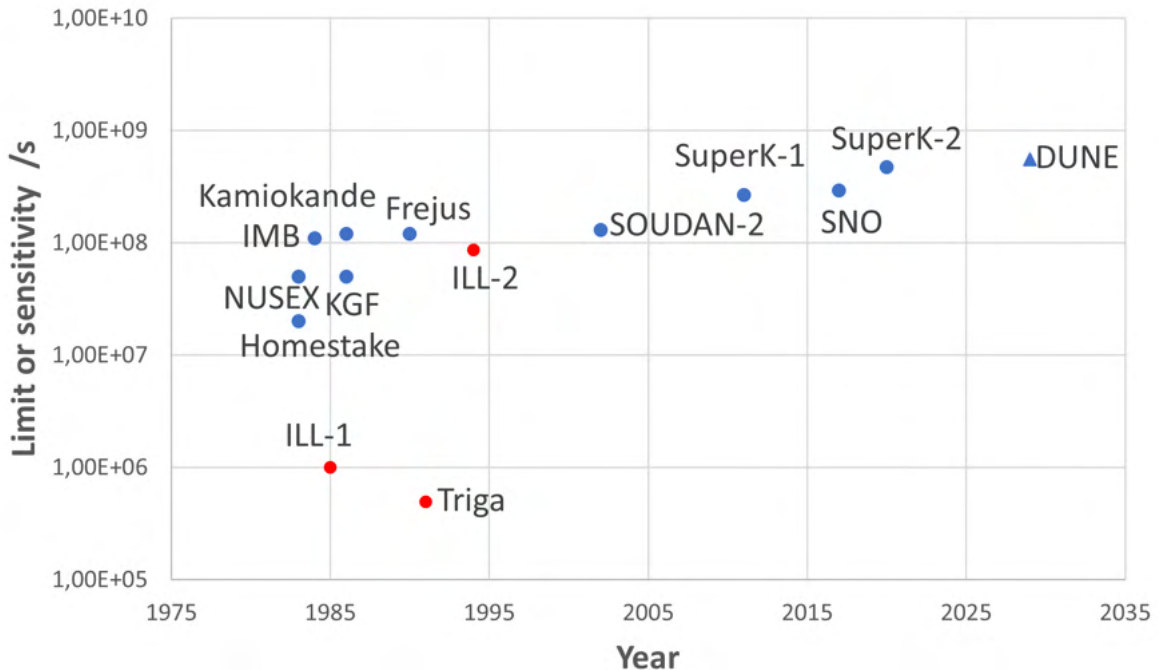


**Figure 185:** Limits from searches with bound neutrons (blue circles) and free neutrons (red circles) and the sensitivities of the future DUNE (blue triangle) experiment.

It should be emphasised that both types of searches (free and bound) are needed. Any comparison between limits from free and bound neutron searches relies model assumptions, such as a point-like conversion process whereas the physics driving a putative conversion is unknown. A signal could potentially appear in one or both search approaches. For example, in one model of low scale BNV, depending on scenario choices, either a suppressed or enhanced bound neutron conversion probability may be expected [249].

### 9.3 Software

In order to calculate the sensitivity of the  $n \rightarrow \bar{n}$  search, it is crucial to undertake the design of the full experiment. This encompasses the development of the ESS lower moderator (see Section 2), the optics system that takes advantage of the Large Beam Port, the creation of a field-free propagation region and the simulation of the NNBAR beamline, and, ultimately, the design of a detector capable of detecting an annihilation signal. Achieving this necessitates a connected series of diverse simulation programs, as emphasized in [250].

An overview of the simulation chain used to construct a comprehensive model of the NNBAR experiment is presented in Figure 186. This simulation chain consists of multiple components, each dedicated to specific aspects of the experiment. It effectively tracks the path of neutrons as they are focused and propagate towards the annihilation detector. The first step is the simulation of the neutron source as described in Section 2. Following this, several different simulations are necessary depending on the particle energy. On the one hand, the reflection and focusing of cold neutrons is modelled using McStas [251] and their propagation in a vacuum tube with suppressed magnetic field region is studied and optimized using the finite-element simulations tool COMSOL [252, 253]. The propagation of fast neutrons, on the other hand, is simulated using MCNP [13] or PHITS [167] in order to determine the required beamline shielding as well as their contribution to the experiment background. The MCPL format [254] is used to exchange particle trajectories between the different tools.

The annihilation detector, which observes the multi-pion final state of the annihilation of antineutron on the carbon foil target must also be modeled. This simulation relies on Geant4 [255], a standard sim-

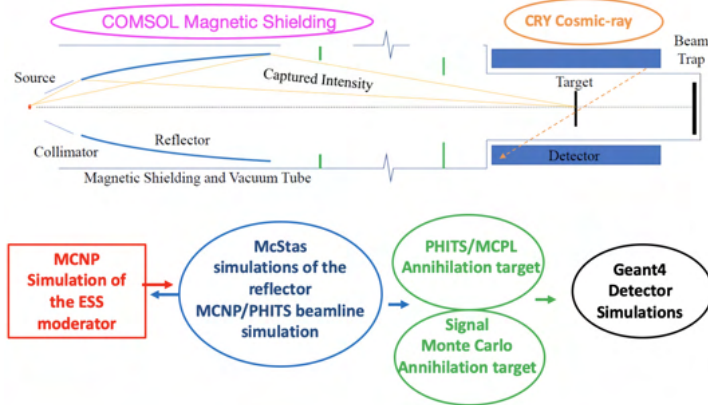


**Figure 186:** Above: An illustrative overview of the essential components required for the NNBAR experiment. Below: A simulation flowchart outlining the simulation and optimization of the NNBAR experiment. MCPL simulations of the ESS lower moderator are used as starting point. The focussing of cold neutrons is studied using McStas while the background stemming from faster neutrons is investigated using MCNP. Finally, Geant4 is used for the detector simulation. The MCPL format is used to exchange data between the different simulations. This figure is sourced from Ref. [5]

ulation toolkit widely employed for detector simulations. The annihilation events are generated using a simulation tool that assumes an initial antineutron interacting with a carbon nucleus [226, 227, 256]. The detector modeling also includes simulating interactions of backgrounds, such as fast spallation products interacting with the foil and external backgrounds, such as those arising from cosmic rays. The cosmic ray particles were generated using the Cosmic-ray Shower Library (CRY) [257].

In addition to the Geant4 full simulation used for the analyses, parameterizations of the detector subsystems were also developed and employed in some cases to provide a fast estimate of the detector response and to cross-check the results obtained from the full simulation.

## 9.4 NNBAR moderator design

The HighNESS project has aimed to design the ideal moderator for NNBAR, which serves as an intense source of cold neutrons. A comprehensive account of the design optimization and engineering studies for this source can be found in Section 2.

## 9.5 The NNBAR beamline

Following their production in the moderator, the neutrons undergo extraction via the Large Beam Port, as detailed in Section 1.1.2. These neutrons are then directed and focused toward the annihilation target, located at a distance of 200 meters from the neutron source.

The LBP holds a central and indispensable role in the NNBAR experiment, being instrumental in achieving the experiment’s sensitivity objectives. It is strategically designed to occupy the equivalent space of three standard ESS beam ports. The LBP’s physical dimensions undergo a gradual increase in size as it extends from a modest area of  $70 \times 105$  square centimeters, situated 2 meters from the neutron source. This expansion culminates with the LBP reaching a size of  $145 \times 110$  square centimeters at the edge of the target monolith. This allows not only to cover a considerable fraction of the solid angle of the lower moderator but to also accept neutrons from the upper moderator at the same time.

However, the LBP serves not only to transport cold neutrons for use in the NNBAR experiment through the target monolith but also leads to a substantial increase in radiation outside of it. Consequently, the NNBAR beamline require additional shielding to handle the heightened dose rate compared to a standard ESS beamline. To determine the necessary amount of shielding, simulations of the entire NNBAR beamline, including the experimental cave and the beam stop, were conducted using the radiation transport code MCNP[13]. A detailed beamline model of the NNBAR beamline was constructed for

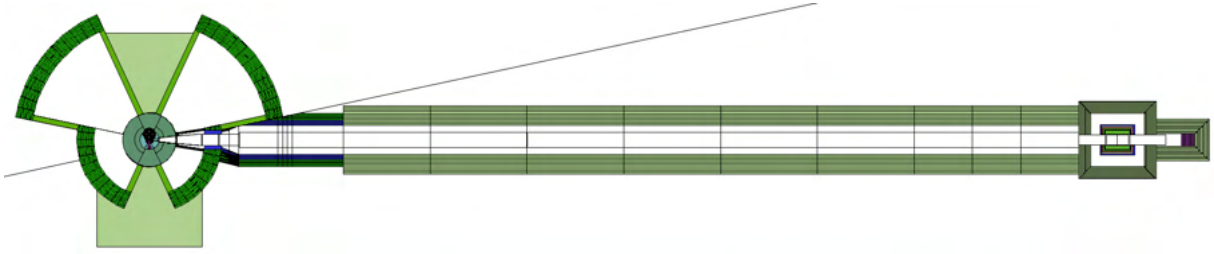


**Figure 187:** Drawing of the NNBAR beamline. The model encompasses the moderator, the Large Beam Port (LBP), the bunker, the NNBAR tunnel, and the NNBAR experimental cave.

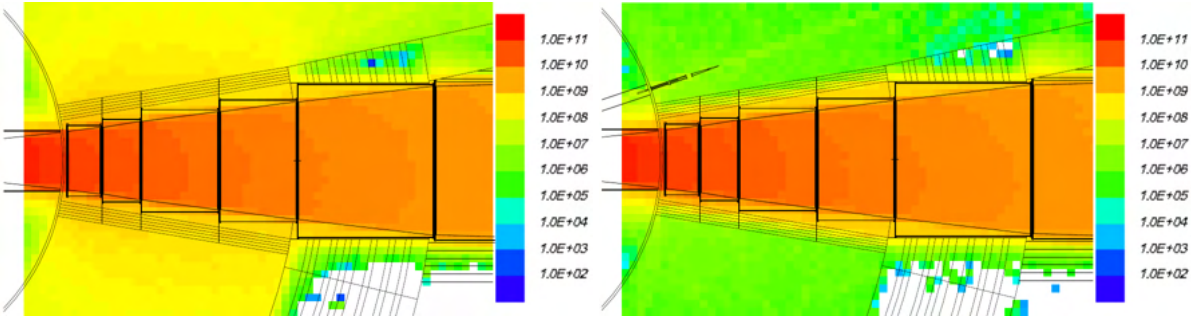


**Figure 188:** Radiation dose map of the inside of bunker close to the Large Beam Port. Left: Radiation dose map without additional shielding. Right: Dose map with 40 cm walls of heavy concrete around the NNBAR beamline.

these simulations using CombLayer[258]. The CombLayer software package allows to define geometry models in C++ and to produce suitable input files for a variety of transport codes. A visual representation of the NNBAR model is provided in Figure 187.

The complete simulation of a beamline, even in the case of a beamline like NNBAR, is computationally expensive. To make these calculations feasible, the simulation of the beamline was split up in separate simulations of different sections of the beamline. For each of these sections, inputs were generated using the duct source method, a standard variance reduction method for long beamlines[259]. However, the unique characteristics of the LBP necessitated the development of a dedicated duct source method. Unlike most regular beamlines at ESS and other neutron facilities, where the neutron distribution can be reasonably assumed to be uniform over the area of their beamport, the large size of the LBP precludes such an assumption. Consequently, when generating the simulation input, it was essential to account for the correlations between neutron position, direction, and kinetic energy.

To achieve this, the coordinates of particles coming from the moderator were sampled to reproduce the distribution at 2 m from the source. The particles were then assigned momenta following the duct source method and kinetic energies following a uniform distribution. Finally, each of these tracks was assigned a particle weight based on the probability density function calculated from their position, momentum and energy in order to reproduce the original distribution[260]. All the beamline calculations presented in this section have been accomplished using this methodology.

Only the radiation doses caused by neutrons were calculated for the results presented in this section. Doses from other particles, e.g. gamma-rays will be evaluated in the future. However, neutrons are expected to be the dominating source of radiation from the LBP and the NNBAR beamline so that the shielding solutions presented here should be still be sufficient when taking other types of radiation into account.

### 9.5.1 NNBAR beamline simulation in the bunker area

The ESS bunker wall was designed with the objective of reducing the radiation dose outside it to a level below the threshold defined as the *supervised area* at the ESS. This threshold is set at  $3 \mu\text{Sv}/\text{h}$ . As per the ESS procedure for shielding calculation, when calculating the expected dose with Monte Carlo

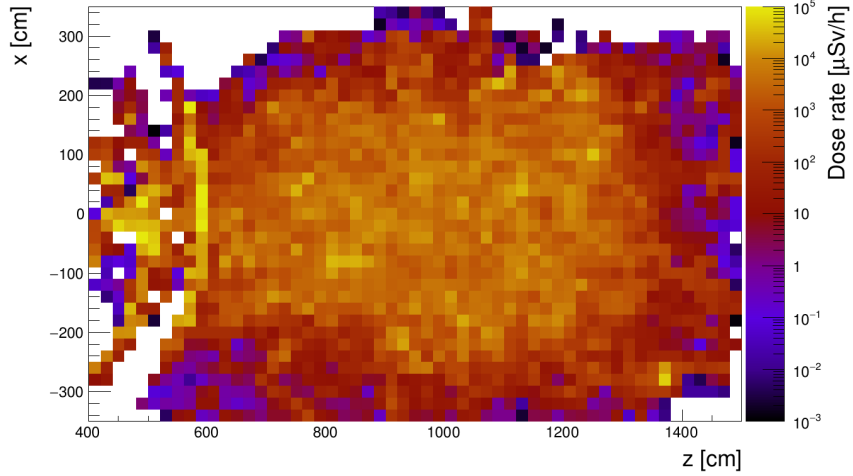


**Figure 189:** Dose map of the top of the existing ESS bunker roof when running the Large Beam Port.

simulations, it is necessary to apply a factor of 2. This factor results in a target value of  $1.5 \mu\text{Sv}/\text{h}$  for the simulation results.

The current design of the bunker wall achieves this target value for the parallel use of 22 standard ESS beamlines at 5 MW without the need for shielding inside the bunker. However, in the case of the NNBAR experiment, due to the size of the LBP, shielding inside the bunker will be necessary. This is illustrated in the left panel of Figure 188 which shows a neutron dose map of the bunker interior. The resulting dose in the vicinity of the beamline exceeds  $100 \text{ mSv}/\text{h}$ , several orders of magnitude higher than what is produced by regular ESS beamlines.

The right panel shows the situation when the beamline is surrounded by 40 cm thick walls of heavy concrete. The dose outside the shielding is reduced by two orders of magnitude and it is similar or somewhat lower of a standard ESS beamline. In Figure 188 above the LBP, the first part of the guide for the HEIMDAL beamline is depicted. As evident, the additional shielding effectively diminishes the background dose generated by the LBP to a level below that produced by HEIMDAL. Thus, it is evident that the dose has been reduced to a sufficient extent, allowing the bunker walls to shield it below the specified limit.

The requirements for the bunker roof differ from those for the wall. Since personnel will not be working regularly on the roof, the established dose limit criteria by the ESS are slightly higher than those for the bunker wall, set at  $25 \mu\text{Sv}/\text{h}$  (with a safety margin of  $12.5 \mu\text{Sv}/\text{h}$  as requested by the safety factor for shielding calculations). The other requirement that was taken into account for the design of the bunker roof was for the dose rates for people outside the experimental area, e.g. the ESS main office building, receive due to skyshine has to be taken into account. The limit for dose received due to skyshine is  $100 \mu\text{Sv}/\text{y}$ [3]. Once again, the design of the bunker roof was selected to meet these limits when operating with the complete set of regular ESS beamlines. However, in the case of NNBAR, it will be necessary to add extra shielding in the area near the LBP. Figure 189 illustrates the situation without any additional shielding. The average dose on top of the roof directly above the LBP is measured at  $3.3(4) \text{ mSv}/\text{h}$ . A conservative estimate of the resulting skyshine can be calculated using the empirical formula:

$$H = h \cdot 7 \cdot 10^4 \sum (H_0 A) \left( \frac{e^{-R/600}}{R^2} \right) \mu\text{Sv}/\text{h}, \quad (24)$$

where  $h$  is the time of exposure,  $\sum(H_0 A)$  is the hadron dose equivalent rate times the surface area and  $R$  is the distance of an exposed person from the source [261]. The calculated dose amounts to  $1.7(2) \text{ mSv}$  per year for an individual working at the ESS Main Office Building, with a working time of  $h = 1800$  hours and a distance of  $R = 136$  meters.

The current study only investigated cases in which the existing roof itself is not modified. This leaves two options to add shielding to the bunker roof. The shielding can be added inside the bunker or on top

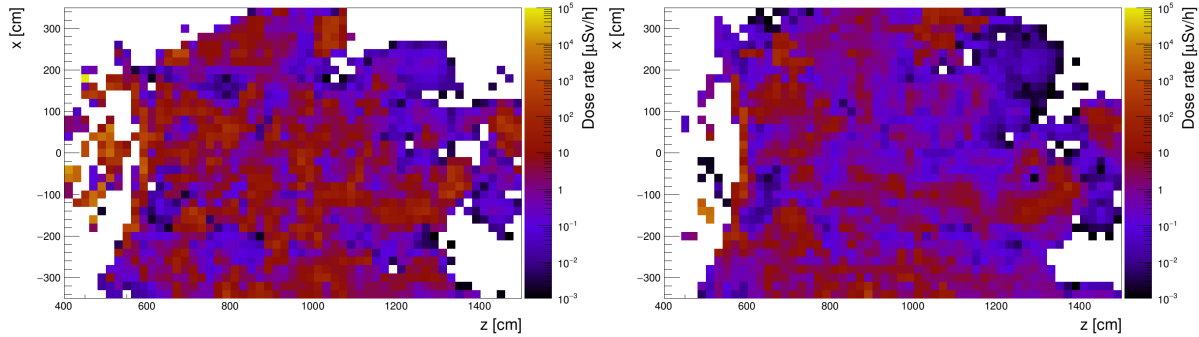


**Figure 190:** Dose map of the top of the existing ESS bunker roof with additional shielding of the LBP. Left panel: Additional shielding of 70 cm inside of the bunker. Right panel: Additional shielding inside the bunker (70 cm of steel) and on top of the roof (40 cm of heavy concrete).

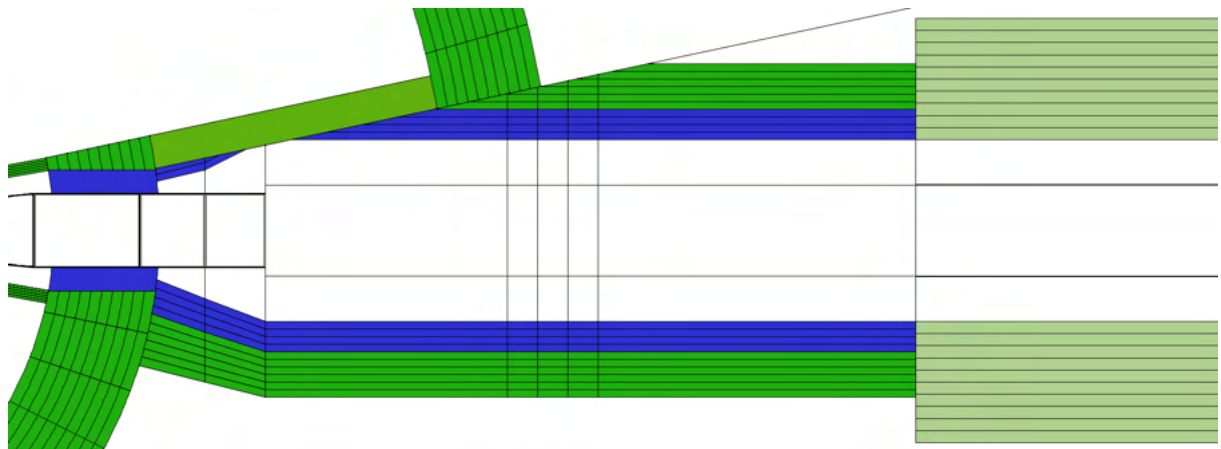


**Figure 191:** Detailed view of the CombLayer model of the NNBAR experiment for the region from the bunker wall until the exit of the experimental hall.

of the existing roof. The size of the NNBAR beamline leaves space to add 70 cm of shielding material between the vacuum pipe and the bunker ceiling. In the current simulation, steel was chosen as material for this additional interior shielding. The left panel of Figure 190 shows the dose map on top of the roof with this addition. The average doses is reduced to 16(2)  $\mu\text{Sv}/\text{h}$  and the skyshine calculated using Equation (24) to 8.5(9)  $\mu\text{Sv}/\text{y}$ . This is at the edge of the dose limit criteria.

The right panel of Figure shows the dose map when also adding 40 cm of heavy concrete on top of the current bunker roof. The average dose is 5.0(7)  $\mu\text{Sv}/\text{h}$  and the skyshine 2.6(4)  $\mu\text{Sv}/\text{y}$ . While more detailed studies are required, this would seem sufficient to fulfill the ESS dose limits.

### 9.5.2 The NNBAR Tunnel

Conducting the NNBAR experiment necessitates the installation of a feed-through in the bunker wall, as well as the creation of an opening large enough to accommodate the NNBAR vacuum pipe and the magnetic shielding structure (refer to Section 9.9).

This necessitates the installation of shielding around the NNBAR vacuum pipe and magnetic shielding to comply with the specified dose limits for the *supervised area*. The vacuum pipe has a rectangular cross section of  $2.4 \text{ m} \times 2 \text{ m}$  up to 18 m. After this, the pipe is round with  $r = 1.5 \text{ m}$ . It's worth noting that existing instruments and infrastructure within the ESS instrument hall impose constraints on the dimensions of the shielding.

The model of the tunnel used in the simulations is shown in Figure 187. Figure 191 provides a more detailed perspective of the area spanning from 10 to 50 meters from the moderator. The initial 25 meters, starting from the bunker, remain within the confines of the D03 experimental hall (as depicted in Figure 7). Within this zone, the NNBAR tunnel's wall configuration comprises 1 meter of steel

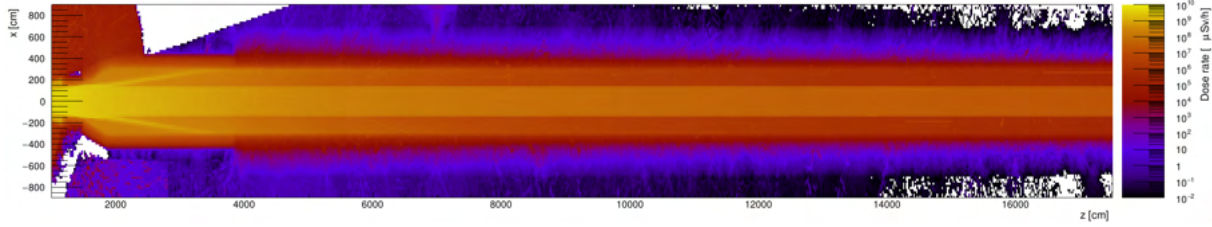


**Figure 192:** Dose map of the NNBAR tunnel.

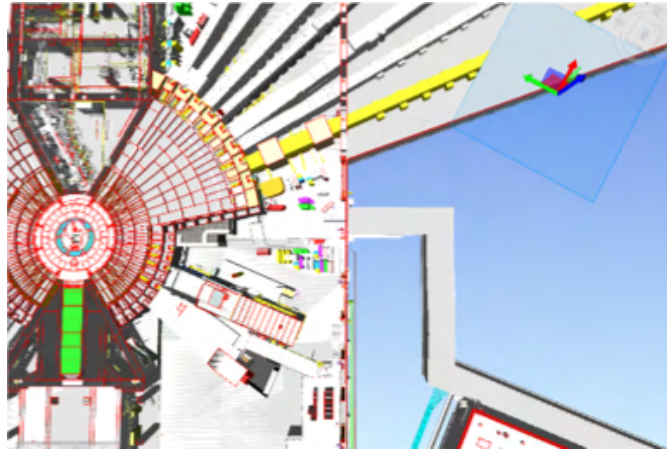


**Figure 193:** The instrument gallery located at the exit of the D03 building

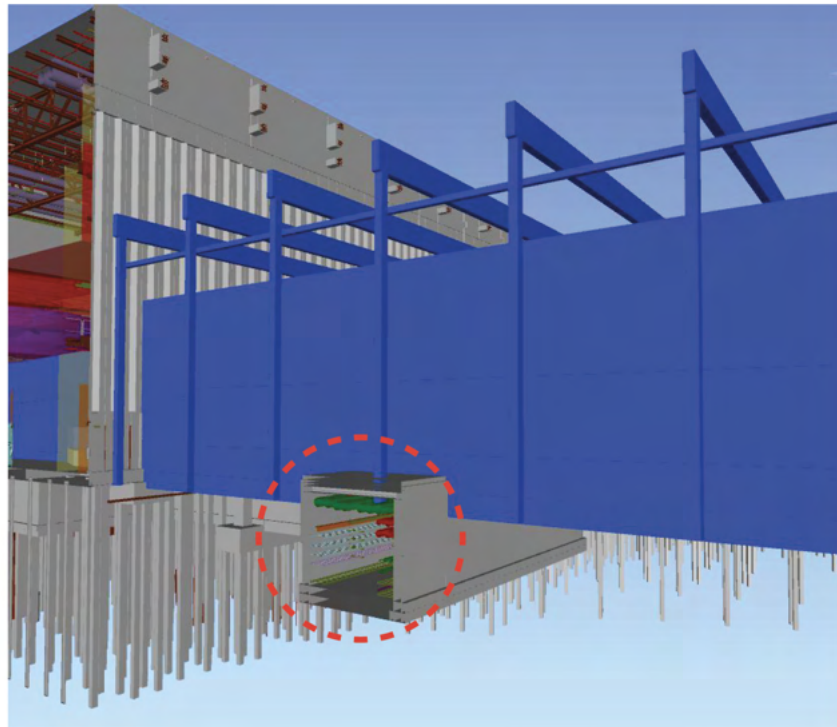
backed by 1.5 meters of heavy concrete. This design was chosen to minimize interference with existing structures and adjacent experiments, notably the LOKI experiment located to the south of the NNBAR experiment. After leaving the bunker, the tunnel widens for a few meters, providing both room for the magnetic shielding of the beamline and facilitating access to the tunnel for tasks such as vacuum maintenance. Beyond the D03 experimental hall, there are fewer space constraints, allowing for the use of regular concrete as the wall material. In the simulations, a uniform wall thickness of 4 meters was initially employed for the entire tunnel. However, the simulation results indicate that this thickness is not required along the entire length.

Figure 192 illustrates the dose map of the NNBAR beamline from the bunker wall up to 175 meters away from the source. The dose rates remain below the limit of  $1.5 \mu\text{Sv}/\text{h}$  for the entire tunnel length. The necessary thickness to achieve this decreases from 400 centimeters just outside the experimental hall to 250 centimeters in proximity to the NNBAR cave. When using heavy concrete outside the experimental hall, the required thickness diminishes to 250 centimeters just outside the experimental hall and 175 centimeters close to the experiment cave.

### 9.5.3 The interface between the NNBAR beamline and the instruments gallery

A particular challenge in designing the shielding for the NNBAR tunnel is the presence of the already existing instrument gallery located beneath the D03 building, as depicted in Figures 193 and 194. The instrument gallery serves the purpose of housing supporting equipment such as ventilation systems and instrument-related pipes. Notably, the gallery intersects with the planned tunnel approximately 30 meters from the moderator, takes a turn, and then runs parallel to the tunnel for approximately 25 meters. The gallery has a roof made of 55 centimeters of regular concrete, which will require replacement and reinforcement. Additionally, to ensure adequate shielding, extra measures will be necessary in front of the gallery.

Different options for the gallery shielding are summarized in Figure 195. In the left panels, while the gallery roof has been replaced, the dimension of the gallery has been kept the same and only the space available between the gallery and the NNBAR beamline has been used for additional shielding. In total,



**Figure 194:** The interface between the NNBAR beamline and the ESS instrument gallery

105 cm of shielding have been placed above the gallery, 60 cm steel and 45 cm of heavy concrete. This is not sufficient to create a safe working environment, with the dose just below the ceiling of the gallery exceeding  $100 \mu\text{Sv}/\text{h}$ . In the middle panel, the shielding thickness has been increased to 75 cm steel and 75 cm heavy concrete. The dose is close to the allowed level of  $1.5 \mu\text{Sv}/\text{h}$  but still exceeds it in places. Finally, the dose in the gallery drops below  $1.5 \mu\text{Sv}/\text{h}$  when increasing the thickness to 90 cm steel and 90 cm heavy concrete. The engineering details of adding this shielding are described in Section 9.6.3.

#### 9.5.4 The NNBAR Cave and Beamstop

At the end of the NNBAR beamline, the annihilation target and the annihilation detector (as described in Section 9.11) will be positioned. This equipment will be housed in an experimental hall referred to as the 'NNBAR cave.' Within this hall, not only will the detector be situated, but it will also accommodate auxiliary electronics and support structures. The NNBAR cave will receive the full NNBAR beam and thus necessitate robust shielding and a beamstop to safely terminate the beam.

In the current model, the front wall of the NNBAR cave is located at a distance of 192 meters from the moderator. At this point, the beamline's radius reduces from 1.5 meters to 1.0 meter. Importantly, the thickness determined for the far end of the tunnel (250 cm concrete or 175 cm heavy concrete) will also meet the ESS dose requirements for a supervised area. The beamstop will be positioned approximately 10 to 15 meters from the annihilation target and is responsible for absorbing the entire neutron beam that travels down the NNBAR beamline. Therefore, it must have a diameter at least as large as that of the beamline itself. Various material combinations and thicknesses have been explored for the beamstop.

In Figure 197, a dose map is presented for a beamstop configuration comprising a thin top layer (0.5 cm) of  $\text{B}_4\text{C}$ , supported by 25 cm of polyethylene, 100 cm of steel, and 320 cm of concrete. The projection illustrates that this configuration is effective in reducing the dose to below  $1.5 \mu\text{Sv}/\text{h}$  behind the beamstop. It's important to note, however, that the activation of the beamstop has not yet been investigated, and such an investigation could impact the selection of materials.

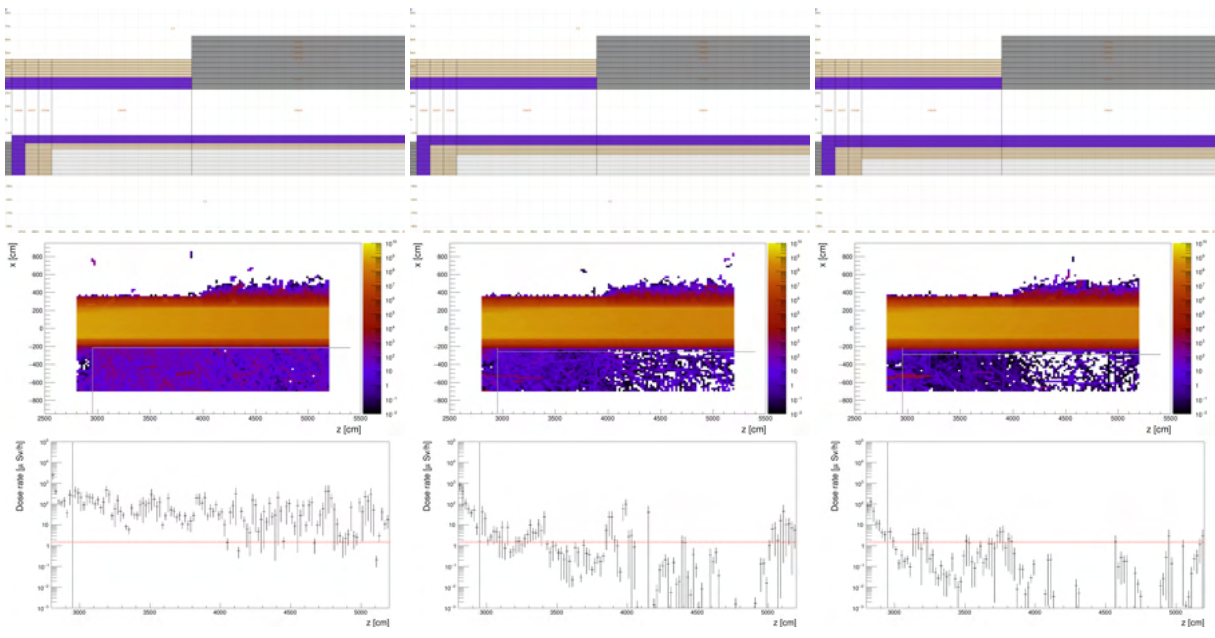


**Figure 195:** Dose maps for the NNBAR beamline and D03 instrument gallery for different shielding options. The investigated geometry is shown in the top row, the middle row shows the respective dose map, the bottom row a projection of the dosemap directly below the ceiling of the gallery for the respective geometry.

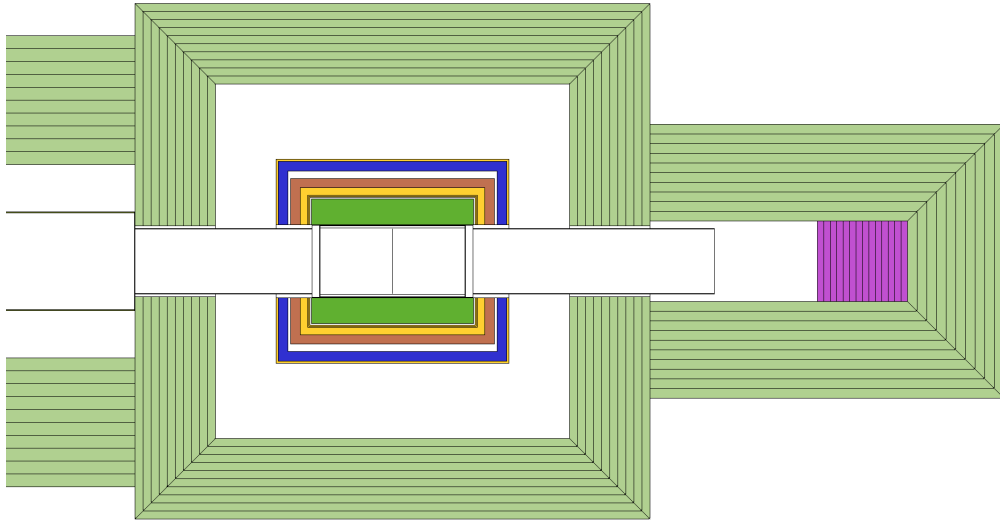


**Figure 196:** Model of the NNBAR cave and beamstop.

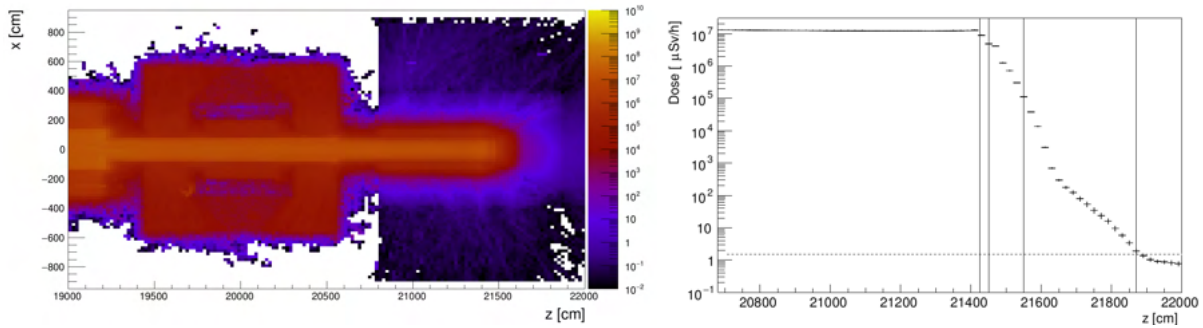


**Figure 197:** Left: Dose map of the NNBAR cave and beamstop. Right: Projection of the dosemap at the center of the beamstop.

## **9.6 Civil Engineering aspects for the NNBAR Project**

The construction of the NNBAR beamline will require a redesign of some parts of the existing facility that are in collision with the proposed beamline. In order to assess potential interfaces, understand the extent of potential collisions, and evaluate associated construction work, a civil engineering project was conducted as part of the HighNESS project. This project was a collaborative effort involving the NNBAR team, the ESS Facility Management division (FM), and the SWECO company<sup>12</sup>. It aimed to determine the required length of the NNBAR beamline, assess its structural requirements, and analyze factors such as width, height, and force loads related to shielding and surrounding structures.

### **9.6.1 Modifications to the bunker area and the D03 instrument hall**

The first 15 m of the NNBAR beamline will be placed inside the neutron bunker (see Section 1.1) in the position currently occupied by the ESS Test Beamline. This beam line will be used in the early day of the ESS project to characterize the neutron source but could be later moved to a different location to allow the construction of the NNBAR experiment. The significantly larger size of the NNBAR beamline will introduce interference with the existing steel structure supporting the bunker roof as shown in Figure 198.

This problem may find a solution, as the steel structure will already undergo significant modifications. These modifications are necessary due to the additional shielding requirements for the bunker roof, driven by the radiation contribution from the NNBAR beamline (see Section 9.5.1). Additionally, modifications to the north sector bunker (see Figure 6 for the explanation of the ESS sectors) wall will be required to accommodate a sufficiently large feed-through.

Beyond the bunker, the subsequent 21 meters of the beamline will be situated within the experimental hall of the D03 building (see Section 1.1). The existing concrete slab of the building has a load capacity of 14 t/m<sup>2</sup> (10 t/m<sup>2</sup> close to the facade) which will prove inadequate to support the heavy load required for the beamline shielding, as discussed in Section 9.5.2. Consequently, the reinforcement of the floor will be necessary. This entails the addition of an extra distribution slab, measuring 750 mm in thickness towards the west sector and 1250 mm for the north sector section outside the bunker area shown in Figure 199.

Furthermore, the length of the beamline makes it necessary to cross the already existing D03 building facade. Given the substantial height and width of the NNBAR beamline and its shielding, it is likely that modifications to the anti-seismic steel structure frame and a section of the building foundation will be necessary. This is because one of the building pillars is situated in the path of the new beamline. However, it's worth noting that the structure has been designed to accommodate the accidental removal of any of these individual columns. This was achieved by designing the truss structure to span a double bay, allowing for the accidental removal of one of the columns in the experimental hall. This design ensures that the structure is robust enough to withstand unforeseen events, such as the loss of a column due to incidents like a vehicle collision or a swinging crane load. Furthermore, this design approach offers a degree of future flexibility, as it allows for the intentional removal of one of the columns during structural alterations, as is the case with the NNBAR beamline. In such a scenario, it will be necessary to reinforce the columns, crane beam, brackets supporting the crane beam, and the walkway support beams on adjacent columns (typically 2 or 4). An independent analysis should assess the feasibility of this undertaking.

### **9.6.2 The area outside the D03 instrument hall**

The proposed NNBAR beamline has a total length of 200 m, with approximately 160 m extending outside the D03 building before reaching the NNBAR cave (see Figure 13). While the optics studies in Section 9.8.3 determined that the 200 m design provides the best trade-off for experiment sensitivity, this section examines the implications of a longer beamline from a civil engineering perspective. As depicted in Figure 200, extending the beamline beyond 200 m would intersect with the circular road encircling

---

<sup>12</sup><https://www.sweco.se>

## Large Beam Port

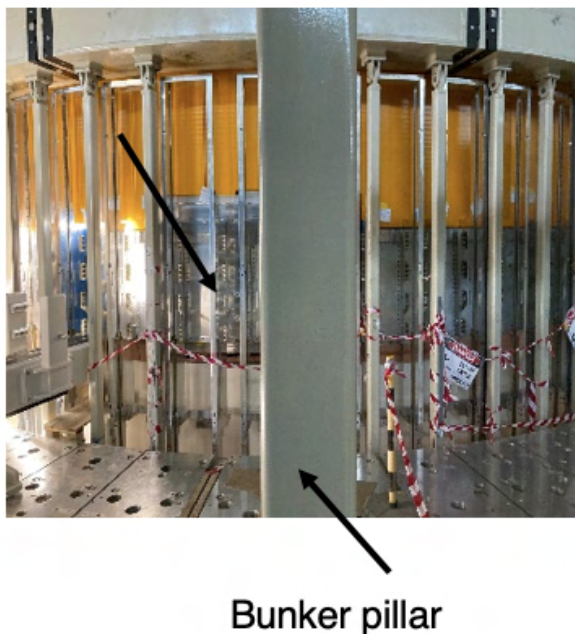


**Figure 198:** Interference between bunker steel structure and NNBAR beamline

the ESS area, necessitating a rerouting of the road. When considering the circular road as a boundary, a detailed analysis of the area near the NNBAR beamline confirmed that there are no conflicts between the beamline foundation and local utilities or subservices. However, a more thorough analysis is required to assess whether local modifications to the foundation are needed to support the loads of the shielding and the instrument cave. Furthermore, an investigation into the necessity of downward shielding to ensure the safety of subservice contents is pending. Nonetheless, given that the subservices are situated at a substantially lower level than the instrument gallery, as discussed in Section 9.6.3, it is very likely that this is not a significant concern.

As presented in Section 9.5, the necessary shielding thickness outside the D03 hall depends on the chosen material and decreases over the length of the beamline. For regular concrete the required thickness ranges from 400 cm to 250 cm, while for heavy concrete, it ranges from 250 cm to 175 cm. The use of heavy concrete is associated with a higher cost of material. A further study of the structure surrounding the shielding resulted in three possible options, as illustrated in Figure 201 using the dimensions for heavy concrete. Figure 201a depicts the simplest option, which consists of a shielding layer without any additional weather protection and an autonomous crane vehicle for moving shielding blocks. Further investigation is needed to determine whether it is feasible to leave the structure unprotected, as exposure to water and wind could lead to damage. This option would require the construction of a service road along the entire length of the beamline. Nevertheless, it is likely the most cost-effective option in terms of construction. The second option is shown in Figure 201b, consisting of shielding and a traverse-crane going along the entire structure, with a simple roof structure as weather protection. This option would also require a service road, but not of the same magnitude as for the first option, as it would not need to be adapted for such heavy vehicles.

Lastly, in Figure 201c, you can see the configuration featuring shielding and a traverse-crane, all enclosed within full weather protection, effectively creating an annex-building connected to the D03 instrument Hall. To accommodate incoming truck or forklift vehicles, the internal communication pathways must be sufficiently wide. This solution offers the advantage of simplified communication between D03 and the NNBAR experimental cave through internal walkways. However, this construction imposes different requirements on installations, such as ventilation, electrical systems, and plumbing.

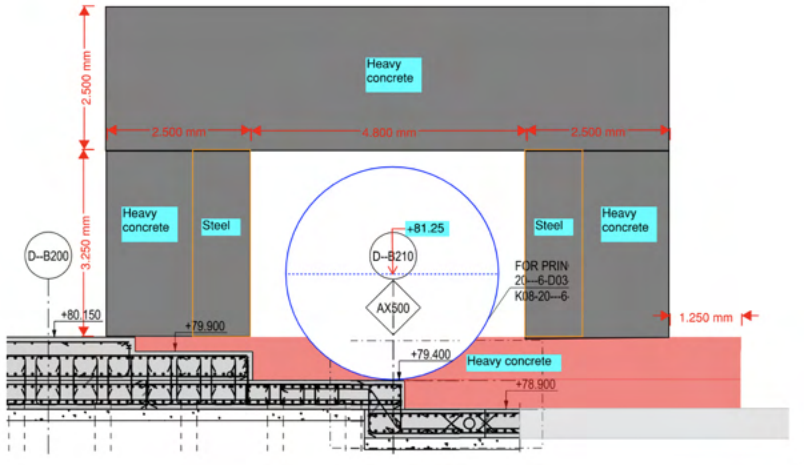


**Figure 199:** Proposed floor reinforcement solution for the NNBAR beamline for the D03 area.

### 9.6.3 Interface between the NNBAR and the instrument gallery

As discussed in Section 9.5.3 and illustrated in Figure 194, the position of the instrument gallery intersects with the NNBAR beamline, resulting in overlapping structures at multiple points, see Figure 202. This situation presents a complex engineering challenge, as it requires both shielding the instrument gallery from the radiation emitted by the beamline and managing the load transferred from the beamline to the gallery.

As was shown in Section 9.5.3, between 150 cm and 180 cm of shielding material (half steel, half heavy concrete) is required to reduce the radiation from the NNBAR beamline to an acceptable level in the instrument gallery. Figure 203 shows a 3D-sketch of the beamline (purple) and the gallery (green). The orange volume shows the space needed for the shielding. The pictures on the right side of Figure 203 show the disassembled beamline, to give an impression of the relation between the instrument gallery and the beamline. It is clear that there is not enough space between for the shielding. This is also illustrated in Figure 204, where the interface between the gallery and the beamline is shown in 5 different positions. Circles highlight the conflicts between the two. This leaves two options, raising the beamline or adding shielding inside the instrument gallery which would require the rerouting of existing pipes.

Figure 204 highlights not only direct conflicts between beamline and gallery but also issues due to the load caused by the shielding. The study of how much load the instrument gallery can manage has been conducted in parallel.

When the instrument gallery was initially designed, it was based on expected loads at that time, as shown in Figure 205. Comparing this to the load produced by the NNBAR shielding in Figure 206, it becomes evident that the additional load exceeds the gallery's capacity. Consequently, the new construction around the beamline must be designed to support this additional load. The principle for solving the problem is illustrated in Figure 207. A substantial beam, supported by drilled steel piles, can effectively transfer the loads around the instrument gallery to the bedrock, isolating the gallery from the new loads.

Additionally, the beam serves as shielding for the instrument gallery. Figure 208 shows a more concrete example for how to implement this in the case of *position 4* from Figure 204, situated outside the D03 hall. The same principle is shown in Figure 209 for inside the experimental hall (*position 3* in Figure 204). In each figure, two possible solutions are presented, both featuring a concrete beam positioned between the gallery and the beamline, supported by drilled steel piles. Lowering the gallery ceiling is necessary to implement these solutions, and additional shielding material is placed inside the instrument gallery in both cases. In the simpler approach, apart from lowering the ceiling (Figures 208a and 209a), the instrument gallery floor remains unchanged. However, it might be necessary to retain the current size of the gallery and to also lower the gallery's floor. Figures 208b and 209b therefore show a scenario in which the floor of the gallery is also lowered.

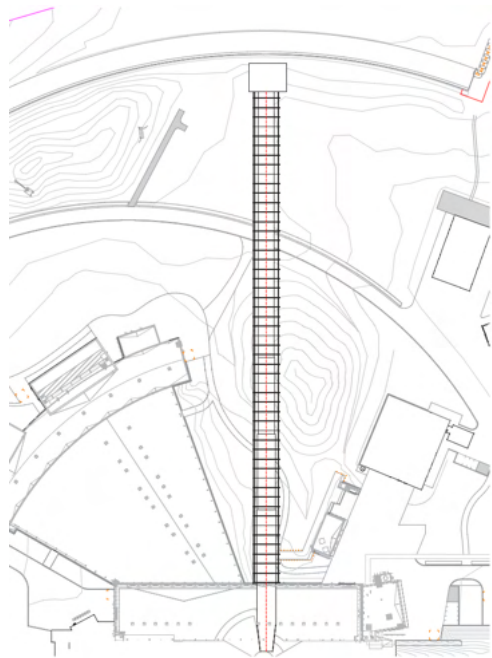


**Figure 200:** Interference between the NNBAR beamline and the ESS circular road for a beamline length  $> 200$  m (here: 300 m).

#### 9.6.4 Future investigations connected to the instrument gallery

The potential solutions are accompanied by important future investigations that must be considered as the project continues. Further examination of the current instrument gallery construction inside the D03 building and the connection between its capacity and the capacity of the building's slab regarding the loads from the shielding and beamline is necessary. An investigation into the possibility of rearranging the installations within the instrument gallery and consideration of groundwater levels, which can impact the extent to which the instrument gallery can be lowered, are necessary.

Space allocations around the NNBAR beamline are crucial. Increasing available space for shielding walls inside the D03 building could simplify the issue of loads on the instrument gallery. Moving the walls farther from the beamline would enable load transfer into the slab, where more piles are present, rather than onto the instrument gallery.

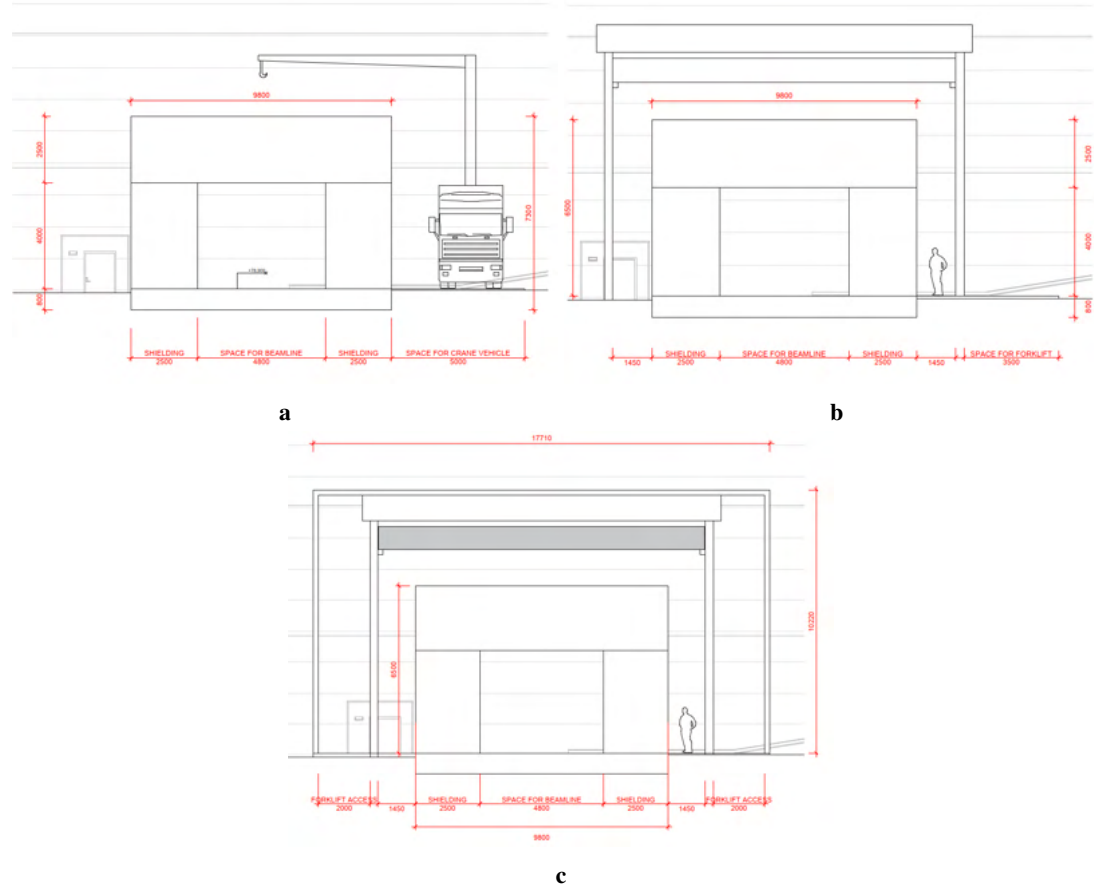


**Figure 201:** Different options for the NNBAR tunnel structure. a: Shielding without weather protection and a crane vehicle. b: Shielding and traverse-crane with roof. c: Shielding, traverse-crane and full weather protection.

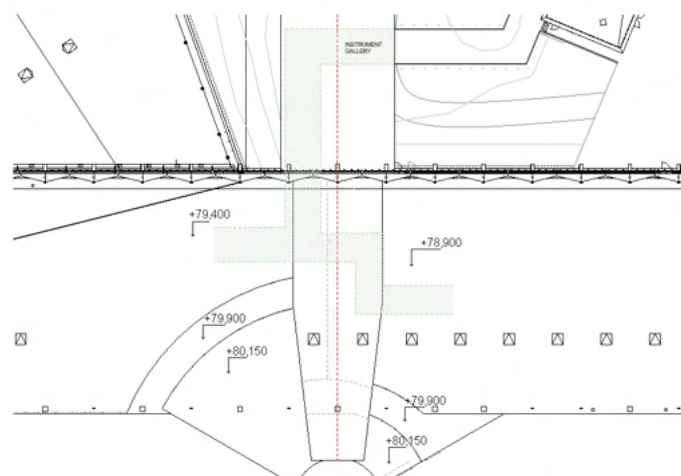


**Figure 202:** Position of the instrument gallery in relation to the beamline. The instrument gallery is shown in green and the beamline in red.

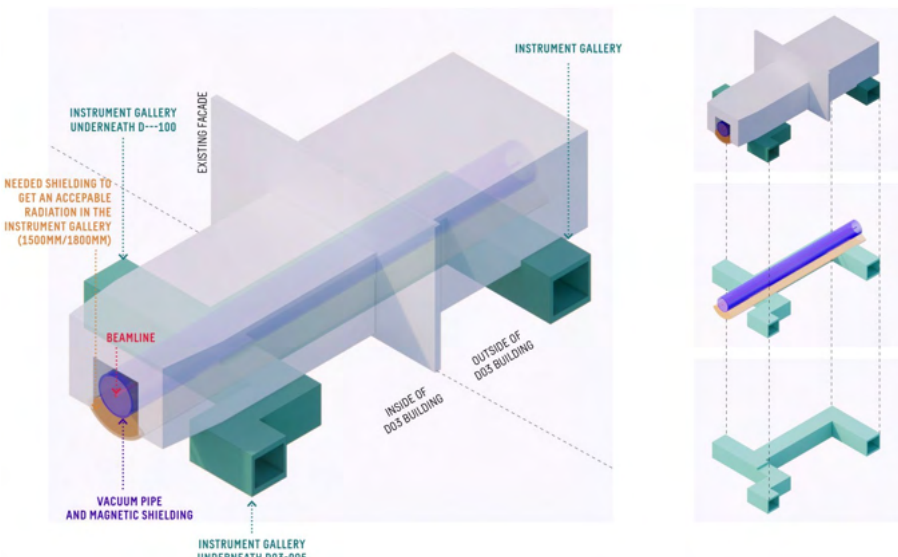


**Figure 203:** Position of the instrument gallery in relation to the beamline. The instrument gallery is shown in green and the beamline in red.

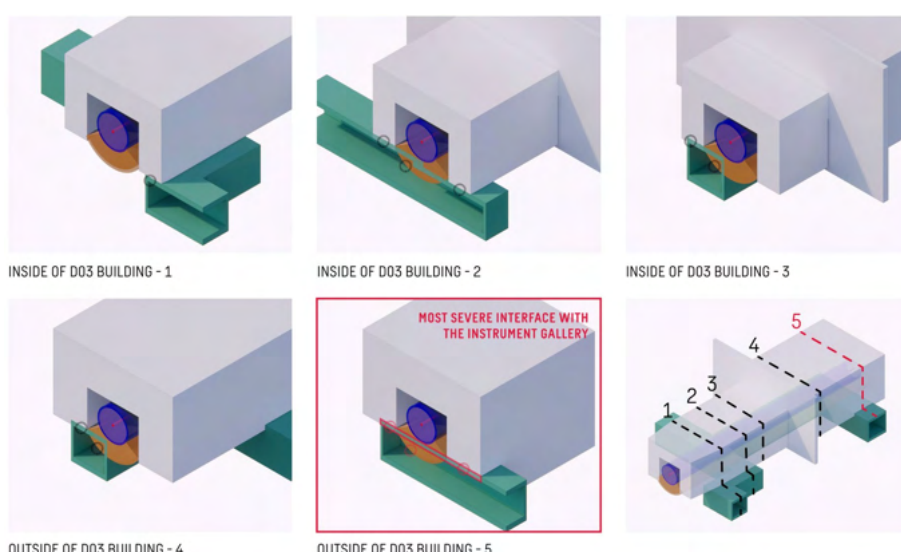


**Figure 204:** Interfaces between the instrument gallery and the NNBAR beamline. Conflicts are highlighted by the circles.

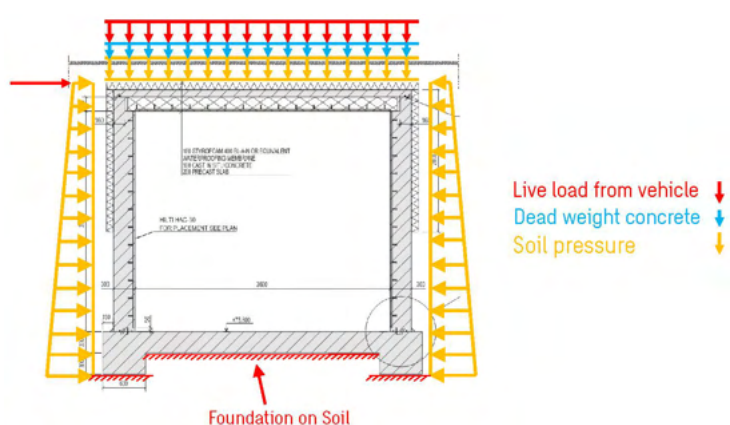


**Figure 205:** The current loads on the instrument gallery, which were the base for its design.

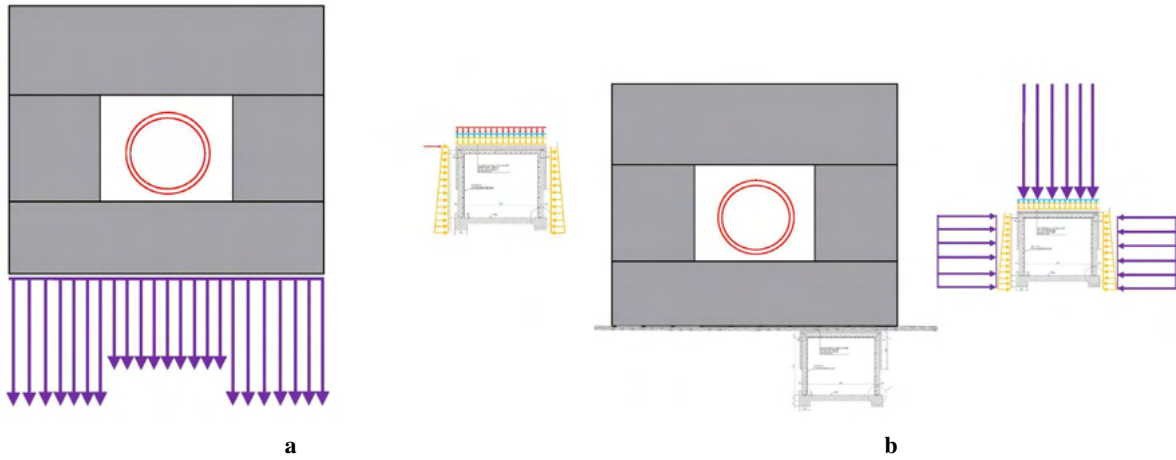


**Figure 206:** a: Estimated loads from the NNBAR shielding. b: Loads from the shielding in relation to the instrument gallery design loads.

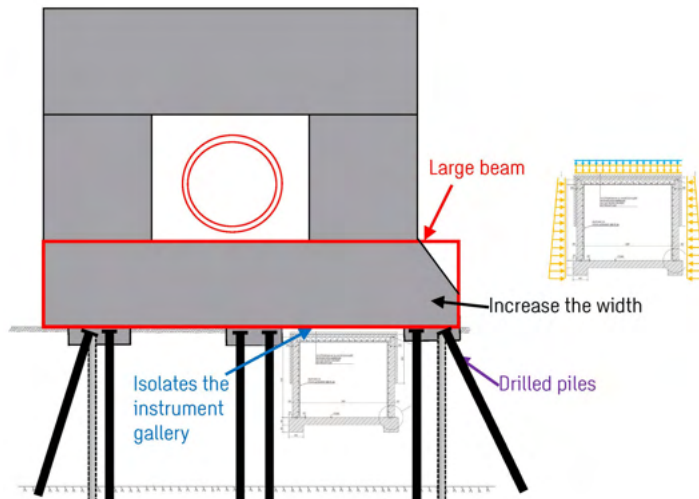


**Figure 207:** Sketch of the proposed solution for removing the load from the ceiling of the instrument gallery.

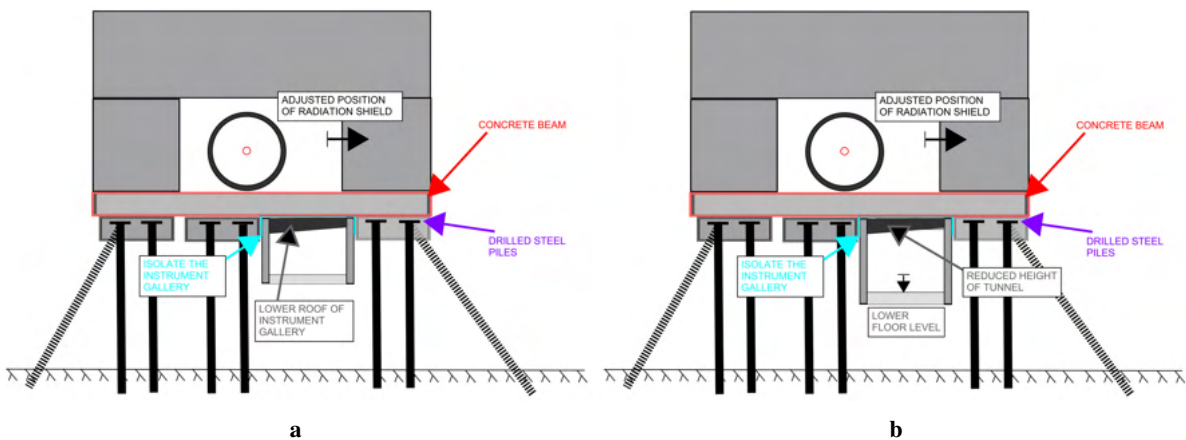


**Figure 208:** Two possible solutions for the interface between beamline and instrument gallery outside the D03 hall. a: Only the ceiling of the gallery is lowered. b: Both ceiling and floor of the gallery are lowered.

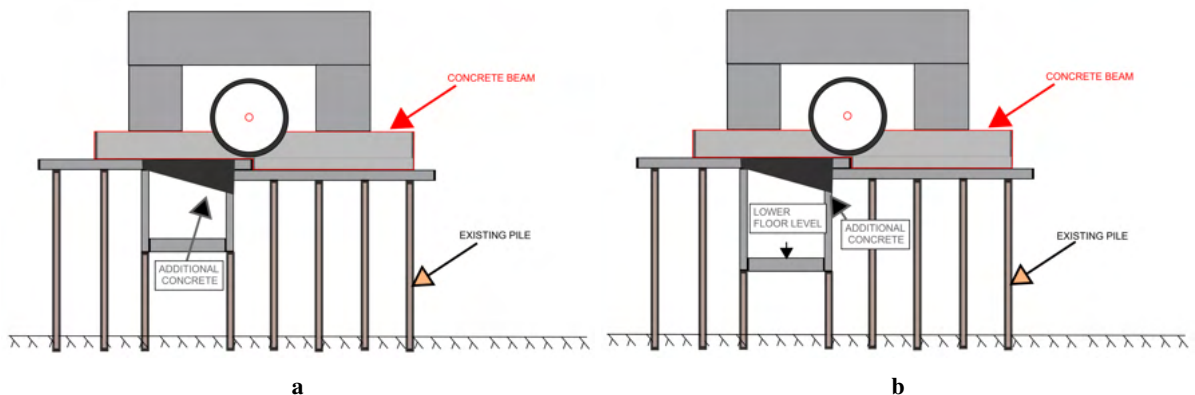


**Figure 209:** Two possible solutions for the interface between beamline and instrument gallery inside the D03 hall.  
 a: Only the ceiling of the gallery is lowered. b: Both ceiling and floor of the gallery are lowered.

## 9.7 The NNBAR focusing reflector

The NNBAR reflector system plays a pivotal role in achieving the goal of a performance increase of three orders of magnitude compared to the previous experiment. The primary requirement for the reflector is to efficiently collect the highest fraction of neutrons emanating from the LBP and direct them through the magnetically shielded region toward the annihilation target situated 200 meters away. Given its size and stringent requirements, this optical system is likely to be one of the most intricate ever developed in the field of neutron research. The design and optimization of this system are detailed in the following section.

### 9.7.1 The optimization of the focusing reflector

The NNBAR Figure of Merit (FOM) has already been described in Section 2.2.3. In our optics simulations, we consider the exact uninterrupted flight time  $t_i$  and the weight (intensity, represented as neutrons per second)  $n_i$  of each neutron arriving at the detector. The FOM is then derived by calculating the sum  $\sum_i n_i \cdot t_i^2$ .

To facilitate comparison with the previous ILL experiment [262], the FOM is normalized, following the procedure described in Ref. [4]. The ILL which ran for one year. As a result, the FOM is quantified in terms of ILL units per year. A value of  $FOM = 1$  signifies a sensitivity level equivalent to that attained at the ILL. Consequently, all FOM values presented in this paper are expressed in this standardized manner. For the sensitivity it is important to note the following. At a distance,  $L$ , from the cold source to the detector, with area,  $A$ , the fraction of neutrons collected by the detector will be proportional to the seen solid angle:  $N \sim \Delta\Omega = A/L^2$ . For neutrons with average velocity,  $v$ , the time-of-flight squared will be  $\langle t^2 \rangle = L^2/v^2$ . It is therefore seen that the sensitivity does not depend directly on  $L$  and an increase is also possible by providing a high flux of slow neutrons with large  $\langle t^2 \rangle$  (see Section 4).

With the above discussion of sensitivity in mind, the concept of the elliptical focusing reflector [263] can be used. Lambertian brightness emission from cold neutron moderator surface can be intercepted by a large open aperture and super-mirror reflector elements installed within this aperture. This directs neutrons to the annihilation target by a single reflection. An important performance parameter of super-mirror reflectors is the  $m$ -value [264]. Given an aperture opening of  $\pm 4^\circ$  degrees one can consider the small element of the mirror reflecting surface located within  $d\Omega = d\cos\theta d\phi$  inside the LBP opening at some distance  $z$  from the cold source and study the question of the quality of super-mirror reflecting material that is needed to provide the change of the neutron trajectory. This change allows neutrons from the source to reach the annihilation target. In Figure 210 such a calculation for the baseline reflector (see Section 9.8 and Figure 219) is depicted for the configuration in an idealized situation with a point-like cold source,  $z$ -axis symmetric reflection, and without taking effects caused due to gravity and off-specular reflection into account. As an example: a nested mirror layout, as described in the following section, that covers an aperture opening of  $\pm 4^\circ$  degrees has gains in terms of FOM for subsequently increased  $m$ -values as collected in Table 46. As expected for an  $m$ -values larger than 6 no further gain is achieved.

**Table 46:** Gains in FOM that can be achieved by increasing the  $m$ -value of a nested mirror reflector that covers an opening of  $\pm 4^\circ$ . After  $m > 6$  no significant gain is attained.

m-value	1	1.5	2	3	4	5	6	7	8
Relative Gain	-	1.11	0.55	0.51	0.16	0.06	0.01	0.00	0.00
Absolute Gain	-	1.11	2.29	3.97	4.74	5.09	5.17	5.23	5.23

### 9.7.2 Nested mirror optics

A possible architecture which transports neutrons diverging from a source to a detector is an elliptical guide. The surfaces of such a device have the shape of an ellipse where, the focal points coincide with

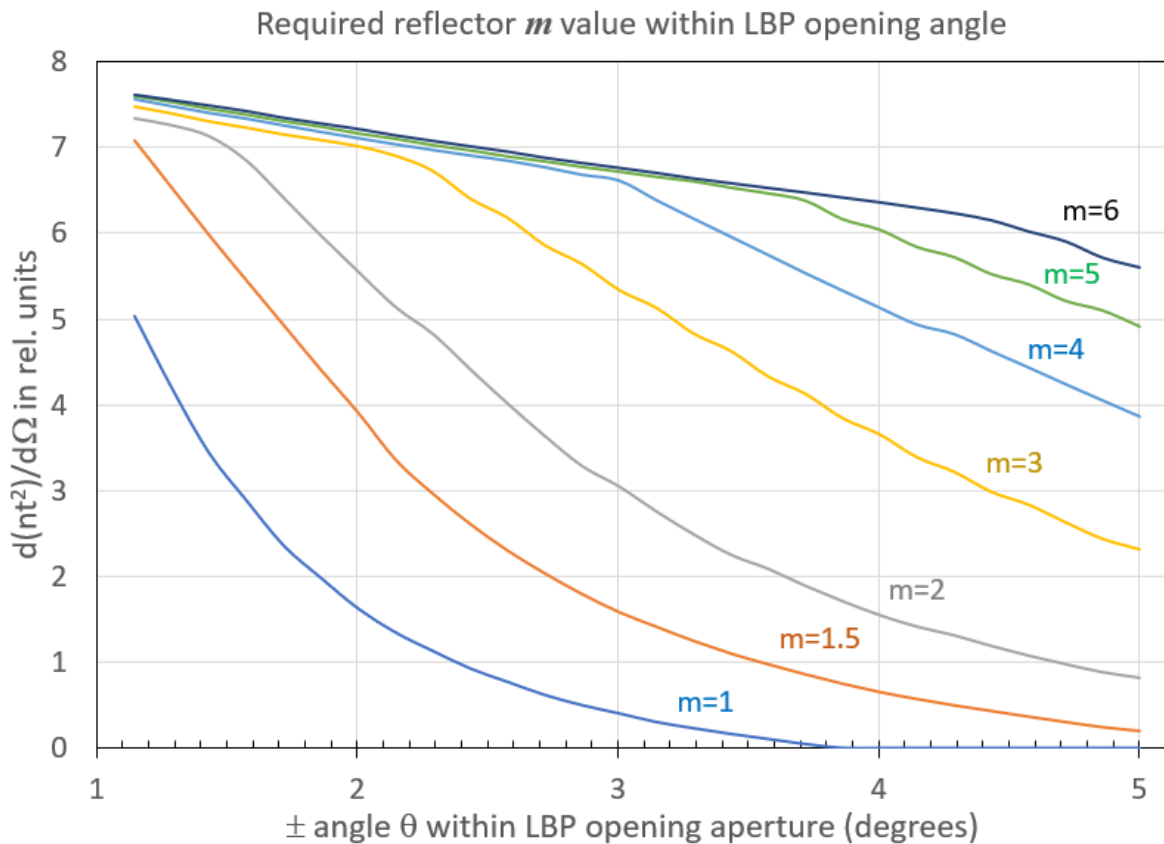


**Figure 210:** The sensitivity  $N < t^2 >$  that can be provided by the  $d\Omega$  element of the super-mirror reflector with different  $m$ -values as a function of the  $\theta$  location of  $d\Omega$  within the LBP opening aperture. For a maximum LBP opening  $\pm 5^\circ$ ,  $m = 6$  reflection quality [264] is adequate for the NNBAR design goal. The total FOM figure should be obtained by integration between minimum and maximum  $\theta$  angles covered by the actual reflectors.

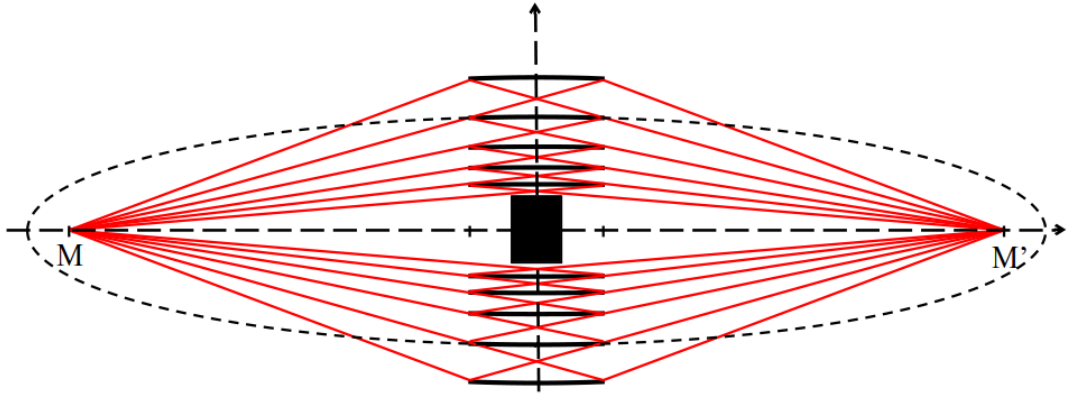


**Figure 211:** Schematic of a nested elliptical guide.  $M$  and  $M'$  are common focal points of the ellipses forming the layers (the dashed line shows one of them.)

the centre of the source and the detector, respectively [151, 170]. An ellipse has the optical property that a beam that emanates from one of its focal points is reflected directly to the other one. Since this feature does not apply to rays starting not at the focal points, the ellipse is therefore a non-imaging device. Nested layers of several guides are able to build up a spatial tight optical component. If the outer layer of such a nested elliptical guide is given, the inner layers can be designed in a recursive manner such that the layers will not shadow themselves. In the diagram shown in Figure 211 the construction principle is shown. The finite size of the optical layers is currently not taken into account.

Different nested layouts of the reflector that are symmetrical around the  $z$ -axis are possible. These are (a) a mono planar, (b) a double planar, and (c) a cylindrical system. In Figure 212 three dimensional diagrams of the different types are shown. In a double mono planar reflector, neutrons would have to be reflected twice in order to be directed to the center of the detector. For the cylindrical symmetrical case, only one reflection is needed. The mono planar reflector comprises two separated devices that are rotated by ninety degrees with respect to each other such that one component acts as a horizontal and the other as a vertical reflector. From an engineering perspective this configuration seems to be particularly promising.

A difficulty of the nested reflector design is the thickness of the glass substrate which is used for the construction of the stable high-quality industrial super-mirrors. Recent developments of self-sustaining substrate less super mirrors [265] offer an elegant possible solution to this problem.

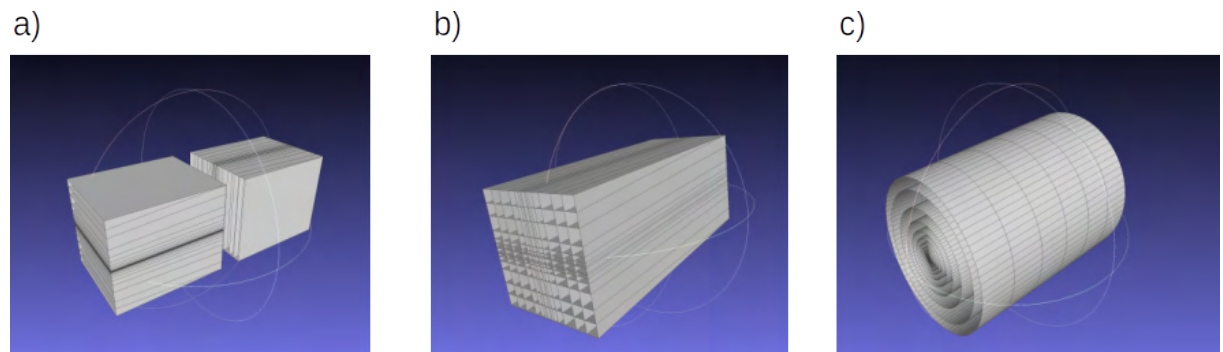


**Figure 212:** Types of nested optical components a) mono planar b) double planar c) cylindrical.

### 9.7.3 Magnification of an elliptical reflector

For any portion of a perfect (without accounting for gravity effects) rotational ellipsoid surface, a point-like emission source in one focal point is projected exactly to the image point in the other focal point. However, as is the case for any realistic optical system, if the source point is displaced from the ellipsoid

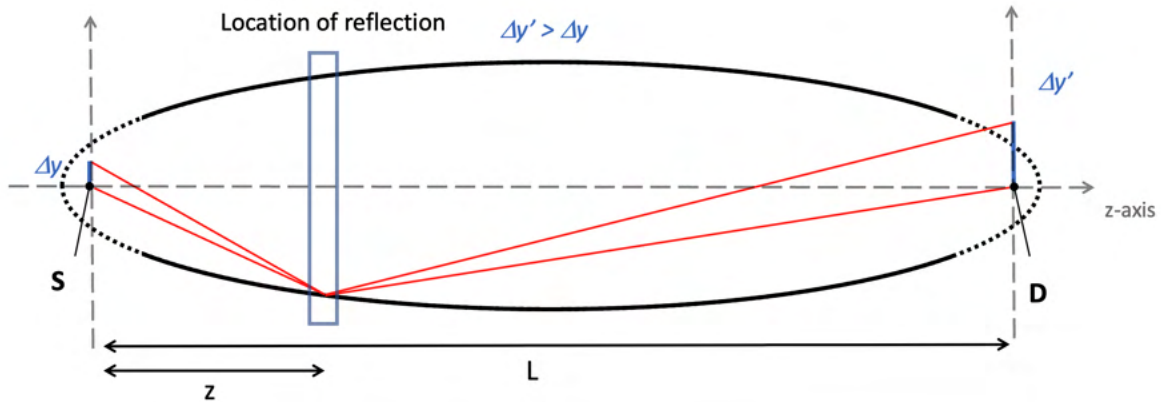


**Figure 213:** Off-Axis magnification of an elliptical reflector. With origin at the Source S in the left focal point,  $L$  distance between focal Points and to the detector D,  $z$  coordinate of reflection along  $z$ -axis.  $\Delta y'$  is the off axis height at the source and  $\Delta y'$  is the height at the detector.

focus lateral to the optical  $z$ -axis then the image point will similarly be laterally displaced with a magnification factor. Figure 213) summarises this situation. The magnification  $M$  for an off axis point of height  $\Delta y$  at left sided focal point is [266]:

$$\Delta y = \frac{L-z}{z} \Delta y' \quad (25)$$

$$M = \Delta y / \Delta y' = \frac{L - z}{z} \quad (26)$$

With the origin in left focal point,  $L$  the distance between focal points and  $z$  the coordinate of reflection along the  $z$ -axis.  $\Delta y'$  is the height at right side focal point. If, therefore, the reflection point  $Z_{refl}$  is 10 m away from the source and the focal distance is  $L = 200$  m, the magnification factor will be  $\sim 20$ . For a detector of radius  $r = 1$  m the most "efficient" emission area of the source will then fall within a radius  $\sim \pm 5$  cm from the ellipsoid axis. This effect of magnification can be studied in simulations; an example is given in Figure 214. The positioning of the reflector between source and detector has a general property such that the nearer the moderator, the larger the covered solid angle albeit with a deterioration of the focusing and vice versa. The optimum position with regards to the FOM is a trade-off between these two effects.

Since the size of the source plays an important role in the capability of the reflector to transport neutrons from it to the detector, the properties and parameters of the focusing reflector are simultaneously optimized with the design of the cold moderator in an iterative process.

#### 9.7.4 Basic Reflector Setup and Simulations

As previously outlined in Section 9.3, the collaboration has developed a dedicated simulation framework for the design of the NNBAR experiment. In this section, our attention will shift towards the simulation aspect pertaining to the optical reflector.

The principal setup for the reflector that is under study has been already shown in Figure 211. The optic is supposed to start at a minimum distance of 10 m from the moderator center and the detector is placed 200 m away from the center of the moderator. The flight time is measured from the point in time of the last interaction (reflection) with the optic. The transversal dimension of the reflector is bounded by a maximum assumed tube width and height of 3 m. Gravity is turned on for all simulations.

To facilitate comparisons between various geometries and the precise positioning of the reflector system, neutron ray-tracing simulations are conducted using McStas [251]. In McStas, the instrument components are defined using a high-level language, which is subsequently compiled into C-Code to execute the Monte Carlo simulations.

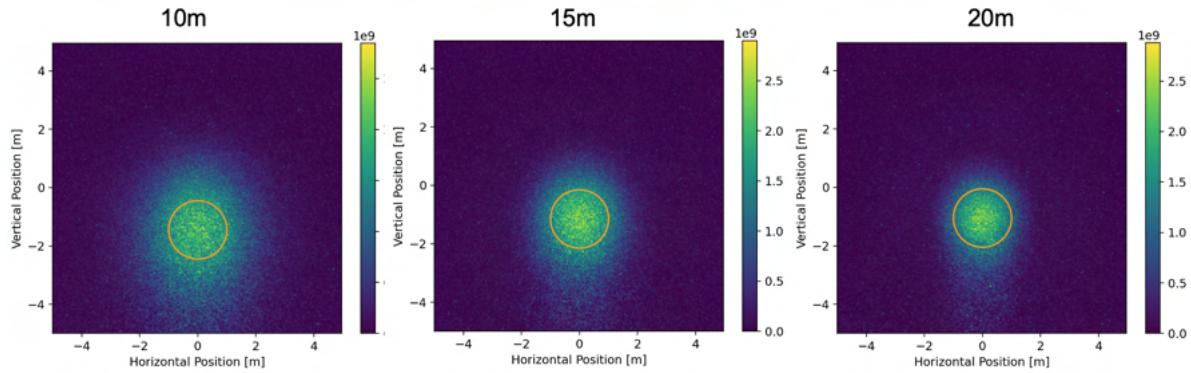


**Figure 214:** The impact of magnification is illustrated using a 4-level nested elliptical reflector with a length of 10 meters, positioned at various starting locations. The representation shows the neutrons arriving at a distance of 200 meters, weighted by the square of their uninterrupted flight time. The orange circle designates the estimated location of the actual antineutron detector, with a radius of 1 meter. The degree of magnification diminishes as the reflector's starting position is farther from the source. However, it's important to note that the FOM is greatest for the 15-meter plot. This variation in FOM is essentially a trade-off between achieving effective focusing and covering a broader solid angle.

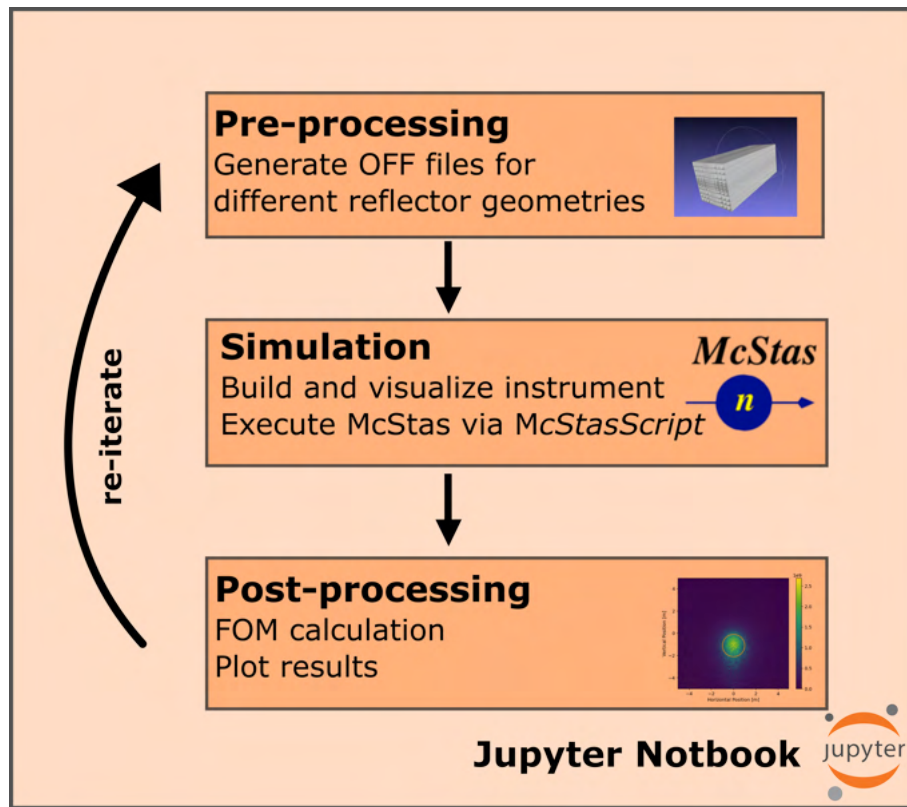


**Figure 215:** Simulation strategy

An extension called McStasScript<sup>13</sup> enables the control of McStas using Python scripting (e.g. in JupyterLab<sup>14</sup> a web-based interactive python development environment). This allows for the entire simulation to be managed and executed within a unified environment. Results can be easily accessed for post-processing tasks, including calculations of the FOM and generating plots. The source term is implemented using an MCPL<sub>input</sub> component [267]. This component reads an MCPL-file [254], which contains an extensive list of neutrons generated as output from a dedicated MCNP [13] simulation of the moderator (see the reference moderator section). In the input file, these neutrons have already been propagated to the region situated 2 m away from the center of the moderator (refer to Figure 216). The

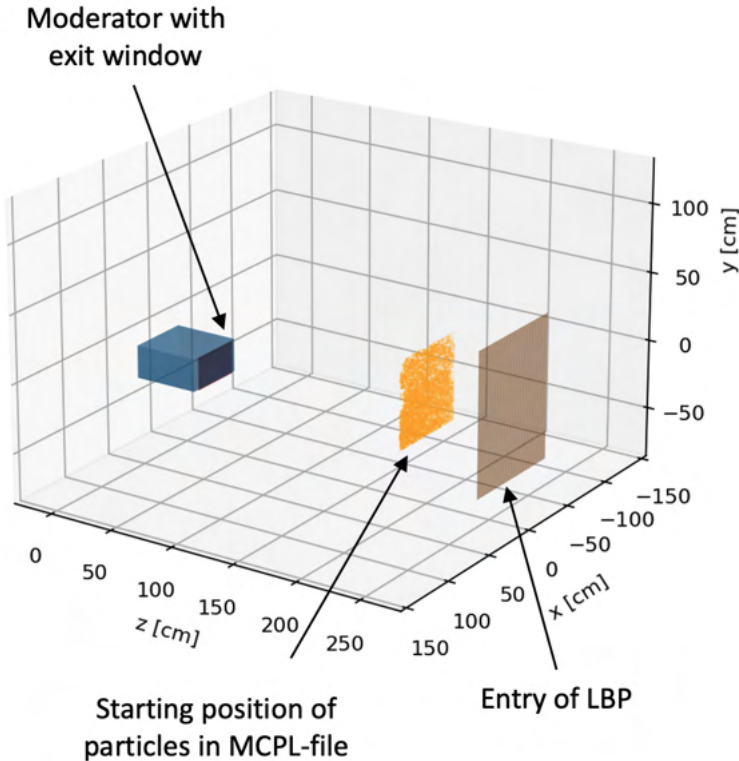


**Figure 216:** Source term calculation with MCPL. The particles are emitted from the moderator window, but already forward propagated to a distance of 2 m, just before the entry of the LBP.

divergence of the neutrons has already been restricted to the solid angle accepted by the LBP. This restriction serves to enhance the count of useful neutrons, decrease the duration of individual runs, and provides a good particle statistics for the Monte-Carlo simulations.

The geometry of the optics is described in the plain text, object file format (OFF-File). This file is automatically generated from a set of input parameters using Python functions. The OFF-file is subsequently employed as input for the McStas component called Guide<sub>anyshape</sub>. This component is responsible for defining and positioning the reflector. Additionally, the LBP is also represented as an OFF-file and is described using the Guide<sub>anyshape</sub> component. Neutrons that collide with the walls of the LBP are absorbed. A Monitor<sub>nD</sub> component is utilized to represent the annihilation detector, where the velocity and flight time of the neutrons are recorded. This virtual detector in the simulation has dimensions of 10 m x 10 m, which makes it notably larger than the actual NNBAR annihilation detector (see Section 9.11). The output from this virtual detector consists of a particle list containing information such as position, velocity, flight time, and weight (neutrons/second). The FOM is calculated within the area of a circle with a radius of 1 m. The position of maximum FOM is determined by varying the center of the

<sup>13</sup><https://mads-bertelsen.github.io/index.html>

<sup>14</sup><https://jupyter.org>

circle.

By conducting simulations with different designs, utilizing various geometries, and adjusting various reflector parameters (e.g., starting position, length, etc.), a substantial number of optical configurations can be explored to identify optimal parameters. Figure 215 illustrates the general sequence of a typical simulation cycle.

The reflectivity  $R$  of the supermirror is calculated in McStas by applying an empirical formula derived from experimental data [267]:

$$R = \begin{cases} R_0 & \text{if } Q \leq Q_c \\ \frac{1}{2}R_0(1 - \tanh[(Q - mQ_c)/W])(1 - \alpha(Q - Q_c)) & \text{if } Q > Q_c. \end{cases} \quad (27)$$

Here  $R_0$  is the low-angle reflectivity,  $Q_c$  is the critical scattering vector,  $\alpha$  is the slope of reflectivity,  $W$  the width of the supermirror cut-off, and  $Q$  (in  $\text{\AA}^{-1}$ ) the length of the scattering vector of the incoming neutron. Non-specular reflection caused by e.g. surface roughness of the mirrors is currently not taken into account. The default settings of McStas,  $R_0 = 0.99$ ,  $Q_c = 0.0219 \text{\AA}^{-1}$ ,  $\alpha = 3 \text{\AA}$  and  $W =$

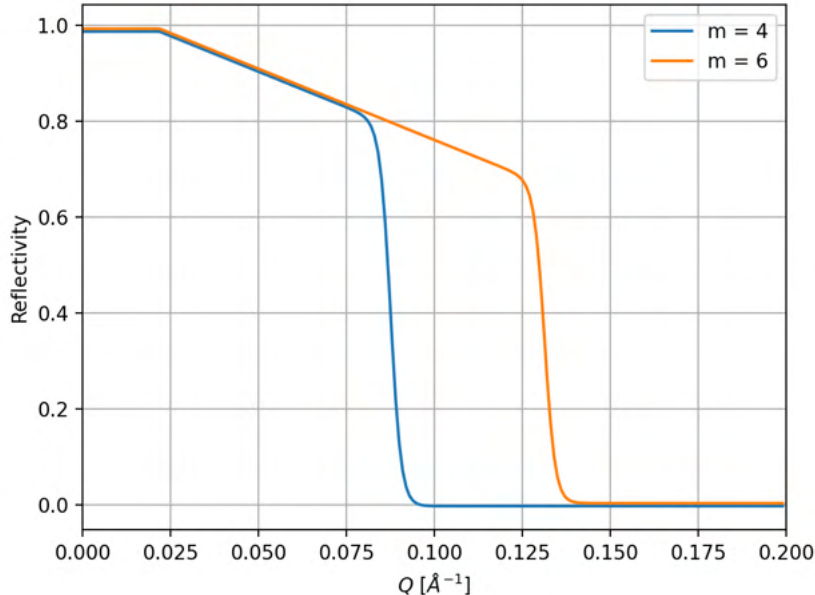


**Figure 217:** Two typical reflectivity curves for a supermirror derived from Equation (27).

$0.003 \text{\AA}^{-1}$ , resemble a typical supermirror and are sufficient to model the reflectors for the NNBAR simulations. Figure 217 displays two exemplary reflectivity curves for  $m = 4$  and  $m = 6$ . It's important to note that the components used in the simulations currently only support an overall reflectivity value, meaning that the  $m$  value cannot vary across the optical component. The simulations conducted for this work used an  $m$  value of 6.

### 9.7.5 Construction of the Nested Optics

If the outer layer of a nested elliptical guide is given, the inner layers can be constructed in a recursive manner. A sketch of the construction is shown in Figure 218 ( $y$  and  $z$  axis have been chosen in to comply with the coordinate system used in McStas). The source  $S$  and the detector  $D$  are located at the ellipses foci.  $b_n$  are the minor half-axes of the  $n^{th}$  nested layers. The distance  $L$  between the two foci of the ellipse is related to the focal distance by the simple relation  $f = L/2$ . The following construction will be valid for start  $z_s$  and end  $z_e$  points that fulfill the criteria:

$$-f < z_s < z_e < f \quad (28)$$

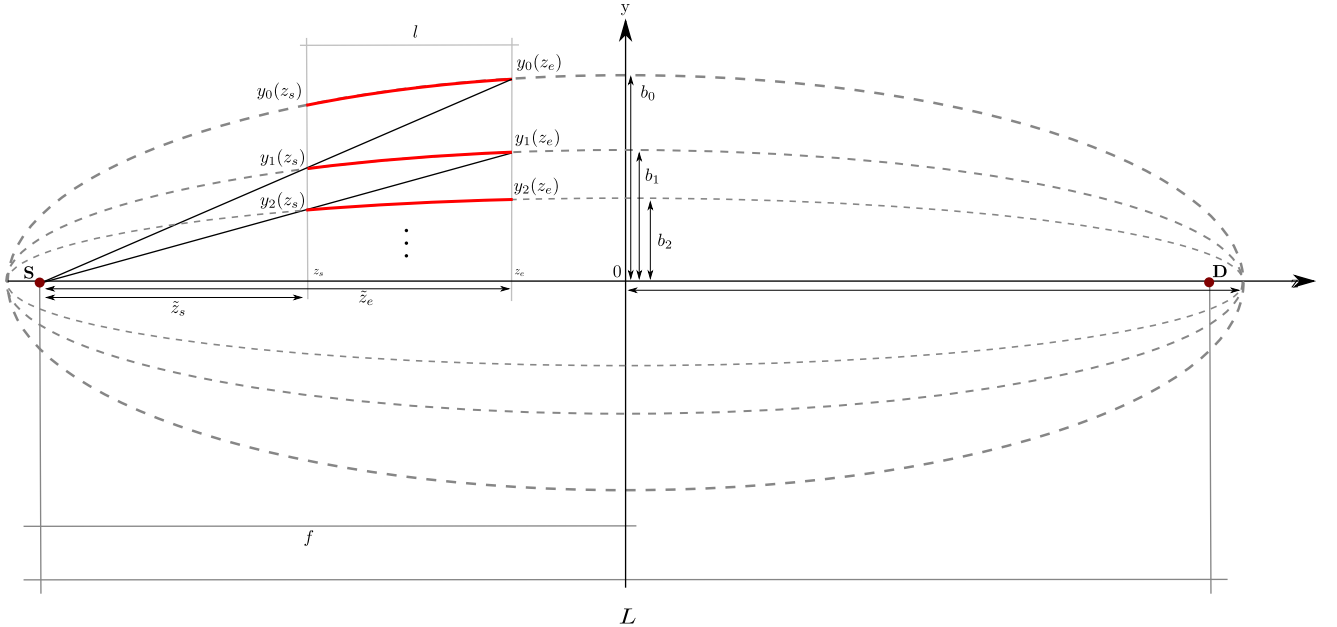


**Figure 218:** Schematic of how the inner nested layers are constructed from the outer ones.

From the sketch (Figure 218) it is seen that a straight lines from the source position  $S$  to the end of the optics from an outer layer (index  $n$ ) defines the starting position of the next layer (index  $n + 1$ ). From this, an analytical expression for the minor half axes  $b_n$  of each layer can be calculated:

$$b_n = \sqrt{-\frac{(f^2 - z^2 - K_n^2)}{2} + \sqrt{\frac{(f^2 - z^2 - K_n^2)^2}{4} + K_n^2 f^2}}, \quad (29)$$

with

$$K_n = \frac{\tilde{z}_s}{\tilde{z}_e} y_{n-1}(z_e), \quad (30)$$

being obtained from the previous levels in recursive manner, where  $\tilde{z}_s$  and  $\tilde{z}_e$  are the distances from focal point  $S$  to the start resp. end of the optic (not to be confused with  $z_s$  ( $z_e$ ) the coordinates of the starting (end) point of the optic). They are related by  $\tilde{z}_s = z_s + f$  and  $\tilde{z}_e = z_e + f$ . Given the parameters of the outermost ellipse ( $f = L/2, b_0$ ), the start and the end of the optics ( $z_s, z_e$ ) all parameters are known to compute the small half-axis  $b_n$  of the inner layers of the nested optics. For all the nested optic variants of Figure 212, functions to generate OFF-files have been developed. In the case of a non-point source like the LD<sub>2</sub> moderator, the use of elliptic mirrors can lead to a smearing and potential screening effect of the nested layers, as discussed in Section 9.7.3. The method described here for calculating the nested levels does not consider these effects. However, it's important to note that the size ratios between the moderator and optical device justify this approach. Nevertheless, when analyzing and interpreting simulation results, these effects should be taken into consideration.

## 9.8 Baseline design and differential reflector

As a starting point for the simulations, a "baseline" design was defined for comparison purposes. This baseline design consists of a cylindrically shaped elliptical reflector with a single layer. The key parameters of this design include: distance of 200 meters between the two foci and a small semi axis  $b$  of 2 m. The center of the source (moderator) is located in one focus, while the center of the detector is located in the other focal point. The reflector covers the part of the ellipse that starts at 10 m from the source and ends at a distance of 50 m and is therefore 40 m long. For this standard baseline configuration, various aspects of the NNBAR experiment have been studied, including different sizes of the cold source moderator(see Section 2), the neutron emission spectra, and the beamline design. This baseline

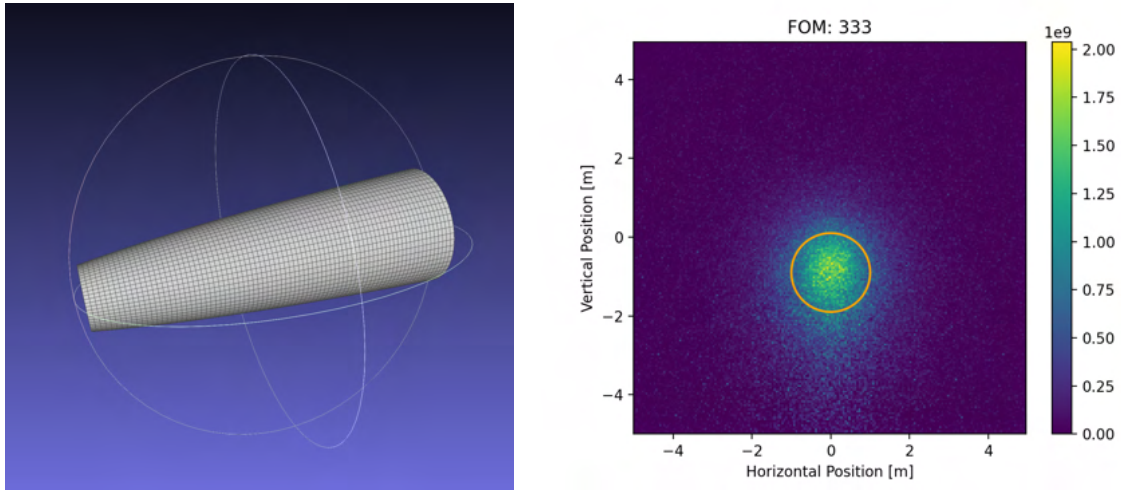


**Figure 219:** (left) 3D Visualization of the 40 m long baseline reflector (axis are not in scale). (right) Result of a McStas simulation with the baseline reflector for Target Power 2 MW. The orange circle marks the detector area of 1 m radius. The FOM is 333.

design scheme has, in addition, been previously used for optimization of parameters and for comparison of several NNBAR configurations in previous publications [4, 268, 180].

A McStas simulation performed with this reflector with the horizontal axis at the center of LBP gave a FOM = 333 with the moderator parameters and spectrum shown in the previous section for ESS power of 2 MW (see Section 1.1.3. The shape of the reflector and the focused beam distribution at the annihilation target obtained in the simulation are depicted in Figure 219.

Given that the center of the lower moderator is approximately 20 cm below the axis of the LBP (as illustrated in Figure 3, a symmetrically placed reflector relative to the moderator may not effectively utilize the entire aperture provided by the LBP.

To cope with that issue the concept of a “differential reflector” was proposed [268]. The reflector is positioned exactly in the middle of the LBP but has a distorted ellipsoid shape (See Figure 220). The constituting panels fulfill the solution of a coupled differential equation, to behave on each position like an elliptical mirror and form a continuous surface. This reflector focuses and bends the neutron beam by a few degrees in the vertical direction at the same time. This will allow the preservation of the FOM with the horizontal beam axis between the centers of the cold source and the annihilation detector.

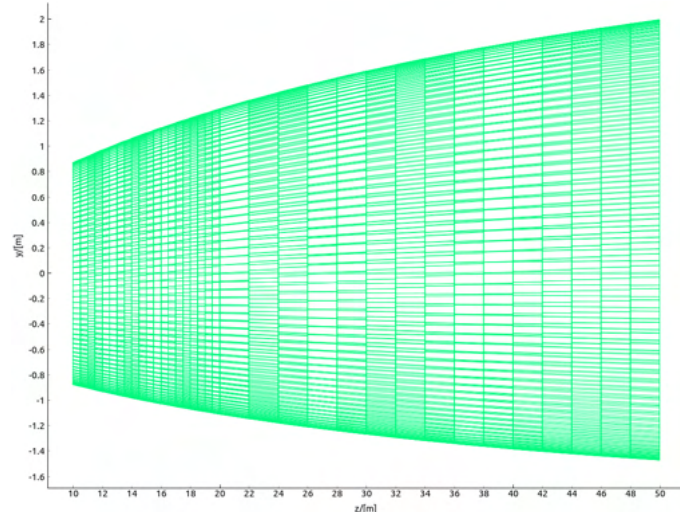


**Figure 220:** Depiction of the differential reflector.

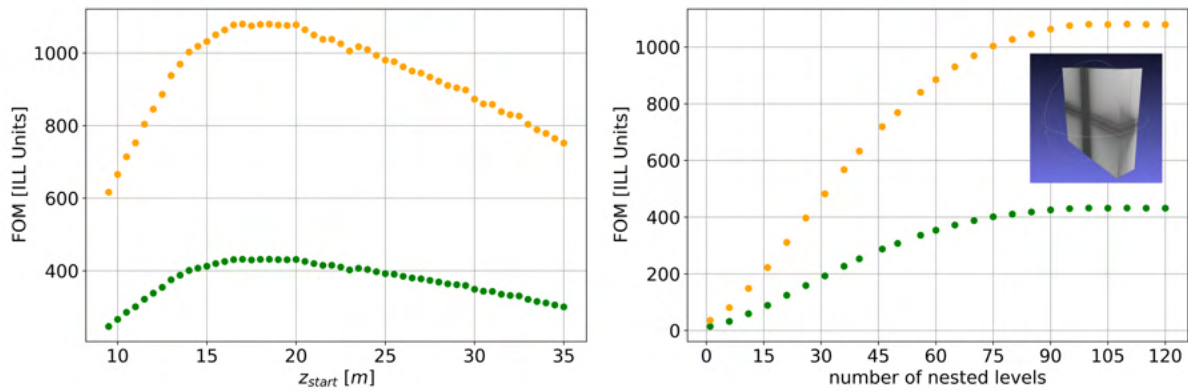


**Figure 221:** Result of simulations for a nested double planar reflector of length 1 m (see inlay) for 2 MW (green) and 5 MW (orange) target power of the ESS. (left) variation of the starting point of the optic, . (right) effect of increasing the number of nested levels.

McStas simulations performed show the comparability of this layout to the baseline design. With the “differential reflector” a  $FOM = 340$  is achieved, which amounts to a small increase of around 1 % compared to the baseline.

### 9.8.1 Optimization of the Nested mirror reflector options

The optimal parameters for various nested mirror optics geometries are determined through extensive simulations, and the resulting figures of merit (FOMs) are compared. Two such parameter scans are depicted in Figure 221 for a double planar nested reflector with a length of 1 m. The scan for the  $z_{start}$  parameter, which represents the start of the optic defined as the distance from the moderator, reveals an optimum at approximately 17 m. It’s important to note that increasing the start-of-optics distance, for example, from 10 meters to 20 meters, would effectively double the size of the reflector face. This demonstrates the need to consider the choice of the start-of-optics parameter in conjunction with the optimization of other parameters that define sensitivity and the overall cost of the experiment.

Regarding the number of nested levels, there appears to be a point of saturation where adding more levels does not lead to a significant further increase in the FOM. This suggests that a balance must be struck between the complexity and cost of the optics system and the achievable sensitivity.

For the simulations of the mono-planar components, the arrangement with mirrors in a horizontal layout was consistently placed in front of the one with mirrors in a vertical layout. This choice was made with magnification in mind. Since the moderator has dimensions of approximately 40 cm in width and 24 cm in height, it is advantageous to have the vertical component with less magnification positioned farther away from the moderator. As the components become shorter, this effect becomes less pronounced.

### 9.8.2 Summary of the simulation results

In Figure 222, the results of the simulations for the various reflector geometries are summarized. The nested components consistently achieve significantly higher FOMs compared to the baseline or the differential reflector. Notably, the cylindrical components slightly outperform the planar ones. This advantage arises because the former require only one reflection to reach the target, while the latter necessitate an additional one. In general, the nested components offer gains of at least 20% over the baseline reflector in terms of FOM.

The results regarding the optimal starting locations, denoted as  $z_{start}$  for the reflectors, are presented in Figure 223. It is observed that the optimal starting location for the reflectors is approximately 17 m

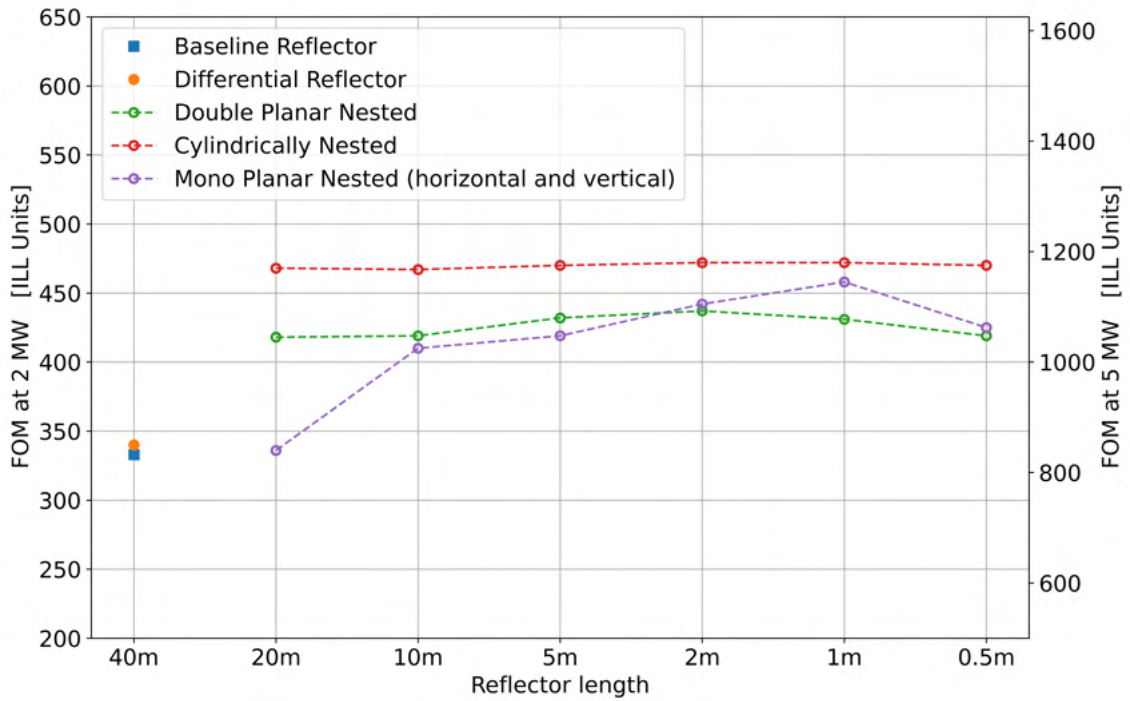


**Figure 222:** Collected FOMs for different reflector geometries (target power 2 MW and 5 MW, respectively).

away from the moderator. Interestingly, as the length of the optics decreases, the optimal starting location shifts farther away from the moderator.

### 9.8.3 Simulations for a physical model of the experiment

The studies conducted in the previous sections did not consider a detailed beamline layout, apart from the limitations imposed by the LBP. To assess the potential impact of further constraints related to the presence of neighboring instruments (e.g., the LOKI instrument located in close proximity to the NNBAR beamline) and the size of the vacuum tube, additional simulations were performed with the following modifications:

- A first rectangular aperture after the LBP at 7.9 m of size 1.8 m x 1.63 m vertically centered at 0.84 m from the top.
- A second rectangular aperture after the LBP at 10 m of size 2.2 m x 2 m vertically centered at 1.0 m from the top.
- A circular aperture at 17 m (respectively after the reflector for starting positions that are larger) of radius 1.5 m centered symmetrically.

With this set of apertures, the available paths for the neutrons are limited to areas that align with the model used for the beamline shielding calculations (as described in Section 9.5).

As a reflector for this study, the monoplanar type with a length of 0.5 m has been chosen (as shown in Figure 224 a) for representation). The reason for this choice is that the construction of this reflector poses fewer engineering challenges compared to the other geometries.

Two possible scenarios for the locations of the reflector have been studied:

- Inside the bunker at 11 m.
- Outside the bunker starting from 15 m.

See also Figure 224.

For both scenarios, the length of the experiment was also varied to study the impact of longer NNBAR baselines on the FOM. The results in the following sections are presented for a 2 MW target power, but

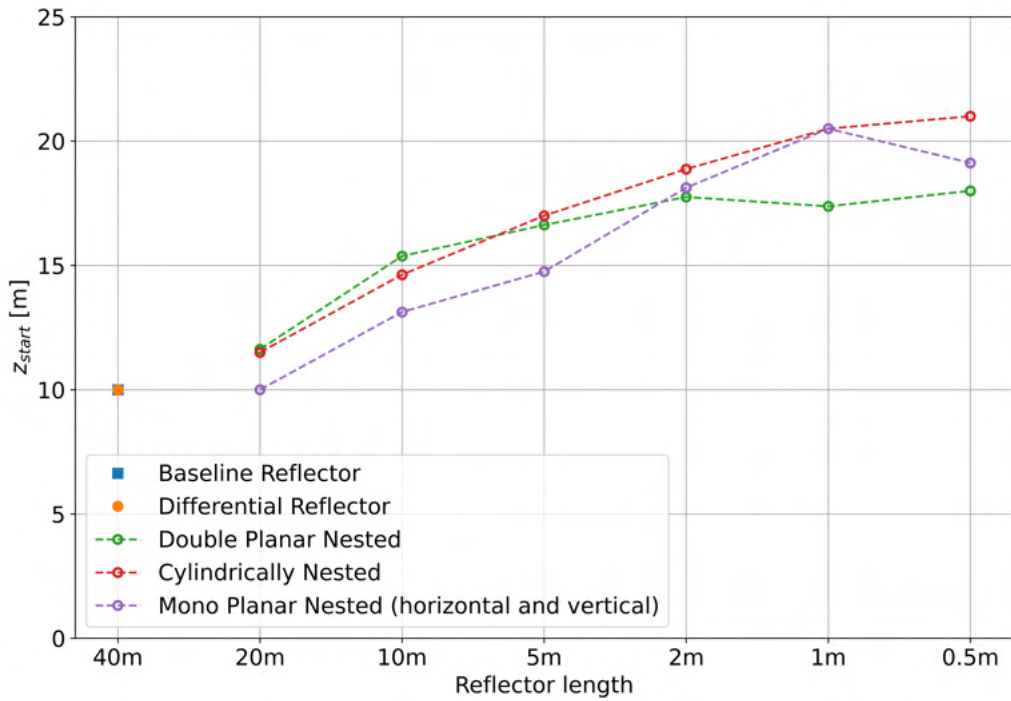


**Figure 223:** Starting position  $z_{start}$  for the different reflector types and lengths. The optimum of shorter reflectors tends to be at positions further upstream.

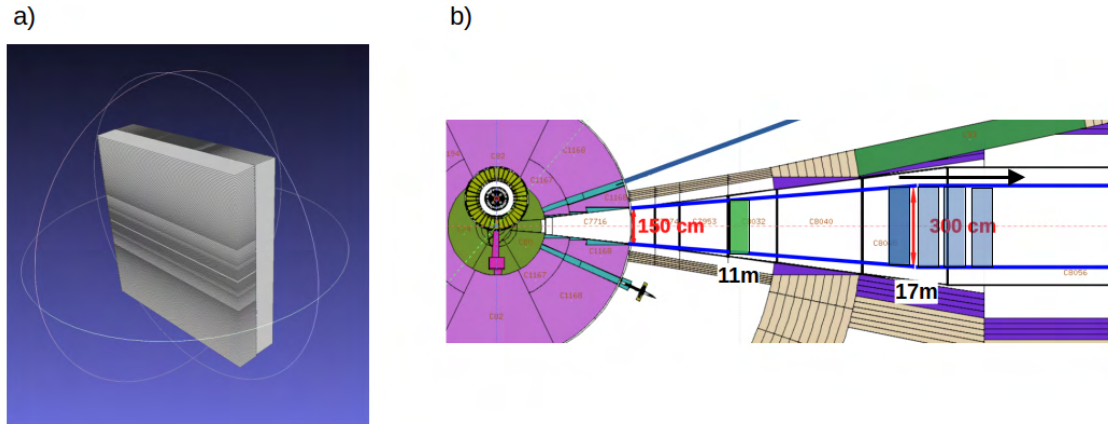


**Figure 224:** Left side: Depiction of the Reflector used for the simulations. Two mono-planar (MP) nested mirror assemblies, each of 0.5 m length. Right Side: Sketch of the placement of the reflectors in the physical model of the experiment; Inside bunker position at 11m (green); Outside bunker( starting at 15m) (blue).

they can be easily scaled to a 5MW power scenario.

**Results for reflector located at 11 m from the source** The results of the simulations for a longer baseline reflector at a distance of 11 m are shown in Figure 225. At a length of 200 m, a Figure of Merit (FOM) of 221 is achieved. Increasing the experiment's baseline length further only leads to marginal gains. This is primarily due to the high magnification factor at this position, which becomes even more significant as the baseline is increased. As a result, the image at the detector becomes smeared out, as

depicted for several lengths in Figure 225.

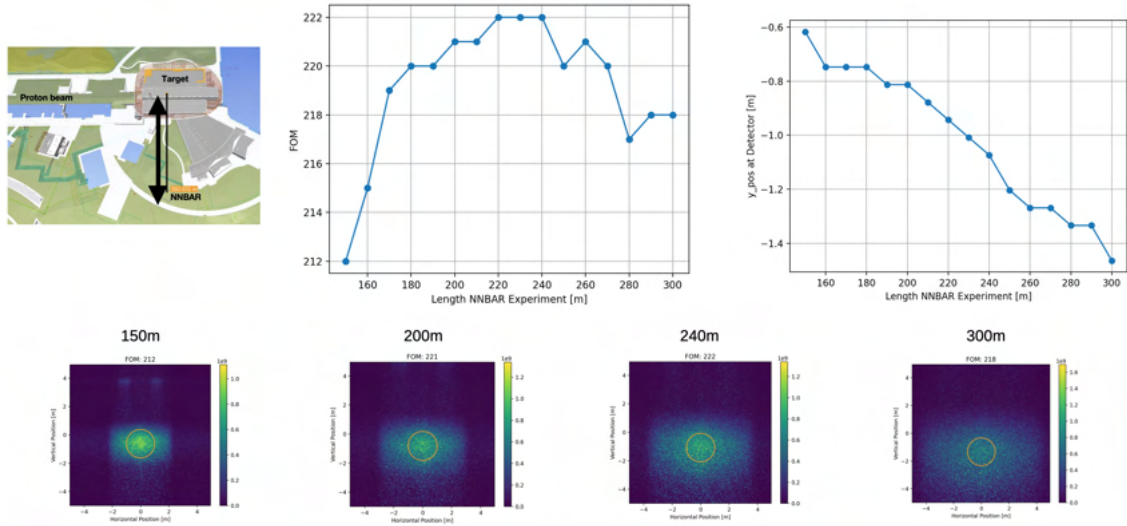
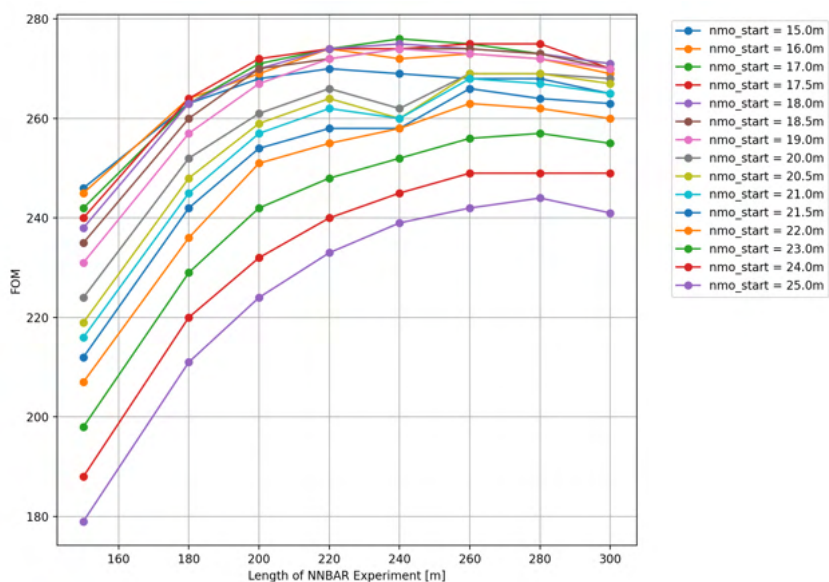


**Figure 225:** Results of simulations for a reflector placed at 11 m. The plot on the right show the shift of the center of intensity on the detector due to gravity fo longer baselines. At the bottom images for selected lengths of the experiment are shown. The blurring is due to the increasing magnification.

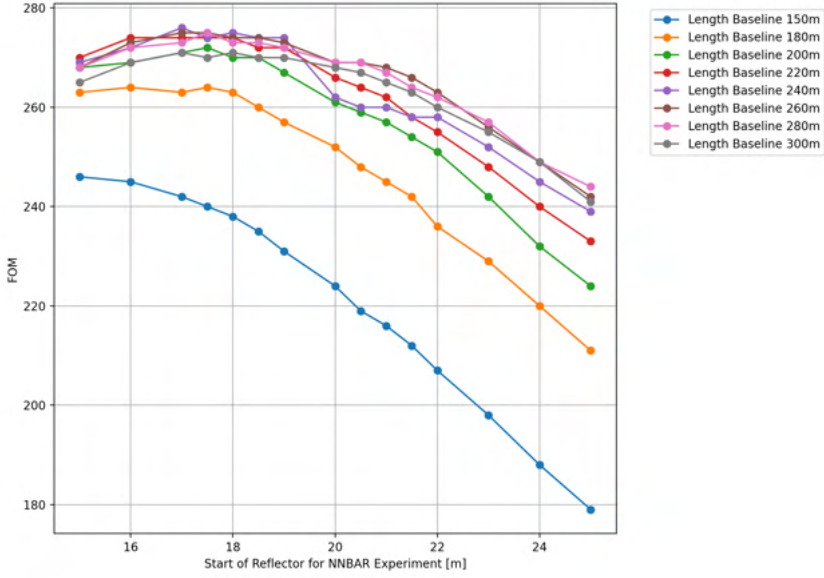
**Results for Reflector located beyond 15 m** In this scenario, both the baseline of the NNBAR experiment and the starting position of the reflector have been varied. The results are visualized in Figure 226 and Figure 227.

Figure 226 shows that the FOM remains relatively constant at lengths of about 200 m. The optimum starting location for the optics outside the bunker scenario is found to be at about 18 m, with a FOM ranging between 270 and 275.

These results suggest that, within the considered parameter space, a baseline length of approximately 200 m and a starting location of around 18 m outside the bunker could provide an optimal configuration for the NNBAR experiment.



**Figure 226:** Results of simulations for a reflector placed beyond 15 m as a function the length of the experiment.



**Figure 227:** Results of simulations for a reflector placed beyond 15 m as a function the starting position. Alternative visualization of the same data as in Figure 226.

The results indicate that using a square-shaped tube section after the optic, which transitions to a circular cross-section after a certain distance, can improve the performance of the NNBAR experiment. Figure 228 shows the results for a reflector placed at 17 m with different lengths of the square-shaped section.

For instance, a length of 20 m for the square-shaped section would result in a FOM of 300. This suggests that modifying the beamline geometry in this manner can lead to a substantial improvement in experimental sensitivity.

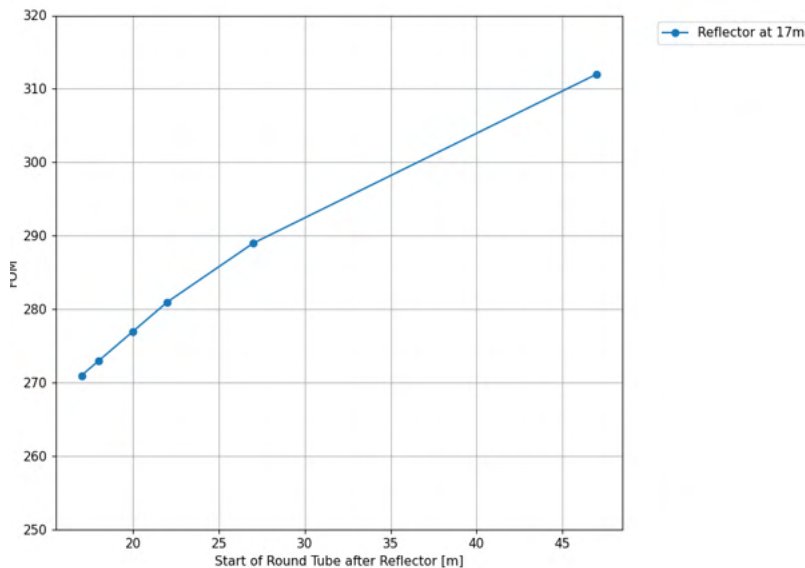


**Figure 228:** Results of simulations when adding a squared shaped tube section after a reflector placed at 17 m. The FOM increases with the length of the section.

#### 9.8.4 Utilizing the ESS pulse shape

There is another possibility that can be explored in simulations, particularly with the mono-planar nested reflector geometry. It is potentially possible to compensate for the gravity effect that effectively cuts off

the slowest neutrons that contribute most strongly to the  $N < t^2 >$  sensitivity. The repetition rate of ESS of 14 Hz means that a 3 ms proton pulse is followed by 68 ms time for neutron flight time. If a mono-planar nested reflector with horizontal reflector planes is positioned e.g. at 10 m from the cold source along the beam axis then slowest neutrons with velocity  $\sim 200$  m/s will arrive to 10 m position for the time between ESS target pulses. Neutrons with such a velocity travelling after the reflection for 1 s a distance about 200 and about 5 m in the vertical direction due to gravity will not hit annihilation target. Vertical motion of neutrons can be corrected at the reflection point if reflection plane will changes its angle starting with each ESS pulse in a programmed way compensating gravity effect. Reflector planes should be driven with high precision (although for small variation) e.g. by ultrasonic piezo-motors allowing motion speed from microns to 100's mm per sec. The motion in the first mono-planar reflector with horizontal planes can compensate for the gravity effect and may increase the sensitivity of the NNBAR experiment. Such motion will not be needed for vertical planes of the second mono-planar reflector. This solution should allow ballistic trajectory for slow neutron that might be limited in height by the diameter of the vacuum and magnetically compensated volume. The length of the reflector planes along the z can be  $\sim 1$  m or shorter as a result of optimization. This idea of a time-varying focusing reflector for the spallation neutron source was discussed previously in [269] and will be part of future studies.

## 9.9 Magnetic Shielding

Magnetic fields must be sufficiently small so as not to inhibit the transition between a neutron and an anti-neutron owing to a lack of degeneracy between the particles caused by their opposite magnetic moments. It is necessary to achieve the quasi-free condition  $\|E\|t \ll 1$ , where  $E$  and  $t$  are neutron energy and propagation time, respectively, and the probability of a transition becomes proportional to the square of the propagation time. Maintaining a magnetic field of less than approximately 5-10 nT achieves this condition [180]. Neutrons travelling 200 m inside a shielded environment will nevertheless be subject to a time-varying field in the rest frame of the particle. This results in gradients, spatial and temporal distortions in the field. It was shown in Ref. [224] that such effects do not significantly suppress the neutron-antineutron transition. The most important quantity is the magnitude of the average field. The goal for NNBAR is therefore to permit neutron propagation with an average field experienced along each neutron trajectory of less than around 10 nT. An additional constraint is that, in order to avoid interactions, the neutrons move in a vacuum. A shielding system, described below, has been designed [270], which gives a typical field of around 5 nT.

### 9.9.1 Magnetic shielding concept

The shield concept is illustrated in Figure 229, a simulated with COMSOL [252, 253]. The model comprises a two-layer octagonal mumetal shield. This is combined with a 316L stainless steel vacuum chamber, which also aids with the shielding. In addition, an external excitation coil is arranged around the shield to monitor the performance. The asymmetric deformation shown arises from the orientation of the earth field.

Mumetal shielding gives a static lowering of the magnetic field in addition to damping changes in the external magnetic field of up to about 10 Hz. The shielding of higher frequencies is given by the combination of the conductivity of the vacuum chamber and the mumetal.

The design of the mumetal shield is based on a proven small-scale design of the magnetic shield which is used for an atomic fountain [271]. This comprises mumetal sheets, deployed in an octagonal shape and which are clamped together. Overlaps of 50 mm width of the mumetal sheets are foreseen to ensure proper magnetic flux connection while being a reasonable compromise with magnetic equilibration. Using this approach, the independent assembly and detachment of the shield parts can be done when needed. The vacuum chamber can be arranged in between the mumetal layers or inside the inner mumetal layer.

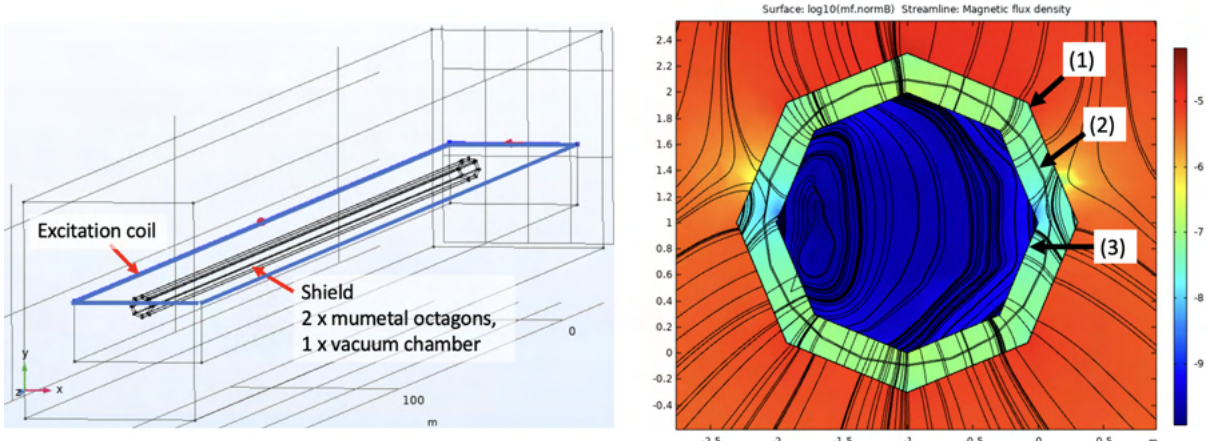


**Figure 229:** Left: The 200 m long and 2 m ID arrangement. This consists of a pair of octagons made from mumetal, with a 200 m length and a stainless-steel vacuum chamber separating them. Right: a shield cross section. A logarithmic scale magnetic field magnitude is shown. (1) Outer mumetal shield; (2) vacuum chamber; (3) inner mumetal shield.

For a low magnetic field, magnetic equilibration of the mumetal is required [272] through a set of coils. These surround each shield layer independently as a toroidal coil. The shield diameter is determined by the volume needed to be accessible to the neutrons together with a distance of around 20 cm shield walls, where the fields after equilibration are too high for the experiment. Furthermore, the gap between the mumetal shells is estimated from simulations and set to a minimum of 20 cm.

**Simulations** Figure 229 shows a schematic diagram of the shield modelled in the simulation. The simulations are made with finite element calculations using the commercial software package COMSOL [252]. For the optimization of parameters, the shield was deployed inside a static background field which is normal to the shield axis. The influence of various static fields from other ESS instrument magnets at LoKi, ESTIA, SKADI, DREAM, HEIMDAL and T-REX [273] were also considered. Representative tests of steel rebar from magnetic concrete and structures were additionally made. A large external coil is deployed surrounding the shield. This produces a magnetic field mostly perpendicular to the shield axis. The coil is placed closer to one open end of the shield than on the other side in order to also study the effect of fields entering the shield longitudinally. Estimates of shielding efficiency were then made for 1, 10 and 100 Hz frequency, which included permeability and currents. The estimation of DC field reduction is not quantitatively possible for fields of very low magnitudes via a magnetostatic approach. However, it should be pointed out that the effect of magnetic equilibration is both well studied and tested and, in specific and simple scenarios, can be calculated [274, 275]. It can thus be scaled from a magnetostatic simulation based on a typical mumetal anhysteric curve. Figure 230 shows the fields inside the shield arising from excitations of frequencies in the range of 1 to 100 Hz, together with an external excitation which has an identical amplitude.

From the ratio of outside and inside magnitude, the shielding factor SF is calculated for the center,  $SF(0.01 \text{ Hz}) \sim 10\text{-}300$ , depending on the position inside the shield. At 50 Hz, the SF is  $> 1000$ , including the vacuum chamber conductivity. After variation and minimization of thicknesses of inner and outer mumetal shield layers, the DC field is expected to be  $< 5 \text{ nT}$  after equilibration for 1.5 mm layer thickness for both shields. For a magnetic field perfectly normal to the shield axis, the length of the shield can be arbitrarily scaled. However, due to a slight tilt of the field at site, the material at the middle sections is thicker than at the end, making the required amount of material larger by 15% compared to naive scaling.

Although the equilibration efficiency is not simulated quantitatively but scaled from experimental findings, the field distribution inside the shield after equilibration is modeled, see Figure 231.

Magnetic equilibration can be realized, as studied in the simulation, using 8 turns for each octagon,

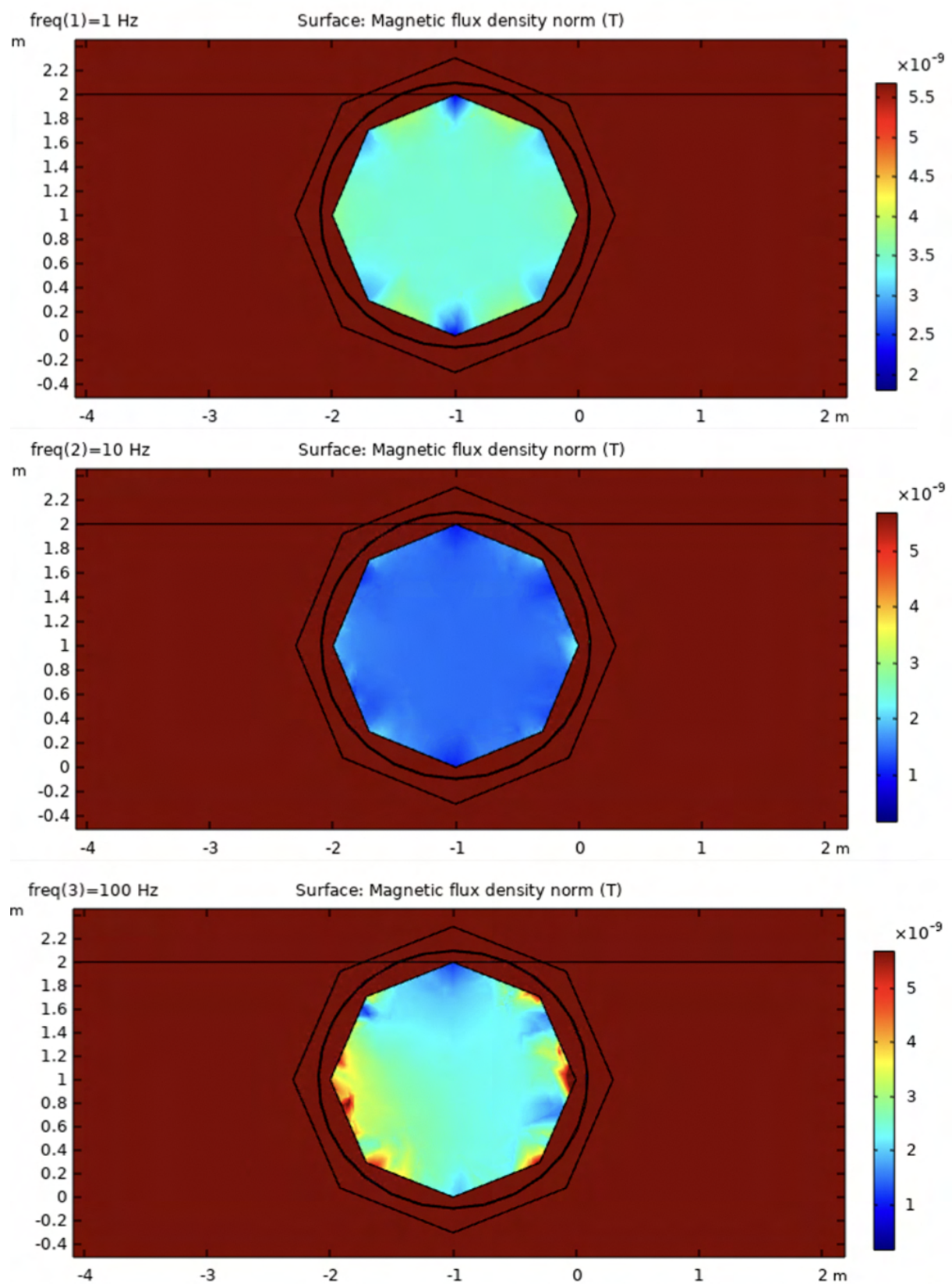


**Figure 230:** Field inside the shield (cross section in middle region), for 1, 10 and 100 Hz external excitation.

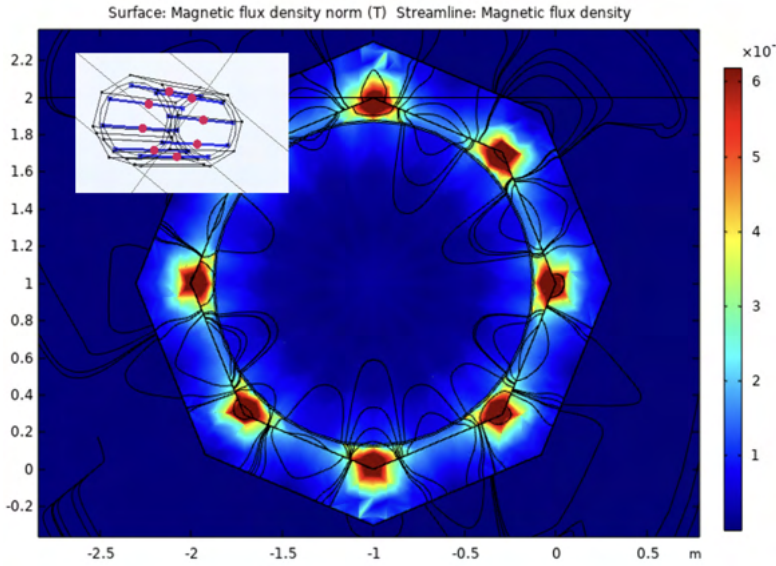


**Figure 231:** The expected field pattern from the magnetic equilibration process.

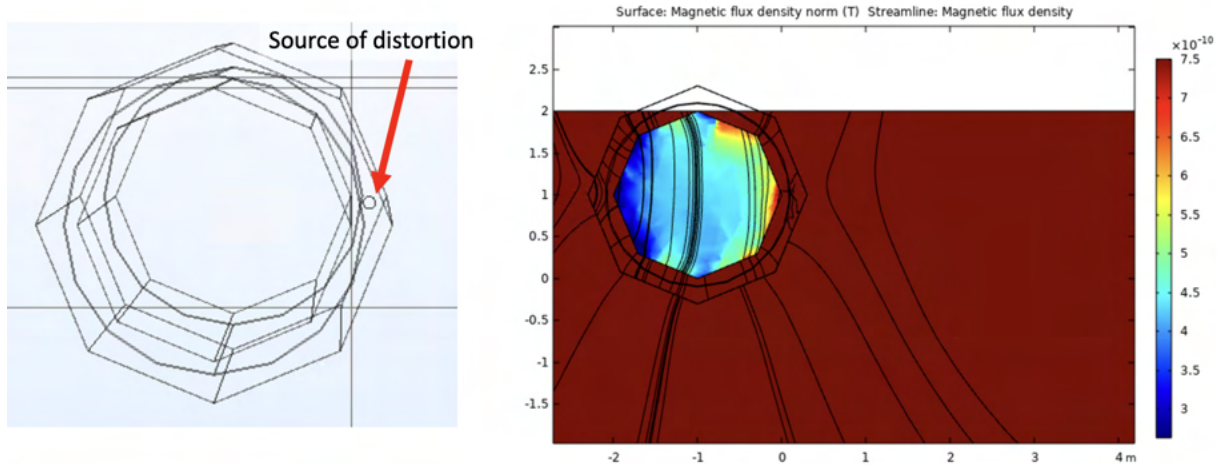


**Figure 232:** An example of a magnetic distortion arising due to a magnetic weld. The impact on the inside field after equilibration is shown.

with 80 Amp-turns. An additional point to consider is the effect of local magnetic distortions which can be their origin, eg, the vacuum chamber or an outside source. The modelling of these is shown in Figure 232. A typical scenario could be a magnetic weld in the vacuum chamber, which can be  $> 1000$  nT extending over distance of few centimeters.

A Monte Carlo study which tracked particles inside the shield using simulated residual field maps has then been carried out. This showed that the efficiency loss due to the presence of the small but finite magnetic field is around several per cent.

## 9.10 NNBAR vacuum

As previously explained, it is necessary to transport neutrons within a magnetically shielded and low-vacuum environment. For quasi-free neutrons, the vacuum pressure should be maintained below  $10^{-5}$  mbar [276, 277, 278]. Meeting these vacuum requirements involves a relatively large volume, approximately 3 meters in diameter and 200 meters in length. This volume is directly connected to the ESS monolith vessel, presenting unique challenges in mechanical, vibrational, vacuum, and radiation safety engineering.

The ESS monolith was designed to be able to operate with He atmosphere (100K Pa) or at a low pres-

sure  $< 1 \times 10^{-2}$  Pa range with a residual composition including He, H<sub>2</sub>O, and light hydrocarbons (CO, CO<sub>2</sub>, CH<sub>4</sub> and other fractions), as part of the expected environment of the spallation process with surface temperatures  $> 373$  K and a mixed environment of neutrons and gamma radiation. A specific vacuum barrier will be necessary to offer the flexibility to work independently on the target and on the NNBAR experiment.

The vacuum vessel will house the neutron optics (as described in Section 9.7.1) in a vacuum environment and will provide support for the external magnetic shield along the entire length of the beamline. During the optimization of the NNBAR optics design, the following approach was adopted for the vacuum pipe: initially, a rectangular vacuum pipe is used from the LBP up to the optics location, which is approximately 17 meters after the moderator (as discussed in Section 9.8.3). Subsequently, the design transitions to a cylindrical vacuum pipe with a 3-meter diameter, extending up to the detector area, where it will then reduce to a 2-meter diameter.

A combination of mechanical pumps (dry rough and turbo-molecular) units for pump down and a combo-type (sputter ion pump and non-evaporable getter) are currently planned as a permanent pump solution to minimise vibration on the optics system and assure a low level of physical access during the periods of operation.

## 9.11 The NNBAR detector

The ultimate goal of the NNBAR detector is the reconstruction of an annihilation event and rejection of background. The signature is an isotropically produced multi-pion final state (between 2 to 8, with an average of  $\sim 5$ ). The constraints in designing such a detector are as follows.

All primary particles hitting the detector should be identified and the directions and energies of annihilation and nuclear products must be measured. Given the constraint of the field-free propagation region, no magnetic field is used in the tracking system. Due to the rare nature of the process being measured, a statistical correction cannot be used, i.e., determining an inferred signal contribution to a large number of selected events in a signal region. As a consequence, combinatorial mistakes must be suppressed. Since the annihilation occurs in a nucleus and not in free space, the rejection power of some observables such as invariant mass and total energy will be degraded, as discussed in Section 9.11.6. This implies that some of the overall demands on the calorimeter energy reconstruction for the signal final-state particles can be relaxed. It is also important that all particles from background processes are identified as such and that these should not degrade the signal, e.g., due to background events piling up in-time with a signal event. Finally, it is of concern that technological and geometrical choices are made such that the final detector is affordable. These points represent an ideal case, but in practice compromises between the different choices will be needed. In order to identify an annihilation event, a combination of different types of evidence from the detector are needed.

The first type of evidence to guide the detector design is topological. A common vertex of origin in the carbon foil with at least two associated charged pion tracks needs to be reconstructed. If a neutral pion is identified, it must be associated with the same vertex as the charged pions. This requires tracking in three dimensions. Three dimensional tracking will allow excellent space resolution of all recorded events.

Figure 233 shows the charged-pion multiplicity from annihilation in  $^{12}\text{C}$ . In 10% of the cases there is only one outgoing charged pion, whereas in 88% of the cases there are two or more charged outgoing pions. The charged pions are the cornerstones of the annihilation topology, since these can be tracked and be used to reconstruct the event. Beyond the charged pions, charged nuclear fragments can also be produced and tracked. For the events that have only one charged pion, a  $\pi^0$  still needs to be reconstructed. For two charged pion events that have been confirmed to originate from inside-out (as opposed to cosmic rays), vertex reconstruction could be performed even in the absence of  $\pi^0$  reconstruction, provided charged nuclear fragments also point to the same vertex.

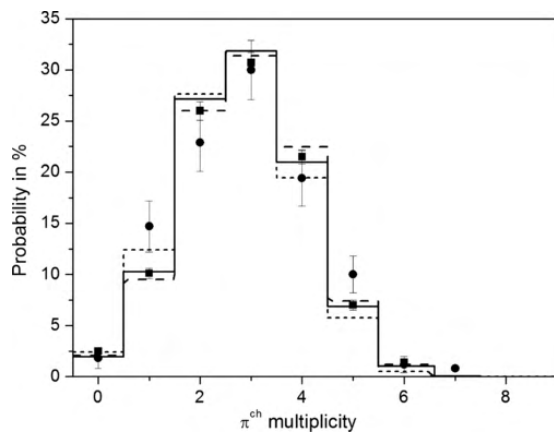


**Figure 233:** The probability (%) of the formation of a specific multiplicity of charged pions in antinucleon-nuclei annihilation. The solid histogram shows data from  $\bar{p}\text{C}$  interactions. Experimental data: circles-[[279]], squares-[[280]]. The dotted histogram shows a  $\bar{n}N$  simulation; the dashed histogram shows an  $\bar{n}\text{Ar}$  simulation. Taken from Reference [226].

Another set of evidence comes from conservation of energy and momentum, which is intrinsically

connected to particle identification (PID). Since a significant fraction of the available energy ( $\sim 30\%$ ) corresponds to the rest masses of the pions, accurate PID and thus measurements of the multiplicities of different types of particles are themselves indirect energy measurements. For a final-state with four pions, nearly 600 MeV of the total energy is accounted for in this way. In principle, the momentum and energies of all annihilation and nuclear products should be measured in order to reconstruct event kinematics and exploit event-level characteristics of the signal event, such as the expected isotropy of produced particles.

### 9.11.1 Detector choices

A number of technologies were considered. Out of the gaseous trackers, a time projection chamber (TPC) was chosen. A TPC is ideal for the purpose of pattern recognition in 3D with minimal combinatorial ambiguities and has a number of other desirable properties such as providing high precision specific energy loss,  $\frac{dE}{dx}$ , on many samples on the track, thus avoiding exceptional values in the Landau tail. A TPC is generally a cost-effective way of tracking over large volumes since the time domain is used for one dimension ( $z$ , along the beam) and the detector medium is only a gas volume. This also leads to a long integration time, which represents a challenge when confronting pile-up background (see Section 9.11.14). However, resolving tracks in 3D is very powerful and this is why, e.g, the ALICE experiment has chosen a TPC as the main tracking detector with up to 10 000 charged particles per collision expected in the TPC in central heavy ion collisions at LHC.

For calorimetry, a scintillator-based hadronic range detector (HRD) and a lead-glass electromagnetic calorimeter (LEC) are the chosen technologies for photon and pion energy measurements. A sampling calorimeter was considered [270] for electromagnetic energy reconstruction. But it was found to have lower  $\pi^0$  mass resolution. Furthermore, the directionality of the Cherenkov shower leads to a lower sensitivity for the LEC to incoming cosmic ray particles than for a sampling calorimeter.

The lower energy charged hadrons ( $p$  and  $\pi$ ) can be stopped gently, by ionization energy loss. The measured energy deposit will then be a correct measurement of the kinetic energy. The higher energies require a substantial amount of material to stop the particle by ionization energy loss. The probability is then high that nuclear reactions will occur before the charged hadron has fully depleted its kinetic energy. An energy deposit will then be a very crude measurement of the kinetic energy. There is no detection way around this fact unless a magnet is introduced. For charged hadrons the energy resolution is poor at high energies and here it will be even worse for hadron calorimetry [281]. Neutral pions decay in almost all cases to 2 photons. A  $\pi^0$  decaying at rest will emit two back-to-back photons with 67.5 MeV each. An increasing kinetic energy of the  $\pi^0$  will cause a smaller opening angle in the laboratory system and higher total photon energy. The markedly distinct behaviour of photons/electrons and charged hadrons in matter normally results in a combination of an electromagnetic calorimeter in front of the hadronic calorimeter. Here, the intention is to measure the hadrons before they scatter and interact, so the order is reversed (hadronic then electromagnetic measurement).

### 9.11.2 Overview of the detector

Figure 234 shows a cut-away of the detector, encased with concrete. This was produced as part of the mechanical construction study (Section 9.11.16).

A Geant4 model was developed to describe this detector. The model includes all major material sources (beampipe, TPC, scintillator staves) though omits smaller items such as electronics<sup>15</sup>. This was used to study light production in the lead-glass and scintillator staves.

A microscopic simulation of tracking in the TPC is a formidable and CPU-expensive task. This is not done here. At this point it is most reliable to utilise experiences from TPC's in operation, mainly the ALICE TPC and its upgrade [282, 283, 284] which is the most modern large scale installation with decades of prior R&D by many experts. In particular the most performance-driving parameter, the drift length, 2.5 meter, is the same for the NNBAR ALICE TPC's. The NNBAR TPC with its shorter track

---

<sup>15</sup>A dedicated MCNP simulation was used to investigate radiation dosages in the electronic, as described in Section 9.11.15.

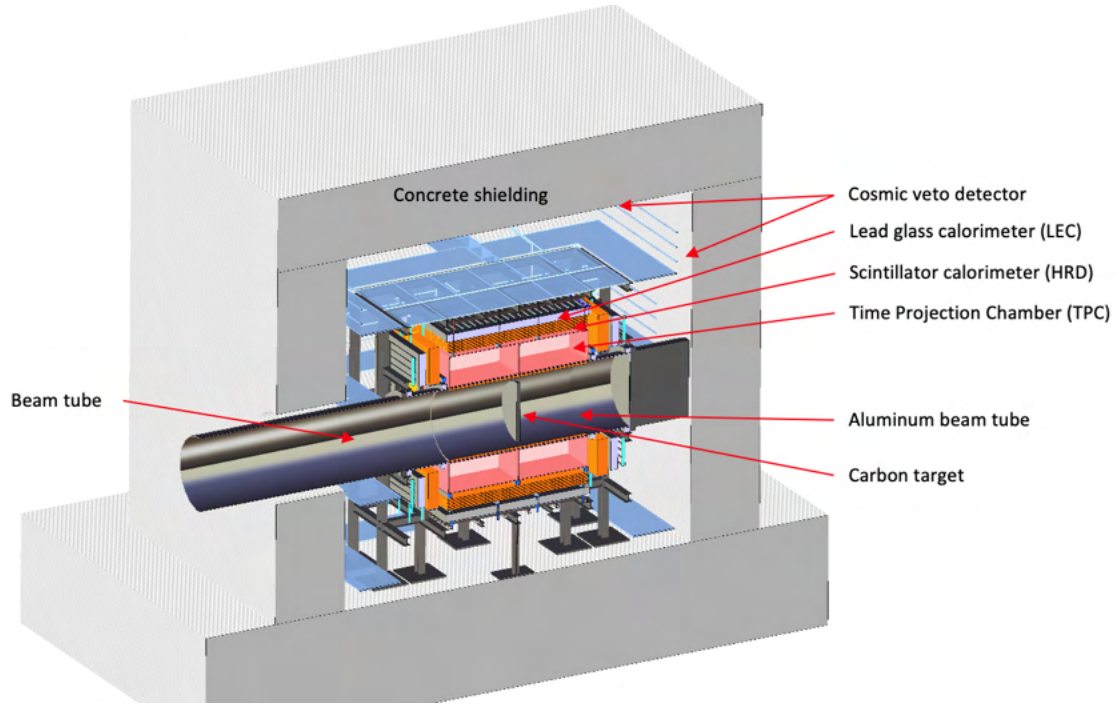


**Figure 234:** The NNBAR annihilation detector layers.

length may have to carefully optimize the drift conditions near the inner and outer edge of the drift field. The ALICE TPC has operated at low B-field which also makes it similar to our zero field. The ALICE TPC with 2.5 m drift length in the drift dimension and with no magnetic field has track residuals (normally claimed as the single point resolution) of about 0.5 mm for tracks parallel to the readout plane. Moderately better at short drift and worse at long. With a tilt angle the residuals deteriorates to mm scale. The single point resolution is, however, not the parameter of interest in a TPC where many points per track are measured. It is the track location and direction obtained by a straight line fit to many coordinates which matters. However, the inherent resolution of the TPC is not a limiting factor for the pointing towards the vertex. It is instead the fact that the measured track direction outside the vacuum chamber is not the same as inside due to multiple scattering in the chamber tube wall (see Section 9.11.5).

**Beam tube and target** Neutrons arriving at the experimental hall enter an evacuated aluminum beam tube with 1m nominal inner radius and 2 cm wall thickness, and encounter a thin ( $100\mu\text{m}$ ) carbon foil annihilation target in the center of the detector. Beam neutrons downstream of the target area are absorbed by a beam stop consisting of a thin boron carbide layer backed by layers of polyethylene, steel and concrete. Additional absorbing materials around the entrance to the beam tube further reduce beam-related backgrounds in the detector.

**TPC** Outside the beam tube is the TPC system, which provides three-dimensional charged particle tracking for event vertex identification and track matching, as well as particle identification capabilities through measurements of the specific energy loss  $\frac{dE}{dx}$  measurements. From the experience with, e.g., ALICE [282, 283] a tracking efficiency for a straight track of an approximately minimum ionising particle of  $\sim 99\%$  and resolution in  $\frac{dE}{dx}\%$  of  $\sim 5\%$  can be obtained. In this work, it is assumed that TPC tracks correspond to a length of at least 15 cm.

The TPC is nominally constructed from eight rectangular chambers each 70 cm deep, 200 cm long and 280 cm wide and contains an assumed 80:20 Ar/CO<sub>2</sub> mixture.

The TPC chamber walls are constructed from fiberglass. Charges are collected at the anode wall by gaseous electron multiplier (GEM) foils read out by 32-channel mixed-signal SAMPA ASICs originally developed for the ALICE TPC and muon chamber upgrades at the LHC. The SAMPA chips provide a

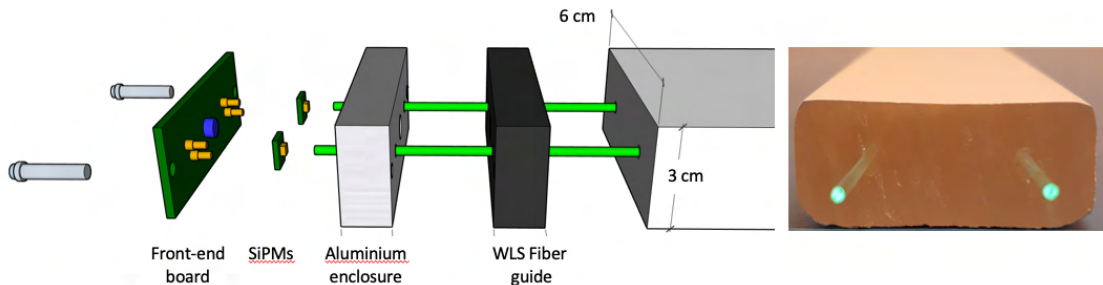


**Figure 235:** Assembly of two SiPM diode arrays and analog front-end electronics at the end of an HRD stave (left), end-view of an HRD stave with two wavelength shifting (WLS) fibers installed

full-on detector readout chain that includes amplification/shaping, digitization, a DSP layer, and readout over multiple parallel 4.8 Gb/s serial links.

The full TPC system contains 256000 GEM channels that can be continuously read out with sample rates as high as 10 MHz, corresponding to more than 5300 4.8 Gb/s serial links.

**HRD** The HRD is a multi-layer calorimeter with plastic scintillator staves that function both as an active material and absorber. It is designed to identify and measure minimum-ionizing energy deposits from low-energy charged pions traversing the scintillator, and is capable of distinguishing between proton and pion tracks by their specific energy loss  $\frac{dE}{dx}$ .

The HRD has a nominal thickness of 30 cm deep, and is built from 10 layers of long scintillating staves with width 6 cm and thickness 3 cm. The full HRD stack corresponds to around 0.6 interaction lengths and around 0.5 radiation lengths. The staves in each HRD layer run perpendicular to those in neighboring layers, producing crossing points for reconstructing minimum ionizing tracks of particles passing through multiple layers. Two embedded wavelength shifting (WLS) fibers running along the length of each stave collect and transport scintillating light to silicon photomultipliers (SiPMs) at the ends and the staves are coated with white reflective paint for optimal light collection in the WLS fibers.

The expected timing resolution of the SiPM stave readout is around  $\sim 1\text{ns}$  [285], and the majority of staves have SiPMs at both ends, allowing position and timing of hits to be estimated from the light propagation timing differences. An exception is at the "end cap" regions where the stave geometry around the beam tube makes this difficult; in the baseline design these shorter staves are therefore read out at only the stave ends furthest from the beam.

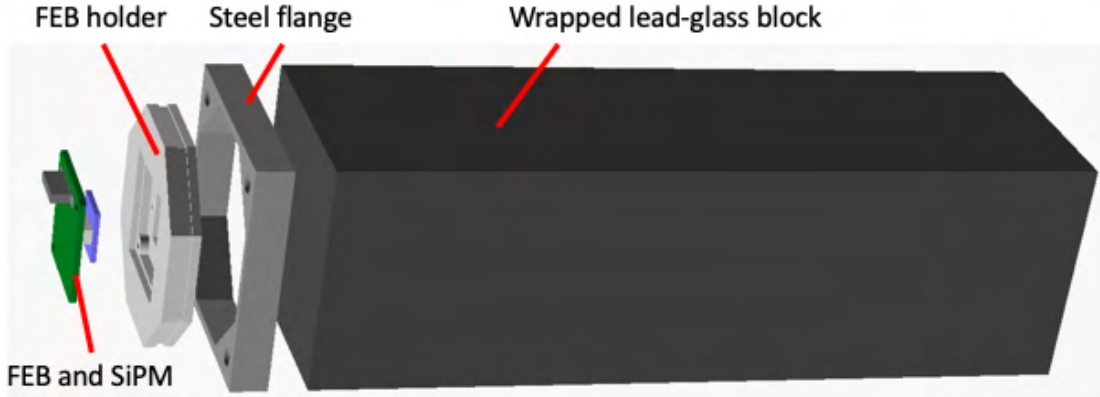
An illustration of SiPM and front-end electronics board (FEB) assembly at the end of each HRD stave is shown in Figure 235, alongside a photograph of a prototype stave. The WLS fiber ends are aligned by a plastic guide glued to the end of the stave, where they are then cut and polished. A milled aluminum enclosure holding the two SiPMs is mounted over the fiber guide. The enclosure also hosts a front-end electronics board (FEB) with analog amplification, shaping and readout circuitry for the SiPMs, calibration LEDs, and low- and high-voltage power distribution.

This HRD design includes more than 3000 scintillating staves with a combined length of more than 9km. The staves are read out by approximately 4500 front-end boards and 9000 SiPMs.

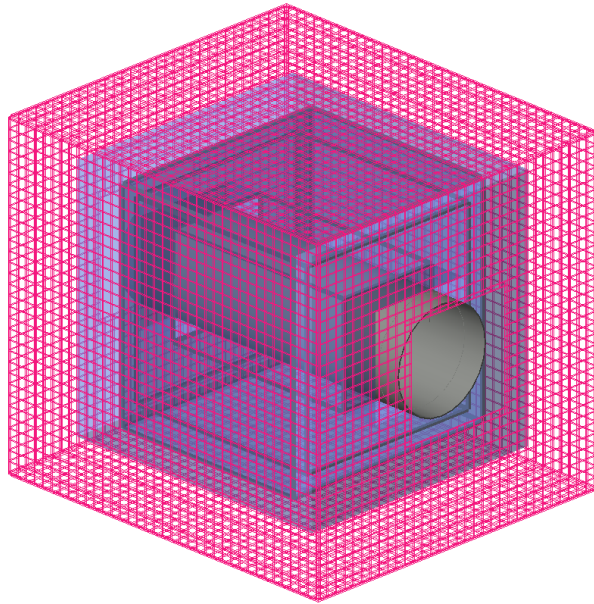
The above gives the broad principle of the HRD baseline design. A more segmented HRD with shorter staves of length 40 cm aimed at mitigating light attenuation in the WLS fiber readout and pile-up is possible. This is used here in simulations of signal and background discrimination. The final design depends on details of accurate and reliable estimates of pile-up.

**LEC** Surrounding the HRD is a lead-glass electromagnetic calorimeter built from over 32000 instrumented glass blocks. The LEC is designed to measure gammas from neutral pion decays, as well as higher-energy charged pions that are not stopped in the HRD.

An exploded view of an LEC glass counter is shown in Figure 236. The lead-glass block faces have  $6 \times 6\text{ cm}$  area and 20 cm depth (corresponding to around 15 radiation lengths), and are read out by SiPM



**Figure 236:** Exploded view of an LEC lead-glass counter.



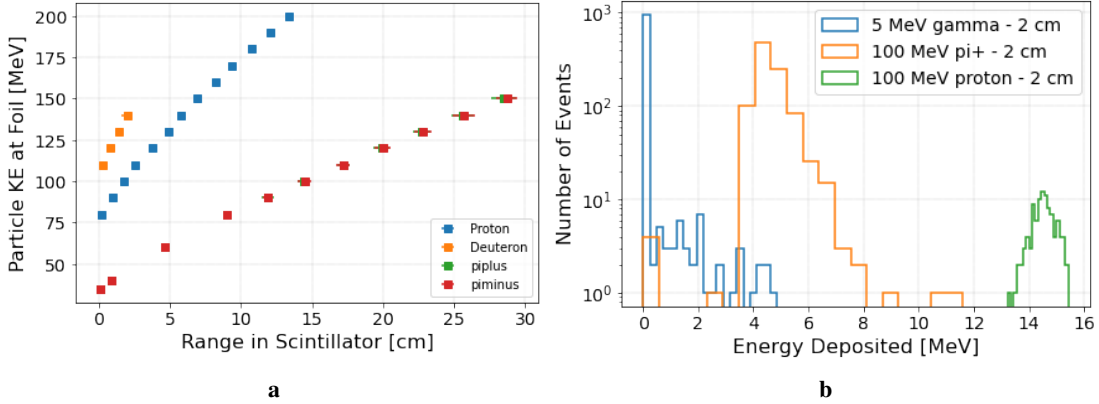
**Figure 237:** Geant model of the cosmic veto detector, including a simplified model of the annihilation detector. The passive shielding has been omitted in the drawing.

photo detector arrays at the back face. For this technology, a resolution of  $\frac{\sigma_E}{E} \sim \frac{6\%}{E[GeV]}$  and a timing resolution of  $\sim 1$  ns is expected, as achieved by PHENIX [286].

Since minimum Cherenkov velocity in a material is inversely proportional to its refractive index, a dense flint glass was chosen with high refractive index of 1.67 (Schott SF5 / CDGM ZF2) in order to improve sensitivity to lower energy charged pions. The sides of the lead-glass blocks are wrapped with enhanced specular reflective film for improved Cherenkov light collection efficiency. To suppress signals from cosmic particles entering from outside the detector, light-absorbing material at the inward-pointing face is used to minimize reflection of Cherenkov light emitted in the "wrong direction".

The LEC counters are mounted in the detector using steel mounting flanges glued to the back face of the glass blocks. The flanges are manufactured from martensitic stainless steel with a thermal expansion coefficient similar to that of the glass to minimize stresses at the steel-glass interface. The center of the flange provides wide open areas for mounting the SiPM arrays and LEC front-end boards. The LEC includes more than 32000 SiPM readout channels, corresponding to one SiPM array and front-end board per glass block.

**Cosmic veto** In the previous search for baryon number violation at ILL, cosmic rays were the dominant contribution to the background [262]. A reliable cosmic ray veto system is therefore crucial for the



**Figure 238:** Simulations of particle interactions in the HRD: (a) the range of particle in the scintillator plastic after passing through the vacuum tube and other detector material (b) energy lost in 2 cm of scintillator plastic for a range of particles and energies. Note that the current design is 3 cm of scintillator. Figure from Reference [287].

NNBAR experiment. For initial studies, a baseline geometry for the veto detector has been created. A baseline model for the veto system produced with Geant 4 is shown in Figure 237. The veto detector geometry is relatively simple, a box with dimensions  $6.4\text{ m} \times 6.4\text{ m} \times 7.2\text{ m}$ , large enough to contain the NNBAR annihilation detector. It comprises two layers of scintillating staves  $20\text{ cm}$  wide and  $3\text{ cm}$  thick, each read out by two WLS fibers to SiPMs at both ends. As for the HRD, the two layers of staves have perpendicular orientation to each other to aid track position measurements. The veto system is read by approximately 900 front-end boards and 1800 SiPM channels.

The passive shielding is omitted in Figure 237. It consists of  $30\text{ cm}$  of steel placed on the inside of the veto detector. Its main purpose is to shield neutral cosmic ray particles as well as showers produced in the active veto itself and prevent them from causing signals in the annihilation detector.

### 9.11.3 Scintillator staves

Geant 4 simulations have been used to study the expected energy loss for various thicknesses of scintillators. Figure 238b shows predictions of the range in the scintillator plastic of particles with different values of kinetic energies at the target foil. A scintillator thickness of  $2\text{ cm}$  will induce energy deposits of close to  $8\text{ MeV}$  for charged pions, and around  $18\text{ MeV}$  for protons. Figure 238 shows simulations of energy deposits in  $2\text{ cm}$  of plastic by photons produced following neutron capture in the carbon target along with energy deposits from  $\pi^+$  and protons. To ensure strong separation from gammas from neutron capture, a thickness of  $3\text{ cm}$  was taken for the detector. These gammas will typically lose their energy in a single scintillator stave, while pions will pass through a number of layers.

The generation of photons in a single scintillator bar and their transport through the scintillator material and the wave-length shifting fibers was investigated with a view of taking a parameterisation of the measured scintillation photons at the SiPM to provide an estimate of detector response. The number of optical photons reaching the SiPMs at the end of each fiber was determined for different particle types and energies while varying the hit position. Fibres were simulated corresponding to the absorption and emission spectra of Kuraray Y-11 fibres. The refractive index of  $n = 1.59$  was taken. Inner ( $n = 1.49$ ) and outer ( $n = 1.42$ ) cladding was also included.

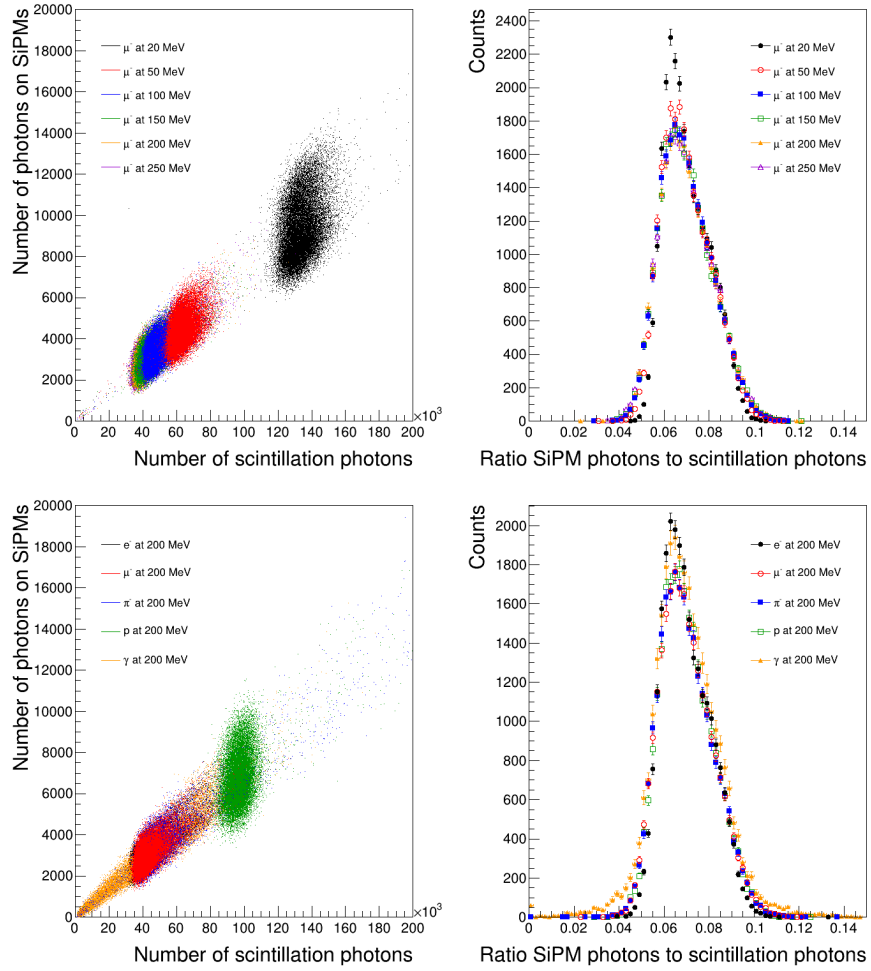


**Figure 239:** Left: the number of optical photons reaching the SiPMs as a function of the produced scintillation photons. Right: The ratio of the number of optical photons at the SiPMs over all scintillation photons. The top distributions show muons at a range of energies. The bottom distributions show distributions for a range of particles at 200 MeV kinetic energy.

Figure 239 shows the number of optical photons reaching the SiPMs as a function of the number of scintillation photons produced for a stave of size  $20 \times 2 \times 320 \text{ cm}^3$ . The data are shown for muons of a range of kinetic energies and a selection of particle types at a kinetic energy of 200 MeV. The fraction of photons reaching the SiPMs is approximately independent on the particle type and energy for a bar of a specific geometry.

To arrive at a parametrization for the expected number of optical photons at a SiPM, the fraction of SiPM hits is considered to be the product of the fraction of scintillation photons being absorbed in a WLS fiber and the fraction of photons re-emitted by the WLS material reaching the end of the fiber without escaping or getting absorbed,

$$\frac{n_{SiPM}}{n_{scint}} = \frac{n_{WLS}}{n_{scint}} \cdot \frac{n_{SiPM}}{n_{WLS}} . \quad (31)$$

The first factor is assumed to only depend on the average distance of the particle track from a fiber  $r$ , while the second one only depends on the average distance from the end of the bar  $z$ . Examples of these dependencies are shown in Figure 240 for incident  $\mu^-$  with  $E_{kin} = 200 \text{ MeV}$ . As is seen in the figure, they can be well described by functions of the form

$$f(r) = \begin{cases} Ae^{r/B} + C & r < d \\ Ae^{d/B} + C & r \geq d \end{cases} \quad (32)$$

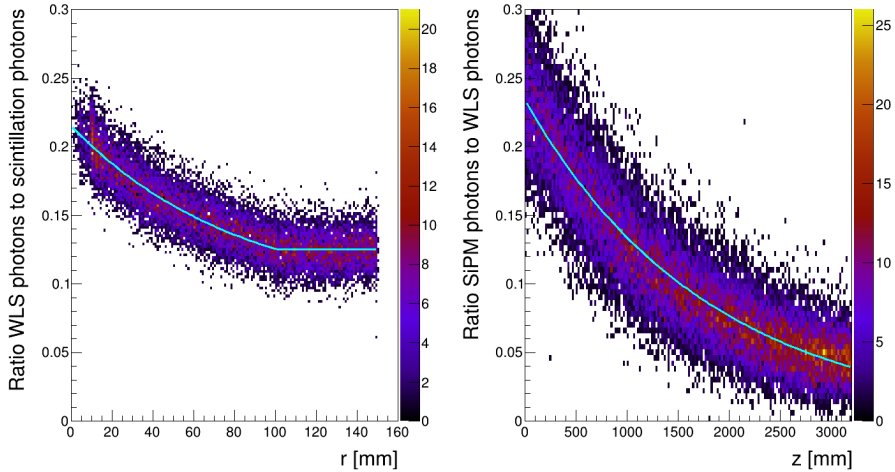


**Figure 240:** Left: Fraction of scintillation photons absorbed by a WLS fiber as a function of distance from the fiber. Right: Fraction of WLS photons reaching the SiPM as a function of  $z$ .

where  $d$  is the distance between the two WLS fibers, and

$$f(z) = D e^{z/E}, \quad (33)$$

respectively. The parameters  $A - E$  depend only on the shape and material of the scintillator bar and WLS fibers. This parameterisation was used in this work.

#### 9.11.4 Lead-glass calorimeter

Simulations with Geant4 were carried out to estimate the required depth and granularity of the lead-glass blocks. The energy resolution for  $\pi^{+/-}$  is expected to be poor due to the low energy of the particles expected at NNBAR and the interactions the particles will undergo with detector material prior to reaching the lead-glass. The purpose of the lead-glass is to measure photons from the decay of  $\pi^0$  produced at the foil. Figure 241 shows simulations of the fraction of energy lost in the lead-glass modules by photons with energies 210 MeV, 355 MeV, and 635 MeV as a function of lead-glass depth. A depth of 20 cm was chosen. For enhanced containment the outer block area was set to  $6 \times 6\text{cm}^2$ . In a more advanced approach, the barycentre of a transverse shower can aid positional determination. Figure 242 shows the GEANT4 simulated number of Cherenkov photons produced in the lead glass as a function of the deposited energy in lead glass by gammas of uniformly distributed from 0 to 450 MeV. This function serves as the basis for reconstructing the energies deposited in the lead glass.

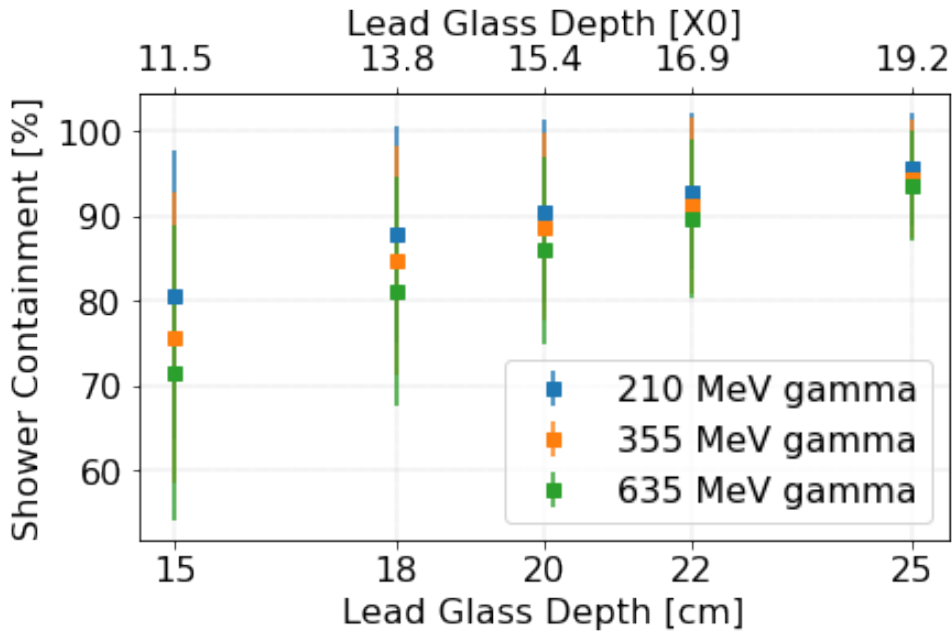


**Figure 241:** Particle shower containment as a function of lead-glass depth for  $4 \times 4 \text{ cm}^2$  lead-glass blocks. Figure from Reference [287].

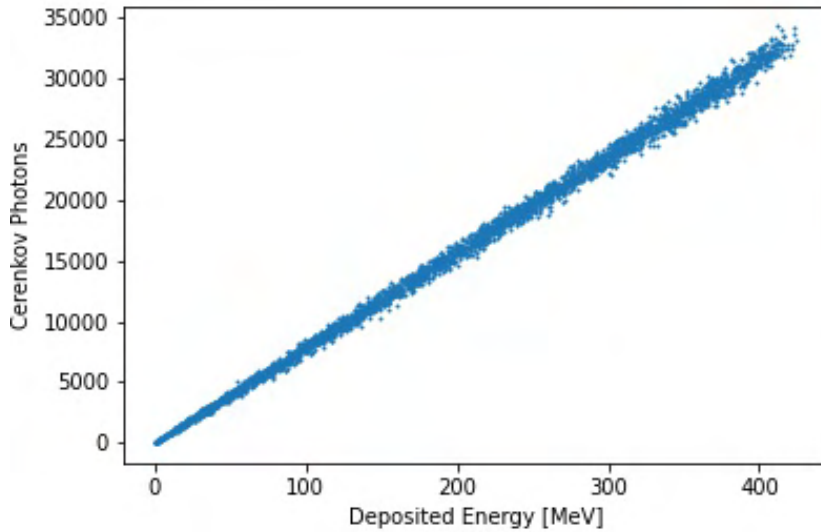


**Figure 242:** The number of Cherenkov photons at the back of the lead-glass module (detected) and the number of Cherenkov photons generated in the lead-glass block versus the deposited energy.

### 9.11.5 Object definition

Object definition is an important tool when building event variables to discriminate between signal and background. Object reconstruction and definition for the NNBAR detector at the beginning of this project [288] and is summarised below.

**Charged particle identification** In the context of free neutron-antineutron oscillation experiments, the differentiation between electrons and positrons, charged pions and protons is important. Electrons and positrons arise via the pair production at low separation angle from photons from neutral pion decays

interacting in the detector. For this work, it is assumed that the closely produced pair and associated large total energy loss allow straightforward identification.

A more sophisticated approach is used for pion and proton discrimination. The energy loss per unit length ( $dE/dx$ ) measured, via a truncated mean approach, in the TPC in conjunction with the number of traversed scintillator layers. Figure 243 shows the TPC  $\frac{dE}{dx}$  distribution of charged pions and protons that can penetrate scintillators at the layers 1, 5, 7 and 10, where the lowest (highest) layer number corresponds to the layer closest to (furthest from) the TPC. Clear separation between protons and pions is observed which increases in layer number. This permits the use of a PID selection for particles penetrating a specific number of layers.

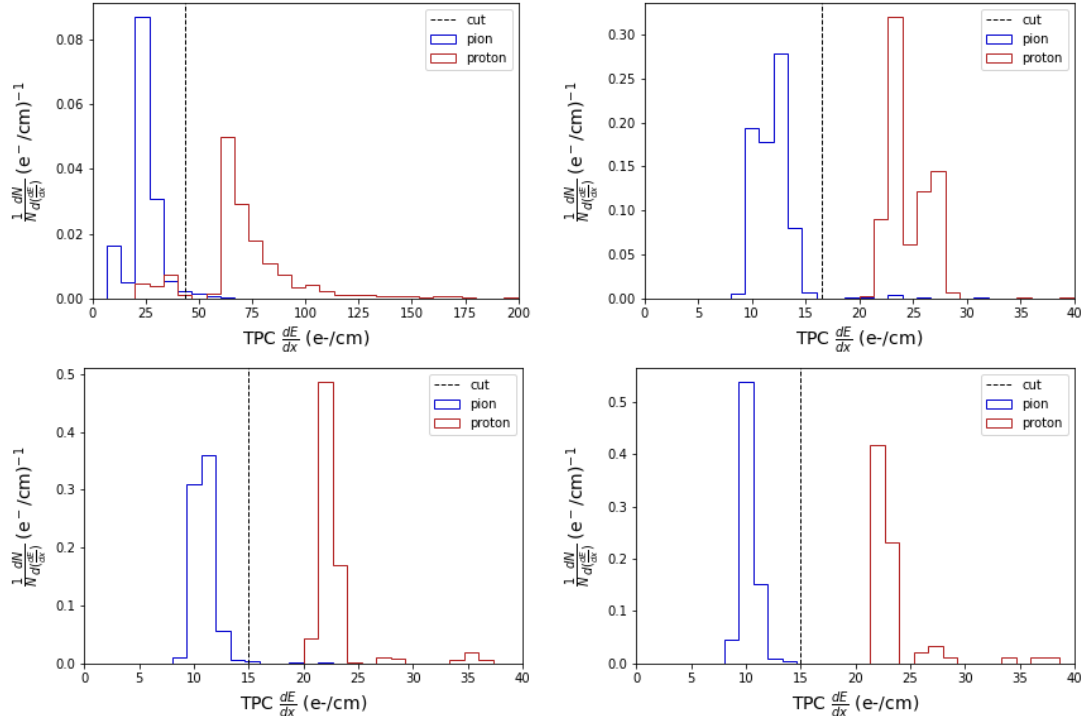


**Figure 243:** Expected distributions of the specific energy loss,  $\frac{dE}{dx}$ , for protons (red) and pions (blue), for different ranges in the scintillator stack.

Figure 244 illustrates the correlation between the TPC  $dE/dx$  and the particle range in the scintillator for annihilation pions and protons, showing two separate regions.

A cut on the TPC  $dE/dx$  as a function of the scintillator range was imposed to facilitate particle discrimination. The optimal cut value for  $dE/dx$  corresponding to each scintillator range was determined through a series of localized optimization procedures targeting the maximization of separation efficiency.

A discriminant region for the acceptance of pions and protons is delineated in Figure 244. Specifically, a particle is classified as a proton if its  $dE/dx$  exceeds the threshold function  $t(R)$ , and as a pion if its  $dE/dx$  falls below  $t(R)$ . Table 47 enumerates the efficiency rates for identifying signal protons and pions under these criteria. The entry in the row labeled  $\pi^\pm$  and column labeled  $\pi^\pm$  indicates that 99% of the signal pions are accurately identified as pions. Conversely, the entry in the row labeled *Proton* and the column labeled  $\pi^\pm$  denotes that only approximately 1% of protons are misidentified as pions. This implies a high degree of fidelity in the particle identification process under the established object definitions.

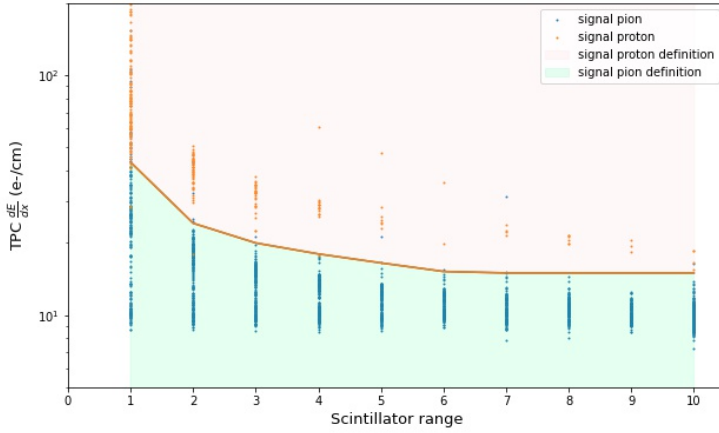


**Figure 244:** The distribution of the relationship between  $dE/dx$  and scintillator range for pions and protons originating from annihilation events. Two specific regions are demarcated on the plot for discrimination between these particle types. The region represented in red serves as the criterion for identifying protons, while the green region is designated for identifying pions. Furthermore, the plot includes a curve representing the threshold function of  $dE/dx$  as a function of scintillator range ( $R$ ), which delineates the boundaries between the defined regions for pions and protons.

**Table 47:** The table provides an assessment of the particle identification efficiency within the experiment. Specifically, it quantifies the likelihood that a signal pion or proton is correctly classified or misclassified.

	Truth Particle Type	
Identified Particle Type	$\pi^\pm$	Proton
$\pi^\pm$	99%	1.3%
Proton	1%	98.7%

**Neutral Objects** Unassociated energy deposits in the calorimeter are grouped into clusters, designated as neutral entities. A subsequent pairing of these neutral objects is conducted for the purpose of invariant mass calculation. The invariant mass  $M$  between a pair of such entities is determined by the equation

$$M = \sqrt{2E_1 E_2 (1 - \cos \theta)}, \quad (34)$$

where  $E_1$  and  $E_2$  denote the observed energy losses for the respective neutral objects within the calorimeter. The angle  $\theta$  signifies the angular separation between the two neutral objects.

This methodology can be empirically validated through Geant4 simulations by directing  $\pi^0$  at the carbon target with a fixed kinetic energy of 100 MeV. Single particle events are generated, with the  $\pi^0$  being directed in random orientations. The reconstructed invariant masses calculated from these simulated events are illustrated in Figure 245.

The multiplicities of neutral and charged pions are key observables to characterise a signal-induced final state. The correlations between generated and detector-level multiplicities of charged and neutral pions and the total number of pions in each annihilation event are shown in Figure 246 for signal Monte Carlo-generated events described in Section 9.11.6. The yield of charged pions at the detector level typically replicates the true number of migration effects that can be seen. For example, some charged pions are lost through geometric limitations. An overestimation of the charged pion yield arises if, e.g., a proton or an electron or positron from a photon conversion is falsely identified as a pion. The detector-level neutral pion multiplicity suffers from a larger migration effect due to the requirement of finding two photons for each pion.

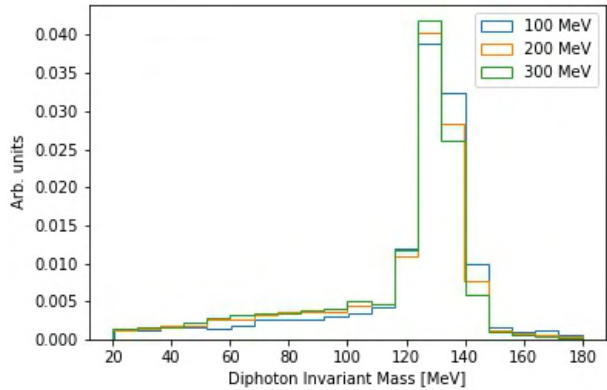


**Figure 245:** Distribution of the diphoton invariant mass.

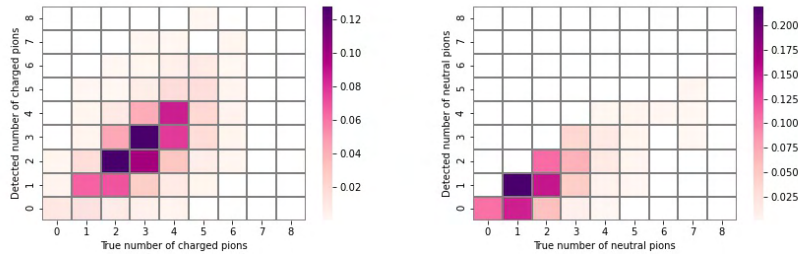


**Figure 246:** True and detector-level multiplicities for charged (left) and neutral pions (right). Figure from Reference [288].

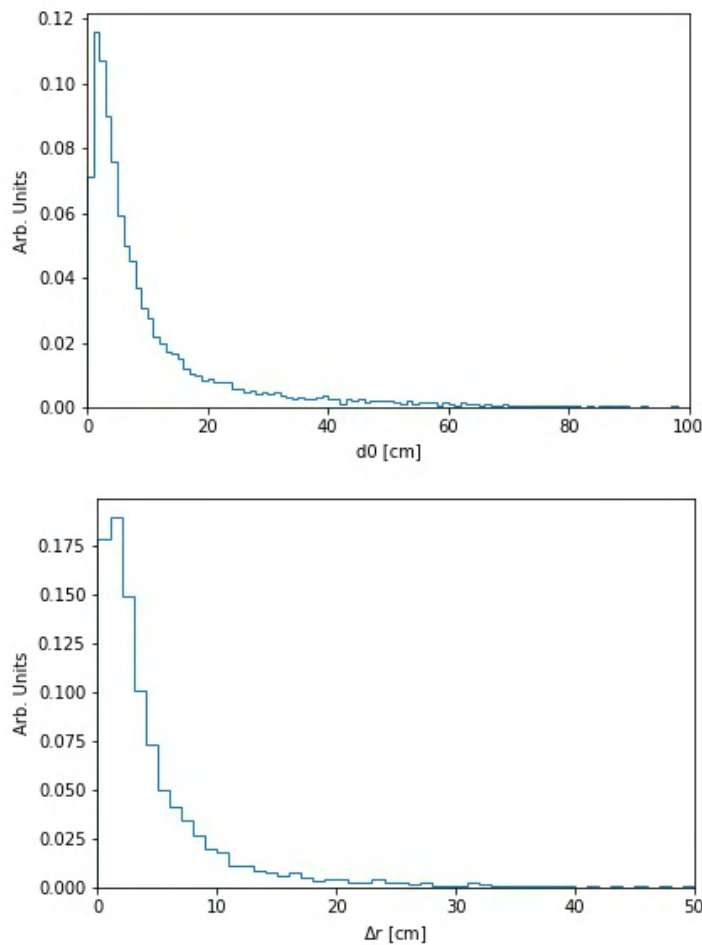
**Vertex resolution** For most signal events, a vertex formed from charged particles emanating from the foil is expected. This is a strong discriminant between signal and backgrounds. Although a full track and vertex reconstruction is not available, the vertex resolution is dominantly determined by the 2 cm thick Al beampipe. As a proxy for the expected vertex performance, an average weighted vertex position was estimated. The weight for each track is  $1/d_0$ , where  $d_0$  is the distance of closest approach between a track extrapolated to the foil and the vertex. The quantity  $d_0$  represents the extrapolated track’s positional uncertainty on the foil. The uncertainty is large for tracks extrapolated over a large distance or produced at near parallel angles to the foil. Figure 247 shows distributions of  $d_0$  and  $\Delta R = \sqrt{(x_{d0} - x_v)^2 + (y_{d0} - y_v)^2}$ , where  $x_{d0}$  and  $y_{d0}$  ( $x_v$  and  $y_v$ ) represent the transverse coordinates of the extrapolated track at distance of closest approach (the transverse coordinates of the vertex). As can be seen, an approximate resolution of around 5-6 cm can be expected. It was checked that the results are insensitive to smearing the TPC tracks with resolutions expected from the operation of the ALICE TPC [282, 283].

### 9.11.6 Signal

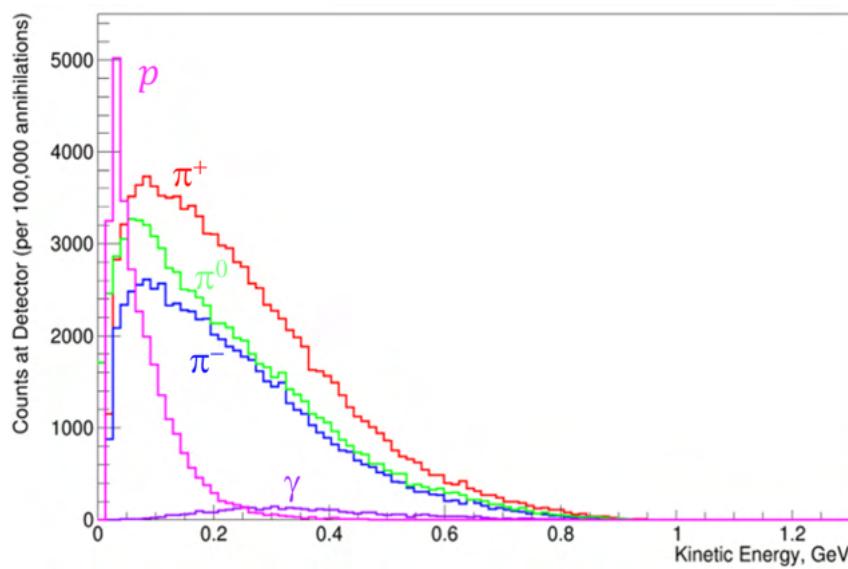
As described in Section 9.2.4, the post-annihilation final states were simulated using a stochastic intranuclear cascade model [225, 226, 227].

Figure 248 displays the distribution of kinetic energy of the final state interactions and scattering-related outgoing particles produced by the annihilation. Included are the decay products of heavy resonances. The energy of pions and photons can reach up to 800 MeV, but their peaks are at about 100 MeV and 300 MeV, respectively. Due to heavy resonance decays, the photon energies are higher. Protons have the lowest kinetic energies; the peak of the distribution occurs at about 50 MeV.

As mentioned in Section 9.2.4, due to final-state interactions invariant mass values significantly lower than two neutron masses are expected. This is illustrated in Figure 249, which displays the initial and final



**Figure 247:** The distance of closest approach  $d_0$  between a track extrapolated to the foil and the vertex (top) and the expected vertex resolution  $\Delta r$  at the foil (bottom).



**Figure 248:** The distribution of the final state kinetic energies of outgoing annihilation-generated particles. In red,  $\pi^+$  are shown; in green,  $\pi^0$ ; blue is  $\pi^-$ ; pink shows protons,  $p$ ; and purple shows photons,  $\gamma$ , resulting from certain heavy resonance decays.

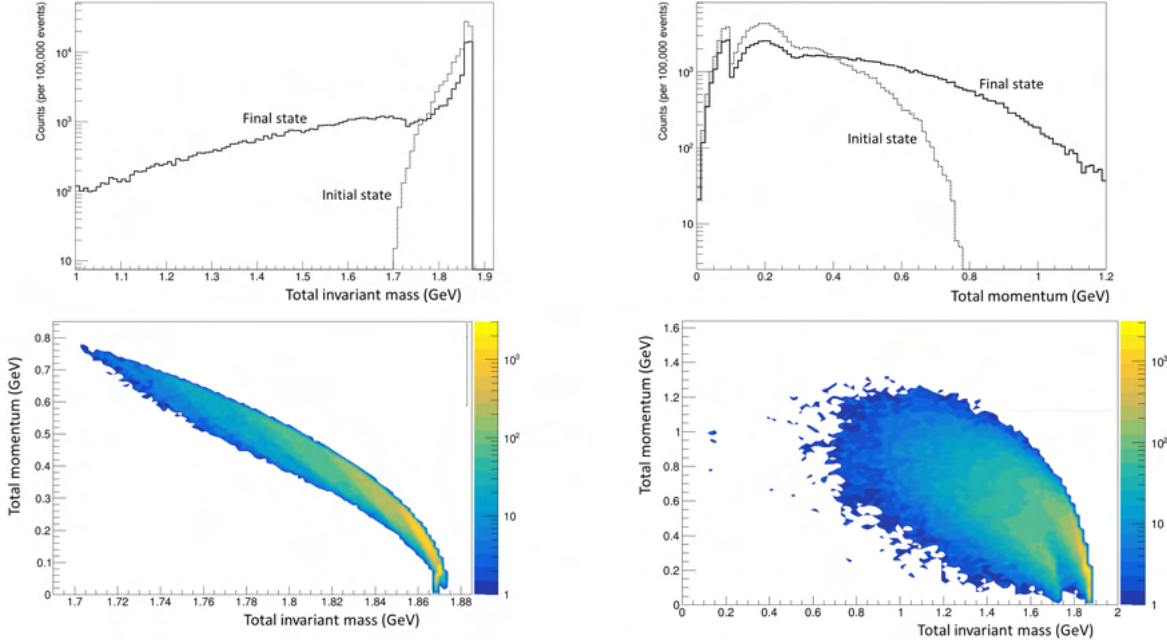


**Figure 249:** The initial and final state distributions of invariant mass (top left), the absolute value of the total momentum (top right), the relationship between the total momentum and invariant mass for the initial (bottom left) and final (bottom right) states.

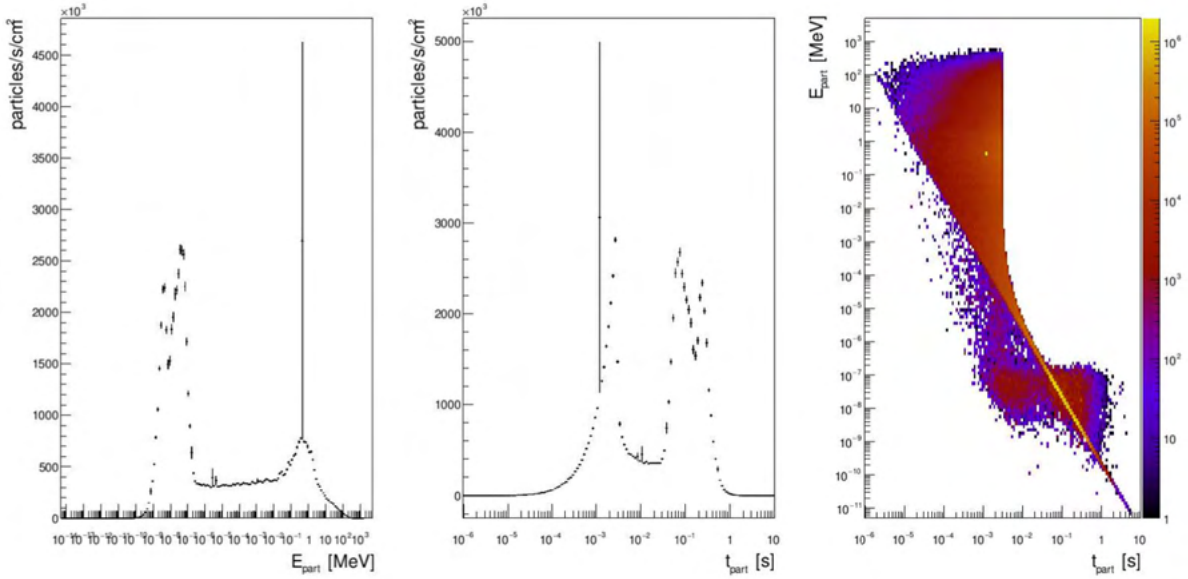
invariant mass distributions of the annihilation process. Here, the "initial state" refers to the mesonic system formed immediately after the antineutron-nucleon annihilation, while the "final state" encompasses the system of pions and photons generated after considering nuclear effects and the decay of resonances. The extended section of the curve, where invariant mass values are low ( $\lesssim 1$  GeV), is a consequence of meson absorption. Additionally, this curve takes into account photons produced as a result of resonance decays.

Figure 249 show the distribution of the total vector sum of momenta for pions. Even in the initial state, this distribution extends to high values due to Fermi motion and the attractive potential of the antinucleon, as explained in Reference [227]. In the final state, the tail of the total vector momentum, considering all pions and photons, becomes elongated. This effect is a result of both meson absorption and the decay of heavy resonances. It generally leads to a greater imbalance in the total vector momentum on an event-to-event basis within the mesonic system. Figure 249 also shows the relationship between the total momentum and invariant mass for both the initial and final states. The distribution in the final state highlights the significance of absorption and rescattering through final state interactions, particularly in predicting the post-annihilation invariant mass.

A sample of around 20,000 events were produced for a cold neutron flux focused over 200m onto the carbon foil.

### 9.11.7 Backgrounds

The principal background sources for the NNBAR experiment is expected to be cosmic rays and beam-generated backgrounds from the spallation source. As shown, the high energy spallation background can be excluded with a timing cut relative to the ESS clock. A key achievement of this work has to design a beamline satisfying safety specifications, demonstrating with MCNP calculations the evolution of the beam over 200 m and allowing the exclusion of fast neutron events with a timing cut. A timing cut can also handle Skyshine, the remainder being suppressed with cosmic ray rejection selections. For cosmic rays, it is shown that a range of selections can be used to suppress the background. While the simulation samples do not statistically replicate the full sample expected for three years of running, the purpose of the study is to demonstrate that the experiment possesses a range of observables that would



**Figure 250:** The intensity of neutrons at the carbon target as a function of neutron energy (left) and time of arrival at the target (middle). The distribution of energy and arrival time is also shown (right).

be used to reject cosmic ray events while retaining a high efficiency. As for other aspects of the NNBAR experiment, the pilot experiment, HIBeam, is needed for data-driven sensitivity estimates.

### 9.11.8 High energy spallation background

The prompt particles from the spallation target include fast neutrons, protons, muons (from pion decays), and photons. These can have energies up to the GeV-scale and thus can potentially produce a pionic signature similar to that expected from a  $\bar{n}N$  process. Unlike cold neutrons, the propagation time for fast particles to reach the carbon target of these particles is strongly correlated with the time of the proton pulse on the tungsten target. As a proxy for fast particles and as the dominant particle component of the beam, the MCNP model was used to track neutrons from the LBP to the carbon target along the beamline described in Section 9.5. Figure 250 shows the neutron intensity at the carbon target, the energy of neutrons at the target and the relationship between the neutron energy and arrival time. As can be seen, the energy extends up to around 1 GeV, albeit as a highly suppressed tail. The arrival time, following the interaction of a proton pulse from the linac on the tungsten wheel is spread over a wide range of time up to around 1 s. A cut of 5 ms from the start of the proton bunch hitting the tungsten target removes the highest energy neutrons, leaving neutrons of energies around 10 eV or less. For a frame interval of 71.4 ms, this leads to an irreducible loss of 7%. The low energy neutrons do not produce a signal-like event but can provide a pile-up contribution to any reconstructed event.

### 9.11.9 Skyshine

Skyshine [289, 290] can be regarded as a fast neutron albedo from the atmosphere. Essentially, skyshine happens when an energetic neutron entirely escapes the facility through the shielding, scatters against the outside air, and returns to the detector region. A comparable term for particles that scatter against the earth is groundshine. Although the NNBAR detector is situated far from the tungsten target, skyshine can extend to several hundred metres. The fast neutron flux entering the atmosphere can be approximated with Equation (35).

$$\phi(r) = \frac{\Phi A}{4\pi r^2} e^{-\frac{r}{\lambda}} \quad (35)$$

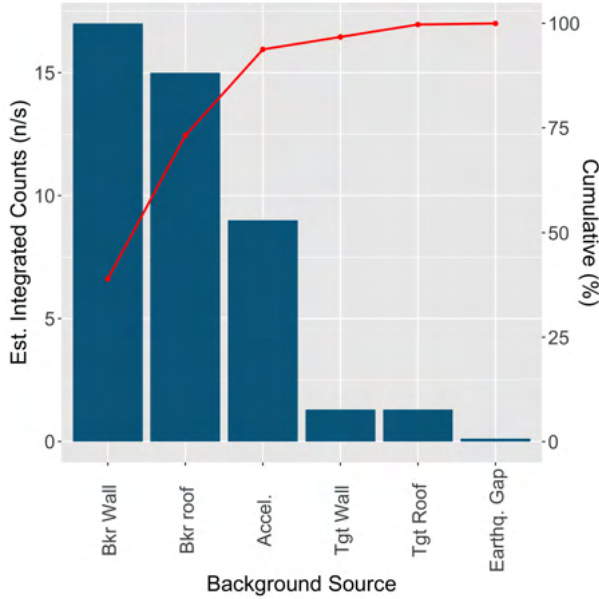


**Figure 251:** Pareto chart of expected background contributions to generic long ESS instrument. Figure from Reference [290].

where  $\Phi$  is the source strength (in units of  $n\text{ m}^{-2}\text{ s}^{-1}$ ) and  $A$  the effective area of the source;  $r$  is the distance from the source (m); and  $\lambda$  is the effective absorption length (m) that depends on the neutron energy.  $\lambda$  is observed to be in the range  $\lambda = 300 - 900$  m for spallation source energies.

The significance of skyshine in the context of the NNBAR experiment primarily stems from two key aspects. Firstly, it holds general relevance for any detector located at a spallation facility due to its capacity to disrupt detector electronics, leading to issues such as radiation-induced noise and single-event upsets. Secondly, skyshine has the potential to coincide with cosmic ray background events, making it imperative to predict the anticipated rate of these events.

In order to estimate the expected background contribution from skyshine we follow Reference [290], assuming no imperfections in the ESS construction for simplicity. Adding up the contributions from all sources including the banker wall, bunker roof, accelerator, target wall, target roof and the so-called earthquake gap, we arrive at a rate of 44 n/s, as shown in Figure 251. A detector response function of 0.1 is assumed for the instrument cave in Figure 251, thus a raw external rate of 440 n/s can be assumed in the case of NNBAR. Since the NNBAR detector area is  $\sim 180\text{ m}^2$ , a total flux of  $2\text{-}3\text{ neutrons m}^{-2}\text{ s}^{-1}$  is expected for NNBAR from skyshine background alone. It is a conservative estimation since it neglects the energy-dependent response function of the detector-shielding system for the NNBAR experiment. While the energy range of skyshine neutrons can extend to as high as  $\sim 400$  MeV, the background represents nothing more than a modest extra contribution to the cosmic ray background and as such, shall be treated using the same tools developed for it. There are of course differences between skyshine and cosmic ray background, in particular, due to having accelerator origin, skyshine background arrives at the detector region relatively soon (5-10 ms) w.r.t. the ESS pulse, while cosmic ray events arrive randomly in time. This effectively means that part of the skyshine contribution is already being suppressed by the 5 ms timing cut to suppress fast neutron background, with the remaining contribution representing no extra challenge compared to cosmic ray background.

### 9.11.10 Cosmic ray background

The simulation of the expected cosmic particle flux over the detector is carried out using the Cosmic-ray Shower Library (CRY) [257] interfaced with the Geant 4 simulation. Cosmic particles are generated on an  $24\text{ m} \times 24\text{ m}$  event plane right on top of 1 m shielding<sup>16</sup>. For each cosmic ray particle species,

<sup>16</sup>This is an overestimate of the expected overburden when also including the material on the ceiling. However, the primary purpose of this section is to demonstrate for a large MC sample, a range of variables that can deal with cosmic ray-induced

20M events were simulated split over the different types of simulated cosmic particle for various energy regions. The flux of different cosmic ray backgrounds over the detector surface, sorted by energy ranges, are shown in Table 48. Table 49 shows the projected number of different cosmic ray backgrounds over the detector surface in 3 years of operation time.

**Table 48:** Simulated cosmic ray background flux at the detector using CRY. The data is sorted by ranges of kinetic energy (KE) and shown for various particle types.

Cosmic Ray Background Particle Flux ( $m^{-2}s^{-1}$ )					
KE(GeV)	Muon	Electron	Proton	Neutron	Gamma
0-0.5	20.9	48.7	2.49	52.2	292
0.5-1	23.7	1.26	0.570	1.72	1.44
1-5	94.2	0.68	0.448	0.855	0.552
5-10	32.1	0.25	0.0202	0.0196	0.0139
10-50	25.3	0.0	0.0121	0.0105	0.00204
>50	2.26	0.0	0.00810	0.000631	0.000150

**Table 49:** The expected number of incoming cosmic particles in 3 years of running time using CRY. The data are split into different ranges of kinetic energy (KE) and shown for various particle types.

Expected number of cosmic ray background particles					
KE(GeV)	Muon	Electron	Proton	Neutron	Gamma
0-0.5	$1.98 \times 10^9$	$4.60 \times 10^9$	$2.36 \times 10^8$	$4.94 \times 10^9$	$2.76 \times 10^{10}$
0.5-1	$2.24 \times 10^9$	$1.19 \times 10^8$	$5.39 \times 10^7$	$1.62 \times 10^8$	$1.36 \times 10^8$
1-5	$8.91 \times 10^9$	$6.41 \times 10^7$	$4.24 \times 10^7$	$8.09 \times 10^7$	$5.22 \times 10^7$
5-10	$3.03 \times 10^9$	$2.40 \times 10^6$	$1.91 \times 10^6$	$1.85 \times 10^6$	$1.31 \times 10^6$
10-50	$2.39 \times 10^9$	0.0	$1.14 \times 10^6$	$10.1 \times 10^5$	$1.93 \times 10^5$
>50	$2.14 \times 10^8$	0.0	$7.67 \times 10^4$	$5.97 \times 10^4$	$1.42 \times 10^4$

**Event selection and background discrimination** Event variables pertinent to the characterization of antineutron-nucleon annihilation events are elaborated upon in Reference [288]. In addition to the variables mentioned, timing window selection is also applied to hits registered in the calorimeter modules. A timing model has been developed to reject out-of-time hits and energy deposits from being used in the estimation of event variables.

The timing window for accepting hits arriving in the scintillator is defined by two key parameters: the time required for a charged pion to arrive at the center of a scintillator stave and a conservative treatment of the timing resolution. The window's start time is calculated as  $(t_{\pi,1000} - 4)ns$  using the time for a fast charged pion (assumed kinetic energy of 1000 MeV) to reach the scintillator stave from the vertex  $t_{\pi,1000}$ . The window's end time is defined as the time needed for a slower 100 MeV kinetic energy charged pion ( $t_{\pi,100}$ ) to reach the stave from the vertex with an offset  $(t_{\pi,100} + 4ns)$ .

Likewise for lead-glass modules, the timing window is determined by the time required for a photon to reach the module from the calculated vertex, represented as  $t_{\gamma}$ . Consequently, the window remains open within the range  $([t_{\gamma} - 4, t_{\gamma} + 4]ns)$ .

Hits are accepted following the application of the timing window. Subsequently, event variables are computed based on the identified objects within the detector. These critical parameters include the multiplicity of charged and neutral pions, the invariant mass ( $W$ ), and the sphericity ( $S$ ) of the detected particle system. Another significant measure involves the total energy loss within the scintillator and lead-glass modules.

The invariant mass of the hadronic system is calculated using the equation:

---

events of all energies.

$$W = \sqrt{\left(\sum_i E_i\right)^2 - \left|\sum_i \vec{p}_i\right|^2} \quad (36)$$

In this formulation, the index  $i$  enumerates the objects that have been identified in the detector. Each object's mass is determined according to predefined criteria. The variable  $E_i$  represents the energy loss for each object, as captured by the corresponding calorimeter modules. The momentum  $\vec{p}_i$  is calculated in a manner consistent with these definitions.

The sphericity ( $S$ ) of the detected particle system is computed using the formula:

$$S = \frac{\lambda_2 + \lambda_3}{2} \quad (37)$$

Here,  $\lambda_i$  ( $i \in \{1, 2, 3\}$ ) are the eigenvalues of the matrix  $M_{xyz}$ , as detailed in Reference [288]. It is assumed that  $\lambda_1 > \lambda_2 > \lambda_3$ .

Another pertinent variable under investigation is the filtered energy loss in the scintillator and lead-glass modules, denoted as  $E_{\text{Scint,filtered}}$  and  $E_{\text{lg,filtered}}$  respectively. These variables are defined as the cumulative sum of the energy losses that occur from hits arriving outside the previously established timing window for scintillator and lead-glass. This metric is particularly useful for distinguishing the annihilation signal events from high-energy cosmic ray background events, which may exhibit substantial late-time energy loss within the lead-glass modules.

A simulation study was conducted to illuminate the distribution of event variables for both annihilation signal and cosmic ray background events. The resulting distributions of invariant mass, sphericity, pion multiplicity, and filtered energies for signal and cosmic ray backgrounds are shown in Figures 252 to 256, respectively.

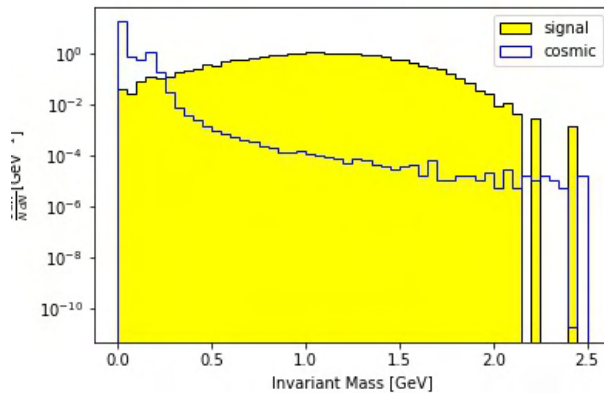


**Figure 252:** The distribution of invariant mass for signal and cosmic ray background events.

A preliminary scheme for discriminating between signal and background events is formulated based on the aforementioned event variables. The cutflow is organized as follows:

1. The first layer of selections focuses on the scintillator modules. The total energy loss must fall within the range  $[t_{\text{scint,lower}}, t_{\text{scint,upper}}]$ .
2. The second layer, denoted as TPC track cut, mandates that at least one track be observed in the TPC. In addition, at least one track in the TPC must be traced back to the foil.
3. The third layer necessitates the identification of at least one pion in the event, either charged or neutral.
4. The fourth layer pertains to the invariant mass, which is required to exceed a predetermined threshold  $t_W$ .

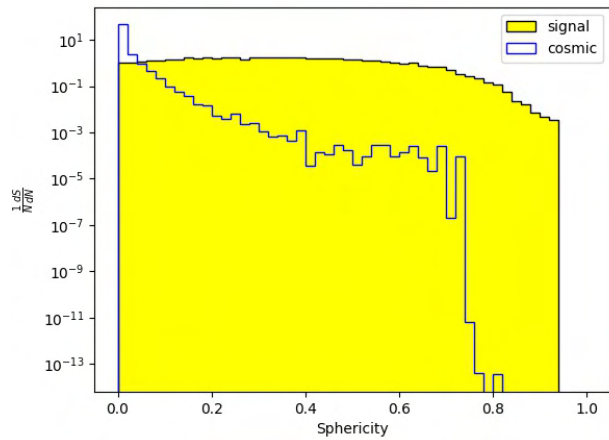


**Figure 253:** The distribution of sphericity for signal and cosmic ray background events.

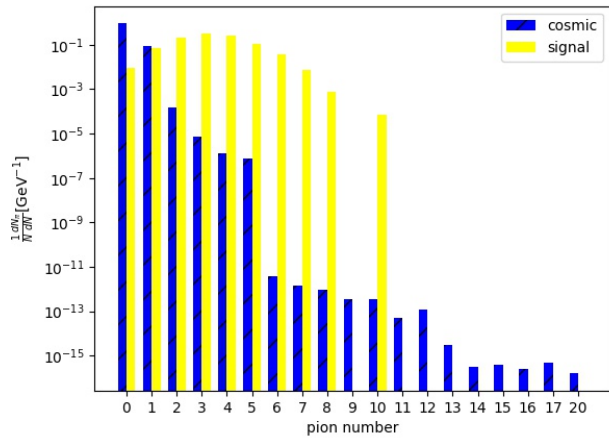


**Figure 254:** Number of pions identified in signal and cosmic ray background events.

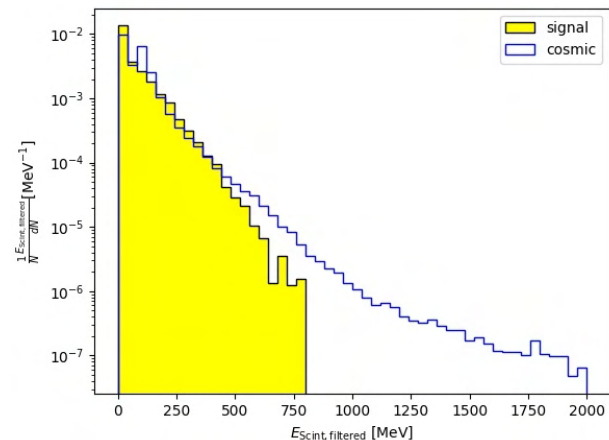


**Figure 255:** The out-of-time energy loss in the scintillators for signal and cosmic ray background events.

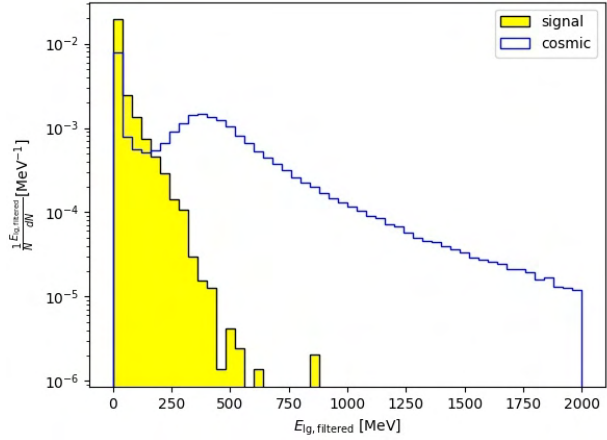


**Figure 256:** The out-of-time energy loss in the lead-glass modules for signal and cosmic ray background events.

5. The fifth layer scrutinizes the sphericity of the event, which must be greater than a specific threshold  $t_S$ .
6. The penultimate layer addresses the filtered energy loss in the scintillator modules, distinguishing between the upper modules with stave center  $y > 0$  and the lower ones with  $y < 0$ , they are denoted by  $E_{\text{scint}, y > 0, \text{filtered}}$  and  $t_{\text{scint}, y < 0, \text{filtered}}$  respectively. The energy lost in the upper scintillator modules should not exceed  $t_{\text{scint}, y > 0, \text{filtered}}$ , while in the lower scintillator modules, it should not surpass  $t_{\text{scint}, y < 0, \text{filtered}}$ .
7. The final layer of the cutflow has two components related to energy loss in the lead-glass modules. Firstly, the energy loss occurring outside the pre-established timing window ( $E_{\text{lg,filtered}}$ ) should not exceed  $t_{\text{lg,filtered}}$ . Secondly, a discretion is applied to the lower lead-glass modules, specifically those with a y-coordinate center less than zero; the energy loss in these modules ( $E_{\text{lg}, y < 0}$ ) should not surpass  $t_{\text{lg}, y < 0}$ .

These layers of the cutflow aim to effectively separate signal events from background, particularly from high-energy cosmic ray events. The thresholds for each layer of the cutflow were globally optimized to achieve two principal objectives: to ensure that no cosmic ray background events survived the series of cuts for a maximal survival fraction of the signal events. As a result, the strategy effectively eliminates all cosmic ray background while retaining a substantial portion of the signal events.

The event survival rate subsequent to each layer of the cutflow with the globally optimized thresholds is tabulated in Table 50. The cutflow achieves a signal acceptance efficiency of 63%, while concurrently maintaining a 100% rejection efficiency (0 % acceptance) for cosmic ray background events. Since neutral cosmic ray particles as well as electrons and protons are overwhelmingly stopped by the concrete overburden, while high energetic muons are able to cross it, the background is split evenly between muon and non-muon background. For the muon background, the active cosmic ray veto system is the main component for suppressing these events.

A simulation of both the active and the passive parts of the cosmic ray veto system was performed in two stages. In the first stage cosmic particles created using the CRY library were transported through the overburden. Surviving particles as well as secondary particles created by reactions in the overburden were then used as input for the second stage which included the cosmic veto detector as well as the inner shielding. A particle was assumed to be successfully vetoed when a number of photons equivalent to 10 keV energy deposition reached each of the 4 SiPMs of at least one scintillator stave. The result of this simulation is that > 98 % of the cosmic ray muons which make it through the overburden are successfully vetoed, with the remaining events identified in the annihilation detector as background, following the described cutflow.

**Table 50:** Survival portion of annihilation signal events, cosmic ray background, and muon after each consecutive cut with globally optimized thresholds.

Selection	Signal	Non-muon background	Muon background
Scintillator energy loss $\in [20, 2000]$ MeV	0.95	0.15	$1.8 \times 10^{-6}$
TPC track cut	0.92	$7.1 \times 10^{-3}$	$1.2 \times 10^{-6}$
Number of pion $\geq 1$	0.86	$6.1 \times 10^{-8}$	$1.1 \times 10^{-8}$
Invariant mass $W \geq 0.5$ GeV	0.83	$1.4 \times 10^{-8}$	$9.5 \times 10^{-9}$
Sphericity $\geq 0.2$	0.73	$8.1 \times 10^{-11}$	$6.1 \times 10^{-9}$
$E_{\text{scint}, y > 0, \text{filtered}} \leq 320$ MeV & $E_{\text{scint}, y < 0, \text{filtered}} \leq 930$ MeV	0.73	-	-

As can be seen, full background rejection for the limited sample of cosmic ray events can be achieved. The purpose of this study is to demonstrate the availability of tools and observables which would be used to control the cosmic ray background level. The above was achieved with a minimal set of observables and a simple linear cutflow. The requirement of, e.g., a vertex would add yet more discriminating power. For the experiment, cosmic ray background would be monitored during non-data-taking periods. Furthermore, a second foil placed 20-30cm downstream of the target foil would provide an estimate of the fake signal rates from cosmic ray events.

### 9.11.11 Cosmic ray interactions in the detector

The interactions of cosmic rays in the detector can give rise to fake signal vertices erroneously associated to the foil. A "danger zone" defined as a cylindrical region centered at the carbon target with a radius of 1.15 m and  $z$  spanning from -5 m to 5 m was considered. Primary and secondary particles resulting from interactions within this zone may traverse the carbon target and yield event signatures resembling that of the signal. Given the potential for confounding the analysis, understanding these events is crucial.

To assess the frequency and nature of such danger zone events in a three-year operational span of the detector, a dedicated study was conducted. Events were selected from cosmic ray background simulation samples, specifically those that exhibited interactions near the beampipe. These events were then scrutinized for several key observables:

- The expected number of particles traversing the carbon target.
- The kinetic energy (KE) distribution of these particles.
- The angle  $\theta$ , defined as the angle between the particle momentum and the positive  $z$ -axis when hitting the carbon target.

Figure 257 and Figure 258 show the KE and  $\theta$  distributions of the particles passing through the carbon target. The y-axis represents the expected count of the particles over a 3-year operation period. Pions originating from cosmic events and passing through the carbon target tend to have kinetic energies that overlap with those of pions from the annihilation signal. However, the likelihood of observing such events remains low over the course of a 3-year operational period. The other particles primarily possess kinetic energies at the MeV or sub-MeV level, which may not be sufficient to produce a signal-like signature in the detector. None of these events are misclassified as signal events through our established event selection criteria.

A principal focus of future work is the study of each type of interaction and how it can contribute to background.

### 9.11.12 Machine Learning

Machine learning (ML) models were studied as an alternative event selection w.r.t. the linear cutflow.

**Correlations** Correlation matrices were used to find any groups of variables and any independent variables. For a group of variables it holds that every variable is correlated to at least one other variable in said group. One correlation matrix was plotted for the signal and all background events respectively. The background events were categorized based on particle and energy range. The independent variables and

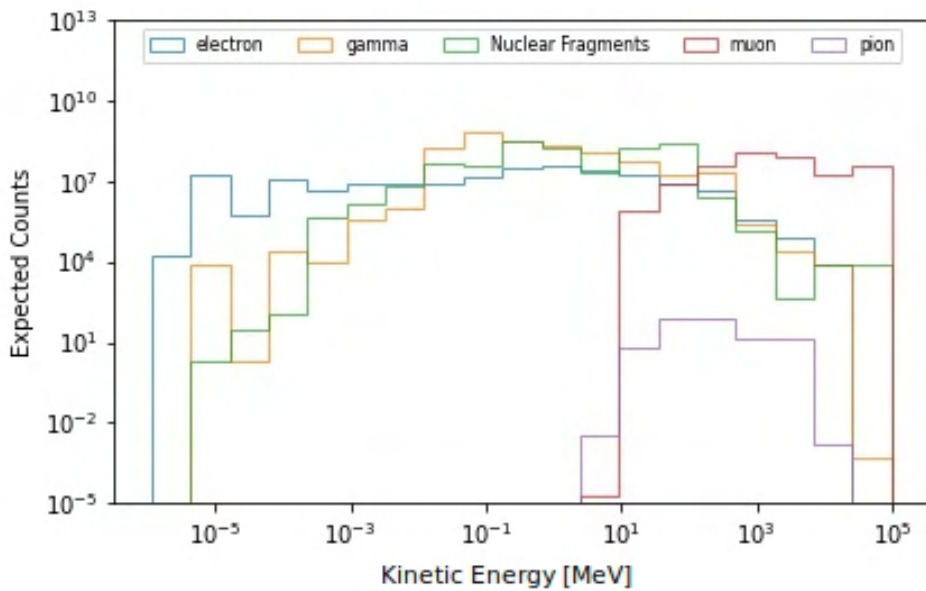


**Figure 257:** The kinetic energy (KE) distribution of electrons, muons, pions, gammas, and nuclear fragments. The *y*-axis represents the expected counts of such particles within a given KE range over a 3-year operational period.

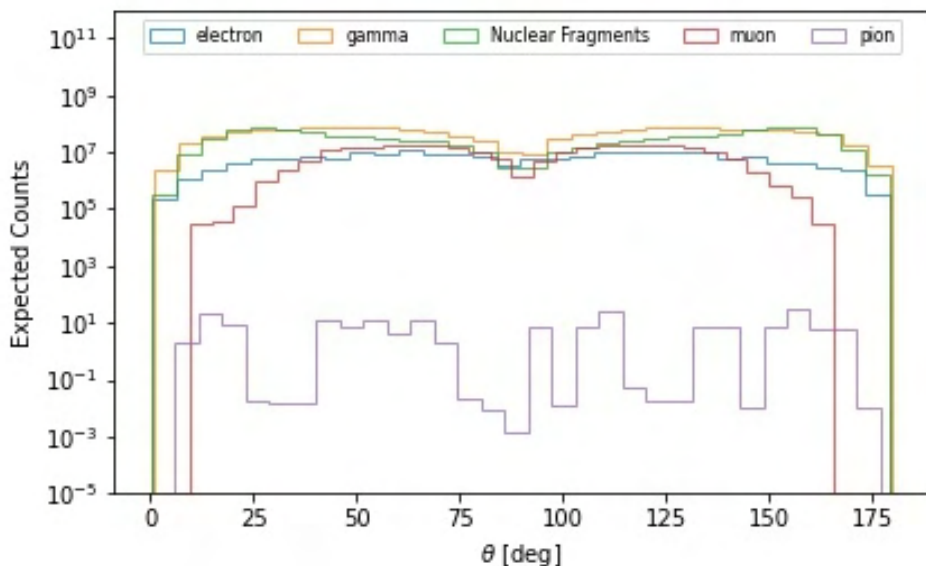


**Figure 258:** The  $\theta$  distribution of electrons, muons, pions, gammas, and nuclear fragments. The *y*-axis represents the expected counts of such particles within a given  $\theta$  range over a 3-year operational period.

groups from each correlation matrix was compared. The selected variables were deposited energy in the scintillators (Scint\_eDep), longitudinal energy in the scintillators (Scint\_E\_L), difference in timing between the first and last hits in the lead-glass and the scintillators, respectively, (Timing\_lg and Scint\_diff), longitudinal energy in the lead-glass (Lead\_glass\_E\_L), numbers of neutral pions based on loose and tight diphoton mass windows (pi0\_loose\_num and pi0\_tight\_num, respectively), sphericity, and invariant mass (Inv\_mass).

Correlation matrices for signal and combined cosmic background are shown in Figure 259.

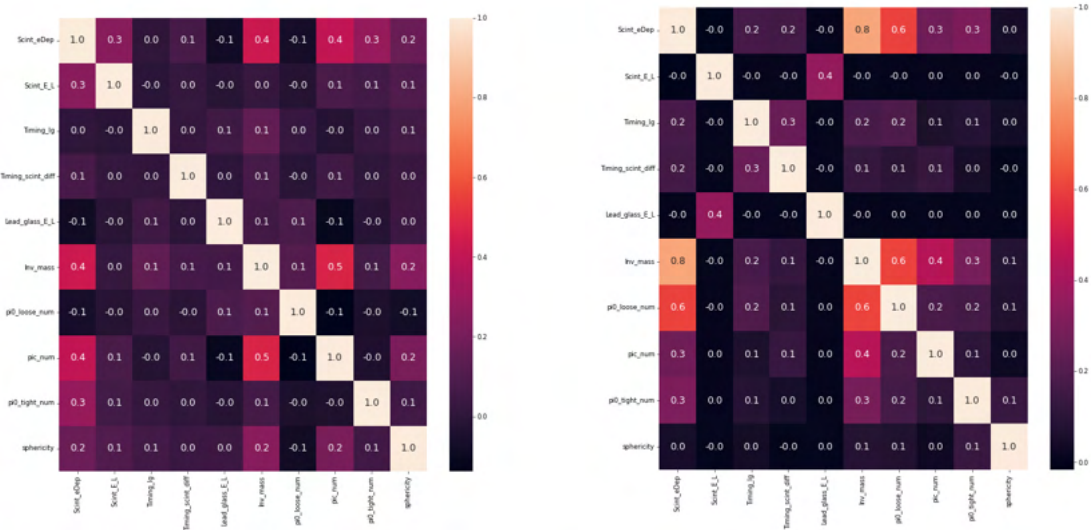


**Figure 259:** Correlation matrices for signal and background events.

**Suitable algorithms** In addition to standard selections, an option for selecting signal events at NNBAR whilst maintaining background rejection is to use ML. A number of algorithms were investigated, including Random Forest Classifier (RFC) [291], Boosted Decision Tree (BDT) [292] and Linear Discriminant Analysis (LDA) [293]. The algorithms were optimized using 20% of the signal. After optimization of performance, tests for signal efficiency and background rejection showed that only the RFC was suitable for NNBAR. Precision Recall (PR) curves[294] were used to determine the skill of the RFC algorithm as well as to detect signs of overtraining[295].

**Results** The area under the PR curve serves as an indicator of skill. When this area approaches 1 for all datasets, it signifies a high level of skill. Conversely, significant variation in this area among different curves is indicative of overtraining. From Figure 260 we see that the RFC is highly skilled and shows no signs of overtraining. The RFC provided 100% background rejection for all cosmic ray samples with a signal efficiency of 71%. A number of different sets of variables were used. The example above is chosen as it represents the most conservative estimate of signal efficiency obtained with full background rejection. The efficiencies for a range of sets of variables obtained range from around 70% to over 90%. The open question with ML is always how a decision is made and whether that decision depends on a difference in the simulation of signal and background that is not realistic. The ML should, therefore, be considered as an interesting and promising area for future study.

### 9.11.13 Comparison with the ILL experiment

When assessing the capability of the NNBAR experiment, a comparison should be made with the ILL experiment [262, 21]. This experiment achieved a selection leading to zero background events using real data. In principle, from the point of view of cosmic ray background, as long as the number of calendar

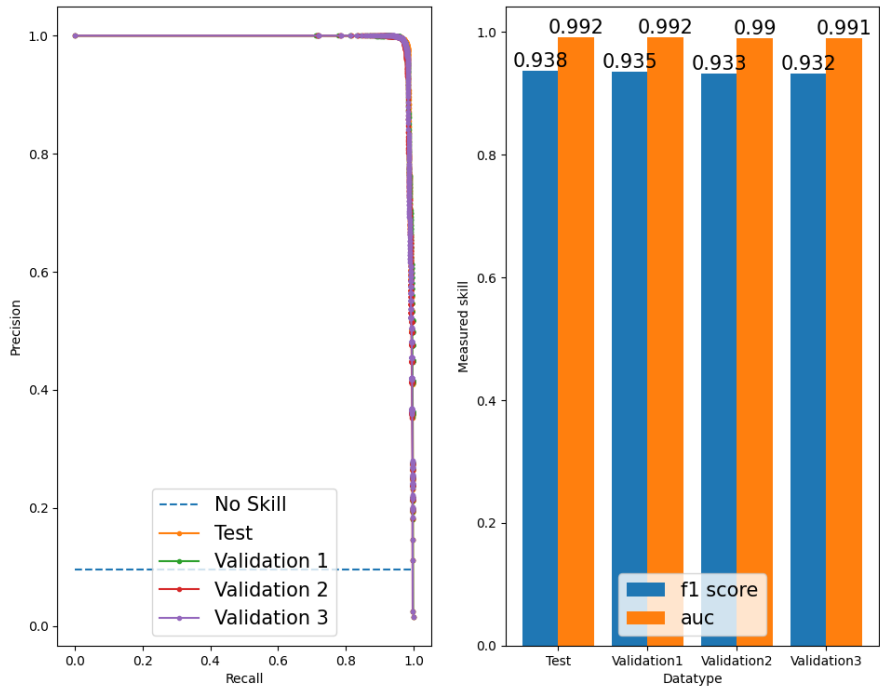


**Figure 260:** Precision Recall curve plotted for the RFC algorithm. The acronym auc stands for Area Under Curve. The f1-score is a measurement of a model’s accuracy. Note: none of the sets of validation data have been used for training or testing.

days for reaching the desired sensitivity is similar, the expected number of cosmic background should be of the same order of magnitude. The ILL experiment ran for a year. Since the NNBAR annihilation detector has, however, a larger area, the expected number of cosmic ray background events is, therefore, larger for NNBAR, with fluxes increasing by the proportion to which the NNBAR overall detector surface area is larger than ILL’s. Should background rejection in NNBAR be demonstrated to be quantitatively superior to ILL’s by at least this factor, zero cosmic ray background expectancy for NNBAR could be argued as a supplement to the detailed simulation-based work shown in Section 9.11.10.

Before comparing each background rejection factor it is thus necessary to compare the two annihilation detector sizes. The total surface of the ILL detector is  $\sim 90 \text{ m}^2$  [262], while the total surface area for NNBAR is around  $180 \text{ m}^2$ . Thus, it must be demonstrated that, for the same data taking period length, that the NNBAR experiment has a background rejection that is superior to ILL by at least a factor of  $\sim 2$ . Given that the NNBAR experiment would likely run three times longer than the ILL experiment, background rejection for NNBAR should be at least 6 times superior than achieved at the ILL.

A direct comparison between NNBAR and the ILL experiment with respect to cosmic ray background rejection is not straightforward, mostly because not all efficiencies to specific selections from the ILL paper are available. However, it is instructive to qualitatively compare the two detectors with respect to different background rejection capabilities, including, but not restricted to, timing, energy, as well as vertex reconstruction.

Generally speaking, timing capabilities of the NNBAR detector are far superior to those at the ILL. To first order this is simply caused by the fact that the NNBAR detector is larger and cosmic ray particles traversing the detector travel therefore longer distances making timing measurements, allowing the flight direction (inwards or outwards) to be determined. This fact is, however, further increased if one observes that it is not only is the scintillator system substantially more granulated with a multiple stave-based HRD but that NNBAR’s electromagnetic calorimeter is also a timing sensitive detector to  $\sim\text{ns}$  precision. It

takes  $\sim 17$  ns for cosmic ray particles to fully traverse the detector from top to bottom by making use of the lead-glass time - a value which is significantly larger than the available resolution. The timing with lead-glass will be useful for particles going outwards. The lead-glass is partially "blind" to particles traveling inwards by using the directionality of Cherenkov light. If successful this would also help rejecting neutral cosmic ray events like e.g. gammas converting in the lead-glass.

Moreover, particle identification for the NNBAR detector is in general far superior. In particular, the NNBAR detector can identify and reconstruct precision-time neutral signal pions while the ILL detector lacked a dedicated electromagnetic calorimeter.

Another important new capability of the NNBAR detector is that due to NNBAR's TPC, tracking in 3 dimensions is available which is a significant gain in pattern recognition. Indeed, the pointing resolution of NNBAR due to the TPC is about ten times better than ILL's.

### 9.11.14 Pile-up

Background events producing a pionic signature and arising from beam interactions on the foil or beamwall arise from fast neutrons that can be excluded with timing selections. Low energy neutrons and their interactions can contribute a sea of low energy particles, largely at the MeV-scale and below. These are dominantly photons and electrons. Neutrons at the eV-scale and below neutrons can also enter the detector.

The flux of particles causing beam-induced noise depends critically on the optimization of beamline around the detector, including recesses, endcap locations, and the choice of type and location of moderator materials and neutron poisons. The optimization of the beamline is a focus area for future work. However, some early MCNP calculations have been made with the unoptimized "worst-case" beamline in the detector area (Section 9.5, around which it is instructive to discuss the issue of beam-induced noise in the detector<sup>17</sup>). Unlike the Geant4 studies, the calculations were made with a coarse-grained detector model in which each component was replaced with a slab of appropriate material. Layers of  $^6\text{LiF}$  and polystyrene were placed inside the beampipe in the beamline area as basic neutron poison and moderator, respectively.

It should first be noted that there will be an irreducible photon background of the order of  $10^7$  photons/second of around 4.5 MeV entering the detector which arise from the activation of the  $^{12}\text{C}$  target foil by the incoming neutron flux. In addition to this, slow neutrons evading the neutron poison will largely either penetrate the beampipe wall, being then captured and causing photon emission in the detector or shielding, or will be captured in the beampipe walls, again producing photons. Photons will Compton scatter in the material causing electrons that can enter the TPC and scintillators.

Threshold cuts are a key tool to study and suppress pile-up in the scintillator arrays owing to the weaker signal left by MeV-scale pile-up particles compared to the  $\sim 10$  MeV left by signal particles in 3 cm of scintillator. However, the absence of a magnetic field in the TPC implies that Compton electrons will appear as tracks.

Table 51 shows the flux of particles in the slow neutron window of (i.e. after the 5 ms timing cut described in Section 9.11.8) entering the different subsystems as estimated with MCNP simulations. For the TPC, ALICE-like conditions may be expected of around 650 tracks per 50ns window, likely necessitating additional scintillators before the TPC to remove timing and track reconstruction ambiguities. The tracks themselves will largely be entering the TPC from random directions. This also requires a dedicated effort for track reconstruction in this high multiplicity environment and the linking of tracks to groups of staves to identify pion tracks from low energy beam-induced particles.

Without the electron background tracks, a traditional TPC with wire chamber readout could be used, even without gated operation. However, the large number of tracks per second due to electron background implies that the issue of the ion backflow from the avalanche region must be addressed. The problem has already been solved by the ALICE TPC upgrade by using GEM instead of multiwire proportional

---

<sup>17</sup>The related issue of radiation dosages is discussed in Section 9.11.15.

chamber (MWPC) readout. Without gating it will then also be possible to use the TPC in continuous readout mode (i.e. none or very loose hardware trigger).

**Table 51:** Estimated flux of particles entering different detector subsystems.

Component	Flux $\text{ncm}^{-2}\text{s}^{-1}$		
	$n$	$e^-$	$\gamma$
TPC	$6 \times 10^3$	$7 \times 10^3$	$1.4 \times 10^6$
Scintillator layer 1	$4 \times 10^3$	$3 \times 10^3$	$1.2 \times 10^6$
Scintillator layer 2	$2 \times 10^3$	$1 \times 10^3$	$1 \times 10^6$
Lead-glass	$2 \times 10^2$	$1 \times 10^2$	$5 \times 10^3$

It should again be emphasised that the fluxes in Table 51 represent the unoptimized beamline in the detector area. An earlier study was made with GEANT4 using incoming slow neutrons. This gave fluxes several orders of magnitude lower than in Table 51. However, a different beamline design around the detector area was assumed. A full determination of the beam-induced noise requires an optimization of the beamline together with the identification and mitigation of sources of large particle fluxes. Predictions from different radiation transport models must be validated against each other and, ultimately, prototype test data.

### 9.11.15 DAQ for NNBAR

The NNBAR data acquisition system must trigger on and read out detector signals with sufficiently precise timing, energy and spatial resolution to effectively discriminate between neutron-antineutron annihilation candidate events and unrelated backgrounds. Balancing this requirement is the need to reduce readout of manageable bandwidth levels and thus avoid dead time.

Table 52 summarizes the estimated channel numbers and readout parameters of the four main NNBAR Subdetectors. Three of them, namely the HRD, LEC and cosmic veto, are "fast" scintillator/Cherenkov detectors with SiPM readout that can measure energy and precise ( $\sim\text{ns}$  level) timing information with low readout latency. The timing precision from these subdetectors is critical for signal/background discrimination, as well as for reading out and matching data from track candidates in the TPC. Since TPC tracks have drift times as high as  $100 \mu\text{s}$ , the baseline NNBAR DAQ design first identifies initial events and track candidates from the "fast" subdetector data, and then adds selected TPC data to the event for track matching, either in the real-time event builder or offline.

The HRD, LEC and veto detector front-end electronics are read out by fast SiPMs, allowing a high degree of commonality between the front-end electronics, digitization and readout between the combined 43000 SiPM channels across the three systems. Collected scintillation/Cherenkov light is converted to fast pulses by SiPMs. The SiPM pulses are then transformed by preamplifier/shaper circuits into analog pulses with amplitude-independent shape and at least 50 ns rise time, which are then continuously digitized at 80 MHz by an on-detector digitizer and readout system based on commercial ADCs read out by programmable logic devices (FPGA). Finite-impulse-response (FIR) filters will allow both amplitude and  $\sim 1 \text{ ns}$  precision timing extraction from the digitized data.

The baseline TPC readout is designed around the SAMPA ASIC, which was designed for the ALICE TPC and muon chamber upgrades at LHC. SAMPA is a 32-channel mixed-signal IC that combines pre-amplification, shaping and digitization, as well as a DSP layer that can be used to apply baseline correction and data compression before reading out the processed data in multiple serial data streams. The SAMPA chip allows triggered readout of zero-suppressed data within programmable-length data frames with up to  $10 \mu\text{s}$  latency, which may be used to limit TPC readout to time frames associated with candidate events seen in the calorimeters. If background rates are high, the TPC can also be read out in continuous mode.

A conceptual layout of the NNBAR DAQ system is shown in Figure 261. As mentioned above, candidate events and track candidates will be initially identified by the "fast" HRD, LEC and veto subdetectors. Unlike at collider experiments where signal events are time-aligned with particle bunch crossings,

Detector	Channels	Dynamic range	Data size	Readout
TPC	256k channels	10 bits	-	Continuous
HRD	9000 SiPMs	10-12 bits	200 bytes	Self-triggered
LEC	32000 SiPM arrays	10-12 bits	200 bytes	Self-triggered
Veto	1000 SiPMs	10 bits	200 bytes	Self-triggered

**Table 52:** Subdetector channel count and data size.

signals and backgrounds in NNBAR will have arbitrary timing, with the additional complication that the flight times and angles of annihilation event products will vary with the vertex position at the target. Therefore, candidate event selection with rejection of unrelated backgrounds requires the absolute timing of particle hits in the fast detectors to be measured with nanosecond or better precision, and a CPU-based trigger/event-builder farm for event candidate selection and reconstruction. Data reduction to the CPU-based trigger is achieved through self-triggered (a.k.a. “triggerless”) readout of fast detector pulses from individual channels, with time stamps included with the digitized pulse data. Initial event selection in the trigger begins with topology and timing-based algorithms from the calorimeter and veto data, with later addition of selected TPC data for the final event selection and reconstruction.

Event selection in the NNBAR trigger will be primarily based on detected hits in the scintillating staves (HRD), lead-glass calorimeter (LEC), and the veto detector. A preliminary signal trigger definition would include a minimum combination of minimum-ionizing “tracks” through multiple layers of staves (a proxy for charged pions) and spatially separated clusters of lead-glass deposits over a given threshold (a proxy for charged pions), with cosmic muon rejection provided by timing and spatial hit data from the veto detector. At the ILL experiment the majority of triggers (2.4 Hz out of 4 Hz), were caused by cosmic muons traversing the detector without triggering the veto. We expect a similar order of magnitude of contribution for the NNBAR trigger, and therefore estimate that the signal trigger rate of NNBAR will also be on the order of a few Hz.

**Front-end system** The baseline solution for global timing distribution at NNBAR is the open-source White Rabbit technology, which has been developed at CERN for distributing sub-nanosecond timing distribution over synchronous Ethernet. White rabbit was initially developed for timing and control, and the conceptual design shown includes a White Rabbit switch network connecting the global timing master and the detector slow-control system with the sub different subdetector systems over gigabit Ethernet links.

While White Rabbit can in principle also be used for general purpose data transfer, this imposes some overheads that can be avoided by instead using separate networks for timing and control (GbE) and readout to the event builder (10GbE), with the latter system comprised of commercial CPUs and network switches.

The self-triggered readout architecture for the calorimeter and veto systems begins with the FPGA-based front-end digitization modules. Sampled data from each channel are locally monitored, and when a valid pulse above a set threshold is identified, the module autonomously transmits the channel data to the off-detector systems for reconstruction and triggering. Since only detected pulses are read out, the total readout bandwidth for the calorimeter and veto systems is highly zero-suppressed. The transmitted data contents will include a time-stamp aligned to a global master clock, as well as the digitized pulse data (typically 10-12 samples) and any additional required information such as checksums and/or status bits. The expected total read out data for a detector pulse is approximately 200 bits, and will be encapsulated into Ethernet packet format by the FPGAs for direct transmission from the digitization system to the event builder farm.

The calorimeter/veto digitization modules are foreseen to be installed in ATCA-type crates equipped with dual-star topology backplanes. To reduce the number of optical links required, one of the star network hubs will contain a network switch that can read out data from up to 12 modules over a single 10 GbE link per crate. The second star hub would contain a timing and control module for distributing

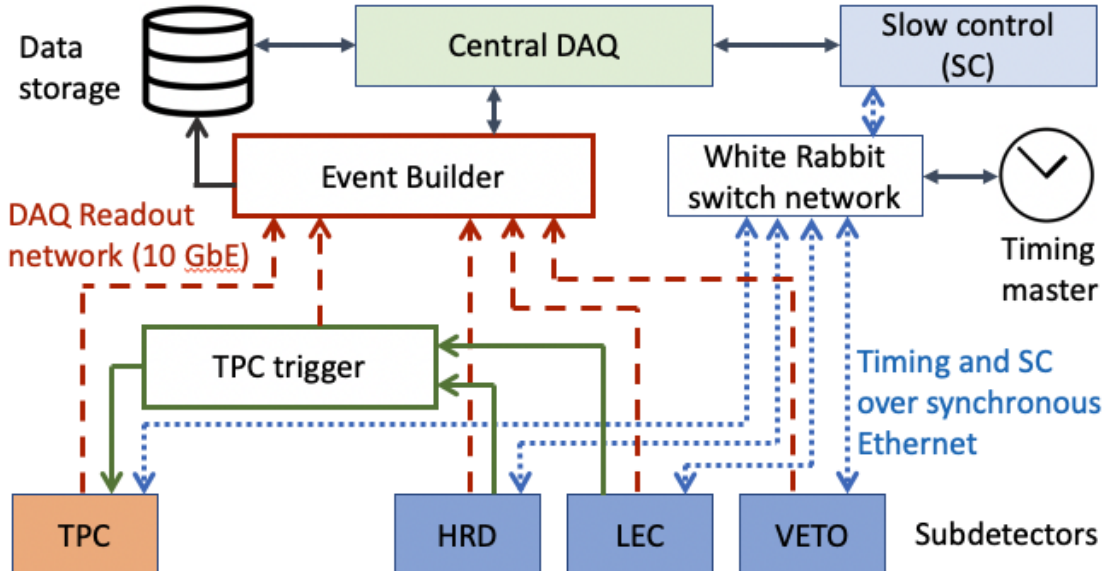


**Figure 261:** Conceptual overview of the baseline NNBAR DAQ.

timing and control signals received from a White Rabbit GbE link.

For the TPC readout, the baseline design in this report assumes pessimistic background estimates and large track multiplicities. In this scenario the SAMPA chips are read out in continuous mode with no zero suppression, over optical fiber links with 4.8 Gbps line rates. The TPC links are received off-detector by FPGA-based boards comparable in design and function to the Common Readout Unit (CRU) developed for the high-luminosity upgrade of ALICE. These boards process and reduce the TPC data (including zero suppression as needed), and then transmit them as Ethernet packets over 10 GbE links to the event builder.

In the event that zero-suppression is insufficient for TPC data reduction, a hardware-based TPC trigger is foreseen that would combine hit data from the HRD and LEC to identify potential particle candidates arriving from the direction of the target, and trigger selective readout of the TPC channels corresponding to the volume through which the track candidate would have passed. The TPC trigger would receive fixed-latency “hit” signals from the front-end digitization and readout modules for the HRD and LEC, and perform FPGA-based topology algorithms. Particle track candidates identified by the TPC trigger would also be included in the event builder readout to help match the TPC data with the relevant events.

**Event builder** Readout from the calorimeters, veto and TPC systems are transmitted off-detector over optical links to the event builder system, where they are distributed through a network of high-capacity ethernet switches to rack-mounted high-performance computing nodes.

A relatively small portion of the computing nodes will perform the initial trigger selection from the HRD, LEC and veto data. Because the readout links from these detectors are sparsely populated, off-detector network switches will further concentrate the data into a smaller number of these nodes. The average event sizes in the calorimeters and veto is expected to be small, in the range of a few kB within a given time interval, and the initial event selection will use relatively simple trigger algorithms such as FIR filters for extracting pulse amplitude and fine timing, and simple event topology calculations based on selection based on the timing and position of detector hits.

The largest portion of the event builder resources is dedicated to readout of the TPC data, which are concentrated by high-performance switches into a significant number of densely populated 100 GbE links for distribution to the computing nodes. After an event candidate has been identified in the initial trigger selection, the corresponding TPC data are extracted and added to the event record. If TPC background rates and computing node resources allow, the online reconstruction stage of the event builder

may include operations like vertex reconstruction, track matching to calorimeter hits and/or further zero-suppression of the TPC data. Otherwise, the event builder may in principle simply read out the corresponding TPC track data and send it to mass storage for further analysis offline.

**Radiation tolerance** The NNBAR detector and front-end electronics systems will be exposed to multiple sources of radiation, including scattered beam neutrons as well as secondary particles from neutron interactions with the target and detector. The TPC front-end electronics are based on radiation-hard ICs developed for much more challenging radiation conditions at LHC/ALICE. On the other hand, the baseline HRD and LEC on-detector systems are planned to use commercial components, so it is important to consider whether such systems will withstand the radiation exposure over the planned 3 years of NNBAR data taking.

Initial estimates of ionizing (TID) and non-ionizing (NIEL) radiation exposure to the detectors and front-end electronics exposure have been produced from detector background simulations using MCNP (see Section 9.11.14), and are summarized in Table 53.

**Table 53:** Estimated annual ionizing (TID) and non-ionizing (NIEL) radiation exposure for the NNBAR detectors and their front-end electronics. The TPC and HRD electronics dose rates vary depending on their position upstream or downstream of the target.

Detector	TID (Gy/year)	NIEL (1 MeV equiv. $n/cm^2/year$ )
TPC	71	
TPC electronics	14-23	$2.0 - 3.2 \times 10^{11}$
Scint. staves (HRD)	23	
HRD electronics	8-33	$5.3 - 5.6 \times 10^{11}$
Lead-glass (LEC)	3	
LEC electronics	0.3	$7.2 \times 10^{10}$

For comparison, the estimated 10-year TID and NIEL doses for the high-luminosity upgrade of the ATLAS hadronic Tile Calorimeter front-end electronics are 22 Gy and  $1 \times 10^{12}$  respectively. Like the HRD and LEC, the upgraded TileCal electronics also use commercial components including fast ADCs, modern FPGAs, and SFP+ optical transceivers. All components in TileCal have been extensively tested and radiation qualified with large safety factors of 8 to 10.

It should be noted that the most radiation sensitive components in the HRD and LEC on-detector electronics will be the FPGAs and other complex digital circuits in the digitization and readout modules. These will be installed outside the LEC, where the TID and NIEL rates will be substantially lower than at the HRD front-end boards.

We therefore conclude that HRD and LEC front-end electronics and on-detector digitization/readout systems will operate in conditions that are compatible with use of radiation-qualified commercial components. Single event effects in the FPGAs will be mitigated with standard methods including triple-mode redundant logic, configuration memory scrubbing, and checksum-protected data readout.

### 9.11.16 Mechanical construction

An early draft design for the baseline NNBAR detector mechanics and support structure has been produced. The main goals of this exercise were to demonstrate that a realistic support structure for the NNBAR subdetectors can be built with a feasible installation plan, while avoiding excessive dead material in the active detector volume that would degrade the detector performance.

**Support structure** Assembly of the annihilation detector begins with construction of a large structure (Figure 262) for supporting the various detector elements and distributing the detector weight evenly across the floor of the experimental hall . A heavy structure of double-T steel beams supports the HRD and LEC calorimeters as well as other service structures such as working platforms, stairs electronics

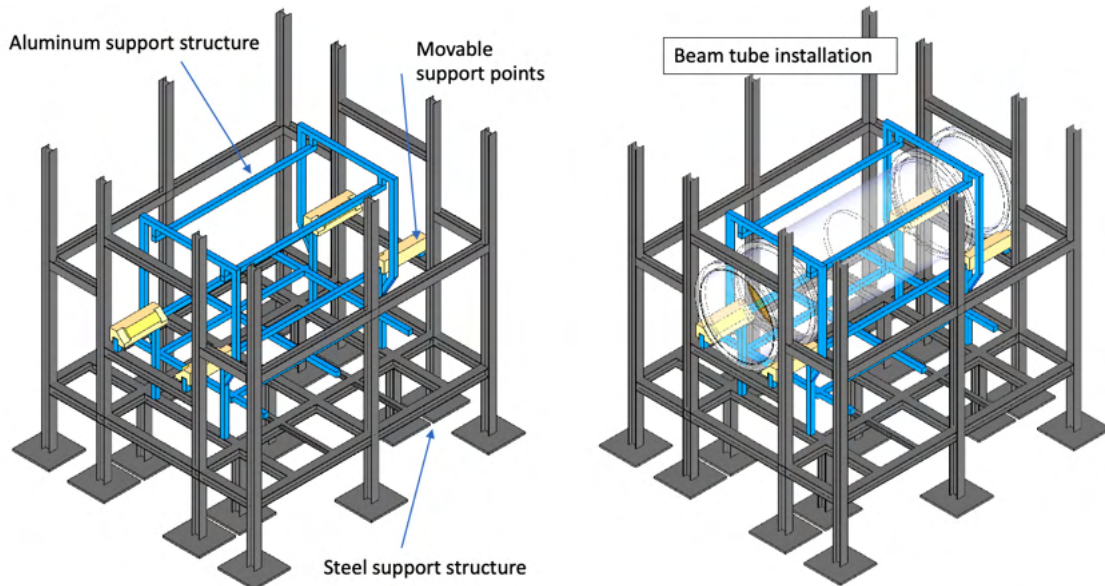


**Figure 262:** Left: The steel and aluminum NNBAR detector support structure with movable support points for installation of the central beam tube. Right: Beam tube installation.

racks, and so forth. An inner framework of aluminum provides a support structure for the TPC and beam tube with minimal dead material.

The steel support structure weighs approximately 40 tons and is designed to support a full annihilation detector weight of nearly 200 tons. The top-most beams are omitted during the early installation stages to allow access for the innermost detector components, and added later for installation of the top-most HRD layers and the LEC.

**Beam tube** The central beam tube is approximately 6.5 meters long and weighs ca. 3.7 tons. Two circular ribs at each end of the tube provide rigidity to prevent the tube from deforming under its own weight. The ribs also serve as mounting points for four sliding supports used during the tube installation process.

**TPC installation** The TPC is also supported by the aluminum frame surrounding the beam tube. To reduce dead material, the TPC chambers can be fixated together to create a more self-supporting structure with a total weight of 600 kg.

**HRD installation** The HRD is pre-assembled in large 10-layer planar sections before transport and installation in the experiment hall. Since the outer edges of the HRD planes are instrumented with SiPMs and front-end boards, assembly and mounting of the HRD sections will require fasteners that pass through the stave structure at regular intervals to aluminum profiles as illustrated in Figure 263. This would necessitate small gaps in the stave structure, but the expected impact on HRD coverage would be negligible.

The total weight of the HRD is estimated at 29 tons.

**LEC installation** The LEC is the largest and heaviest subdetector, with more than 32000 lead-glass counters and a total assembled weight of nearly 100 tons. To facilitate installation a commercial "slide guide" system of extruded aluminum profiles is used to support pre-assembled modular blocks of 9 lead-glass counters in a  $b3 \times 3$  arrangement. The slide-guide system would be mounted to the double T-beam structure of the steel support structure, with adjustable plates for alignment during assembly.

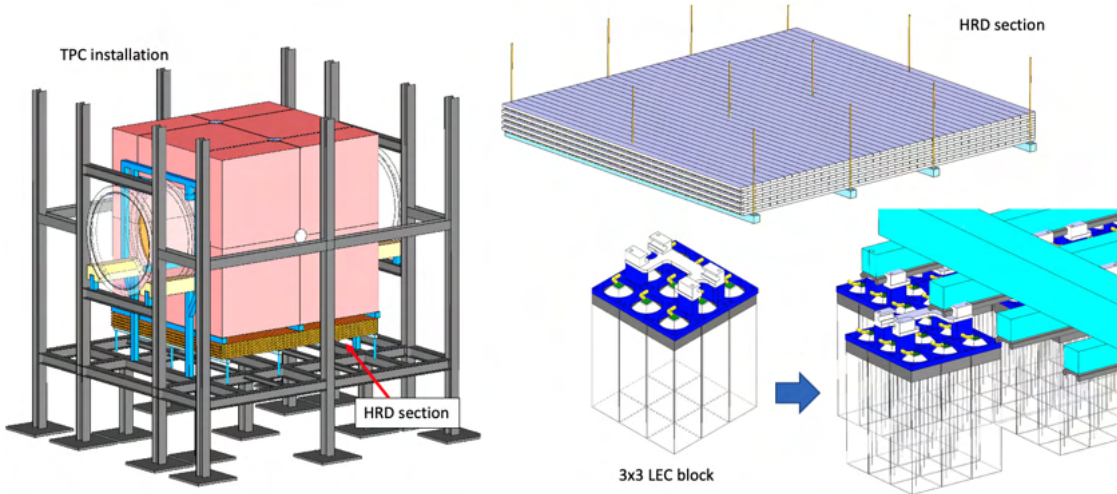


**Figure 263:** Clockwise from left: TPC installation around the central beam tube, with an HRD section below; A hanging HRD section with aluminum supports; LEC installation detail with modular assemblies of 9 counters each mounted on aluminum slide-guide profiles.

**Working platforms and stairs** The annihilation detector design also includes working platforms and stairs to allow safe access to all parts of the detector for installation and maintenance work (Figure 264).

**Shielding and Veto** The cosmic veto system is mounted on the concrete shielding walls surrounding the annihilation detector.

### 9.11.17 Future steps

As discussed in Section 9.11.14, a major future focus on the design of the beamline around the detector which dictates the low energy particle flux in the detector. While this will not cause a signal, it can degrade the ability of the detector to reconstruct signal and distinguish it from background events.

Related to this is a focus on dealing with the constraints of the vacuum vessel and, in particular, the deployment of a tracking system inside the vacuum. Accurate estimates of the low energy particle flux and associated dosages are needed. This work must therefore be performed in tandem with beamline optimization.

Being a large surface, the wall of the vacuum vessel has to be strong to withstand the air pressure outside. A cylindrical shape is thus preferred. In the simulations a homogeneous 2 cm Al tube has been used as it has proven to be strong enough in other applications. The thickness is however critical from the detection point of view. Multiple scattering in the wall will cause angular deviations in so that directions measured outside will not correspond fully to the real directions inside and thus the pointing to the vertex will not be as accurate as it could be. Another obstacle is that a large fraction of the proton spectrum will stop in the wall and will thus not contribute to the vertex definition.

To overcome these problems, a possibility is to place detectors inside the vacuum. The angular deviation by multiple scattering is not large so with good pattern recognition pointing inwards from outside, two high resolution coordinates inside can be sufficient to restore the original direction. Protons stopping in the wall would however not be adequately measured with only two coordinates. A proton track with two coordinates could however still support a hypothetical vertex defined by at least two other tracks. To deal fully with tracks stopping in the wall would require three coordinates. An inner detector system will have the layers to be placed at radial positions of 1 – 1.5 m depending on position resolution. This amounts to an areal size in excess of around  $30 \text{ m}^2$  per layer. An absorber layer composed of LiF with some backing will likely have to be deployed in front of an inner detector to prevent slow neutrons to enter the tracking. This would also stop the large number of electrons coming from beta decay of free neutrons flying by. This would also serve as a radiation shield radiation shield against cold neutrons.

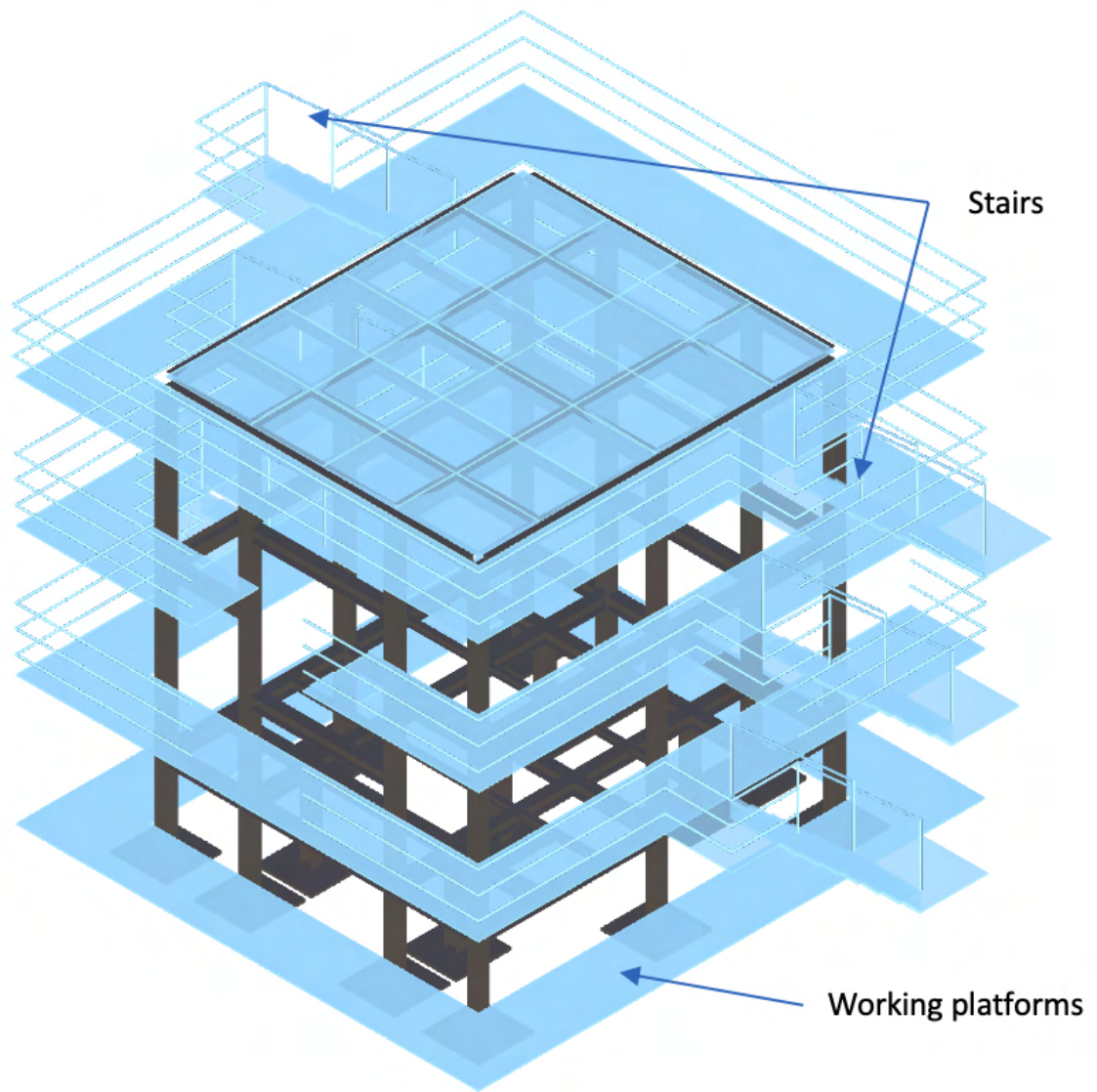


**Figure 264:** Working platforms and stairs in the experimental hall.

However, inner detectors (and to some extent also outer) can not be shielded from the prompt flux of faster neutrons. Dosages for outer detectors are discussed in Section 9.11.15.

The obvious choice for detectors in the vacuum would be Si-strip detectors. Since space points are needed it needs crossed strips for each coordinate station. Most pions are minimum ionizing so the noise level is important. A position resolution in the  $\sim 0.1$  mm range appears to be adequate if coordinates are around 20 cm apart. The cost of a system with 2 layers (ca  $60\text{m}^2$ ) would most likely, however, be financially prohibitive. Three layers to manage the lower energy protons even more difficult.

If an inner tracker made of Si Strip detectors could be sufficient for safe tracking one could save money on the outside by omitting the 70 cm taken up by the TPC. That could mean substantial savings on the calorimetry. However a Si-only tracker would most likely need at least 4 stations since normal tracking also uses a known vertex which we don't have here. The rate of background tracks is of course essential. A helpful property of Si detectors is a quite good time resolution which helps pattern recognition. Another positive aspect is that it performs well not only for perpendicular tracks because of the tiny thickness.

As an alternative to Si, with gas as the detector medium, radiation effects are negligible. Since the particles to track, the pions, are normally minimum ionizing, a gas medium cannot be at low pressure, otherwise efficiency will be lost. Around 50% of normal air pressure would still probably be OK for tracking while energy loss resolution is worsened. Gas detectors placed inside the vacuum must, in addition to being extremely gas tight, also have walls strong enough to withstand the pressure difference to the vacuum. The only possible solution to this would be straw tubes where the cylindrical containment of the gas offers the mechanically strongest barrier. The big obstacle with straws is that they are only position sensitive in 1 dimension (plus the straw radial location). For space points stereo layers of straws will be required, adding to the problem of combinatorial ambiguities. If pattern recognition is provided from outside this may be overcome. The possibility to use the low energy part of the proton spectrum is likely to be diminished or lost if the track is not recognized on the outside.

Construction of straws is a challenge. To cover 5 m at 1 m radius is a bigger project than the ATLAS straw tube project [296]. Probably, for gas tightness one would have to use metallic tubing. One simplification is to use larger tube diameter. That will on the other hand be at the expense of the search window in time to compose coordinates and tracks increases. With 4 mm tubes as in ATLAS the window is 75 ns. This would add to the combinatorial concerns. The diameter of the big vacuum tube will also increase since tubes have to be straight. How feasible this type of solution is depends a lot on the background conditions. The low energy electron background will make long tracks. The cosmic ray showers, which are the most problematic possible source of fake annihilation signals, have several nearby tracks and will be ambiguous to reconstruct by crossed straws alone. External pattern recognition should help.

An additional alternative is a scintillating fibre tracker. The upgraded forward scintillating fiber tracker of LHCb is a very elegant tracking solution [297]. It requires U,V stereo geometry to obtain space coordinates. Because if its very small readout cell (0.25mm) one obtains 0.07 mm position resolution perpendicular to the fibre direction. The granularity is very good and the time resolution when assembling coordinates and tracks is on a ns scale. Thus combinatoric ambiguities should be much better in control compared to the straw tubes. Since fibers can adapt (bent) to the cylindrical shape of the tube, the tube diameter does not have to be increased to house the stereo fibers. In size, a 3 station straw tracker for NNBAR would be comparable to the LHCb straw tracker (which has straight fibers) [298]. Outgassing from fibers in vacuum and the sensitivity to radiation are questions that need careful study.

The simulated tube of 2 cm Al is a motivated baseline choice for a conventional beampipe to maintain a vacuum. However, as discussed, it has negative consequences for the experiment. As an alternative to placing detectors inside the tube, which adds a lot of complication to the setup, a possibility is to spread the 2 cm material in two 1 cm cylinders with spacers between. The strength could be maintained. The inner tracking station as above, could be placed between the cylinders at normal pressure. The material where multiple scattering would stop many protons would be halved. A more advanced solution could be to have a pressure gradient, e.g., 50% of the ambient air pressure in the intermediate volume between

the cylinders. Then both cylinder materials could be reduced. One could even place a gaseous tracker operating at 50% of air pressure in the intermediate volume. This volume in itself could be the gas container of that detector. This would be quite elegant if it could be implemented with enough safety (the danger is pressure failure (up or down) In the middle volume.)

It is also possible to provide the mechanical strength to the cylinder allowing non-uniform thickness and include a skeleton of stronger supports. At first sight this may appear non-optimal, but with external tracking in 3D pointing back to the cylinder, it will be known if a track has passed the thicker material. Such tracks from the analysis can be omitted or weighted down when analysing data.

A further means of mitigating the effect of low energy particles in the tracker is to deploy a magnetic field of up to 0.1 T. This would curl up the Compton electrons. However, it is a notable technical challenge, given the nT-level requirement along the beam path. A possible realization is a toroidal coil in the detector directly at the end of the magnetically shielded vacuum tube. The magnetic shield will then require modifications to separate the flux close to the imperfect toroidal coil and the low-field region,

## 9.12 Cost estimation of the experiment

### 9.12.1 Parametric Costing Analysis

In addition to the usual spreadsheet-based costing breakdown that one would typically use for a project of this scale, a parametric study was performed to understand the cost-benefit curves in part of the effort to arrive at a baseline specification. This study was based on a costing tool developed in python at the ESS for regular neutron experiments, in order to establish the correct strategy to maximise return on investment in instrumentation [299].

The original software used manufacturer quotes from 2013 for all the major components of a “normal” neutron instrument and was heavily benchmarked against other neutron facilities around the world. Those generic functions were then adapted specifically for the work on NNBAR in the current project, including the specialised detector technology that is needed. The construction of the ESS has allowed the refinement of a number of engineering and materials costs since 2013, and these were updated. Finally, a more recent quote was obtained from a neutron optics vendor, which takes into account recent economic changes since 2013, along with improvements in manufacturing efficiency and the scale involved in the optical components of this project.

The tool encapsulates most of the relationships found in multiple spreadsheets. It also calculates on-the-fly various geometrical relationships between optics, shielding, construction engineering, and electronics.

A useful curve to understand the design optimisation is the total instrument cost *vs* beam radius,  $r$ . Whilst the performance of the beam might be expected to increase roughly as a function of beam area, and therefore proportional to  $r^2$  as also shown in Figure 265, the variation of the cost is not so obvious when one considers vacuum systems, shielding etc. This is seen in the Figure to be essentially linear. This of course raises interest in the expected cost-to-benefit ratio, which is shown by varying with beam radius. The baseline point with  $1000 \times$  the total number of ILL data events, assuming a 3 year operational cycle, is indicated.

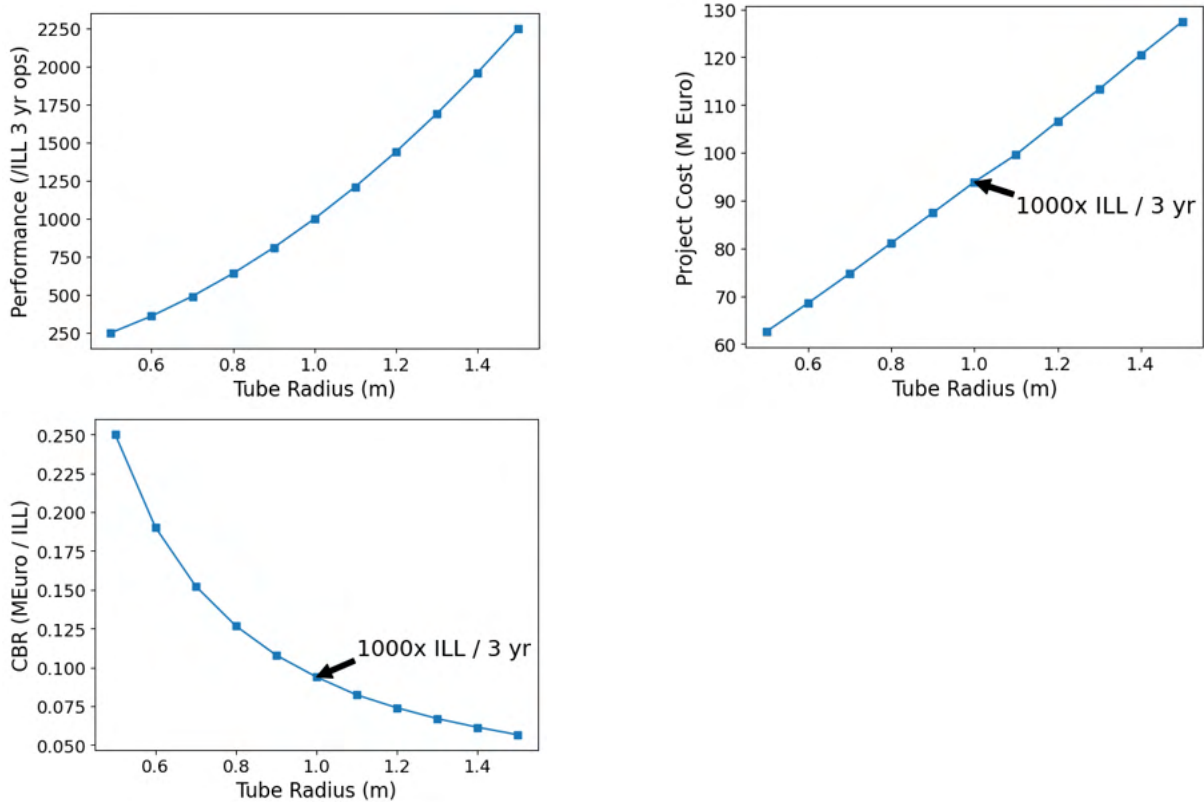


**Figure 265:** Top: variation of the instrument performance *vs* beam radius. Bottom left: variation of instrument cost *vs* beam radius. Bottom right: Variation of the instrument cost-benefit ratio *vs* beam radius. The baseline point with  $1000 \times$  the total number of ILL data events, assuming a 3 year operational cycle, is indicated.

The breakdown of the cost is shown for the baseline  $r=1$  m in Figure 266. The figure also shows the cost breakdown for a varying beampipe radius.

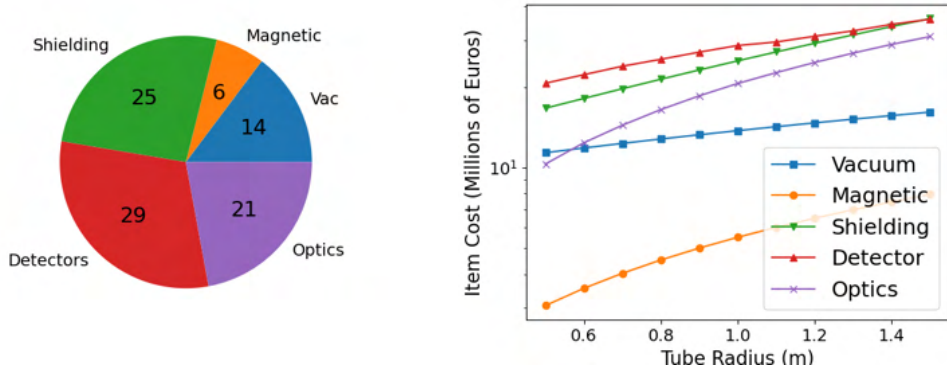


**Figure 266:** Left: breakdown of costs for different parts of the experiment for the baseline selection. Right: breakdown of costs for different parts of the experiment as a function of beam radius.

A tabulated breakdown of all the costs for the baseline specifications (length = 200 m,  $m=6.0$ , radius = 1 m) is shown in Table 54.

The cost breakdown given assumes a baseline design with both the vacuum tube and carbon film target having 1m radius. If the vacuum tube radius is increased by 10 cm to avoid target interactions close to the vacuum tube wall, the overall detector cost would be expected to increase by approximately 4 percent.

From the cost breakdown in Table 266, it can be seen that the lead glass calorimeter (LEC) accounts

Item	Cost (M €)
Carbon target	0.07
Vacuum tube	4.76
Vacuum system	9.0
Magnetic shielding	5.5
Steel shielding	3.05
Beam tube concrete shielding	11.07
Detector cave concrete shielding	1.42
Detector mechanical construction	0.75
Counting house	0.03
Beamstop	4.78
TPC and front-end electronics	3.53
TPC readout to DAQ	1.94
Lead glass	7.07
Lead glass SiPM and analog front-end	13.60
Stave scintillators	0.12
Stave SiPM and analog front-end	0.46
Stave WLS	0.36
Veto scintillators	0.07
Veto WLS	0.19
Veto SiPM and analog front-end	0.38
Calorimeter/Veto digitization and readout	2.11
Timing and slow control	0.19
DAQ system	2.11
Optical elements	20.66
<b>Total</b>	<b>93.22</b>

**Table 54:** Cost breakdown of an instrument with the baseline specifications, i.e. length = 200 m,  $m=6.0$ , and radius = 1 m, rounded to nearest k€.

for the majority of the detector cost. The LEC has a channel count of more than 32000, which is comparable to calorimeters at LHC experiments, and the majority of the cost per LEC counter is the for the silicon photomultipliers (SiPM) used to read out the channels. SiPMs are a relatively economical solution compared to photomultiplier tubes for light detection with high quantum efficiency, and they would be an essential component of any electromagnetic calorimeter design for NNBAR.

The next largest cost comes from the lead-glass blocks. From our experience with the LEC prototype, the glass cost itself represents about 40 percent of this. The type of glass used is mass-produced for applications such as X-ray shielding windows, and the cost per kg assumes raw glass ingots like those purchased for the prototype blocks. The remaining 60 percent of the cost is processing, and based on our cooperation with the Cerfav R&D center in Saint-Gobain for cutting and polishing the glass blocks. Some efficiencies of scale may be possible for the full-scale detector production.

Similarly, the costing for the scintillating stave HRD and veto detectors are based on experience with the HRD prototype, which uses staves from the same Fermilab production facility as those produced for the Mu2e and LDMX experiments.

The TPC prototype developed at LUND is based on the same SAMPA ASICs and similar front-end readout architecture as the ALICE high-luminosity upgrade, and provides the basis for the costing model of that subdetector.

Cost for magnetic shielding is mainly comprised of the material costs of the passive shielding material of about 60 t of sheet material, currently costing 3.7 M Euros annealed; structures amounting to about 1.3 M Euros and 0.5 M Euros for engineering of one section and the adaptation for extreme length. However, with the recent proof of scalability of long octagonal shields in length, the design costs are a fixed offset only.

## 9.13 Sensitivity of the experiment

The sensitivity (FOM and  $n \rightarrow \bar{n}$  conversion time) of the experiment depends on several factors.

1. The ESS power. Two scenarios are considered: 2MW and 5MW.
2. The background level. As shown in Section 9.11, a timing selection of at least 5 ms after the proton beam hits the tungsten target will suppress high energy spallation background. Given the ESS repetition rate of 14 Hz, this corresponds to an acceptance of  $\epsilon_{time} = 93\%$ . For cosmic rays and late skyshine, cut-based selections and machine learning algorithms can be made which retain around  $\epsilon_{sig} = 70\%$  signal efficiency while removing all of the simulated background hitting the detector (Section 9.11.10). Furthermore, a range of sensitive observables are available and the detector is more advanced than that used at the ILL experiment which drove a zero background experiment as discussed in Section 9.11.13. A zero background experiment represents feasible performance although more work is needed to conclusively demonstrate this. Sensitivities are therefore calculated for a stated zero background scenario.
3. The extent to which the quasi-free condition is maintained. Neutrons propagate through a low but not zero field region (Section 9.9). A Monte Carlo study stepping slow neutrons through the simulated field, and evaluating the cumulative effect of average values of a non-zero magnetic field at each position, showed that the quasi-free efficiency is around 98 – 99%. Analytical calculations of the departure from the quasi-free conditions for fields of the size in NNBAR imply an inefficiency of around 5% for a 200 m propagation length [224]. An efficiency of  $\epsilon_{free} = 95\%$  is taken as a conservative value.
4. Operation time. The ILL experiment ran for one year. It is anticipated that NNBAR would operate for at least three years.

The FOM is calculated with respect to the previous experiment at the ILL. For an ESS power of 2 MW and a reflector deployed around 18 m from the bunker, the FOM is 300 ILL units per year (Section 9.8.3).

An enhanced FOM ( $FOM_{full}$ ) can be calculated that takes into account the differences in signal efficiency between NNBAR and the ILL experiment's overall efficiency ( $\epsilon_{ILL} = 50\%$  at the ILL), timing losses at the ESS, and a running time of three years.

$$FOM_{full} = FOM \times 3 \times \frac{\epsilon_{sig} \times \epsilon_{time} \times \epsilon_{free}}{\epsilon_{ILL}} = 1065 \quad (38)$$

The sensitivity to the  $n \rightarrow \bar{n}$  oscillation time varies with the square root of the FOM. Taking the ILL limit of  $0.86 \times 10^8$  s, this leads to a sensitivity of  $2.8 \times 10^9$  s at 90% Confidence Level. For 5MW ESS operation, the  $FOM_{full}$  and conversion time sensitivities are  $FOM_{full} = 2663$  and  $4.4 \times 10^9$  s, respectively. Figure 267 shows, for comparison, the limits from searches with bound neutrons and free neutrons and the sensitivities of the future DUNE experiment. The sensitivities of the NNBAR experiment at 2MW and 5MW for a zero background search are also shown.

It should be emphasised that the relevant quantity when considering the capability of a search for neutrons converting to antineutrons is the ability of the experiment to observe such a process. This is directly proportional to the figures of merit discussed here and is thus the relevant quantity to show an experiment's discovery potential.

The above sensitivities correspond to a baseline of a 2 m diameter beamline in the detector area. As shown in Section 9.12, variations in the diameter, while also maintaining the same detector acceptance, can enhance or degrade the FOM.

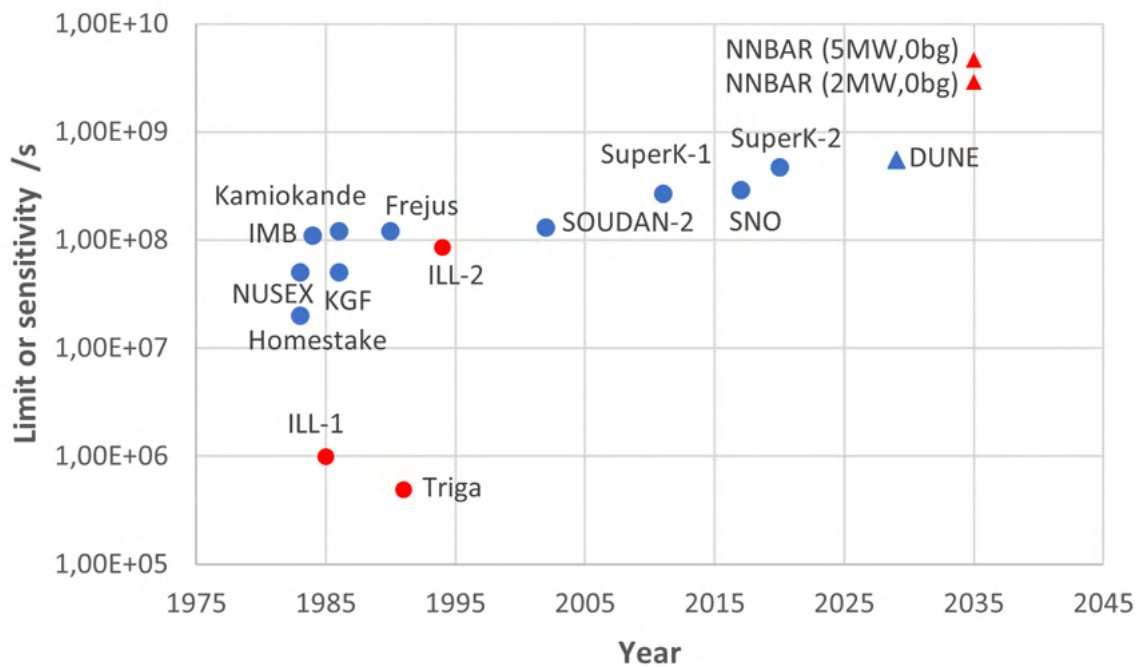


**Figure 267:** Limits from searches with bound neutrons (blue circles) and free neutrons (red circles) and the sensitivities of the future DUNE (blue triangle) experiment. The sensitivities of the NNBAR experiment at 2MW and 5MW for a zero background search are also shown (red triangles).

## 9.14 Summary

The European Spallation Source will open up a new discovery window for searches for baryon number violation. The NNBAR experiment can search for neutrons converting to anti-neutrons with a sensitivity that is potentially three orders of magnitude greater than previously achieved. A discovery of free neutron conversions would falsify the Standard Model and address a number of open questions in modern physics including baryogenesis.

This paper outlines a conceptual design of the NNBAR experiment using a dedicated cold moderator. As part of this work, a beamline was designed and civil engineering aspects studied. All aspects of the experiment: neutron focusing, propagation in a field-free region and anti-neutron detection were considered.

This paper also identifies a number of areas of further study including pile-up and the possibility of in-vacuum tracking.

## 10 Thermal Scattering Libraries

### 10.1 Introduction

Here we present the development of simulation software for describing neutron interactions in novel moderator and reflector materials considered of interest for the HighNESS project. The main interest is the development of software in order to describe neutron interactions in NDs, magnesium hydride, graphitic compounds with extended Bragg-edges compared to normal graphite, and the clathrate hydrates. To support this work, several methods were developed to include new physics processes, such as small-angle neutron scattering and magnetic scattering, into the Monte-Carlo simulation process.

Traditionally, thermal neutron scattering data for Monte-Carlo simulations are usually distributed as part of the thermal scattering sublibrary (TSL) of major evaluated nuclear data libraries (ENDF/B [300], JEFF [301] and JENDL [302]). In the past decade, these libraries have seen an increase in activity related to the development of the TSL, in part due to the work of the Subgroup 48 of the Working Party for Evaluation Cooperation [303]. Nevertheless, the coverage of materials, and particularly of materials of interest in the development of cold neutron sources, is limited.

In addition, these libraries are also restricted by the ENDF format [304]. In its current version, elastic scattering can be either represented using a coherent or incoherent model. In December 2020, a format change was proposed [305] to include both components in what is called *mixed elastic* scattering. To make use of this format, the tool that is currently freely available for the generation of thermal scattering libraries, the LEAPR module of NJOY[306], must be modified and recompiled to support the calculation of coherent scattering in new materials. In addition, there is no simple way to include additional physics processes such as small-angle neutron scattering and magnetic scattering through this approach.

To overcome these limitations, we investigated a number of approaches for including improved thermal neutron scattering data in Monte-Carlo simulations. These include approaches based on extended thermal neutron scattering libraries in a modified ENDF format in addition to calling the code NCystal [307, 308, 309] on-the-fly during a Monte-Carlo simulation.

Each of the above mentioned developments used input based on state-of-the art molecular modelling systems. This included the usage of both density-functional-theory (DFT) techniques in addition to classical molecular dynamics.

An important part of the process of development of new models and tools is benchmarking against experimental data. Data for this purpose is in particular very limited for materials of interest to very-cold and ultra-cold neutron applications. For this reason, we also carried out an experimental campaign at the BOA instrument at the Paul Scherrer Institute to explore its possible use as a neutron beamline for this purpose and also to investigate in particular extend Bragg-edge graphitic compounds.

In the following, we first present the molecular modelling simulations, followed by advancements in nuclear libraries and extension of NCystal to include new physics, and finally work on benchmarking and investigations with the BOA instrument.

### 10.2 Molecular Modelling

To support the development of new neutron scattering models, extensive molecular modelling calculations were carried out using a variety of techniques. The main outcomes of such calculations are the structure, in the form of the atomic positions, and the phonon frequency distribution. These two quantities can be used as input to the neutron scattering models.

#### 10.2.1 Molecular modelling for MgH<sub>2</sub> / MgD<sub>2</sub>

The phonon spectra inputs for the MgH<sub>2</sub>, and its deuterated variant MgD<sub>2</sub>, libraries were generated using Density Functional Perturbation Theory (DFPT) [310] with the Perdew-Burke-Ernzerhof (PBE) [311] approximation for the exchange and correlation energy functional. The calculations also employed ultrasoft pseudopotentials [312, 313] and plane wave expansions of Kohn-Sham orbitals as given in the

Quantum-ESPRESSO (QE) package [314]. The PDOS of  $\text{MgH}_2$  and  $\text{MgD}_2$  are shown in Figure 268 [315].

The results for  $\text{MgH}_2$  are very similar to previous ab-initio works [316, 317]. In particular, in [316] the overall validity of the isotropic approximation of the mean square displacement is assessed at different temperatures. The high-frequency phonons, due to the motion of hydrogen, are almost exactly scaled by a factor  $\sqrt{2}$  by isotopic substitution while the acoustic part of the spectrum is essentially unchanged.

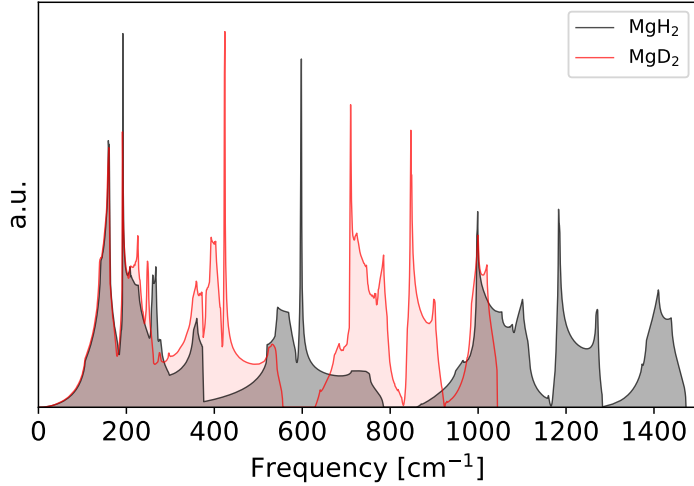


**Figure 268:** Comparison of the theoretical phonon DOS for  $\text{MgH}_2$  and  $\text{MgD}_2$  (from Ref. [315]).

### 10.2.2 Nanodiamonds

NDs of interest as reflector materials for cold neutrons are synthesized by detonation techniques [318]. The resulting samples consist of nanoparticles with a distribution in diameter centered at about 5 nm [318]. Transmission electron microscopy (TEM) measurements of NDs synthesized under different conditions revealed a mostly diamond-like structure of the nanoparticles with, however, a partial surface graphitization whose extent depends on the preparation conditions, thermal history, and purification process [319]. Full transformation of NDs into carbon onions was in fact observed by heating at about 1670 K [320]. Impurities such as H, N and O are also present, resulting from the purification methods or from oxidation in air. A fraction of about 5 atomic % of H was measured, for instance, in commercial samples of detonation NDs used by Vasiliev et al. in ref. [321] to measure the heat capacity as a function of temperature. This latter work shows that the heat capacity of 5 nm NDs is notably larger than that of bulk diamond up to 300 K.

This result suggests a sizable difference in the phonon density of states (PDOS) of the NDs with respect to the bulk which is confirmed by the inelastic neutron scattering data reported by Shiryaev et al. in Ref. [322].

Since the PDOS is expected to affect both the elastic (via the Debye-Waller factor) and the inelastic contributions to the neutron scattering cross section, it is important to have reliable structural models of the NDs to provide both atomic positions and the phonon DOS for the calculation of the total neutron scattering cross section.

To this aim, we generated models of NDs by molecular dynamics (MD) simulations with the classical interatomic potential AIREBO [323]. This potential is suitable for generating reliable structural models of NDs as shown by several previous works, including the formation of a graphitic shell upon annealing [324]. However, the classical potential is less reliable in reproducing the PDOS, which is the key property needed to compute the neutron scattering cross section. Our strategy thus consists of using the classical potential to investigate the dependence of the structural properties on the annealing process and then to use the NDs models generated with the AIREBO potential to compute the PDOS with a more reliable,

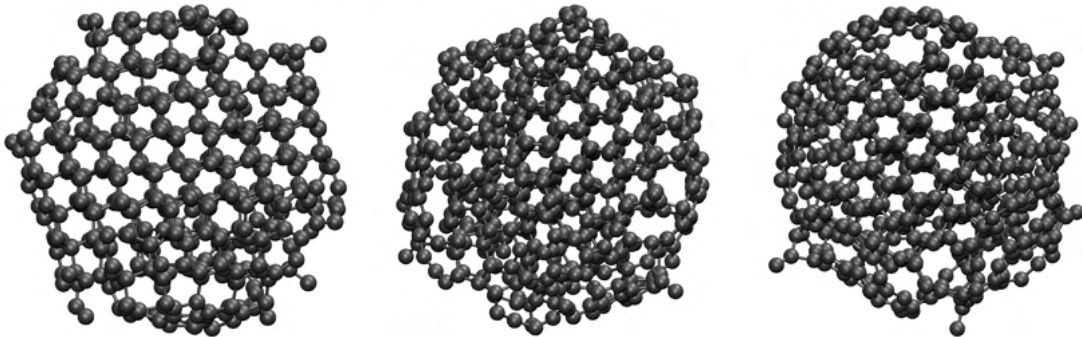


**Figure 269:** Snapshots of the evolution of the 2.5 nm ND annealed at 2000 K with the AIREBO potential extracted at (left) 10 ps, (central) 500 ps and (right) 1 ns. The initial configuration was built by the Wulff construction.

but much more computationally demanding scheme. To this aim we chose the Gaussian Approximation Potential (GAP) from Ref. [325].

We have investigated NDs with diameters of 1.4, 2.5 nm and 5 nm, containing about 200, 750, and 5900 atoms, respectively. The initial configuration of the ND was built in two different ways, either as a spherical shape or by using the Wulff construction that minimizes the overall surface energy. To this aim we used the theoretical surface energies of the surfaces of diamonds from Ref. [326], obtained from Density Functional Theory (DFT).

We then annealed the models at several different temperatures in the range 500-3000 K for 1 ns. Snapshots of the evolution of the 2.5 nm ND as a function of time at 2000 K are shown in Figure 269. A partial graphitization of the outermost layers is clearly visible.

Preliminary calculations of PDOS with the AIREBO potential show that the PDOS is more similar to that of the bulk diamond for annealing at the lower temperatures while sizable changes occur at and above 2000 K due to partial graphitization with a reduction of the optical peak and an increase of the PDOS due to acoustic phonons at low frequency. This effect is reduced by increasing the size of the NDs as also shown by the results of Ref. [324] on 1442-atom NDs.

To compare with experimental data we resort, however, to the more accurate GAP potential. In Figure 270 we compare the theoretical PDOS of the largest 5 nm ND annealed at 500 K temperatures with INS data from Ref. [322]. The PDOS was obtained by Fourier transforming the velocity-velocity correlation function extracted from simulations 20 ps long. The agreement with experimental data is overall good and it improves for the models annealed at higher temperatures which corresponds to a higher degree of graphitization. These theoretical PDOS have been used to compute the neutron scattering cross section presented in the sections below.

### 10.2.3 Graphitic compounds

We have explored several graphitic compounds through DFT calculations. This includes graphite oxide and intercalated graphite oxide, also in deuterated forms, and fullerite. We present below a selection of these calculations, where further details can be found in [134] for fullerite.

Graphite oxide (GO) is made of graphitic layers with a fraction of carbon atoms bound to oxygen atoms either in an epoxy group ( $C-O-C$ ) or within a hydroxyl ( $C-OH$ ). This leads to a wrinkled hexagonal structure with a typical 6-7 Å distance between the layers [328, 329, 330], which is also ruled by the presence of hydrogen bonds among hydroxyls in adjacent layers. Intercalated water molecules bound to the hydrophilic hydroxyl groups have a marginal effect on the structure of the individual layers, but they lead to a further expansion of the interlayer distance [330]. The C/O and C/H ratio of graphite oxide depends on the preparation conditions with reported compositions ranging from  $C_8O(OH)_2$  to  $C_{12}O(OH)_2$  (see Ref. [331] for a review).

To provide structural and phononic data for the calculation of the neutron scattering cross sections, we optimized the geometry of different models of GO by means of DFT calculations. We first considered the model with composition  $C_8O(OH)_2$  proposed in Ref. [331]. The supercell contains two graphitic planes

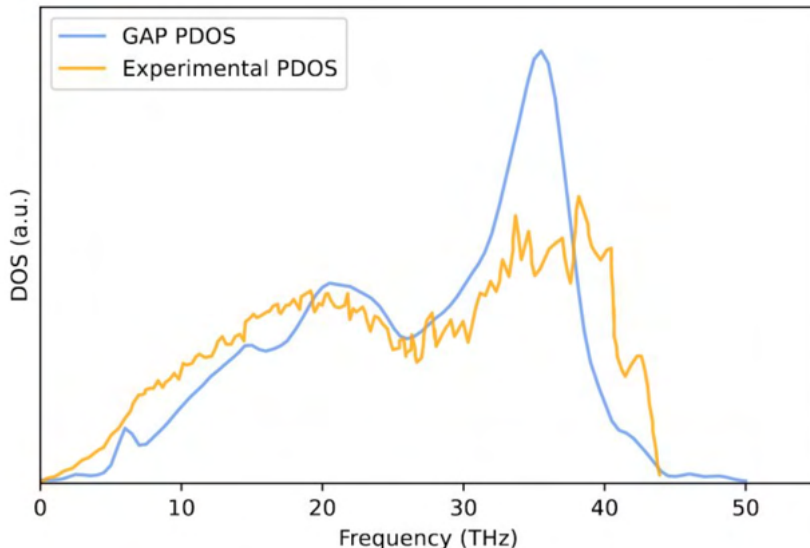


**Figure 270:** Phonon density of states computed with the GAP potential for the 5.0 nm ND annealed at 500 K (from Ref. [327]), compared with experimental data from inelastic neutron scattering from Ref. [322].

each made of 2x2 unit cells of a single graphite layer (8 carbon atom per layer) with one epoxy group and two hydroxyl groups per layer pointing in opposite directions with respect to the graphitic plane. The two graphitic planes in the unit cell have oxygen atoms and hydroxyls in the same positions but the planes can slide one with respect to the other during the geometry optimization. We then considered a second larger model with a supercell containing two graphitic planes each made of 3x3 unit cells of a single graphite layer (18 carbon atom per layer) with one epoxy group and two hydroxyl groups per layer, still pointing in opposite directions with respect to the graphitic plane, which corresponds to a composition  $C_{18}O(OH)_2$ .

Finally, we considered a hydrated form of the small model by adding a water molecule in the van der Waals gap between adjacent graphitic layers which corresponds to a composition  $C_8O(OH)_2\text{-H}_2\text{O}$ . The geometry of these models have been optimized by DFT calculations with the QE suite of programs [314], the PBE [311] approximation for the exchange and correlation energy functional, ultrasoft pseudopotentials [312] and a plane wave expansion of Kohn-Sham orbitals. We also included semiempirical van der Waals interactions à la Grimme (D2) [332].

The side views of the final configuration of the small and large model of GO are shown in Figure 271. The sliding of the two graphitic planes leads to the formation of H-bonds among the hydroxyls and between one hydroxyl and the epoxy group. There are two different interplanar distances corresponding to 5.244 and 4.525 Å in the small model and to 4.616 and 4.699 Å in the large one. In the hydrated model, with composition  $C_8O(OH)_2\text{-H}_2\text{O}$ , the water molecules induce a swelling of the structure with larger interlayer distances of 6.131 and 6.141 Å.

We then computed the PDOS for all models within DFPT [310] as implemented in the QE code. We also computed the PDOS for deuterated models. Examples of the PDOS projected on different atomic species, each normalized to one, are shown in Figure 272 for the small and large models with no intercalated water. Atomic positions and PDOS of the models discussed above have been used as input to the neutron scattering models.

#### 10.2.4 Clathrate hydrates

The initial configuration of the THF-containing hydrogenated clathrate hydrates in structure II was taken from Ref. [333]. The unit cell of the face centered cubic lattice contains 34  $\text{H}_2\text{O}$  molecules and two THF molecules inserted in the large cages. The unit cell was replicated to build the conventional cubic cell with 136  $\text{H}_2\text{O}$  and 8 THF molecules. The initial position of the THF molecules was selected by

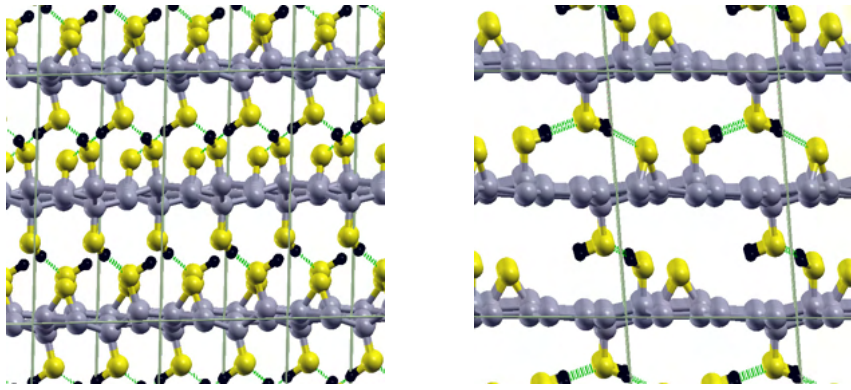


**Figure 271:** Side views of (right) the small model of GO (composition  $C_8O(OH)_2$ ) and (left) the large model of GO (composition  $C_{18}O(OH)_2$ ). Several replicas of the supercell are shown. Hydrogen bonds are depicted by green lines. Carbon, oxygen and hydrogen atoms are depicted by gray, yellow and black spheres.

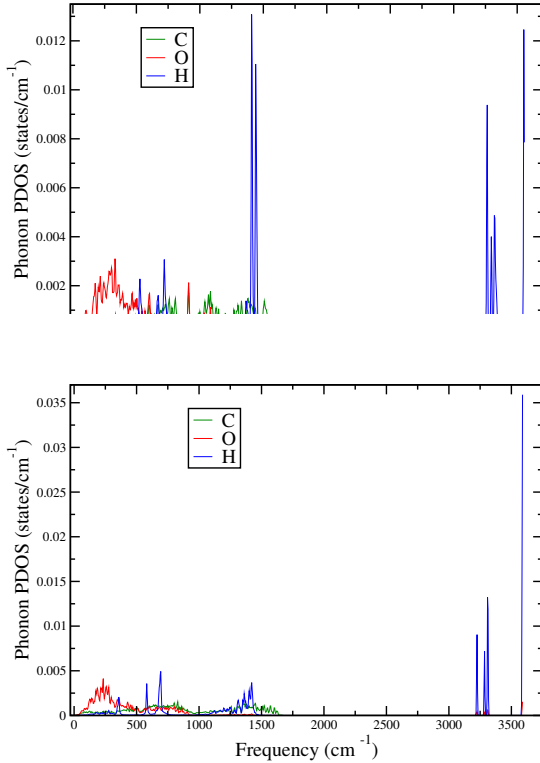


**Figure 272:** Phonon density of states (PDOS) projected on different atomic species, each normalized to one for (left panel) the small model with composition  $C_8O(OH)_2$  and (right panel) in the large model with composition  $C_{18}O(OH)_2$ .

performing classical MD simulations with GROMACS [334] using the SPC/E potential for water [335] and the general Amber force field for THF and THF-water interactions [336]. The initial structure was optimised by means of DFT calculations with CP2k [337]. We employed the PBE approximation for the exchange and correlation functional [311], norm conserving pseudopotentials [338]. The Kohn-Sham orbitals were expanded in a triple-zeta-valence plus polarisation basis set while the electronic density was expanded in plane waves as implemented in CP2k. Semiempirical van der Waals interactions were included according to Grimme (D3) [339]. The phonons were computed using CP2k combined with phonopy [340] at the experimental lattice parameter. The force constant matrix was computed from forces at finite atomic displacements in the conventional cubic cell (136 water molecules). The

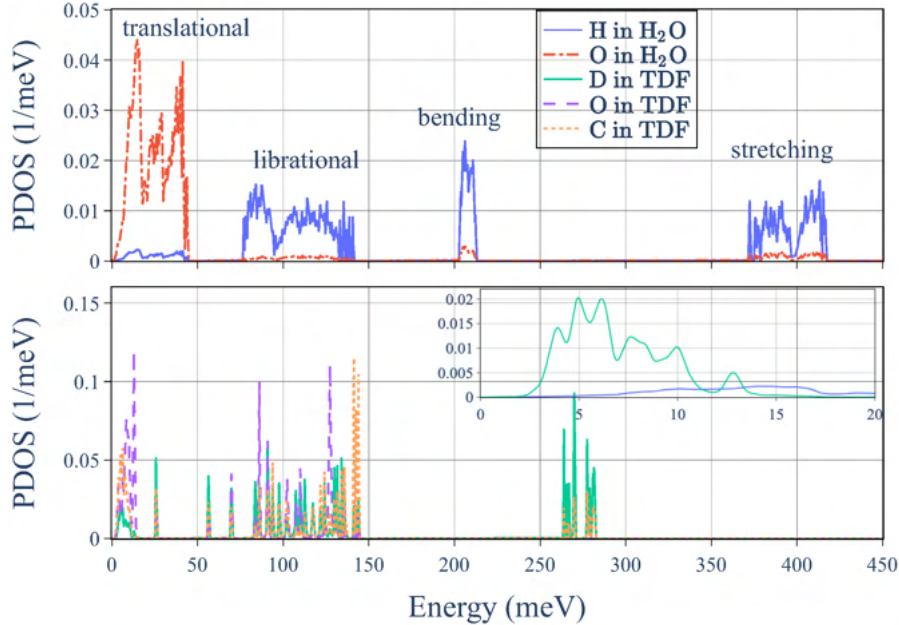


**Figure 273:** Normalised PDOS of TDF-containing hydrogenated clathrate hydrate projected on different atomic species from DFT calculations. The global PDOS can be obtained by summing the projected PDOS multiplied by the number of corresponding atoms in the unit cell.

Coulombic long range contribution was computed analytically from effective charges and the dielectric constant obtained in turn from ionic forces and polarisation at finite electric field within the Berry phase approach [341] implemented in CP2k.

The PDOS was computed for all possible four combinations of TDF/THF and hydrated/deuterated clathrate. As an example, we show in Figure 273 the PDOS projected on different atomic species for the TDF-H<sub>2</sub>O clathrate. At low energy, the translational modes of the H<sub>2</sub>O molecules dominate. In this spectral region, the experimental neutron weighted PDOS of type II clathrate hydrates has two characteristic peaks at about 7 and 10.5 meV [131, 342]. This double peak feature is less evident in the theoretical PDOS projected on the water molecules. The position of the two peaks is also blue-shifted to about 10 and 14.5 meV. This double peak feature is instead better reproduced by classical simulations with rigid water molecules as reported for instance in Refs. [343, 342]. A possible improvement of the theoretical PDOS would then result from the use of the DFT-PDOS for the intramolecular modes and the classical result for the PDOS in the translational low frequency region as we will discuss later on. The band from 70 meV to 150 meV is due to molecular librations. At higher energy, intramolecular modes are dominant with O-H bending and O-H stretching at around 200 meV and 400 meV, respectively. The PDOS of atoms bound in the TDF molecules are illustrated in the lower panel of Figure 273. The PDOS of the THF-H<sub>2</sub>O and TDF-D<sub>2</sub>O can be found in Ref. [124]. The PDOS of the cage can be transferred to other clathrates, based on weak guest-host coupling assumption as discussed in Ref. [131].

We considered two other type II clathrates, which include the clathrate with O<sub>2</sub> molecules in the large and small cages [344] and a mixed clathrate with THF in the large cages and O<sub>2</sub> molecules in the small cages. For these structures, we performed classical MD simulations at 200 K with the same force-field with rigid water molecules and partially rigid THF used for the generation of the initial structure of the THF-clathrate mentioned previously. We considered a supercell made of 2×2×2 conventional cubic cells each containing 136 water molecules. The PDOS were computed by Fourier transforming the velocity-velocity autocorrelation function extracted from MD trajectories.

To include in the PDOS the contribution from intramolecular modes of the water molecule, we used the DFT results obtained for the type II clathrate containing THF discussed above. In the approximation of weak coupling between water and the guest molecules in the cage, we expect that the intramolecular modes of H<sub>2</sub>O would be little affected by the replacement of THF by O<sub>2</sub> at least for the purpose of the

calculation of the neutron scattering cross section.

To describe both the intermolecular and intramolecular modes we then built a PDOS by merging the classical PDOS in the low frequency region of translational and librational modes with the DFT PDOS in the high frequency region for the intramolecular modes of water. The resulting PDOS projected on the different atomic species are shown in shown in Figure 274. The simulated PDOS serve to compare with the measurements presented in Section 4.

### 10.3 Advancements in Nuclear Data Libraries

The design of reactors, neutron sources, and nuclear systems requires calculations of neutron distributions using radiation transport codes. A major source for nuclear data used in radiation transport codes, such as MCNP, OpenMC, and PHITS, are the ENDF files. These files include sub-libraries for different kinds of particles, in particular thermal neutron scattering data in form of TSL and written in ENDF-6 format [304]. In ENDF format, File 7 stores the thermal neutron scattering data in two sections: one for elastic and one for inelastic scattering. In general, the scattering cross section of neutrons can be decomposed into four parts: coherent elastic, incoherent elastic, coherent inelastic, and incoherent inelastic scattering. Elastic scattering represents the scattering of a neutron without the exchange of energy with the target material in the laboratory frame of reference, while inelastic scattering represents the scattering of a neutron where it either gains or loses energy. Coherent scattering contains the interference terms of the scattering and therefore is sensitive to the structure of the material, whereas incoherent elastic scattering depends on the self correlation for each atom at different times.

At the moment, in the ENDF-6 format, the elastic section stores either the coherent elastic or incoherent elastic cross section only. In the inelastic section, either the incoherent inelastic cross section is stored in the incoherent approximation or the inelastic is stored as a sum of incoherent and coherent inelastic parts calculated in the incoherent approximation. To overcome the limitation in the elastic section, a change was recently proposed [305] for the thermal scattering format, which will in this paper be referred to as the “mixed-elastic format”. Implementation of the new format makes it possible to store both the coherent and incoherent elastic cross sections in the elastic section, one after another one, in the same format in which they were stored before individually. This is important for materials like MgD<sub>2</sub> which have a significant coherent and incoherent elastic component. Without the new format, thermalization of neutrons couldn’t be properly calculated for such a material using the current format.

Thermal scattering files can be produced with the LEAPR module of NJOY, which is available under a free software license but its support for coherent elastic scattering is limited. On the other hand, the NCrytal library [307, 308, 309] has an extensive treatment of the calculation of thermal neutron scattering cross sections directly but cannot generate ENDF-6 formatted files. In order to remedy this, we have combined these two tools, using NCrytal to generate the microscopic data that is later used by NJOY to produce thermal scattering libraries. Additionally, we have modified NJOY to support the proposed mixed-elastic format and produce thermal scattering .ACE files with coherent and incoherent elastic scattering. The Monte-Carlo code OpenMC was modified as well to support this new format. This development is described in the NJOY+NCrytal paper [345] in great detail, however a summary is given below.

Since MgH<sub>2</sub> and MgD<sub>2</sub> have significant incoherent and coherent elastic components, the main motivation for developing NJOY+NCrytal was to enable accurate calculations of thermalization and moderation of neutrons in these materials, in both the current and proposed format. Additionally, NJOY+NCrytal was motivated by a need to implement the mixed-elastic format proposal in an open source code, such as NJOY. In essence, NJOY+NCrytal is a customized version of NJOY that relies on NCrytal to provide the necessary information for the calculations of the coherent and incoherent elastic components. Additionally, both NJOY and NCrytal utilize CMake and GitHub repositories for the installation, hence making the integration smoother.

The changes to NJOY can be split into two parts. The first part is to provide an interface between LEAPR and NCrytal so that LEAPR can calculate coherent and incoherent elastic cross section components for any crystalline material. The calculated elastic components are then stored in the tsl-ENDF

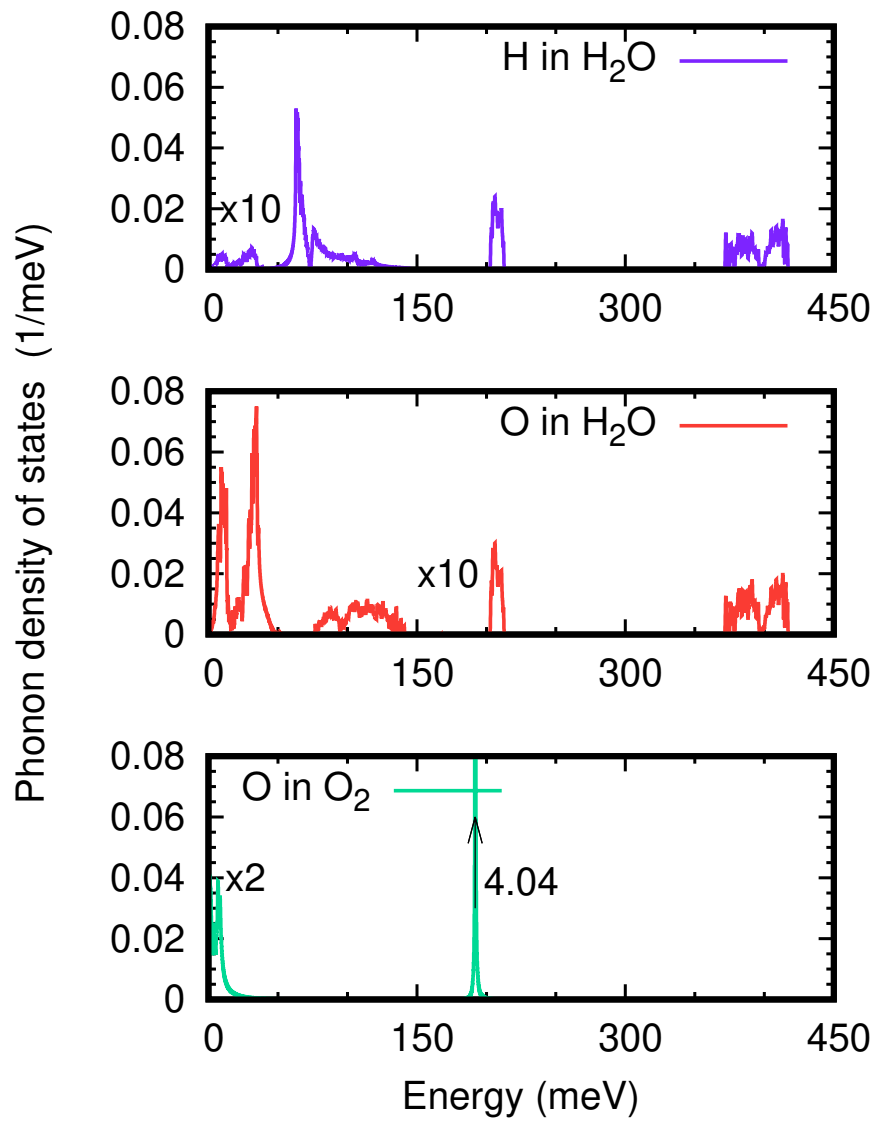


**Figure 274:** The phonon density of states of  $\text{O}_2\text{-H}_2\text{O}$  clathrate projected on the different atomic species obtained from atomistic simulations (see text). Each projected PDOS is normalized to one. The total PDOS can be obtained by summing the projected PDOS multiplied by the number of corresponding atoms in the unit cell. For the sake of clarity, the projected PDOSs are multiplied by ten below 50 meV for H and above 70 meV for O in water, and by two below 50 meV for O in  $\text{O}_2$ .

file for both the current and proposed mixed-elastic format. The second part consists of implementing changes to the THERMR and ACER modules of NJOY so that the new mixed-elastic format can be read and handled properly in order to produce .ACE files used by Monte-Carlo particle transport codes to sample neutron scattering events. A summary of the generated libraries are given below.

### 10.3.1 MgH<sub>2</sub> / MgD<sub>2</sub>

We computed the total scattering neutron cross sections of polycrystalline MgH<sub>2</sub> and its deuterated variant MgD<sub>2</sub> using the NJOY + NCystal tool and input from the DFT simulations described above. MgH<sub>2</sub> recently emerged as a good candidate material for cold neutron reflectors [169], while MgD<sub>2</sub> is of interest because of an even lower absorption cross section. As mentioned before, calculating the total cross section of a material is one of the most important validation tests of the newly created libraries.

From the calculated phonon spectra, tsl-ENDF files were created for both MgH<sub>2</sub> and MgD<sub>2</sub>, using the NJOY + NCystal tool. In Figure 275 it can be seen that the agreement between the measured total cross section data from Granada [169] and the calculated curves (which include an absorption cross section ( $\sigma_{2200}^H = 0.3326$  b,  $\sigma_{2200}^{Mg} = 0.063$  b) is excellent. Since MgH<sub>2</sub> is an incoherent scatterer, due to the large incoherent cross section of hydrogen, if MEF option cannot be utilized, the CEF option is a good approximation as well. MEF stands for mixed-elastic format, while CEF stands for current ENDF format. The latter includes approximations within the ENDF format and can be used in standard versions of Monte-Carlo software, as described in more detailed in [345].

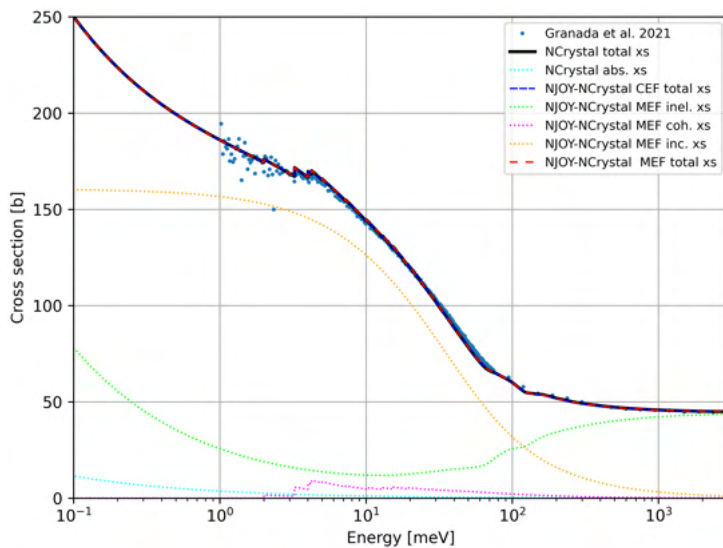


**Figure 275:** Total scattering cross section comparison for MgH<sub>2</sub>. From [345].

Figure 276 shows a comparison between the NCystal and the NJOY+NCystal calculated total cross sections for MgD<sub>2</sub>, as well as different scattering components as calculated in NJOY+NCystal and NCystal. It can be seen that the total cross section for MgD<sub>2</sub> is orders of magnitude lower than for MgH<sub>2</sub>. This arises from the incoherent hydrogen, which has a cross section of 82.02 barns, and is replaced with coherent deuterium with a cross section of 7.64 barns. Although the CEF option is not recommended for deuterated materials due to the presence of both coherent and incoherent cross sections, the approximation for compounds works well in terms of total cross section because the coherent component is assigned to the Mg(MgD<sub>2</sub>) library and the incoherent component to the D(MgD<sub>2</sub>) library.

### 10.3.2 Other materials

In addition to including the MgH<sub>2</sub> and MgD<sub>2</sub> evaluations, the NJOY+NCystal library contains 213 tsl-ENDF evaluations, created for 112 new or updated materials, in both the current ENDF-6 format and

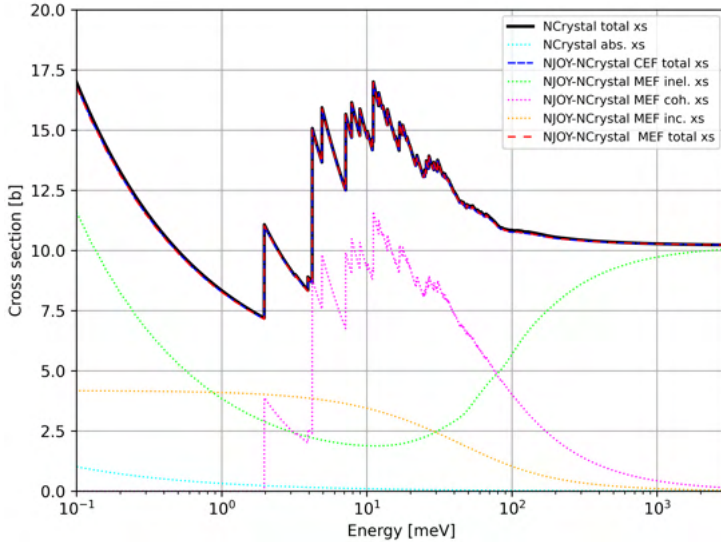


**Figure 276:** Total scattering cross section comparison for  $\text{MgD}_2$ . From [345].

in the new proposed mixed-elastic format. A summary of the NJOY+NCrystal library is given in the NJOY+NCrystal paper [345].

Different methodologies were employed to create the final tsl-ENDF files. Some of the materials were created from existing .ncmat files in current and previous versions of NCrystal. For some of the materials, mostly monoatomic metals, the VDOS curves in existing .ncmat files were updated, mostly using different sources from the literature. For the rest of the materials, phonon curves were obtained by utilizing ab-initio calculations from a phonon database at Kyoto University [346, 347, 348, 349]. In summary, the files from the database were used with Phonopy [340] to calculate phonon eigenvalues and eigenfrequencies, which were then utilized with oClimax [350] to extract partial phonon spectra. A detailed explanation of how the phonon spectrum and crystal structure was obtained for each material and is provided in the comments section of the tsl-ENDF files.

The experimental data for the validation of the tsl-ENDF files is scarce. Wherever experimental data were available, tsl-ENDF files were validated against total cross-section measurements and diffraction data, while all materials were validated against specific heat capacity curves as a minimum standard for acceptance. The link to the exact files used for each material at the Kyoto University database can be found inside the tsl-ENDF files in the HighNESS Github repository. For validation, the correct crystal structure was a starting point (a reference for each crystal structure can be found inside tsl-ENDF files as well), followed by comparison with the experimental specific heat capacity and if available, total cross section measurements. For  $\alpha$  and  $\beta$  SiC, diffraction data was used as well as a means of validation of the libraries.

### 10.3.3 Libraries for the THF- and TDF-clathrates

The lattice parameters, atomic positions of the crystalline structure, and the PDOS from the molecular modelling calculations were converted into input files for the NCrystal toolkit. Figure 277 shows the total scattering cross section of the THF-containing deuterated clathrate hydrate, which is the sum of coherent elastic, incoherent elastic and inelastic cross sections. Incoherent elastic scattering is dominant for neutron energy below a few meV because of the large incoherent cross section of hydrogen [351]. It should be pointed out that these scattering cross sections are calculated based from Figure 273.

The large Bragg cutoff (around 0.2 meV or 20 Å) is an advantage for cold neutron moderation because neutrons can be reflected within the cage structure thus increasing the interactions with the guest molecules. The cross sections of the totally hydrogenated and deuterated THF-clathrates are presented in Ref. [124]. These theoretical neutron scattering cross sections serve to compare against the measurements performed at the ILL as shown in Section 4.

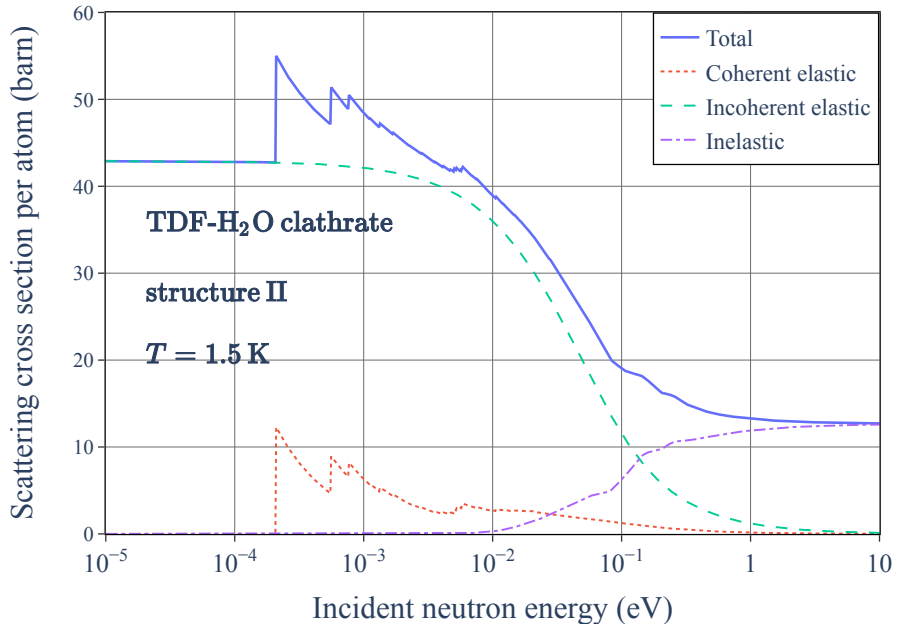


**Figure 277:** Neutron scattering cross sections of type II TDF-containing hydrogenated clathrate hydrate.

#### 10.3.4 Libraries for graphitic compounds

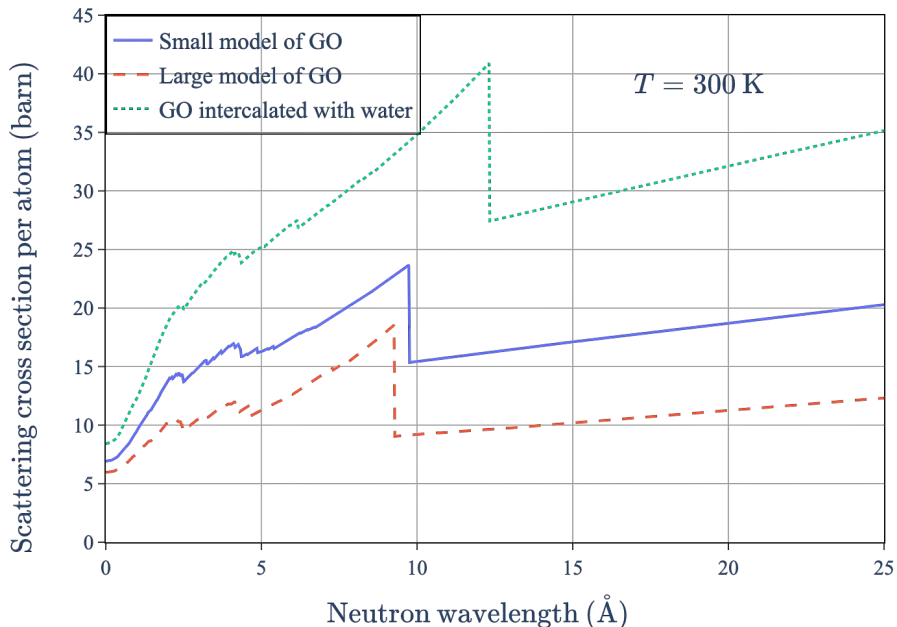


**Figure 278:** Neutron scattering cross sections of the small and large models of hydrogenated GO, and hydrogenated GO intercalated with water molecule.

For the graphitic material presented in Section 10.2.3, the crystalline structure and the corresponding PDOS are merged into a .ncmat file by using the NCrystal internal tool. Examples of the theoretical neutron scattering cross sections are presented in Figures 278 and 279.

Figure 278 show the results for GO for the two different simulation models in addition to GO including water intercalation. It can be seen that the addition of the water extends the Bragg-cutoff to higher wavelengths. The scattering cross section per atom of the small model ( $C_8O(OH)_2$ ) is larger than that of the large model ( $C_{18}O(OH)_2$ ), because the atomic density of hydrogen is higher in the small model. The effect of deuteration is to lower the cross-sections, due to the exchange of H to D, which results in a

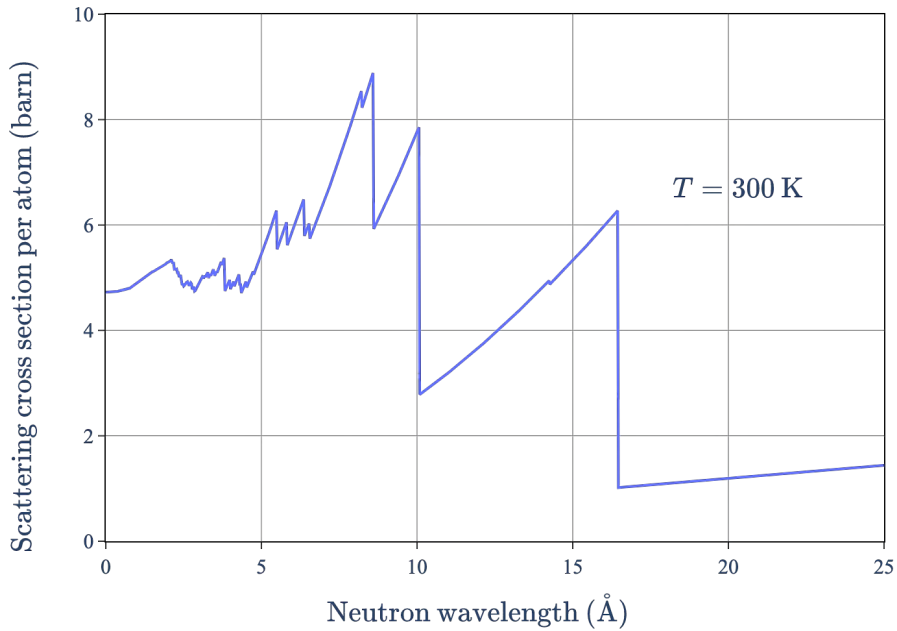


**Figure 279:** Neutron scattering cross section of fullerite, calculated based on the PDOS and crystalline structure presented in Ref. [134].

lower incoherent elastic scattering in the material.

Figure 279 shows the results for the fullerite model, which exhibits an extension of the Bragg-cutoff to even higher wavelengths, compared to the graphite oxide models. The neutron scattering cross section is obtained using the crystalline structure and the DFT-calculated PDOS which are detailed in Ref. [134].

In addition to the above, the .ncmat files for all graphite compounds investigated can be found in the HighNESS Github repository. This includes deuterated graphite oxide, deuterated intercalated graphite oxide, and a couple other intercalated graphites.

## 10.4 Extensions of NCrystal to include new physics

A unique feature for the code NCrystal is that it can be called on-the-fly during a Monte-Carlo simulation. This makes it possible to avoid limitations in the ENDF nuclear data format and include new physics that were not possible before through usage of plugins.

The support for plugins was introduced in NCrystal release versions 2.2.x-2.4.x and they are to be developed according to the descriptions given on the wiki pages [352, 353]. The development process includes picking a name for the plugin, forking the plugin template library and developing the plugin to combine new physics models with the existing models in NCrystal. A template repository and example infrastructure to facilitate validation, debugging and bench-marking of the new plugin are provided to make it easier for new users to get started. After the plugin is developed, it can be compiled as a shared library or directly into a given NCrystal installation and all plugins developed should appear as forks of the ncplugin-template repository [354]. In addition, NCrystal release version 2.1.0 includes the ability to define custom data in the NCrystal material data files, which can be used by the new physics models developed in the plugin. These developments have made it possible to include small-angle neutron scattering, magnetic scattering, and texture effects directly into NCrystal and will be described below.

### 10.4.1 Small-angle neutron scattering plugin

The design and optimization of reflector systems for very-cold and ultra-cold neutron sources based on NDs critically relies on an efficient and validated implementation of SANS. For this reason, we investigated different approaches for integrating in Monte-Carlo codes a pre-existing empirical model for SANS in NDs powder. The first possibility consists of extending the NCrystal poly-crystalline kernel by adding the SANS process through a plugin which is interfaced through NCrystal with other radiation transport codes, e.g. McStas, Geant4 or OpenMC. The other possibility is to implement the ND calculation directly in the Monte-Carlo code and use a modified .ACE SANS file, as was done in [135]. This work has been presented in earlier papers [355, 356].

The empirical model that serves as a starting point for both implementations is based on the work by Granada et. al. [135][169] and was implemented prior to the beginning of this project [356]. The idea is to fit a simple model to the SANS structure factor measured by Teshigawara et. al. [318]. This approach takes into consideration the nanoparticle size distribution, because it affects the experimental SANS structure factor.

In the Teshigawara work, the experimental results were fit using the unified exponential/power-law approximation, as expressed in Eq.3 in [357], while this implementation further simplifies the fit function in a piecewise power law:

$$I(Q) = \begin{cases} A_1 Q^{b_1} & Q < Q_0 \\ A_2 Q^{b_2} & Q > Q_0 \end{cases} \quad (39)$$

The results, along with the initial  $I(Q)$  data are shown in Figure 280. By using the relation between the SANS structure factor and the SANS cross section, and considering that for neutron energies  $E_n > 0.01$  meV (lower limit in many Monte Carlo simulation software) it is always true that the incident wavenumber  $k_0$  satisfies  $k_0 > 6.95 \times 10^{-2} \text{ \AA}^{-1} > Q_0 = 5.11 \times 10^{-2} \text{ \AA}^{-1}$ , then it is possible to use the following expression for the total SANS cross section:

$$\begin{aligned} \sigma(k_0) &= \frac{\sigma_0}{2k_0^2} \int_0^{2k_0} q I(q) dq = \frac{\sigma_0}{2k_0^2} \left( \int_0^{Q_0} q I(q) dq + \int_{Q_0}^{2k_0} q I(q) dq \right) \\ &= \frac{\sigma_0}{2k_0^2} \left[ \frac{A_1}{b_1 + 2} Q_0^{b_1 + 2} + \frac{A_2}{b_2 + 2} (2k_0)^{b_2 + 2} - \frac{A_2}{b_2 + 2} Q_0^{b_2 + 2} \right] \end{aligned} \quad (40)$$

This cross section as a function of the wavevector  $k_0$  is used by Monte-Carlo codes during run-time to compute the macroscopic total cross section and sample the distance to next collision. If there is a collision, the code randomly picks the reaction based on the ratio of its cross section to the total one. For

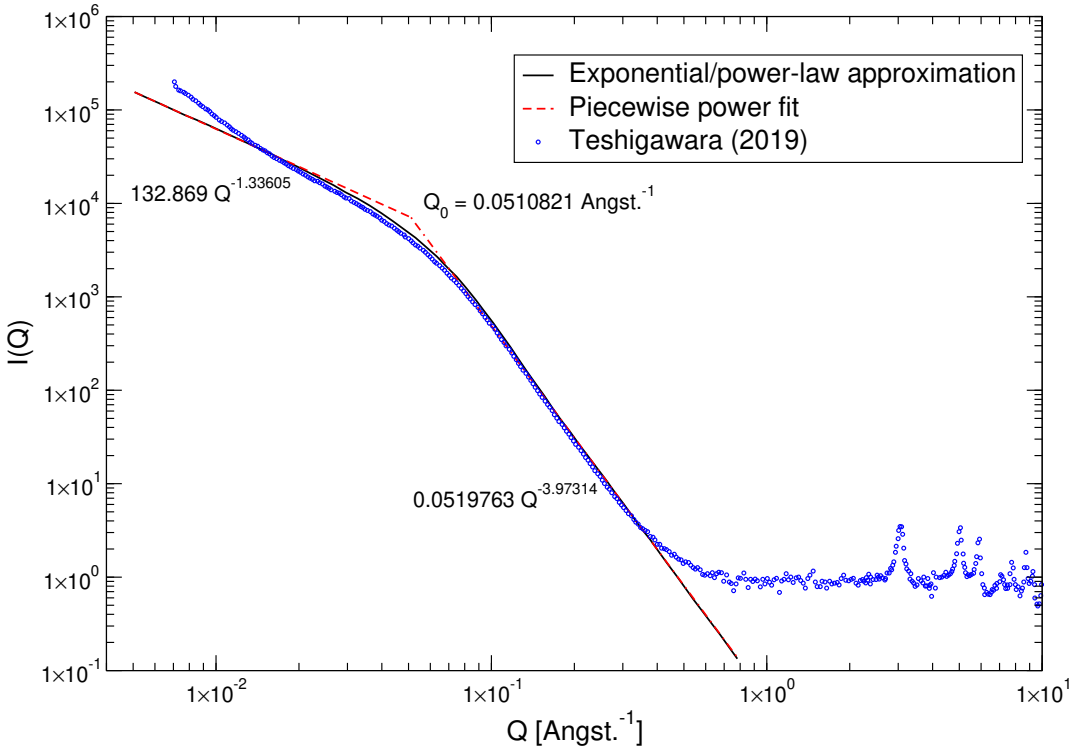


**Figure 280:** Structure factor  $I(Q)$  in the Teshigawara paper fitted by a power-exponential law and then further simplified into a piecewise power law fit.

different types of scattering, the outgoing energy and direction are sampled according to the underlying physics. In the case of SANS, there is no energy exchange, but the direction still need to be determined. The cumulative probability distribution for the scattering vector  $Q$  is given by:

$$CDF(k_0, Q) = \begin{cases} \frac{\sigma_0}{2k_0^2} \frac{A_1}{b_1 + 2} Q^{b_1+2} & Q < Q_0 \\ \frac{\sigma(k_0)}{\sigma_0} \left[ \frac{A_1}{b_1 + 2} Q_0^{b_1+2} + \frac{A_2}{b_2 + 2} Q^{b_2+2} - \frac{A_2}{b_2 + 2} Q_0^{b_2+2} \right] & Q > Q_0 \end{cases} \quad (41)$$

The value of the outgoing  $Q$  is sampled by first inverting analytically Equation (41) and then evaluating  $CDF^{-1}(\xi)$  at a random number  $\xi \sim U(0, 1)$ . The scattering cosine is finally computed as  $\mu = 1 - \frac{1}{2} \left[ \frac{Q}{k_0} \right]^2$ .

This model has been implemented as a plugin in NCrystal and has been extensively benchmarked in [355].

In Figure 281 we can see the calculated total scattering cross-sections using the phonon frequency distribution for perfect diamond and the one based on the finite size of the ND particles using the NCrystal plugin. It can be seen that the scattering cross-section is dominated by small-angle neutron scattering at low-energies, while the finite size of the NDs impacts the inelastic component of the cross-section.

#### 10.4.2 Magnetic scattering plugin

Clathrate hydrates hosting oxygen are considered as promising candidates due to neutron inelastic magnetic scattering with oxygen [110]. A tiny energy around 0.4 meV, which corresponds to the zero-field splitting constant, can be removed from the neutrons due to the magnetic interactions with the electrons of oxygen molecules in paramagnetic states. Based on the theory derived by Zimmer [110], the equations of the magnetic scattering kernels are implemented as a plugin named ncplugin-MagScat in NCrystal.

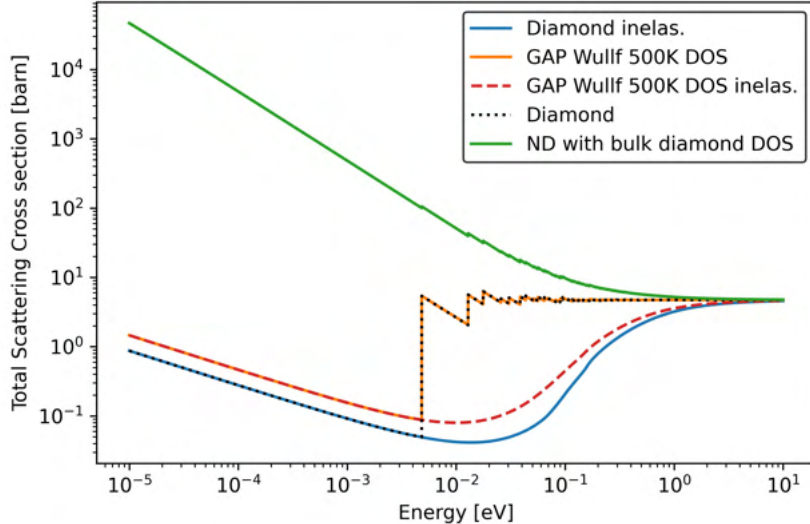


**Figure 281:** Calculated scattering cross-sections and components for NDs using the phonon frequency distribution of perfect diamond and the phonon frequency spectrum based on a finite-size of the ND particles. From [327]

At low temperatures, molecules in crystalline oxygen appear to be antiferromagnetically ordered [358, 359]. Oxygen molecules are in paramagnetic states when they are kept sufficiently far away to avoid magnetic ordering, e.g., enclathrated in clathrate hydrates [110]. Paramagnetic molecular oxygen possesses a spin triplet ground state characterising the spin state projection along the symmetry axis of the molecule. The transition of the magnetic levels or spin orientation results in changing the neutron kinetic energy with 0.4 meV due to the molecular zero-field splitting. The physics of neutron scattering with paramagnetic oxygen is derived in Ref. [110]. Nevertheless, only the inelastic magnetic cross sections are given, the derivation of the theoretical outgoing neutron distribution or the scattering kernels required by Monte-Carlo simulations remains undone. Scattering kernels or  $S(\vec{Q}, \omega)$  are tabulated data giving the probability of neutron scattering with target nuclei or electron system as a function of neutron wave vector transfer  $\vec{Q} = \vec{k} - \vec{k}'$  and energy transfer  $\hbar\omega = E - E'$ . The approximation of neglecting the Debye-Waller factor in the calculations of paramagnetic scattering cross sections in Ref. [110] can also be improved. The physics of neutron nucleus scattering can be included to take into account the impacts of atoms presented in the cage structure.

The aim is thus to include and validate the physics of neutron scattering with paramagnetic oxygen in the Monte-Carlo neutron transport simulations. To this end, we use the open source software package NCystal to calculate the neutron nucleus scattering kernels and benefit from its flexibility and versatility to include the magnetic physics in a plugin named ncplugin-MagScat. NCystal is able to be used as a backend for the Monte-Carlo particle transport code OpenMC, which provides a possibility to validate the implemented magnetic scattering model by comparing with the experimental measurements reported in the literature, performed by Chazallon et al. on O<sub>2</sub> clathrate hydrate [344] and Renker et al. on O<sub>2</sub>-C<sub>60</sub> [360], respectively.

Based on Ref. [110], the neutron magnetic scattering kernels or dynamic structure factors  $S_{\text{mag}}(Q, \omega)$  are derived. In this section we only present the final form of the equations. Without external magnetic fields, the double differential magnetic scattering cross section for unpolarised neutrons is given by

$$\frac{d^2\sigma_{\text{mag}}}{d\Omega dE'} = b_m^2 \left( \sqrt{\frac{E'}{E}} S_{\text{mag},\pm}(Q, \omega) + S_{\text{mag},0}(Q, \omega) \right), \quad (42)$$

where  $b_m = 5.404 \text{ fm}$  is the magnetic scattering length,  $Q$  is the neutron wavenumber transfer,  $\hbar\omega = E - E'$  is the neutron energy transfer,  $S_{\text{mag},\pm}(Q, \omega)$  and  $S_{\text{mag},0}(Q, \omega)$  represent respectively the magnetic inelastic (+ for up-scattering and - for down-scattering) and elastic scattering kernels and is

given by

$$S_{\text{mag},\pm}(Q, \omega) = \exp \left( -(\langle u^2 \rangle + \frac{\ln(2)}{\Gamma_{\text{mag}}^2}) Q_{\pm}^2 \right) g_{\pm}(T) \delta(\hbar\omega \pm D), \quad (43)$$

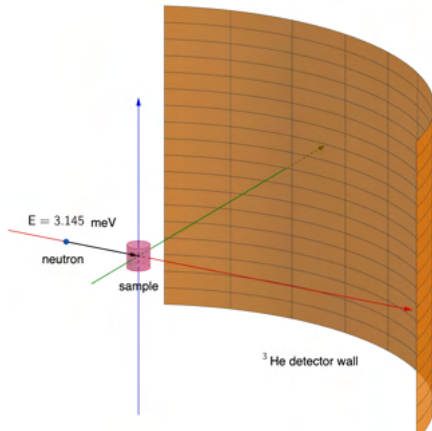
and

$$S_{\text{mag},0}(Q, \omega) = \exp \left( -(\langle u^2 \rangle + \frac{\ln(2)}{\Gamma_{\text{mag}}^2}) Q_0^2 \right) g_0(T) \delta(\hbar\omega). \quad (44)$$

$\langle u^2 \rangle$  is the mean-squared displacement (MSD) which is temperature-dependent and can be calculated from the PDOS.  $\Gamma_{\text{mag}} = 15 \text{ nm}^{-1}$  represents the half width at half maximum (HWHM) of the magnetic form factor which is approximated by a Gaussian function [361].  $D$  is the zero-field splitting constant and  $g(T)$  are functions which contain thermal average of spin matrix elements.



a IN6



b Simplified model

**Figure 282:** Time-of-flight spectrometer IN6 at ILL.

The above model has been integrated into a NCystal plugin and more details are listed in Ref. [134]. It is pointed out in Ref. [110] that the inelastic neutron scattering due to magnetic effects was observed in the experiments performed by Chazallon et al. [344] on O<sub>2</sub>-clathrate and Renker et al. [360] on O<sub>2</sub>-C<sub>60</sub>. Both of the measurements were performed on the time-of-flight spectrometer IN6 (Figure 282a) at ILL. The incident neutron wavelength was set to be 5.1 Å (3.145 meV) for these two measurements. The incident wavelength is larger than the Bragg cutoff of aluminum (Al) ( $\approx 4.6 \text{ \AA}$ ), which has the advantage to avoid possible contamination from Al. In our work, we investigate the magnetic effects through Monte-Carlo simulations. Similar to the process developed for simulating neutron diffraction measurements on uranium dioxide [362], the calculation scheme is composed of MD and DFT calculations, Monte-Carlo simulations, and experimental correction.

MD and DFT calculations are detailed in Ref. [134]. The simulations were performed by using the Monte-Carlo particle transport code OpenMC. From version 0.13.3, OpenMC enables users to define materials through the NCystal .ncmat file and call the corresponding neutron scattering cross sections on-the-fly. The neutron magnetic scattering kernels calculated by the developed plugin ncplugin-MagScat and the neutron nucleus scattering kernels generated from PDOS can thus be taken into account in the Monte-Carlo simulations.

Based on detailed characteristics found on the website [363], a simplified model of IN6 spectrometer (Figure 282b) was used in the OpenMC simulations. The distance between the sample position and the cylindrical <sup>3</sup>He detector wall is  $L = 2.48 \text{ m}$ . The detector wall of IN6 covers a large azimuthal angular range from 10° to 115° and a vertical angular range near to ±15°. The detector wall is composed of

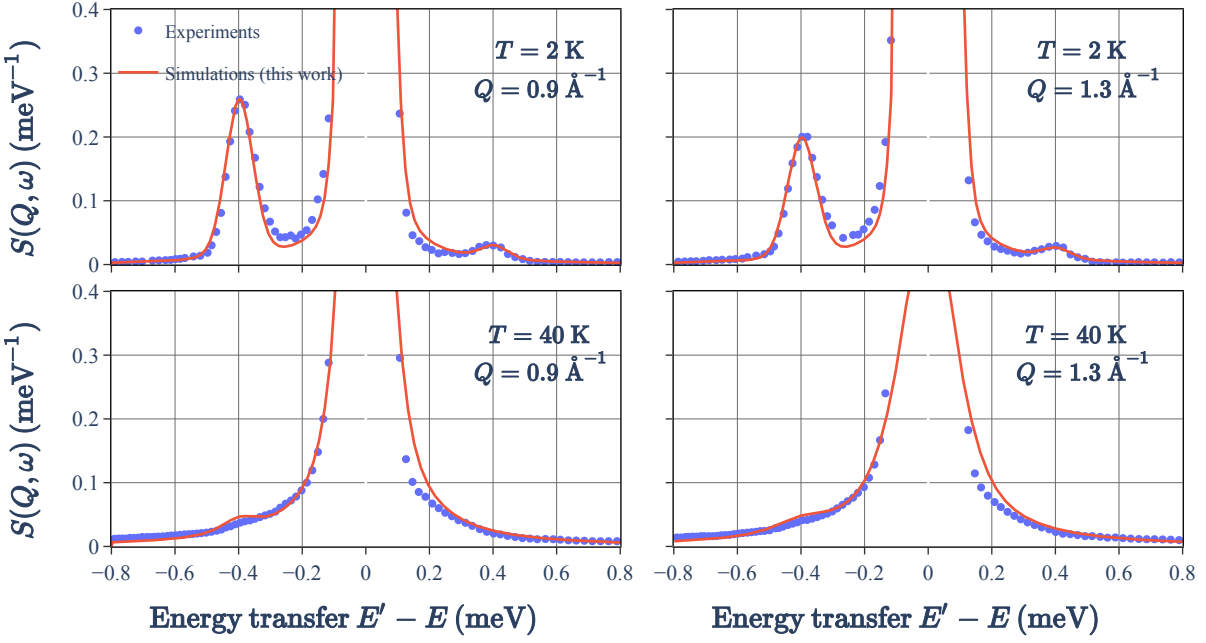


**Figure 283:** Comparisons between simulated and experimental  $S(Q, \omega)$  on O<sub>2</sub>-clathrate [344] at 2 K and 40 K.

337×109 grids along the azimuthal and vertical angular ranges, respectively. The spatial resolution is thus equal to 1.3 cm × 1.2 cm.

The experimental corrections were performed to take into account the resolution of the detectors and the motions of the guest oxygen molecules which are temperature-dependant. Good agreement is obtained between the simulated and experimental  $S(Q, \omega)$  at 2 K and 40 K (see Figure 283), confirming the magnetic scattering physics implemented in the developed plugin. The results on O<sub>2</sub>-C<sub>60</sub> are detailed in Ref. [134]. Preliminary investigations of the magnetic model in the VCN production is presented in Section 4.

#### 10.4.3 Texture plugin

A polycrystalline material, whose grains are randomly oriented, is referred to as a powder. The calculation of the coherent elastic scattering cross section  $\sigma_{\text{coh}}^{\text{el}}(\lambda)$  for powder in NCystal is given by [307, 309]:

$$\sigma_{\text{coh}}^{\text{el}}(\lambda) = \frac{\lambda^2}{2V_{\text{uc}}} \sum_{hkl} d_{hkl} |F_{hkl}|^2, \quad (45)$$

where  $V_{\text{uc}}$  is the volume of the unit cell of the crystal,  $d_{hkl}$  represents the distance between adjacent atomic planes (hkl), and  $|F_{hkl}|^2$  is the form factor depending on the Debye-Waller coefficient or mean squared displacement of the atoms.

Nevertheless, grains having a preferred orientation or texture are observed in polycrystalline materials. The presence of texture can have a significant impact on  $\sigma_{\text{coh}}^{\text{el}}(\lambda)$ . The texture can be described using the orientation distribution function (ODF) which gives the probability of finding grains with a specific orientation in a polycrystalline material [364]. It exists different models which incorporate the ODF in the calculation or correction of  $\sigma_{\text{coh}}^{\text{el}}(\lambda)$  [365, 366, 367, 368]. In our work, we implemented the March-Dollase model as a plugin in NCystal to investigate the texture effects in graphitic materials in transmission measurements.

The March-Dollase model assumes an axially symmetric orientation distribution around the beam direction [369]. Equation (45) is corrected by multiplying the following term  $P_{hkl}(\lambda, d_{hkl})$ :

$$P_{hkl}(\lambda, d_{hkl}) = \frac{1}{2\pi} \int_0^{2\pi} \left( R^2 B_{hkl}^2 + \frac{1 - B_{hkl}^2}{R} \right)^{-\frac{3}{2}} d\phi, \quad (46)$$

where

$$B_{hkl} = \cos(A_{hkl}) \sin(\theta_{hkl}) + \sin(A_{hkl}) \cos(\theta_{hkl}) \sin(\phi), \quad (47)$$

$$A_{hkl} = \arccos\left(\frac{hH + kK + lL}{\sqrt{h^2 + k^2 + l^2}\sqrt{H^2 + K^2 + L^2}}\right), \quad (48)$$

$$\theta_{hkl} = \arcsin\left(\frac{\lambda}{2d_{hkl}}\right), \quad (49)$$

and  $(HKL)$  is the preferred orientation axis parallel to the beam direction.  $R$  is a coefficient representing the degree of crystallographic anisotropy. A polycrystalline material can have more than one preferred orientation. We use the fraction  $f_{hkl}$  and  $R_{hkl}$  associated to each preferred orientation  $hkl$  with  $\sum f_{hkl} = 1$ .

The March-Dollase model has been implemented in the NXS code [370]. The coherent elastic cross sections for aluminum calculated by NXS and our NCystal plugin are compared in Figure 284. We obtain an excellent agreement for powder aluminum. In Equation (45), when  $R = 1$ ,  $P_{hkl}(\lambda, d_{hkl})$  becomes a constant equal to 1, representing the random orientation of grains. The identical cross section obtained by putting  $R = 1$  serves to verify our implementation for the texture model. For  $R$  different from 1, the texture effects on the coherent elastic cross sections are clearly observed. We obtained a good agreement with the NXS code. A zoomed up image of the three peaks is presented in Figure 285. Our calculations show finer peaks compared to the NXS code because we use a finer neutron wavelength discretization. The comparison of cross section with NXS serves to verify our implementation of the March-Dollase model in the developed plugin.

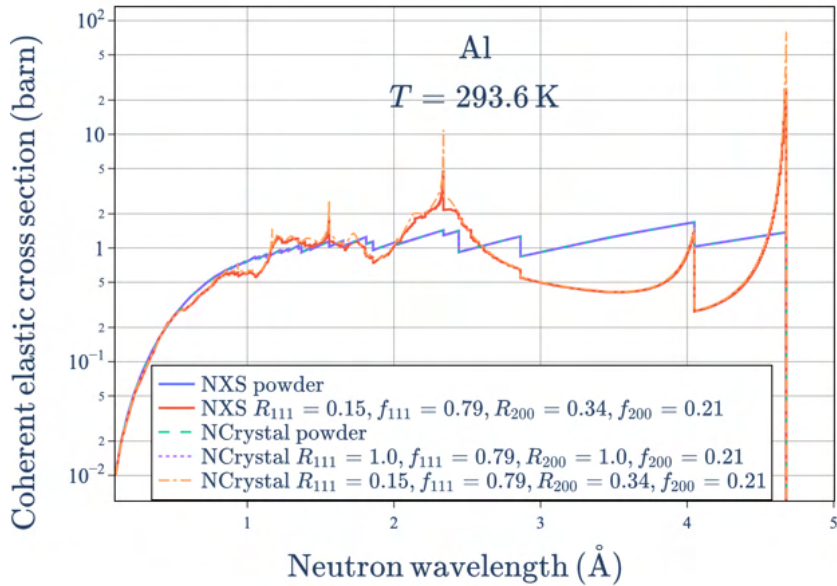


**Figure 284:** Comparison of coherent elastic scattering cross section calculated by the NXS code and the NCystal plugin for aluminum with and without texture.

## 10.5 Experimental investigations of graphitic compounds

To support the work on the graphitec compounds, we carried out a series of measurements at the BOA [371] beamline as the Paul Scherrer Institute. These measurements were deemed necessary due to the lack of information of neutronic properties of expanded Bragg-edge graphitic compounds, and as a way to understand better the structural and dynamical properties of the material.

For the measurements, we prepared several different graphitic compound samples in flake form. These included normal graphite, graphite oxide, deuterated graphite oxide, graphite oxide intercalated with water and deuterated graphite oxide intercalated with heavy water.

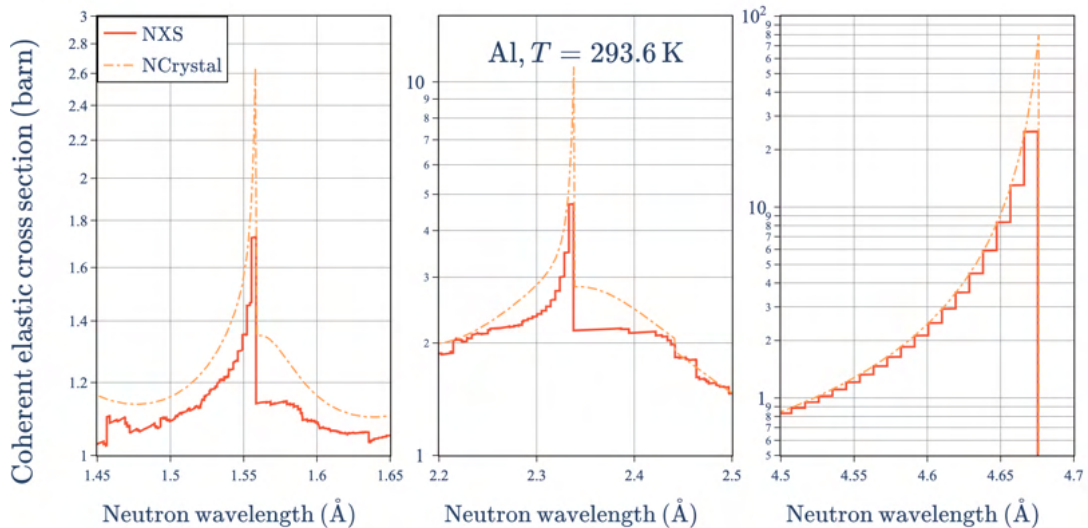


**Figure 285:** Zoom of cross section for aluminum with texture shown in Figure 284.

Figure 286 shows examples of (wide-angle X-ray scattering) WAXS data collected at the CoSAXS beamline at MAX-IV for graphite, graphite oxide, and graphite oxide mixed with water. The plot clearly shows a decreasing value of  $q$  for the narrow peak, which indicates an increased interplanar spacing and thus a larger Bragg cutoff. The shift in the peak between graphite and graphite oxide is due to the oxidation of the graphite, while the shift in peak between graphite oxide and the graphite oxide mixed with water sample is due to the intercalation of water molecules between the planes of the graphite oxide.

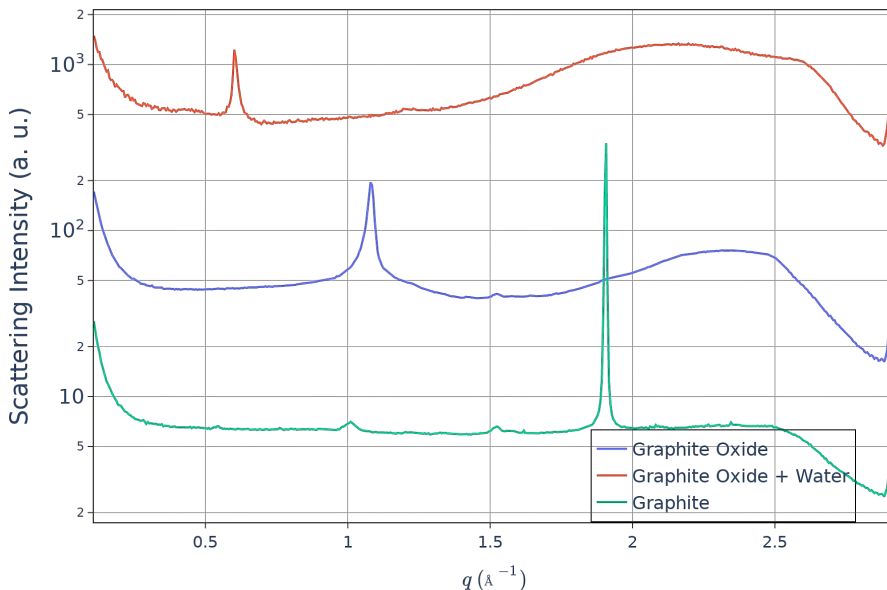


**Figure 286:** Examples of diffraction data collected at CoSAXS.

For the experimental campaign at BOA, we also developed a triaxial transmission sample holder (Figure 287), which provides the same optical depth and the same center for the three directions. This was used to explore texture effects in the samples.

The measurements were carried out over three different beamtimes at BOA. In the first experiment we used the imaging setup of the instrument, however it was found that the background levels above 8 Å were too high in order to resolve Bragg-edges above this limit.

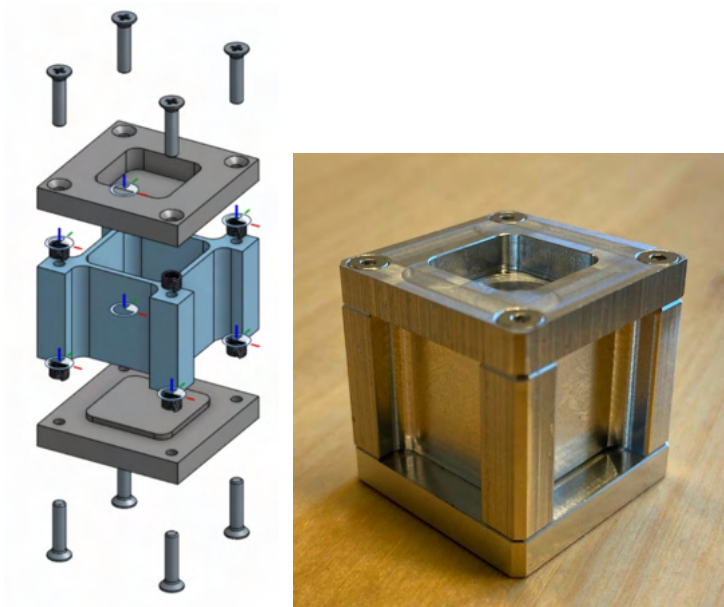


**Figure 287:** Sample holder for triaxial transmission experiments.

For the second measurement, we made major revisions to the setup in order to reduce the background above about  $8 \text{ \AA}$ . This included the usage of a neutron collimation system from the PSI Neutron Optics and Computing Group, in combination with a flat, 8.5 mm thick multi-tube He-3 detector. We also used a flat  $m = 4$  mirror for a better separation of the cold neutron beam from the fast beam component, which we identified as a contribution to the background in the first run. A main goal of this experiment was to determine the best geometry of the optics, shielding and detector that maximizes the signal-to-background ratio. The resulting spectrum from the revised setup compared to the spectrum from the first measurement is shown in Figure 288. As seen in the figure, the reduction in the background level was dramatic, resulting in a spectrum reaching up to around  $25 \text{ \AA}$  in wavelength. Figure 289 shows the resulting total cross-section for graphite oxide using the revised setup, where it is now possible to see clearly a Bragg edge appearing around  $12 \text{ \AA}$ .

The main aim of the third measurement at BOA was to investigate texture effects in the graphite oxide samples. The spectrum obtained from this measurement is also shown in Figure 288, where the differences at lower wavelength appear as the mirror was not used in the latter measurements.

A preliminary analysis of the results confirms the presence of texture in the samples, which can be appropriately represented using the March-Dollase texture implemented in NCrystal. Figure 290 shows the total cross section in the direction of compression for graphite flakes can be well represented by a combination of a texture model, to include the orientation of the flakes during the filling of the sample holder, and a SANS model to include the microscopic porosity of the graphites. This combination of models will also be used for further analysis of the measured spectra for other graphitic materials.

## 10.6 Advances on NCrystal

In addition to the above mentioned developments, NCrystal has undergone extensive upgrades over the course of the HighNESS project. This goes back to NCrystal release version 2.1.0. These releases include developments motivated not only by the HighNESS project, but also by outside projects and cover a wide range of areas such as improvements to the code and data format, extending and introducing new features and data, and bug fixes, just to name a few. A limited selection of specific examples are highlighted below. More information can also be found in the change logs [372], covering developments not only related to this work but also outside projects. Several of these developments are listed below.

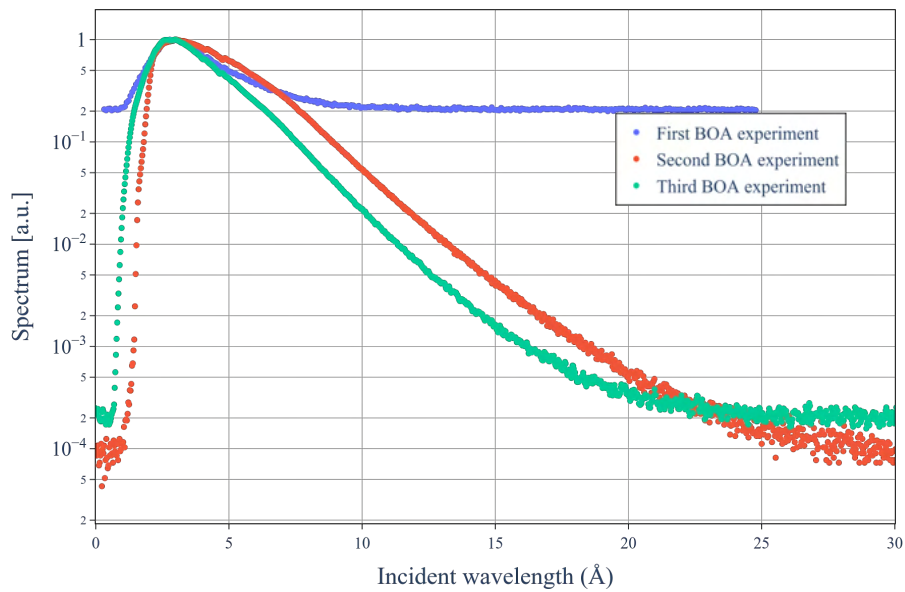


**Figure 288:** Measured spectra for the three experiments at BOA in PSI. From the first to the second experiment, background was significantly reduced, which resulted in an increase of the usable wavelength range. From the third experiment, the neutron mirror was removed, which made it possible to measure in the range  $1 - 2 \text{ \AA}$ , at the expense of the long wavelength region.

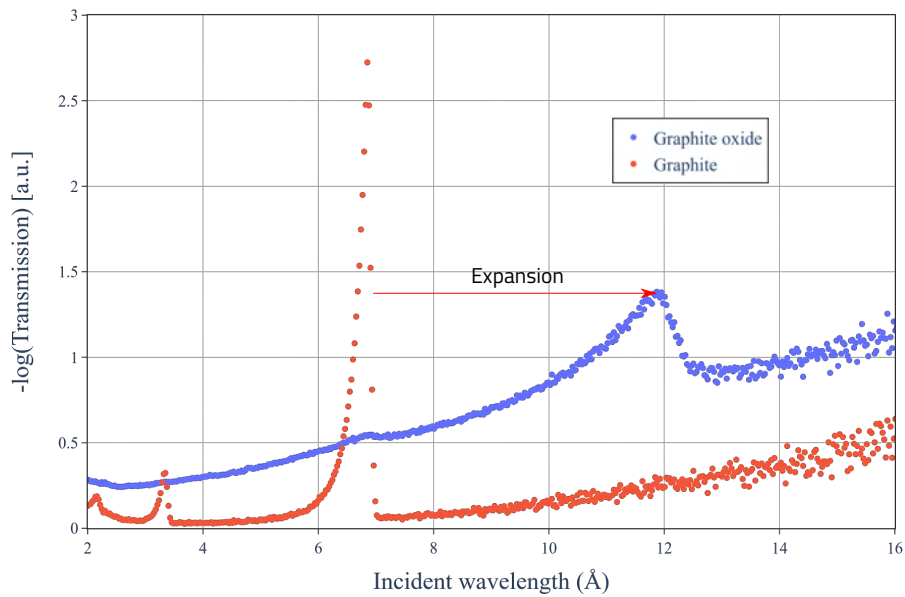


**Figure 289:** Measured total cross-sections for graphite and graphite oxide in the second PSI experiment.

NCrystal version 2.5.0 was a major technical upgrade to NCrystal which included changes to more than 200 files amounting to around 15,000 lines of code. The main motivation for these improvements was to bring NCrystal code up to modern C++ standards, improve caching strategies, provide support for multi-threading, and to prepare for future improvements in NCrystal, for example for better support for integration with Monte-Carlo codes such, as Geant4 and OpenMC, and future possibilities for describing thermal neutron scattering in multi-phase materials. Of particular interest is the support for multi-threading. This allows NCrystal to be run safely in the multi-thread mode of a given Monte-Carlo

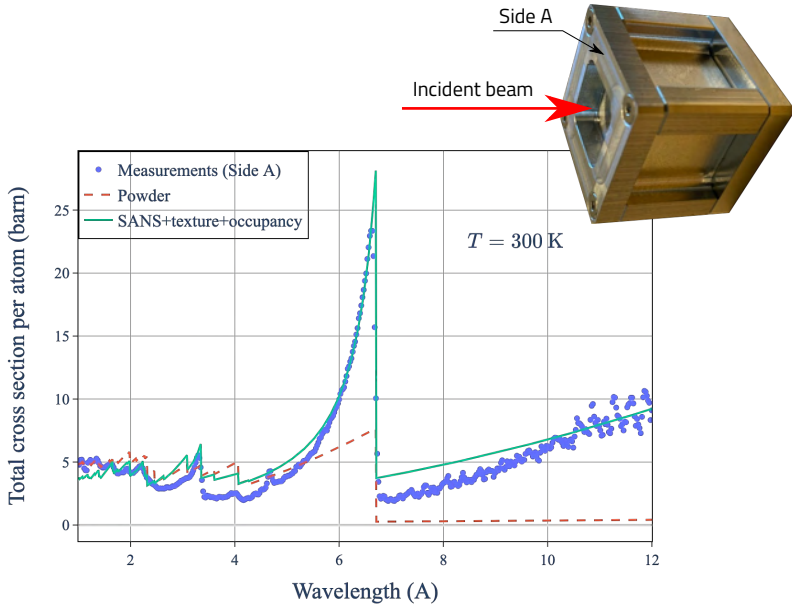


**Figure 290:** Total cross section for graphite flakes, measured and computed in the direction of compression.

code, such as OpenMC, thus making it possible to take advantage of the gains in efficiency due to multi-threading.

Release version 2.6.x includes improvements to handling observed artifacts in calculated inelastic cross-sections due to low-granularity beta-grids and phonon density of states curves in addition to the possibility to estimate atomic mean-squared-displacements from the phonon density of states. The latter contribution improves the reliability of the Debye-Waller factors at low-temperatures in elastic scattering components.

Release version 2.7.0 [373] of NCrystal includes a massive addition of 64 new crystalline materials to the NCrystal library. Many of the new materials are of wide interest to the nuclear community, but serve as an important validation for NCrystal. Included in this library are also the data generated in this work for magnesium hydride and magnesium deuteride. The release also contains the useful scripts, ncrytal\_verifyatompos and ncrytal\_onlinedb2ncmat, for verification of input of the crystal structure of a material and also against multiple online databases (such as materialprojects.org or the Crystallography Open Database), respectively.

NCrystal was also updated to include improved sampling of scattering kernels for very-cold and ultra-cold materials. This was included in the release 3.1.0 of NCrystal. One practical challenge, facing in particular UCN moderator design studies, is that only a tiny fraction of scattered neutrons will normally be left with an energy at the desired UCN scale (hundreds of neV). Thus, in order to get sufficient statistics, while keeping computational requirements reasonable, it is necessary to employ some sort of biasing or variance reduction scheme. This is facilitated by making it possible to split a scattering process into two components: a down-scatter-to-UCN-regime process and a process with the rest of the physics, by respectively appending ";" comp=inelas;ucnmode=only" and ";" ucnmode=remove" to a given NCrystal material cfg-string. Furthermore, the dedicated UCN process is implemented with a special improved model which is believed to be completely free of any modelling artifacts. A new configuration parameter, ucnmode is used to control this UCN process split-up (cf. CfgRefDoc for details). Note that in order to divide neutrons into UCN and non-UCN regimes, the code also needs the definition of a UCN threshold energy. If not set explicitly, this will default to 300neV ( $\approx 522 \text{ \AA}$ ).

In order to properly implement and validate the work described above, several internal utilities were added related to scattering kernels. This includes code for easily evaluating scattering kernels at any alpha and beta point, as well as utilities for what is essentially exact sampling or integration for cross

sections. These utilities are useful as they allow us to validate scattering kernel models better, are used directly in the new UCN-production models, and will hopefully facilitate future improvements.

Lastly, NCrystal was improved in order to facilitate the HighNESS thermal neutron scattering school. These include for example better material creation via a python API. These tools were used during the thermal neutron scattering school held in May 2023 at the ESS.

## 10.7 Contents of the HighNESS repository

The software described here is freely available in the Github repository of HighNESS and is hosted in the Github platform, following the directives of the HighNESS Data Management Plan. The following is a list of the major software developments within the project.

- OpenMC+Ncrystal:  
[https://github.com/highness-eu/openmc/tree/mixed\\_ncrystal](https://github.com/highness-eu/openmc/tree/mixed_ncrystal)
- NCrystal NDs plugin<sup>18</sup>:  
<https://github.com/highness-eu/ncplugin-SANSND>
- NJOY+Ncrystal:  
[https://github.com/highness-eu/NJOY2016/tree/njoy\\_ncrystal](https://github.com/highness-eu/NJOY2016/tree/njoy_ncrystal)  
[https://github.com/highness-eu/ncrystal/tree/njoy\\_ncrystal](https://github.com/highness-eu/ncrystal/tree/njoy_ncrystal)
- NJOY+Ncrystal Library (MgH<sub>2</sub>, MfD<sub>2</sub> and additional materials):  
<https://github.com/highness-eu/NJOY-NCrystal-Library>
- OpenMC with modifications to support mixed-elastic scattering:  
[https://github.com/highness-eu/openmc/tree/njoy\\_ncrystal](https://github.com/highness-eu/openmc/tree/njoy_ncrystal)
- Texture Plugin:  
<https://github.com/highness-eu/ncplugin-CrysText>
- NCMAT files for graphitic materials:  
<https://github.com/highness-eu/ncmat-graphitic>
- Magnetic Scattering Plugin:  
<https://github.com/highness-eu/ncplugin-MagScat>
- NCMAT files for clathrates:  
<https://github.com/highness-eu/ncmat-clathrates>

## 10.8 Conclusions

In this section we have presented developments of simulation software for describing neutron interactions in novel moderator and reflector materials considered of interest for the HighNESS project. The main focus has been the development of software to describe interactions in ND particles, magnesium hydride, graphitic compounds with extended Bragg-edges compared to normal graphite, and the clathrate hydrates.

For this purpose we have investigated two main approaches for including thermal neutron scattering data in Monte-Carlo simulations. In the first case we developed the tool NJOY+NCrystal to support a number of options for creating nuclear data in the format for Monte-Carlo simulations. The tool supports the creation of libraries for polycrystalline materials in a format that can be directly used with these codes, or in an improved mixed-elastic format which can be used with modified Monte-Carlo codes.

This approach is however still limited to polycrystalline materials with standard elastic and inelastic scattering components. Thus to include effects, like small-angle neutron scattering and magnetic scattering, we developed a plugin feature for NCrystal. Through this approach Monte-Carlo codes can access NCrystal on-the-fly, instead of accessing a nuclear data library, making it possible to extend the types of physics process included in the simulation.

Additionally, we have carried out extensive molecular modelling simulations in order to provide updated and new data for input to the neutron scattering models. For example, we investigated finite

---

<sup>18</sup>Plugin support requires installing NCrystal version 2.2.0 or later: <https://github.com/mctools/ncrystal>

size effects on the phonon frequency spectrum of ND particles in addition to producing new data for magnesium hydride, graphitic compounds and the clathrate hydrates.

Finally, we carried out an experimental campaign at the BOA beamline of PSI in order to aide in the benchmarking of the graphitic compound models, in addition to investigating the possibiities of using this beamline for measurements of very-cold neutron scattering cross-sections. We demonstrated through these experimental efforts that the background on the instrument could be reduced to a level where it was possible to resolve the Bragg-edges around 12 Å in our graphitic compound samples.

## 11 Experimental campaign with advanced reflectors

In this section, the experimental efforts to test the advanced reflector configurations highlighted during the HighNESS project are presented. In line with the plan described in the HighNESS proposal, the optimal beam extraction configuration for a mock-up experiment is identified in Section 11.1. The host institute chosen for this experiment is the Budapest Neutron Center (BNC), where a cold moderator test facility (CMTF) has been constructed [374]. The purpose of a CMTF is to provide users with a facility designed to test moderators, both for high-power and compact sources. In this setup, an out-of-pile moderator and reflector system is fed by the fast and thermal neutrons coming from the 10 MW BNC research reactor. The setup of the HighNESS experiment is designed to test the effect of advanced reflectors both around the cold source and in the beam extraction, taking into account the constraints imposed from the facility.

After having approximated the appropriate dimensions for the reflector layer and the diffusive extraction channel, this information was transferred to the engineering team, and served as starting point for the engineering design. Several iterations between neutronics and engineering design were done before the prototype was manufactured. First neutron and gamma dose measurements were performed at 1 MW reactor power at the channel outlet (near reflector) and outside the bunker on June 5<sup>th</sup> 2023. The low level of the background allowed for the beamline to also be opened at 10 MW. The outside bunker measurements were found to be within the local regulation limits; some parts of the bunker, however, needed to be reinforced.

In the context of a separate experiment planned by the Mirrotron company, the CMTF installation was completed in the reactor hall on June 23<sup>rd</sup> 2023, making it possible to obtain a 2D image from the moderator using a pin-hole system. Due to delays linked to reactor operation, however, the HighNESS measurement campaign was postponed until September 18<sup>th</sup> through the 29<sup>th</sup>.

After the preliminary experiment in Budapest Neutron Center, an opportunity arose to perform an additional experiment at the test station built in the Big Karl area of the Institute of Nuclear Physics (IKP) in Forschungszentrum Jülich (FZJ), a newly build accelerator-driven neutron source [375]. Here we investigated only the effect of putting advanced reflectors around the cold source (cryogenic methane). In this case, due to the short time between the invitation to participate and the allotted beamtime, no prior neutronics study was performed. However, the experience acquired by the engineers from the neutronics design for the experiment in Budapest was utilized in adapting this second experiment to the specific conditions related to the new facility.

In general, the characteristics of the facility that are required for the experiment and were considered in the planning phase are:

- The availability of a cold and stable moderator
- Sufficient room to install the prototype
- The availability of neutron detectors, with sufficient resolution to clearly quantify performance difference with a void prototype of same dimensions

With these conditions in mind, in this section we describe both the experiment performed at the BNC reactor and the experiment performed at the JULIC accelerator in FZJ.

### 11.1 Mock-up experiment at the Budapest Neutron Center

The proof-of-concept experiment at the CMTF facility at BNC was designed to test the reflective properties of both ND and MgH<sub>2</sub> in a representative beam-extraction configuration. In this section, the neutronic design of the experiment is discussed in some depth.

#### 11.1.1 Introduction to CMTF and the HighNESS experiment

The BNC's objective is to provide users with a prototype of a low-dimensional liquid para-hydrogen cold neutron source with a significantly higher brightness than previously developed neutron moderators, in

order to replace the existing moderator. The beamline, sketched in Figure 291, has been built at channel 4 of the 10 MW BNC reactor. The BNC reactor was commissioned in 1959 at 2.5 MW, refurbished and then upgraded to 10 MW in 1992. The maximum thermal flux is  $2.5 \times 10^{14} \text{ n/cm}^2\text{s}$ .

The CMTF design starts with a steel collimator coupled with one of the reactor channel outlets and with a high-purity box-shaped lead reflector. A 5 cm diameter beryllium disk is placed in the beam path to better diffuse the neutrons coming from the reactor. The moderator vessel consists of a 150-mm-long aluminum alloy tube with a diameter of 25 mm filled with liquid parahydrogen at 20 K placed at an angle of  $45^\circ$  with respect to the direct beam path. The beamline components of the moderator test facility include a collimator, a set of choppers, and a pin-hole imaging system to measure the brightness of the moderator cell based on the camera-obscura principle [376].

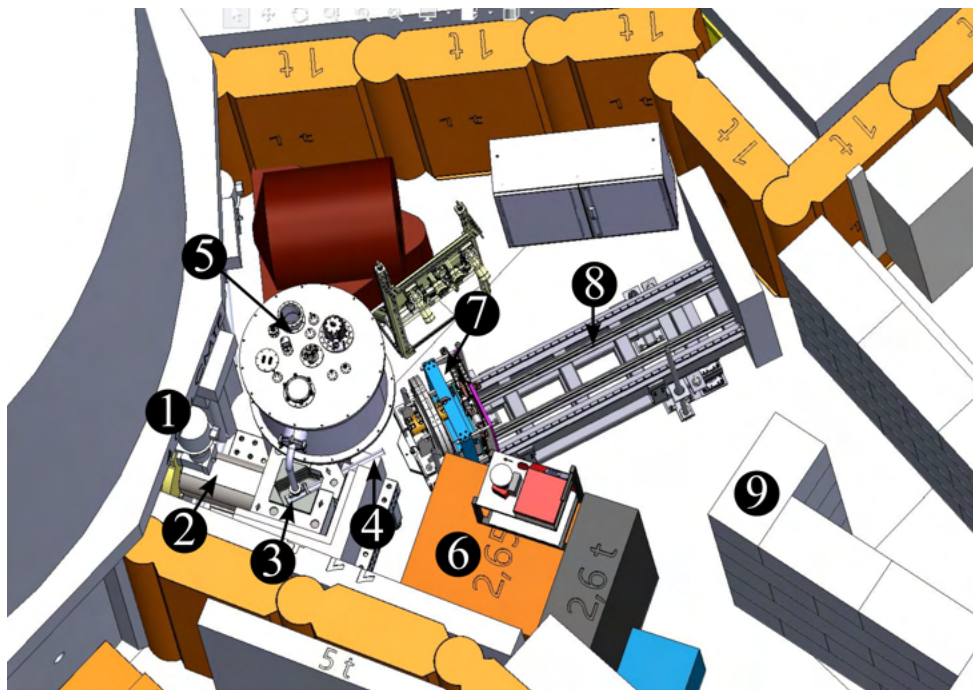


**Figure 291:** Sketch of the channel #4 beam line of the 10 MW Budapest Research Reactor of the Budapest Neutron Center (BNC). (1) Channel #4 shutter drive, (2) primary carbon steel beam collimator, (3) lead reflector-moderator block, (4) extraction system (5), cryo-cooler tank (6), beam stop (7), pin-hole assembly (8), rail support system (9), bunker's shielding walls.

Sectional views in Figure 292 from the engineering drawings show important features of the reflector-moderator block. The lead reflector is composed of different blocks, which can be removed to accommodate more components, like advanced reflector jackets and an extraction system. The section just above the moderator is left uncovered and is meant to house the pipes of the cryogenic system. Finally, it is important to mention that this design is the result of a long process in the context of a facility that was still under construction. Many features have changed since it was first designed in 2021 and several details were re-defined during the construction (e.g. shielding).

The CMTF concept was the starting point for the design of the HighNESS experiment. The possibility for reusing some of the CMTF components and to adapt them to the HighNESS purposes saved on manufacturing costs, but also imposed some constraints on the neutronic design of the experiment. In particular, we decided to retain the collimator, the lead reflector, and the detection system, which means that the best option for the source was to keep the same low-dimensional design based on parahydrogen and focus the work solely on the extraction system.

In the extraction channel, a thin layer of ND powder is expected to give a significant increase in the cold neutron flux [377]. This is mainly due to the quasi-specular reflectivity exhibited by ND in the cold energy range. Meanwhile,  $\text{MgH}_2$  is expected to be much more effective than ND in reflecting the neutrons back into the source, where the environment is dominated by large-angle scattering, hence

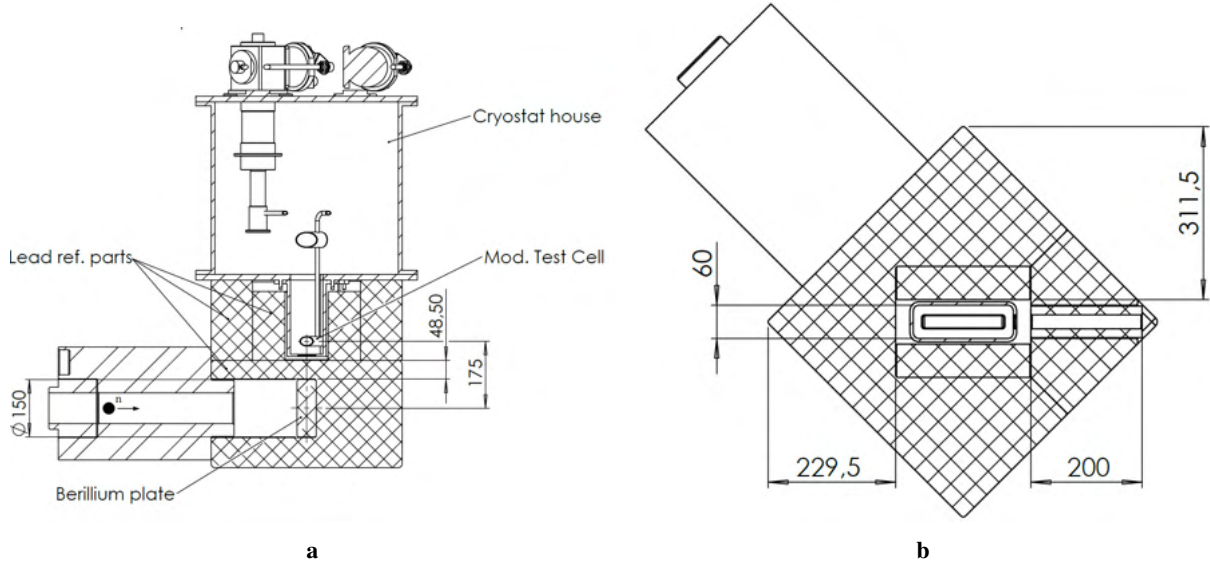


**Figure 292:** Section drawings of the lead reflector-moderator block at the CMTF. (a) vertical section (b) horizontal section at the height of the moderator vessel.

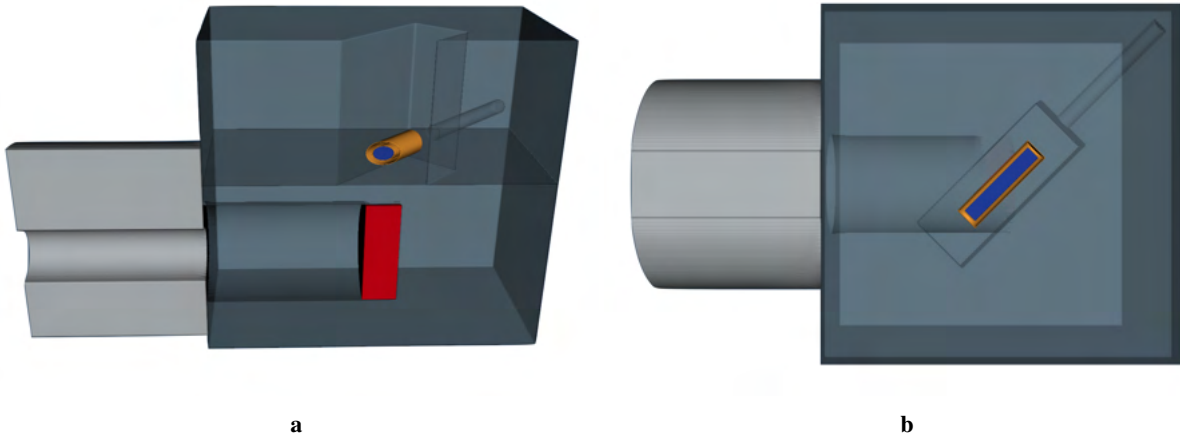


**Figure 293:** MCNP model of the lead reflector-moderator block at CMTF produced according to the engineering drawings in Figure 292. (a) vertical section (b) horizontal section at the height of the moderator vessel.

limiting the neutron leakage in the cold energy range [378]. For these reasons, the proposed set-up for the HighNESS experiment makes the following additions to the CMTF design:

- A reflector vessel that wraps the moderator tube on all sides, except the extraction side.
- An extraction guide with a thin inner layer of ND powder, coupled with the moderator vessel.

In the next section, we present the neutronic calculations that lead us to the final dimensions for the prototype of such a system.

### 11.1.2 Neutronic modeling

The MCNP model of the CMTF moderator, produced based on the technical drawings provided by BNC (Figure 292), is shown in Figure 293. The source spectrum coming out of channel 4 (Figure 294) used in the simulations was calculated from the full MCNPX reactor model and presented in [374]. The spectrum presents both a thermal and a fast peak around, respectively, 70 meV and 2.8 MeV, up to a maximum energy of 12.5 MeV. A more accurate measurement of the source using gold foil activation is foreseen in the future. Preliminary calculations on this starting model confirmed some of the neutronic

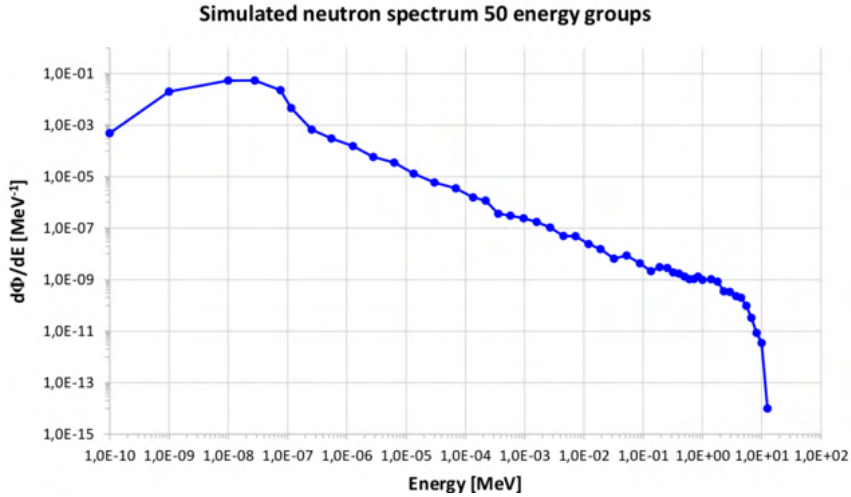


**Figure 294:** Neutron source spectrum used in the calculations and showed at ICNS 2022 [374]

features one would expect from such a concept:

- Fast and thermal neutrons from the source are diffused by the beryllium disk and the lead blocks. The efficient diffusion of fast and thermal neutrons, although it is optimal to increase the flux at the moderator, is also expected to give a significant contribution to the noise in the extraction channel (Figure 295a and Figure 295b);
- In a similar way, an intense fast and thermal flux is coming out of the collimator and the reflector. However, the shielding around these components and, more generally, the issues regarding background and safety (e.g. activation after exposure) have been studied separately.
- The flux map in the cold energy range, below 5.11 meV, (Figure 295c) shows that the parahydrogen in the moderator vessel is indeed a cold source. The flux map also confirms that a cold neutron reflector capable of reducing the leakage around the moderator would considerably increase the performance of the system.

The first test of the HighNESS concept was done with the model described in Figure 296. The dimensions of the lead reflector were reduced in the inner section to make room for the reflector and the trumpet. In reality, the space for the installation of these external components came from the removal of lead blocks and does not precisely coincide with the simple assumption of the model. Also, details like cooling pipes and metal support structures were not taken into account at this stage of the modeling.

The runs with this model were affected by a crippling low neutron transport efficiency from the source to the exit of the trumpet. As a result, the tallies far from the moderator exit could not statistically converge for any large amount of primary particles in the source. The initial explanation for the problem was a poor definition of geometry importance in the simulation, which would have made MCNP waste time in tracking the diffused neutrons in the region of the large reflector far away from the extraction channel. The actual reason for this behavior was related to a wrong spatial definition of the source beam. To simplify the problem, we decided to study the extraction with a simpler geometry that has all the essential characteristics of the full model. This corresponding *toy model* is shown in Figure 297.

The main difference between the toy model and the original one is the lead reflector. The original 49 cm × 49 cm × 46 cm box-shaped reflector was substituted by a sphere with a radius of 13 cm centered between the moderator and the beryllium disk. The moderator is also closer to the disk and forms a 90° angle with the source beam. The neutron source and the other relevant dimensions (e.g. moderator length and radius etc...) are identical to the ones in the original model. As we are studying relative gains due to the enhancing effect of advanced reflectors, the toy model appears to be a very convenient tool.

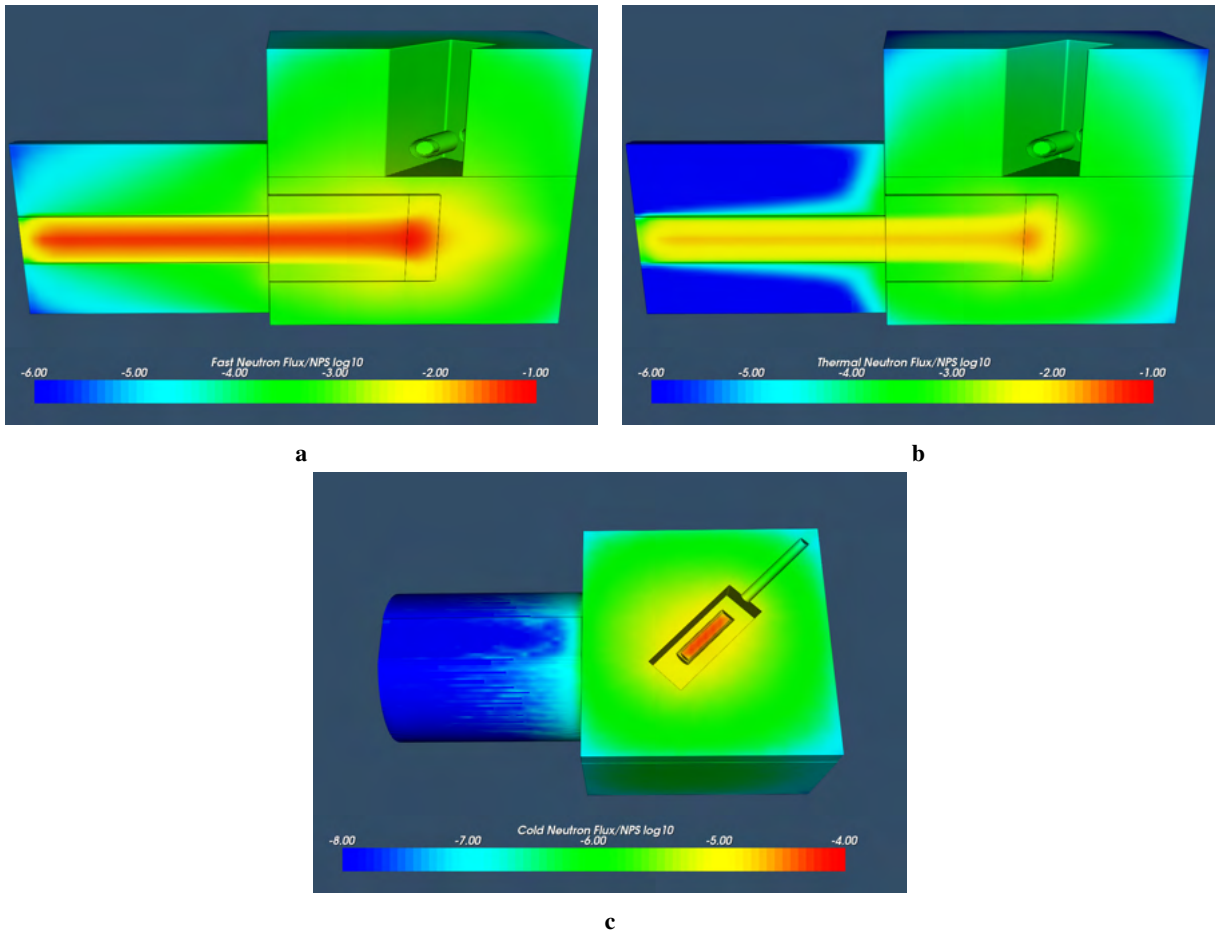


**Figure 295:** Energy-integrated flux maps in  $\text{n}/\text{cm}^2$  per source neutron. (a) Vertical section with energy integrated between 81 meV and 25 MeV. (b) Vertical section with energy integrated between 13 meV and 81 meV (c). Horizontal section at the moderator height with energy integrated below 5.11 meV (4 Å)

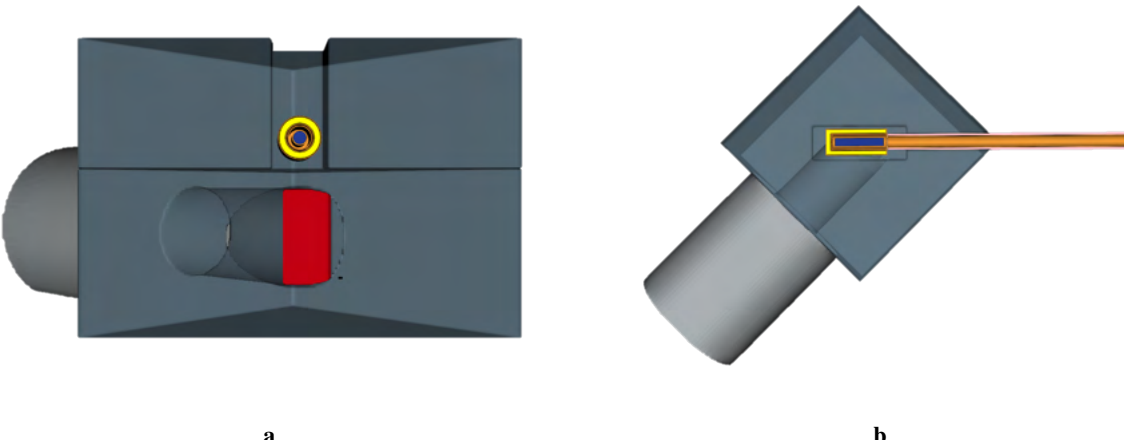


**Figure 296:** MCNP model of the lead reflector-moderator block for the HighNESS experiment. (a) vertical section with a view of the reflector (b) horizontal section at the height of the moderator vessel with a view of the extraction system.

### 11.1.3 Optimization of the source aperture

The moderator vessel is coupled with the extraction system through a cadmium plate with a circular opening. The reason to have a Cd window is to block the diffused thermal neutrons while allowing

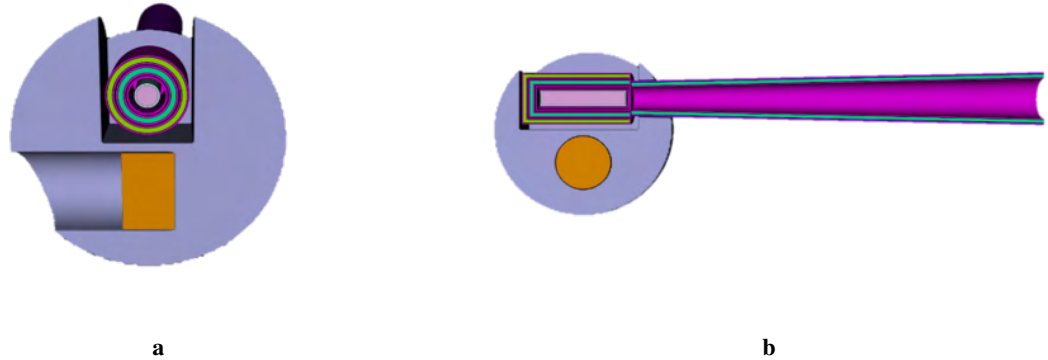


**Figure 297:** MCNP toy model of the lead reflector-moderator block for the HighNESS experiment. (a) vertical section parallel to the neutron beam with a view of the reflector (b) section perpendicular to the neutron beam with a view of the extraction cone.

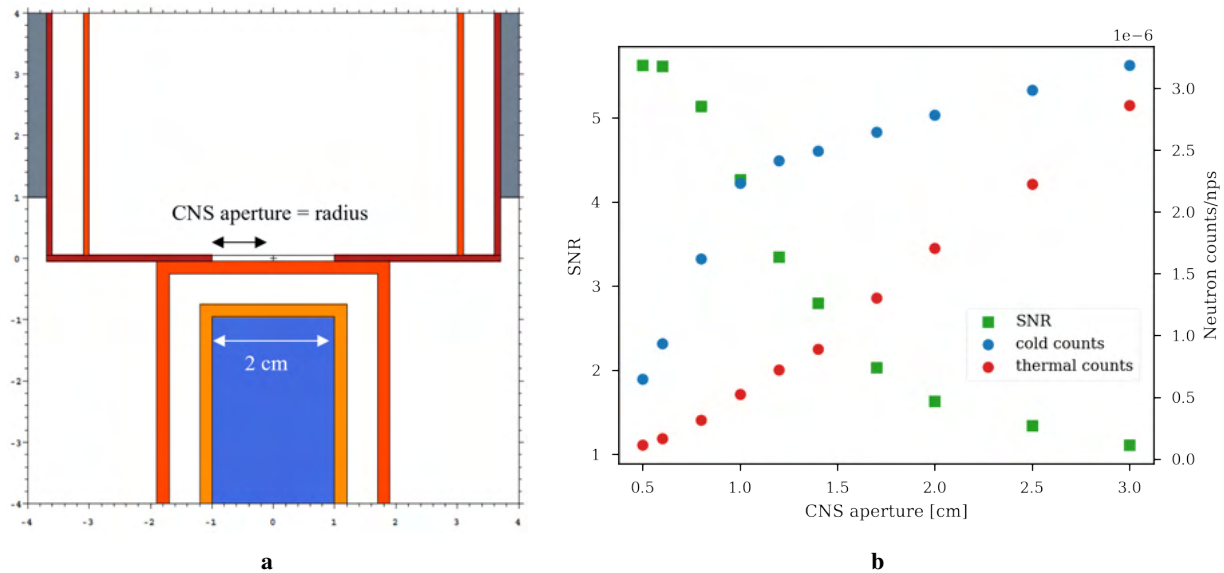


**Figure 298:** Optimization of the CNS aperture with the toy model. (a) MCNP model without reflector and ND in the extraction. The cadmium plate is dark red. (b) SNR, CN, and thermal neutron count as a function of the CNS aperture.

in the extraction tube mostly the cold neutrons coming from the moderator. To study separately the contributions from the components, we removed the advanced reflector around the source and in the extraction channel. A close-up of this interface in the MCNP model is shown in Figure 298.

The thickness of the cadmium layer between the moderator and the extraction system is 1 mm in the simulation, but here we assumed perfect collimation, i.e. every neutron that enters the cell is absorbed. Similarly, we added a layer of cadmium around the extraction tube to prevent the thermal neutrons diffused in the lead reflector to reach the detector. The radius of the empty tube at this step is 3 cm, but the aperture in the cadmium is independent of the extraction and its radius can be optimized separately. If we define cold neutrons as all the neutrons with  $\lambda > 1.8 \text{ \AA}$  and thermal as the ones with  $0.5 \text{ \AA} < \lambda < 1.8 \text{ \AA}$ , then the optimal aperture for the cold neutron source (CNS) should maximize the following signal-to-noise ratio (SNR):

$$\text{SNR} = \frac{C_c}{C_t} \quad (50)$$

where  $C_c$  and  $C_t$  are the cold and thermal neutron counts respectively. It is clear that considering all the thermal neutrons as noise is a rough approximation since they are also part of the spectrum emitted by

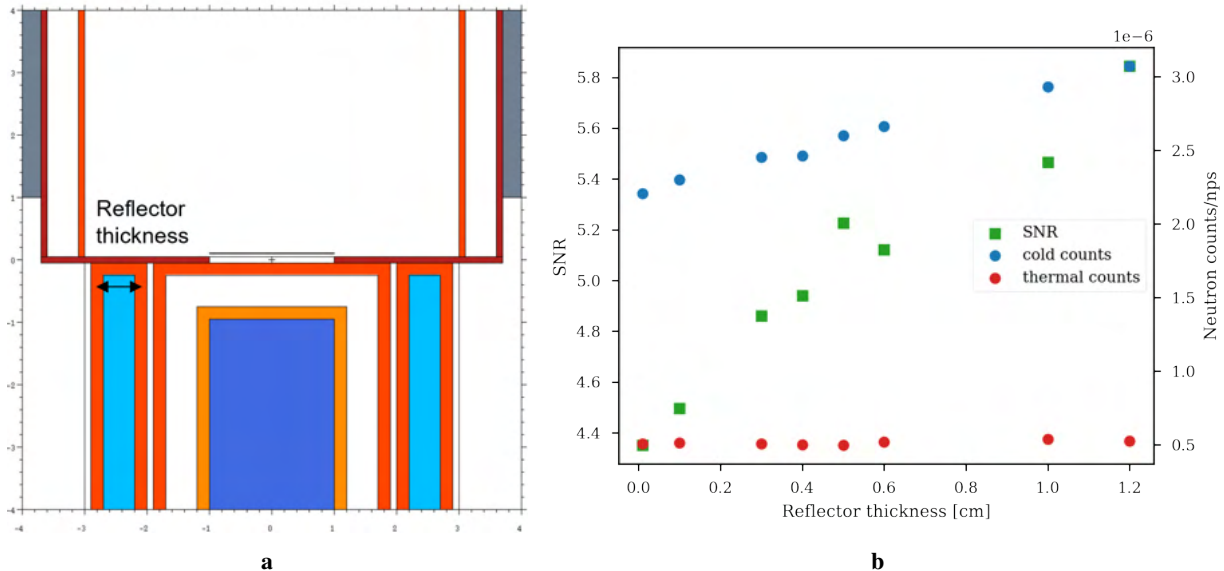


**Figure 299:** Optimization of the CNS reflector thickness with the toy model. (a) MCNP model without ND in the extraction. CNS aperture is 1 cm (b) SNR, CN, and thermal neutron counts as a function of the reflector thickness.

the cold moderator. However, it is reasonable to assume that the contribution from the diffused thermal field would quickly dominate as the aperture gets bigger. Hence, this simple definition still allows us to effectively optimize the aperture for the moderator's signal. The SNR can be calculated both at the aperture and at the end of the extraction tube. The plot in Figure 298b shows the neutron counts and the SNR as a function of the CNS aperture when recording at 60 cm from the emission surface (end of the extraction). The maximum value for the SNR is obtained for 0.5 cm, which is simply the smallest radius chosen as input. However, this corresponds also to the minimum for the counts. A good compromise between SNR and count rate is found at the knee of the CN counts curve, which is precisely the radius of the moderator. In other words, it is not convenient to have the cadmium aperture larger than the moderator itself, since the expected increase in diffused thermal neutrons is not balanced anymore by the gain in the cold flux.

#### 11.1.4 Optimization of the source reflector

We fixed the CNS aperture to 1 cm and study the optimal size for the advanced reflector around the CNS. The reflector jacket is made of aluminum with 2-mm-thick walls. The gap between the moderator vacuum jacket and the reflector is 1 mm. The close-up of the geometry is shown in Figure 299a.

We inserted room temperature  $MgH_2$  in the simulation with increasing vessel thickness. The results on the cold and thermal counts and the SNR are shown in Figure 299b. It is clear that the increase in the cold neutron counts is correlated with the amount of  $MgH_2$  in the system, and gains higher than 30% are observed when putting 1.2 cm of this material around the CNS. In this case, where the calculations show that the more reflector material the better performance, the optimal value 1 cm is the upper limit physically allowed inside the lead reflector. ND was also tested as reflector material, but no gain was observed in the cold range at any thickness value. However, an enhancing effect in the VCN range could not be observed due to poor tally convergence, but it is reasonable to expect a similar, if not higher, gain factor. For this reason, we prepared also a reflector jacket filled with ND.

#### 11.1.5 Optimization of the extraction system

The last component of the HighNESS experiment to study was the extraction system including the layer of ND powder. As a first approximation, we can fix the thickness of the ND layer to 5 mm (and  $0.6 \text{ g/cm}^3$  as density). The total length of the component was fixed to 60 cm by the available space between the

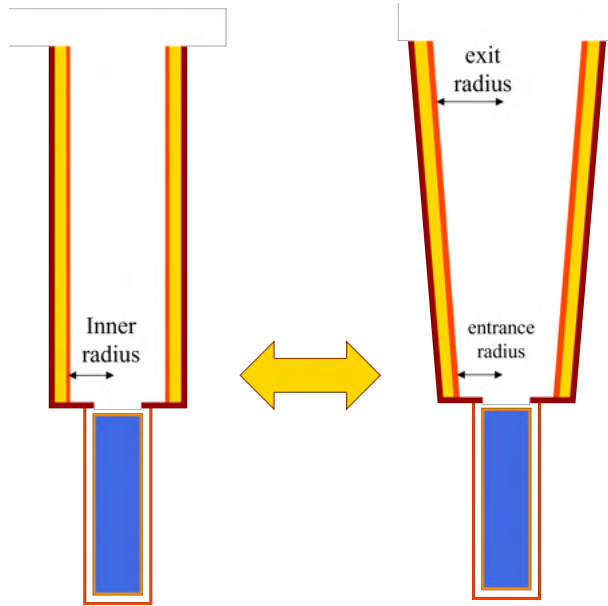


**Figure 300:** Illustration of the two shapes for the extraction system, straight tube (left) and diverging cone (right) with their parameters. Not to scale.

moderator-reflector assembly and the collimation of the pin-hole system. We can also ignore the CNS reflector to isolate the effect of the extraction. The CNS aperture is still 1 cm. Two examples of extraction systems are sketched in Figure 300.

From the neutronics point of view, the most convenient shape is a divergent cone. Similarly to what happens with the total reflection inside a mirror guide, quasi-specular reflections on divergent walls will progressively reduce the divergence of the beam at the expense of a higher emission surface. From the engineering point of view instead, thin aluminum walls are achievable only with cylindrical pipes, while cone-shaped ones can be manufactured with no less than 2 mm walls. At the same time, the thickness of the internal wall can heavily influence the neutronics performance of the extraction system, since the path in the aluminum rapidly increases for grazing neutrons, hence increasing the chances of being absorbed. In Figure 301 we report the SNR for several combinations of entrance and exit radii (size of the inner vacuum channel) for the extraction system and two Al wall thicknesses, of 1 and 2 mm, respectively.

When  $R_{OUT} > R_{IN}$  the shape is a divergent cone, while for  $R_{OUT} = R_{IN}$  it is a cylindrical tube. It is clear that the best neutronics performance is obtained with a small 1-mm-thick slightly divergent aluminum cone, but the difference with a tube with the same dimensions is relatively small while increasing the wall thickness to 2 mm has a bigger impact. The best compromise between neutronics and engineering is then an extraction cylindrical tube with a radius of 1.4 cm and wall thickness of 1 mm.

### 11.1.6 Global optimization

So far we have optimized the setup varying one or two parameters at a time while keeping the others constant. In this section, we wanted to study what would be the optimal solution in a more global sense. In other words, we tried to answer the question: what is the best setup when the CNS aperture, the entrance and the exit extraction radii, the reflector thickness, and the ND layer thickness are all free to vary?

Once again we used Dakota to solve the problem in a fast and robust way. We first studied the parameters by optimizing one FOM at a time. Although they do not combine fairly the needs of the experiment, these single-objective designs represent, within the statistical uncertainty, the best possible configurations for each FOM taken individually, so they can be used as maximum achievable values when making compromises in the multi-objective optimization. The results are summarized in Table 55. In light of the previous optimization effort, these values are not surprising: smallest CNS aperture and extraction radius for maximum SNR (opposite for CN counts) and tube over cone shape (1 mm over 2 mm Al walls) for both FOMs.

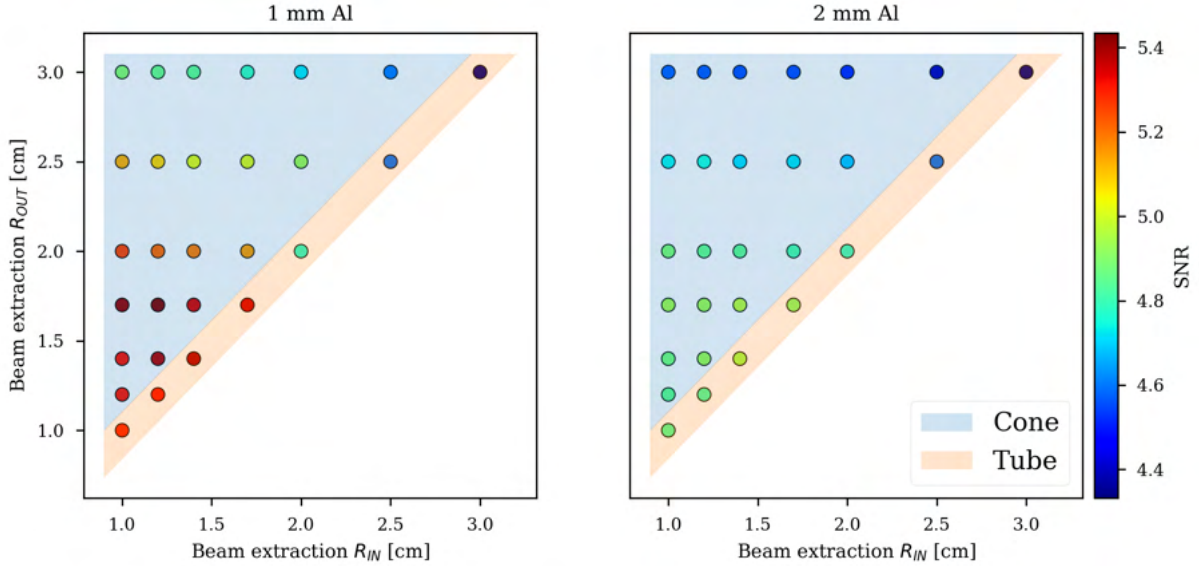


**Figure 301:** SNR values for several configurations of the extraction system. The points where  $R_{IN} < R_{out}$  correspond to a divergent cone, while  $R_{IN} = R_{out}$  correspond to a straight tube. On the left, the inner Al walls separating the vacuum and the ND are 1 mm-thick. On the right, the same inner walls are 2 mm-thick. From an engineering point of view, a divergent cone with 1 mm walls is not feasible.

The ultimate goal is to optimize the setup for both SNR and cold neutron counts, which means optimizing two objective functions at the same time. There are several approaches one can adopt, but the method we chose relies on the concept of the Pareto front. In a multi-objective problem, the optimal design is not a point. Rather, it is a set of points that satisfy the Pareto *optimality criterion*, which is stated as follows in [18]: “a feasible vector  $X'$  is Pareto optimal if exists no other feasible vector  $X$  which would improve some objective without causing a simultaneous worsening in at least one other objective”. A feasible point  $X_0$  is said to be dominated if can be improved on one or more objectives simultaneously. Points along the Pareto front are said to be non-dominated.

The first step in the Pareto-set optimization method is reducing the multi-objective problem in a single-objective problem. Namely, Dakota optimizes a weighted sum of SNR and CN counts, each normalized by the maximum value achieved in the respective single-objective optimization. The normalization is essential since the SNR is orders of magnitude bigger than the counts per nps, hence, without the normalization, Dakota would be biased almost entirely toward the SNR. The weighted sum is the new objective function. Finally, the composition of the two FOMs was evaluated using a set of weights (SNR, CN counts). In Table 56 the results of the simulations for a chosen weights set are summarized. As a sanity check, we made sure the results for the weights (1,0) and (0,1) were the same as the single-objective optimizations (within the statistical uncertainty).

The analysis of the results of a multi-dimensional double-objective optimization is inevitably a complex task. We would like to point out some of the findings arising from this study:

- Despite the increasing importance of the CN counts weight, the CNS aperture is kept small to avoid a quick drop in the SNR. Only when the SNR has a small weight, the CNS aperture is “allowed” to increase. This shows how important is to shield the extraction system from the intense diffused thermal field;
- increasing the ND thickness in the extraction layer has a minimal impact on the CN counts;
- almost half of the CN, compared to the single objective optimization, are obtained already with a small opening configuration. Hence, there is no need to have a large extraction system to observe the enhancing effect.

Taking into account all the previous optimization results and several iterations with the WP5 team, we decided to build a prototype with the following characteristics:

**Table 55:** Optimized designs for single-objective approach. The FOM in bold are the ones optimized for that run.

Parameters [cm]	Optimized FOM	
	SNR	CN counts [n/nps]
CNS aperture	1.0	3.0
Entrance extraction radius	1.0	3.0
Exit extraction radius	1.0	3.0
CNS reflector	1.0	1.0
ND layer extraction	1.0	1.0
<b>FOMs</b> <sup>1</sup>		
SNR	<b>7.33</b>	0.98
CN counts [n/nps]	$4.61 \times 10^{-7}$	$7.32 \times 10^{-6}$

<sup>1</sup> In bold the values corresponding to the optimized FOM.

**Table 56:** Optimized designs from the Pareto-set approach.

Parameters [cm]	Weight sets (SNR,CN counts)				
	(0.75,0.25)	(0.65,0.35)	(0.5,0.5)	(0.35,0.65)	(0.25,0.75)
CNS aperture	1.0	1.0	1.0	2.8	3.0
Entrance extraction radius	1.0	1.0	1.0	2.3	3.0
Exit extraction radius	3.0	3.0	3.0	3.0	3.0
CNS reflector	1.0	1.0	1.0	0.89	0.85
ND layer extraction	0.67	0.73	2.3	2.0	2.5
<b>FOM ratio to max</b>					
SNR	0.80	0.80	0.80	0.16	0.14
CN counts	0.48	0.48	0.48	0.93	1.0

- The CNS aperture in the cadmium disk is 1 cm, matching the moderator size, to reduce the spurious thermal contribution to the detector;
- the space around the cold source is enough to accommodate a reflector jacket 1 cm thick;
- the extraction system is a tube with an inner radius of 1.4 cm and wall thickness of 1 mm.

### 11.1.7 Expected performance

The values found in the optimization phase are then inserted in the original full model (Figure 296) to check the expected gains from the setup. We can divide the effect of the reflector from the effect of adding the extraction system filled with ND (sometimes indicated as +ND in the following summary). Hence, we define the common baseline as the model without both reflector and extraction tube and we calculate the gains after adding a 1-cm-thick jacket when it is empty, filled with ND, or with MgH<sub>2</sub>. All these cases, baseline included, are also calculated with ND in the extraction tube. A scheme summarizing the set of the eight measurements is shown in Figure 302.

To this set we added at the end one last case to test the performance of a standard reflector, i.e. room temperature water. Hence we planned a total of ten measurements during the experiment. The gains we expect to observe are summarized in Figure 303, while a more detailed overview of the simulation results can be found in Table 57.

In Figure 303a, we can see how more than 40% gains over the baseline can be obtained with a MgH<sub>2</sub>

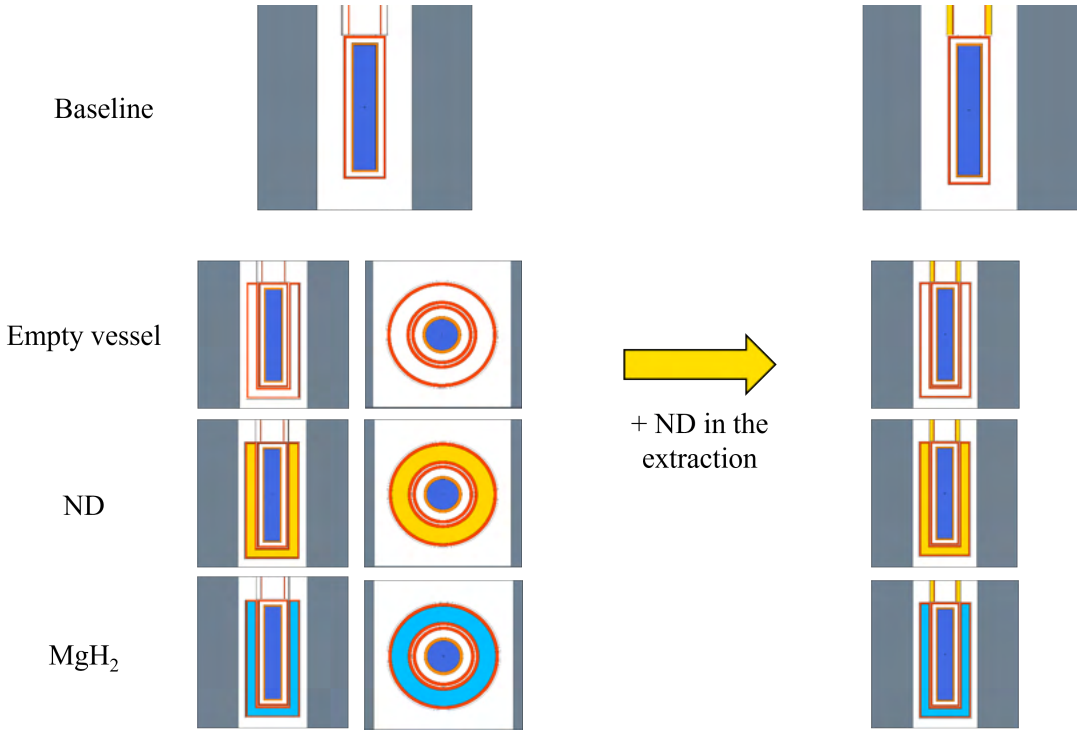


**Figure 302:** Graphical scheme of the measurements to perform at BNC facility in the context of the HighNESS experiment.

reflector. However, similar performances are observed with standard room temperature water, while ND do not seem to have a measurable effect in the energy range studied. When adding ND to the extraction system, the gain factor goes well above 2 in the  $4\text{ \AA}$  to  $10\text{ \AA}$  range, corresponding to the energy peak for quasi-specular reflection. The reason for similar results between water and  $\text{MgH}_2$  is to be ascribed to the inelastic scattering on H. As shown in Figure 9 in [378], for energies above 0.1 eV, the inelastic cross section is dominated by down-scattering processes, hence in an intense thermal/fast field the dominating interaction with H is inelastic, while one could expect the reflector behavior to be dominant at low energies. Even though the effect is not purely due to the advanced cold reflector properties of  $\text{MgH}_2$ , it is still interesting to study the material and its applicability in different environments.

Finally, in Figure 304, we show the calculated spectra for all the cases, where an overview of the gains as a function of energy is given.

### 11.1.8 Dose and background calculations

The following step was to add increasing details to the model in order to simulate the whole experimental environment. In particular, we studied two quantities that are crucial for the measurements: the neutron and photon dose rates inside and outside the experimental hall and the background level at the detector compared to the signal from the moderator.

The first step toward a more realistic model was made by adding the cryogenic system to the reflector-moderator assembly. In particular, we were interested in quantifying the effect on the neutronics of the piping case as well as the piping itself. These components are made of aluminum to reduce the impact on the performance, however, a strip of reflector must be removed to make space for them, which can be expected to further reduce the initial yield. The MCNP model, manually made from a simplified version of the CAD drawings, is shown in Figure 305. The components further away from the moderator vessel, like the cryogenic tank and external transfer pipes, are made of stainless steel. The negative impact of the cryogenics at the exit of the extraction tube was estimated to be between 20% to 30% depending on the neutron energy (higher at lower wavelength) for the case with  $\text{MgH}_2$  as CNS reflector and ND in the extraction. This effect is almost entirely due to the aluminum structure, hence should not affect the

**Table 57:** Overview of the 10 simulations of measurements that are going to be performed at the CMTF.

Counts/nps	Without ND in the extraction									With ND in the extraction								
	$\lambda > 20 \text{ \AA}$			$10 \text{ \AA} < \lambda < 20 \text{ \AA}$			$4 \text{ \AA} < \lambda < 10 \text{ \AA}$			$1.8 \text{ \AA} < \lambda < 4 \text{ \AA}$			$1.8 \text{ \AA} < \lambda < 0.5 \text{ \AA}$					
	Value	% Rel. Err.	Value	Value	% Rel. Err.	Value	% Rel. Err.	Value	% Rel. Err.	Value	% Rel. Err.	Value	% Rel. Err.	Value	% Rel. Err.	Value	% Rel. Err.	
Baseline	$3.40 \times 10^{-10}$	9	$4.04 \times 10^{-9}$	3	$6.39 \times 10^{-8}$	0.6	$2.14 \times 10^{-7}$	0.4	$6.28 \times 10^{-8}$	0.8								
Empty vessel	$3.34 \times 10^{-10}$	11	$4.18 \times 10^{-9}$	3	$6.34 \times 10^{-8}$	0.6	$2.15 \times 10^{-7}$	0.4	$6.17 \times 10^{-8}$	0.8								
ND	$3.13 \times 10^{-10}$	10	$3.77 \times 10^{-9}$	3	$6.29 \times 10^{-8}$	0.6	$2.13 \times 10^{-7}$	0.4	$6.62 \times 10^{-8}$	0.9								
MgH <sub>2</sub>	$4.70 \times 10^{-10}$	7	$5.70 \times 10^{-9}$	3	$8.99 \times 10^{-8}$	0.6	$2.92 \times 10^{-7}$	0.3	$8.01 \times 10^{-8}$	0.7								
Water	$4.51 \times 10^{-10}$	7	$5.81 \times 10^{-9}$	2	$9.22 \times 10^{-8}$	0.6	$2.98 \times 10^{-7}$	0.3	$8.22 \times 10^{-8}$	0.7								
Counts/nps	Without ND in the extraction									With ND in the extraction								
	$\lambda > 20 \text{ \AA}$			$10 \text{ \AA} < \lambda < 20 \text{ \AA}$			$4 \text{ \AA} < \lambda < 10 \text{ \AA}$			$1.8 \text{ \AA} < \lambda < 4 \text{ \AA}$			$1.8 \text{ \AA} < \lambda < 0.5 \text{ \AA}$					
	Value	% Rel. Err.	Value	Value	% Rel. Err.	Value	% Rel. Err.	Value	% Rel. Err.	Value	% Rel. Err.	Value	% Rel. Err.	Value	% Rel. Err.	Value	% Rel. Err.	
Baseline	$4.02 \times 10^{-10}$	8	$6.62 \times 10^{-9}$	2	$1.12 \times 10^{-7}$	0.3	$2.39 \times 10^{-7}$	0.4	$6.56 \times 10^{-8}$	0.8								
Empty vessel	$4.13 \times 10^{-10}$	9	$6.63 \times 10^{-9}$	2	$1.11 \times 10^{-7}$	0.4	$2.39 \times 10^{-7}$	0.4	$6.45 \times 10^{-8}$	0.8								
ND	$3.99 \times 10^{-10}$	28	$6.54 \times 10^{-9}$	2	$1.10 \times 10^{-7}$	0.4	$2.38 \times 10^{-7}$	0.4	$6.91 \times 10^{-8}$	0.8								
MgH <sub>2</sub>	$6.17 \times 10^{-10}$	6	$9.17 \times 10^{-9}$	2	$1.58 \times 10^{-7}$	0.3	$3.26 \times 10^{-7}$	0.3	$8.39 \times 10^{-8}$	0.7								
Water	$5.96 \times 10^{-10}$	6	$9.32 \times 10^{-9}$	2	$1.61 \times 10^{-7}$	0.3	$3.34 \times 10^{-7}$	0.3	$8.55 \times 10^{-8}$	0.7								

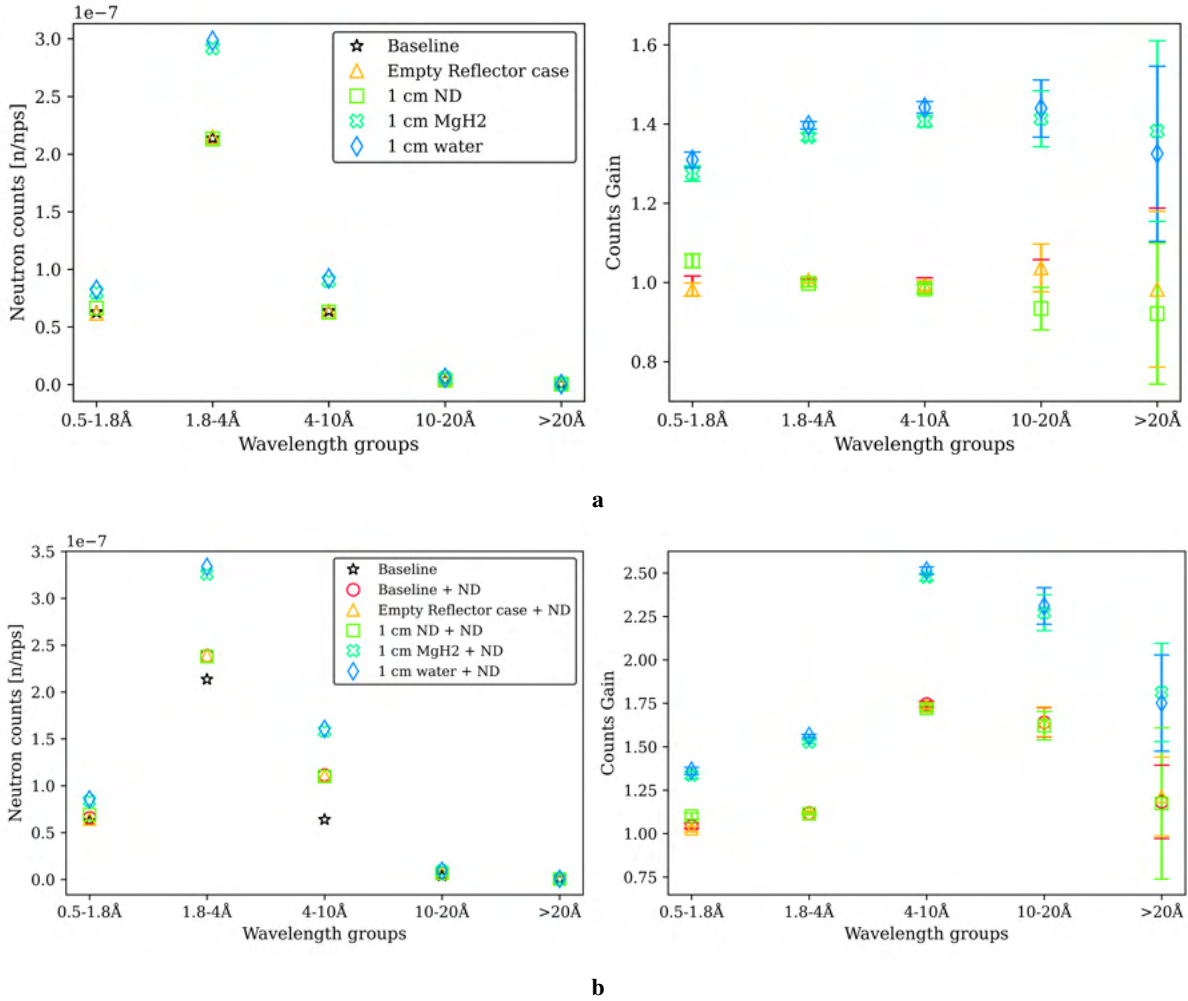


**Figure 303:** (left) Normalized neutron counts at the exit of the extraction tube for five wavelength groups for (a) all the cases without the thin ND layer in the extraction (b) with ND. (right) counts gains over the baseline

relative gains.

To have a better estimate of the background at the detector position, we modeled the essential pieces of the detection system: the chopper, the pin-hole system, and the steel table according to the specifications provided (cfr. Figure 291). In particular, the pin-hole system is made of several layers of metals, like lead and copper, and neutron shielding material like cadmium and boron plastic (Mirrobor™). The result is shown in Figure 306.

The last piece necessary for the study is the model of the experimental bunker. A temporary model of the neighbor channel #2 was used for preliminary calculations of the background at the detector position, which already highlighted how critical it was to carefully shield the reflector-moderator block and the detector from the intense diffused epithermal and thermal neutron flux. Later we received a close-to-final model of the experimental room designed by BNC, which included a concrete floor, a simple model for the heavy-concrete reactor, and external walls made of boric acid bath and Mirrotron boron concrete. The shielding around the reflector is made of mostly Mirrobor™ sheets (80 wt% B<sub>4</sub>C + CH<sub>2</sub>O) and paraffin wax. The complete MCNP model used for the exploratory analysis is shown in Figure 307. In the figure, the geometry is mirrored along the horizontal direction compared to Figure 291.

At this point it should be noted that this model is still missing a design for the bunker ceiling and the shielding around the collimator at the beam port. At the time of writing, the CMTF construction phase has been recently completed with a design for the ceiling made of structural steel and several layers of borated HDPE. The space around the collimator, between the reactor's wall and the reflector, has been filled with paraffin wax blocks. However, these recent changes have not been implemented in the model

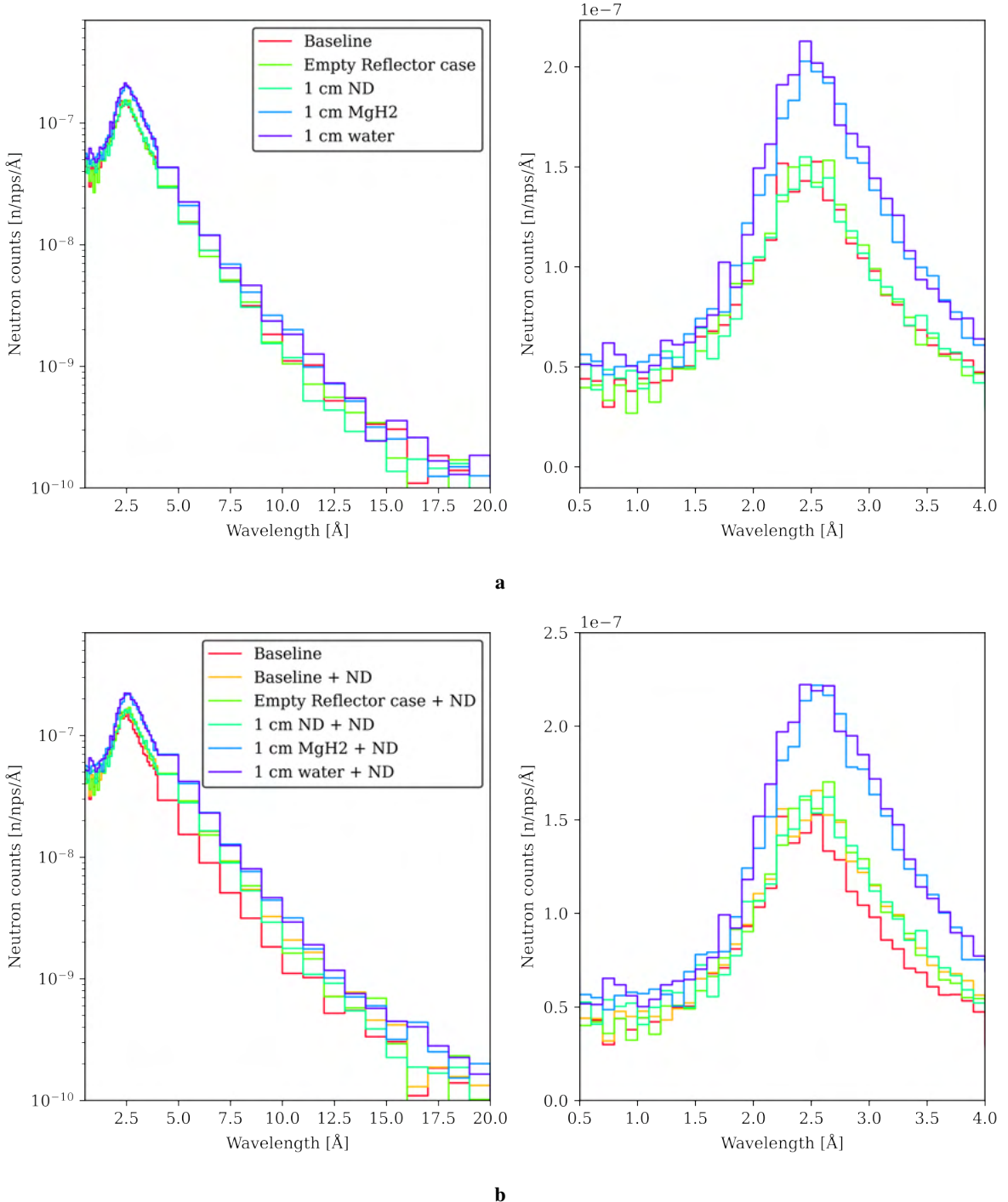


**Figure 304:** Normalized neutron counts wavelength spectra at the exit of the extraction tube for (a) all the cases without the thin ND layer in the extraction (b) with ND.

yet.

### 11.1.9 Background

A preliminary assessment of the background at the detector position with the full model shown in Figure 307 can be made by looking at the neutron flux map at different energy-groups. The neutron flux in  $\text{n}/\text{cm}^2/\text{nps}$  at the height of the moderator is shown in Figure 308 (fast and epithermal) and Figure 309 (thermal and cold) with a spatial resolution of  $10 \text{ cm} \times 10 \text{ cm} \times 10 \text{ cm}$ . The highly diffused neutron field in the epithermal (81.8 meV to 1 MeV) and thermal (13 meV to 81.8 meV) energy range appears to be

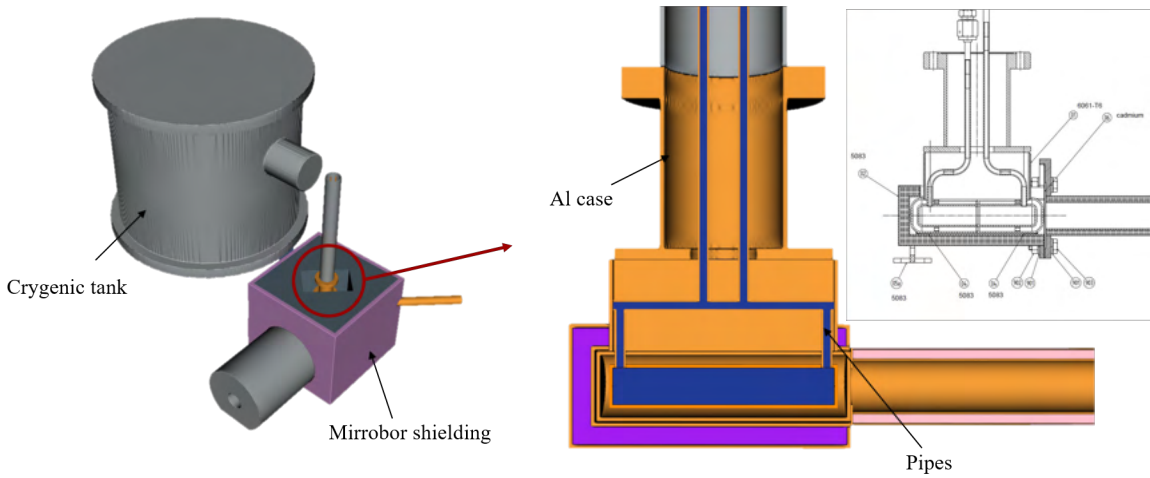


**Figure 305:** MCNP model of the cryogenic system for the HighNESS experiment. The stainless steel cryogenic tank is shown on the left. On the right, an enlarged view of the moderator pipes and case according to the engineering CAD (top right).

Neutron flux [n/cm <sup>2</sup> /nps]	Cold	Thermal	Epithermal	Fast
without shielding	$2.43 \times 10^{-8}$	$2.55 \times 10^{-7}$	$3.75 \times 10^{-7}$	$3.85 \times 10^{-9}$
with shielding	$2.79 \times 10^{-11}$	$1.41 \times 10^{-10}$	$4.79 \times 10^{-8}$	$1.73 \times 10^{-9}$

**Table 58:** Neutron flux values in n/cm<sup>2</sup>/nps measured at the detector position with the next-event estimator (F5) tally with and without the Mirrobot™ shielding and for four different energy-groups: fast (1 MeV to 100 MeV), epithermal (81.8 meV to 1 MeV), thermal (13 meV to 81.8 meV) and cold neutrons (5.11 meV to 13 meV). The relative error for all the values is 1%. Due to the incompatibility of the library with the next-event estimator, ND were removed from the extraction tube for this test.

1 or 2 orders of magnitude higher than the cold flux in the detector position. While these flux values do not take into account the energy-dependent resolution of the detector, they still highlight the importance of reducing the diffusion out of both the collimator and the reflector. As an example, in the temporary model of the neighbor channel #2 we observed that adding a layer of an ideal absorber (all neutrons get killed when entering the cell) around both the collimator and the lead block had the effect of reducing the high energy neutron flux by more than a factor 10.

In the case of the latest model, we estimated the effect of shielding the 20 cm × 20 cm detector with 2 cm Mirrobot™ sheets all the way from the pin-hole assembly. The model is shown in Figure 310. The calculations are made with a point detector tally (next-event estimator) placed at the center of the detector position along the beam direction. Due to the incompatibility of the library with the next-event estimator, ND were removed from the extraction tube for this test. The results are reported in Table 58 with the same energy-groups as the flux maps. From the reported values, it is clear that this solution is effective in shielding diffused cold and thermal neutrons, but it is not enough for epithermal neutrons.

### 11.1.10 Dose rate

The measurement of the dose rates outside the bunker is an important task to guarantee the safety of the people working at the facility during the experiment. The estimation of the same dose rates with a model is needed not only to ensure the validity of the model itself but also to study what are the worse case scenarios and how to act preventively. A preliminary safety assessment with the channel #4 beam shutter open and reactor power of both 1 and 10 MW was performed by the radiation protection group in week 23 of 2023. A temporary lead reflector and paraffin wax shielding (Figure 311a) was mounted in the room, and also a temporary ceiling made of borated HDPE sheets was built. Neutron and gamma dose rates were measured at five points outside the boron concrete walls. In all the cases, the values

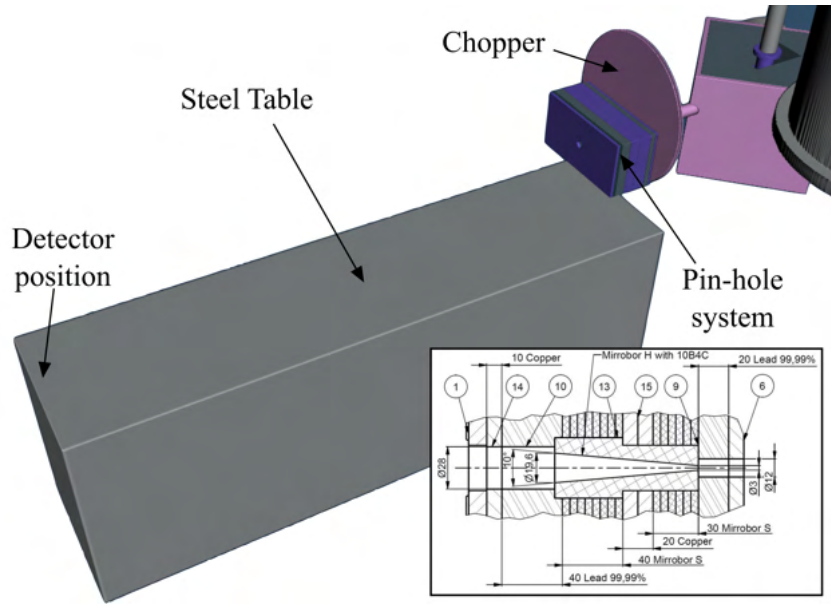


**Figure 306:** MCNP model of the detection system for the HighNESS experiment. The model has only the essential elements: the chopper, the pin-hole system, and the steel table with the support rails for the detector. The detailed drawings of the pin-hole system are reported in the bottom right corner.

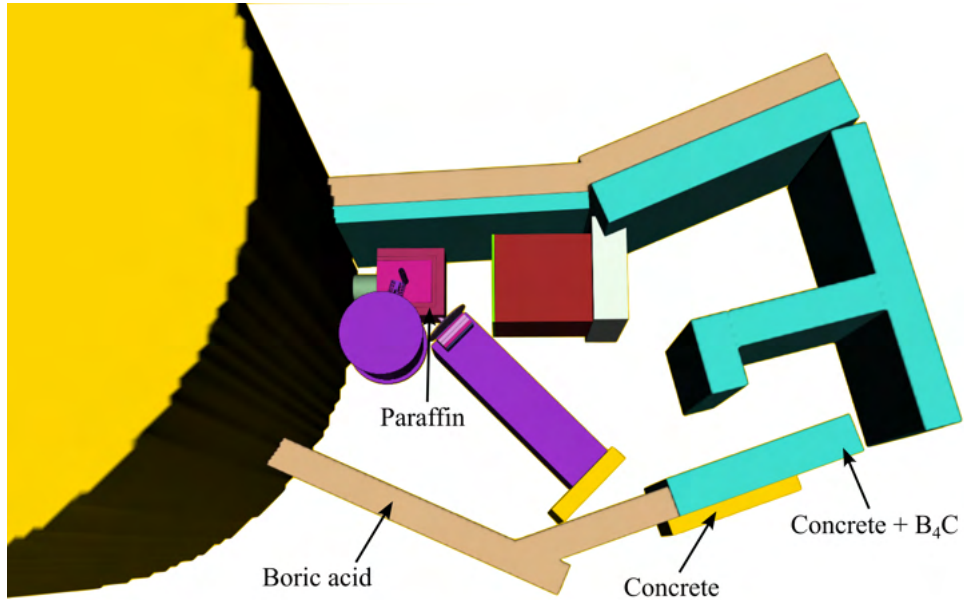


**Figure 307:** MCNP model of the experimental room for the HighNESS experiment. The different materials for the external and reflector shielding are highlighted. Mirrored along the horizontal direction compared to Figure 291.

Dose rate [ $\mu\text{Sv}/\text{h}$ ]	P1	P2	P3	P4	P5
Neutron	3	3	8	6	1.6
Gamma	2	4	2.9	2.1	2.5

**Table 59:** Neutron and gamma dose rates measured by the reactor radiation protection group in week 23 of 2023. Reactor power was 10 MW. Values obtained by private communication.

were below the legal requirement of  $10 \mu\text{Sv}/\text{h}$  (see Table 59). We adapted the previous model by adding the dummy lead reflector and the temporary HDPE roof to compare the calculated dose rates with the

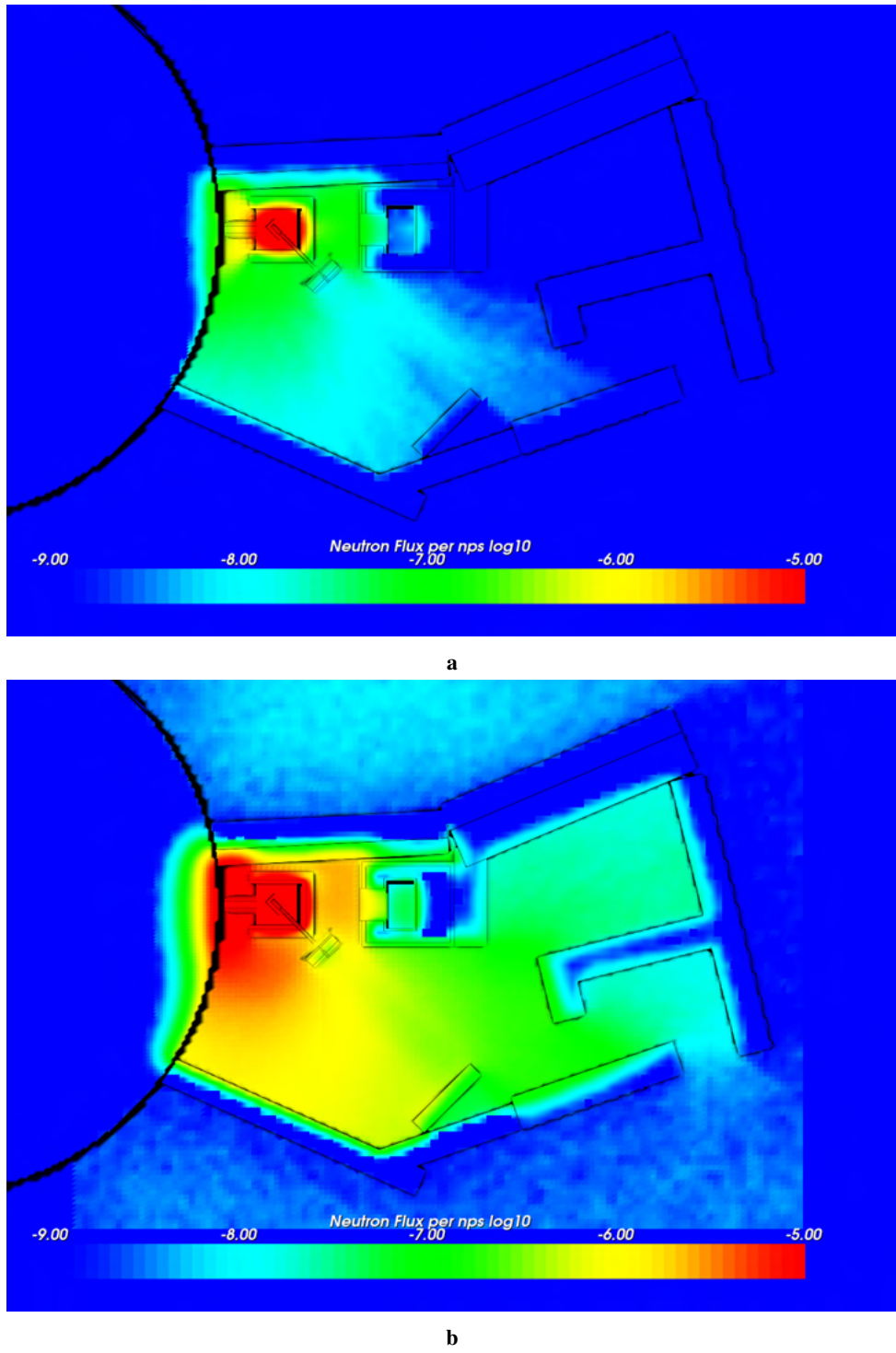


**Figure 308:** Neutron flux map at the moderator height with a spatial resolution of  $10\text{ cm} \times 10\text{ cm} \times 10\text{ cm}$  for (a) fast neutrons (1 MeV to 100 MeV) (b) epithermal neutrons (81.8 meV to 1 MeV). Units are  $\text{n}/\text{cm}^2/\text{nps}$  in log scale.

measured one. The model and the five points measured are shown in Figure 311b.

The dose rates are calculated using the Neutron Fluence-to-Dose Rate Conversion Factors based on ICRP-116 and assuming a neutron current of  $2.81 \times 10^{11} \text{ n/s}$  through the beam port of Channel #4 (value calculated with the reactor full model in MCNPX). The resulting dose rate map is shown in Figure 312. Considering how preliminary these calculations are, we found a good agreement with the measured dose rate, at least in the order of magnitude. It should be noted that it was not possible to compare the gamma dose rate since no gamma source was included in the model. A pessimistic estimation of the gamma

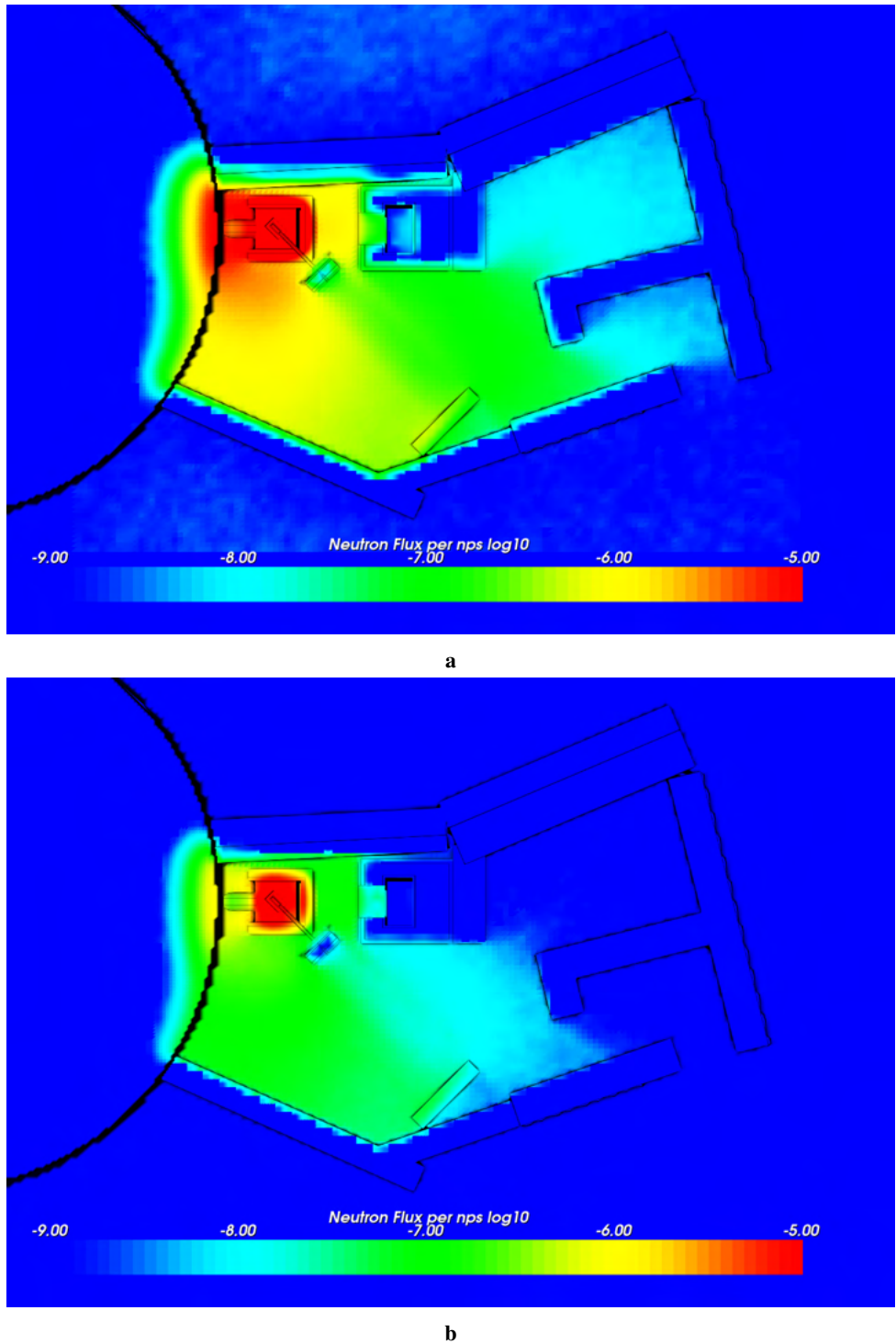


**Figure 309:** Neutron flux map at the moderator height with a spatial resolution of  $10\text{ cm} \times 10\text{ cm} \times 10\text{ cm}$  for (a) thermal neutrons (13 meV to 81.8 meV) (b) cold neutrons (5.11 meV to 13 meV). Units are  $\text{n/cm}^2/\text{nps}$  in log scale.

flux out of the beam port based on measurements in channel #2 was proposed as a back-of-the-envelope solution to include gammas in the model. Moreover, it is clear that a dedicated study that measures precisely the flux in the five regions and improves the statistical convergence of the tallies is needed.

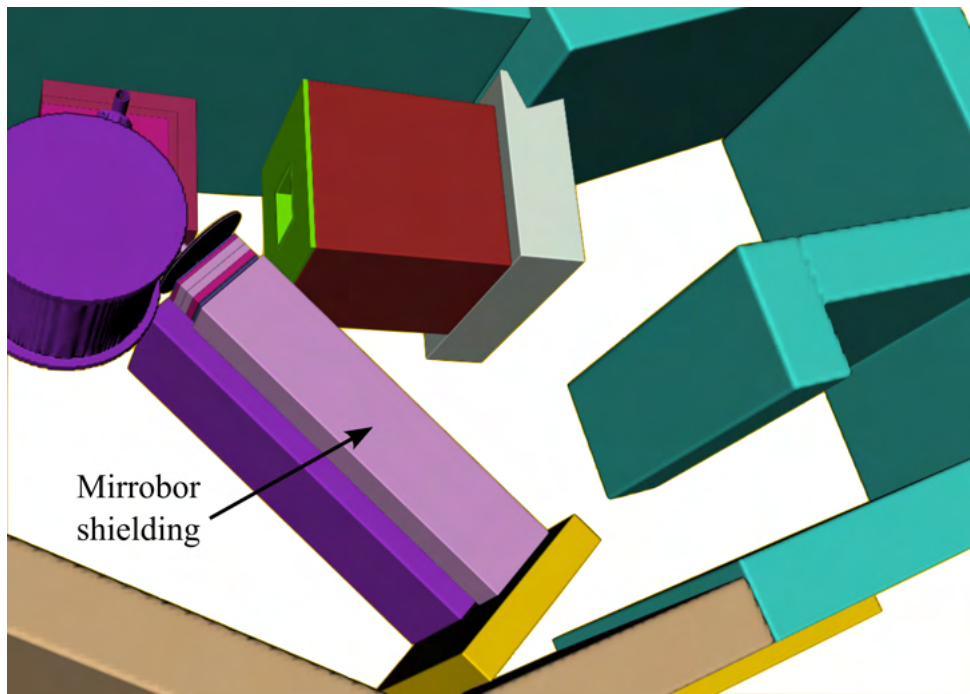


**Figure 310:** MCNP model of the shielded detector for the HighNESS experiment. The shielding is made of 2 cm Mirrobor<sup>TM</sup>(80 wt% B<sub>4</sub>C + CH<sub>2</sub>O), is 20 cm × 20 cm and covers the gap from the pin-hole assembly to the detector position.

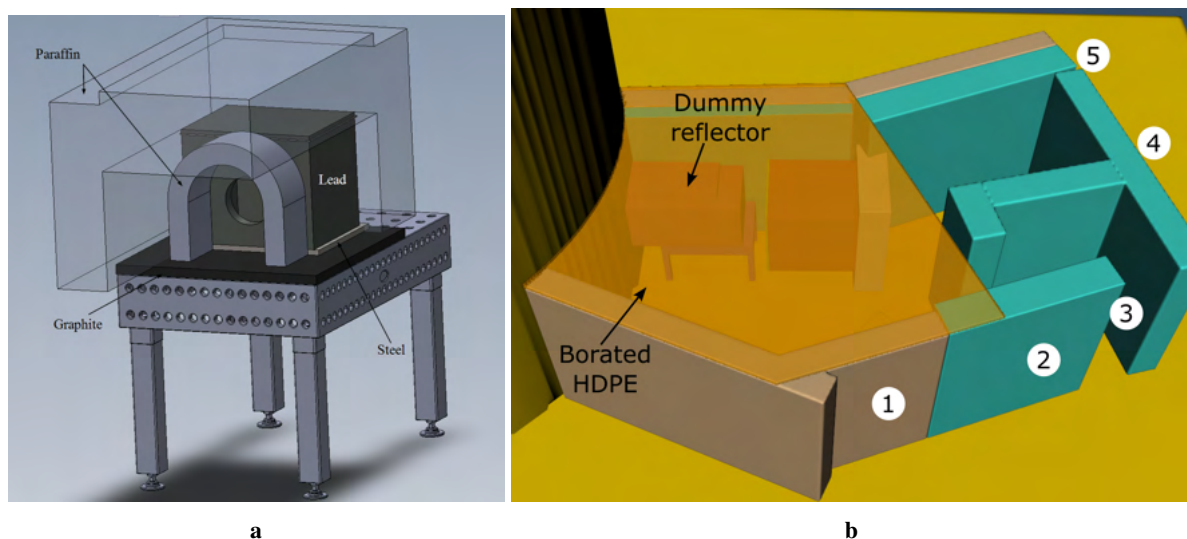


**Figure 311:** (a) Dummy lead reflector with temporary paraffin wax shielding. (b) MCNP model of the experimental room adapted for the configuration of the dose rate measurements with the dummy reflector and the temporary roof. The five points where the dose rates were measured are also shown.

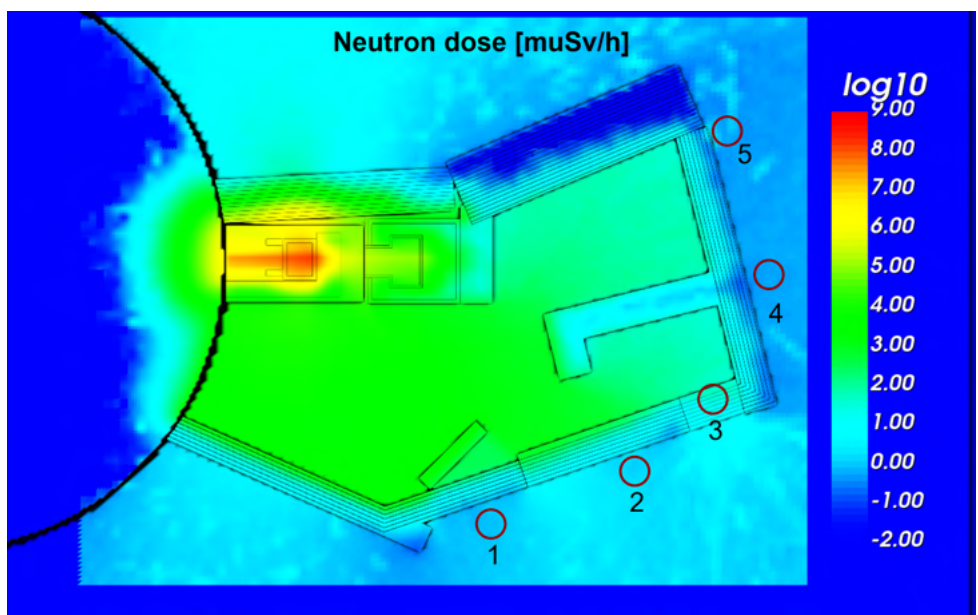


**Figure 312:** Neutron dose rate map with a spatial resolution of  $10\text{ cm} \times 10\text{ cm} \times 10\text{ cm}$ . The dose rates are calculated using the Neutron Fluence-to-Dose Rate Conversion Factors based on ICRP-116 and assuming a neutron current of  $2.81 \times 10^{11}\text{ n/s}$  through the beam port of Channel #4. Units are  $\mu\text{Sv/h}$  in log scale. The five points where the dose rates were measured are also shown.

### 11.1.11 Activation calculations

Based on the neutronics model previously described, the activation of the experimental setup components was also studied, in particular the activation of the reflector vessels that have to be exchanged during the experiment to assess the effect of the different reflector materials and of the FZJ cryostat for shipping and future re-use purposes. The calculations were performed at the Oak Ridge National Laboratory. The following hypotheses were considered:

- 40 hours of operation at  $2.81 \times 10^{11}$  n/s, which corresponds to 4-5 measurements per day of 1 to 2 hours
- 30 minutes, 1 h, 8 h, 1 day, 1 week and 1 month of decay time.

The dose rate limits to access the bunker are:

- In normal working conditions to access inside the bunker (reactor in operation, channel closed): below 30 microSv/h,
- Extreme conditions, e.g. for short immediate operations (reactor in operation, channel open): below 500 microSv/h – max 1 hour cumulated dose for 2 months span.

Due to issues in using the external supply line of H<sub>2</sub>, a smaller cryostat than the one described in D6.2, self-supplied, was used for the experiment as described later on in Figure 323. The cryostat was modelled according to the CAD description of this component. The neutron fluxes were volume-averaged over whole parts. The constant 40 hours of operation were assuming that the chopper and the pin-hole were in closed positions. Regarding the materials definitions, in carbon steels, a cobalt percentage of 0.05% was considered and 0.2% for stainless steel. Figure 313 presents photon dose rate maps through moderator center. After 30 minutes of decay, the limit of 500 microSv/h corresponding to the extrem conditions is exceed in the area where the vessel filled with advanced material is located. It can be also seen that the dose rates in the area where the cryostat is located are exceeding the 30 microSv/h limit for normal operating conditions but after one day of decay, this dose rate decreases to 2.5 microSv/h for both areas of concern. After 8 hours of decay time, the vessels to be exchanged are still in an area where the calculated dose rates are more than 80 microSv/h, which tends to indicate that a tool can be needed for remote handling of that component.

After 40 hours of irradiation and 1 day of decay, the dose rate on contact at the surface of the cryostat is calculated as 2.5 uSv/hr. After a week of decay, the dose rate decreases by a factor of 10. The internal copper structure was taken into account. Figure 314 gives the total activity in function of time of the cryostat. In stainless steel the activation is mainly dominated by <sup>56</sup>Mn as shown in Figure 314. The two other main contributors are <sup>51</sup>Mn and <sup>60</sup>Co and in copper, the activation is mainly due to <sup>64</sup>Cu as reported in Figure 315. It should be noticed that this model is not taking into account any shielding around nor in the collimator.

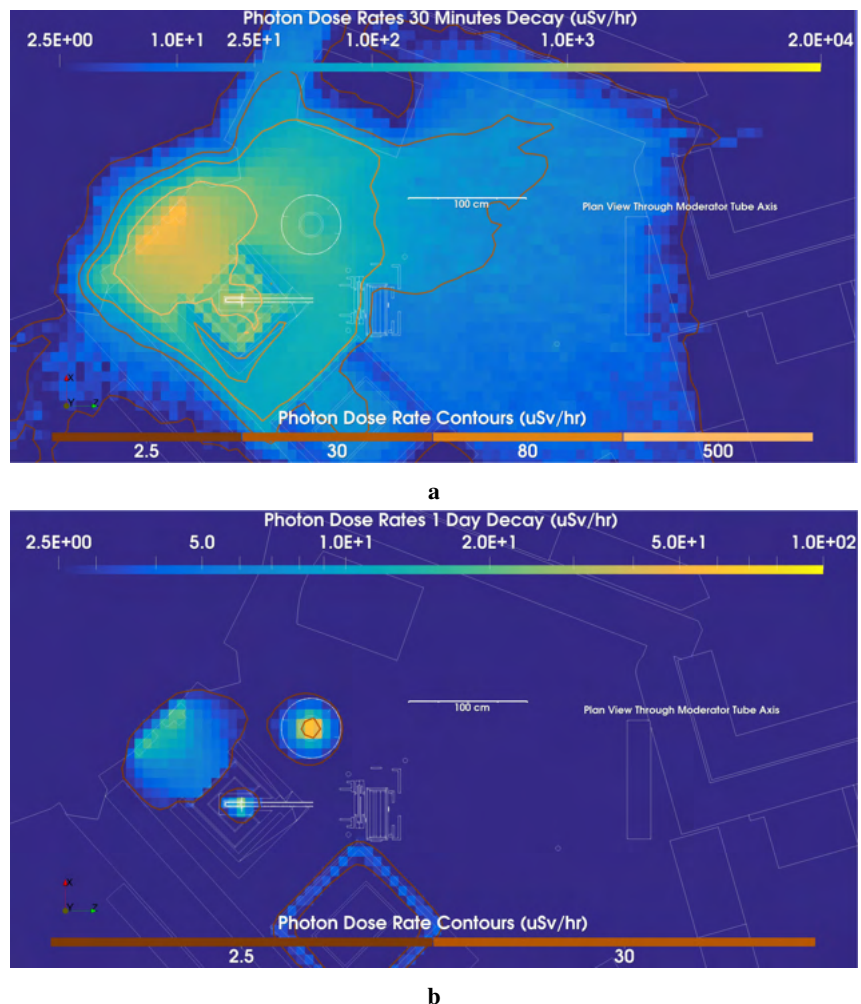


**Figure 313:** Photon dose rates - 30 minutes of decay (a) (b) 1 day of decay

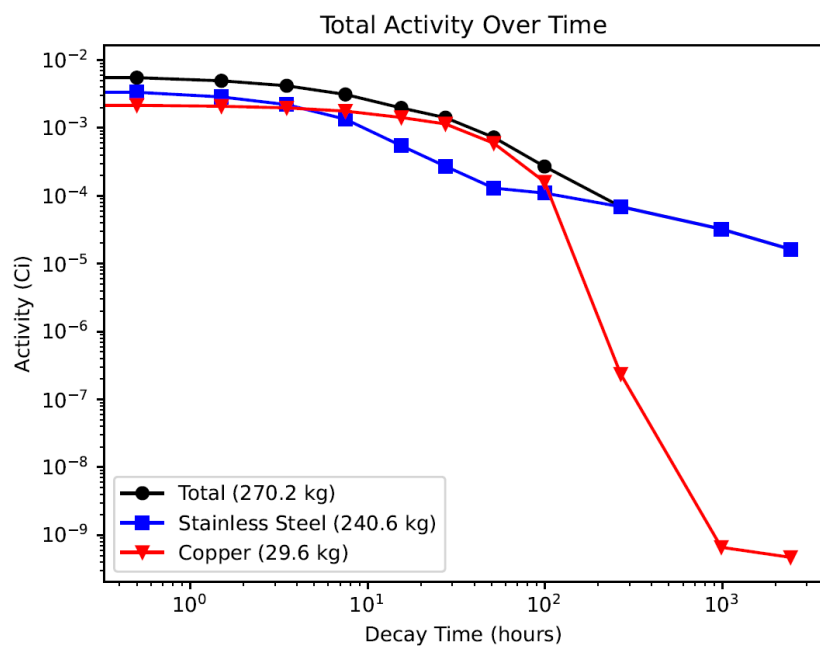


**Figure 314:** Total activity over time of the FZJ cryostat

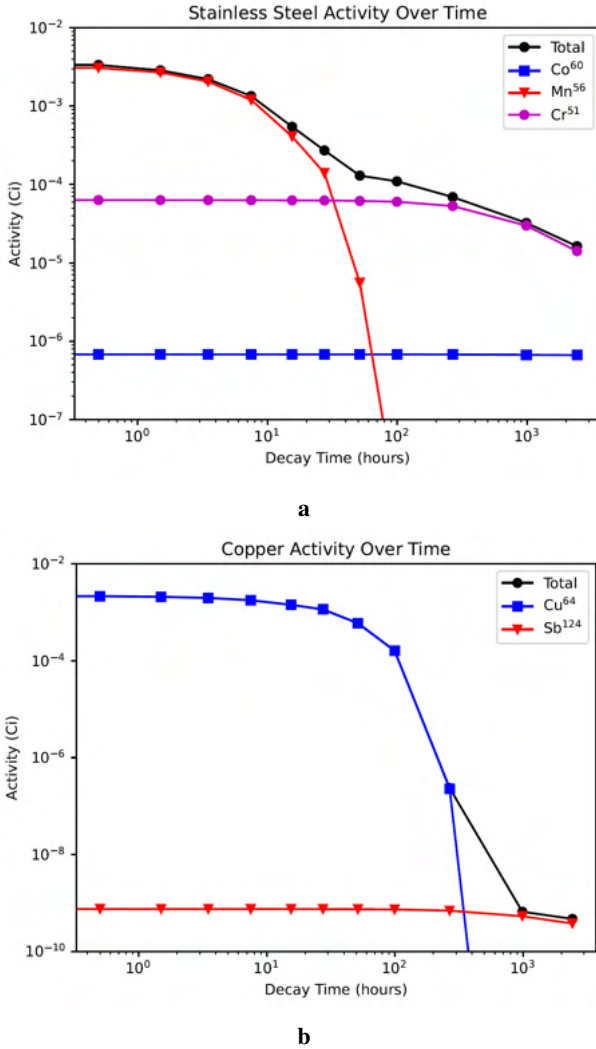


**Figure 315:** (a) Activation of the FZJ cryostat - Contribution of Stainless steel (b) Contribution of copper

## 11.2 Engineering of the experimental setup

The engineering team (WP5) designed a moderator & reflector unit, surrounded by advanced reflector materials as well as an associated beam extraction channel based on advanced reflector materials for the BNC experiment. To be able to quantify the effect of the advanced reflectors, a control measurement with an empty reflector vessel should be carried out first as reference. This initial measurement can then be followed by a measurements performed with ND and MgH<sub>2</sub> vessel respectively. Those interchangeable vessels filled with 10 mm thick layers of ND or MgH<sub>2</sub> powder have to be placed around the cold para hydrogen moderator, which is fed by neutrons of the Budapest research reactor. These reflectors can be exchanged to perform measurements with different configurations, shown in Figure 316. The moderated neutrons of the moderator/reflector assembly are led into a 600 mm long beam-tube, surrounded by a 5 mm thick ND powder layer to extract the cold neutrons from the moderator. The spectra of reflector/moderator/guide assembly are measured by a pin-hole (“camera obscura”) time-of-flight (TOF) setup. All structures which are placed in the neutron beam are manufactured of aluminum to reduce activation and allow fast exchanging of the reflector vessels. The H<sub>2</sub> supply lines are led into the cryostat system outside the bunker, where the LH<sub>2</sub> liquefaction takes place and a high para H<sub>2</sub> concentration will be generated. [379]

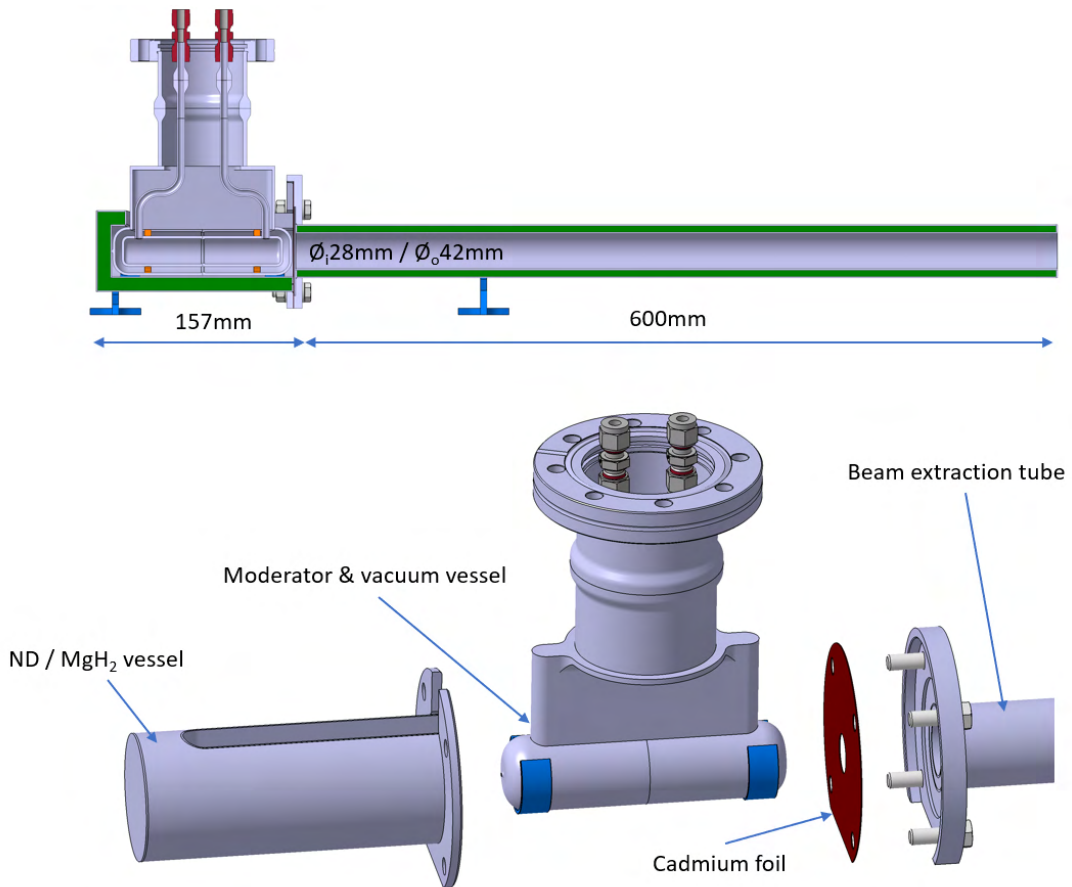


**Figure 316:** Experimental moderator/reflector/guide setup with interchangeable configurations placed inside the neutron beam.

### 11.2.1 Assembly and welding of the components

The moderator itself consists of two half-tubes with back walls, which are milled from one piece of aluminum EN AW-5083 each. They are joined by EB welding to minimize the heat input during the process. This reduces bending and distortion issues during the welding process significantly. After the welding, spacer rings made of polyimide are put onto the vessel, to ensure proper alignment of the moderator in the surrounding vacuum vessel. Polyimide is chosen as material, because of its low heat conductivity, while being resistant to the low temperatures the moderator will reach, as it uses liquid para-hydrogen ( $LH_2$ ) as the moderating medium at a temperature of around 20 K. This reduces the required cooling power of the cryostat, because it reduces thermal losses due to thermal insulation. In the next step, the supply pipes for the liquid hydrogen ( $LH_2$ ) are welded on by tungsten inert gas welding (TIG) (Figure 317 & Figure 319 left).

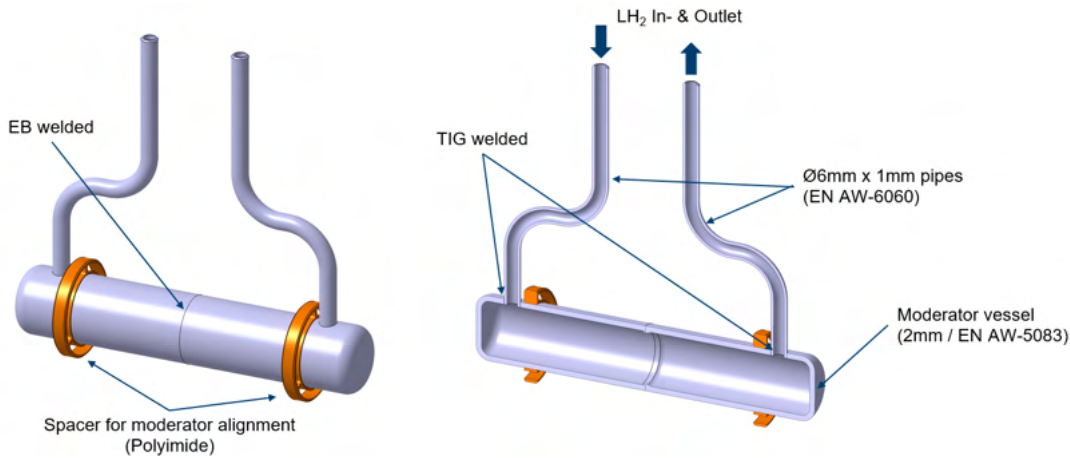


**Figure 317:** Design of the LH<sub>2</sub> moderator.

The vacuum vessel shown in Figure 318 and Figure 319 (right) ensures the insulation vacuum for the cryogenic parts of moderator system. This is necessary, because it affects the required cooling power that is needed for the low temperature of around 20 K of the moderating medium liquid hydrogen (LH<sub>2</sub>). The jacket surrounds the moderator and the supply pipes. It is also joined by EB welding, for minimal heat input and less distortion when welding. There are two interfaces in this vacuum vessel. One is the connection of the LH<sub>2</sub> supply pipes and the other is the vacuum connection flange. On both interfaces, a transition of aluminum to stainless-steel is needed, because aluminum is too soft to ensure a re-useable connection. Therefore, at the pipes, a friction welding adapter is used, so that the cutting ring fitting for the connection to the transfer-lines can be adapted to the stainless-steel end of the adapter. The CF-flange at the outer vacuum jacket is also made of stainless-steel. This transition from aluminum to stainless steel is solved with an explosive cladding adapter, which has a titanium (Ti) layer in between. This material mix is due to the cladding procedure via explosion itself and has no special reason for the usage of the adapter.

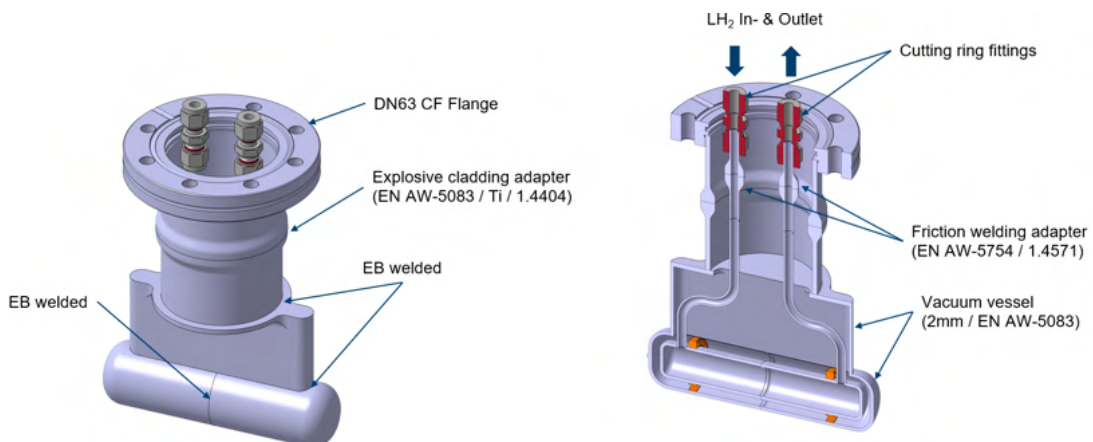


**Figure 318:** Design of the vacuum vessel.



**Figure 319:** Manufactured cold moderator (left: hydrogen vessel, right: vacuum jacket).

The ND & MgH<sub>2</sub> vessels are basically made of an inner and an outer part, as it is shown in Figure 320. The inner and outer tubes are made of aluminum EN AW-6060 and are both closed with a disc also made of EN AW-6060, which is EB welded, due to the small wall-thicknesses of 1 mm. They built a concentric vessel with a 10 mm overall layer in between, that has been filled with either ND or MgH<sub>2</sub>. The packing density of the ND vessels is 0.25 g/cm<sup>3</sup> and for MgH<sub>2</sub> 0.60 g/cm<sup>3</sup>.

For a control measurement, one of the three vessel assemblies will stay empty. After the filling process, the vessels are closed with a ring-shaped disc by EB-welding. To be able to connect the assembly to the beam extraction channel, a custom flange is tack welded onto the outer vessel part by laser beam welding.

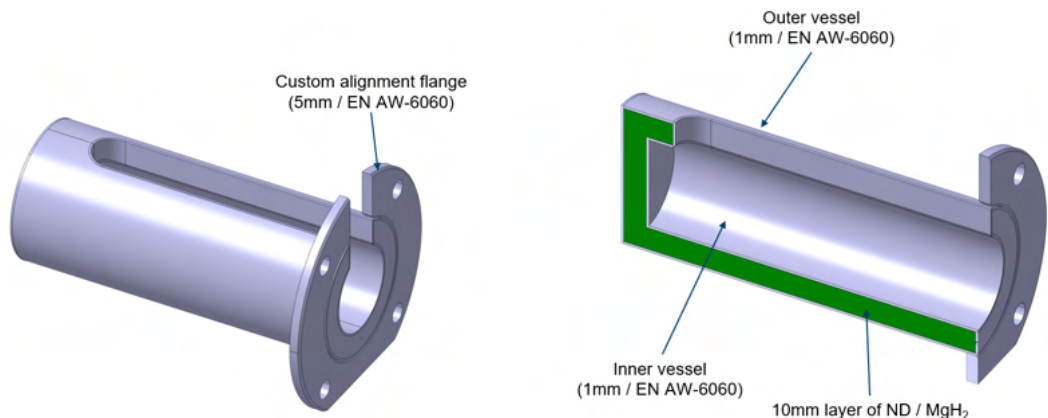


**Figure 320:** Design of ND & MgH<sub>2</sub> vessel.

The ND beam extraction channel in Figure 321 & Figure 322 is generally of a very similar design, as the vessels described before in Figure 320. It consists of an inner and an outer tube, which are in a first step closed from one side with a ring-shaped disc. They built a concentric vessel with a 5 mm layer in between, which is filled with ND. The filling was carried out under a fume hood while the tube/vessel was placed on a shaker. After the filling process, the vessel is closed with a second ring-shaped disc. All parts are made of EN AW-6060 and for the joining process, EB-welding is used again, due to the small wall-thicknesses of 1 mm. To be able to connect the assembly to the ND- & MgH<sub>2</sub>-vessels, a custom flange is tack welded onto the outer tube by laser beam welding.

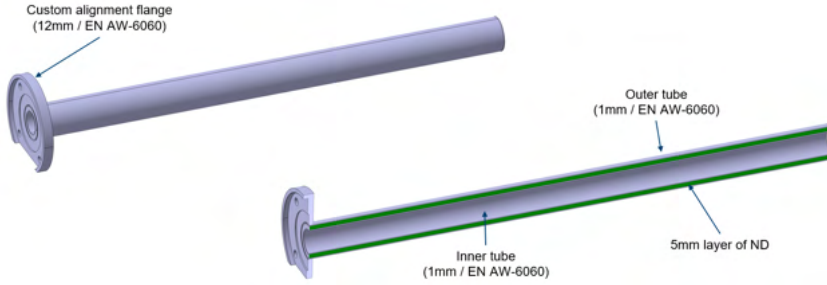


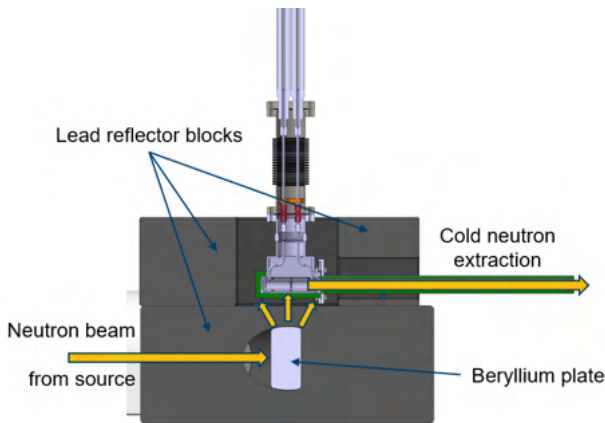
**Figure 321:** Design of the ND beam extraction channel.



**Figure 322:** Manufactured ND beam extraction channel.

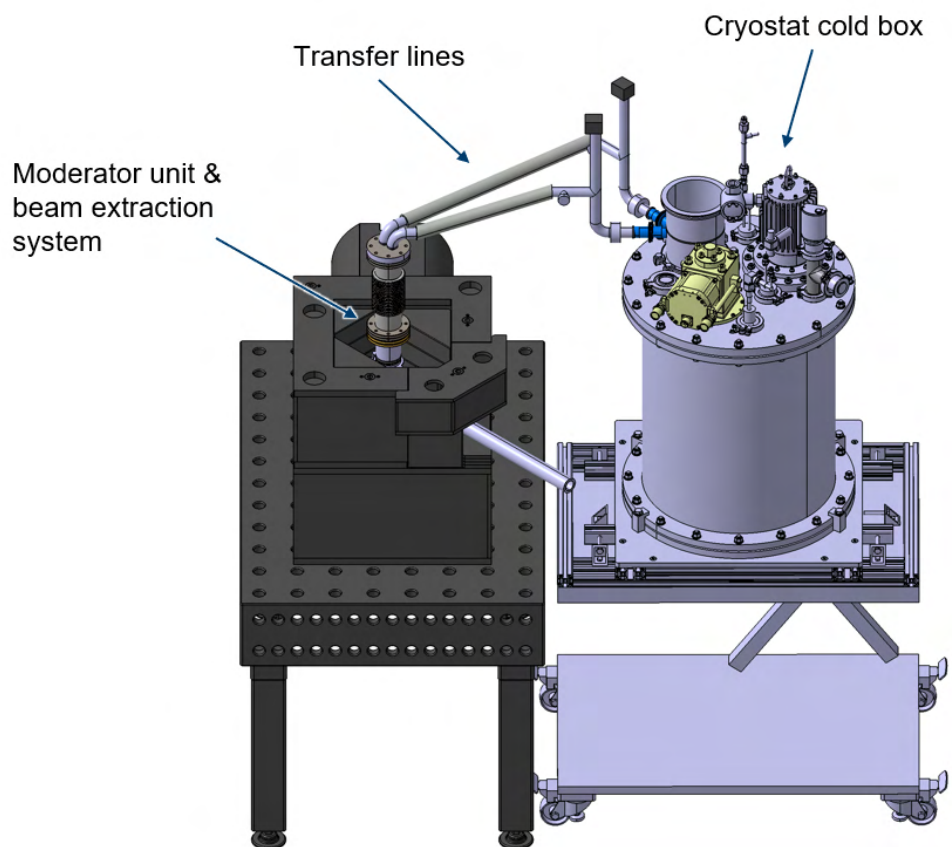
### 11.2.2 Assembly of the moderator & beam extraction system into the test facility

Figure 323 shows a side view cut-section of the moderator test facility at the Budapest Neutron Centre (BNC) with the integrated moderator and beam extraction systems. The neutron beam from the reactor source enters the test station through an assembly of lead blocks and hits a plate made of beryllium (Be). This Be-plate is located directly below the test area for the moderator units and scatters the thermal neutrons, so that they are fed into the moderator and reflector assembly. After the neutrons are slowed down to cold neutron energies, they exit through the ND beam extraction system into the detector area.



**Figure 323:** Integration into moderator test facility

Figure 324 shows the moderator unit and the beam extraction system, located in the Budapest Neutron Centre (BNC) moderator test facility setup. Figure 325 is showing a view of the cryostat. The vacuum vessel surrounding the cold moderator and the LH<sub>2</sub> supply pipes are connected via vacuum insulated transfer lines with the cryostat cold box. This cryostat is also made and owned by Forschungszentrum Juelich and was used to perform to the experiment. It is needed to supply the cold moderator with LH<sub>2</sub> in a closed loop using a circulation pump. A cold head with 40 W @ 20 K is used to liquefy and to cool down the hydrogen to 20 K inside the cryostat via a heat exchanger. In addition, a catalyst ensures that the moderator is supplied with almost 100 % para hydrogen. The concentration ratio is monitored using Raman spectroscopy. It also supplies the insulation vacuum, which is necessary to maintain the cold temperatures inside the transfer lines and the vacuum jacket.



**Figure 324:** Moderator system with cryostat cold box



**Figure 325:** Assembled cold moderator system

### 11.2.3 Results and discussion

In preparation for experiments to be performed using the Channel 4 at the BNC reactor, the channel radiation protection environment was successfully tested on June 5<sup>th</sup> 2023 through neutron and gamma dose rates measurements performed at 1 MW reactor power at the channel outlet, near the reflector and outside the bunker area of the channel. The low level of the background allowed for a channel opening at 10 MW. The outside bunker measurements were found to be within the local regulation limits and gave information on how the shielding should be reinforced. In order to benefit from feedback for the future HighNess measurements, WP4 and WP6 did participate in the setup of the experimental campaign dedicated to the test of a low dimensional moderator performed by the Mirrotron company from June 12<sup>th</sup> to June 23<sup>rd</sup> 2023. On June 23<sup>rd</sup> 2023, the CMTF installation was completed: channel-collimator, reflector, Be, outlet collimator, pin-hole system were fully installed and all components (pin-hole slit system, choppers and the detector) were working as shown in Figure 326. The roof on top of the experi-

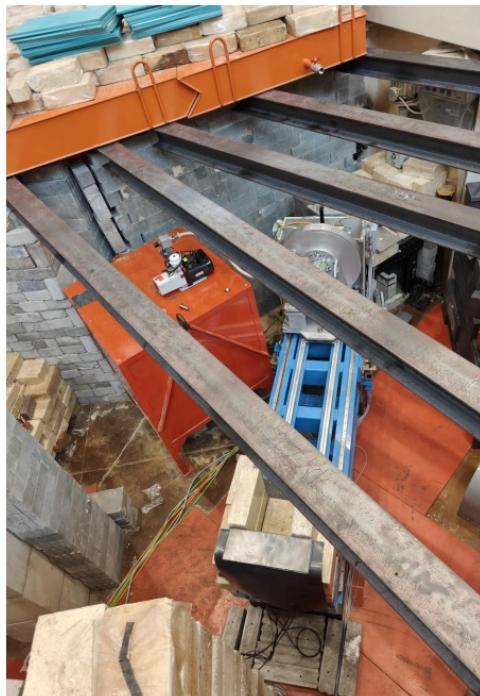


**Figure 326:** CMTF beamline installed in bunker- June 2023, Courtesy of L. Rosta

mental room was also completed. A 2D image from the moderator via the pin-hole system was recorded (see Figure 327), no TOF analysis was performed due to time limitation as the reactor had to stop but a fundamental milestone was reached at this point, showing a proof that the beamline can be operated safely with all the components installed, according to the design documents and the safety analysis report. First neutron measurements were performed at 10 MW reactor power with the completed assembly of the test facility. The HighNess measurement campaign took place from September 18<sup>th</sup> to September 29<sup>th</sup>. The roof on top of the experiment room was completed and closed on and the beam was opened on September 21<sup>st</sup>, allowing for first measurements. In particular, the dose rate measurements confirmed the results given by the activation calculations previously performed by the Oak Ridge National Laboratory. At the moderator position, considering the shutter closed, the dose rate recorded was 80  $\mu\text{Sv}/\text{h}$  and 400  $\mu\text{Sv}/\text{h}$  at the reflector surface, at shutdown after 1 hour of irradiation, decreasing to the level of 10  $\mu\text{Sv}/\text{h}$ , which is below the safety limit, after few hours of cooling time. The measurement performed during the first week of the campaign clearly confirmed the need of reducing the background. As illustrated in Figure 328, paraffin blocks were added to surround the collimator and the lead shielding encapsulating the experimental set-up. A tunnel made of Mirrobor™ plates (natural rubber and boron powder based flexible plates) was installed on the detector table, also combined with paraffin blocks.

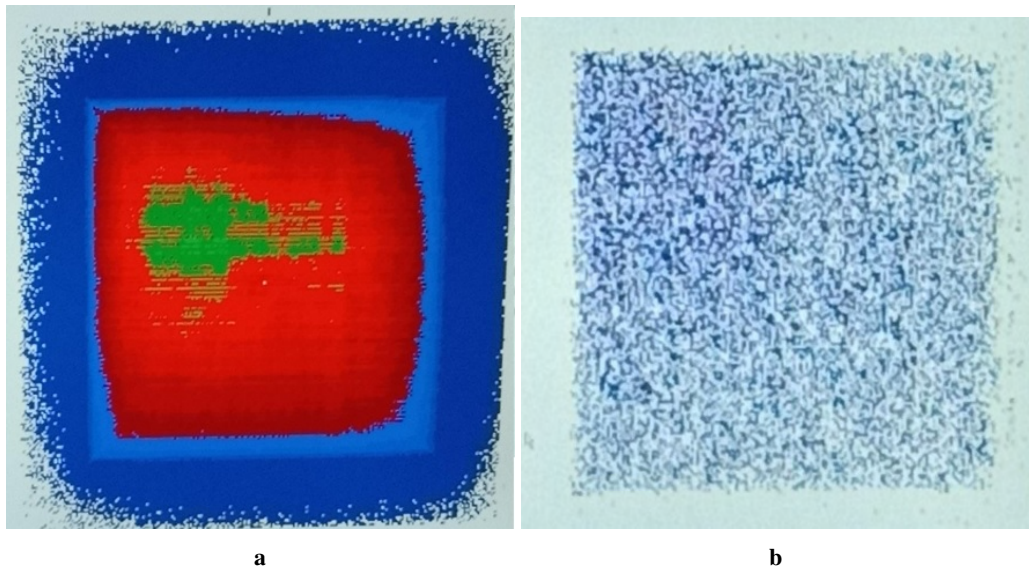


**Figure 327:** (a) 2D image on the He-3 detector from the moderator at 10 MW (b) Background at closed beam.



**Figure 328:** (a) Paraffin blocks shielding (b) Shielding on the detector table.

Placing a layer of Mirrobor™ between the chopper and the detector led to a count rate decrease of 10%, highlighting the fact that the background was mainly due to fast neutrons.

The reactor was stopped at 14:00 on September 22<sup>th</sup> 2023. A last spectrum was recorded just before this shutdown. The efforts done to reinforce the shielding lead to a significant background reduction. Reinforcing the shielding around the detector and especially from its backside led to a reasonable background-to-noise ratio. In summary, the first week of the campaign was dedicated to the shielding improvement in order to reduce the background. The cryogenic system was put in place during the second week. Cooling of hydrogen started on September 28<sup>th</sup>. Figure 329 illustrates the status of the facility at this time. At the time of writing, even if the tight schedule does not allow for measurements with vessel exchange, the successful building of the beamline and manufacturing of the different components of the experimental setup and the first images of the moderator obtained are giving the proof that such measurements can be performed, which is already an important milestone reached, and is promising for future campaigns.



a



b

**Figure 329:** Status of BNC experiment on September 27<sup>th</sup> 2023 (a) View of the roof with compressor installed (b) Interior of the experimental room.

## 11.3 Experiment at the JULIC Neutron Platform

The construction of a test Target-Moderator-Reflector (TMR) unit is part of the High Brilliance Neutron Source (HBS) project [380], which aims to develop a High Current Accelerator-driven Neutron Source (HiCANS) which is competitive and cost-efficient. The test TMR station was developed over two years through a collaboration between JCNS and Central Institute of Engineering, Electronics and Analytics (ZEA-1) at FZJ and built in the ‘Big Karl’ area of the IKP. The neutrons are produced by 45 MeV protons accelerated by the JUELich Light Ion Cyclotron (JULIC), delivered via a dedicated proton transfer beamline, and impinging on a newly developed high-power tantalum target with an internal microfluidic water-cooling loop. A schematic representation is shown in Figure 330. The subsequent fast neutrons emitted are moderated to thermal and cold range by, respectively, a high-density polyethylene (HDPE) premoderator and two cold sources, a low-dimensional hydrogen source and a methane moderator, both at cryogenic temperature. The TMR is surrounded by a 68-ton heavy concrete biological shielding with a unique modular design that can accommodate up to eight individual experiments. The first neutrons were produced on the target on December 12<sup>th</sup> 2022. Due to the low current of the proton beam ( $5 \mu\text{A}$  peak current), the neutron yield produced is relatively low ( $\approx 10^{10} \text{ s}^{-1}$ ), so the facility is optimal for proof-of-principle experiments like the one planned within HighNESS. The HighNESS experiment took place at the HiCANS test station from August 30<sup>th</sup> 2023 to September 3<sup>rd</sup> 2023.

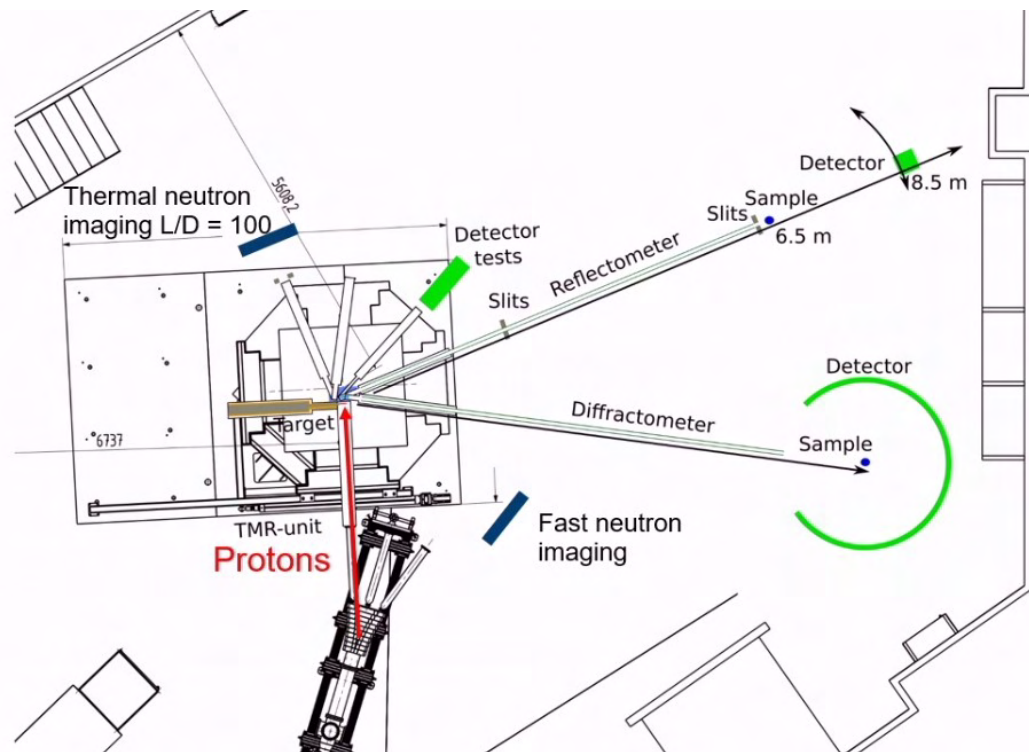


**Figure 330:** Schematic of the HiCANS test station at the Big Karl area of the IKP.

### 11.3.1 Experimental setup

The protons hitting the target are extracted from the plasma of the ion source for the JULIC Cyclotron, the pre-accelerator of the COoler SYnchrotron (COSY), where they are accelerated from 4 keV to 45 MeV. During the period of the beamtime, the accelerator was operating in two modes:

- 25 Hz frequency and 0.8 Å pulse length
- 10 Hz frequency and 1 or 3 ms pulse length

The first set of parameters was intended for most of the other experiments, with resolution-sensitive measurements where the cold and very cold tail of the moderator spectrum was not crucial. On the other hand, the low frequency and long pulse length mode was specifically tailored for the HighNESS needs, where fine resolution was not so important and the cold flux was essential. The accelerator operational schedule during the beamtime included the change of parameters early in the morning and in the afternoon after the HighNESS measurements were finished. During the preparation of the experiment, pulse lengths of 1 ms and 2 ms were also investigated in order to assess what would be the best trade-off between resolving the shorter wavelengths and having a high flux at long wavelengths. Since the factor 3 in neutron flux was deemed more important, we decided to add only one short measurement at 1 ms before switching to 3 ms.

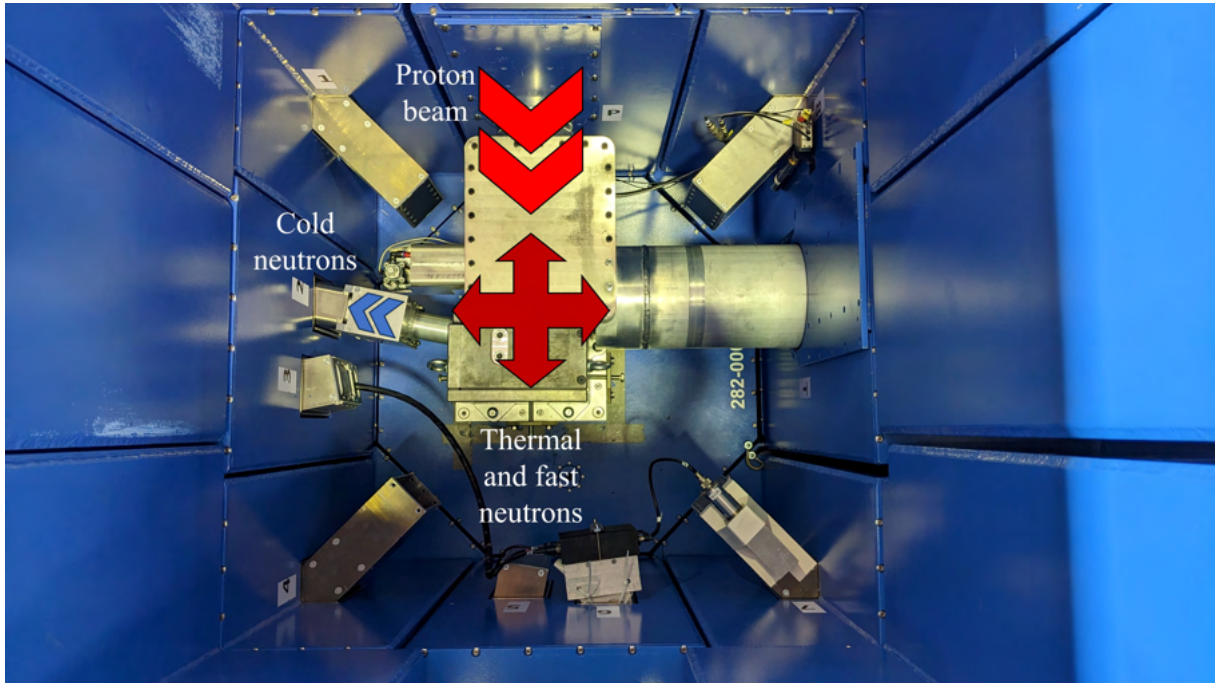


**Figure 331:** Target-Moderator-Reflector (TMR) area seen from above. Protons are coming from top. Cold neutrons moderated in the solid methane are extracted from beamline number 2.

The TMR station presented in Figures 331 and 332a is equipped with two cold sources: a liquid para-hydrogen moderator and a solid methane one (Figure 332b). The two moderators are embedded in a HDPE block which acts as a premoderator. A lead case around the HDPE reflects the thermal neutrons and shields the sources from the gamma radiations. The effect of the advanced reflectors was tested at the diffractometer of the facility (beamline number 2, see Figure 330), which looks into the solid methane cold source. The moderator vessel is an aluminum cylinder of 36 mm in diameter and 53 mm in length, with an inner cavity of 22 mm in diameter and 33 mm in length corresponding to the moderating volume. The source is kept at the cryogenics temperatures by liquid helium flowing in channels carved around the outer layer of the vessel. The poor thermal conductivity of solid methane is improved by inserting an aluminum foam which increases the thermal coupling with the vessel for a better heat removal. For the duration of the experiment, the source target temperature was set to 22 K. The choice of the temperature was motivated by the need to keep the moderator conditions as stable as possible. Cooling the moderator at a lower temperature would have implied a higher cold flux, but also a much larger consumption of He to maintain that condition stable, which in turn would have meant a need of several He tank exchanges with a procedure which requires to warm up and re-solidify the methane, with no guarantee to go back to the same experimental conditions. During the measurements, the temperature stability was checked and noted in the logbook at the beginning and at the end of the run, with a resolution of 1 K. Unfortunately, due to a software crash of the monitoring system, only the logs from the first day were available for the data analysis.



**Figure 332:** Pictures of the (a) TMR with lead shielding around the HDPE premoderator and the extraction system for beamline 2 (b) Closer look at the two moderator outer vessels without the HDPE block. Above, the hydrogen moderator and below, the methane one with the HighNESS reflector cup surrounding it. (c) neutron optical guide (d)  ${}^3\text{He}$  tube detectors at the sample area. The central tube in front of the guide exit is the detector used to record the signal.

The cold neutrons moderated inside the methane are transported out of the shielding to the sample area by a neutron guide with a  $30\text{ mm} \times 44\text{ mm}$  section and coated by  ${}^{58}\text{Ni}$  ( $m=1.18$ ). The distance from the moderator surface to the guide exit is 6.83 m. A  ${}^3\text{He}$  tube placed in front of the window at the exit of the guide measures the intensity of the neutrons as a function of the time of flight. On both sides of the detector, two identical tubes measure the background in its proximity. Since the guide section is bigger

than the dimensions of the moderator, also fast neutrons from the TMR are reaching the sample area. Here they can get thermalized or scattered by the borated polyethylene shielding, with a second chance to reach the detector as background. Thus, the tubes on the sides should give a good estimates of this small effect.

A set of useful monitors, synchronized with the same time-of-flight trigger as the detector for the signal, were scattered around the hall at the following locations: inside the TMR station (visible in the bottom right corner in Figure 331), outside the biological shielding, inside and outside the sample station shielding, and the array of tubes from the banana detector of the diffractometer (visible in Figure 332d). The time resolution was 0.2 ms for a full-scale range of 50 ms.

### 11.3.2 Materials and Methods

The experiment consisted in the insertion of several aluminum cups around the methane moderator, as shown in Figure 332b, two of them had a cavity filled with, respectively, ND and MgH<sub>2</sub>, one had an empty cavity for comparison, acting as reference, and the last one was entirely made of polyethylene, the same material as the premoderator. The cups, manufactured by the WP5 engineering team in FZJ, are aluminum hollow cylinders with an outer diameter of 74.5 mm and inner diameter of 56.5 mm. In the circular crown, a 5 mm gap hosts the reflector material in powder form, while the walls are 2 mm thick. The powders were poured in the gap from a hole in the back of the cup, and sealed with a screw and a plastic ring.

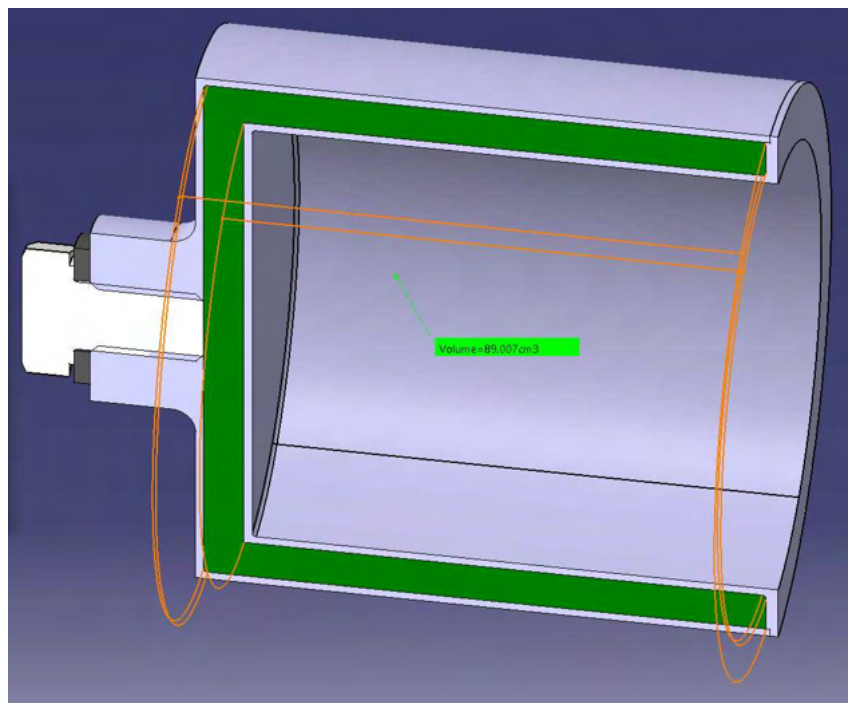


**Figure 333:** Diagram of the aluminum cap showing the calculated internal volume.

The nanodiamond powder used is commercial Detonation NanoDiamonds (DND) for nuclear applications [381]. The average particle size is 5 nm and the purity declared by the manufacturer for the ash residues is < 0.1 wt %. The size distribution of the same product was characterized in [318], while an independent elemental analysis with inductively coupled plasma mass spectrometry (ICP-MS) technique performed in FZJ showed a total metallic impurity content of 185 mg/kg, made up by traces of Ca (60 mg/kg), Mn (49 mg/kg), Na (27 mg/kg), Fe (23 mg/kg) and other elements in lower concentrations. After filling the cup, the mass of powder in the jacket was 21.8 g. This means that, with a jacket volume of 89 cm<sup>3</sup> taken from the CAD (Figure 333), the achieved fill density was 0.245 g/cm<sup>3</sup>.

Similarly, the MgH<sub>2</sub> was used in the form of a powder to fill the cavity of a second cup. The average

size of the particles is  $15\text{ }\mu\text{m}$ , for a nominal density of  $1.45\text{ g/cm}^3$ . Also in this case, the manufacturer declared a purity of 99.9% [382]. The powder density measured after filling the cup is  $0.66\text{ g/cm}^3$ .

During the five days of the beamtime, the schedule of the experiment was meant to limit as much as possible the change of the accelerator parameters, while giving the same share of time to all the users of the facility. The schedule for the first four days is summarized in Figure 334, while for the last day the accelerator parameters were fixed to a 10 Hz and 3 ms with two cup exchanges. The procedure for the cup exchange consisted in shutting down the accelerator, letting the target decay for at least two hours, perform a radiation survey of the area, entering into the modular biological shielding, removing the back lead panel of the reflector, extracting the old cup from behind and inserting the new one (Figure 335). Manipulation of activated components was performed by radiologically qualified personnel from FZJ and under supervision of radiation protection officers.

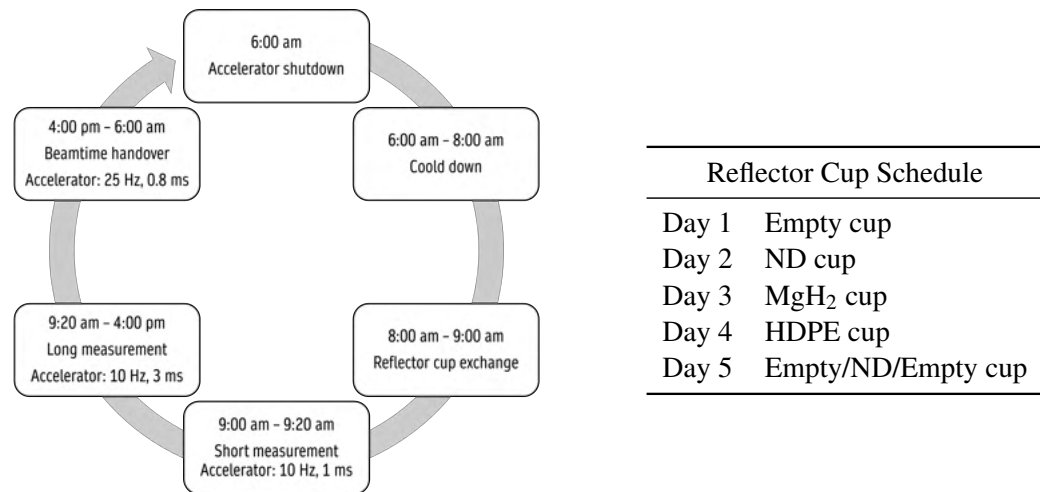


**Figure 334 & Table 60:** (Left) Schematic of the experiment schedule for the first four days. (Right) Reflector cup used for each day of experiment.

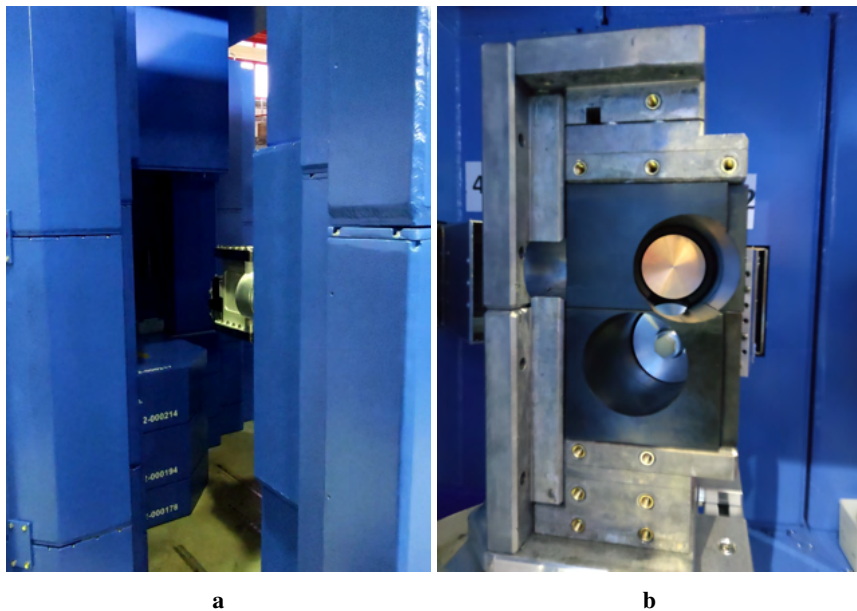


**Figure 335:** (a) Opened modular biological shielding with target (b) Example of the view of the TMR when the back lead panel of the reflector is removed for the cup exchange.

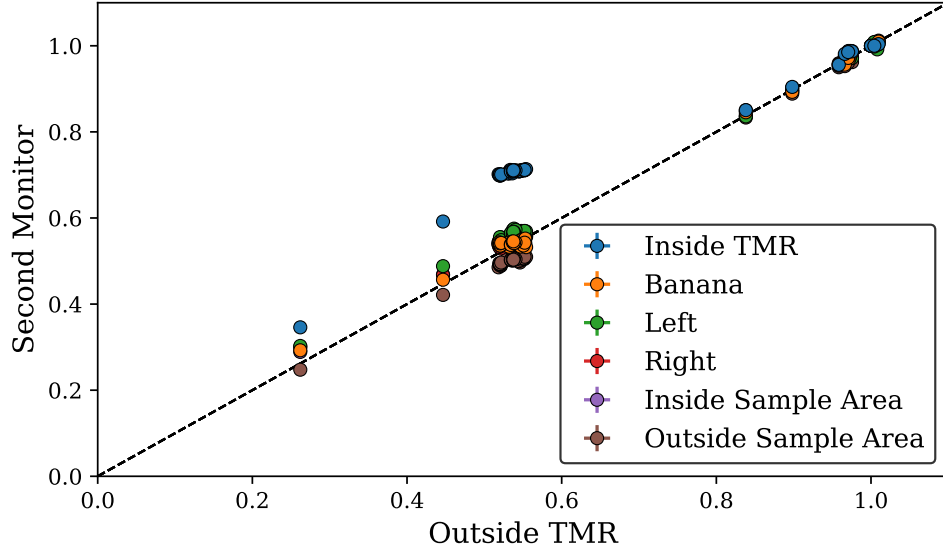


**Figure 336:** Plot showing the correlation between the integrated counts of the monitor outside the TMR shielding and all the other monitors. The counts are normalized by both the acquisition time and the counts for the first run (T0).

### 11.3.3 Data Analysis

The measurement of the time-of-flight spectrum was subdivided into multiple acquisitions of 20-30 min each. In this way we could study the stability of the source during the data acquisition. After subtracting the background contribution, which is almost negligible for cold neutrons with this setup, the spectra are normalized with the respective integrated monitor counts. Some of the runs were affected by statistically meaningful deviations from the average measurement, which are related to malfunctioning parts of the setup (more details will be given on this topic in the discussion part). Once identified the cause of the systematic deviation, those runs were discarded from the analysis. The resulting averaged and corrected spectrum was calculated as:

$$\overline{S^*}(t) = \sum_i^N \frac{1}{N} \frac{S^i(t) - B^i(t)}{\sum_t M^i(t)} \quad (51)$$

where  $S^i(t)$  is the signal from the main detector for the  $i$ -th run,  $B^i(t)$  are the average background counts from the two  ${}^3\text{He}$  tubes on the left and on the right of the main detector, and  $M^i(t)$  are the monitor counts used for normalization. The conversion from time-of-flight bin in ms to wavelength bin in Å is obtained as:

$$\lambda = \frac{3956 \text{ Å m/s}}{6.83 \text{ m}} * t [\text{ms}] * 0.001 = 0.5792 \text{ Å s}^{-1} * t [\text{ms}] \quad (52)$$

In order to study the effect of the advanced reflector around the moderator on the cold spectrum, the ratio between the cases with the reflector and the empty cup is evaluated:

$$r(\lambda) = \frac{\overline{S_R^*}(\lambda)}{\overline{S_{empty}^*}(\lambda)} \quad (53)$$

It is clear that the stability of both the signal and the monitor is critical in evaluating  $r(\lambda)$ , since uncorrelated systematic drifts in the two terms could cause ratios greater or smaller than 1 even when there is no real effect. In Figure 336, the sum of the counts for the monitor situated outside the TMR for all runs, normalized by both the acquisition time and the counts of the first run (T0), is plotted against the same quantity for all the other monitors. Variations in absolute counts can be caused by fluctuations of the proton current, but the correlation between the monitors is expected to stay constant, which is not happening for the monitor located inside the TMR. The two largest clusters of runs are separated by an intensity gap due to a decrease in the accelerator current that occurred after the second day and caused by

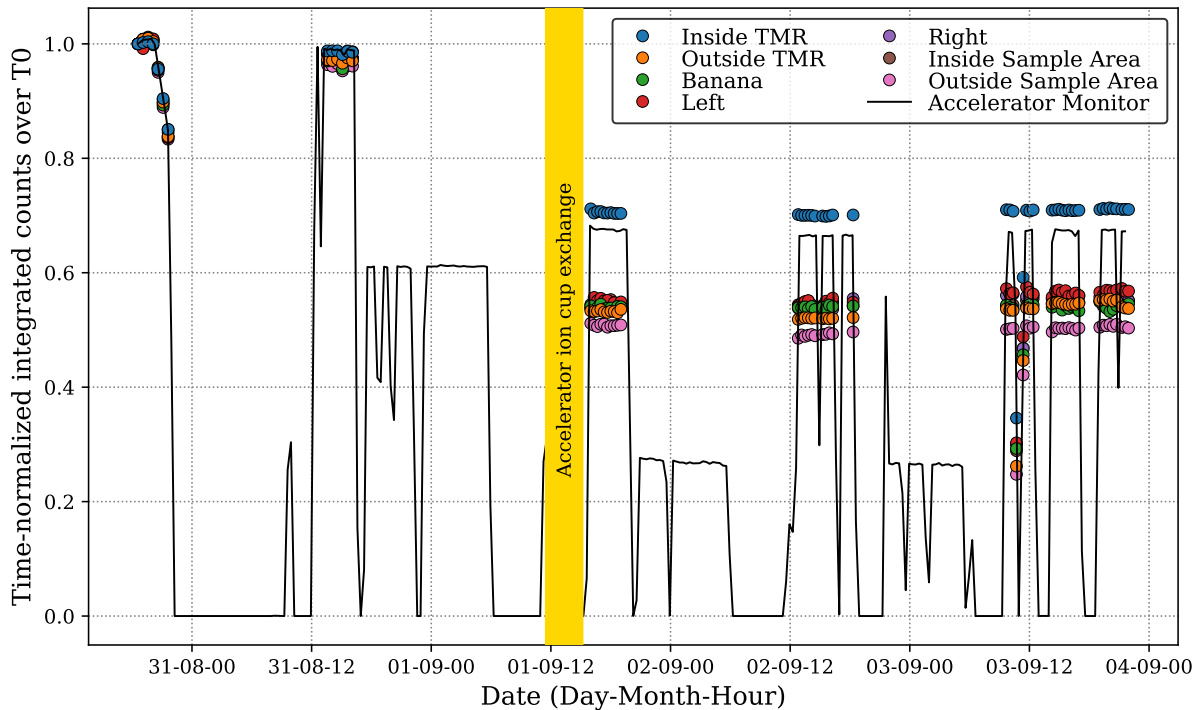


**Figure 337:** Plot showing the correlation between the accelerator monitor counts and all the other monitors. The counts are normalized by both the running time and the counts for the first run at T0. The time window for the exchange of the accelerator cup is shown. The lower peaks in-between the HighNESS experiment correspond to the shorter pulse length regime.

the exchange of the accelerator ion cup, after which the current went from  $8 \mu\text{A}$  to  $6.3 \mu\text{A}$ . This effect is more visible in Figure 337, where the time-normalized integrated counts for all monitors, further divided by the counts at T0, are plotted as a function of the time and compared with the accelerator monitor, also normalized in the same way. After the exchange of the ion cup, the 20% decrease in current results in 30% less counts for the monitor inside the TMR area and almost 50% for the other monitors. The accelerator monitor was not considered reliable for normalization by the instrument scientist since, after a change in the ADC threshold to allegedly avoid overflow, no extensive testing was conducted on the relation between the proton current and the monitor. In this respect, the analysis of the correlations among the network of monitors highlights that probably also the monitor located inside the TMR area is not reliable for normalization. A possible explanation for this effect could hence be that both monitors are underestimating the count drop after the ion cup exchange due to overflow. Thus, the monitor outside the TMR shielding is used for normalization in the data analysis.

The integrated counts are not the only measure of the system stability. After the exchange of the accelerator ion cup, we systematically measured a different pulse shape. In Figure 338a the counts of the monitor inside the TMR area, divided by the total counts and averaged over the stable runs, are shown as a function of the time, while in Figure 338b we calculated the ratio of the same curves over the empty cup. We decided to show the monitor inside the TMR area because the pulse shape is easily recognizable, although the same behavior is observed in all the monitors. Also, for clarity sake, only the runs from the first four days are shown. The ion cup was exchanged between the ND and MgH<sub>2</sub> cup measurements. The question that arises is if this could produce a systematic impact on both the spectra and, most importantly, the ratio with the empty cup. Since a similar effect was also observed the first day during the measurements with the empty cup (Figure 339), we can study that case to isolate as much variables as possible and try to answer the initial question.

The cause of the proton pulse shape change in the first day was due to two decoupled clocks signals that were slowly drifting out of synchronization and cutting the proton pulse. We noticed the presence of the drift only the day after, and the problem was quickly fixed before starting the new measurements.

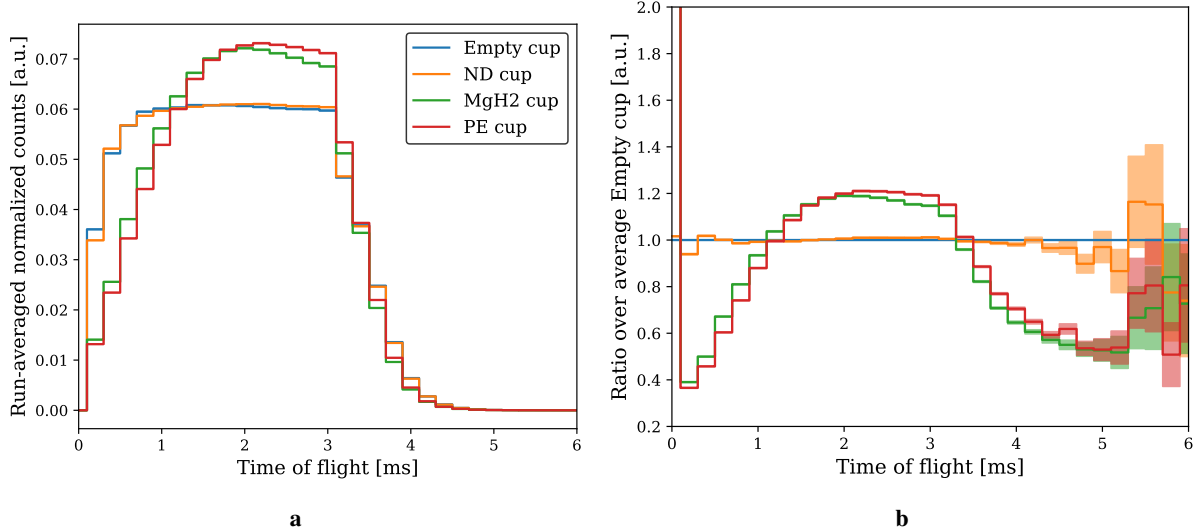


**Figure 338:** (a) Monitor counts inside the TMR area as a function of time, divided by the total counts and averaged over the stable runs for measurements from Day 1-4. (b) ratio of the same curves over the empty cup. The shaded area indicates the standard deviation.

In Figure 339a, this drift is clearly visible in the runs 4 to 6, but probably already started in run 3. These runs are hence discarded from the calculation of the average and marked with an x in the plots. The normalization hides the differences in absolute counts (lower for runs 3 to 6), but highlights the different shapes and allows to calculate the ratios in Figure 339b. The study of the signal from the main detector, calculated with Equation (51), in Figures 339c and 339d shows that a drift of 10%-20% in the pulse shape is positively correlated to a statistically significant increase/decrease of 5%-10% in the counts of the cold signal up to  $\approx 20 \text{ \AA}$ . A potential confounding factor worth to study in this case is the temperature of the moderator. The only log data available is the temperature as a function of time of the liquid He flowing in and out of the moderator vessel during the first measurements. This set of data is reported in Figure 340. According to the responsible of the source, the nominal temperature of the moderator is the one of the inflow. While a warming trend is clearly visible, an absolute variation of 0.4 K would be hardly appreciable in the final spectrum. This conclusion comes from the experiences with temperature drifts during the last day of beamtime, which suggest that differences of 2-3 K are necessary to start obtaining a measurable effect on the spectra. In conclusion, since we cannot rule out that the pulse shape has an effect on the signal, the results from day 1 and day 2 cannot be compared with the measurements taken after the ion cup exchange. The first set of results represents the first attempt to measure the effect of the ND cup over the empty cup of Day 1. The second set, including MgH<sub>2</sub>, polyethylene, and a second ND attempt, uses the first measurement of empty cup from Day 5.

### 11.3.4 Results

**First attempt with ND cup** The first two days we measured the empty cup and the ND cup for the first time. As already mentioned, at the end of the measurement with the empty cup, the accelerator pulse was unstable, but it was promptly fixed by the end of the day. The data collected during the accelerator drifts were not included in the average. For the ND cup, the first thing we noticed after the cup exchange was an increase in the moderator temperature. The monitoring system was reporting a liquid He in-flow temperature of 23.8 K. Before starting the runs, the temperature was restored to 22 K by increasing the flow of coolant. In Figure 341 the results are presented for both the monitor outside the TMR and the signal from the main detector. The ratio in Figure 341d is calculated with Equation (53) and shows a small, but statistically significant, increase in counts of the case with the ND cup over the empty cup above 5  $\text{\AA}$ . The increase reaches up to 5% at longer wavelengths. Even if there is a difference in pulse shape in Figure 341b, it is probably too small to produce the observed effect in the signal. In any case, the increment at such a short wavelengths needs to be investigated further, since the reflectivity of the

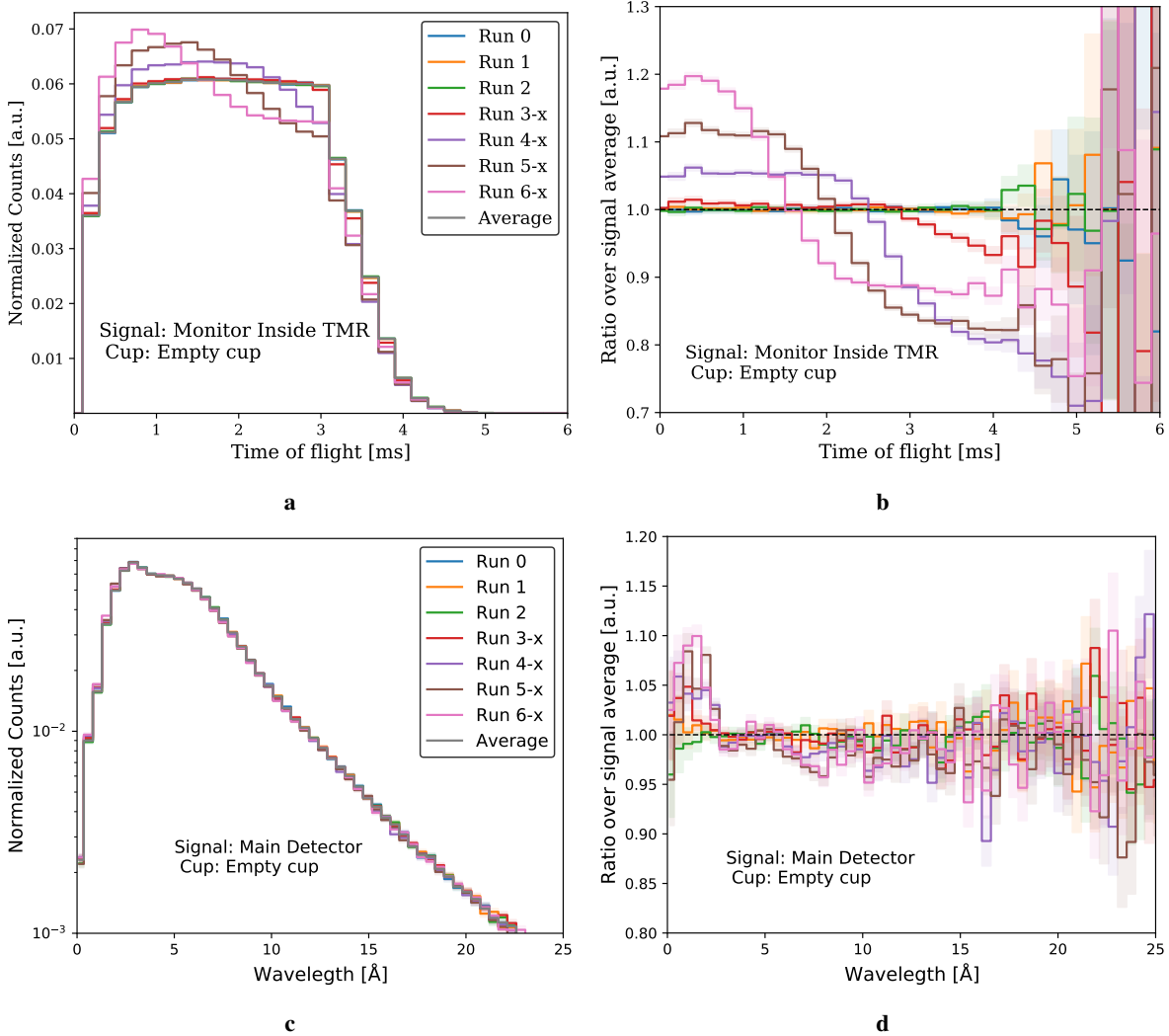


**Figure 339:** Normalized counts for each run and ratio over average for the empty cup measurement for: (a) and (b) Monitor inside the TMR area, (c) and (d) main detector. The signal from the main detector is re-binned by a factor 4 ( $0.46 \text{ \AA}$ ). All the runs not included in the stable average are marked by an x.

ND is expected to kick off above  $\approx 20 \text{ \AA}$ .

**Second attempt with ND cup** During the last day, we had the chance to take three measurements with 2 cup exchanges: empty, ND and empty cup a second time. The reason to plan the first two in the same day was to prevent as much as possible any source of instability, e.g. changes in the accelerator parameters. Unfortunately, even these measurements were not flawless in terms of stability. During the first shut down to exchange the cup, the moderator cooling control system crashed and the moderator warmed up to 70 K, but the methane mass flow was still 0, so most likely it was still frozen by the time it was brought back to 22 K for ND cup runs. After 9 runs with the ND cup, we noticed that the moderator temperature was once again rising up to 24 K because the He flow was getting smaller. This caused a systematic drift in the different ND runs that produced, by the time of the last run, 4% less counts integrated above  $5 \text{ \AA}$ . For this reason, we decided to keep only the first 20 min run, the closest to the nominal temperature of 22 K. For the second cup exchange, we decided to put back the empty cup to rule out any possible spurious contribution from the first re-cooling of the day. The results for both the empty cups and the ND cup are presented in Figure 342. The ratio between the empty cups in Figure 342d suggests that the two measurements are not equivalent and the unexpected warm up had, indeed, a negative effect on the initial conditions. In particular, the same trend is also visible when the ND cup signal is compared with the first empty cup. In this regard, the ratio between the signals from

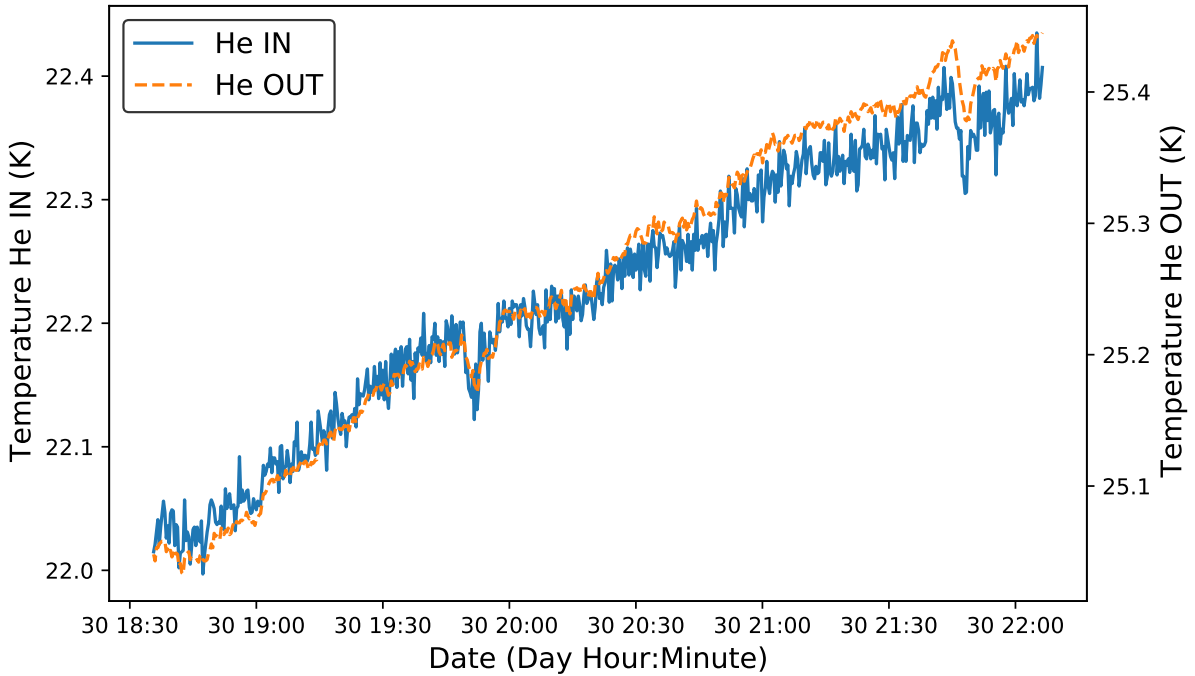


**Figure 340:** Variation of the He temperature flowing IN and OUT of the moderator during the empty cup measurement on Day 1.

the first ND run and the second empty cup is probably the most reliable. The lower statistic, resulting from keeping only the first ND run, does not allow to measure any statistically significant effect above the unity. Thus, we could not confirm the result from the first days (Figure 341d).

**Magnesium hydride cup** The cup with the MgH<sub>2</sub> was put right before the accelerator ion cup broke. After the exchange and the restart of the accelerator, many tests were conducted on the accelerator parameters. The inconsistencies we report in Figure 343, where we assume that the average is given by the first run only, are most likely due to an unsettled accelerator pulse that lasted for the whole measurements. Unfortunately, we were not able to catch it on time to find a solution. Thus, we conclude that the ratio with the first Empty cup signal taken on Day 5 would not be meaningful.

**Polyethylene cup** The PE cup inserted on Day 4 benefited from stable accelerator conditions that remained until the next day when we measured with the first Empty cup on Day 5. However, toward the end of the day the cooling control system crashed, and the moderator melted. After the restart of the system and the slow cooling of the source back to 22 K, we were able to collect one more 20-min-long run. The spectrum from this run was still distinctively a warm-up spectrum, so it is not considered for the average value. Early in the morning the next day, a quick run before the shut down with the accelerator at 10 Hz and 1 ms was acquired and compared with the equivalent short runs of day before, showing good agreement. This suggests that the cooling process was most likely not over by the time of the last measurement, but it eventually reached the starting point over the course of the evening. Hence, the most reliable set of the data we have is the one taken before the melting of the moderator. However, the results shown in Figure 344, and in particular Figures 344c and 344d, suggests that the polyethylene cup uniformly increases the thermal and cold production of the source by 15%. Due to its hydrogen content, the removal of pre-moderation material in an intense high-energy neutron field to accommodate an advanced reflector is a key factor to take into account.

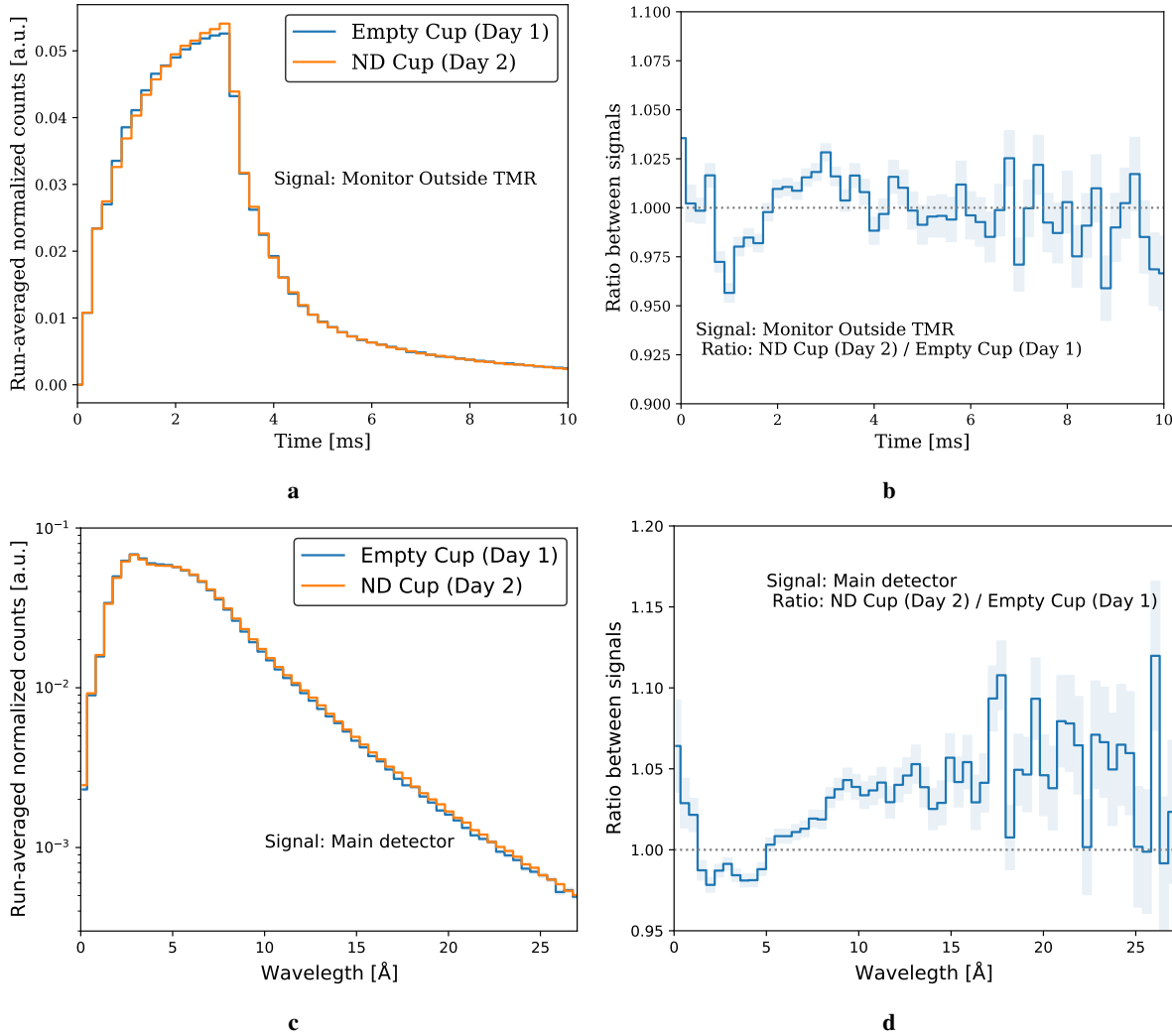


**Figure 341:** Run-averaged normalized counts and ratio between signals: (a) and (b) Monitor inside the TMR area, (c) and (d) main detector for the ND cup and Empty cup cases. The signal from the main detector is re-binned by a factor 4 (0.46 \AA).

### 11.3.5 Discussion

The experimental campaign at the HiCANS test station was part of a series of efforts by HighNESS to characterize the advanced reflectors. The models we have developed and used in the simulations so far confirmed their promising application to cold, very cold and ultra-cold neutron sources. The experiment, first attempt to verify these effects, was not originally part of the HighNESS plan and it was arranged at the eleventh hour when the opportunity arose. The insights we had gained from the design of the experiment at BNC were transposed to the setup for the test station, but the impromptu decision made it hard to perform an in-depth study beforehand. This fact may have contributed to have inconclusive results from the beamtime. Nevertheless, this experience allows us to pin down the technical criticality involved in performing this kind of experiment and possible improvements:

- The stability of the source should certainly be the first concern, in terms of both the accelerator and moderator. A careful examination of the options has to take into account how to minimize the risk of disruptions and malfunctioning. In order to quantify the stability sought, the setup can be studied beforehand with simulations that include the relevant features;
- the monitoring of stability of the systems can be improved with a calibrated measures of the accelerator pulse and a reliable temperature control system;
- The procedure of exchanging the cup required long shutdown/restart time of the facility. An

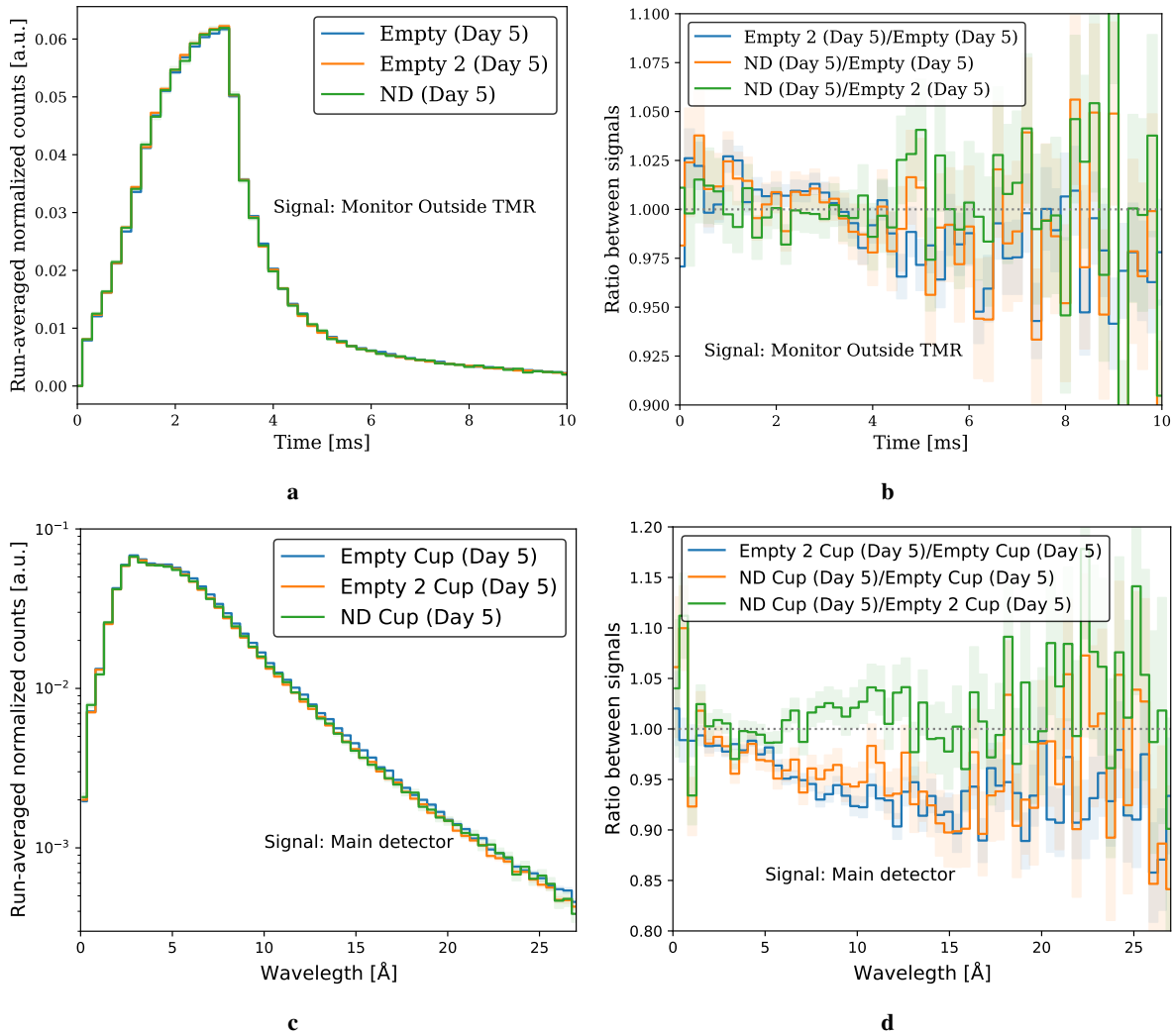


**Figure 342:** Run-averaged normalized counts and ratio between signals: (a) and (b) Monitor inside the TMR area, (c) and (d) main detector for the ND cup and Empty cups cases of Day 5. The signal from the main detector is re-binned by a factor 4 (0.46 Å).

out-of-pile source may possibly be advantaged in this regard, but background could become a problem. Minimizing the exchanges and maximizing the time window for each measurement would be undoubtedly beneficial;

- Studying the possibility of compressing the powder inside the cups, or inserting bigger cups, would increase the relative effect, hence relaxing the requirements on the stability. This contribution should also be investigated with appropriate simulations;
- In order to understand better the limits of application, it would be interesting to test the cup concept in an in-beam setup with a pure cold source. This setup can possibly highlight better the properties of the advanced reflector over common hydrogen-rich materials, e.g. polyethylene, which can almost in all cases provide higher hydrogen density than advanced reflector powders. While this is undoubtedly advantageous for an in-pile source in high-energy neutron field, a pure cold beam could emphasize the reflector properties without the premoderator component.

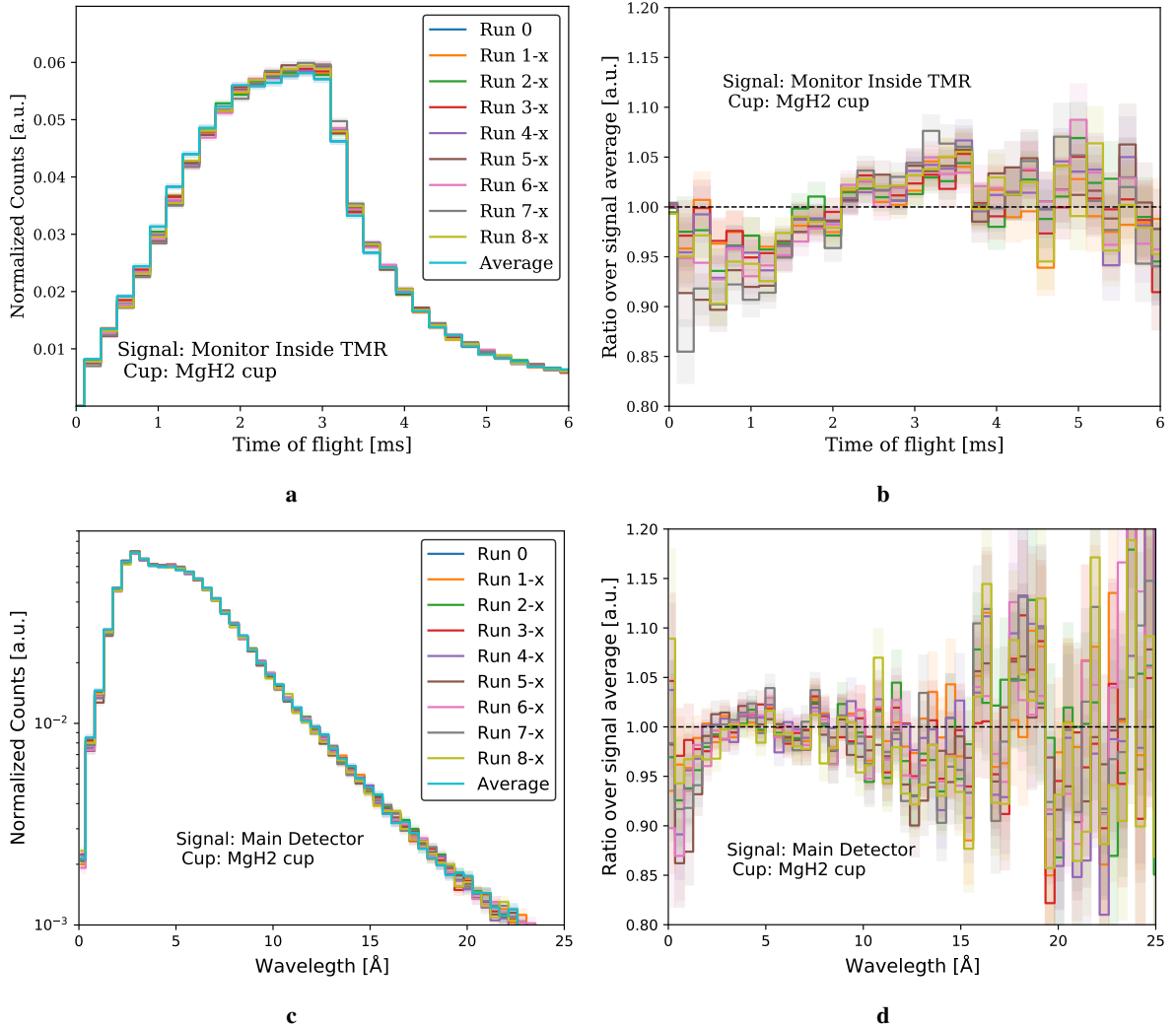


**Figure 343:** Normalized counts for each run and ratio over average for the MgH<sub>2</sub> cup measurement for: (a) and (b) Monitor inside the TMR area, (c) and (d) main detector. The signal from the main detector is re-binned by a factor 4 (0.46 Å). Only the first run is used for the average, so all the other runs are marked by an x.

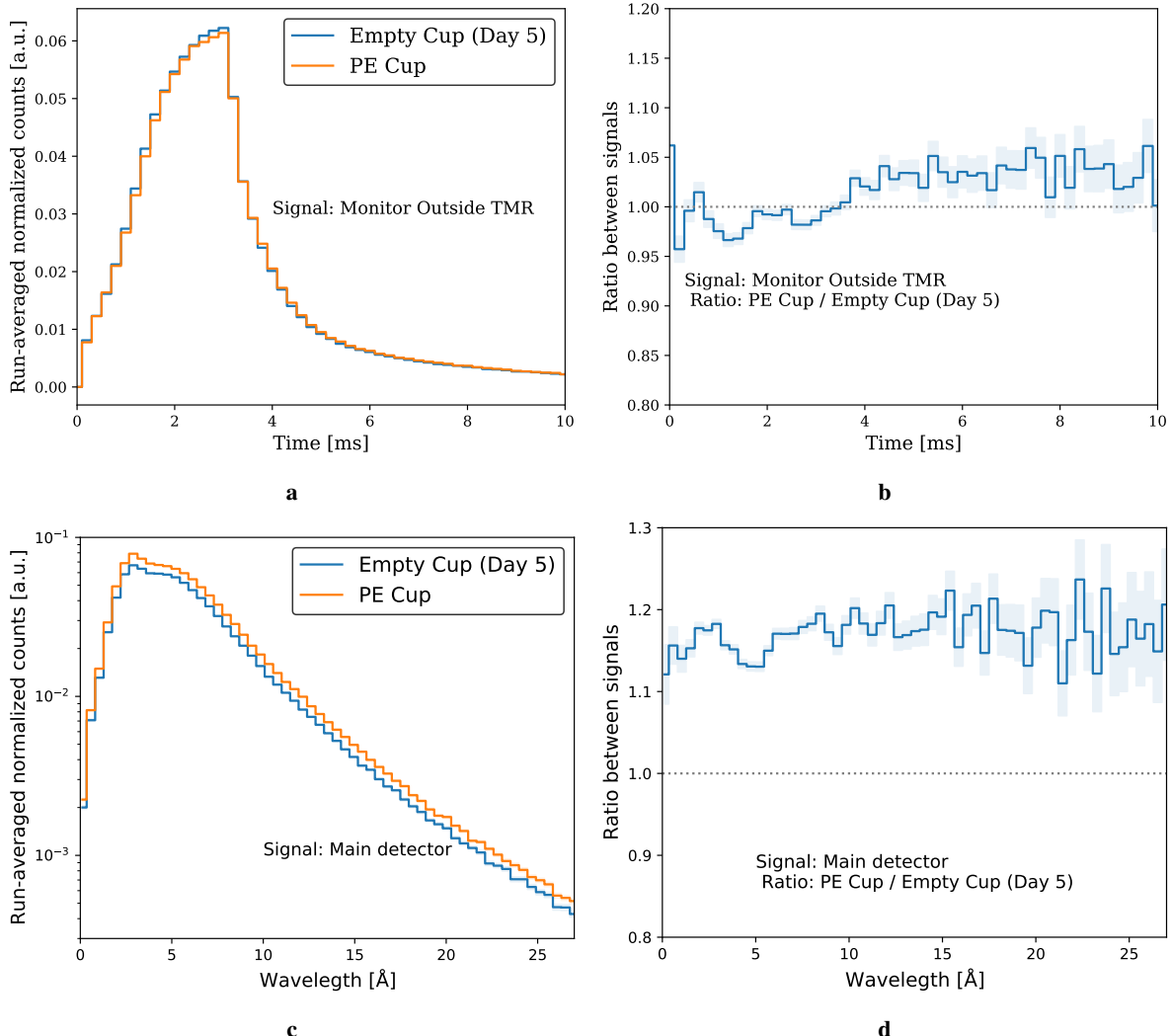


**Figure 344:** Run-averaged normalized counts and ratio between signals: (a) and (b) Monitor inside the TMR area, (c) and (d) main detector for the PE cup and first Empty cup case of Day 5. The signal from the main detector is re-binned by a factor 4 (0.46  $\text{\AA}$ ).

## 12 Conclusions

The primary goal of the HighNESS project was the design of a second neutron source to complement the high-brightness bi-spectral source which is placed above the spallation target and serves all the neutron scattering instruments of the initial suite planned for ESS. To achieve this objective, the HighNESS project outlined a scientific case in its proposal, encompassing various neutron scattering techniques and including the NNBAR experiment, which aims to detect neutron to antineutron oscillation.

At the heart of the project is the design of a high-intensity cold source, which will directly serve instruments and experiments, but also secondary VCN and UCN sources. Without a source delivering at least several times the intensity of the upper moderator, it would not be possible to achieve the ambitious scientific goals outlined in the proposal. The choice of liquid deuterium, used for decades at reactors and continuous spallation sources, was confirmed to be the only viable option for such a source. The final design is able to deliver an intensity above 4 Å of a factor of 10 greater than the upper moderator, thus exceeding the proposal expectations. This remarkable outcome is crucial for enabling the NNBAR experiment to reach its anticipated sensitivity levels, as discussed further below. Additionally, the cold source features an extended emission surface compared to the upper moderator. This property has been duly exploited in the design of novel SANS and imaging instruments that will complement and outperform the ones under construction at ESS (see below).

The design of the cold source was an iterative process between the neutronic and engineering teams. A detailed engineering study of the cold moderator was performed including stress analysis and fluid dynamics simulations, to operate and cool the liquid deuterium, the aluminum structure and the cold beryllium filter that increases the cold flux for NNBAR. The design was reviewed by an international team of experts. However a few further investigations are recommended, which are detailed at the end of Section 3.

To guide the optimization of the cold source, the HighNESS project included a design of a small suite of conceptual instruments that takes advantage of the increased source intensity. The suite included two SANS instruments – one using a conventional design and one based on focusing with Wolter optics – as well as an imaging instrument. The performance of these instruments were evaluated with different proposed models for the source, and the results were considered when deciding which source models to pursue further. With the current design of the cold source it was found that the Wolter optics based SANS instrument in particular would have world-leading capabilities with impressive flux, bandwidth, minimum  $Q$ , and resolution simultaneously. The larger source also allowed for a simple pinhole imaging beamline that would have a large homogeneous field of view, still offering modest wavelength resolution for advanced imaging techniques, and thus complementing the ESS instrument ODIN, which is under construction.

In addition to the cold source developments, the HighNESS project aimed to ambitiously extend the range of available neutrons for ESS users into the VCN and UCN ranges. The project achieved significant results in both of these areas. Let's first discuss the VCNs.

The desire for an intense source of VCNs has been a longstanding aspiration within the user community, spanning at least two decades. The realization of such a source has faced challenges primarily due to the lack of knowledge regarding the properties of low-temperature materials, which were considered the most promising candidates for such a source. To enable reliable Monte Carlo simulations and, consequently, the design of a neutron source, the availability of thermal scattering cross-section libraries is essential. In the HighNESS project, these libraries were developed for candidate VCN moderator and reflector materials, including deuterated clathrate hydrates and nanodiamonds. Additionally, new libraries for solid deuterium were developed through collaboration with another EU program called EURIZON. The development of these libraries stands as a significant achievement within the HighNESS project. It can be deemed a major breakthrough in the field of source design. HighNESS has not only created these thermal scattering libraries but also made them readily accessible to the community, adhering to the open-source policy outlined in the project proposal. This step was taken to ensure the wider dissemination of the project's outcomes. This contribution unfolded during a period of notably vibrant development, partly due to recent advancements in compact neutron source design.

Thanks to these developments, it was possible to tackle the task of designing a VCN source. The results were very compelling. As in the case of the cold source development, another *factor of 10* manifested: this time, it is the increase in the brightness for neutrons above 40 Å, compared to the brightness of a conventional cold source placed in the same location below the spallation target. Such a breakthrough is due to the use of solid deuterium at 5 K, in combination with nanodiamonds, and to its reduced upscattering of VCNs, compared to liquid deuterium at 22 K which is used for the intense cold source. If duly exploited, this type of dedicated VCN could be a game changer for several neutron scattering techniques such as SANS and spin-echo. However, both SANS and spin-echo beamlines using a VCN source would need optics that counteract the effects of gravity. Such systems were already investigated as a part of the project and highly encouraging results were obtained with focusing optics corrected by prisms.

The scientific case, along with general design concepts for VCN and UCN sources, underwent extensive discussions during two dedicated workshops organized at ESS by HighNESS in collaboration with the League of European Neutron Sources (LENS). These workshops saw active participation from over 100 members of the community. One of the most encouraging outcomes of these workshops was the multitude of ideas generated for UCN sources at ESS. This not only underscores the potential that ESS offers but also validates the feasibility of the upgrade paths explored by HighNESS. Following the workshop's directions, the HighNESS team conducted neutronic design studies for most of the proposed UCN source options. Both in-pile and in-beam designs were considered, utilizing two commonly used materials for UCN production: solid deuterium and superfluid helium. The results have been highly promising, positioning ESS for a world-leading UCN source.

The choice of the optimal UCN source for ESS depends on various factors, including technical feasibility (e.g., cooling of the source and UCN extraction) and the integration of the three source categories developed in HighNESS. The project explored at least eight potential integration options for CN, VCN, and UCN sources, as discussed in detail in Section 7. These options should be subject to further study and development in future projects, and they represent a valuable legacy of the HighNESS project.

To achieve its goals, the HighNESS project also conducted an extensive experimental program. This program involved the measurement of cross sections for various materials relevant to the project, with a particular focus on clathrate hydrates and graphite compounds. These measurements were conducted at facilities such as ILL (using the IN5 and PANTHER beamlines) and PSI (utilizing the BOA beamline).

Another aspect of the experimental program involved the measurement of prototype advanced reflectors designed to enhance the VCN flux, as outlined in the HighNESS proposal. In this case, a significant challenge arose due to the limited availability of operational facilities where prototype measurements could be conducted. At the time the proposal was written, there was only one such facility, which was the LENS facility in Indiana. Unfortunately, this facility shut down at the beginning of the HighNESS project. Another facility under development was located at the Budapest Neutron Center, and the HighNESS project provided strong support for its development. As part of this effort, the project organized a collaborative measurement involving a cold moderator with advanced reflectors made of nanodiamonds and MgH<sub>2</sub>. However, it is important to note that this moderator test facility was still in the developmental phase throughout the duration of the HighNESS project. During this time, only preliminary measurements involving dose rates and background were conducted using an ambient water moderator. The project team remains hopeful that the planned tests can be carried out in the near future once the facility reaches full operational capacity. Another facility that came online recently (December 2022) is the JULIC Neutron Platform in Forschungszentrum Jülich. The HighNESS team had the opportunity to perform a first pilot measurement of a simplified setup of the Budapest measurement.

Regarding the NNBAR experiment, in the HighNESS proposal and in the NNBAR white paper, it was suggested that NNBAR could achieve a sensitivity compared to the previous search that is 1000 times higher, with ESS operating at 5 MW power. This estimate was based on a very preliminary study that did not take into account the ESS design and engineering constraints, which typically tend to decrease sensitivity. However, thanks to the developments in the HighNESS project, including the design of a top-performing cold source, nested mirror optics, and detector studies, the NNBAR collaboration is able

to achieve the proposed sensitivities at 2 MW power instead of 5 MW. Furthermore, at 5 MW power, the expected sensitivities have more than doubled. Further studies on background levels and the development of prototype experiments are required to establish that this sensitivity improvement can be realized.

Finally, in addition to delivering outstanding results as promised in the proposal, the HighNESS consortium has devoted considerable time and effort to training young scientists, including both Ph.D. students and postdoctoral researchers. This training involved not only supervisory roles but also dedicated activities such as organizing the first International School on Thermal Neutron Scattering Kernel Generation, which took place at ESS from May 22 to May 26, 2023 and attracted 40 participants worldwide.

## 13 Outlook

There are a number of developments recommended to fully capitalize on the success of the HighNESS project, and some of them have already been hinted in the previous section.

**Source design.** One aspect concerns the technical challenges related to operating the sources at the high power of ESS. ESS will operate for many years at 2 MW, with an eventual upgrade to 5 MW. The liquid deuterium moderator will most likely operate at 2 MW but currently, there is no design that can guarantee its functionality at 5 MW. Toward the conclusion of the HighNESS project, the design was significantly simplified, including a simpler shape for the reentrant hole and fewer flow channels inside the vessel. However, further work is required in this area to develop a high-performing design that can operate reliably at 5 MW.

For a solid deuterium moderator the situation is even more uncertain, since such a moderator has never been operated at the MW power level. We have identified and started to investigate some possible engineering solutions however the development of a VCN source capable of operating in a high radiation environment, would require a major R&D program.

**Instrument design.** A successful design of a VCN source should be accompanied by a dedicated design of experiments using VCN beams. In fact, most of the instrument design in HighNESS concerned the high intensity cold neutron beams delivered by the liquid deuterium moderator. The study of an optics system to transport VCNs and counteract the effect of gravity mentioned above showed promising results, and could be the basis to begin designing dedicated VCN instruments for neutron scattering. The design of NNBAR with VCN should also be investigated as also a dedicated VCN fundamental physics program.

**Experimental program.** HighNESS has provided major input toward the development of new facilities to test moderators, in particular the moderator test facility at the Budapest Research Center and the Big Karl facility in Jülich. A key necessary step in the continuation of the research initiated by HighNESS would be the realization of prototypes of VCN sources based on solid deuterium and nanodiamonds, as well as deuterated clathrate hydrates. Prior to the implementation of such prototypes in the in-pile positions of the aforementioned moderator test facilities, characterization with cold and very cold neutron beams are envisaged. Suitable sites for such investigations are the cold neutron beam facility PF1B and the very cold neutron beam of PF2 at the ILL.

**Measurement and calculation of cross sections.** HighNESS has established a process to calculate thermal scattering libraries and perform experimental validations. More developments are certainly recommended to deepen the experimental and theoretical knowledge of such materials, as well as to support the inclusion of these materials in Monte Carlo simulations. Notable examples are the measurement of the cross sections of solid deuterium at 5 K for VCNs, and superfluid helium below 1 K for UCNs. Furthermore, measurements on binary clathrate hydrates, hosting both fully deuterated THF and molecular oxygen are needed to benchmark the developed scattering kernels for these compounds.

## **14 Acknowledgements**

We would like to acknowledge the Paul Scherrer Institute for access to beam time at the facility under proposal numbers 20212829, 20221100 and 20222657. We acknowledge MAX IV Laboratory for time on Beamline COSAXS under Proposal 20221553. Research conducted at MAX IV, a Swedish national user facility, is supported by the Swedish Research council under contract 2018-07152, the Swedish Governmental Agency for Innovation Systems under contract 2018-04969, and Formas under contract 2019-02496. We would also like to acknowledge the support by ILL services in performing the experiments carried out there. We would also like to thank the ESS Manufacturing Workshop and the ESS sample environment group for machining the triaxial and cylindrical sample holders. HighNESS is funded by the European Union Framework Programme for Research and Innovation Horizon 2020, under grant agreement 951782

## References

- [1] Roland Garoby et al. “The European Spallation Source Design”. In: *Physica Scripta* 93.1 (Dec. 2017), p. 014001. DOI: 10.1088/1402-4896/aa9bff. URL: <https://doi.org/10.1088/1402-4896/aa9bff>.
- [2] “The ESS instrument suite, a capability gap analysis”. 2018. URL: <https://europeanspallationsource.se/instruments/capability-gap-analysis>.
- [3] L. Zanini et al. “Neutronic Design of the Bunker Shielding for the European Spallation Source”. In: *Journal of Surface Investigation: X-ray, Synchrotron and Neutron Techniques* 14.1 (2020), S251–S253. DOI: 10.1134/S1027451020070538.
- [4] A. Addazi et al. “New high-sensitivity searches for neutrons converting into antineutrons and/or sterile neutrons at the HIBeam/NNBAR experiment at the European Spallation Source”. In: *Journal of Physics G: Nuclear and Particle Physics* 48.7 (June 2021), p. 070501.
- [5] F. Backman et al. “The development of the NNBAR experiment”. In: *Journal of Instrumentation* 17.10 (Oct. 2022), P10046. DOI: 10.1088/1748-0221/17/10/P10046. URL: <https://dx.doi.org/10.1088/1748-0221/17/10/P10046>.
- [6] V. Santoro et al. “Development of high intensity neutron source at the European Spallation Source”. In: *Journal of Neutron Research* 22.2-3 (2020), pp. 209–219. DOI: <https://doi.org/10.3233/JNR-200159>.
- [7] V. Santoro et al. “The HighNESS Project at the European Spallation Source: Current Status and Future Perspectives”. In: *Nuclear Science and Engineering* 0.0 (2023), pp. 1–33. DOI: 10.1080/00295639.2023.2204184. eprint: <https://doi.org/10.1080/00295639.2023.2204184>. URL: <https://doi.org/10.1080/00295639.2023.2204184>.
- [8] T. Goorley et al. “Initial MCNP6 release overview. MCNP6 version 0.1”. In: *Nuclear technology* 180 (Dec. 2012), pp. 298–315. DOI: 10.13182/NT11-135.
- [9] Zanini, L., Takabayev, L., Klinkby, L., Kokai, L., Marquez-Damian, J. I., Ramic, K., Rizzi, N., Santoro, V., Samothrakitis, S., Wagner, R., Zimmer, O. *Baseline document with figure of merit to be used in the moderator design*. HighNESS Deliverable 4.1. 2021.
- [10] E. Dian et al. *HighNESS Deliverable 4.2: Neutronic design of the liquid deuterium moderator*. HighNESS Deliverable 4.2. 2022.
- [11] K. H. et al. Andersen. “The Instrument Suite of the European Spallation Source”. In: *Nucl.Instr.Meth.* 957 (2020), p. 163402.
- [12] Carpenter and Loong. *Elements of slow-neutron scattering*. Cambridge University Press., 2016.
- [13] J. Goorley, Michael James, et al. *Initial MCNP6 Release Overview*. Tech. rep. LA-UR-13-22934. Los Alamos National Laboratory, 2013.
- [14] K. Lefmann and K. Nielsen. “McStas, a general software package for neutron ray-tracing simulations”. English. In: *Neutron News* 10.3 (1999), pp. 20–23. ISSN: 1044-8632.
- [15] Thomas Kittelmann et al. “Monte Carlo Particle Lists: MCPL”. In: *Comput. Phys. Commun.* 218 (2017), pp. 17–42. DOI: 10.1016/j.cpc.2017.04.012. arXiv: 1609.02792 [physics.comp-ph].
- [16] A. P. Serebrov et al. “The Project of Ultracold Neutron Sources at the PIK Reactor with Superfluid Helium as a Moderator”. In: *Technical Physics Letters* 40.1 (Jan. 2014), pp. 10–12. ISSN: 1063-7850, 1090-6533. DOI: 10.1134/S1063785014010118. URL: <http://link.springer.com/10.1134/S1063785014010118> (visited on 09/08/2021).
- [17] Albert Steyerl. *Ultracold Neutrons*. World Scientific, May 2020. ISBN: 9789811212727.
- [18] B.M. Adams et al. *Dakota, A Multilevel Parallel Object-Oriented Framework for Design Optimization, Parameter Estimation, Uncertainty Quantification, and Sensitivity Analysis: Version 6.18 User’s Manual*. Sandia Technical Report SAND2020-12495. May 2023.
- [19] L. Zanini et al. “Design of the cold and thermal neutron moderators for the European Spallation Source”. en. In: *Nuclear Instruments and Methods in Physics Research Section A: Accelerators, Spectrometers, Detectors and Associated Equipment* 925 (May 2019), pp. 33–52. ISSN: 0168-9002. DOI: 10.1016/j.nima.2019.01.003. URL: <http://www.sciencedirect.com/science/article/pii/S0168900219300087> (visited on 11/11/2020).
- [20] Esben Klinkby et al. *Voluminous D2 source for intense cold neutron beam production at the ESS*. 2014. arXiv: 1401.6003 [physics.ins-det].
- [21] M. Baldo-Ceolin et al. “A New experimental limit on neutron - anti-neutron oscillations”. In: *Z. Phys. C* 63 (1994), pp. 409–416. DOI: 10.1007/BF01580321.
- [22] Tadahiko Murata, Hisao Ishibuchi, et al. “MOGA: multi-objective genetic algorithms”. In: *IEEE international conference on evolutionary computation*. Vol. 1. IEEE Piscataway. 1995, pp. 289–294.

- [23] R. Wagner et al. “Design of an optimized nested-mirror neutron reflector for a NNBAR experiment”. In: *Nuclear Instruments and Methods in Physics Research Section A: Accelerators, Spectrometers, Detectors and Associated Equipment* 1051 (2023), p. 168235. ISSN: 0168-9002. DOI: <https://doi.org/10.1016/j.nima.2023.168235>. URL: <https://www.sciencedirect.com/science/article/pii/S0168900223002255>.
- [24] V. Santoro et al. “The HighNESS Project at the European Spallation Source: Current Status and Future Perspectives”. In: *Nuclear Science and Engineering* 0.0 (2023), pp. 1–33. DOI: 10.1080/00295639.2023.2204184. eprint: <https://doi.org/10.1080/00295639.2023.2204184>. URL: <https://doi.org/10.1080/00295639.2023.2204184>.
- [25] “Development of High Intensity Neutron Source at the European Spallation Source, Proposal”. In: (2019).
- [26] Inc Ansys. *ANSYS CFX-Solver Theory Guide*. 2023R2. Canonsberg, PA: ANSYS, 2023.
- [27] John M. Carpenter and Bradley J. Micklich. “Proceedings of the Workshop on Applications of a Very Cold Neutron Source”. In: (Dec. 2005). URL: <https://www.osti.gov/biblio/1248367>.
- [28] Ferenc Mezei. “Very cold neutrons in condensed matter research”. In: *Journal of Neutron Research* 24.2 (2022), pp. 250–210. DOI: 10.3233/JNR-220012.
- [29] Florian M. Piegsa. “New concept for a neutron electric dipole moment search using a pulsed beam”. In: *Phys. Rev. C* 88 (4 Oct. 2013), p. 045502. DOI: 10.1103/PhysRevC.88.045502. URL: <https://link.aps.org/doi/10.1103/PhysRevC.88.045502>.
- [30] Florian M. Piegsa. “Novel concept for a neutron electric charge measurement using a Talbot-Lau interferometer at a pulsed source”. In: *Phys. Rev. C* 98 (4 Oct. 2018), p. 045503. DOI: 10.1103/PhysRevC.98.045503. URL: <https://link.aps.org/doi/10.1103/PhysRevC.98.045503>.
- [31] H. Abele et al. “Particle physics at the European Spallation Source”. In: *Physics Reports* 1023 (2023). Particle Physics at the European Spallation Source, pp. 1–84. ISSN: 0370-1573. DOI: <https://doi.org/10.1016/j.physrep.2023.06.001>. URL: <https://www.sciencedirect.com/science/article/pii/S0370157323001898>.
- [32] Florian M. Piegsa and Guillaume Pignol. “Limits on the Axial Coupling Constant of New Light Bosons”. In: *Physical Review Letters* 108.18 (May 2012), p. 181801. ISSN: 0031-9007, 1079-7114. DOI: 10.1103/PhysRevLett.108.181801. URL: <https://link.aps.org/doi/10.1103/PhysRevLett.108.181801> (visited on 04/12/2023).
- [33] J. S. Nico et al. “Measurement of the neutron lifetime by counting trapped protons in a cold neutron beam”. In: *Phys. Rev. C* 71 (5 May 2005), p. 055502. DOI: 10.1103/PhysRevC.71.055502. URL: <https://link.aps.org/doi/10.1103/PhysRevC.71.055502>.
- [34] A. T. Yue et al. “Improved Determination of the Neutron Lifetime”. In: *Phys. Rev. Lett.* 111 (22 Nov. 2013), p. 222501. DOI: 10.1103/PhysRevLett.111.222501. URL: <https://link.aps.org/doi/10.1103/PhysRevLett.111.222501>.
- [35] Stephan Paul. “The puzzle of neutron lifetime”. In: *Nuclear Instruments and Methods in Physics Research Section A: Accelerators, Spectrometers, Detectors and Associated Equipment* 611.2-3 (Dec. 2009), pp. 157–166. DOI: 10.1016/j.nima.2009.07.095. URL: <https://doi.org/10.1016%2Fj.nima.2009.07.095>.
- [36] A Addazi et al. “New high-sensitivity searches for neutrons converting into antineutrons and/or sterile neutrons at the HIBeam/NNBAR experiment at the European Spallation Source”. In: *Journal of Physics G: Nuclear and Particle Physics* 48.7 (June 2021), p. 070501. DOI: 10.1088/1361-6471/abf429. URL: <https://dx.doi.org/10.1088/1361-6471/abf429>.
- [37] Valery Nesvizhevsky. “Why very cold neutrons could be useful for neutron-antineutron oscillation searches”. In: *Journal of Neutron Research* 24.2 (2022). Publisher: IOS Press, pp. 223–227. ISSN: 1023-8166. DOI: 10.3233/JNR-220003. URL: <https://content.iospress.com/articles/journal-of-neutron-research/jnr220003> (visited on 06/04/2023).
- [38] K. Eder et al. “The new very-cold-neutron optics facility at ILL”. In: *Nuclear Instruments and Methods in Physics Research Section A: Accelerators, Spectrometers, Detectors and Associated Equipment* 284.1 (1989), pp. 171–175. ISSN: 0168-9002. DOI: [https://doi.org/10.1016/0168-9002\(89\)90273-8](https://doi.org/10.1016/0168-9002(89)90273-8). URL: <https://www.sciencedirect.com/science/article/pii/0168900289902738>.
- [39] H. Rauch and Samuel A. Werner. *Neutron interferometry : lessons in experimental quantum mechanics, wave-particle duality, and entanglement*. eng. 2nd ed. Oxford: Oxford University Press, 2015. ISBN: 9780191780813.
- [40] R. Colella, A. W. Overhauser, and S. A. Werner. “Observation of Gravitationally Induced Quantum Interference”. In: *Phys. Rev. Lett.* 34 (23 June 1975), pp. 1472–1474. DOI: 10.1103/PhysRevLett.34.1472. URL: <https://link.aps.org/doi/10.1103/PhysRevLett.34.1472>.
- [41] G van der Zouw et al. “Aharonov–Bohm and gravity experiments with the very-cold-neutron interferometer”. In: *Nuclear Instruments and Methods in Physics Research Section A* 440.3 (2000), pp. 568–574. ISSN: 0168-9002. DOI: [https://doi.org/10.1016/S0168-9002\(99\)01038-4](https://doi.org/10.1016/S0168-9002(99)01038-4). URL: <https://www.sciencedirect.com/science/article/pii/S0168900299010384>.

- [42] J. Klepp et al. “Diffraction of slow neutrons by holographic SiO<sub>2</sub> nanoparticle-polymer composite gratings”. In: *Phys. Rev. A* 84 (1 July 2011), p. 013621. DOI: 10.1103/PhysRevA.84.013621. URL: <https://link.aps.org/doi/10.1103/PhysRevA.84.013621>.
- [43] J. Baumann et al. “Experimental limit for the charge of the free neutron”. In: *Phys. Rev. D* 37 (11 June 1988), pp. 3107–3112. DOI: 10.1103/PhysRevD.37.3107. URL: <https://link.aps.org/doi/10.1103/PhysRevD.37.3107>.
- [44] Florian M. Piegsa. “Novel concept for a neutron electric charge measurement using a Talbot-Lau interferometer at a pulsed source”. In: *Phys. Rev. C* 98 (4 Oct. 2018), p. 045503. DOI: 10.1103/PhysRevC.98.045503. URL: <https://link.aps.org/doi/10.1103/PhysRevC.98.045503>.
- [45] A. G. Klein and A. Zeilinger. “WAVE OPTICS WITH COLD NEUTRONS”. eng. In: *Journal de Physique Colloques* 45.C3 (1984), pp. C3-239–C3-242. ISSN: 0449-1947.
- [46] Ferenc Mezei. “Very cold neutrons in condensed matter research”. en. In: *Journal of Neutron Research* 24.2 (Jan. 2023), pp. 205–210. ISSN: 14772655, 10238166. DOI: 10.3233/JNR-220012. URL: <https://www.medra.org/servlet/aliasResolver?alias=iospress&doi=10.3233/JNR-220012> (visited on 04/12/2023).
- [47] D.S. Hussey et al. “Design of a neutron microscope based on Wolter mirrors”. In: *Nuclear Instruments and Methods in Physics Research Section A: Accelerators, Spectrometers, Detectors and Associated Equipment* 987 (2021), p. 164813. ISSN: 0168-9002. DOI: <https://doi.org/10.1016/j.nima.2020.164813>. URL: <https://www.sciencedirect.com/science/article/pii/S0168900220312109>.
- [48] D.F.R. Mildner and M.V. Gubarev. “Wolter optics for neutron focusing”. In: *Nuclear Instruments and Methods in Physics Research Section A: Accelerators, Spectrometers, Detectors and Associated Equipment* 634.1, Supplement (2011). Proceedings of the International Workshop on Neutron Optics NOP2010, S7–S11. ISSN: 0168-9002. DOI: <https://doi.org/10.1016/j.nima.2010.06.093>. URL: <https://www.sciencedirect.com/science/article/pii/S0168900210012830>.
- [49] Adam Kubec et al. “An achromatic X-ray lens”. en. In: *Nature Communications* 13.1 (Mar. 2022). Number: 1 Publisher: Nature Publishing Group, p. 1305. ISSN: 2041-1723. DOI: 10.1038/s41467-022-28902-8. URL: <https://www.nature.com/articles/s41467-022-28902-8> (visited on 06/29/2023).
- [50] Frédéric Ott. “Opportunities in the use of Very Cold Neutrons in reflectometry techniques”. In: *Journal of Neutron Research* 24 (2022), pp. 211–221.
- [51] V. Santoro et al. “Workshop on very cold and ultra cold neutron sources for ESS”. In: *Journal of Neutron Research* (2022), pp. 73–75.
- [52] Valery Nesvizhevsky. “Why very cold neutrons could be useful for neutron-antineutron oscillation searches”. In: *Journal of Neutron Research* (2022), pp. 223–227.
- [53] F.X. Gallmeier et al. “Options for a very cold neutron source for the second target station at SNS”. In: *Journal of Physics Conference Series* 1021(1) (2018), p. 012083.
- [54] M. Huerta Parajon, and Bermejo F. J. “A review of the cold neutron moderator materials: neutronic performance and radiation effects”. In: *Physics Procedia* 60 (2014), p. 74.
- [55] O. Zimmer. “Neutron conversion and cascaded cooling in paramagnetic systems for a high-flux source of very cold neutrons”. In: *Phys. Rev. C* 93 (2016), p. 035503.
- [56] H. Conrad et al. “Inelastic scattering and spectral measurements of advanced cold moderator media”. In: *Physica B* 350 (2004), e647.
- [57] A. Frei. “The Source for Ultra-Cold Neutrons at the FRM II, these proceedings”. In.
- [58] Wolfgang Bernnat, Jürgen Keinert, and Margarete Mattes. “Evaluation of Scattering Laws and Cross Sections for Calculation of Production and Transport of Cold and Ultracold Neutrons”. In: *Proceedings of the 6th International Workshop on Advanced Cold Moderators, Jülich, Sept 11-13, 2002*. 2004.
- [59] Wolfgang Bernnat, Jürgen Keinert, and Margarete Mattes. “Scattering laws and cross sections for moderators and structure materials for calculation of production and transport of cold and ultracold neutrons”. In: *Journal of Nuclear Science and Technology* 39.sup2 (2002), pp. 124–127.
- [60] JR Granada. “Neutron scattering kernel for solid deuterium”. In: *Europhysics Letters* 86.6 (2009), p. 66007.
- [61] Yunchang Shin et al. “Microscopic model for the neutron dynamic structure factor of solid methane in phase II”. In: *Nuclear Instruments and Methods in Physics Research Section A: Accelerators, Spectrometers, Detectors and Associated Equipment* 620.2 (2010), pp. 382–390. ISSN: 0168-9002. DOI: <https://doi.org/10.1016/j.nima.2010.03.109>. URL: <https://www.sciencedirect.com/science/article/pii/S0168900210006911>.
- [62] Heidrun Barnert-Wiemer. *Conceptual design of a cold methane moderator system for the European Spallation Source (ESS)*. 2002.

- [63] A Serebrov et al. “Studies of a solid-deuterium source for ultra-cold neutrons”. en. In: *Nuclear Instruments and Methods in Physics Research Section A: Accelerators, Spectrometers, Detectors and Associated Equipment* 440.3 (Feb. 2000), pp. 658–665. ISSN: 01689002. DOI: 10.1016/S0168-9002(99)01058-X. URL: <https://linkinghub.elsevier.com/retrieve/pii/S016890029901058X> (visited on 08/10/2023).
- [64] CM Lavelle et al. “Ultracold-neutron production in a pulsed-neutron beam line”. In: *Physical Review C* 82.1 (2010), p. 015502.
- [65] F Atchison et al. “Investigation of solid D<sub>2</sub>, O<sub>2</sub> and CD<sub>4</sub> for ultracold neutron production”. In: *Nuclear Instruments and Methods in Physics Research Section A: Accelerators, Spectrometers, Detectors and Associated Equipment* 611.2-3 (2009), pp. 252–255.
- [66] Tomasz Bryś. “Extraction of ultracold neutrons from a solid Deuterium source”. en. Diss., Eidgenössische Technische Hochschule ETH Zürich, Nr. 17350, 2007. Doctoral Thesis. Zürich: ETH Zurich, 2007. DOI: 10.3929/ethz-a-005540305.
- [67] Ekaterina Korobkina et al. “Growing solid deuterium for UCN production”. In: *Journal of Neutron Research* 24.2 (2022). Publisher: IOS Press, pp. 179–191. ISSN: 1477-2655. DOI: 10.3233/JNR-220010.
- [68] C. L. Morris et al. “Measurements of Ultracold-Neutron Lifetimes in Solid Deuterium”. en. In: *Physical Review Letters* 89.27 (Dec. 2002), p. 272501. ISSN: 0031-9007, 1079-7114. DOI: 10.1103/PhysRevLett.89.272501. URL: <https://link.aps.org/doi/10.1103/PhysRevLett.89.272501> (visited on 01/09/2023).
- [69] JR Granada, F Cantargi, and Jose Ignacio Marquez Damian. “Neutron cross sections libraries for methane in Phase II and solid deuterium”. In: *J. Korean Phys. Soc* 59 (2011), p. 1076.
- [70] Kemal Ramić et al. “NJOY+NCrystal: an open-source tool for creating thermal neutron scattering libraries with mixed elastic support”. In: *Nuclear Instruments and Methods in Physics Research Section A: Accelerators, Spectrometers, Detectors and Associated Equipment* 1027 (2022), p. 166227.
- [71] ESS Spallation Physics Group. *Thermal scattering files for solid deuterium*. 2022. URL: <https://git.esss.dk/spallation-physics-group/solid-deuterium>.
- [72] C-Y Liu et al. “Coherent Neutron Scattering in Polycrystalline Deuterium and its Implications for Ultracold Neutron Production”. In: *arXiv preprint arXiv:1005.1016* (2010).
- [73] Christopher John Werner et al. “MCNP Version 6.2 Release Notes”. In: (Feb. 2018). DOI: 10.2172/1419730. URL: <https://www.osti.gov/biblio/1419730>.
- [74] S. M. Chernyavsky et al. “Enhanced directional extraction of very cold neutrons using a diamond nanoparticle powder reflector”. In: *Review of Scientific Instruments* 93.12 (2022). Publisher: American Institute of Physics, p. 123302. ISSN: 0034-6748. DOI: 10.1063/5.0124833. URL: <https://aip.scitation.org/doi/10.1063/5.0124833> (visited on 04/18/2023).
- [75] A. Anghel et al. “Solid deuterium surface degradation at ultracold neutron sources”. en. In: *The European Physical Journal A* 54.9 (Sept. 2018), p. 148. ISSN: 1434-6001, 1434-601X. DOI: 10.1140/epja/i2018-12594-2. URL: <http://link.springer.com/10.1140/epja/i2018-12594-2> (visited on 01/09/2023).
- [76] Chao Zhang et al. “A Predicting Model for the Effective Thermal Conductivity of Anisotropic Open-Cell Foam”. In: *Energies* 15.16 (2022). ISSN: 1996-1073. DOI: 10.3390/en15166091. URL: <https://www.mdpi.com/1996-1073/15/16/6091>.
- [77] Ahmad Hilmi Khalid et al. “Heat conductivity and permeability of aluminium foam”. In: *IOP Conference Series: Materials Science and Engineering* 834.1 (Apr. 2020), p. 012029. DOI: 10.1088/1757-899X/834/1/012029. URL: <https://dx.doi.org/10.1088/1757-899X/834/1/012029>.
- [78] Nidia C Gallego and James W Klett. “Carbon foams for thermal management”. In: *Carbon* 41.7 (2003), pp. 1461–1466. ISSN: 0008-6223. DOI: [https://doi.org/10.1016/S0008-6223\(03\)00091-5](https://doi.org/10.1016/S0008-6223(03)00091-5). URL: <https://www.sciencedirect.com/science/article/pii/S0008622303000915>.
- [79] James W. Klett. “The role of precursor modification on the production of graphite foam”. In: *Carbon* 144 (2019), pp. 43–54. ISSN: 0008-6223. DOI: <https://doi.org/10.1016/j.carbon.2018.11.046>. URL: <https://www.sciencedirect.com/science/article/pii/S0008622318310777>.
- [80] Michio Inagaki, Yutaka Kaburagi, and Yoshihiro Hishiyama. “Thermal Management Material: Graphite”. In: *Advanced Engineering Materials* 16.5 (2014), pp. 494–506. DOI: <https://doi.org/10.1002/adem.201300418>. eprint: <https://onlinelibrary.wiley.com/doi/pdf/10.1002/adem.201300418>. URL: <https://onlinelibrary.wiley.com/doi/abs/10.1002/adem.201300418>.
- [81] Mahmoud Moeini Sede and J.M. Khodadadi. “Thermal conductivity improvement of phase change materials/graphite foam composites”. In: *Carbon* 60 (2013), pp. 117–128. ISSN: 0008-6223. DOI: <https://doi.org/10.1016/j.carbon.2013.04.004>. URL: <https://www.sciencedirect.com/science/article/pii/S0008622313002960>.

- [82] Hong Ye, Mingyang Ma, and Qing Ni. "An experimental study on mid-high temperature effective thermal conductivity of the closed-cell aluminum foam". In: *Applied Thermal Engineering* 77 (2015), pp. 127–133. ISSN: 1359-4311. DOI: <https://doi.org/10.1016/j.aplthermaleng.2014.12.029>. URL: <https://www.sciencedirect.com/science/article/pii/S1359431114011582>.
- [83] Kong Chunhui et al. "Thermal Conductivity of Open Cell Aluminum Foam and Its Application as Advanced Thermal Storage Unit at Low Temperature". In: *Rare Metal Materials and Engineering* 47.4 (2018), pp. 1049–1053. ISSN: 1875-5372. DOI: [https://doi.org/10.1016/S1875-5372\(18\)30118-8](https://doi.org/10.1016/S1875-5372(18)30118-8). URL: <https://www.sciencedirect.com/science/article/pii/S1875537218301188>.
- [84] J. W. Klett et al. "The role of structure on the thermal properties of graphitic foams". en. In: *Journal of Materials Science* 39.11 (June 2004), pp. 3659–3676. ISSN: 1573-4803. DOI: 10.1023/B:JMSC.0000030719.80262.f8. URL: <https://doi.org/10.1023/B:JMSC.0000030719.80262.f8> (visited on 06/08/2023).
- [85] Adam L. Woodcraft. "Predicting the thermal conductivity of aluminium alloys in the cryogenic to room temperature range". en. In: *Cryogenics* 45.6 (June 2005), pp. 421–431. ISSN: 0011-2275. DOI: 10.1016/j.cryogenics.2005.02.003. URL: <https://www.sciencedirect.com/science/article/pii/S0011227505000391> (visited on 06/02/2023).
- [86] Zeju Weng et al. "Cryogenic thermal conductivity of 7050 aluminum alloy subjected to different heat treatments". en. In: *Cryogenics* 116 (June 2021), p. 103305. ISSN: 0011-2275. DOI: 10.1016/j.cryogenics.2021.103305. URL: <https://www.sciencedirect.com/science/article/pii/S0011227521000631> (visited on 05/30/2023).
- [87] B. Baudouy and A. Four. "Low temperature thermal conductivity of aluminum alloy 5056". en. In: *Cryogenics* 60 (Mar. 2014), pp. 1–4. ISSN: 0011-2275. DOI: 10.1016/j.cryogenics.2013.12.008. URL: <https://www.sciencedirect.com/science/article/pii/S0011227513001252> (visited on 05/30/2023).
- [88] Adam L. Woodcraft et al. "Thermal conductivity measurements of pitch-bonded graphites at millikelvin temperatures: Finding a replacement for AGOT graphite". en. In: *Cryogenics* 49.5 (May 2009), pp. 159–164. ISSN: 0011-2275. DOI: 10.1016/j.cryogenics.2008.10.024. URL: <https://www.sciencedirect.com/science/article/pii/S0011227509000174> (visited on 05/30/2023).
- [89] Ctirad Uher. "Thermal conductivity of several exfoliated graphites from 2 k to 300 k". In: *Cryogenics* 20 (1980), pp. 445–447.
- [90] Liang Chen, Shuangtao Chen, and Yu Hou. "Understanding the thermal conductivity of Diamond/Copper composites by first-principles calculations". In: *Carbon* 148 (2019), pp. 249–257. ISSN: 0008-6223. DOI: <https://doi.org/10.1016/j.carbon.2019.03.051>. URL: <https://www.sciencedirect.com/science/article/pii/S0008622319302751>.
- [91] JAHM Software, Inc. *Material Properties Database MPDB v7.91*. North Reading, USA.
- [92] H M Roder et al. "Survey of the properties of the hydrogen isotopes below their critical temperatures". In: (Aug. 1973). URL: <https://www.osti.gov/biblio/4244810>.
- [93] E. D. Marquardt, J. P. Le, and Ray Radebaugh. "Cryogenic Material Properties Database". In: *Cryocoolers 11*. Boston, MA: Springer US, 2002, pp. 681–687. ISBN: 978-0-306-47112-4. DOI: 10.1007/0-306-47112-4\_84. URL: [https://tsapps.nist.gov/publication/get\\_pdf.cfm?pub\\_id=913059](https://tsapps.nist.gov/publication/get_pdf.cfm?pub_id=913059).
- [94] Lu Zhao et al. "A review of the coefficient of thermal expansion and thermal conductivity of graphite". In: *New Carbon Materials* 37.3 (2022), pp. 544–555. ISSN: 1872-5805. DOI: [https://doi.org/10.1016/S1872-5805\(22\)60603-6](https://doi.org/10.1016/S1872-5805(22)60603-6). URL: <https://www.sciencedirect.com/science/article/pii/S1872580522606036>.
- [95] TOULOUKIAN Y. S. "Vol.1(Thermal Conductivity-Metallic Elements and Alloys)and 4(Specific Heat-Metallic Elements and Alloys)". In: *Thermophysical Properties of Matter* (1970). URL: <https://cir.nii.ac.jp/crid/1572261548993384960>.
- [96] Ichiro Tanaka. "Refining technology and low temperature properties for high purity aluminium". In: (2013). URL: <https://www.sumitomo-chem.co.jp/english/rd/report/2013/>.
- [97] Bisma Parveez et al. "Microstructure and Mechanical Properties of Metal Foams Fabricated via Melt Foaming and Powder Metallurgy Technique: A Review". In: *Materials* 15.15 (2022). ISSN: 1996-1944. DOI: 10.3390/ma15155302. URL: <https://www.mdpi.com/1996-1944/15/15/5302>.
- [98] C. Hutter et al. "Heat transfer in metal foams and designed porous media". In: *Chemical Engineering Science* 66.17 (2011), pp. 3806–3814. ISSN: 0009-2509. DOI: <https://doi.org/10.1016/j.ces.2011.05.005>. URL: <https://www.sciencedirect.com/science/article/pii/S0009250911002995>.
- [99] C.-Y. Liu, A. R. Young, and S. K. Lamoreaux. "Ultracold neutron upscattering rates in a molecular deuterium crystal". In: *Physical Review B* 62.6 (Aug. 2000). Publisher: American Physical Society, R3581–R3583. DOI: 10.1103/PhysRevB.62.R3581. URL: <https://link.aps.org/doi/10.1103/PhysRevB.62.R3581> (visited on 01/09/2023).

- [100] E.B. Iverson and J.M. Carpenter. “Kinetics of irradiated liquid hydrogen”. In: *Conrad, H. (Ed.) ACoM-6 - 6th international workshop on advanced cold moderators Proceedings* (2004), p. 236. URL: [https://inis.iaea.org/collection/NCLCollectionStore/\\_Public/36/069/36069444.pdf?r=1](https://inis.iaea.org/collection/NCLCollectionStore/_Public/36/069/36069444.pdf?r=1).
- [101] F. Atchison et al. “Measured Total Cross Sections of Slow Neutrons Scattered by Solid Deuterium and Implications for Ultracold Neutron Sources”. In: *Physical Review Letters* 95.18 (Oct. 2005). Publisher: American Physical Society, p. 182502. DOI: 10.1103/PhysRevLett.95.182502. URL: <https://link.aps.org/doi/10.1103/PhysRevLett.95.182502> (visited on 01/09/2023).
- [102] Ingo Rienäcker. “Improving ultracold neutron yields and the search for mirror neutrons at the PSI UCN source”. en. Doctoral Thesis. Zurich: ETH Zurich, 2022. DOI: 10.3929/ethz-b-000579840.
- [103] Nicola Rizzi et al. “Benchmarking of the NCystal SANS Plugin for Nanodiamonds”. In: *Nuclear Science and Engineering* 0.0 (2023), pp. 1–9. DOI: 10.1080/00295639.2023.2196926. eprint: <https://doi.org/10.1080/00295639.2023.2196926>. URL: <https://doi.org/10.1080/00295639.2023.2196926>.
- [104] F. Atchison et al. “Diffuse reflection of ultracold neutrons from low-roughness surfaces”. en. In: *The European Physical Journal A* 44.1 (Apr. 2010), pp. 23–29. ISSN: 1434-601X. DOI: 10.1140/epja/i2010-10926-x. URL: <https://doi.org/10.1140/epja/i2010-10926-x> (visited on 01/11/2023).
- [105] R. Cubitt et al. “Quasi-specular reflection of cold neutrons from nano-dispersed media at above-critical angles”. en. In: *Nuclear Instruments and Methods in Physics Research Section A: Accelerators, Spectrometers, Detectors and Associated Equipment* 622.1 (Oct. 2010), pp. 182–185. ISSN: 0168-9002. DOI: 10.1016/j.nima.2010.07.049. URL: <http://www.sciencedirect.com/science/article/pii/S0168900210016591> (visited on 12/11/2020).
- [106] Aleksander Aleksenskii et al. “Clustering of Diamond Nanoparticles, Fluorination and Efficiency of Slow Neutron Reflectors”. en. In: *Nanomaterials* 11.8 (Aug. 2021). Number: 8 Publisher: Multidisciplinary Digital Publishing Institute, p. 1945. DOI: 10.3390/nano11081945. URL: <https://www.mdpi.com/2079-4991/11/8/1945> (visited on 08/02/2021).
- [107] V.V. Nesvizhevsky et al. “The reflection of very cold neutrons from diamond powder nanoparticles”. en. In: *Nuclear Instruments and Methods in Physics Research Section A: Accelerators, Spectrometers, Detectors and Associated Equipment* 595.3 (Oct. 2008), pp. 631–636. ISSN: 01689002. DOI: 10.1016/j.nima.2008.07.149. URL: <https://linkinghub.elsevier.com/retrieve/pii/S0168900208011261> (visited on 04/12/2023).
- [108] Valery Nesvizhevsky et al. “Fluorinated nanodiamonds as unique neutron reflector”. en. In: *Carbon* 130 (Apr. 2018), pp. 799–805. ISSN: 0008-6223. DOI: 10.1016/j.carbon.2018.01.086. URL: <http://www.sciencedirect.com/science/article/pii/S0008622318300952> (visited on 12/02/2020).
- [109] E. Dendy Sloan and Carolyn A. Koh. *Clathrate Hydrates of Natural Gases*. eng. 3. Berkeley, California: CRC Press, Taylor & Francis, 2008. ISBN: 978-0-8493-9078.
- [110] Oliver Zimmer. “Neutron conversion and cascaded cooling in paramagnetic systems for a high-flux source of very cold neutrons”. In: *Phys. Rev. C* 93 (3 Mar. 2016), p. 035503. DOI: 10.1103/PhysRevC.93.035503. URL: <https://link.aps.org/doi/10.1103/PhysRevC.93.035503>.
- [111] Valentin Czamler et al. “Clathrate hydrates as novel moderator material for sources of very cold neutrons”. In: *Proceedings of the 8th European Conference on Neutron Scattering* (2023).
- [112] M Celli et al. “Phonon density of states in different clathrate hydrates measured by inelastic neutron scattering”. In: *Journal of Physics: Conference Series* 340.1 (Feb. 2012), p. 012051. DOI: 10.1088/1742-6596/340/1/012051. URL: <https://dx.doi.org/10.1088/1742-6596/340/1/012051>.
- [113] H Conrad et al. “Inelastic scattering and spectral measurements of advanced cold moderator media”. en. In: *Physica B: Condensed Matter*. Proceedings of the Third European Conference on Neutron Scattering 350.1, Supplement (July 2004), E647–E650. ISSN: 0921-4526. DOI: 10.1016/j.physb.2004.03.173. URL: <https://www.sciencedirect.com/science/article/pii/S0921452604003898> (visited on 08/25/2021).
- [114] Masato Kida et al. “Mechanical properties of polycrystalline tetrahydrofuran hydrates as analogs for massive natural gas hydrates”. In: *Journal of Natural Gas Science and Engineering* 96 (2021), p. 104284. ISSN: 1875-5100. DOI: <https://doi.org/10.1016/j.jngse.2021.104284>. URL: <https://www.sciencedirect.com/science/article/pii/S1875510021004820>.
- [115] S. R. Gough and D. W. Davidson. “Composition of Tetrahydrofuran Hydrate and the Effect of Pressure on the Decomposition”. en. In: *Canadian Journal of Chemistry* 49.16 (Aug. 1971), pp. 2691–2699. ISSN: 0008-4042, 1480-3291. DOI: 10.1139/v71-447. URL: <http://www.nrcresearchpress.com/doi/10.1139/v71-447> (visited on 04/17/2023).
- [116] Oliver Zimmer et al. <https://doi.ill.fr/10.5291/ILL-DATA.1-10-42.2020>.
- [117] Juan Rodríguez-Carvajal. “Recent advances in magnetic structure determination by neutron powder diffraction”. In: *Physica B: Condensed Matter* 192.1 (1993), pp. 55–69. ISSN: 0921-4526. DOI: [https://doi.org/10.1016/0921-4526\(93\)90108-I](https://doi.org/10.1016/0921-4526(93)90108-I). URL: <https://www.sciencedirect.com/science/article/pii/092145269390108I>.

- [118] Juan Rodriguez-Carvajal. “Recent developments of the program FULLPROF, commission on powder diffraction”. In: *IUCr Newsl.* 26 (Jan. 2001).
- [119] R.A. Young. *The Rietveld method*. eng. International Union of Crystallography. Monographs on Crystallography 5. Oxford [u.a.]: Oxford Univ. Press, 1993. ISBN: 0198555776.
- [120] R. J. Hill and C. J. Howard. “Quantitative phase analysis from neutron powder diffraction data using the Rietveld method”. eng. In: *Journal of Applied Crystallography* 20.6 (1987), pp. 467–474. ISSN: 1600-5767.
- [121] Juan Rodriguez-Carvajal. *An Introduction into the Program Fullprof 2000 (Version July 2001)*. Jan. 2001.
- [122] Jacques Ollivier, Mohamed Zbiri, and Jerome Halbwachs. *Instrument Layout: Disk chopper time-of-flight spectrometer IN5*. <https://www.ill.eu/users/instruments/instruments-list/in5>. Grenoble, France.
- [123] Bjorn Fak, Michael Marek Koza, and Olivier Meulien. *Instrument Layout: Thermal neutron time-of-flight spectrometer PANTHER*. <https://www.ill.eu/users/instruments/instruments-list/panther>. Grenoble, France.
- [124] S. Xu et al. “Theoretical calculations of neutron scattering cross sections for tetrahydrofuran-containing clathrate hydrates at low temperature”. In: 2023.
- [125] Joachim Wuttke. “Improved sample holder for multidetector neutron spectrometers”. In: *Physica B: Condensed Matter* 266.1 (1999), pp. 112–114. ISSN: 0921-4526. DOI: [https://doi.org/10.1016/S0921-4526\(98\)01503-8](https://doi.org/10.1016/S0921-4526(98)01503-8). URL: <https://www.sciencedirect.com/science/article/pii/S0921452698015038>.
- [126] Mantid. *Manipulation and Analysis Toolkit for Instrument Data. Mantid Project*. <http://dx.doi.org/10.5286/SOFTWARE/MANTID>. 2013.
- [127] O. Arnold et al. “Mantid—Data analysis and visualization package for neutron scattering and  $\mu$  SR experiments”. In: *Nuclear Instruments and Methods in Physics Research A* 764 (2014), pp. 156–166. ISSN: 0168-9002. DOI: <https://doi.org/10.1016/j.nima.2014.07.029>. URL: <http://www.sciencedirect.com/science/article/pii/S0168900214008729>.
- [128] Mantid. *Mantid Documentation. Algorithm Contents*. <https://docs.mantidproject.org/nightly/algorithms/index.html>. 2023.
- [129] Oliver Zimmer et al. <https://doi.ill.fr/10.5291/ILL-DATA.1-10-49>. 2021.
- [130] B. Chazallon et al. “Anharmonicity and guest–host coupling in clathrate hydrates”. In: *Phys. Chem. Chem. Phys.* 4 (19 2002), pp. 4809–4816. DOI: 10.1039/B202464K. URL: <http://dx.doi.org/10.1039/B202464K>.
- [131] H. Schober et al. “Guest-host coupling and anharmonicity in clathrate hydrates”. In: *The European Physical Journal E* 12.1 (2003), pp. 41–49. DOI: 10.1140/epje/i2003-10026-6. URL: <https://doi.org/10.1140/epje/i2003-10026-6>.
- [132] Daniel Broseta, Livio Ruffine, and Arnaud Desmedt, eds. *Gas Hydrates I: Fundamentals, Characterization and Modeling*. en. 1. Hoboken, NJ, USA: John Wiley & Sons, Inc., June 2017. ISBN: 978-1-119-33268-8. DOI: 10.1002/9781119332688. (Visited on 01/20/2022).
- [133] Paul K. Romano et al. “OpenMC: A state-of-the-art Monte Carlo code for research and development”. In: *Annals of Nuclear Energy* 82 (2015). Joint International Conference on Supercomputing in Nuclear Applications and Monte Carlo 2013, pp. 90–97. ISSN: 0306-4549. DOI: <https://doi.org/10.1016/j.anucene.2014.07.048>. URL: <https://www.sciencedirect.com/science/article/pii/S030645491400379X>.
- [134] S. Xu et al. “Monte-Carlo simulations of inelastic neutron magnetic scattering of oxygen molecules hosted in deuterated clathrate hydrates and fullerite  $C_{60}$ ”. In: *to be submitted for the journal* (2023).
- [135] J Rolando Granada, J Ignacio Márquez Damián, and Christian Helman. “Studies on reflector materials for cold neutrons”. In: *EPJ Web of Conferences*. Vol. 231. EDP Sciences. 2020, p. 04002.
- [136] Y. B. Zeldovich. “Storage of cold neutrons”. In: *JETP* 9 1389 (1959).
- [137] V V Vladimirovskii. “Magnetic mirrors, channels and bottles for cold neutrons”. In: *Zhur. Eksppl'. i Teoret Fiz.* Vol: 39 (Oct. 1960). URL: <https://www.osti.gov/biblio/4094905>.
- [138] F L Shapiro. “ELECTRIC DIPOLE MOMENTS OF ELEMENTARY PARTICLES”. In: *Soviet Physics Uspekhi* 11.3 (Mar. 1968), p. 345. DOI: 10.1070/PU1968v01n03ABEH003840. URL: <http://dx.doi.org/10.1070/PU1968v01n03ABEH003840>.
- [139] V I Lushchikov et al. “Observation of ultracold neutrons.” In: *JETP Lett. (USSR) (Engl. Transl.)*, 9: 23-6(Jan. 5, 1969). (Jan. 1969). URL: <https://www.osti.gov/biblio/4744673>.
- [140] A. Steyerl. “Measurements of total cross sections for very slow neutrons with velocities from 100 m/sec to 5 m/sec”. In: *Physics Letters B* 29.1 (1969), pp. 33–35. ISSN: 0370-2693. DOI: [https://doi.org/10.1016/0370-2693\(69\)90127-0](https://doi.org/10.1016/0370-2693(69)90127-0). URL: <https://www.sciencedirect.com/science/article/pii/0370269369901270>.
- [141] PDG. *History Plots*. 2023. URL: <https://pdg.lbl.gov/2023/reviews/rpp2022-rev-history-plots.pdf>.

- [142] R. Golub and J. M. Pendlebury. “The electric dipole moment of the neutron”. In: *Contemporary Physics* 13.6 (1972), pp. 519–558. DOI: 10.1080/00107517208228016. eprint: <https://doi.org/10.1080/00107517208228016>. URL: <https://doi.org/10.1080/00107517208228016>.
- [143] V. Nesvizhevsky et al. “Quantum states of neutrons in the Earth’s gravitational field”. In: *Nature* 415 (2002), pp. 297–299. URL: <https://doi.org/10.1038/415297a>.
- [144] H. Abele et al. “Particle Physics at the European Spallation Source”. In: *Phys. Rept.* 1023 (2023), pp. 1–84. DOI: 10.1016/j.physrep.2023.06.001. arXiv: 2211.10396 [physics.ins-det].
- [145] A. Serebrov and V Lyamkin. “Development of UCN sources at PNPI”. In: *Journal of Neutron Research* 24 (2022), pp. 145–166.
- [146] A. Steyerl et al. “A new source of cold and ultracold neutrons”. In: *Physics Letters A* 116.7 (1986), pp. 347–352. ISSN: 0375-9601. DOI: [https://doi.org/10.1016/0375-9601\(86\)90587-6](https://doi.org/10.1016/0375-9601(86)90587-6). URL: <https://www.sciencedirect.com/science/article/pii/0375960186905876>.
- [147] O. Zimmer et al. “In-beam superfluid-helium ultracold neutron source for the ESS”. In: *Journal of Neutron Research* 24 (2022), pp. 95–110.
- [148] L. Zanini et al. “Very cold and ultra cold neutron sources for ESS”. In: *Journal of Neutron Research* 24 (2022), pp. 77–93.
- [149] R. Golub and J.M. Pendlebury. “Super-thermal sources of ultra-cold neutrons”. In: *Physics Letters A* 53.2 (1975), pp. 133–135. ISSN: 0375-9601. DOI: [https://doi.org/10.1016/0375-9601\(75\)90500-9](https://doi.org/10.1016/0375-9601(75)90500-9). URL: <https://www.sciencedirect.com/science/article/pii/0375960175905009>.
- [150] S. Degenkolb, P. Fierlinger, and O. Zimmer. “Approaches to high-density storage experiments with in-situ production and detection of ultracold neutrons”. en. In: *Journal of Neutron Research* 24.2 (Jan. 2023), pp. 123–143. ISSN: 14772655, 10238166. DOI: 10.3233/JNR-220044. URL: <https://www.medra.org/servlet/aliasResolver?alias=iospress&doi=10.3233/JNR-220044> (visited on 04/12/2023).
- [151] Oliver Zimmer. “Multi-Mirror Imaging Optics for Low-Loss Transport of Divergent Neutron Beams and Tailored Wavelength Spectra”. In: (2016). arXiv: 1611.07353.
- [152] E. Chanel et al. “Concept and strategy of SuperSUN: a new ultracold neutron converter”. In: *to be published in J. Neutron Research* () .
- [153] Skyler Degenkolb, Peter Fierlinger, and Oliver Zimmer. “In-situ production and detection of ultracold neutrons”. In: *Journal of Neutron Research* 24 (2022), p. 123.
- [154] Tomasz Bryś. “Extraction of ultracold neutrons from a solid deuterium source”. PhD thesis. ETH Zurich, 2007.
- [155] Stefan Döge. “Scattering of Ultracold Neutrons in Condensed Deuterium and on Material Surfaces”. PhD thesis. Technical University of Munich, 2018.
- [156] Oliver Zimmer. “Superfluid-helium ultracold neutron sources: concepts for the European Spallation Source?” In: *Physics Procedia* 51 (2014), pp. 85–88.
- [157] Robert Golub. “On the storage of neutrons in superfluid 4He”. In: *Physics Letters A* 72(4-5) (1979), pp. 387–390.
- [158] Robert Golub et al. “Operation of a superthermal ultra-cold neutron source and the storage of ultra-cold neutrons in superfluid Helium-4”. In: *Z. Phys. B* 51 (1983), pp. 187–193.
- [159] A Frei et al. “Understanding of ultra-cold-neutron production in solid deuterium”. In: *Europhysics Letters* 92.6 (2011), p. 62001.
- [160] F Atchison et al. “Cold neutron energy dependent production of ultracold neutrons in solid deuterium”. In: *Physical review letters* 99.26 (2007), p. 262502.
- [161] L. Zanini et al. *HighNESS Deliverable 4.4: Report Neutronic Design of an In-pile UCN Source*. HighNESS Deliverable 4.4. 2023.
- [162] P. Schmidt-Wellenburg, K.H. Andersen, and O. Zimmer. “Ultra cold neutron production by multiphonon processes in superfluid helium under pressure”. In: *Nuclear Instruments and Methods in Physics Research Section A: Accelerators, Spectrometers, Detectors and Associated Equipment* 611.2 (2009). Particle Physics with Slow Neutrons, pp. 259–262. ISSN: 0168-9002. DOI: <https://doi.org/10.1016/j.nima.2009.07.085>. URL: <https://www.sciencedirect.com/science/article/pii/S0168900209015393>.
- [163] J.R. Granada et al. In: *Nuclear Instruments and Methods in Physics Research Section A: Accelerators, Spectrometers, Detectors and Associated Equipment* 1053 (2023), p. 168284. ISSN: 0168-9002. DOI: <https://doi.org/10.1016/j.nima.2023.168284>. URL: <https://www.sciencedirect.com/science/article/pii/S0168900223002747>.
- [164] R. Granada et al. “Neutron scattering kernel for superfluid He-4”. In: *ICNS 2022 - International Conference on Neutron Scattering, Buenos Aires, Argentina* (2022).

- [165] K. F. Eckerman et al. “Availability of nuclear decay data in electronic form, including beta spectra not previously published”. In: *Health Physics* 67.4 (1994), pp. 338–345. ISSN: 0017-9078. DOI: 10.1097/00004032-199410000-00004.
- [166] M. Adib and M. Kilany. “On the use of bismuth as a neutron filter”. In: *Radiation Physics and Chemistry* 66.2 (2003), pp. 81–88. ISSN: 0969-806X. DOI: [https://doi.org/10.1016/S0969-806X\(02\)00368-7](https://doi.org/10.1016/S0969-806X(02)00368-7). URL: <https://www.sciencedirect.com/science/article/pii/S0969806X02003687>.
- [167] Tatsuhiko Sato et al. “Features of Particle and Heavy Ion Transport code System (PHITS) version 3.02”. In: *Journal of Nuclear Science and Technology* 55.6 (2018), pp. 684–690. DOI: 10.1080/00223131.2017.1419890.
- [168] Anatolii Serebrov and Vitaliy Lyamkin. “Development of UCN sources at PNPI”. en. In: *Journal of Neutron Research* 24.2 (Jan. 2023), pp. 145–166. ISSN: 14772655, 10238166. DOI: 10.3233/JNR-220007. URL: <https://www.medra.org/servlet/aliasResolver?alias=iospress&doi=10.3233/JNR-220007> (visited on 04/25/2023).
- [169] JosÚ Rolando Granada et al. “Development of neutron scattering kernels for cold neutron reflector materials”. In: *Journal of Neutron Research* 23.2-3 (2021), pp. 167–177.
- [170] Oliver Zimmer. “Imaging Nested-Mirror Assemblies – A New Generation of Neutron Delivery Systems?” In: *Journal of Neutron Research* 20.4 (Jan. 2019), pp. 91–98. ISSN: 14772655, 10238166. DOI: 10.3233/JNR-190101. (Visited on 09/14/2021).
- [171] E. Korobkina et al. “Production of UCN by Downscattering in Superfluid He4”. In: *Physics Letters A* 301.5-6 (Sept. 2002), pp. 462–469. ISSN: 03759601. DOI: 10.1016/S0375-9601(02)01052-6. arXiv: cond-mat/0204635. URL: <http://arxiv.org/abs/cond-mat/0204635> (visited on 02/03/2022).
- [172] P. Schmidt-Wellenburg et al. “Experimental Study of Ultracold Neutron Production in Pressurized Superfluid Helium”. In: *Physical Review C* 92.2 (Aug. 17, 2015), p. 024004. ISSN: 0556-2813, 1089-490X. DOI: 10.1103/PhysRevC.92.024004. URL: <https://link.aps.org/doi/10.1103/PhysRevC.92.024004> (visited on 03/02/2022).
- [173] O. Zimmer et al. *HighNESS Deliverable 4.3: Report Neutronic Design of an In-beam UCN Source*. HighNESS Deliverable 4.3. 2023.
- [174] Estelle Chanel et al. “Concept and strategy of SuperSUN: A new ultracold neutron converter”. en. In: *Journal of Neutron Research* 24.2 (Jan. 2022). Publisher: IOS Press, pp. 111–121. ISSN: 1023-8166. DOI: 10.3233/JNR-220013. URL: <https://content.iospress.com/articles/journal-of-neutron-research/jnr220013> (visited on 09/26/2023).
- [175] Ken Holst Andersen et al. “Optimization of moderators and beam extraction at the ESS”. In: *Journal of Applied Crystallography* 51.2 (Apr. 2018), pp. 264–281. DOI: 10.1107/S1600576718002406. URL: <https://doi.org/10.1107/S1600576718002406>.
- [176] L. Zanini et al. “The neutron moderators for the European Spallation Source”. In: *Journal of Physics: Conference Series* 1021.1 (May 2018), p. 012066. DOI: 10.1088/1742-6596/1021/1/012066. URL: <https://dx.doi.org/10.1088/1742-6596/1021/1/012066>.
- [177] Hans Wolter. “Spiegelsysteme streifenden Einfalls als abbildende Optiken für Röntgenstrahlen”. In: *Annalen der Physik* 445.1-2 (1952), pp. 94–114. DOI: <https://doi.org/10.1002/andp.19524450108>. eprint: <https://onlinelibrary.wiley.com/doi/pdf/10.1002/andp.19524450108>. URL: <https://onlinelibrary.wiley.com/doi/abs/10.1002/andp.19524450108>.
- [178] David F. R. Mildner. “Resolution of small-angle neutron scattering with a reflective focusing optic”. In: *Journal of Applied Crystallography* 47.4 (2014), pp. 1247–1251. DOI: <https://doi.org/10.1107/S1600576714011364>. eprint: <https://onlinelibrary.wiley.com/doi/pdf/10.1107/S1600576714011364>. URL: <https://onlinelibrary.wiley.com/doi/abs/10.1107/S1600576714011364>.
- [179] A. J. Jackson, K. Kanaki, and C. I. Lopez. *LoKI - A broad band high flux SANS instrument for the ESS*. Tech. rep. JAEA-Conf-2015-002. Japan, 2016, pp. 263–271. URL: [http://inis.iaea.org/search/search.aspx?orig\\_q=RN:48014673](http://inis.iaea.org/search/search.aspx?orig_q=RN:48014673).
- [180] D. G. Phillips II et al. “Neutron-Antineutron Oscillations: Theoretical Status and Experimental Prospects”. In: *Phys. Rept.* 612 (2016), pp. 1–45. DOI: 10.1016/j.physrep.2015.11.001. arXiv: 1410.1100 [hep-ex].
- [181] R. Barbier et al. “R-parity violating supersymmetry”. In: *Phys. Rept.* 420 (2005), pp. 1–202. DOI: 10.1016/j.physrep.2005.08.006. arXiv: hep-ph/0406039.
- [182] R. N. Mohapatra. “Neutron-antineutron Oscillation: Theory and Phenomenology”. In: *J. Phys. G* 36 (2009), p. 104006. DOI: 10.1088/0954-3899/36/10/104006. arXiv: 0902.0834 [hep-ph].
- [183] Lorenzo Calibbi et al. “Baryon number violation in supersymmetry: neutron-antineutron oscillations as a probe beyond the LHC”. In: *JHEP* 05 (2016). [Erratum: *JHEP* 10, 195 (2017)], p. 144. DOI: 10.1007/JHEP05(2016)144. arXiv: 1602.04821 [hep-ph].

- [184] K. S. Babu, R. N. Mohapatra, and S. Nasri. “Post-Sphaleron Baryogenesis”. In: *Phys. Rev. Lett.* 97 (2006), p. 131301. DOI: 10.1103/PhysRevLett.97.131301. arXiv: hep-ph/0606144.
- [185] K. S. Babu et al. “Post-Sphaleron Baryogenesis and an Upper Limit on the Neutron-Antineutron Oscillation Time”. In: *Phys. Rev. D* 87.11 (2013), p. 115019. DOI: 10.1103/PhysRevD.87.115019. arXiv: 1303.6918 [hep-ph].
- [186] Zurab Berezhiani. “More about neutron - mirror neutron oscillation”. In: *Eur. Phys. J. C* 64 (2009), pp. 421–431. DOI: 10.1140/epjc/s10052-009-1165-1. arXiv: 0804.2088 [hep-ph].
- [187] Zurab Berezhiani et al. “Neutron Disappearance and Regeneration from Mirror State”. In: *Phys. Rev. D* 96.3 (2017), p. 035039. DOI: 10.1103/PhysRevD.96.035039. arXiv: 1703.06735 [hep-ex].
- [188] Zurab Berezhiani. “A possible shortcut for neutron–antineutron oscillation through mirror world”. In: *Eur. Phys. J. C* 81.1 (2021), p. 33. DOI: 10.1140/epjc/s10052-020-08824-9. arXiv: 2002.05609 [hep-ph].
- [189] European Strategy Group Collaboration et al. *Update of the European Strategy for Particle Physics, CERN-ESU-015-2020*. 2020.
- [190] A. D. Sakharov. “Violation of CP Invariance, C asymmetry, and baryon asymmetry of the universe”. In: *Pisma Zh. Eksp. Teor. Fiz.* 5 (1967). [Usp. Fiz. Nauk 161, no. 5, 61 (1991)], pp. 32–35. DOI: 10.1070/PU1991v034n05ABEH002497.
- [191] Shmuel Nussinov and Robert Shrock. “N - anti-N oscillations in models with large extra dimensions”. In: *Phys. Rev. Lett.* 88 (2002), p. 171601. DOI: 10.1103/PhysRevLett.88.171601. arXiv: hep-ph/0112337.
- [192] G.R. Dvali and Gregory Gabadadze. “Nonconservation of global charges in the brane universe and baryogenesis”. In: *Phys. Lett. B* 460 (1999), pp. 47–57. DOI: 10.1016/S0370-2693(99)00766-2. arXiv: hep-ph/9904221.
- [193] Gerard ’t Hooft. “Symmetry Breaking Through Bell-Jackiw Anomalies”. In: *Phys. Rev. Lett.* 37 (1976). Ed. by Mikhail A. Shifman, pp. 8–11. DOI: 10.1103/PhysRevLett.37.8.
- [194] Peter Brockway Arnold and Larry D. McLerran. “Sphalerons, Small Fluctuations and Baryon Number Violation in Electroweak Theory”. In: *Phys. Rev. D* 36 (1987), p. 581. DOI: 10.1103/PhysRevD.36.581.
- [195] Frans R. Klinkhamer and N. S. Manton. “A Saddle Point Solution in the Weinberg-Salam Theory”. In: *Phys. Rev. D* 30 (1984), p. 2212. DOI: 10.1103/PhysRevD.30.2212.
- [196] N. S. Manton. “Topology in the Weinberg-Salam Theory”. In: *Phys. Rev. D* 28 (1983), p. 2019. DOI: 10.1103/PhysRevD.28.2019.
- [197] K. Abe et al. “The Search for  $n - \bar{n}$  oscillation in Super-Kamiokande I”. In: *Phys. Rev. D* 91 (2015), p. 072006. DOI: 10.1103/PhysRevD.91.072006. arXiv: 1109.4227 [hep-ex].
- [198] J. Gustafson et al. “Search for dinucleon decay into pions at Super-Kamiokande”. In: *Phys. Rev. D* 91.7 (2015), p. 072009. DOI: 10.1103/PhysRevD.91.072009. arXiv: 1504.01041 [hep-ex].
- [199] S. Sussman et al. “Dinucleon and Nucleon Decay to Two-Body Final States with no Hadrons in Super-Kamiokande”. In: (2018). arXiv: 1811.12430 [hep-ex].
- [200] Sudhakantha Girmohanta and Robert Shrock. “Improved Upper Limits on Baryon-Number Violating Dinucleon Decays to Dileptons”. In: *Phys. Lett. B* 803 (2020), p. 135296. DOI: 10.1016/j.physletb.2020.135296. arXiv: 1910.08356 [hep-ph].
- [201] K. Abe et al. “Neutron-Antineutron Oscillation Search using a 0.37 Megaton-Year Exposure of Super-Kamiokande”. In: *Phys. Rev. D* 103 (2021), p. 012008. DOI: 10.1103/PhysRevD.103.012008. arXiv: 2012.02607 [hep-ex].
- [202] S. L. Glashow. “The Future of Elementary Particle Physics”. In: *NATO Sci. Ser. B* 61 (1980), p. 687. DOI: 10.1007/978-1-4684-7197-7\\_\\_15.
- [203] Rabindra N. Mohapatra and R. E. Marshak. “Local B-L Symmetry of Electroweak Interactions, Majorana Neutrinos and Neutron Oscillations”. In: *Phys. Rev. Lett.* 44 (1980). [Erratum: *Phys. Rev. Lett.* 44, 1643 (1980)], pp. 1316–1319. DOI: 10.1103/PhysRevLett.44.1316.
- [204] Mei Bai et al. “Ultimate Limit of Future Colliders”. In: *JACoW NAPAC2022* (2022), pp. 321–324. DOI: 10.18429/JACoW-NAPAC2022-TUZD3. arXiv: 2209.04009 [physics.acc-ph].
- [205] Sumathi Rao and Robert Shrock. “ $n \leftrightarrow \bar{n}$  Transition Operators and Their Matrix Elements in the MIT Bag Model”. In: *Phys. Lett. B* 116 (1982), pp. 238–242. DOI: 10.1016/0370-2693(82)90333-1.
- [206] Sumathi Rao and Robert E. Shrock. “Six Fermion ( $B - L$ ) Violating Operators of Arbitrary Generational Structure”. In: *Nucl. Phys. B* 232 (1984), pp. 143–179. DOI: 10.1016/0550-3213(84)90365-1.
- [207] Enrico Rinaldi et al. “Neutron-antineutron oscillations from lattice QCD”. In: *Phys. Rev. Lett.* 122.16 (2019), p. 162001. DOI: 10.1103/PhysRevLett.122.162001. arXiv: 1809.00246 [hep-lat].
- [208] Enrico Rinaldi et al. “Lattice QCD determination of neutron-antineutron matrix elements with physical quark masses”. In: *Phys. Rev. D* 99.7 (2019), p. 074510. DOI: 10.1103/PhysRevD.99.074510. arXiv: 1901.07519 [hep-lat].

- [209] Michael I. Buchoff and Michael Wagman. “Perturbative Renormalization of Neutron-Antineutron Operators”. In: *Phys. Rev. D* 93.1 (2016). [Erratum: *Phys. Rev. D* 98, 079901 (2018)], p. 016005. DOI: 10.1103/PhysRevD.93.016005. arXiv: 1506.00647 [hep-ph].
- [210] Michael I. Buchoff and Michael Wagman. “Neutron-Antineutron Operator Renormalization”. In: *PoS LATTICE2014* (2015), p. 290. DOI: 10.22323/1.214.0290. arXiv: 1502.00044 [hep-lat].
- [211] John H. Schwarz. “Superstring Theory”. In: *Phys. Rept.* 89 (1982), pp. 223–322. DOI: 10.1016/0370-1573(82)90087-4.
- [212] Sudhakantha Girmohanta and Robert Shrock. “Baryon-Number-Violating Nucleon and Dinucleon Decays in a Model with Large Extra Dimensions”. In: *Phys. Rev. D* 101.1 (2020), p. 015017. DOI: 10.1103/PhysRevD.101.015017. arXiv: 1911.05102 [hep-ph].
- [213] Sudhakantha Girmohanta and Robert Shrock. “Nucleon decay and  $n-\bar{n}$  oscillations in a left-right symmetric model with large extra dimensions”. In: *Phys. Rev. D* 101.9 (2020), p. 095012. DOI: 10.1103/PhysRevD.101.095012. arXiv: 2003.14185 [hep-ph].
- [214] Zurab Berezhiani and Arkady Vainshtein. “Neutron-Antineutron Oscillation as a Signal of CP Violation”. In: (2015). arXiv: 1506.05096 [hep-ph].
- [215] P. S. Bhupal Dev and Rabindra N. Mohapatra. “TeV scale model for baryon and lepton number violation and resonant baryogenesis”. In: *Phys. Rev. D* 92.1 (2015), p. 016007. DOI: 10.1103/PhysRevD.92.016007. arXiv: 1504.07196 [hep-ph].
- [216] Rouzbeh Allahverdi, P. S. Bhupal Dev, and Bhaskar Dutta. “A simple testable model of baryon number violation: Baryogenesis, dark matter, neutron–antineutron oscillation and collider signals”. In: *Phys. Lett. B* 779 (2018), pp. 262–268. DOI: 10.1016/j.physletb.2018.02.019. arXiv: 1712.02713 [hep-ph].
- [217] K. S. Babu, P. S. Bhupal Dev, and R. N. Mohapatra. “Neutrino mass hierarchy, neutron - anti-neutron oscillation from baryogenesis”. In: *Phys. Rev. D* 79 (2009), p. 015017. DOI: 10.1103/PhysRevD.79.015017. arXiv: 0811.3411 [hep-ph].
- [218] Lorenzo Calibbi et al. “Baryon number violation in supersymmetry: Neutron-antineutron oscillations as a probe beyond the LHC”. In: *PoS LHCP2016* (2016). Ed. by Johan Bijnens, Andreas Hoecker, and Jim Olsen, p. 152. DOI: 10.22323/1.276.0152.
- [219] G. Senjanovic and Rabindra N. Mohapatra. “Exact Left-Right Symmetry and Spontaneous Violation of Parity”. In: *Phys. Rev. D* 12 (1975), p. 1502. DOI: 10.1103/PhysRevD.12.1502.
- [220] Goran Senjanovic. “Spontaneous Breakdown of Parity in a Class of Gauge Theories”. Other thesis. 1979. DOI: 10.1016/0550-3213(79)90604-7.
- [221] Rabindra N. Mohapatra and Goran Senjanovic. “Neutrino Masses and Mixings in Gauge Models with Spontaneous Parity Violation”. In: *Phys. Rev. D* 23 (1981), p. 165. DOI: 10.1103/PhysRevD.23.165.
- [222] T. Bitter and D. Dubbers. “Test of the quasifree condition in neutron oscillation experiments”. In: *Nuclear Instruments and Methods in Physics Research Section A: Accelerators, Spectrometers, Detectors and Associated Equipment* 239.3 (1985), pp. 461–466. ISSN: 0168-9002. DOI: [https://doi.org/10.1016/0168-9002\(85\)90024-5](https://doi.org/10.1016/0168-9002(85)90024-5). URL: <http://www.sciencedirect.com/science/article/pii/0168900285900245>.
- [223] U. Schmidt et al. “Long distance propagation of a polarized neutron beam in zero magnetic field”. In: *Nuclear Instruments and Methods in Physics Research Section A: Accelerators, Spectrometers, Detectors and Associated Equipment* 320.3 (1992), pp. 569–573. ISSN: 0168-9002. DOI: [https://doi.org/10.1016/0168-9002\(92\)90952-Z](https://doi.org/10.1016/0168-9002(92)90952-Z). URL: <http://www.sciencedirect.com/science/article/pii/016890029290952Z>.
- [224] E. David Davis and Albert R. Young. “Neutron-antineutron oscillations beyond the quasifree limit”. In: *Phys. Rev. D* 95.3 (2017), p. 036004. DOI: 10.1103/PhysRevD.95.036004. arXiv: 1611.04205 [nucl-ex].
- [225] E.S. Golubeva and L.A. Kondratyuk. “Annihilation of low energy antineutrons on nuclei”. In: *Nucl. Phys. B Proc. Suppl.* 56 (1997). Ed. by H. Koch, M. Kunze, and K. Peters, pp. 103–107. DOI: 10.1016/S0920-5632(97)00260-0.
- [226] Elena S. Golubeva, Joshua L. Barrow, and Charles G. Ladd. “Model of  $\bar{n}$  annihilation in experimental searches for  $\bar{n}$  transformations”. In: *Phys. Rev. D* 99.3 (2019), p. 035002. DOI: 10.1103/PhysRevD.99.035002. arXiv: 1804.10270 [hep-ex].
- [227] Joshua L. Barrow et al. “Progress and simulations for intranuclear neutron-antineutron transformations in  $^{40}_{18}Ar$ ”. In: *Phys. Rev. D* 101.3 (2020), p. 036008. DOI: 10.1103/PhysRevD.101.036008. arXiv: 1906.02833 [hep-ex].
- [228] G. Bressi et al. “Search for Free Neutron antineutron Oscillations”. In: *Z. Phys. C43* (1989), pp. 175–179. DOI: 10.1007/BF01588203.
- [229] G. Bressi et al. “Final results of a search for free neutron antineutron oscillations”. In: *Nuovo Cim. A103* (1990), pp. 731–750. DOI: 10.1007/BF02789025.

- [230] G. Fidecaro et al. “Experimental search for neutron antineutron transitions with free neutrons”. In: *Phys. Lett.* 156B (1985), pp. 122–128. DOI: 10.1016/0370-2693(85)91367-X.
- [231] M. I. Cherry et al. “Experimental test of baryon conservation: a new limit on neutron antineutron oscillations in oxygen”. In: *Phys. Rev. Lett.* 50 (1983), pp. 1354–1356. DOI: 10.1103/PhysRevLett.50.1354.
- [232] M. R. Krishnaswamy et al. “Results From the Kgf Proton Decay Experiment”. In: *Nuovo Cim.* C9 (1986). [Conf. Proc.C850418,97(1985)], pp. 167–181. DOI: 10.1007/BF02514839.
- [233] G. Battistoni et al. “Nucleon Stability, Magnetic Monopoles and Atmospheric Neutrinos in the Mont Blanc Experiment”. In: *Phys. Lett.* 133B (1983), pp. 454–460. DOI: 10.1016/0370-2693(83)90827-4.
- [234] T. W. Jones et al. “A Search for  $N\bar{N}$  Oscillation in Oxygen”. In: *Phys. Rev. Lett.* 52 (1984), p. 720. DOI: 10.1103/PhysRevLett.52.720.
- [235] M. Takita et al. “A Search for Neutron - antineutron Oscillation in a  $^{16}\text{O}$  Nucleus”. In: *Phys. Rev.* D34 (1986), p. 902. DOI: 10.1103/PhysRevD.34.902.
- [236] Christoph Berger et al. “Search for Neutron - antineutron Oscillations in the Frejus Detector”. In: *Phys. Lett.* B240 (1990), pp. 237–242. DOI: 10.1016/0370-2693(90)90441-8.
- [237] J. Chung et al. “Search for neutron antineutron oscillations using multiprong events in Soudan 2”. In: *Phys. Rev.* D66 (2002), p. 032004. DOI: 10.1103/PhysRevD.66.032004. arXiv: hep-ex/0205093 [hep-ex].
- [238] B. Aharmim et al. “Search for neutron-antineutron oscillations at the Sudbury Neutrino Observatory”. In: *Phys. Rev.* D96.9 (2017), p. 092005. DOI: 10.1103/PhysRevD.96.092005. arXiv: 1705.00696 [hep-ex].
- [239] C. B. Dover, A. Gal, and J. M. Richard. “Neutron antineutron oscillations in nuclei”. In: *Phys. Rev.* D27 (1983), pp. 1090–1100. DOI: 10.1103/PhysRevD.27.1090.
- [240] W.M. Alberico, A. Bottino, and A. Molinari. “A New Evaluation Of The Neutron-Antineutron Oscillation Time”. In: *Phys. Lett. B* 114 (1982), pp. 266–270. DOI: 10.1016/0370-2693(82)90493-2.
- [241] W.M. Alberico et al. “Neutron-Antineutron Mixing Inside Nuclei”. In: *Nucl. Phys. A* 429 (1984), pp. 445–461. DOI: 10.1016/0375-9474(84)90691-2.
- [242] C. B. Dover, A. Gal, and J. M. Richard. “Neutron antineutron Oscillations in Nuclei”. In: *Nucl. Instrum. Meth.* A284 (1989), p. 13. DOI: 10.1016/0168-9002(89)90239-8.
- [243] W. M. Alberico, A. De Pace, and M. Pignone. “Neutron - antineutron oscillations in nuclei”. In: *Nucl. Phys.* A523 (1991), pp. 488–498. DOI: 10.1016/0375-9474(91)90032-2.
- [244] Jorg Hufner and Boris Z. Kopeliovich. “Neutron - antineutron oscillations in nuclei revisited”. In: *Mod. Phys. Lett. A* 13 (1998). Ed. by Anthony W. Thomas and K. Tsushima, pp. 2385–2392. DOI: 10.1142/S0217732398002540. arXiv: hep-ph/9807210.
- [245] E. Friedman and A. Gal. “Realistic calculations of nuclear disappearance lifetimes induced by n anti-n oscillations”. In: *Phys. Rev. D* 78 (2008), p. 016002. DOI: 10.1103/PhysRevD.78.016002. arXiv: 0803.3696 [hep-ph].
- [246] Douglas Bryman. “Two nucleon (B - L)-conserving reactions involving tau leptons ”. In: *Phys. Lett.* B733 (2014), pp. 190–192. DOI: 10.1016/j.physletb.2014.04.042. arXiv: 1404.7776 [hep-ex].
- [247] V. Takhistov et al. “Search for Nucleon and Dinucleon Decays with an Invisible Particle and a Charged Lepton in the Final State at the Super-Kamiokande Experiment”. In: *Phys. Rev. Lett.* 115.12 (2015), p. 121803. DOI: 10.1103/PhysRevLett.115.121803. arXiv: 1508.05530 [hep-ex].
- [248] Babak Abi et al. “Deep Underground Neutrino Experiment (DUNE), Far Detector Technical Design Report, Volume II DUNE Physics”. In: (Feb. 2020). arXiv: 2002.03005 [hep-ex].
- [249] Zurab Berezhiani. “Neutron–antineutron oscillation and baryonic majoron: low scale spontaneous baryon violation”. In: *Eur. Phys. J. C* 76.12 (2016), p. 705. DOI: 10.1140/epjc/s10052-016-4564-0. arXiv: 1507.05478 [hep-ph].
- [250] Joshua Barrow et al. “Computing and Detector Simulation Framework for the HIBeam/NNbar Experimental Program at the ESS”. In: *EPJ Web Conf.* 251 (2021), p. 02062. DOI: 10.1051/epjconf/202125102062. arXiv: 2106.15898 [physics.ins-det].
- [251] Peter Willendrup, Emmanuel Farhi, and Kim Lefmann. “McStas 1.7 - a new version of the flexible Monte Carlo neutron scattering package”. In: *Physica B: Condensed Matter* 350.1, Supplement (2004). Proceedings of the Third European Conference on Neutron Scattering, E735–E737. ISSN: 0921-4526. DOI: <https://doi.org/10.1016/j.physb.2004.03.193>. URL: <https://www.sciencedirect.com/science/article/pii/S0921452604004144>.
- [252] COMSOL AB. *COMSOL Multiphysics® v. 6.1*. COMSOL AB, Stockholm, Sweden, 2022. URL: <https://www.comsol.se>.
- [253] COMSOL Multiphysics. “Introduction to COMSOL multiphysics®”. In: *COMSOL Multiphysics, Burlington, MA, accessed Feb 9 (1998)*, p. 2018.

- [254] T. Kittelmann et al. “Monte Carlo Particle Lists: MCPL”. In: *Computer Physics Communications* 218 (2017), pp. 17–42. ISSN: 0010-4655. DOI: <https://doi.org/10.1016/j.cpc.2017.04.012>. URL: <https://www.sciencedirect.com/science/article/pii/S0010465517301261>.
- [255] S. Agostinelli et al. “GEANT4—a simulation toolkit”. In: *Nucl. Instrum. Meth. A* 506 (2003), pp. 250–303. DOI: 10.1016/S0168-9002(03)01368-8.
- [256] Joshua L. Barrow. “Towards Neutron Transformation Searches”. PhD thesis. U. Tennessee, Knoxville, 2021.
- [257] C. Hagmann, D. Lange, and D. Wright. “Cosmic-ray shower generator (CRY) for Monte Carlo transport codes”. In: *2007 IEEE Nuclear Science Symposium Conference Record*. Vol. 2. 2007, pp. 1143–1146. DOI: 10.1109/NSSMIC.2007.4437209. URL: <https://www.sciencedirect.com/science/article/abs/pii/S0920563297002600?via%5C3Dihub>.
- [258] S. Ansell. “CombLayer - A fast parametric MCNP(X) model constructor”. In: *JAEA-Conf-2015-002* (2016). DOI: <https://doi.org/10.11484/jaea-conf-2015-002>.
- [259] D. Di Julio et al. “Simulating neutron transport in long beamlines at a spallation neutron source using Geant4”. In: *Journal of Neutron Research* 22.2-3 (2020), pp. 183–189.
- [260] Matthias Holl et al. *Beamline Simulation for the NNBAR Experiment at the European Spallation Source*. 2022. arXiv: 2209.08997 [physics.data-an].
- [261] A. H. Sullivan. “A Guide to Radiation and Radioactivity Levels Near High Energy Particle Accelerators”. In: *Nuclear Technology Publishing* ().
- [262] M. Baldo-Ceolin et al. “A new experimental limit on neutron-anti neutron transitions”. In: *Phys. Lett. B* 236 (1990), pp. 95–101. DOI: 10.1016/0370-2693(90)90601-2.
- [263] Y Kamyshkov et al. “Use of Cold Source and Large Reflector Mirror Guide for Neutron-Antineutron Oscillation Search”. In: (1995), pp. 843–849. URL: <https://http://www.neutronresearch.com/parch/1995/01/199501008430.pdf>.
- [264] “Swiss Neutronics Co., Supermirrors for Neutrons”. In: (2021). URL: <https://www.swissneutronics.ch/products/neutron-supermirrors/>.
- [265] H.M. Shimizu. *Optimization of Supermirror*. 2014. URL: <https://indico.esss.lu.se/event/171/contributions/1335/attachments/1140/1796/20140612-shimizu.pdf>.
- [266] Damian Martin Rodriguez, Shane J. Kennedy, and Phillip M. Bentley. “Properties of Elliptical Guides for Neutron Beam Transport and Applications for New Instrumentation Concepts”. In: *Journal of Applied Crystallography* 44.4 (Aug. 1, 2011), pp. 727–737. ISSN: 0021-8898. DOI: 10.1107/S0021889811018590. URL: <https://scripts.iucr.org/cgi-bin/paper?S0021889811018590> (visited on 11/07/2022).
- [267] P Willendrup et al. *Component Manual for the Neutron Ray-Tracing Package McStas*. <http://www.mcstas.org/documentation/manual/mcstas-2.7-components.pdf>. 2020.
- [268] Matthew Frost. “Observation of Baryon Number Violation via Cold Neutron Sources”. PhD thesis. University of Tennessee, Knoxville, 2019. URL: [https://trace.tennessee.edu/utk\\_graddiss/5951](https://trace.tennessee.edu/utk_graddiss/5951) (visited on 03/22/2022).
- [269] Y. Kamyshkov, M. Snow, and G. Greene. “Time-variable neutron optics (unpublished)”. In: (2014).
- [270] F. Backman et al. “The Development of the NNBAR Experiment”. In: *Journal of Instrumentation* 17.10 (Oct. 1, 2022), P10046. ISSN: 1748-0221. DOI: 10.1088/1748-0221/17/10/P10046. URL: <https://iopscience.iop.org/article/10.1088/1748-0221/17/10/P10046> (visited on 11/02/2022).
- [271] E Wodey et al. “A scalable high-performance magnetic shield for very long baseline atom interferometry”. In: *Review of Scientific Instruments* 91.3 (2020), p. 035117.
- [272] I Altarev et al. “Minimizing magnetic fields for precision experiments”. In: *Journal of Applied Physics* 117.23 (2015), p. 233903.
- [273] *European Spallation Source Instruments*. Accessed on September 26, 2023. URL: <https://europceanspallationsource.se/instruments>.
- [274] Z Sun et al. “Dynamic modeling of the behavior of permalloy for magnetic shielding”. In: *Journal of Applied Physics* 119.19 (2016), p. 193902.
- [275] Zhiyin Sun et al. “Limits of low magnetic field environments in magnetic shields”. In: *IEEE Transactions on Industrial Electronics* 68.6 (2020), pp. 5385–5395.
- [276] G. Costa and P. Kabir. “Environmental effects on possible  $n - \bar{n}$  transitions”. In: *Phys. Rev. D* 28 (3 Aug. 1983), pp. 667–668. DOI: 10.1103/PhysRevD.28.667. URL: <https://link.aps.org/doi/10.1103/PhysRevD.28.667>.

- [277] B.O. Kerbikov. “Lindblad and Bloch equations for conversion of a neutron into an antineutron”. In: *Nuclear Physics A* 975 (2018), pp. 59–72. ISSN: 0375-9474. DOI: <https://doi.org/10.1016/j.nuclphysa.2018.04.006>. URL: <https://www.sciencedirect.com/science/article/pii/S0375947418300782>.
- [278] V. Gudkov et al. “A new approach to search for free neutron-antineutron oscillations using coherent neutron propagation in gas”. In: *Physics Letters B* 808 (2020), p. 135636. ISSN: 0370-2693. DOI: <https://doi.org/10.1016/j.physletb.2020.135636>. URL: <https://www.sciencedirect.com/science/article/pii/S0370269320304391>.
- [279] Lewis E. Agnew et al. “Antiproton Interactions in Hydrogen and Carbon below 200 Mev”. In: *Phys. Rev.* 118 (5 June 1960), pp. 1371–1391. DOI: [10.1103/PhysRev.118.1371](https://doi.org/10.1103/PhysRev.118.1371). URL: <https://link.aps.org/doi/10.1103/PhysRev.118.1371>.
- [280] J. Riedlberger et al. “Anti-proton Annihilation at Rest in Nitrogen and Deuterium Gas”. In: *Phys. Rev. C* 40 (1989), pp. 2717–2731. DOI: [10.1103/PhysRevC.40.2717](https://doi.org/10.1103/PhysRevC.40.2717).
- [281] P. A. Zyla et al. “Review of Particle Physics”. In: *PTEP* 2020.8 (2020), p. 083C01. DOI: [10.1093/ptep/ptaa104](https://doi.org/10.1093/ptep/ptaa104).
- [282] Betty Bezverkhny Abelev et al. “Performance of the ALICE Experiment at the CERN LHC”. In: *Int. J. Mod. Phys. A* 29 (2014), p. 1430044. DOI: [10.1142/S0217751X14300440](https://doi.org/10.1142/S0217751X14300440). arXiv: [1402.4476](https://arxiv.org/abs/1402.4476) [nucl-ex].
- [283] David Rohr et al. “GPU-based Online Track Reconstruction for the ALICE TPC in Run 3 with Continuous Read-Out”. In: *EPJ Web Conf.* 214 (2019). Ed. by A. Forti et al., p. 01050. DOI: [10.1051/epjconf/201921401050](https://doi.org/10.1051/epjconf/201921401050). arXiv: [1905.05515](https://arxiv.org/abs/1905.05515) [physics.ins-det].
- [284] J. Adolfsson et al. “The upgrade of the ALICE TPC with GEMs and continuous readout”. In: *JINST* 16.03 (2021), P03022. DOI: [10.1088/1748-0221/16/03/P03022](https://doi.org/10.1088/1748-0221/16/03/P03022). arXiv: [2012.09518](https://arxiv.org/abs/2012.09518) [physics.ins-det].
- [285] W. Baldini et al. “Measurement of parameters of scintillating bars with wavelength-shifting fibres and silicon photomultiplier readout for the SHiP Muon Detector”. In: *JINST* 12.03 (2017), P03005. DOI: [10.1088/1748-0221/12/03/P03005](https://doi.org/10.1088/1748-0221/12/03/P03005). arXiv: [1612.01125](https://arxiv.org/abs/1612.01125) [physics.ins-det].
- [286] L Aphecetche et al. “PHENIX calorimeter”. In: *Nucl. Instrum. Meth. A* 499 (2003), pp. 521–536. DOI: [10.1016/S0168-9002\(02\)01954-X](https://doi.org/10.1016/S0168-9002(02)01954-X).
- [287] K. Dunne, B. Meirose, D. Milstead, A. Oskarsson, V. Santoro, S. Silverstein, and S.-C. Yiu. “The HIBeam/NNbar Calorimeter Prototype”. In: (2021). arXiv: [107.02147](https://arxiv.org/abs/107.02147) [hep-ex].
- [288] Sze-Chun Yiu et al. “Status of the Design of an Annihilation Detector to Observe Neutron-Antineutron Conversions at the European Spallation Source”. In: *Symmetry* 14.1 (2022), p. 76. DOI: [10.3390/sym14010076](https://doi.org/10.3390/sym14010076).
- [289] Graham Roger Stevenson and RH Thomas. “A simple procedure for the estimation of neutron skyshine from proton accelerators”. In: *Health physics* 46.1 (1984), pp. 115–122.
- [290] Phil Bentley. “Simulated Fast Neutron Instrument Backgrounds at a MW Spallation Source”. In: (Sept. 2022). arXiv: [2209.02452](https://arxiv.org/abs/2209.02452) [physics.ins-det].
- [291] L Breiman. “Random Forests”. In: *Machine Learning* 45 (Oct. 2001), pp. 5–32. DOI: [10.1023/A:1010950718922](https://doi.org/10.1023/A:1010950718922).
- [292] Jerome H Friedman. “Greedy function approximation: a gradient boosting machine”. In: *Annals of statistics* (2001), pp. 1189–1232.
- [293] Alan Julian Izenman. “Linear Discriminant Analysis”. In: *Modern Multivariate Statistical Techniques: Regression, Classification, and Manifold Learning*. New York, NY: Springer New York, 2008, pp. 237–280. ISBN: 978-0-387-78189-1. DOI: [10.1007/978-0-387-78189-1\\_8](https://doi.org/10.1007/978-0-387-78189-1_8). URL: [https://doi.org/10.1007/978-0-387-78189-1\\_8](https://doi.org/10.1007/978-0-387-78189-1_8).
- [294] David M. W. Powers. “Evaluation: from precision, recall and F-measure to ROC, informedness, markedness and correlation”. In: *CoRR* abs/2010.16061 (2020). arXiv: [2010.16061](https://arxiv.org/abs/2010.16061). URL: <https://arxiv.org/abs/2010.16061>.
- [295] TMVA group D. Jason Koskinen H. Voss (MPIK). *Lecture 10: Multivariate Method - Boosted Decision Tree*. 2021.
- [296] Bartosz Mindur. “ATLAS Transition Radiation Tracker (TRT): Straw tubes for tracking and particle identification at the Large Hadron Collider”. In: *Nucl. Instrum. Meth. A* 845 (2017). Ed. by G. Badurek et al., pp. 257–261. DOI: [10.1016/j.nima.2016.04.026](https://doi.org/10.1016/j.nima.2016.04.026).
- [297] Roel Aaij et al. “The LHCb upgrade I”. In: (May 2023). arXiv: [2305.10515](https://arxiv.org/abs/2305.10515) [hep-ex].
- [298] A. Augusto Alves Jr. et al. “The LHCb Detector at the LHC”. In: *JINST* 3 (2008), S08005. DOI: [10.1088/1748-0221/3/08/S08005](https://doi.org/10.1088/1748-0221/3/08/S08005).
- [299] P. M Bentley. “Instrument suite cost optimisation in a science megaproject”. In: *Journal of Physics Communications* 4 (2020), p. 045014. DOI: [10.1088/2399-6528/ab8a06](https://doi.org/10.1088/2399-6528/ab8a06).

- [300] D.A. Brown et al. “ENDF/B-VIII.0: The 8th Major Release of the Nuclear Reaction Data Library with CIELO-project Cross Sections, New Standards and Thermal Scattering Data”. In: *Nuclear Data Sheets* 148 (2018). Special Issue on Nuclear Reaction Data, pp. 1–142. ISSN: 0090-3752. DOI: <https://doi.org/10.1016/j.nds.2018.02.001>. URL: <http://www.sciencedirect.com/science/article/pii/S0090375218300206>.
- [301] A.J.M Plompen et al. “The joint evaluated fission and fusion nuclear data library, JEFF-3.3”. In: *Eur. Phys. J. A* 181 (2020), p. 56.
- [302] Osamu Iwamoto et al. “Japanese evaluated nuclear data library version 5: JENDL-5”. In: *Journal of Nuclear Science and Technology* 60 (2023), pp. 1–60.
- [303] International Evaluation Collaboration. *Thermal Scattering Law S(a,b): Measurement, Evaluation and Application*. [https://www.oecd-nea.org/jcmts/pl\\_23901/international-evaluation-co-operation-volume-42](https://www.oecd-nea.org/jcmts/pl_23901/international-evaluation-co-operation-volume-42). 2020.
- [304] M Herman, A Trkov, et al. “ENDF-6 formats manual”. In: *Brookhaven National Laboratory* (2009).
- [305] M. Zerkle. *TSL mixed elastic scattering format*. <https://indico.bnl.gov/event/7233/contributions/43822/>. 2020.
- [306] Robert Macfarlane et al. *The NJOY nuclear data processing system, version 2016*. Tech. rep. Los Alamos National Lab.(LANL), Los Alamos, NM (United States), 2017.
- [307] X.-X. Cai and T. Kittelmann. “NCrystal: A library for thermal neutron transport”. In: *Computer Physics Communications* 246 (2020), p. 106851. ISSN: 0010-4655. DOI: <https://doi.org/10.1016/j.cpc.2019.07.015>. URL: <http://www.sciencedirect.com/science/article/pii/S0010465519302280>.
- [308] X.-X. Cai et al. “Rejection-based sampling of inelastic neutron scattering”. In: *Journal of Computational Physics* 380 (2019), pp. 400–407. ISSN: 0021-9991. DOI: <https://doi.org/10.1016/j.jcp.2018.11.043>. URL: <https://www.sciencedirect.com/science/article/pii/S0021999118307885>.
- [309] T. Kittelmann and X.-X. Cai. “Elastic neutron scattering models for NCrystal”. In: *Computer Physics Communications* 267 (2021), p. 108082. ISSN: 0010-4655. DOI: <https://doi.org/10.1016/j.cpc.2021.108082>. URL: <https://www.sciencedirect.com/science/article/pii/S0010465521001946>.
- [310] Stefano Baroni et al. “Phonons and related crystal properties from density-functional perturbation theory”. In: *Reviews of Modern Physics* 73.2 (July 2001), pp. 515–562. ISSN: 00346861. DOI: <10.1103/RevModPhys.73.515>. arXiv: 0012092v1 [arXiv:cond-mat]. URL: <http://link.aps.org/doi/10.1103/RevModPhys.73.515>.
- [311] J.P. Perdew, K. Burke, and M. Ernzerhof. “Generalized Gradient Approximation Made Simple”. In: *Phys. Rev. Lett* 77 (1996), p. 3865.
- [312] David Vanderbilt. “Soft self-consistent pseudopotentials in a generalized eigenvalue formalism”. In: *Phys. Rev. B* 41 (11 Apr. 1990), pp. 7892–7895. DOI: <10.1103/PhysRevB.41.7892>. URL: <https://link.aps.org/doi/10.1103/PhysRevB.41.7892>.
- [313] Andrea Dal Corso. “Pseudopotentials periodic table: From H to Pu”. In: *Computational Materials Science* 95 (2014), pp. 337–350. ISSN: 0927-0256. DOI: <https://doi.org/10.1016/j.commatsci.2014.07.043>. URL: <http://www.sciencedirect.com/science/article/pii/S0927025614005187>.
- [314] Paolo Giannozzi et al. “QUANTUM ESPRESSO: a modular and open-source software project for quantum simulations of materials”. In: *J. Phys.: Condens. Matter* 21.39 (2009), p. 395502. URL: <http://stacks.iop.org/0953-8984/21/i=39/a=395502>.
- [315] Kemal Ramic et al. *NJOY+NCrystal: an open-source tool for creating thermal neutron scattering libraries*. 2021. arXiv: 2108.11737 [physics.ins-det].
- [316] Ohba N. et al. “First-principles study on thermal vibration effects of MgH<sub>2</sub>”. In: *Phys. Rev. B* 70 (2004), p. 035102.
- [317] H.G. Schimmel et al. “The vibrational spectrum of magnesium hydride from inelastic neutron scattering and density functional theory”. In: *Mat. Sci. and Eng. B* 108 (2004), p. 38.
- [318] M Teshigawara et al. “Measurement of neutron scattering cross section of nano-diamond with particle diameter of approximately 5 nm in energy range of 0.2 meV to 100 meV”. In: *Nuclear Instruments and Methods in Physics Research Section A: Accelerators, Spectrometers, Detectors and Associated Equipment* 929 (2019), pp. 113–120.
- [319] V. N. Mochalin et al. “The properties and applications of nanodiamonds”. In: *Nature Nanotechnology* 7 (2011), p. 11. DOI: <10.1038/NNANO.2011.209>.
- [320] Z. Qiao et al. “Graphitization and microstructure transformation of nanodiamond to onion-like carbon”. In: *Scripta Materialia* 54 (2006), p. 225. DOI: <10.1016/j.scriptamat.2005.09.037>.
- [321] O. O. Vasiliev et al. “Special Features of the Heat Capacity of Detonation Nanocrystalline Diamond”. In: *Journal of Superhard Materials* 37 (6 2015), p. 388. DOI: <10.3103/S1063457615060039>.

- [322] Andrey A. Shiryaev et al. “Inelastic neutron scattering: a novel approach towards determination of equilibrium isotopic fractionation factors. Size effects on heat capacity and beta-factor of diamond”. In: *Phys. Chem. Chem. Phys.* 22 (23 2020), pp. 13261–13270. DOI: 10.1039/D0CP02032J. URL: <http://dx.doi.org/10.1039/D0CP02032J>.
- [323] S. J. Stuart, A. B. Tutein, and J. A. Harrison. “A reactive potential for hydrocarbons with intermolecular interactions”. In: *J. Chem. Phys.* 112 (14 2000), p. 6472.
- [324] H. Matsubara et al. “Evaluation of thermal conductivity and its structural dependence of a single T nanodiamond using molecular dynamics simulation”. In: *Diamond and Related Materials* 102 (2020), p. 107669. DOI: 10.1016/j.diamond.2019.107669.
- [325] P Rowe et al. “An accurate and transferable machine learning potential for carbon”. In: *J. Chem. Phys.* 153 (2020), p. 034702. DOI: 10.1063/5.0005084.
- [326] R. Tran et al. “Surface Energies of Elemental Crystals”. In: *Scientific Data* 3 (2013), p. 160080.
- [327] DiJulio, Douglas D. et al. In: *EPJ Web of Conf.* 284 (2023), p. 17013.
- [328] M. Mermoux, Y. Chabre, and A. Rousseau. “FTIR and  $^{13}\text{C}$  NMR study of graphite oxide”. In: *Carbon* 29 (1991), p. 469.
- [329] A. Lerf et al. “Structure of Graphite Oxide Revisited”. In: *J. Phys. Chem. B* 102 (1998), p. 4477.
- [330] T. Szabó et al. “Evolution of Surface Functional Groups in a Series of Progressively Oxidized Graphite Oxides”. In: *Chem. Mater.* 18 (2006), p. 2740.
- [331] D. W. Boukhvalov and M. I. Katsnelson. “Modeling of Graphite Oxide”. In: *J. Am. Chem. Soc.* 130 (2008), p. 10697.
- [332] S Grimme. “Semiempirical GGA-type density functional constructed with a long-range dispersion correction”. In: *J. Comp. Chem.* 27 (2006), p. 1787.
- [333] Annika Lenz and Lars Ojamäe. “Structures of the I-, II- and H-Methane Clathrates and the Ice-Methane Clathrate Phase Transition from Quantum-Chemical Modeling with Force-Field Thermal Corrections”. In: *The Journal of Physical Chemistry A* 115.23 (2011), p. 6169. ISSN: 1089-5639. DOI: 10.1021/jp111328v. URL: <https://doi.org/10.1021/jp111328v> (visited on 03/01/2022).
- [334] B. Hess et al. In: *J. Chem. Theory Comput.* 4 (2008), p. 435.
- [335] H. J. C. Berendsen, J. R. Grigera, and T. P. Straatsma. In: *J. Chem. Phys.* 91 (1987), p. 6269.
- [336] J. Wang et al. In: *J. Comp. Chem.* 25 (2004), p. 1157.
- [337] Joost VandeVondele et al. “Quickstep: Fast and accurate density functional calculations using a mixed Gaussian and plane waves approach”. In: *Comput. Phys. Commun.* 167 (2005), p. 103. ISSN: 0010-4655. DOI: <https://doi.org/10.1016/j.cpc.2004.12.014>. URL: <https://www.sciencedirect.com/science/article/pii/S0010465505000615>.
- [338] S. Goedecker and M. Teter. “Separable dual-space Gaussian pseudopotentials”. In: *Phys. Rev. B* 54 (1996), p. 1703. DOI: 10.1103/PhysRevB.54.1703.
- [339] S. Grimme et al. “A consistent and accurate ab initio parametrization of density functional dispersion correction (DFT-D) for the 94 elements H-Pu”. In: *J. Chem. Phys.* 132 (2010). ISSN: 00219606. DOI: 10.1063/1.3382344.
- [340] Atsushi Togo and Isao Tanaka. “First principles phonon calculations in materials science”. In: *Scripta Materialia* 108 (2015), pp. 1–5. ISSN: 1359-6462. DOI: <https://doi.org/10.1016/j.scriptamat.2015.07.021>. URL: <https://www.sciencedirect.com/science/article/pii/S1359646215003127>.
- [341] I. Souza, J. Iniguez, and D. Vanderbilt. In: *Phys. Rev. Lett.* 89 (2002), p. 117602.
- [342] M Celli et al. “Phonon density of states in different clathrate hydrates measured by inelastic neutron scattering”. In: *Journal of Physics: Conference Series* 340.1 (Feb. 2012), p. 012051. DOI: 10.1088/1742-6596/340/1/012051. URL: <https://dx.doi.org/10.1088/1742-6596/340/1/012051>.
- [343] C. J. Burnham and N. J. English. In: *J. Chem. Phys.* 144 (2015), p. 051101.
- [344] B. Chazallon et al. “Anharmonicity and guest–host coupling in clathrate hydrates”. In: *Phys. Chem. Chem. Phys.* 4 (19 2002), pp. 4809–4816. DOI: 10.1039/B202464K. URL: <http://dx.doi.org/10.1039/B202464K>.
- [345] Kemal Ramić et al. “NJOY+NCrystal: An open-source tool for creating thermal neutron scattering libraries with mixed elastic support”. In: *Nuclear Instruments and Methods in Physics Research Section A: Accelerators, Spectrometers, Detectors and Associated Equipment* 1027 (2022), p. 166227. ISSN: 0168-9002. DOI: <https://doi.org/10.1016/j.nima.2021.166227>.
- [346] A. Togo. *Phonon database at Kyoto University*. <http://phonondb.mtl.kyoto-u.ac.jp/>. [Online]. 2015.
- [347] Anubhav Jain et al. “Commentary: The Materials Project: A materials genome approach to accelerating materials innovation”. In: *APL Materials* 1.1 (2013), p. 011002. DOI: 10.1063/1.4812323. eprint: <https://doi.org/10.1063/1.4812323>. URL: <https://doi.org/10.1063/1.4812323>.

- [348] Shyue Ping Ong et al. “Python Materials Genomics (pymatgen): A robust, open-source python library for materials analysis”. In: *Computational Materials Science* 68 (2013), pp. 314–319. ISSN: 0927-0256. DOI: <https://doi.org/10.1016/j.commatsci.2012.10.028>. URL: <https://www.sciencedirect.com/science/article/pii/S0927025612006295>.
- [349] Shyue Ping Ong et al. “The Materials Application Programming Interface (API): A simple, flexible and efficient API for materials data based on REpresentational State Transfer (REST) principles”. In: *Computational Materials Science* 97 (2015), pp. 209–215. ISSN: 0927-0256. DOI: <https://doi.org/10.1016/j.commatsci.2014.10.037>. URL: <https://www.sciencedirect.com/science/article/pii/S0927025614007113>.
- [350] Y. Q. Cheng et al. “Simulation of Inelastic Neutron Scattering Spectra Using OCLIMAX”. In: *Journal of Chemical Theory and Computation* 15.3 (2019), pp. 1974–1982.
- [351] Javier Dawidowski et al. “Appendix - Neutron Scattering Lengths and Cross Sections”. In: *Neutron Scattering – Fundamentals*. Ed. by Felix Fernandez-Alonso and David L. Price. Vol. 44. Experimental Methods in the Physical Sciences. Academic Press, 2013, pp. 471–528. DOI: <https://doi.org/10.1016/B978-0-12-398374-9.09989-7>.
- [352] NCrystal development team. *NCrystal Plugins*. <https://github.com/mctools/ncrystal/wiki/Plugins>.
- [353] NCrystal development team. *Plugins Development*. <https://github.com/mctools/ncrystal/wiki/PluginsDevelopment>.
- [354] NCrystal development team. *Forks*. <https://github.com/mctools/ncplugin-template/network/members>.
- [355] Nicola Rizzi et al. “Benchmarking of the NCrystal SANS Plugin for Nanodiamonds”. In: *Nuclear Science and Engineering* (2023), pp. 1–9. DOI: [10.1080/00295639.2023.2196926](https://doi.org/10.1080/00295639.2023.2196926).
- [356] Jose Ignacio Marquez Damian, Douglas D DiJulio, and Günter Muhrer. “Nuclear data development at the European Spallation Source”. In: *Journal of Neutron Research Preprint* (2021), pp. 1–10.
- [357] Mikhail V. Avdeev et al. “The spatial diamond–graphite transition in detonation nanodiamond as revealed by small-angle neutron scattering”. en. In: *Journal of Physics: Condensed Matter* 25.44 (Sept. 2013). Publisher: IOP Publishing, p. 445001. ISSN: 0953-8984. DOI: [10.1088/0953-8984/25/44/445001](https://doi.org/10.1088/0953-8984/25/44/445001). URL: <https://doi.org/10.1088/0953-8984/25/44/445001> (visited on 07/22/2021).
- [358] Yu.A. Freiman and H.J. Jodl. “Solid oxygen”. In: *Physics Reports* 401.1 (2004), pp. 1–228. ISSN: 0370-1573. DOI: <https://doi.org/10.1016/j.physrep.2004.06.002>. URL: <https://www.sciencedirect.com/science/article/pii/S037015730400273X>.
- [359] C-Y. Liu and A. R. Young. “Ultra-cold Neutron Production in Anti-ferromagnetic Oxygen Solid”. In: *arXiv: Nuclear Theory* (2004).
- [360] B. Renker et al. “Intercalation of molecular gases into C<sub>60</sub>”. In: *Phys. Rev. B* 64 (20 Nov. 2001), p. 205417. DOI: [10.1103/PhysRevB.64.205417](https://doi.org/10.1103/PhysRevB.64.205417). URL: <https://link.aps.org/doi/10.1103/PhysRevB.64.205417>.
- [361] W. H. Kleiner. “Magnetic Scattering of Slow Neutrons from O<sub>2</sub> Gas”. In: *Phys. Rev.* 97 (2 Jan. 1955), pp. 411–418. DOI: [10.1103/PhysRev.97.411](https://doi.org/10.1103/PhysRev.97.411). URL: <https://link.aps.org/doi/10.1103/PhysRev.97.411>.
- [362] S. Xu et al. “Atomic scale Monte-Carlo simulations of neutron diffraction experiments on stoichiometric uranium dioxide up to 1664 K”. In: *Nuclear Instruments and Methods in Physics Research Section A: Accelerators, Spectrometers, Detectors and Associated Equipment* 1002 (2021), p. 165251. ISSN: 0168-9002. DOI: <https://doi.org/10.1016/j.nima.2021.165251>. URL: <https://www.sciencedirect.com/science/article/pii/S0168900221002357>.
- [363] *SHARP+ Cold neutron time-focussing time-of-flight spectrometer*. Accessed: 2023-03-10. URL: <https://www.ill.eu/users/instruments/instruments-list/sharp/characteristics>.
- [364] S.I. Wright. “Orientation Texture”. In: *Encyclopedia of Condensed Matter Physics*. Ed. by Franco Bassani, Gerald L. Liedl, and Peter Wyder. Oxford: Elsevier, 2005, pp. 221–233. ISBN: 978-0-12-369401-0. DOI: <https://doi.org/10.1016/B0-12-369401-9/00696-3>. URL: <https://www.sciencedirect.com/science/article/pii/B0123694019006963>.
- [365] Victor Laliena, Miguel Ángel Vicente-Álvarez, and Javier Campo. “Monte Carlo simulation of neutron scattering by a textured polycrystal”. In: *Journal of Applied Crystallography* 53.2 (Apr. 2020), pp. 512–529. DOI: [10.1107/S1600576720002290](https://doi.org/10.1107/S1600576720002290). URL: <https://doi.org/10.1107/S1600576720002290>.
- [366] J.R. Santisteban et al. “Texture imaging of zirconium based components by total neutron cross-section experiments”. In: *Journal of Nuclear Materials* 425.1 (2012). Microstructure Properties of Irradiated Materials, pp. 218–227. ISSN: 0022-3115. DOI: <https://doi.org/10.1016/j.jnucmat.2011.06.043>. URL: <https://www.sciencedirect.com/science/article/pii/S0022311511006386>.

- [367] Florencia Malamud et al. “Texture analysis with a time-of-flight neutron strain scanner”. In: *Journal of Applied Crystallography* 47.4 (Aug. 2014), pp. 1337–1354. DOI: 10.1107/S1600576714012710. URL: <https://doi.org/10.1107/S1600576714012710>.
- [368] L.L. Dessieux et al. “Neutron transmission simulation of texture in polycrystalline materials”. In: *Nuclear Instruments and Methods in Physics Research Section B: Beam Interactions with Materials and Atoms* 459 (2019), pp. 166–178. ISSN: 0168-583X. DOI: <https://doi.org/10.1016/j.nimb.2019.09.010>. URL: <https://www.sciencedirect.com/science/article/pii/S0168583X19306032>.
- [369] Hirotaka Sato, Takashi Kamiyama, and Yoshiaki Kiyanagi. “A Rietveld-Type Analysis Code for Pulsed Neutron Bragg-Edge Transmission Imaging and Quantitative Evaluation of Texture and Microstructure of a Welded  $\alpha$ -Iron Plate”. In: *MATERIALS TRANSACTIONS* 52.6 (2011), pp. 1294–1302. DOI: 10.2320/matertrans.M2010328.
- [370] Mirko Boin. “nxs: a program library for neutron cross section calculations”. In: *Journal of Applied Crystallography* 45.3 (June 2012), pp. 603–607. DOI: 10.1107/S0021889812016056. URL: <https://doi.org/10.1107/S0021889812016056>.
- [371] M. Morgano et al. “Neutron imaging options at the BOA beamline at Paul Scherrer Institut”. In: *Nuclear Instruments and Methods in Physics Research Section A: Accelerators, Spectrometers, Detectors and Associated Equipment* 754 (2014), pp. 46–56. ISSN: 0168-9002. URL: <https://www.sciencedirect.com/science/article/pii/S016890021400360X>.
- [372] NCystal development team. *CHANGELOG*. <https://github.com/mctools/ncystal/blob/master/CHANGELOG>.
- [373] NCystal development team. *Announcement Release2.7.0*. <https://github.com/mctools/ncystal/wiki/Announcement-Release2.7.0>.
- [374] A. Szakál. “Out-of-pile moderator test facility at the Budapest Neutron Centre”. In: Presented at the International Conference on Neutron Scattering (ICNS 2022), Buenos Aires, Argentina, 2022.
- [375] Paul Zakalek et al. “A flexible target station for Hi-CANS”. In: International Symposium UCANS9, online by RIKEN, Japan (online event), 28 Mar 2022 - 31 Mar 2022. Mar. 28, 2022. URL: <https://juser.fz-juelich.de/record/906983>.
- [376] J. Füzi. “Direct measurement of cold neutron moderator spectra”. In: *Nuclear Instruments and Methods in Physics Research Section A: Accelerators, Spectrometers, Detectors and Associated Equipment* 586 (2008), pp. 41–45. DOI: 10.1016/j.nima.2007.11.055.
- [377] Mostafa Jamalipour et al. “Improved beam extraction at compact neutron sources using diamonds nanoparticles and supermirrors”. In: *EPJ Web Conf.* 1033 (2022), p. 166719. DOI: <https://doi.org/10.1016/j.nima.2022.166719>. URL: <https://www.sciencedirect.com/science/article/pii/S0168900222002510>.
- [378] J. Rolando Granada, J. Ignacio Márquez Damián, and Christian Helman. “Studies on Reflector Materials for Cold Neutrons”. en. In: *EPJ Web of Conferences* 231 (2020). Publisher: EDP Sciences, p. 04002. ISSN: 2100-014X. DOI: 10.1051/epjconf/202023104002. URL: [https://www.epj-conferences.org/articles/epjconf/abs/2020/07/epjconf\\_ucans82020\\_04002/epjconf\\_ucans82020\\_04002.html](https://www.epj-conferences.org/articles/epjconf/abs/2020/07/epjconf_ucans82020_04002/epjconf_ucans82020_04002.html) (visited on 09/11/2023).
- [379] V. Santoro et al. “Development of a High Intensity Neutron Source at the European Spallation Source: The HighNESS project”. In: *14th International Topical Meeting on Nuclear Applications of Accelerators*. Apr. 2022. arXiv: 2204.04051 [physics.ins-det].
- [380] Paul Zakalek et al. “High-brilliance neutron source project”. In: *Journal of Physics: Conference Series*. Vol. 1401. 1. IOP Publishing. 2020, p. 012010.
- [381] *Commercial Nanodiamonds by Ray Techniques Ltd*. <https://nanodiamond.co.il/>. [Online; accessed 17-September-2023].
- [382] *Commercial Magnesium Hydride by American Elements*. <https://www.americanelements.com/magnesium-hydride-7693-27-8>. [Online; accessed 17-September-2023].